Université Fédérale
Toulouse Midi-Pyrénées

THÈSE

En vue de l'obtention du

DOCTORAT DE L'UNIVERSITÉ DE TOULOUSE

Délivré par :

Université Toulouse 3 Paul Sabatier (UT3 Paul Sabatier)

Cotutelle internationale avec:
Université de Carthage/ Institut National Agronomique de Tunisie (INAT)

Présentée et soutenue par :
Sameh Saadi
le vendredi 16 février 2018

Titre :

Estimation spatialisée de l'évapotranspiration réelle et des volumes d'irrigation à l'aide de modèles de bilans hydrique et énergétique forcés par des données de la télédétection optique (VIS/PIR/IRT)

École doctorale et discipline ou spécialité :
ED SDU2E : Surfaces et interfaces continentales, Hydrologie

Unité de recherche :
Centre d'Études Spatiales de la BIOsphère (CESBIO UMR 5126) / GREEN-TEAM-INAT

Directeur/trice(s) de Thèse :

Gilles Boulet, Directeur de recherche IRD, CESBIO
Zohra Lili Chabaane, Professeur, Université de Carthage, INAT

Jury :

Albert Olioso, Directeur de Recherche,INRA Centre de recherche PACA	Rapporteur
Mladen Todorovic, Professeur,Institut Agronomique Méditerranéen de Bari	Rapporteur
Hamadi Habaieb, Professeur, Université de Carthage, INAT	Examinateur
Hedia Chakroun, Maître de conférences, Université Tunis El Manar, ENIT	Examinateur
Jean-Philippe Gastellu-Etchegorry, Professeur, Université UPS	Examinateur
Said Khabba, Professeur, Université Cadi Ayyad	Examinateur
Vincent Simonneaux, Ingenieur de recherche IRD, CESBIO	Co-encadrant de thèse

وما استعصى على قوم منال
إذا الإقدام كان لهم ركابا
وما نيل المطالب بالتمنـي
ولكن تؤخذ الدنيا غلابا
أحمد شوقي

Soyez réalistes, demandez l'impossible !

Slogan de Mai 68

Dédicaces

À la mémoire de la grande dame, ma grand-mère *MIMA HADHRIA*, qui en quittant le navire il y'a de cela quatre années, a œuvré bien malgré elle à mon passage vers le monde des grands.

À la mémoire de ma chère grand-mère *HABIBA*.

À mon cher Papa *MUSTAPHA*. Tu as été le premier à m'encourager à aller si loin dans mes études. Tu m'as inculqué le goût du travail, de la rigueur et de l'ambition. J'ai voulu mener à terme cette thèse pour que tu sois toujours fier de moi. Merci Papa pour ton soutien, ta confiance, tes sacrifices; merci pour tout. Je te dédie ce travail modeste qui est pour toi et grâce à toi.

À la plus belle créature sur terre, à cette source de tendresse, de patience et de générosité, à Mama NAJOUA. Tu m'as toujours poussé et motivé dans mes études. Sans toi, je n'aurais certainement pas fait d'études longues. Cette thèse représente l'aboutissement du soutien et des encouragements que tu m'as prodigués. Que tu te sois remerciée par cette trop modeste dédicace.

À mon âme sœur, mon mari *AKRAM*. Sans ton soutien moral et matériel, tes conseils, tes encouragements et tes énormes sacrifices, ce travail n'aurait jamais vu le jour. Que dieu réunisse nos chemins pour un long commun serein.

C'est à toi mon adorable ange, ma joie, mon petit trésor que maman dédie ce travail pour te dire que tu resteras pour toujours le rayon du soleil qui égaye sa vie. Je t'aime *YOUSSEF* et je te souhaite tout le bonheur du monde.

À mon ange gardien et mon fidèle compagnon dans les moments les plus délicats de cette vie, mon cher frère *ANIS*. Je te dédie ce travail avec tous mes vœux de bonheur, de santé et de réussite, ainsi qu'à ta douce femme *RACHIDA*.

À mes beaux-parents *ABDELHAFIDH* et EMNA, merci pour votre tendresse, affection et énorme aide, ainsi qu'à mes beaux-frères et belle-sœur. Vous m'avez accueilli à bras ouverts dans votre famille. Je vous dédie ce travail en témoignage de l'attachement, de l'amour et de l'affection que je porte pour vous.

À *TOUTA*. Merci pour ton amour sincère et ta présence continue.

À mes chers oncles *SADOK* et *SOFIENE*. Que Dieu vous donne santé et longue vie.

Sameh

Dedication

To the memory of *MIMA HADHRIA* and of my grandmother *HABIBA*.

To my dear father *MUSTAPHA*, who made me what I am today, who gave me all the love, support and encouragement for what I would remain grateful.

To my dear mother *NAJOUA*, who has never ceased to surround me with her affection and her most delicate attentions all along my life and to whom I have an unwavering devotion.

To my soul mate, my understanding and patient husband *AKRAM* who has been a great source of motivation and inspiration.

To my little angel, my baby *YOUSSEF*. May God bless you.

To my dear brother *ANIS* who shared all my moments with a lot of joy and encouragement, and to his sweet wife *RACHIDA*.

To my parents-in-law *ABD EL HAFIDH* and *EMNA*, brothers-in-law and sister-in-law.

To my uncles *TOUTA*, *SADOK* and *SOFIENE*.

Sameh

Remerciement

J'ai toujours imaginé que la rédaction de cette page me serait particulièrement savoureuse. La cerise sur le gâteau en quelque sorte. Au cours de ces 4 années, j'ai longuement eu le loisir d'imaginer cet instant. C'était un bon leitmotiv qui m'a porté dans les bons comme dans les moments les plus durs. Je remercie ALLAH de m'avoir donné la grâce et la force pour continuer jusqu'à la fin et ne jamais baisser les bras. Pourtant à cet instant, je dois avouer que le doux sentiment de saveur escompté est légèrement entaché d'une pointe de nostalgie. Certains souvenirs affluent en moi au moment même où je franchis la ligne. Il n'est pas si aisé de ponctuer 4 années riches en rencontres et en apprentissage ; et ceci malgré un nouveau quotidien nettement plus enviable que ces derniers mois de labeur. C'est donc dans un état d'esprit mitigé que je rédige ces quelques lignes afin de remercier toutes les personnes qui ont contribué implicitement ou explicitement à l'ensemble de ce travail.

À mon directeur de thèse, Mr Gilles Boulet et mon Co-encadrant, Mr Vincent Simonneaux pour la confiance et la liberté qu'ils m'ont accordés pour mener à bien ce doctorat. Malgré la distance, ils ont su être disponibles et à l'écoute à chaque moment décisif. Leurs soutiens m'ont permis d'aller jusqu'au bout de cette belle aventure sans difficulté et dans un climat amical et détendu. J'ai beaucoup apprécié la multitude de leurs idées et critiques constructives. J'aurais difficilement pu imaginer mieux comme encadrement.

À ma directrice de thèse, Mme Zohra Lili Chabaane, qui m'a fait confiance dès mon arrivée. Merci pour m'avoir aiguillée et donné ma chance en me confiant ce projet de thèse. Merci pour votre écoute et votre efficacité qui m'ont permis de garder le cap et de ne jamais me décourager ! Vos grandes qualités humaines et scientifiques m'auront permis de mener à bien cette thèse.

Aux Mr Mahmoud Elyes Hamza et Mr Faiçal Ben Jeddi, directeurs de l'Institut National Agronomique de Tunisie INAT, Mr Yann Kerr et Mr Laurent Polidoro, directeurs du Centre d'Etudes Spatiales de la BIOsphère CESBIO et Mr Olivier Pringault, directeur de l'institut de Recherche pour le Développement IRD.

Aux membres de mon comité de thèse, Mme Valérie Demarez, Mr Salah Er-raki et Mr Netij Ben Mechlia pour leurs commentaires et pistes de recherche.

À Mr Mladen Todorovic et Mr Albert Olioso d'avoir accepté être rapporteurs de cette thèse. Leurs commentaires et leurs questions tant sur la forme que sur le fond du manuscrit, ont contribué à l'améliorer de manière significative. Je tiens également à remercier Mr Hamadi Habaieb, Mme Hedia Chakroun, Mr Said Khabba et Mr Jean Philippe Gastellu-Etchegorry pour avoir accepté d'être membres du jury de cette thèse.

À Mme Zeineb Kessouk pour ses encouragements ainsi qu'à tout le personnel de l'IRD-CESBIO : Mr Bernard Mougenot, Mr Hassan Ayari, Mr Pascal Fanise, Mr Michèle Lepage, Mme Dominique Tarrise, Mme Valérie Le Dantec, Mme Anne-Marie Ouertani, Mme Rim Ouannes et Mr Messouaf Ahmed.

Une pensée particulière à tous les membres du LMI TREMA, professeurs et doctorants, qui m'ont chaleureusement accueillie lors de mon séjour à Marrakech.

À tous ceux qui m'ont entouré pendant ces 4 années, c'était que du bonheur. Et certains collègues sont devenus des amis : Azza, Nesrine, Safa, Amal, Wafa, Nissaf, Ons, Fajr, Nadhima, Nesrine, Raja, Hamza, Marouen et Houssem. Je n'oublierai jamais nos discours interminables autour de la table de déjeuner, ni les beaux moments de jogging, de shopping, de vélo, et les fous rires avec Azza à Toulouse, ni les ruptures du jeûne du fameux Ramadan 2017 avec Safa et Wafa au campus IAS.

Aux amis d'ici et d'ailleurs. Ils ont tous été les gardiens de mon équilibre psychologique durant ces quatre ans. Ils sont tellement nombreux à m'avoir soutenu... je n'ai pas besoin de les citer, ils se reconnaitront. Je vous aime !

Aux membres de ma famille. Une chose est sûre, je n'aurais rien pu faire sans vous ! Tout ce que vous avez fait signifie tellement pour moi. Je vous adore !

Je vous dédie cette thèse, elle est à vous, pour vous, grâce à vous !

Sameh

Janvier, 2018

Acknowledgment

First, I thank ALLAH for giving me grace to endure until the end.

My deep gratitude is expressed to my supervisors Mr. Gilles Boulet, Mr. Vincent Simonneaux and Mrs. Zohra Lili Chabaane for guidance of my PhD thesis, precious advice, relevant remarks and never-ending support. It was a great honor and pleasure to work with you. Thanks for all the time devoted to me.

I would like to express my deep thanks to Mr. Mahmoud Elyes Hamza and Mr. Faiçal Ben Jeddi, Directors of the National Agronomic Institute of Tunisia INAT, Mr. Yann Kerr and Mr. Laurent Polidoro, Directors of the Center for Space Studies of the BIOsphere CESBIO and Mr. Olivier Pringault, Director of the Research Institute for Development IRD.

My sincere regards to the members of my thesis committee, Mrs. Valérie Demarez, Mr. Salah Er-raki and Mr. Netij Ben Mechlia; for their valuable comments and advice.

I would like to express my deep thanks to Mr. Mladen Todorovic and Mr. Albert Olioso to have accepted to be reporters of this thesis. Their comments and questions on both the form and the content of the manuscript helped to significantly improve it. I would like also to thank Mr. Hamadi Habaieb, Mrs. Hedia Chakroun, Mr. Said Khabba and Mr. Jean Philippe Gastellu-Etchegorry for agreeing to be members of the jury of my thesis.

My deep regards to Mrs. Zeineb Kessouk for her encouragement and to all IRD-CESBIO staff: Mr. Bernard Mougenot, Mr. Hassan Ayari, Mr. Pascal Fanise, Mr. Michèle Lepage, Ms. Dominique Tarrise, Mrs. Valérie Le Dantec, Mrs. Anne-Marie Ouertani, Mrs. Rim Ouannes and Mr. Messouaf Ahmed.

A special thought to all members of LMI TREMA, professors and PhD students, who warmly welcomed me during my stay in Marrakech.

I would like to express my deep appreciation for all the happy moments shared with my precious friends at INAT. This joyful company has filled my life with cheerful days and was source of support and encourage. Thanks to all my colleagues and close friends Azza, Nesrine, Safa, Amal, Wafa, Nissaf, Ons, Fajr, Nadhima, Nesrine, Raja, Hamza, Marouen and Houssem.

Thanks my lovely family, for your constant support.

Sameh

January, 2018

Spatial estimation of actual evapotranspiration and irrigation volumes using water and energy balance models forced by optical remote sensing data (VIS / NIR / TIR)

Abstract

In arid and semi-arid regions, water availability is a major limitation to crop production. Efficient agricultural water management is therefore a major issue, mainly in irrigated areas. The design of tools that provide an estimate of water balance components, especially of Evapotranspiration (ET), at the regional scale may help sustainable management of limited water resources in the water scarce regions. Remotely sensed Earth observation has become a major research field for agricultural water resources management. It provides regularly distributed data over large geographic areas about actual vegetation temporal dynamics (through the Normalized Difference Vegetation Index NDVI) and water availability under water stress (through the land surface temperature T_{surf}) which are crucial factors controlling ET.

The main objective of this thesis is to develop and test efficient techniques and methods to estimate hydrological variables (ET and irrigation volumes) in order to assess, in space (at "metric" and "kilometric" resolution) and over relatively long time periods (four agricultural seasons), the crop water requirements in the Kairouan plain (central Tunisia), as well as the extracted irrigation volumes from the overexploited aquifer. The adopted approach combines field experimentation, modeling and the use of multi-sensor / multi-resolution remote sensing data. Two types of tools to estimate ET and irrigation volumes are used: (a) a daily water balance model, SAMIR (SAtellite Monitoring of Irrigation), simulating water fluxes at a daily time step, and (b) an energy balance model, SPARSE (Soil Plant Atmosphere and Remote Sensing Evapotranspiration), which characterizes the water status at the satellite overpass time. For this purpose, two main research focuses have been explored: (i) to develop methods to integrate *in situ* data and high-resolution (VIS-NIR) remote sensing data (SPOT5 imagery) in the SAMIR model (calibrated using flux measurements by Eddy Covariance) to draw up the distributed water balance of irrigated areas in the Kairouan plain during four agricultural seasons (2008-2009 and 2011-2014) and (ii) to test the performance of the SPARSE model in monitoring the water status of a heterogeneous landscape in the study area and determine whether the low-resolution remote sensing data in the VIS-NIR and TIR domains (Terra-MODIS and Aqua-MODIS) are useful for spatializing the key variables of the energy balance (sensible and latent heat fluxes) in a semi-arid context.

ET and irrigation volumes, estimated with the SAMIR model, are assessed using field measurements (flux measurements by Extra Large Scintillometer XLAS along a path length of 4 km), and field surveys (observed irrigation volumes), respectively. The validation of the SPARSE results was carried out by means of XLAS flux measurements. Special attention has been paid to the extrapolation of the modeled latent heat flux by SPARSE from instantaneous to daily estimates. The seasonal irrigation volumes estimated by the SAMIR model are acceptable, even though results at finer timescales (monthly and below) needed to be improved, in particular

by translating our knowledge of the agricultural practices into algorithmic constraints in the model. Hence, the SAMIR model parameters, especially non calibrated ones (market gardening and trees), are revisited in order to enhance the results of distributed ET and irrigation volumes. The SAMIR model was recalibrated by using simultaneously latent heat flux and soil moisture measurements of three cereals fields (irrigated and rainfed). This calibration aims to get a unique set of parameters for cereals taking into account irrigated and rainfed cereals in order to better parameterize the model in a context of various cropping practices, which is the case in the area below the XLAS transect. For the SPARSE model, the estimates of the sensible and latent heat fluxes are in close agreement with those obtained from the XLAS. These results indicate that the XLAS can be effectively used to validate large-scale sensible heat flux derived from remote sensing data (and residual latent heat flux), in particular for the results obtained at the satellite overpass time. However, the extrapolation from instantaneous to daily ET is less obvious. The daily latent heat fluxes derived from the XLAS agreed rather well with those modeled using SPARSE, which shows the potential of SPARSE in water consumption monitoring over heterogeneous landscape in semi-arid conditions, and especially to identify the most affected areas by water stress.

Key words: Evapotranspiration, irrigation management, remote sensing, hydrological modeling, water balance model, energy balance model.

Estimation spatialisée de l'évapotranspiration réelle et des volumes d'irrigation à l'aide de modèles de bilans hydrique et énergétique forcés par des données de la télédétection optique (VIS/PIR/IRT)

Résumé

Dans les régions arides et semi-arides, la disponibilité de l'eau est le principal facteur limitant de la production agricole. La gestion efficace de l'eau est ainsi un problème majeur, principalement dans les zones irriguées. La conception d'outils fournissant des estimations régionales des composantes du bilan hydrique, en particulier l'évapotranspiration (ET), composante principale du bilan hydrique, peut aider à la gestion durable de la ressource en eau dans ces régions. La télédétection par satellite a démontré un très fort potentiel pour le suivi à différentes échelles des ressources hydriques agricoles. Elle fournit des données réparties sur de grandes zones géographiques et à intervalles réguliers, permettant, ainsi, de suivre la dynamique de la végétation (à travers des indices de végétation tel que l'indice de végétation par différence normalisée NDVI) et la détection du stress hydrique (à travers la température de surface terrestre Tsurf) qui sont des facteurs cruciaux contrôlant l'ET.

L'objectif principal de ce travail de thèse est de développer des techniques et des méthodes efficaces pour estimer les variables hydrologiques (ET et les volumes d'irrigation) afin d'évaluer, dans l'espace (résolution "métrique" et "kilométrique"), les besoins en eau des cultures du couvert végétal de la plaine de Kairouan (Tunisie centrale) ainsi que les volumes d'irrigation extraits de son aquifère surexploité. L'approche adoptée combine l'expérimentation, la modélisation et l'utilisation de données de télédétection multi-capteurs / multi-résolutions. Les deux types d'outils utilisés pour estimer l'ET et les volumes d'irrigation sont le modèle de bilan hydrique journalier SAMIR (SAtellite Monitoring of Irrigation), simulant les flux d'eau à un pas de temps journalier et le modèle SPARSE (Soil Plant Atmosphere and Remote Sensing Evapotranspiration), qui caractérise l'état hydrique du sol et du couvert végétal au temps de passage du satellite. deux axes de recherche principaux ont été explorés à cette fin; (i) développer des méthodes pour intégrer des données *in situ* et des données de télédétection haute résolution (VIS-NIR) (imagerie SPOT5) dans le modèle SAMIR (calibrées à l'aide de mesures de flux par Eddy Corrélation) pour établir le bilan hydrique spatialisé des zones irriguées de la plaine de Kairouan pendant quatre saisons agricoles (2008-2009 et 2011-2014) et (ii) tester la performance du modèle SPARSE dans l'estimation de l'état hydrique d'un couvert agricole hétérogène dans la zone d'étude et déterminer l'utilité des données de télédétection basse résolution dans les domaines VIS-PIR et IRT (Terra-MODIS et Aqua-MODIS) dans la spatialisation des variables clés du bilan d'énergie dans un contexte semi-aride: les flux de chaleur sensible et latente.

Les variables estimées avec le modèle SAMIR; ET et volumes d'irrigation; sont validés à l'aide des mesures terrain (mesures de flux par un scintillomètre à extra-large ouverture XLAS, le long d'un « transect » de 4 km) et des enquêtes de terrain (volumes

d'irrigation observés), respectivement. Alors que la validation des résultats SPARSE a été réalisée au moyen des mesures de flux XLAS. Une attention particulière a été portée à l'extrapolation des résultats instantanés du flux de chaleur latente SPARSE, au pas de temps journalier pour des applications hydrologiques. Les volumes d'irrigation saisonniers estimés par le modèle SAMIR sont acceptables, même si les résultats à des échelles de temps plus fines (mensuelles) doivent être améliorés, notamment en traduisant notre connaissance des pratiques agricoles en contraintes algorithmiques dans le modèle. Ainsi, les paramètres du modèle SAMIR, en particulier les paramètres non calibrés, sont revisités afin d'améliorer les performances de simulation de l'ET et des volumes d'irrigation. Pour le modèle SPARSE, les estimations des flux de chaleur sensible et latente sont en étroit accord avec celles obtenues à partir du XLAS. Ces résultats indiquent que les mesures d'un scintillomètre XLAS peuvent être utilisées avec succès pour valider du flux de chaleur sensible dérivé des données de télédétection (et du flux de chaleur latente résiduelle), en particulier pour les résultats obtenus au temps de passage du satellite. Cependant, l'extrapolation de l'ET instantanée au pas de temps journalier est moins évidente. Les flux de chaleur latente journalier dérivés du XLAS conviennent plutôt bien avec ceux modélisés par SPARSE, ce qui montre le potentiel du modèle SPARSE dans la surveillance de la consommation de l'eau agricole dans un paysage à couvert végétal hétérogène en conditions semi-arides, et notamment pour la localisation des zones les plus touchées par le stress hydrique.

Mots clés : Evapotranspiration, gestion de l'irrigation, télédétection, Modélisation hydrologique, modèle de bilan hydrique, modèle de bilan d'énérgie.

تقدير كمية النتح والتبخر و كميات الري باستخدام نماذج توازن الماء والطاقة و بيانات الاستشعار عن بعد

الخلاصة

تهدف هذه الاطروحة أساساً إلى تطوير التقنيات الفضائية المرئية لتقدير كمية النتح والتبخر فضلا عن كميات الري المستخرجة من طبقة المياه الجوفية المستغلة استغلالا مفرطا و ذلك بالمناطق شبه القاحلة عامة وبسهل القيروان خاصة . إن المنهج المتبع في هذه الدراسة يجمع بين القياسات الميدانية والنمذجة واستخدام بيانات الاستشعار عن بعد.

وفي هذا الاطار تم إستعمال صور الأقمار الصناعية SPOT5 لحساب المؤشر الإحصائي NDVI وذلك لإستعماله في النموذج SAMIR بهدف تقدير كمية النتح والتبخر و كميات الري خلال أربعة مواسم فلاحية (2008-2009 و 2011-2014). و قد تم إثبات فعالية نتائج النموذج SAMIR بمقارنتها بكميات الري المسجلة فعلاً من خلال مسح ميداني شمل ثلاثة مناطق مروية في سهل القيروان.

و من ناحية أخرى تم إختبار مدى نجاعة النموذج SPARSE في تقدير الحالة المائية للغطاء الزراعي غير المتجانس بالإضافة إلى تحديد جدوى بيانات الاستشعار عن بعد منخفضة الاستبانة (MODIS) في حساب متغيرات توازن الطاقة، و التي افضت إلى تقدير كمية النتح والتبخر خلال موسمين فلاحيين 2012-2013 و-2013-2014. وبهدف إثبات فعالية نتائج النموذج SPARSE تمت مقارنتها مع قياسات التدفق XLAS على طول 4 كم من المنطقة التي شملتها الدراسة.

الكلمات الدليلية:النتح والتبخر ،التحكم في مياه الري،الاستشعار عن بعد مرئي، النمذجة الهيدرولوجية، نموذج توازن المياه، نموذج توازن الطاقة.

Table of Content

List of figures

List of tables

Preface

This doctoral thesis was carried out within the framework of a joint international PhD involving the University of Toulouse 3 Paul Sabatier (UPS), under the main supervision of Mr. Gilles Boulet and Mr. Vincent Simonneaux, and the University of Carthage (UCAR) / National Agronomic Institute of Tunisia (INAT), under the supervision of Mrs. Zohra Lili Chabaane.

The study had been accomplished within the frame of several projects dedicated to the monitoring of the water resources evolution in the Merguellil basin (Kairouan Plain, central Tunisia), and based on the coupling between remote sensing, land surface modeling and in-situ observations:

- Project ANR / AMETHYST (2013-2017) "Assessment of changes in MEdiTerranean Hydro resources in the South: river basin Trajectories": Joint development of water resources and uses in the Mediterranean, coordinated by Mr. Mehrez Zribi;

- The PHC Maghreb project 14 MAG 22 (2014-2016) coordinated on the Tunisian side by Mrs. Zohra Lili Chabaane (INAT) and on the French side by Mrs. Valérie Ledantec (UPS).

- CNES/TOSCA program for the EVA2IRT project coordinated by Mr. Gilles Boulet;

- MISTRALS/SICMED program for the ReSAMEd project coordinated by Mr. Gilles Boulet;

This thesis report is the result of four years of work (first registration in January 2014 at the INAT and in September 2014 at the UPS), carried out at the Institute of Research for Development (IRD) at INAT, at the Center for Space Studies of the BIOsphere (CESBIO) in Toulouse, at the Laboratory of InteGRatEd managemEnt of Natural resources: remoTE sensing, spatial Analysis and Modeling (GREEN-TEAM) in INAT and at the International Mixed Laboratory "Remote Sensing and Water Resources in the Semi-Arid Mediterranean (TREMA)" at the Cadi Ayyad University in Marrakech (UCAM).

During the course of the thesis three steering committees took place; the members of those comittees included Ms Valérie Demarez (Lecturer at UPS), Mr Salah Erraki (Professor at the UCAM / Semlalia Faculty of Sciences) and Mr Netij Ben Mechlia (Professor at INAT).

During the thesis, I benefited from the scholarship "Allocation de Recherche pour une Thèse au Sud" ARTS (24 months); mobility to CESBIO and TREMA was funded by the Carthage University's Alternance Scholarships, the ARTS Scholarship and the PHC Maghreb 14 MAG 22 program.

Introduction

Scientific context

About 71 percent of the Earth's surface is covered by water. Oceans hold about 96.5 percent of all Earth's water, the remainder freshwater is distributed between frozen and glaciated areas (1.74%), underground water tables (1.69%), and surface water, which includes rivers, lakes and soil moisture (about 0.07%) (USGS, 2016).

According to the United Nations Environmental Program (UNEP, 2000), the freshwater scarcity is viewed by scientists and politicians as the second most important environmental issue of the 21st century. "The world water cycle seems unlikely to be able to cope with demands in the coming decades" (UNEP, 2000). Water requirements are generally associated with access to drinking water for the population, whereas it is also crucial for agriculture and many industrial and agro-food sectors. Indeed, the water use has continuously intensified and diversified since the beginning of the 20th century (Sauer *et al.*, 2010; Shiklomanov, 2000; Siebert *et al.*, 2005; Wisser *et al.*, 2008).

Water is one of the most important inputs required in agricultural production. Over 90% of fresh biomass is essentially water that complements carbon dioxide as a major substrate in carbon fixation, photosynthesis, a process that is the essence of life on Earth. Agriculture water use through crop irrigation accounts for 70 % of all water use in the world and as much as 95 percent in many developing countries (Assessment Millennium Ecosystem, 2005). Irrigated agricultural lands occupy less than 20% of all cropped area but produce 40–45% of the world's food. It is generally expected that irrigated agriculture will have to be considerably extended in the future in order to feed growing population, which has more than doubled between 1960 and 2008, from about 2.9 billion to more than 6.7 billion. Consequently, total agricultural output has increased by almost 170 % globally between 1961 and 2008 with an average increase of 2.2% per year (Wik *et al.*, 2008). However, the gap between available water supply and water demand is increasing in many parts of the world (Figure 1), limiting future expansion of irrigation (Assessment Millennium Ecosystem, 2005).

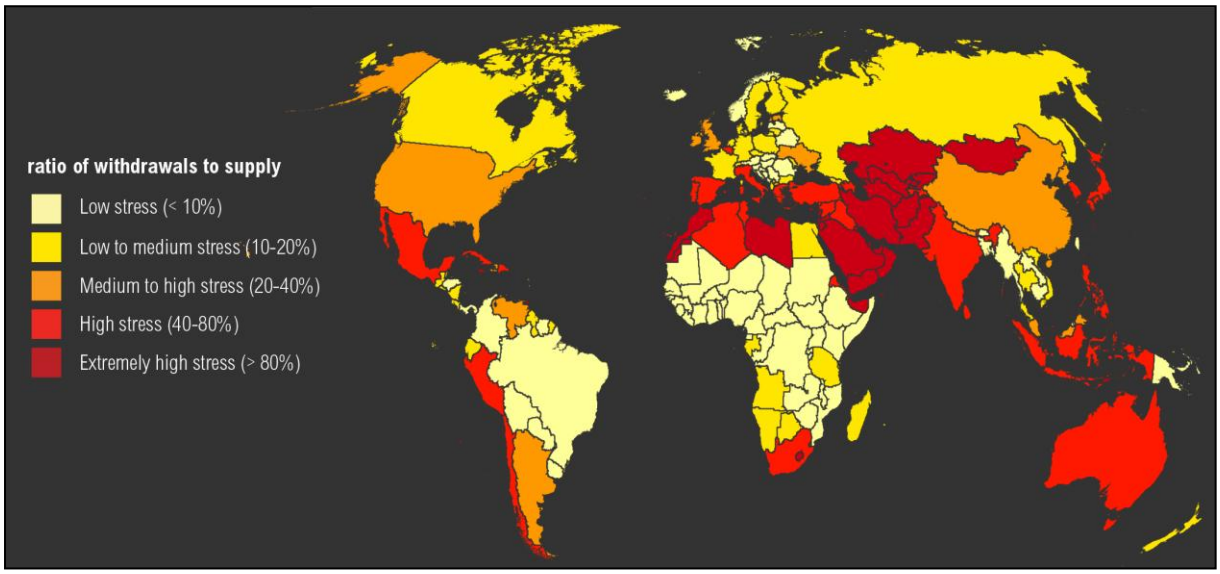

Figure 1: Water stress by country; this map shows the average exposure to water stress of water users in each country, *i.e.* the ratio of total withdrawals to total renewable supply in a given area. A higher percentage means more water users are competing limited supplies.(Source: Gassert *et al.* (2013))

Indeed, the distribution of populations is not correlated with water availability. The arid zones receive only 2.2% of the world's water but are home to 21.5% of the population (Frérot, 2011). Moreover, in regions subject to a monsoon climate, almost all-annual rainfall and most river flows are concentrated for a short period, about two months. In many countries, surface water exploitation has almost reached its limit and large volumes are taken from underground aquifers to fuel agriculture, industrial and domestic consumption. Thus, most of the world's aquifers are overexploited (Wada *et al.*, 2012). This overexploitation is critical for both quantitative and qualitative aspects since it often goes together with water quality degradation. This is particularly the case for saline intrusions for coastal aquifers.

In addition to the food requirements linked to the world population growth, agricultural production is one of the important sectors that might be significantly affected by climate change, since crop yields depend mainly on climate conditions (rainfall patterns and temperature). The Mediterranean region is one of the most prominent "Hot-Spots" in future climate change projections (Giorgi and Lionello, 2008) due to an expected larger warming than the global average and an increase in precipitation inter-annual variability. Indeed, the major part of the southern Mediterranean countries, already suffering from water scarcity, show a growing water deficit, due to the combined effect of the increase in water consumption (increased domestic use and extension of irrigated areas), and the reduction of resources (temporary drought and/or climate change). According to Blue Plan Note N°11 (UNEP, 2009), Mediterranean water demand is likely to increase by 50 km^3 by 2025 and reach 330 km^3/year. The major portion of this increase would be due to the Southern and Eastern Mediterranean countries where, in view of demographic growth and of the immediate impacts of changes in the water cycle, it is estimated that, by 2050, about 290 million people would end up in a situation of severe water scarcity (Figure 2).

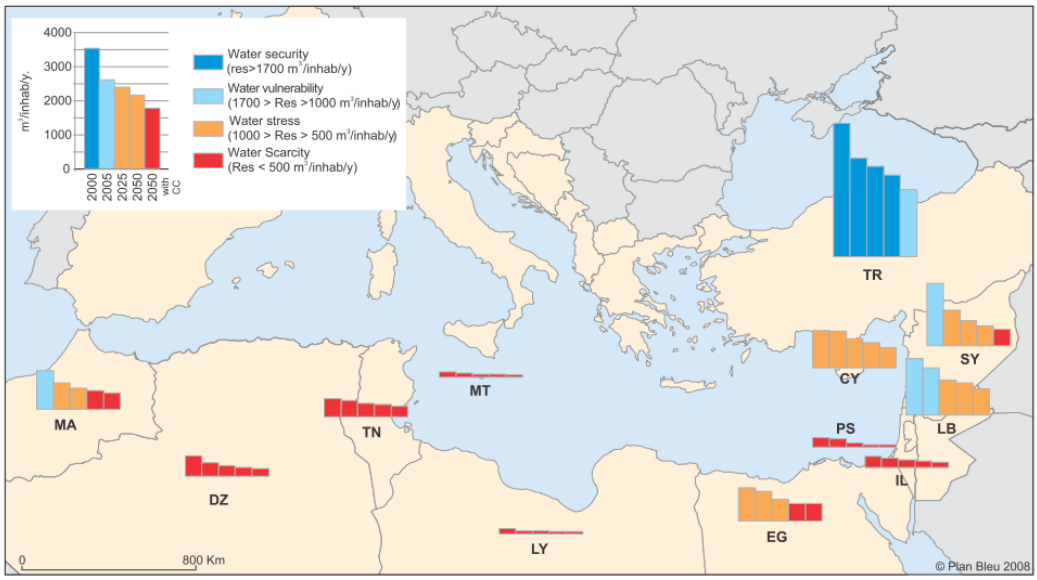

Figure 2: Evolution of water resources per inhabitant in the Southern and Eastern Mediterranean countries between 2000 and 2050 (Source: UNEP (2009))

Tunisia is mainly an arid to semi-arid country facing the problem of water scarcity (water resources per inhabitant are below the water shortage threshold with 460m³/inhabitant/year). Strong tensions are being expressed on water access and sharing; hence, monitoring of agricultural water resources is of paramount importance. The Kairouan plain, in central Tunisia, is a semi-arid area that has experienced a strong development of irrigated crops during the last decades of 20th century. As in many parts of the Maghreb region, surface water is scarce and groundwater uptake is a dominant source. Annual consumption exceeds the annual recharge of the water table resulting in a piezometric decrease of between 0.5 m and 1 m per year (Leduc *et al.*, 2004).

In order to understand the reasons of this "hydrological crisis" and to find solutions, the Kairouan plain has been the subject of several investigations and scientific studies in the complementary fields of hydrology, anthropology, soil science, geology, hydrogeology, remote sensing, etc. Their main research topics were surface and groundwater resources management linked to irrigation (Cudennec, 2005; Feuillette, 2001; Le Goulven *et al.*, 2009; Leduc *et al.*, 2007; Massuel *et al.*, 2017; Pradeleix *et al.*, 2015). Poussin *et al.* (2008) simulated regional irrigation water demand using a representation of agricultural activities based on typologies of farms and cropping systems. More recently, some studies dealt with the use of remote sensing for soil water balance assessment, including soil moisture estimation (Amri, 2013; Gorrab, 2016), soil texture mapping (Shabou *et al.*, 2015; Zribi *et al.*, 2012), distributed evapotranspiration and irrigation water requirement estimation using low (Amri *et al.*, 2014) and high-resolution remote sensing data (Guermazi *et al.*, 2016) and cereal yield prediction (Chahbi *et al.*, 2014).

In this context, estimating the water consumption of crops is useful to address the issue of regional planning and management of water resources, which requires an overall understanding and quantification of the water cycle components (precipitation, evapotranspiration, run-off, infiltration). Evapotranspiration (ET) is of paramount importance since it represents the preponderant component of the terrestrial water balance; it is the second greatest component after precipitation at the global scale and the most relevant one in arid and semi-arid regions. Thus, ET quantification is a key factor for water management in arid and semi-arid environments. In this regard, some studies

aimed to compute distributed ET in Tunisia in view of regional agricultural water management. The majority of these studies was dealing with distributed reference ET (Baccour *et al.*, 2012; Habaieb and Masmoudi Charfi, 2003; Jabloun and Sahli, 2008) or plot scale actual ET estimation (Boudhina *et al.*, 2017). Some works combined the FAO56 method (Allen *et al.*, 1998) to remotely sensed data in order to estimate low-resolution distributed maximum ET in the Mejerda watershed in north Tunisia (Mjejra *et al.*, 2014) and high-resolution distributed actual ET as well as irrigation water requirement in the Regueb watershed in central Tunisia (Guermazi *et al.*, 2016).

While the farmer generally has enough information to manage water for his property, agricultural land fragmentation, heterogeneous landscapes and the lack of relevant information on actual water use collected by authorities are important constraints for regional water management. Hydrologic applications in agriculture and water resource management require ET information over a range of temporal and spatial scales, from hourly to monthly to seasonal time steps, and at field to global scales. Therefore, without resorting to modern technologies of information gathering and management, this task would require a considerable human effort, an exorbitant financial cost and prohibitive delays.

On the other hand, Earth Observation by satellites allows the acquisition of spatially distributed information on a regular acquisition basis. The type of biophysical variables that can be monitored through remote sensing (RS) varies according to the observed spectral range: vegetation cover (visible and near infrared domain, VIS-NIR), surface temperature (thermal infrared domain, TIR), surface soil moisture (microwave domain). These data must be combined and integrated into operational models, representing the elementary processes involved at the soil-vegetation-atmosphere interface, in order to produce information on the evolution of the various components of the surface water and energy budgets. Therefore, the techniques using RS information are essential when dealing with hydrological processes to understand water and plant functioning at different decision-making scales (farms, irrigated perimeter, and sub-watershed). Over the past decades, RS has shown a great potential for characterizing land surfaces (land use, vegetation coverage, soil moisture, water stress, etc.).

Data acquisition in the microwave domain makes it possible to estimate soil moisture in the first centimeters (Wang and Qu, 2009). Active microwave sensors are characterized by high spatial resolutions (10-20 m) while the passive microwave sensors exhibit lower resolutions having no reliable applications when dealing with cropped soils. The plant available water, *i.e.* mainly the water stored in the first meter of soil depth, depends not only on the evolution of the surface moisture but also more widely on the water supply (precipitation and irrigation) and the soil structural properties (porosity, density). Hence, the microwave data cannot estimate directly the total quantity of water mobilized at the soil-vegetation-atmosphere interface.

The VIS-NIR domain data allows to estimate relatively accurately the vegetation cover fraction and therefore the leaf area involved in photosynthesis and evapotranspiration (Baret *et al.*, 1989; Richardson and Everitt, 1992). In addition, since ET is the most effective means of dissipating the energy received as radiation, the surface temperature is a good indicator of water stress. When ET is limited by the water availability, the surface temperature increases above the theoretical surface temperature calculated under potential conditions (*i.e.* with the characteristics of the current climate and vegetation but with the assumption that water availability is not limiting). Thus, the use of information acquired in

the TIR domain is a good tool of estimating actual evapotranspiration (Boulet *et al.*, 2007; Hain *et al.*, 2009).

In the recent decades, the various spectral domains have often been used independently: microwave experts have focused on soil moisture estimation, TIR domain experts have focused on stress retrieval, etc. It is only recently that joint efforts have been made between these different communities but also within and between international space agencies: NASA (with the Earth Observing System (EOS) program), ESA (with Living Planet and Copernicus programs) and JAXA (with the Global Change Observation GCOM mission program). There has been a growing number of space programs aimed at creating a multi-spectral synergy. A recent example of this motivation is the new Sentinel satellite constellation (ESA, 2017). VIS-NIR, TIR and C-band microwave data are available with unprecedented spatio-temporal resolution. These strategies are based on the development of a system of complementary observations in order to better characterize the continental surfaces.

However, there are several limitations in the efficient use of RS observation for agricultural and hydrological applications. For instance, the accuracy of the measurement is as important as the measurement itself, since, it gives an idea of the observations quality. In most studies, it is defined as the uncertainty associated with instrumentation and inversion models. However, with the use of satellite images for agro-hydrology, it is also important to take into account the notion of spatial representativeness of the measurement, which plays a major role in the agrohydrological variables one wants to retrieve. Let's take the example of MODIS leaf area index (LAI) and land surface temperature (T_{surf}) products. Global MODIS LAI products were validated using a global LAI field measurement database created on the basis of a literature review and major validation campaigns, showed uncertainties of 1.0–1.2 (Fang *et al.*, 2012). Fensholt *et al.* (2004) showed also that MODIS LAI is overestimated by approximately 2–15% in comparison with LAI field measurements. Moreover, the reported error in MODIS T_{surf} is less than 1 K, as validated over homogenous land surface patches by Wan *et al.* (2002). However, this error is greater over bare soil, and biases reach 3.8 K in comparison with ASTER T_{surf} product (Duan *et al.*, 2017). Better accuracy of MODIS T_{surf} was found when evaluated against ground observations in an arid area of northwest China, with an average bias of 0.36 K and minus 0.58 K during daytime and nighttime, respectively (Li *et al.*, 2014). Furthermore, daily T_{surf} products (MOD/MYD11A1) accuracy in relation to land cover in China's arid and semi-arid areas was studied by Yu *et al.* (2014) and show a mean absolute error of 2–3 K in comparison with *in situ* longwave radiation measurements at 12 stations; higher accuracy was observed for stations with homogeneous land cover.

Spatial and temporal resolutions are of paramount importance to realistically integrate spatial observations into bio-physical models. The spatial resolution depends mainly on the sensitivity of the sensor to receive energy emitted by the surface. This sensitivity is strongly dependent on the wavelength domain and plays an important role since it determines the size of the region observed and the size of the objects that will be possible to characterize. For example, SMOS operating in passive L-band has a spatial resolution of 40 km that is too wide to be directly integrated into agro-hydrological models. Hence, spatial resolution must be chosen according to the objects observed and / or modeled (Figure 3); in other words, the spatial representativeness of the observation. The revisit frequency that governs the temporal availability of RS data is the time required for the satellite to perform a complete orbital cycle, that is, to observe exactly the same scene

again from the same point in space. The temporal resolution is related to the spatial resolution for a given wavelength domain because it depends on the orbit of the satellite. For example, in the thermal infrared, Landsat data have a spatial resolution of 100 m but a temporal resolution of 16 days whereas the MODIS data have a spatial resolution of 1 km but a frequency of twice a day at least. Recently, the concept of satellite constellation with several satellites having the same characteristics allows to secure the acquisition in case of failure and also to increase the revisit frequency. For example, the Sentinel-2 mission (10-60 m of spatial resolution) includes two satellites allowing an acquisition frequency of five days. Similarly, to the spatial resolution, the temporal resolution must be chosen according to the characteristic timescale of the variation for the objects one wants to observe and / or model (Figure 3). Finally, it is important to note that all visible images are sensitive to cloud cover, which can amplify the time gap between the available data. The recent increased high temporal resolutions cannot completely solve the problem of cloudiness even in semi-arid areas and combination with other VIS-NIR high-resolution sensors like Landsat 8 should still be useful.

Currently, in the solar and TIR domains, two types of observation are available. In one hand, wide swath / low-resolution sensors (e.g. SPOT-VEGETATION, TERRA-MODIS or PROBA-V) allow daily observation of the entire globe, but at a resolution (~1 km) generally much larger than the size of an agricultural field. On the other hand, high spatial resolution sensors (less than 100 m, e.g. Landsat 8, SPOT, Sentinel-2) allow only one to six observations per month in nominal mode (orbital cycle) on smaller scenes (e.g. 60 km for SPOT, 180 km for Landsat and 290 km for Sentinel-2). At the beginning of this work, *i.e.* before 2016, it was quite difficult to obtain series of high spatial resolution images to study an area as large as the Kairouan plain (3000 km^2) over long periods. Moreover, the cost of these data was prohibitive when we had to program acquisition of SPOT image time series. Today, the situation is quite different with the breakthrough represented by the lunch of Sentinel-2. However, in a context of operational water resources management, the use of medium to low spatial resolution sensors, freely available on the internet, is still interesting. Indeed, they offer a daily acquisition frequency allowing to cope with cloudiness, and MODIS provides daily thermal acquisition which are still not available at high-resolution and frequency (Landsat images are acquired only every 16 days and subjected to clouds) although they are very useful for agricultural water monitoring. However, the major drawback of low-resolution sensors is that pixels usually contain several types of surfaces (mixed pixel).

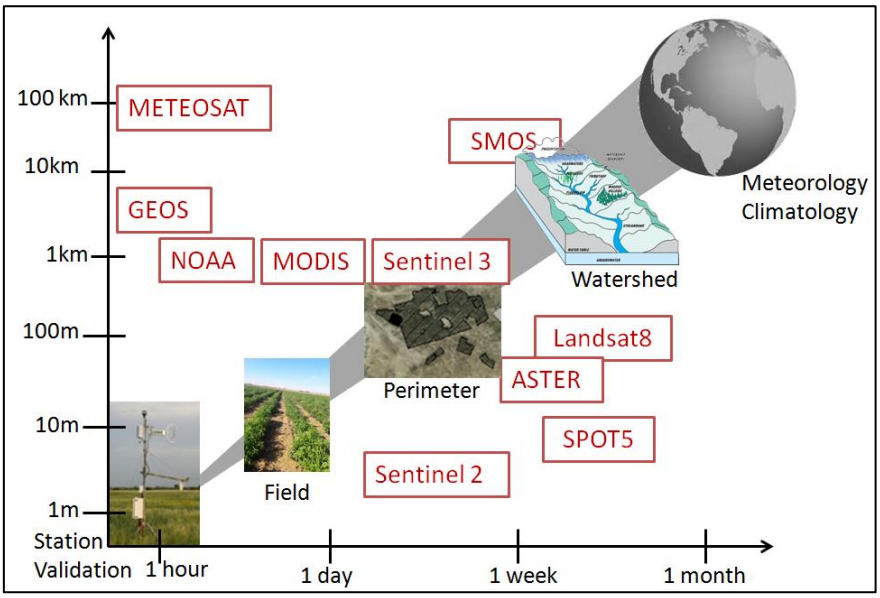

Figure 3: Multi-sensor / multi-resolution remote sensing data for crop monitoring and agro-hydrological applications (inspired from Malbéteau, (2016))

Contrarily to *in-situ* data (sparse network), RS provides exhaustive monitoring (complete coverage) over large regions; this contributes to strengthen decision-making tools designed for resource managers. However, the remotely sensed variables or parameters are generally only one component of these tools, which must integrate other sources of information. Broadly speaking, these tools are based on "agro-meteorological" models simulating the different elementary processes involved in the plant covers dynamics (phenology, photosynthesis, biomass production etc.) and in the soil water balance (evapotranspiration, infiltration, runoff etc.). The joint use of agro-meteorological models and remotely sensed data, regularly distributed in space and time, is a particularly dynamic research path allowing the establishment of water resources and agricultural production systems observatories at regional scale.

Several models have been developed to estimate surface evapotranspiration from RS optical data and meteorological data (Bastiaanssen *et al.*, 2000; Garatuza-Payan and Watts, 2005; Neale *et al.*, 2005). These methods are roughly divided into those fed with solar (VIS-NIR) RS data and those fed with TIR RS data (Figure 4). The first group is based on the fact that evapotranspiration is strongly linked to the green vegetation amount present at the surface, which is well quantified using remote sensing in the solar domain, typically vegetation indices. These approaches are thus based on agro-hydrological models fed by remote sensing. The second group relies on the fact that evapotranspiration is a component of the energy budget, which is strongly linked with surface temperature.

Regarding the first group, one of the most popular approaches used in agriculture for crop water budget modeling is the FAO-56 set of evapotranspiration models (Allen *et al.*, 1998) recommended by the Food and Agriculture Organization (FAO). It is attractive because it requires a relatively small amount of input data and has a relatively good precision on evapotranspiration under standard conditions (unstressed vegetation). However, these models assume a precise knowledge of water supplies to work well. These models have long been coupled with remote sensing providing estimates of the crop coefficients representing the vegetation activity. Indeed, some pioneers provided empirical evidence about the direct relationship between crop coefficients and vegetation

indices (VI) derived from multispectral satellite images (Heilman *et al.*, 1982; M. U. Neale *et al.*, 1990). Monitoring crop development and crop ET over the growing season for the purpose of irrigation management requires dense time series of multispectral imagery delivered in real time and at a spatial resolution high enough to assume an homogeneous land cover in the pixel (Calera *et al.*, 2017). Accordingly, the virtual constellation of Landsat 8 and Sentinel-2 currently provides, at no cost, a time resolution of around one image per week, which is adequate for the monitoring of crop development. In this dissertation, as Sentinel-2 images were not yet available, high-resolution SPOT images are used to feed a VI-based soil water balance (SWB) model run at field and irrigated perimeter scales to compute distributed ET and irrigation volumes. Nevertheless, the major drawback of SWB methods, even the relatively simple FAO-56 one, is the high number of required parameters (often crop specific) but also the lack of real irrigation information needed to compute actual ET (Figure 4). SWB parameters are difficult to estimate especially when dealing with heterogeneous land surface at a regional scale.

At the regional scale, the second group of methods based on surface energy balance (SEB) is often used for ET estimation by combining remotely sensed T_{surf} with vegetation parameters and meteorological variables (Figure 4). The pixel size of T_{surf} sensors ranges from 100 m for the thermal sensor on board Landsat 8 to 1000 m for MODIS-AQUA, MODIS-TERRA and Sentinel-3. The advantage of these models, from a crop management point of view, is to provide ET under actual soil water conditions, including vegetation stress, and further indicators of water stress. Despite their high temporal resolution (e.g. twice a day for MODIS), the spatial resolution of TIR images provided by the most operational platforms is not appropriate for small agricultural fields (Allen *et al.*, 2011b) since the pixels may overlay broad mixtures so that surface temperature signals are mixed and the ET retrievals are difficult to interpret. Otherwise, medium spatial resolution TIR images (e.g. 60 and 100m for Landsat 7 and Landsat 8, respectively), have low temporal resolution (16 days for Landsat) which, combined with the cloudiness issue, does not allow an adequate monitoring of crop development. Disaggregation techniques, using typically high-resolution Normalized Difference Vegetation Index (NDVI) images to "distribute" the T_{surf} of thermal images, are relatively new tools for solving spatial resolution problems and increasing the effective spatial resolution from satellite thermal imagery, in order to reach spatial resolutions comparable to the most common multispectral images (Semmens *et al.*, 2016). Furthermore, aerial images and growing advances in airborne thermal cameras show very promising perspectives to produce temperature maps at very high spatial resolution (Berni *et al.*, 2009; Zarco-Tejada *et al.*, 2012).

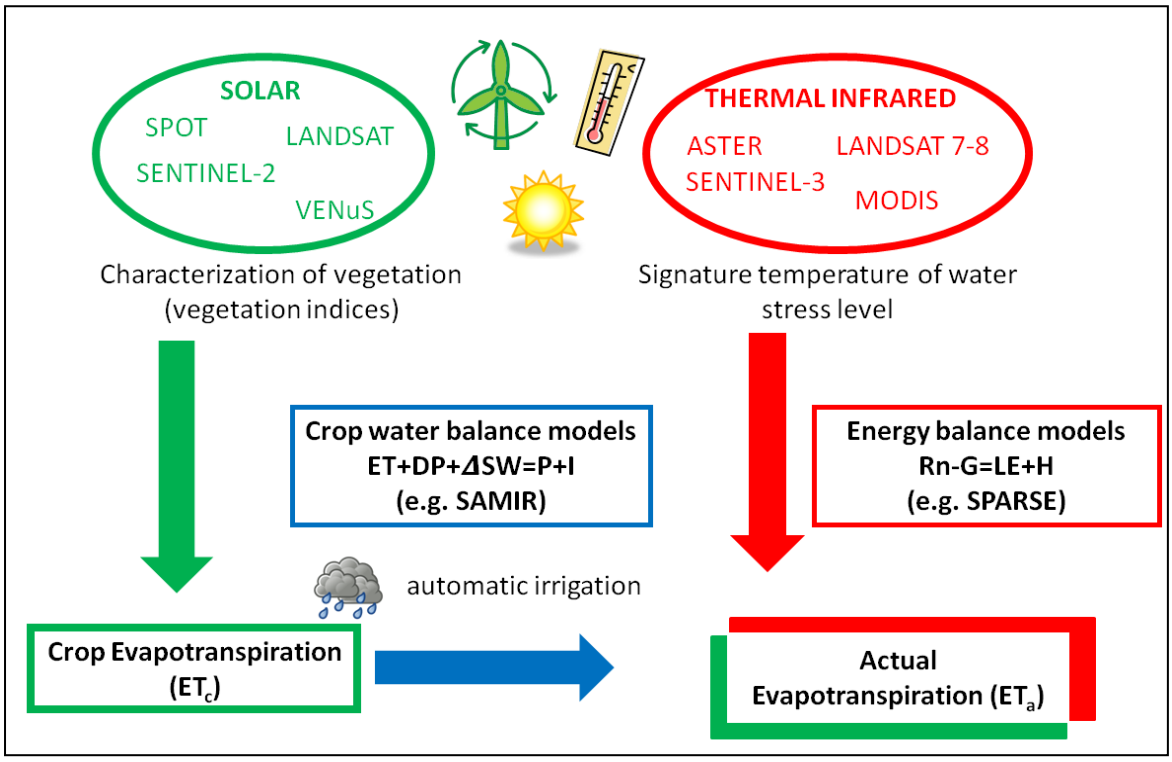

Figure 4: Actual evapotranspiration estimation using soil water balance and surface energy balance models fed by VIS-NIR and TIR remote sensing data, respectively.

PhD motivation, objectives and methodological approach

The central question of my PhD thesis is the control of agrometeorological models by satellite data from optical and thermal sensors to monitor the crop water budget in semi-arid environments. The general objective of this work, entitled "Spatial estimation of actual evapotranspiration and irrigation volumes using water and energy balance models forced by optical remote sensing data (VIS/ NIR/TIR)", is to develop and test methods for estimating the hydrological variables related to crop water budget, *i.e.* evapotranspiration, crop water requirements and irrigation volumes, at scales ranging from plot to regional level and for relatively long time periods (up to the agricultural season). The operational perspective is to provide tools for irrigation and watershed management. Our study area is the Kairouan semi-arid plain located in central Tunisia, occupied by irrigated agriculture and where most of the water is extracted from an overexploited aquifer.

The adopted approach combines field experimentation, modeling and the use of multi-sensor / multi-resolution remote sensing data. Both types of tools used to estimate hydrological variables (ET and irrigation volumes) are: i) a daily water balance model, SAMIR (Simonneaux *et al.*, 2009), simulating water fluxes at a daily time step and ii) an instantaneous energy balance model, SPARSE (Boulet *et al.*, 2015), which characterizes the water status at the satellite overpass time.

For this purpose, two main research focuses have been explored:

- The first was the development of methods to integrate *in situ* data and high-resolution (VIS-NIR) remote sensing data (SPOT imagery) in the SAMIR model to draw up the spatialized water balance of irrigated areas in the Kairouan plain during four agricultural seasons (2008-2009 and 2011-2014).

The model was calibrated using plot scale measurement of evapotranspiration (eddy correlation) and the control output variables, ET and irrigation volumes were assessed using field fluxes measurements by Extra Large Scintillometer XLAS and irrigation volumes obtained by field surveys, respectively.

- The second focus was to test the performance of the SPARSE energy balance model in monitoring the water status of a heterogeneous landscape in the Kairouan Plain and to determine whether the low-resolution data from Terra-MODIS and Aqua-MODIS satellites in the VIS-NIR and TIR domains were useful for spatializing the key variables of the energy balance in a semi-arid context, *i.e.* sensible and latent heat fluxes. Validation of the results was carried out by means of the XLAS sensible heat flux measurements. Special attention has been paid to the extrapolation of the instantaneous ET estimates to daily time step for hydrological applications.

This manuscript is organized in five chapters:

- The first chapter reviews general notions concerning the soil water balance components and the various methods to estimate them. A particular interest is given to ET and irrigation with a comparison between water balance and energy balance-based methods for ET modeling. The potential of multi-sensor/multi-resolution spatial remote sensing data in ET modeling is also discussed.

- The second chapter decribes the study area, the experimental set-up and the satellite datasets, as well as the pre-processing of the *in situ* data.

- The third chapter studies the possibility of using high-resolution VIS-NIR imagery in an agro-meteorological modeling scheme through the SAMIR model (after calibration for irrigated cereal-crops) in order to establish maps of daily ET and irrigation volumes at the scale of the irrigated perimeter for four agricultural seasons (2008-2009 and 2011-2014). Observed irrigation volumes at field, farm and perimeter scale were used to validate the modeled irrigation volumes, while ET derived from the XLAS scintillometer measurements (operated continuously for more than two years from March 2013 to June 2015) was used to validate the modeled ET of the last two seasons.

- In the fourth chapter, the parameterization of SAMIR model was revisited, since the comparison of daily modeled ET with the scintillometer derived ET shows shortcomings mainly attributed to the parameterization of the non calibrated crops (trees and vegetables). Also, the calibration for cereal crops was redone based on both ET (eddy covariance) and soil moisture measurements. Since no calibration was possible for trees and vegetables parameters, they were enhanced based on literature.

- In the last chapter, the operational use of the SPARSE model was tested and the accuracy of the modeled sensible heat flux (H) and of the modeled daily ET over a semi-arid land surface, in a context of high land cover complexity (*i.e.* trees, winter cereals, summer vegetables) was assessed. The validation was based on the comparison of modeled H and ET with the scintillometer measured H and derived ET, respectively.

Finally, we present the conclusions of this work and the research prospects.

Chapter 1: Soil water balance components' estimation methods

This chapter introduces theoretically the main processes of interactions at the Soil-Vegetation-Atmosphere interface involved in coupled water and energy cycles, on which are based the soil water balance model and the surface energy balance model applied in this dissertation, i.e. SAMIR and SPARSE, respectively. We synthesize here the different types of evapotranspiration and irrigation estimation methods, mainly those based on Soil-Vegetation-Atmosphere Transfer modeling and assimilation of optical remote sensing data in the visible (VIS), near infrared (NIR) and thermal infrared (TIR) domains.

The determination of water fluxes at the soil-plant-atmosphere (SPA) interface is of fundamental interest for agro-hydrological management purposes. Information on water balance components under cropped soils is crucial for irrigation planning (Calera *et al.*, 2017) and crop water stress monitoring (Ihuoma and Madramootoo, 2017) at field and regional scales. The water balance equation is usually applied to the unsaturated zone of the soil. Mass conservation is thus expressed for agricultural systems as:

$$P + I + W - ET - R - \mathrm{D} - \mathrm{Icp} = \frac{[\pm \Delta S]_0^z}{\Delta \mathrm{t}} \qquad (1.\ 1)$$

where P is precipitation, I is irrigation, W is contribution from water table by capillary rise, ET is evapotranspiration, R is runoff, D is the deep percolation, Icp is interception and $\boldsymbol{\Delta}$S is soil water storage variation within the time step Δt in the soil layer where the roots are active to supply water to the plant (between the surface and the root zone depth z in meter). All the term in equation 1.1 are expressed in rates (millimeters per unit time).

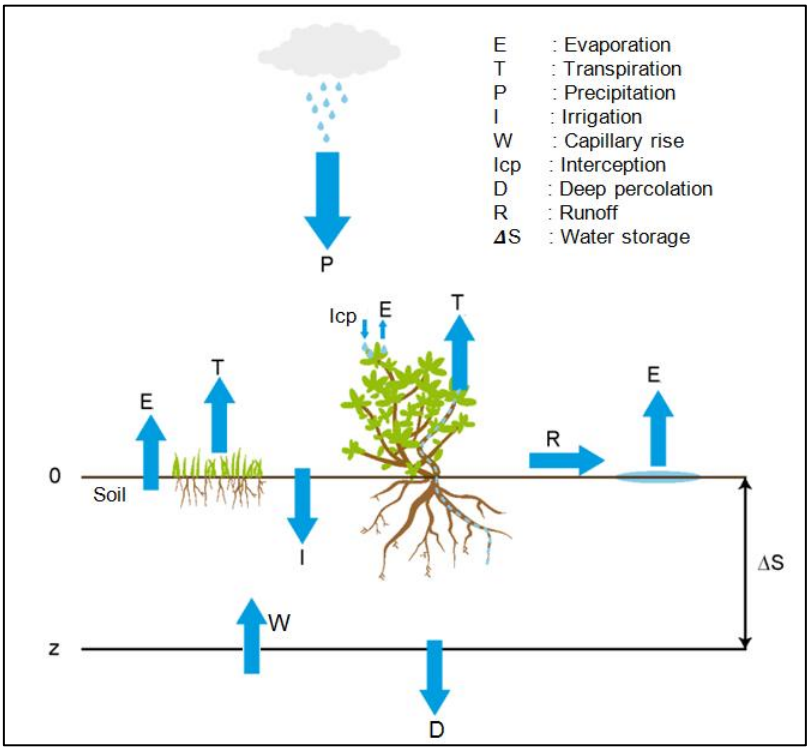

Figure 1. 1: Components of the soil water balance (Source: Velluet (2014), modified)

Since it is often very difficult to accurately measure all terms of Eq. (1.1), a number of simplifications are generally made. For application over flat terrain, condition that prevails in many agricultural regions, the runoff term R could be neglected (e.g. Holmes, 1984) but, actually, it depends on the occurrence and characteristics of precipitation (amount, duration and intensity) and can only be neglected for a particular type of soil (Jensen *et al.*, 1990), *i.e.* coarse (sand and loamy sand) and moderately coarse (sandy loam) in absence of other factors such as the presence of crust, overland flow for gravity irrigation etc. On the other hand, deep percolation is a major unknown of equation (1.1). Some researchers suggest that it can be neglected in dry regions (e.g. Holmes, 1984), but actually it depends on the soil depth, slope, permeability and surface storage (Jensen *et al.*, 1990) and needs to

be checked in each particular case (Brutsaert, 2013), depending also on the climate and irrigation practices. For operational applications in irrigation management, the soil water balance equation can be expressed in its simplified form as follows:

$$P + I = \mathrm{ET} + \frac{[\pm \Delta S]_0^r}{\Delta t} \quad (1.\ 2)$$

The precipitation term can be estimated from a network of rainfall stations (rain gauge measurements) or weather radar data (Arkin and Xie, 1994), from satellite-based precipitation products like the Tropical Rainfall Measuring Mission (TRMM) (Huffman *et al.*, 2007), the Global Satellite Mapping of Rainfall (Ushio *et al.*, 2009), the Naval Research Laboratory blended-satellite rainfall technique (Turk *et al.*, 2010) or from meteorological model outputs (Clark *et al.*, 2016). Therefore, the evapotranspiration and irrigation terms become the key terms of the water balance equation.

Strictly speaking, crop water requirement refers to the water transpired by the plant, the water evaporated from the soil and the water stored by the plant for its metabolic processes. Since evaporation from soil (E) and transpiration by the plant (T) occur simultaneously, the term evapotranspiration (ET) is used to describe the total loss of water from vegetated land surfaces to the atmosphere. Furthermore, since the water used for the plant metabolism is substantially negligible as compared to E and T, the term crop water requirement is frequently alternative to evapotranspiration in standard/optimum conditions.

The crop ET under optimal conditions (unstressed crop), referred to as ETc (for "ET crop"), is the evapotranspiration from crops grown under standard management and environmental conditions. When cultivating crops in fields, the actual crop evapotranspiration, referred to as ETa, often deviates from ETc due to non-optimal conditions (pests and diseases, soil salinity, low soil fertility, water scarcity or water logging) that reduce the evapotranspiration rate.

The amount of water required to cover the theoretical water demand by the plant, e.g. ETc, is defined as crop water requirement (CWR). Although the values for ETc and CWR are identical, crop evapotranspiration refers to the amount of water that is evaporated and transpired while CWR refers to the amount of water that needs to be available in the soil for making such crop consumption possible. The CWR always refers to a crop grown under optimal conditions, *i.e.* a uniform crop, actively growing, completely shading the ground, free of diseases, and favorable soil conditions (including fertility and water). The crop thus reaches its full production potential under the given environment. CWR mainly depends on the weather conditions (major climatic factors influencing the CWR are solar radiation, air temperature and humidity and wind speed), the crop type and the phenological/growing stage of the crop. The influence of the climate on CWR is synthesized into the reference crop evapotranspiration (ETo) which is the evapotranspiration of an hypothetical reference grass cover (Allen *et al.*, 1998). The CWR can be supplied to the crops by rainfall, by irrigation or by a combination of irrigation and rainfall. Efficient agricultural water management requires reliable estimation of the CWR (or ETc) and the corresponding irrigation requirement to meet CWR complementary to rainfall.

1.1 Soil water storage

The water balance computation consists in describing the evolution of the stock of water available in the soil, *i.e.* the profile distribution of the water content in the various soil horizons.

In order to calculate the soil water budget, an estimate of the soil's ability to store water is required. Available water capacity is the maximum amount of water a soil can provide to the plant. It is the water held between the soil field capacity (FC) and the permanent wilting point (WP) in the root zone. The FC or drained upper limit (Figure 1.2) is defined as the water content of a soil that has reached equilibrium with gravity after several days of drainage. The WP or lower limit of available water (Figure 1.2) is defined as the water content at which plants can no longer extract a sustainable quantity of water from the soil and begin to wilt. Typical suction values associated with the FC and WP are -3.3 kPa (-0.33 bars) and -1500 kPa (-15 bars) respectively. Like water content, FC and WP are defined as a volume of water per volume of soil. Given these two definitions, the water available for evapotranspiration after drainage *i.e.* the available water retention capacity is defined as the FC minus the WP.

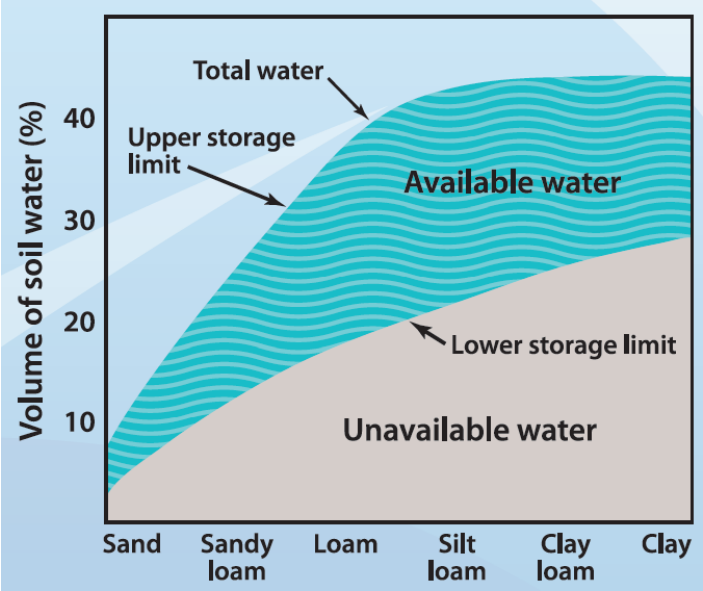

Figure 1. 2: The relative amounts of water available and unavailable for plant growth in soils with textures from sand to clay (Source: Soil-Quality (2017))

There are different methods to provide these soil hydrodynamic properties, which are function of soil texture and organic content. They may be prescribed from literature values when available (Table 1.1 gives some typical values of available water retention capacity). The *in situ* measurement of these properties is costly and time consuming, in addition to implementation difficulties, linked to soil manipulation and data interpretation. Moreover, proxy data on the soil texture, structure, organic matter content, porosity or dry bulk density, can be used to find the hydrodynamic parameters of the soil by applying functional mathematical relationships *i.e.* pedotransfer functions or PTF. However, PTF performance is quite variable and depends on several factors such as the

similarity between the application region and the database's source region, climate, geology or measurement techniques (Wösten *et al.*, 2001).

Table 1. 1: Water retention properties for agricultural soils

Soil Type (USA Soil Texture Classification)	Soil water characteristics		
	$\boldsymbol{\theta}_{FC}$ [m^3/m^3]	$\boldsymbol{\theta}_{WP}$ [m^3/m^3]	$\boldsymbol{\theta}_{FC}$ - $\boldsymbol{\theta}_{WP}$ [m^3/m^3]
Sand	0.07 - 0.17	0.02 - 0.07	0.05 - 0.11
Loamy sand	0.11 - 0.19	0.03 - 0.10	0.06 - 0.12
Sandy loam	0.18 - 0.28	0.06 - 0.16	0.11 - 0.15
Loam	0.20 - 0.30	0.07 - 0.17	0.13 - 0.18
Silt loam	0.22 - 0.36	0.09 - 0.21	0.13 - 0.19
Silt	0.28 - 0.36	0.12 - 0.22	0.16 - 0.20
Silt clay loam	0.30 - 0.37	0.17 - 0.24	0.13 - 0.18
Silty clay	0.30 - 0.42	0.17 - 0.29	0.13 - 0.19
Clay	0.32 - 0.40	0.20 - 0.24	0.12 - 0.20

Source: FAO paper N°56 (Allen *et al.*, 1998)

For soil water balance calculations, it is necessary to know the total available water retention capacity in a soil profile. This value is typically expressed in mm and can be obtained by integrating the available water-holding capacity over the effective depth of the soil, *i.e* the soil depth where the roots have access. If the initial soil moisture is unknown, which is usually the case, a soil moisture evolution model can be used to force the net change in soil moisture from the beginning to the end of a specified period (for which the soil moisture at the end can be considered similar to one at the beginning, e.g. an hydrological year), use the final moisture profile as the initial one and run the model again over the same period, and repeat the process until the first and the last profile of the period are similar (long-term equilibrium) according to a given precision (Ghosh, 2016); this method is called "spin-up".

Wang-Erlandsson *et al.* (2016) described six approaches for the root zone water storage capacity estimation, and showed that remote sensing-based studies are generally based on field observations and look up tables (Sánchez *et al.*, 2010; Sánchez *et al.*, 2012).

1.2 Evapotranspiration

The evapotranspiration process involves a phase change of water from liquid to gaseous state, with latent heat requirement of about 2.47 MJ per kg of water evaporated. Most of the energy required in ET process comes from solar and atmospheric radiation. The large amount of energy involved in the processes of evaporation and transpiration means a coupling between the water and energy cycles. Actual ET (ET_a)– or its energy equivalent, the total latent heat flux LE (E is the rate of evaporation of water [$kg.m^{-2}.s^{-1}$] and L is the latent heat of vaporization of water [$J.kg^{-1}$]) – depends on three factors: weather, soil water availability and vegetation cover, which are highly variable in time and space. Depending on the application, an estimation of ET_a is required at hourly (weather applications), daily (hydrology, agronomy) or monthly (surface-subsurface interactions) time steps (Lagouarde and Boulet, 2016).

Transpiration occurs through different organs, involving many processes. It is driven by the water vapor difference between the stomata cavity and the surrounding air: as water evaporates through the stomata, it creates a negative pressure (also called tension or suction) within the leaves and the xylem cells, which exerts a pulling force on the water in the soil to be absorbed by the roots and draws the water upward from the root system to the air system by the conductive system. Water is then disseminated in liquid form through the leaf intercellular spaces and stomata (small orifices of a few micrometers in diameter ensuring and regulating the gas exchange (CO_2 and H_2O) between the plant and the atmosphere); T includes the transfer towards the atmosphere through the boundary layer around the leaf.

In addition to the intrinsic specificities of the plant itself, root extraction depends on soil texture, soil moisture, and the climatic conditions. If the water is insufficiently abundant in the soil, the plant is under water stress and the leaf potential decreases. The critical leaf potential represents the water potential of the stomata under which the plant can no longer extract water to the atmospher. When this threshold is reached, the plant adapts its morphology to meet its needs, reducing for example the opening of the stomata, developing its root system or decreasing its leaf area.

The capability to predict levels of actual ET is a valuable asset for water resource managers, as it describes the water consumption from vegetation. ET can be either measured or estimated via modeling (even though most models require field measurements). Conventionally, if ET is quantified by the use of an instrument, it is 'directly' measured and when it is found by means of a relationship among several observations, it is 'indirectly' measured (Rana and Katerji, 2000). Conversely, ET is considered as 'estimated' if it is expressed by a model.

1.2.1 Direct measurements of ET

The ET measurement methods are based on concepts which can be critical under semi-arid and arid environments for several reasons: (*i*) representativeness (*ii*) instrumentation (*iii*) microclimate and (*iv*) applicability. Therefore, to establish the degree of accuracy of the obtained ET measurement and the validity of a method, it is necessary to consider all these parameters (Allen *et al.*, 2011b).

1.2.1.1 Hydrological approach: Weighing lysimeters

Weighing lysimeters have been developed to give a direct measurement of ET. In general, it is a device, a tank or container, to define the water movement across a boundary (depth level of the soil). Lysimeters of many different designs, sizes, shapes, and measurement systems have been built over the years (Howell *et al.*, 1991). The main advantage of the lysimeter *in situ* measurements is that water consumption of vegetation can be performed under approximately realistic field conditions. However, a lysimeter measurement requires elaborate preparation. Moreover it is typically limited to only few individual trees or a small surface area of agricultural crops (Verstraeten *et al.*, 2008). A Major limitation of lysimeters is that capillary rise is not taken into consideration because the water table can be supposed to be at a considerable depth (Makkink, 1959); moreover, root extension is sometimes limited.

1.2.1.2 Plant physiology approaches

Methods based on plant physiology either measure the water loss from a whole plant or a group of plants. They may include methods such as tracer technique and porometry but here, only two of the most common methods will be analysed: the sap flow method and the chamber system.

a. Sap flow method

Sap flow measures only plant transpiration by means of simple accurate models; sap flow can be measured by two basic methods: (i) heat pulse and (ii) heat balance. The most popular sap flow method is the heat balance method, based on the concepts proposed by Čermák *et al.* (1973) and Steinberg *et al.* (1990). The plant transpiration can be estimated by determining the sap mass flow; this is done using gauges that are attached to or inserted in the plant stem. For the heat balance method, a heater element is placed around the plant stem to provide energy to the system. Thermocouples are used to determine how much heat is lost by conduction up, down and radially in the stem from the heater element. The difference between the heat input and these losses is assumed to be dissipated by convection with the sap flow up the stem and may be directly related to water flow (Kjelgaard *et al.*, 1997). The mass flow rate F [$g.t^{-1}$] is expressed by the relationship:

$$F = \frac{Q_h - Q_v - Q_r}{c_w \delta T} \quad (1.\ 3)$$

where Q_h is input heat, Q_v is vertical conductive heat, Q_r is radial heat loss to environment, c_w [$J.g^{-1}.K^{-1}$] is specific heat of water and δT is the temperature difference between the upstream and downstream thermocouples.

Direct measurements of actual transpiration can also be performed with the heat pulse-sap flow technique, which has been applied in vineyards (Yunusa *et al.*, 2004) and olive groves (Testi *et al.*, 2006; Williams *et al.*, 2004). Sap flow method is a very good alternative to lysimeter experiments; however, operation of sap-flow sensors requires a vast technical input and maintenance effort.

b. Chambers system

The chamber system method was described for the first time by Reicosky and Peters, (1977). The first chambers system version was portable (by means of a tractor, for example) and the ET rate was calculated as a difference (latent heat storage) between two measurements by a psychrometer: one acquisition before the chamber was lowered on the plot and another one minute later. Chambers system is easier to implement than the weighing lysimeter (Reicosky *et al.*, 1983), but it is not suitable for long term ET measurements. The most serious problem of almost all chambers is the microclimate modification (solar radiation balance; air temperature, wind speed) during the measurement period.

1.2.1.3 Micrometeorological approaches

ET consumes energy; this energy corresponds to what is required to transport water from the inner intercellular space in the leaves and plant organs to the atmosphere; it is therefore expressed as a flux density in [W.m^{-2}].

Micrometeorological methods based on physical principles require accurate measurements of meteorological parameters on a small temporal scale (1 h or less). Their accuracy depends on the validity of some hypothesis such as the flux conservation, which implies that measurements are performed over a large flat area with uniform vegetation.

a. Aerodynamic method

Assuming that a flux density can be related to the gradient of the concentration in the atmospheric surface layer (ASL), the latent heat flux by the aerodynamic technique can be determined directly by means measurement of the vapour pressure at different heights above the crop. LE is then calculated by means of the scaling factors u* and q* (Grant, 1975; Saugier and Ripley, 1978):

$$LE = L\rho u^* q^* \quad (1.\ 4)$$

where L [J.kg-1] is the latent heat of vaporization of water, ϱ [kg.m^{-3}] is the air density, q* is scale of the specific air humidity [kg. kg^{-1}], and u* [m.s^{-1}] is the friction velocity derived from the wind profile measurement as follows:

$$u^* = \frac{ku}{ln\left(\frac{z-d}{z_0}\right) - \psi_m} \quad (1.\ 5)$$

where k=0.41 is the von Karman constant, d (m) is the zero plane displacement height, z_0 (m) is the roughness length of the surface and ψ_m is the stability correction function for momentum transport. q* is determined similarly from the humidity profile measurement:

$$q^* = \frac{k(q - q_0)}{\ln\left(\frac{z - d}{z_0}\right) - \psi_v} \quad (1.\ 6)$$

where q_0 is the air humidity extrapolated at $z=d+z_0$ and ψ_v is the stability correction function for latent heat transport.

The major difficulty with this technique is the correct measurement of the vapor pressure at different heights above the crop. For this reason, LE can also be derived indirectly by the energy balance (see section 1.2.2.1) where the sensible heat flux can be determined by the flux-gradient relation for temperatures:

$$H = -\rho c_p u^* T^* \quad (1.\ 7)$$

where c_p [J.kg^{-1}.K^{-1}] is the specific heat of air at constant pressure, ϱ [kg.m^{-3}] is density of air and T*, the temperature scale, is deduced by the air temperature profile:

$$T^* = \frac{k(T-T_0)}{\ln\left(\frac{z-d}{z_0}\right)-\psi_h} \quad (1.\ 8)$$

where T_0 is the temperature extrapolated at $z=d+z_0$ and ψ_h is the correction function for the heat transport.

Under this form, the main advantage of the aerodynamic technique consists in avoiding complex high frequency humidity measurements. Nevertheless, the accuracy depends on the number of measurement levels for the wind speed and temperature profiles. In fact, equations (1.8) and (1.9) require at least three or four levels (Webb, 1965), but accuracy is improved when many more levels are used (Wiernga, 1993). This method showed good results (Pieri and Fuchs, 1990), when the stability correction functions of Dyer and Hicks (1970) and Paulson (1970) were used.

b. Eddy covariance

The transport of scalar (vapor, heat, carbon dioxide CO_2) and vectorial amounts (*i.e.* momentum) in the lower atmosphere in contact with the canopies is mostly governed by air turbulence. In recent decades, methods for measuring turbulent flows have been been improved, both in terms of reliability and in terms of operationality. The eddy covariance method (EC) is considered as the standard method for measuring surface turbulent fluxes. The first complete scientific contributions to this topic were given by Dyer (1961) and Hicks (1970); extensive details of the theory can be found in Baldocchi, (2003), Falge (2017) and Stull (2012) .

EC method is a direct measurement of the turbulence in order to get the surface fluxes of sensible and latent heat and of CO_2 with high accuracy.

The mean vertical flux density (F_x) of a physical quantity (X, for example temperature, water vapor or CO_2) in the turbulent layer is proportional to the covariance between the vertical velocity (w) and the concentration of this quantity (Van Dijk, 2004). In general, the instantaneous vertical flux density (F_x) per unit of time and surface can be written:

$$F_x \approx wX \quad (1.\ 9)$$

Using the Reynolds decomposition ($W = \overline{w} + w'$ and $X = \overline{X} + X'$), the average flux ($\overline{F}$) can be approximated by the following formula:

$$\overline{F_x} \approx \overline{wX} = \overline{(\overline{w} + w')(\overline{X} + X')} \quad (1.\ 10)$$

By expanding this expression and using the fact that $\overline{\overline{X}} = \overline{X}$ and the fluctuations mean is zero, equation (1.10) becomes:

$$\overline{F_x} \approx \overline{w}.\overline{X} + \overline{w'X'} \quad (1.\ 11)$$

In a horizontal homogeneous boundary layer flow, the average vertical wind speed is zero by definition (Brunet Y., 1995), hence $\overline{w} = 0$.

Finally, for the flux density, we obtain:

$$\overline{F_x} \approx \overline{w'X'} \quad (1.\ 12)$$

Turbulent fluxes (momentum, sensible heat, latent heat and gas concentration) can be expressed as the product of the vertical wind speed fluctuations term by the considered quantity fluctuations term.

The sensible heat flux density H, is given by:

$$H = -\rho c_p \overline{w'T'} \quad (1.\ 13)$$

where c_p [J.kg^{-1}.K^{-1}] is the specific heat of air at constant pressure, ϱ [kg.m^{-3}] is density of air, w is the instantaneous deviation of vertical wind velocity from mean vertical wind velocity ($\overline{w}$) and T' is the instantaneous deviation of air temperature from mean temperature ($\overline{T}$).

The latent heat flux density LE, is given by:

$$LE = -\rho \overline{w'q'} \quad (1.\ 14)$$

where w is the instantaneous deviation of vertical wind velocity from mean vertical wind velocity ($\overline{w}$) and q' is the instantaneous deviation of specific humidity from mean specific humidity ($\overline{q}$). The negative sign appears because velocity is conventionally defined as positive towards the surface while the flux is negative due to the sign convention used for vertical velocity.

To measure ET directly by the EC method, vertical wind fluctuations have to be measured (by the sonic anemometer) and acquired synchronously to the vapour density fluctuations (by fast response hygrometer); both have to be acquired at a typical frequency of 10–20 Hz.

Despite problems linked to the correct management of the sensors, complex data processing, and the management of 'closure error' (the sum of measured LE+H does not equal measured Rn−G) of about 10-30% (Foken, 2008; Twine *et al.*, 2000; Wilson *et al.*, 2002), this method has very good performances both at hourly and daily scale, also in semi-arid environments. Examples of eddy correlation measurements can be found in Er-Raki *et al.* (2009), Hoedjes *et al.* (2007), Hoedjes *et al.* (2008), Liu *et al.* (2016) and Williams *et al.* (2004). The EC method has the advantage of allowing the measurement of the fluxes of all kinds of molecules other than water, and in particular CO_2.

c. Scintillometer

Large-scale turbulent fluxes are difficult to evaluate since the above methods are mostly valid only on small homogeneous surfaces. Indeed, the heterogeneity of most landscapes generates large flux variability, which is difficult to measure with the conventional techniques. Hence, indirect turbulent flow measurement techniques have been developed, the most promising is the scintillometery. Scintillometry has emerged as one of the most widely used tools to quantify average fluxes over heterogeneous land surfaces (Brunsell *et al.*, 2011). Scintillometer operating at wavelengths λ of about 1μm are

called optical scintillometer, whereas when λ is ranged between 1 and 10 mm these are called microwave scintillometers.

Scintillometer consists of a transmitter and a receiver at both ends of an atmospheric propagation path (measurement transect). Fluxes of sensible heat and momentum cause atmospheric turbulence close to the ground, and creates, with surface evaporation, refractive index fluctuations due mainly to air temperature and humidity fluctuations (Hill *et al.*, 1980). The receiver detects and evaluates the intensity fluctuations of the transmitted signal, called scintillations, which are linked to surface fluxes of sensible and latent heat. The magnitude of the fluctuations in the refractive index is usually measured in terms of a structure parameter of the refractive index of air integrated along the optical path C_{n^2} [$m^{-2/3}$] (Tatarskii, 1961). Scintillometers measure sensible and latent heat fluxes (H and LE) by relating C_{n^2} to the structure parameter of temperature C_{T^2} and the structure parameter of humidity C_{TQ}, respectively, through the Monin Obukhov stability parameters. Temperature fluctuations given by C_{T^2} are the dominant cause of scintillation in the optical wavelengths, and therefore optical scintillometers can be applied to measure *H* without making measurements of, or assumptions on, humidity fluctuations. Scintillometers can provide average H estimates over areas comparable to those observed by satellites (Hemakumara *et al.*, 2003; Lagouarde *et al.*, 2002) along a path length ranginge from a few hundred meters to 5 km (the case of large aperture scintillometers LAS) up to 10 km (the case of extra large aperture scintillometers XLAS).

Since the optical scintillometer provides spatially averaged H, LE can be computed as the energy balance residual term (LE =Rn-G-H) assuming 100% energy balance closure. The estimation of a representative value for the available energy (Rn-G) across the transect is therefore crucial for the accuracy of LE retrieved values.

Since the upwind area contributing to the flux (*i.e.* the flux footprint) varies according to wind direction and atmospheric stability, it must be estimated if one wants to compare scintillometer measurements to, say, pixel derived estimates of the flux (Brunsell *et al.*, 2011). The footprint of a flux measurement defines the spatial context of the measurement, *i.e.* the source areas that influence the sensors. Assessing the upwind area contributing to the flux can be done using several footprint models (Horst and Weil, 1992; Leclerc and Thurtell, 1990). These models have been developed to determine what area is contributing the the flux. Contributions of upwind locations to the measurement depend on the height of the vegetation, height of the instrumentation, wind speed, wind direction, and atmospheric stability conditions (Chávez *et al.*, 2005).

The scintillometry technique has been evaluated and analyzed over heterogeneous landscapes against EC measurements (Bai *et al.*, 2009; Chehbouni *et al.*, 2000; Ezzahar *et al.*, 2009) and also against model outputs (Marx *et al.*, 2008; Samain *et al.*, 2012; Watts *et al.*, 2000). Few studies dealt with extra large aperture scintillometer (XLAS) data (Kohsiek *et al.*, 2006; Kohsiek *et al.*, 2002; Moene *et al.*, 2006). An historical survey, the theoretical rationale as well as recent works in applied research are reviewed in De Bruin and Wang (2017). Calculations of the sensible heat flux measured by scintillometry as well as the footprint computation are detailed in the next chapter (see section 2.5.3).

1.2.2 Remote sensing based method for ET estimation

Direct measurement of ET is only possible at local scale (for a single plot mostly); it is much more difficult at larger scales (irrigated perimeter or watershed) due to the complexity of hydrological processes (Minacapilli *et al.*, 2007). Moreover, at these scales, land cover is usually heterogeneous and this affects the land-atmosphere exchanges of heat, water and other constituents (Giorgi and Avissar, 1997). ET estimates for various temporal and spatial scales, from hourly to monthly to seasonal time steps, and from field to global scales, are required for hydrologic applications in water resource management (Anderson *et al.*, 2011). Techniques using remote sensing (RS) information are therefore essential when dealing with processes that cannot be represented by point measurements only. In fact, RS capabilities for monitoring vegetation and its physical properties on large areas have been identified for years now (Tucker, 1978). Jackson *et al.* (1977) were ones of the major pioneers in determining ET by remote sensing, with the use of infrared thermometry for the estimation of wheat water consumption.

As explained in the introduction of this thesis, RS provides periodic data about some major ET drivers, amongst others, land surface temperature and vegetation properties (e.g. NDVI and Leaf Area Index LAI) from plot to regional scales (Li *et al.*, 2009; Mauser and Schädlich, 1998). Many methods using remotely-sensed data to estimate ET are reviewed in Courault *et al.* (2005;) and Liou and Kar (2014). According to Courault *et al.* (2005), these methods are difficult to classify because their complexity depends on the balance between the empirical and physically based used modules.

1.2.2.1 Surface energy budget methods

The quantity of water released by a surface into the atmosphere can be directly related to the energy that was necessary for its transformation into vapor by the following equation:

$$LE = \varrho \times L \times ET \quad (1.\ 15)$$

Where LE [$W.m^{-2}$] is the latent heat flux expressed in, L [J.kg-1] is the latent heat of vaporization of water, representing the energy required for the vaporization of one kilogram of water. ET represents the evaporation rate of the surface in cubic meter of water per square meter of surface per unit of time and ϱ [$kg.m^{-3}$] is the density of the water .

The vegetation cover intercepts only part of the radiative energy emitted by the sun and the atmosphere, the complementary part being reflected towards the atmosphere. A small fraction of the energy absorbed by vegetation (usually neglected in energy balance expression) is used for photosynthesis, which is crucial for crop development. Most of the intercepted radiative energy is redistributed by the vegetation cover in its near environment under different propagation modes: emission of radiative energy (thermal infrared), conduction of heat into the ground or convection in the atmosphere. All these components allow introducing the concept of energy balance based on the principle of energy conservation in the environment. Conventionally, the radiative fluxes received by the surface are positive, whereas those emitted are negative. More generally, the heat

fluxes are positive if they represent a loss of energy for the surface and negative for a contribution.

Assuming an uniform and vegetation cover of large extension, and therefore no advection of heat from neighbouring areas, the energy exchange can be considered as purely vertical, and the equation of the energy balance at the surface is written as follows:

$$R_n - G = LE + H \quad (1.16)$$

where LE is the latent heat flux, H is the sensible heat flux, Rn is the net radiation and G is the conduction flux in the soil. The difference (Rn-G) is called the available energy, an amount that is converted into H+λE, the turbulent fluxes. This latter denomination is used because they depend largely and in the same way on the intensity of convection in the atmospheric surface boundary layer. (Rn-G) is partitioned according to the surface water status between the two turbulent fluxes H and LE. When water is present in the soil in sufficient quantity, available energy is mostly converted into LE, while under water stress, this distribution is instead in favor of H.

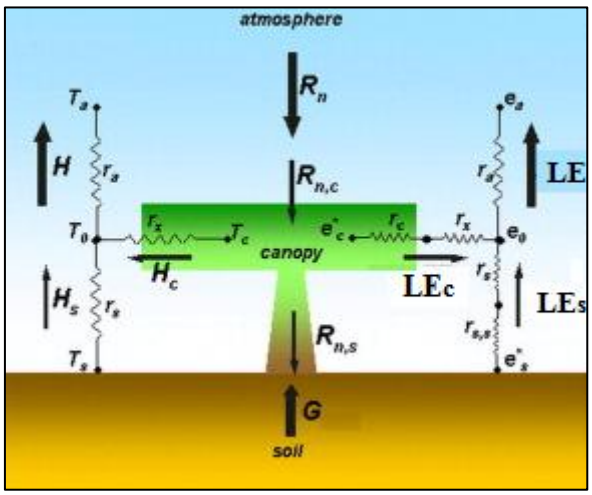

Figure 1. 3 : Components of the energy balance at the soil-vegetation-atmosphere interface ("c", "s" and "a" refer to crop, soil and air, respectively and r_x [$s.m^{-1}$] is the resistance of the canopy boundary layer)

Radiative exchanges

The radiations involved in the surface energy processes are i) the solar radiation (short wavelengths), part of which belongs to the visible spectral domain (0.3-5.0 μm), another to the ultraviolet domain (0.3-0.4 μm) and the remainder to the near and middle infrared range (0.8-5.0 μm) and ii) the thermal infrared radiation (long wavelengths, 5-100 μm) emitted and received by the surface.

Incident short wavelengths radiation *i.e.* global radiation Rg [$W.m^{-2}$] reaching the land surface consists of two components: the incident solar radiation that has not been absorbed by the atmosphere and has not been diffused in other directions as well as the solar radiation diffused by the atmosphere towards the surface. A fraction of the global radiation, the albedo α [-], is reflected by the surface, hence, the reflected short wavelengths radiation by the surface is therefore αRg (Equation 1.17). The surface albedo

α depends both on the optical properties of the bare soil α_s and vegetation cover α_v which in turn depend on the foliage structure affecting light interception (leaf size, orientation and spatial distribution). Hence, the leaf behaves as a semi-transparent surface for radiations coming from the atmosphere and those reflected from the ground; with absorption, transmission and reflection capacities depending on the solar spectrum wavelengths. The net surface radiation of short wavelengths (Rn_s) is the resultant of these two emitted and reflected short wavelengths radiation (Equation 1.17).

$$Rn_s = Rg - \alpha Rg = (1 - \alpha)\, Rg \quad (1.\ 17)$$

The atmosphere emits thermal infrared radiation towards the surface, following the principle of a black body (Mandel and Wolf, 1995). Downward atmospheric radiation, or incident longwave radiation $R_{atm} = \varepsilon_a \sigma T_a^4$ [W.m^{-2}], results from the gases and aerosols. Ta [K] and ε_a [-] are air temperature and emissivity, respectively. Atmospheric radiation increases with cloud cover. The surface reflects a fraction of the atmospheric radiation, depending on its absorption coefficient assimilated to the surface emissivity ($(1 - \varepsilon_{surf})R_{atm}$) under the assumption of the surface thermal homogeneity. Furthermore, the Earth surface emits like a gray body at land surface temperature T_{surf} [K] and with an "effective" surface emissivity ε_{surf} [-] which takes into account the long wavelengths radiation exchanges in the canopy. Hence, it emits thermal infrared radiation according to the Stephan-Boltzmann law ($\varepsilon_{surf}\sigma T_{surf}^4$) (Johnson, 2012). The net surface radiation of long wavelengths (Rn_l) is the resultant of these emitted and reflected long wavelengths radiation (Equation 1.18).

$$Rn_l = \varepsilon_a \sigma T_a^4 - \left[(1 - \varepsilon_{surf})\varepsilon_a \sigma T_a^4 + \varepsilon_{surf}\sigma T_{surf}^4\right] = \varepsilon_{surf} R_{atm} - \varepsilon_{surf}\sigma T_{surf}^4 \quad (1.\ 18)$$

Consequently, the net surface radiation Rn [W.m^{-2}] (Figure 1.3) is the balance of energy between incoming and outgoing shortwave and longwave radiation fluxes at the land-atmosphere interface can be written as follows:

$$R_n = Rn_s + Rn_l = (1 - \alpha)\, Rg + \varepsilon_{surf} R_{atm} - \varepsilon_{surf}\sigma T_{surf}^4 \quad (1.\ 19)$$

where σ is Stefan-Boltzmann constant=5.67×10^{-8} W.m^{-2}.K^{-4}

Heat conduction

The associated flux with heat conduction is the conduction heat flux, referred G [W.m^{-2}] (Figure1.3). The conductive heat exchanges in the soil are controlled by the vertical temperature gradient at the soil surface, according to the law of Fourier (Lienhard, 1981). The G flux is positive during the day (the skin surface temperature is greater than the below ground temperature) and negative at night. The diurnal and nocturnal conductive fluxes roughly compensate each other and the average daily flux is low. G depends on several factors including soil composition, amount of organic matter, minerals, water (which is strongly conductive) and air (which is weakly conductive). In the absence of sufficiently accurate spatial information on these factors, the G flux is conventionally expressed as a fraction of total net radiation (ξ=G/Rn). Generally, G represents 5-20% of Rn during daylight hours (Kalma *et al.*, 2008). Since G cannot be

directly measured remotely, several models have been proposed to estimate G based on the G/Rn ration as a function of soil and vegetation characteristics (Bastiaanssen, 1995; Burba *et al.*, 1999; Choudhury *et al.*, 1987; Jackson *et al.*, 1987; Kustas and Daughtry, 1990; Kustas *et al.*, 1993; Ma *et al.*, 2002; Payero *et al.*, 2001; Tasumi, 2003).

Heat Convection

Convection is the predominant mode of mass transfer between the surface and the atmosphere; it propagates thermal energy via eddies. The associated fluxes with this mode of energy propagation are the sensible heat flux H [W.m^{-2}] depending on a vertical temperature gradient and the latent flux LE [W.m^{-2}] associated with the quantity of water vapor introduced into the atmosphere (Figure1.3). Convective exchanges depend on fluctuations in wind speed and atmospheric scalars (temperature, humidity). In general, convective fluxes Fc are expressed, by analogy with the laws of diffusion, as the product of a transfer coefficient Kt and a vertical concentration gradient dC/dz (Lagouarde and Boulet, 2016).

$$F_C = -K_t \frac{dC}{dz} \quad (1.\ 20)$$

This equation is strictly valid in the atmosphere, but it has been extended between the surface itself and a reference level above (Figure 1.5). Assuming that the convective fluxes are conservative, and linking the turbulent diffusivities to resistive terms by an electrical analogy (Figure 1.4), it can be shown that sensible heat flux H in the case of a uniform surface and latent heat flux LE can be written as:

$$H = \rho\, c_p \frac{T_{aero} - T_a}{r_a} \quad (1.\ 21)$$

$$LE = \frac{\rho c_p}{\gamma} \frac{e_s(T_{aero}) - e_a}{r_a + r_s} \quad (1.22)$$

where ϱ [kg.m^{-3}] is the air density, c_p [J.kg^{-1}.K^{-1}] is the specific heat of air at constant pressure, $\boldsymbol{\gamma}$ [K.Pa.C^{-1}] is the psychrometric constant, T_a [K] and e_a [Pa] are respectively the air temperature and vapor pressure at the reference level z_a, T_{aero} is the aerodynamic temperature which is equivalent to an air temperature within the canopy at the evaporation level z_{aero}=d+z_{om} where d is the displacement height of the wind speed profile and z_{om} is the bare soil roughness length; e_s(T) [Pa] denotes the saturation water vapor pressure curve as a function of temperature T and r_a [s.m^{-1}] and r_s [s.m^{-1}] are the aerodynamic and bulk surface resistances, respectively. These two resistances depend on turbulent diffusivities, turbulent characteristics (wind speed, thermal gradients) and the surface and vegetation cover characteristics (height, roughness, stomatal functioning, leaf area). r_a is dependent on the turbulent properties of the atmospheric boundary layer above the surface. An unstable and therefore more mixed atmosphere (this is often the case during the day) will tend to facilitate vertical energy transfers and thus decrease atmospheric resistance while a more stable and stratified atmosphere (mostly at night) will oppose strong resistance to energy transfer (Penman, 1948) .

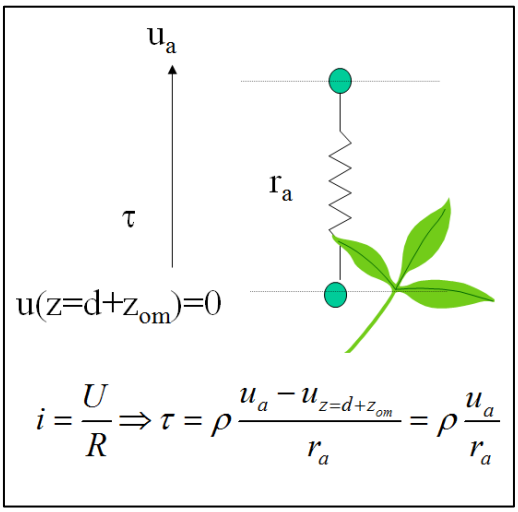

Figure 1. 4: Electrical analogue of aerodynamic resistance (I [A] is the current through a conductor between two points, U [V] is the voltage measured across the conductor , R [Ohm] is the resistance of the conductor, d [m] is the displacement height and z_{om} [m] is the bare soil roughness length; "a" refers to air).

In fact, surface temperature affects all four terms of the energy balance of equation 1.16, which takes the following form by replacing each of terms with expressions (1.19), (1.21) and (1.22):

$$(1-\xi)\left[(1-\alpha)Rg + \varepsilon_s R_{atm} - \varepsilon_s \sigma T_{surf}^4\right] = \rho\, c_p \frac{T_{aero}-T_a}{r_a} + \frac{\rho c_p}{\gamma} \frac{e_s(T_{aero})-e_a}{r_a+r_s} \qquad (1.23)$$

In the case of reduced water availability, the surface temperature adjusts so that the other dissipative terms, H and G (as well as the long wavelength radiation emitted by the surface, included in the radiation net), all of which are positive functions of temperature, compensate for the decrease in latent heat flux. The resulting increase in temperature is all the more significant as the decrease in LE is significant. There is therefore a clear relationship, in the case of vegetated surfaces, between water stress and surface temperature.

Remote sensing based energy budget models are reviewed in Courault *et al.* (2005), Farahani *et al.* (2007), Glenn *et al.* (2007), Kalma *et al.* (2008), Overgaard *et al.* (2006) and Verstraeten *et al.* (2008). The majority considers the land surface as an electrical analogue, which means that the rate of exchange of a quantity (heat or mass) between two points is driven by a difference in potential (temperature or concentration) and controlled by a number of resistances that depend on the local atmospheric environment and internal properties of the land surface and vegetation.

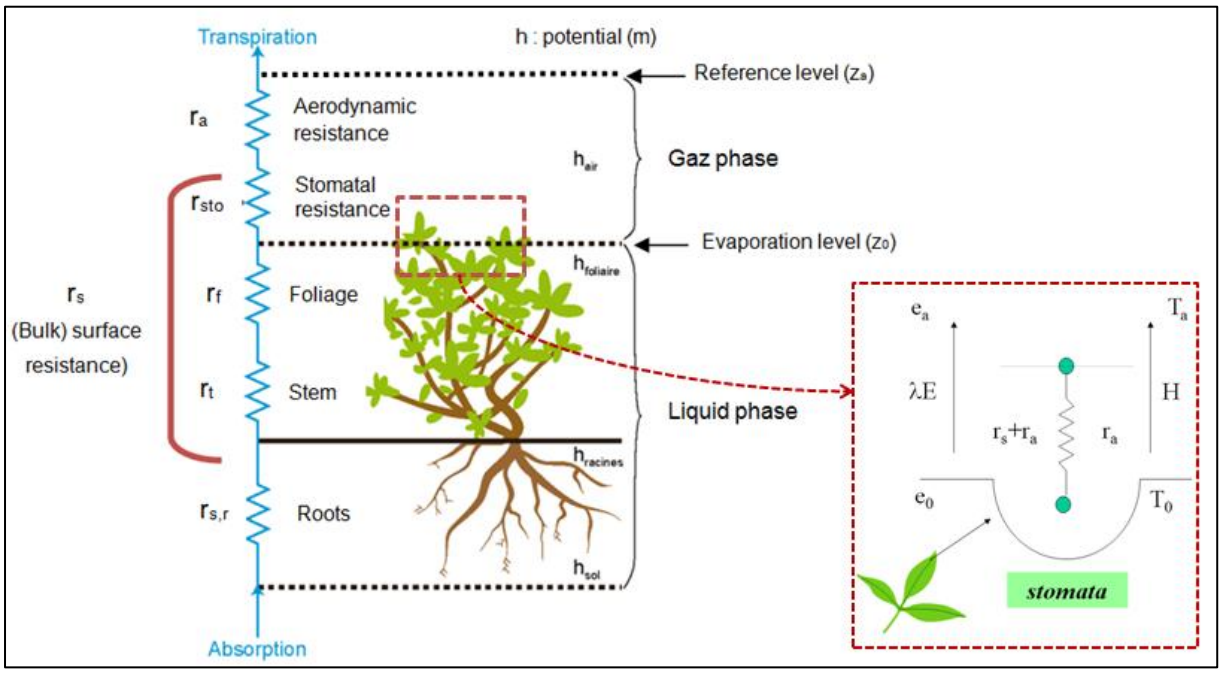

Figure 1. 5: Analogous schematization of the transpiration process under the hypothesis of a conservative transpiration flow (Source: Guyot (1999) and Boulet (2003), modified).

Two types of methods are currently used to compute LE: the so-called "single pixel" methods use information from each pixel independently of any other pixel in the image, while the "contextual" methods take advantage of thermal contrasts in the image. They provide instant estimates of latent heat flux at the time of the satellite overpass. "Single pixel" estimation methods solve the energy balance at the surface for a given pixel, independent of the rest of the image. Calculation of atmospheric resistances distributed over large areas is therefore a major challenge for these models, partly because of the difficulties encountered in the spatialized estimation of the roughness properties of the surface. To circumvent this problem, the "contextual" methods exploit the spatial variability of the surface properties, placing each pixel in its context and locating it with respect to endmembers. The most cited contextual models are the "Surface Energy Balance Algorithm for Land model (SEBAL)" (Bastiaanssen *et al.* 1998), "Mapping EvapoTranspiration with High-resolution and Internalized Calibration (METRIC)" (Allen *et al.* 2007), "Triangle method" (Carlson, 2007) and "Simplified Surface Energy Balance Index (S-SEBI)" (Roerink *et al.*, 2000). These models are based on a "single-source" (see later) scheme, and solve for *H* through a relationship with temperature gradient. The near-surface air temperature gradient obtained by solving the energy balance over carefully selected "hot and cold" (or dry and wet) pixels identified using the thermal (radiometric surface temperature) and shortwave (surface albedo and NDVI) bands of the satellite image. METRIC is based on the same structure as SEBAL but uses a reference ET (Penman-Monteith) to express the potential evapotranspiration rate. In what follows, we focus on "single pixel" methods because at kilometric-resolution (e.g. MODIS images) endmembers (spectra chosen to represent pure surface in a spectral image) are difficult to found. Moreover, SPARSE model applied in this dissertation is based on these methods.

"Single pixel" methods

Residual methods use information from each pixel independently of any other pixel in the image. Here after, we focus on these methods mainly those using thermal infrared remote sensing data on which is based the SPARSE model applied in this dissertation. A common approach to LE estimation from RS is to calculate LE as the residual term of the energy budget, *i.e.* the difference between available energy (Rn-G) and H as follows:

$$LE = Rn - G - \rho\, c_p \frac{T_{aero} - T_a}{r_a} \quad (1.24)$$

This equation is widely used for the estimation of instantaneous LE. When estimated at midday, it provides a good indicator of plant water status for irrigation scheduling. When dealing with seasonal, monthly or daily estimations, the use of ground-based ET from weather data is necessary to make temporal interpolation.

The main issue of estimating ET as a residual is the need to measure or estimate Rn and G accurately, which can be problematic under conditions such as with sparse or heterogeneous vegetation. G is normally considered a fixed fraction of the net radiation (Anderson *et al.*, 1997; Boegh and Soegaard, 2004; Norman *et al.*, 1995), and since previous studies have shown that net-radiation can be accurately determined from RS data (e.g. Boegh *et al.*, 1999), the main task becomes the determination of sensible heat flux from remote sensing data using the electrical analogue from.

SEB models employ various expressions for the aerodynamic resistance. In the reviews by Kalma *et al.* (2008) and Overgaard *et al.* (2006) , three broad approaches to describe the surface and its resistance network are distinguished: (i) "one source" methods considering the surface as a homogeneous mixture of soil and vegetation without distinction between soil evaporation and vegetation transpiration (Monteith, 1965; Penman, 1948); (ii) "two source" models taking into account vegetation and bare soil as two separate sources for energy transfers (Shuttleworth and Wallace, 1985); (iii) "multisource" models, which are essentially extensions of the "two source" model (figure 1.6) . Moreover, these models use different representations of the soil water storage, from conceptual to physical or mechanistic modeling (Boulet, 1999): Single-reservoir model, two-reservoir model derived from the Force-Restore model (Deardorff, 1978) and the discretized model which decompose the column of soil into several horizons, among which the equations of water and heat dissipation in the soil derived from Richards (1931) are applied (figure 1.6).

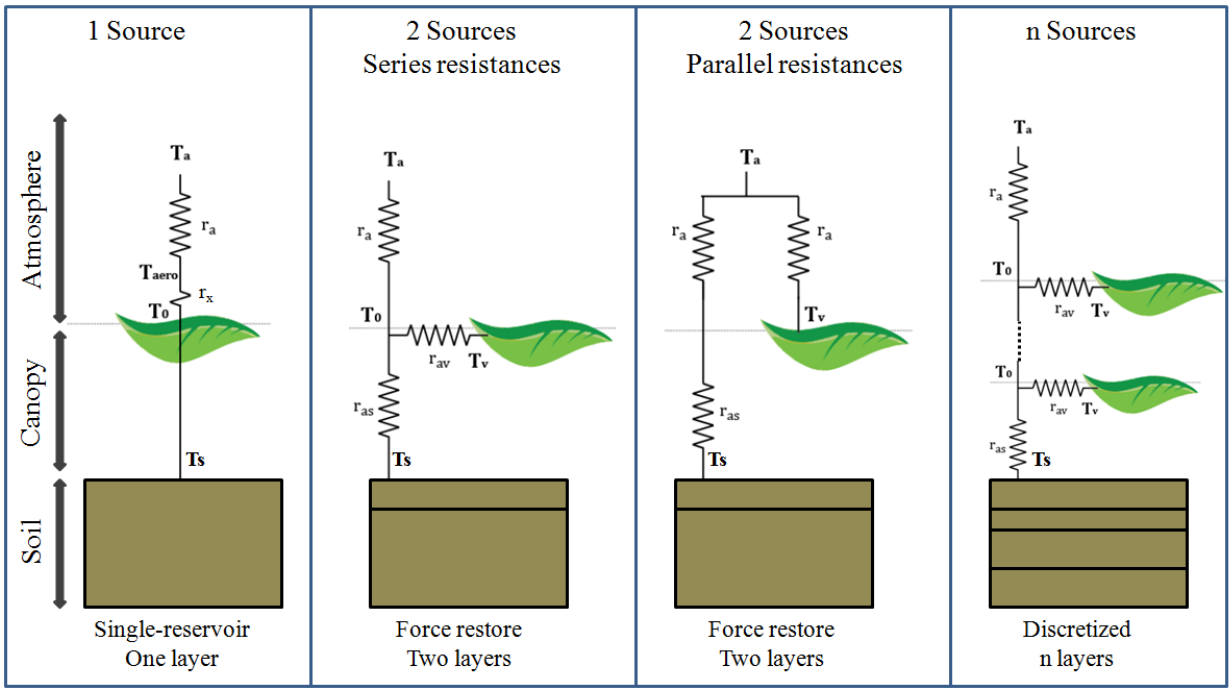

Figure 1. 6: Complexity levels of the soil and schematic diagram of the electrical resistance analogy to one-source, two-source (series and parallel approaches) and multi-layer models (Source: Boulet (1999) and Chirouze (2009), modified)

❖ *One source model*

One layer or one source models, often referred to "big-leaf" models, are derived from the approach proposed by Monteith (1965) which recognize the role of surface controls but do not distinguish between soil evaporation and transpiration in the heat exchange. They are well adapted to estimate the evapotranspiration of dense canopies (Monteith and Unsworth, 1990). They consider a stomatal resistance of the vegetation cover and an aerodynamic resistance between the surface and the atmosphere. The "big-leaf" concept assumes that the canopy is horizontally homogeneous and that the vertical distribution of surface fluxes (sensible heat and latent heat) can be represented by a single source at the "big-leaf" surface located at the conceptual height $z=d+z_{om}$ *(*figure 1.6*)*.

The one dimensional equations based on aerodynamic theory and energy balance (Monteith and Unsworth, 2007; Penman, 1948), have proved very useful in the actual crop ET estimation; because they take into account both the canopy properties and meteorological conditions (Black *et al.*, 1970; Szeicz and Long, 1969; Szeicz *et al.*, 1973). The most widely used form of the combination equation, called Penman-Monteith equation, can be expressed under the following form:

$$LE = \frac{\Delta(R_n - G) + \rho_a c_p \frac{e_s(Taero) - e_a}{ra}}{\Delta + \gamma\,(1 + \frac{r_s}{r_a})} \qquad (1.25)$$

where Rn-G [W.m^{-2}] is available energy, $\boldsymbol{\Delta}$ [kPa C^{-1}] is the slope of the saturation vapour pressure temperature relationship, (e_s-e_a) [kPa] is the vapour pressure deficit of the air, ϱ_a [kg.m^{-3}] is the air density, c_p [J.kg^{-1}.K^{-1}] is the air specific heat at constant pressure, γ

[kPa.C^{-1}] is the psychrometric constant, r_a [s.m^{-1}] is the aerodynamic resistance and r_s [s.m^{-1}] is the bulk (surface) resistance. In Equation 1.25 we can distinguish non-parametric variables (available energy, vapor pressure deficit Δ and γ) which are standard measurable climatic data; and the parametric variables (r_a and r_s) which are not directly measurable and need to be modeled.

The difficulty of using this equation, especially at regional scale, is the estimation of r_a . Differences in crop height and leaf area index (LAI) determine crop roughness and thereby r_a. Crop rooting characteristics, root water uptake and LAI describe the value of canopy resistance (r_s). The lack of information on aerodynamic properties for r_a or on the soil water status necessary for r_s makes the Penman-Monteith equation difficult to implement in operational hydrology and water management studies. This shortcoming has been solved in the irrigation community by introducing the concept of crop reference ET and crop coefficients accounting for a rough estimate of the vegetation development and a global soil moisture level deduced from a simplified water budget equation.

The temperature at the aerodynamic level T_{aero} is defined as the temperature of the air at the aerodynamic level within the canopy, and can be represented as an average temperature of the surface elements, weighted by their relative contributions to global atmospheric conductance (Moran *et al.*, 1989). This temperature is more a conceptual variable than a quantity one can measure *in situ* (Kalma and Jupp, 1990). Single source models require a method to relate T_{aero} and the remotely-sensed surface temperature (Matsushima, 2005). It has been showed that T_{aero} and T_{surf} may differ by several degrees (Kustas and Norman, 1996; Stewart *et al.*, 1994; Troufleau *et al.*, 1997). T_{aero} is greater than T_{surf} in stable conditions and lower in unstable conditions (Kalma and Jupp, 1990). This difference essentially depends on the geometric distribution of the canopy (height of the canopy, vegetation cover ratio, leaf distribution). It is compensated by adding an additional resistance term r_x , related to a factor kB^{-1} as follows (Stewart *et al.*, 1994):

$$r_x = \frac{kB^{-1}}{ku_*} \tag{1.26}$$

This kB^{-1} factor is usually determined empirically or semi-empirically as a function of atmospheric conditions, LAI and the height of the canopy (Boulet *et al.*, 2012). Several formulations have been proposed in the literature to determine kB^{-1} (e.g. the SEBS model (Su, 2002)). Other methods for linking T_{aero} and T_{surf} introduce a β factor $\beta = (T_{aero}-T_a)/(T_{surf}-T_a)$ determined empirically from LAI (Boulet *et al.*, 2012; Chehbouni *et al.*, 1997). Whereby, the radiometric surface temperature can substitute the aerodynamic surface temperature. Hence, H can be written as:

$$H = \rho\, c_p \frac{LST - T_a}{r_a + r_x} \tag{1.27}$$

❖ *Two-source models*

The one source approach makes no distinction between the soil evaporation (E) and the vegetation transpiration (T); therefore the resistances are not well defined (Raupach and Finnigan, 1988). To address these concerns, two sources energy balance models such as described by Shuttleworth and Wallace (1985) include a canopy layer in which heat and

mass fluxes from the soil and from the vegetation are allowed to interact. These models treat ET as the sum of separate flux-profile relationships governing E and T and have been initially developed for sparse canopies (e.g. Jupp *et al.*, 1998; Kustas and Norman, 1999; Lhomme *et al.*, 1994; Norman *et al.*, 1995).

In that sense, dual-source models provide a more realistic description of the main water and heat fluxes, even if the vegetation is seen as a single "big leaf" and the soil as a single "big pore" (Kustas and Norman, 1996), which is especially true for sparse vegetation, when commonly used scalar profiles within the canopy no longer apply. It also avoids the use of a parameterized kB^{-1} (Kustas and Anderson, 2009).

The two sources model assumes that in most agro-systems vegetation has access to enough water in the root zone to transpire at a potential rate, so that a modeled potential transpiration rate is a valid first guess to estimate T. This assumption implies that, if vegetation stress is not properly taken into account, the resulting evaporation will decrease to unrealistic levels (negative fluxes) in order to maintain the same total surface temperature, so that a retrieved negative evaporation is a good witness of plant water stress. The original version of two sources energy balance model (Norman *et al.*, 1995) provides two algorithms to describe the soil–vegetation–atmosphere interactions, representing, respectively, the "patch" and "layer" approaches following the terminology proposed by Lhomme *et al.* (2012). In the "layer" approach, the vegetation layer completely covers the ground and prevents the soil from interacting directly (in terms of radiation and turbulent heat transfer) with the atmospheric reference level: soil and vegetation heat sources are fully coupled through a resistance network organized in series (Figure 1.6). In the "patch" approach, soil and canopy sources are located side by side, and the soil interacts directly with the air above the canopy: soil and vegetation heat sources are thermally uncoupled and fluxes are computed with two parallel resistance schemes (Figure 1.6).

The two sources energy balance model requires land surface temperature T_{surf} observations adjusted for atmospheric effects and corrected for surface emissivity in the thermal infrared (TIR) band to produce accurate results.

❖ ***Multilayer models***

Multi-layer models have been developed since the 1960s (Waggoner *et al*, 1969), they take into account the vertical structure of the vegetation (three or more vegetation levels) (Raupach *et al.*, 1989); hence, a stomatal resistance is added for each vegetation layer, as well as a resistance to control the interactions with the overlying and underlying layers. These models are not considered suitable for hydrological modeling because they require a large number of parameters that would be very difficult to obtain.

Assimilation of TIR data in SEB models

Land surface temperature (T_{surf}), as frequently referred to as the skin temperature of the Earth's surface and is derived from remotely sensed TIR data. It is the result of the thermodynamic equilibrium dictated by the energy balance at the atmosphere, surface, and subsurface interface, and the efficiency by which the surface transmits radiant energy into the atmosphere (Kustas *et al.*, 2003). T_{surf} plays a key role in the partitioning of available energy between turbulent fluxes of sensible and latent heat. There is a strong link

between water availability in the soil and surface temperature under water stress, hence, in order to estimate soil moisture status as well as actual ET at relevant space and timescales, information in the TIR domain (8–14 μm) is frequently used (Boulet *et al.*, 2007).

Major improvements in large scale estimates of actual ET have been obtained through remote sensing methods based on TIR data, available from a variety of satellite systems (Cammalleri *et al.*, 2014). These approaches reviewed in Kalma *et al.* (2008) and Liang *et al.* (2010); appear to accurately reproduce ET over a wide range of conditions at both the satellite overpass time and daily time scales. The basic idea behind these approaches is that surface radiative temperature, and by association the surface turbulent energy fluxes, are dependent on the surface soil water content.

T_{surf} is highly variable in space and time (Prata *et al.*, 1995), mainly due to the meteorological forcing variability and of to surface properties heterogeneity. The environmental conditions impacting the T_{surf} are climatic conditions, topography, vegetation cover (density, phenology etc.), surface and root zone soil moisture, soil hydrodynamic properties (texture, porosity, etc.) and the radiative properties (albedo, emissivity).

Given the complexity of this variable, ground measurements are not satisfactory, especially when dealing with large areas. Hence, remote sensing provides the possibility of observing the T_{surf} in the spectral range of thermal infrared (8 to 14 μm) with varying temporal and spatial resolutions.

Satellite-based thermal datasets currently available and main TIR missions are summarized in annex 1. These datasets reflect a tradeoff between temporal and spatial resolution such that the systems have either high-spatial/low-temporal resolution (e.g., Landsat Thematic Mapper (TM); and Landsat Enhanced Thematic Mapper Plus (ETM+) or low-spatial/high-temporal resolution (e.g., National Oceanic and Atmospheric Administration-Advanced Very High-resolution Radiometer (NOAA-AVHRR); Terra/Aqua-Moderate Resolution Imaging Spectrometer (MODIS); Geostationary Operational Environmental Satellite (GOES). ASTER data are only available by demand and therefore provide only sporadic temporal coverage at a given site.

1.2.2.2 Soil water balance method: crop coefficient approach

The most common and practical approach used for estimating ET is the FAO-56 method (Allen *et al.*, 1998), previously adopted by Doorenbos and Pruitt (1977), on which is based the SAMIR model used in this dissertation. It is used to estimate crop water requirements based on the reference evapotranspiration (ETo) and crop coefficients.

According to the FAO drainage and irrigation paper N°56 (Allen *et al.*, 1998), distinctions are made between reference crop evapotranspiration (ET_o), crop evapotranspiration (ETc) and actual evapotranspiration (ETa). ETo is the evapotranspiration rate from a hypothetical grass reference crop with an assumed crop height of 0.12 m, a fixed surface resistance of 70 $s.m^{-1}$ and an albedo of 0.23. ETo was often confused with potential ET (ETp) (Douglas *et al.*, 2009; Torres *et al.*, 2011; Zhang *et al.*, 2010). ETc is the water lost by crops that are grown in large fields under optimum soil moisture, excellent management and environmental conditions, and achieve full

production under the given climatic conditions. ETa involves all conditions of the vegetated surface. Due to sub-optimal crop management and environmental constraints that affect crop growth and limit evapotranspiration, ETa is generally smaller than ETc.

The FAO-56 method is applied in three steps: (i) determine the climatic reference ETo, ii) apply a single (Kc) or double crop coefficient (Ke and Kcb) to get ET of a given crop under standard conditions *i.e.* optimal agronomic conditions (ETc), and (iii) apply a water stress coefficient Ks to get ET under non-standard conditions *i.e.* stress conditions (ETa) also called actual ET (ETc_{adj}).

The FAO-56 method is based on two underlying assumptions: (1) ETo represents the climate effect and (2) Kc (and Kcb) varies mainly with the specific characteristics of the crop, allowing the use of these coefficients regardless of the climates and environmental conditions (Allen *et al.*, 1998).

In the single crop coefficient approach, ETa is computed as follows:

$$ET_c = K_c * ET_0 \quad (1.28)$$

In the dual crop coefficient approach, the effects of crop transpiration and soil evaporation are determined separately. Two coefficients are used: the basal crop coefficient (Kcb) to describe plant transpiration and the soil water evaporation coefficient (Ke) to describe evaporation from the soil surface. ETc and ETa are computed as follows:

$$ET_c = (K_{cb} + K_e) \times ET_0 \quad (1.29)$$

$$ET_a = (K_s \times K_{cb} + K_e) \times ET_0 \quad (1.30)$$

More exactly, the basal crop coefficient, Kcb, is defined as the ratio of ETc to ETo when the soil surface layer is dry but where the average soil water content of the root zone is adequate to sustain full plant transpiration. Thus, it is the sum of transpiration and evaporation due to capillary rise from the root compartment passing through the dry soil surface, which explains why the Kcb during the initial stage for annual crops (before vegetation appears), as proposed in the FAO-56 paper, is above zero. In other words, the Kcb represents the baseline potential Kc in the absence of the additional effects of soil wetting by irrigation or precipitation. If the soil is wet following rain or irrigation, Ke may be large. However, the sum of Kcb and Ke can never exceed a maximum value, Kc_{max}, determined by the energy available for ET at the soil surface. As the soil surface becomes drier, Ke becomes smaller and falls to zero when no water is left for evaporation. The estimation of Ke requires a daily water balance computation for the calculation of the soil water content remaining in the upper topsoil. The dual crop coefficient approach is best for real time irrigation scheduling and for soil water balance computations.

The evaporation coefficient Ke is driven by both the water content in the soil surface and the fraction of soil actually subject to evaporation, *i.e.* exposed and wet (few).

The total evaporable water of the surface layer (TEW) [mm] is defined by water content at field capacity and wilting point (θ_{fc} [-], θ_{wp} [-]) and the depth of the evaporation layer Ze [mm] as follows:

$$TEW = (\theta_{fc} - \left(\frac{\theta_{wp}}{2}\right)).Ze \quad (1.31)$$

REW [mm] is the readily evaporable water, *i.e.* the fraction of TEW evaporating without resistance, related to soil texture and defined by the user. When the water depletion in the evaporation layer (De) [mm] is higher than the easily evaporable water (REW), a reduction factor Kr [-] is computed as follows to reduce evaporation:

$$Kr = \frac{TEW - De}{TEW - REW} \leq 1 \quad (1.32)$$

Kr is equal to 1 as long as De < REW, *i.e.* as long as there is readily evaporable water.

The fraction of soil actually subjected to evaporation, f_{ew} [0-1], is determined by to parameters: the fraction of soil wetted by irrigation (fw), linked to the type of irrigation (typically 1 for gravity irrigation, <1 for drip irrigation), and the fraction of soil actually exposed to evaporation, *i.e.* not shadowed by vegetation.

$$f_{ew} = min(1 - fc, fw) \quad (1.33)$$

For example, for flood irrigation where evaporation is not limited by the wetted fraction of soil (fw = 1), few is only controlled by the fraction cover of vegetation, f_{ew} = 1-fc.

Finally, Ke is computed using the following equation:

$$Ke = Min(Kr.(Kcmax - Kcb)\ ;\ f_{ew}.Kcmax) \quad (1.34)$$

where the first term accounts for limitation due to available energy and soil water content, and the second term accounts for limitation due to few.

The estimation of Ks requires a daily water balance computation for the root zone in order to highlight the effect of water stress on crop ET and irrigation requirement. Soil water balance is calculated on a daily basis following the scheme illustrated in Figure 1.7, although in our case surface runoff is neglected. It is expressed in terms of water depletion in the effective root zone, Dr [mm], at the end of each day i through the following equation (Allen *et al.*, 1998):

$$Dr_i = Dr_{i-1} - P_i - I_i - W_i + ETa_i + D_i \quad (1.35)$$

where Dr_i [mm] is root zone depletion at the end of day i, Dr_{i-1} [mm] is root zone depletion at the end of the previous day i-1, P_i [mm] is effective rainfall on day i [mm], I_i [mm] is net irrigation depth on day i that infiltrates the soil [mm], W is contribution from water table by capillary rise on day i, ETa_i [mm] is crop evapotranspiration on day i and D_i [mm] is water loss out of the root zone by deep percolation on day i.

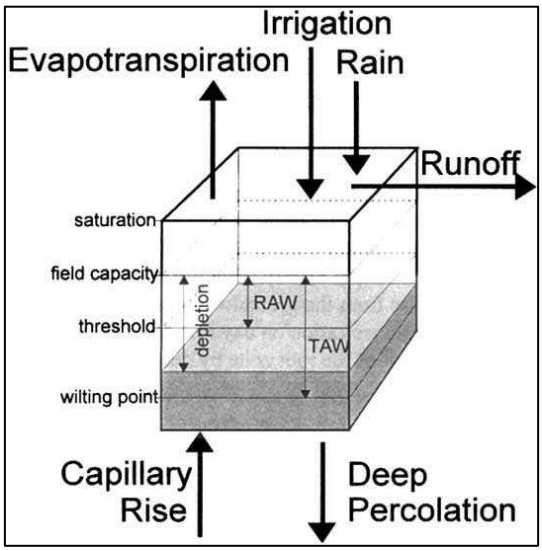

Figure 1. 7: Water balance components in the root zone (Source: Allen *et al.* (1998))

At field capacity, Dr is zero. When soil water is extracted by ET, the depletion increases and stress will be induced when Dr becomes larger than the readily available water (RAW). When the root zone depletion is smaller than RAW, then Ks = 1. For root zone depletion greater than RAW, the water stress coefficient is computed as (Allen *et al.*, 1998):

$$K_s = \frac{TAW - Dr}{TAW - RAW} = \frac{TAW - Dr}{(1 - p)\,TAW} \tag{1.36}$$

where Ks [-] is a dimensionless transpiration reduction factor dependent on available soil water ranging between 0 and 1, Dr [mm] is root zone depletion, TAW [mm] is total available soil water in the root zone [mm], RAW [mm] is readily available water in the root zone and p [-] is the fraction of TAW (*i.e.* RAW/TAW) that the crop can extract from the root zone without causing water stress.

The total available water (TAW) in the root zone is linked to the root depth and to the difference between the water content at field capacity and wilting point as expressed in equation 1.37. The two latter terms depends on the type of soil.

$$TAW = (\theta_{fc} - \theta_{wp}).Zr \tag{1.37}$$

Complementarily of the FAO-56 method and remote sensing

The FAO-56 method has long been used to monitor plot scale water budget with tools like CROPWAT (Clarke, 1998) using most of the time crop coefficients taken from the FAO tables. RS provides spatial and updated information about vegetation. The satellite images not only allow distinguishing different types of land use, but also, provide further information about the actual development of vegetation. This information is well correlated with the photosynthetic activity of plants, which is itself determinant of ET.

To compute ET on larger areas, some tools have been developed based mainly on the use of thermal remote sensing for energy balance methods, like METRIC (Allen Richard

et al., 2007). However, the increasing availability of high-resolution NDVI time series arose the coupling of the FAO-56 with remotely sensed crop coefficients (González-Dugo *et al.*, 2013; Mateos *et al.*, 2013; Neale *et al.*, 2007; Simonneaux *et al.*, 2008). This trend lead to the emergence of tools like the DEMETER concept (Calera-Belmonte *et al.*, 2005) providing Kc to farmers, the HYDROMORE tool (Sánchez *et al.*, 2010) computing the water budget of crops, or the TOPS-SIM "system-of-system" for irrigation management (Melton *et al.*, 2012). Zhang and Wegehenkel (2006) developed a model based on the FAO-56, lumped in a more complex model including the whole watershed system, and using essentially low-resolution MODIS images. Minacapilli *et al. (*2008) proposes the SIMODIS model based on a variant of FAO-56 where Kc is determined analytically using vegetation and climatic parameters, and a more physical soil modeling.

Spatio-temporal monitoring of vegetation dynamics by remote sensing is possible through the use of reflectance combinations through vegetation indices (VI). VIs are based essentially on the red band (R) corresponding with a high absorption of the radiation and the infrared band (NIR) offering a high reflectance. VIs determined over the last thirty years by different authors and their fields of application are summarized in annex 3.

The first researches relating vegetation development and canopy reflectance was carried out during the 1970s (Kanemasu, 1974; Tucker, 1979), It has been shown that the crop coefficients were linked to the VIs (Er-Raki *et al.*, 2007; Glenn *et al.*, 2011; Hunink *et al.*, 2017; Hunsaker *et al.*, 2005a; Hunsaker *et al.*, 2005b; Simonneaux *et al.*, 2008). The arguments in favor of the causal Kcb-VI relationship include the direct relationship between Kcb and the fraction of photosynthetic active radiation absorbed by the canopy (fPAR) and the relationship of these parameters with the VIs (Calera *et al.*, 2017). Ke is linked to the bare soil fraction, complementary of the fractional vegetation cover (fc) which can also be related to visible RS data (Huete *et al.*, 1985). Although the relations proposed between Kcb, fc and VIs are not theoretically fully linear, they can usually be approximated by linear relations (Choudhury *et al.*, 1994; Gonzalez-Dugo and Mateos, 2008). One pitfall of RS methods based on crop coefficient is their requirement for crop specific relations providing crop coefficient from RS data (Gowda *et al.*, 2008). Some relations may be found in the literature, either directly estimating crop coefficients from VIs, or assessing them from vegetation parameters like the leaf area index (LAI) or fc. This difficulty also applies to the relation between VIs and fractional vegetation cover (fc) required running the FAO-56. Furthermore, establishing a unique relationship between crop coefficient and spectral vegetation indices is an ongoing research topic (Er-Raki *et al.*, 2010) and many empirical linear relationships available in the literature have been derived experimentally. The interest for coupling the FAO-56 method (Allen et al, 1998) with remotely-sensed crop coefficients is raising alongside the increasing availability of high-resolution NDVI time series (González-Dugo *et al.*, 2013; Mateos *et al.*, 2013; Neale *et al.*, 2007; Simonneaux *et al.*, 2008). The low availability of such data, for financial as well as technical reasons, combined with the intermittent presence of cloud, has been a restraint to their use (J. Trout *et al.*, 2008; Pinter *et al.*, 2003; Takeuchi *et al.*, 2003). However, the recently lunched Sentinel-2 mission offers a unique opportunity to improve this monitoring thanks to high-resolution (10 m) and high repetitivity (5 days) visible and near infrared (VIS-NIR) remote sensing. Main VIS-NIR missions are detailed in annex 2.

1.2.2.3 Deterministic methods

Surface processes are driven by three important interlocking mass and energy budgets, a water balance, an energy balance and a carbon budget (Figure 1.8). Deterministic methods are based on more complex models such as land surface models (LSM) which compute the different components of energy and/or water balance. Water and energy balances are coupled by the ET flux, in the water balance; which is called LE in the energy balance. The development of LSMs since the 1960s has allowed the understanding of the complex biophysical, hydrological, and biogeochemical interactions between land surface and the atmosphere at micro- and mesoscales by providing a simple and realistic way to represent the transfer of energy, water and carbon fluxes between the land surface and the atmosphere (Zhao and Li, 2015). Soil-Vegetation-Atmosphere Transfer (SVAT) models are a subgroup of the LSMs, they solve the coupled water and energy budget equations via ET. They are generally mechanical models, describe the vertical exchanges (one-directional 1-D vertical transfers are considered while lateral interactions are neglected), and rely on a simplified representation of the vegetation cover. SVAT models are mainly used for estimating ET, surface-energy exchanges and water balance components (Olioso *et al.*, 2005) (Figure 1.8). Their application has often been limited by the lack of *in situ* data required for models forcing, calibration and evaluation. The over-parameterization of SVAT models due to their physical nature requires a multi-criteria analysis (*i.e.* several variables) over a sufficiently long period. Indeed, a major problem related to the degree of complexity of SVAT models is the equifinality problem (Beven, 2006), which is to say that the good performance of the global description of a complex model does not mean that its components are estimated correctly. Indeed, there are theoretically an infinite number of possible combinations between the different variables of the system that can lead to the same overall result. This means, for example, that a precise estimate of the ET rate of the surface does not mean that the evaporation and transpiration components are correctly simulated. Moreover, in studies of land–atmosphere interactions, a SVAT model is assumed to respond in a realistic way to changes in land surface properties, despite the fact that the model may be validated only for specific locations or surface types. However, model response is potentially sensitive not only to changes in land surface properties, but also to interactions between them (Beringer *et al.*, 2002).

Remote sensing data are used at different SVAT modeling levels, either for forcing the model input, or correcting the course of state variables in the model each time remote sensing data are available (sequential assimilation) or re-initializing unknown parameters using data sets acquired over temporal windows of several days/weeks (variational assimilation) (Courault *et al.*, 2005).

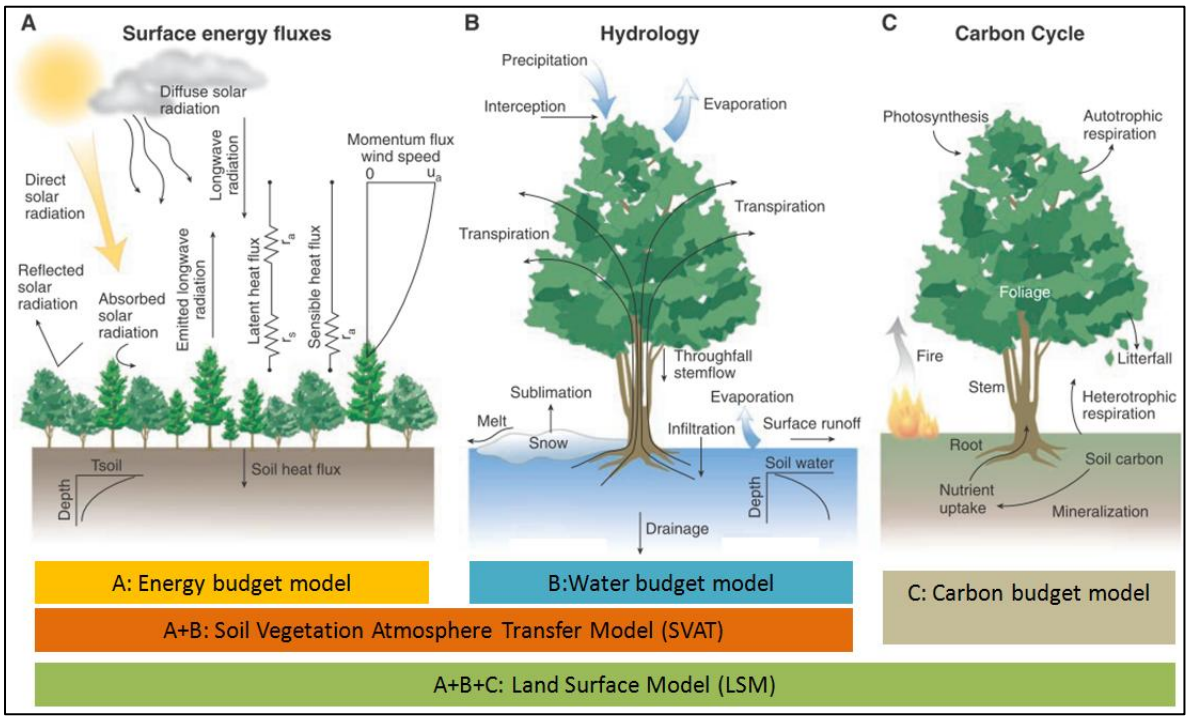

Figure 1. 8: The current generation of land surface models (LSM) treats the biosphere and atmosphere as a coupled system based on modeling the transfers of (A) energy, (B) water and (C) carbon fluxes between land surface and atmosphere. Soil Vegetation Atmosphere (SVAT) models are based on the coupled water and energy cycles (Source: Bonan (2008), modified)

1.2.2.4 Inter comparisons of ET estimation methods

Soil water balance (SWB) and the surface energy budget (SEB) approaches, as well as both approaches integrated into SVAT modeling, use remote sensing data to estimate spatially distributed ET (Minacapilli *et al.*, 2009). The SWB approach exploits only visible-near-infrared (VIS-NIR) observations to perceive the spatial variability of crop parameters. The SEB modeling approach uses visible (VIS), near infrared (NIR) and thermal (TIR) data to solve the SEB equation by forcing remotely sensed estimates of the SEB components (mainly the land surface temperature T_{surf}). The SWB approach has the advantage of high-resolution and frequency VIS-NIR remote sensing data availability against limited availability of high-resolution thermal imagery for the SEB approach. Indeed, satellite data such as Landsat or Advanced Spaceborne Thermal Emission and Reflection Radiometer (ASTER) provide accurate field scale (30–100 m) estimates of ET (Allen *et al.*, 2011a), but they have a low temporal resolution (16 day-monthly) (Anderson *et al.*, 2011).

Three categories of methodologies for the integration of satellite data in the models are distinguished; (i) forcing consists of directly integrating the data in the model as input data of the system; (ii) calibration consists of estimating a set of constant parameters of the model so that its estimates are optimal over a given period or study area. The validity of this set of parameters over other time periods or study zones can be questioned; and (iii) data assimilation is a set of techniques for combining data from a variety of sources (satellite observations, field measurements, model outputs) in order to estimate a system variables that are statistically optimal (Bouttier and Courtier, 2002; Gu *et al.*, 2009). A

classic assimilation scheme is composed of three elements: a set of observations, a dynamic model and an assimilation technique (Robinson and Lermusiaux, 2000). These techniques make it possible to use the distributed satellite data in order to correct and improve the spatialized predictions of land surface models, and also help calibrate them on large study areas.

SWB and SEB models each have their strengths and weaknesses. The RS-based SWB models provide estimation of ET, soil water content, and irrigation requirements in a continuous way. For instance, at plot scale, accurate estimates of seasonal ET and irrigation can be obtained by SWB modeling using high-resolution remote sensing forcing. However, for an appropriate estimation of ET, the SWB model requires knowledge of the water inputs (precipitation and irrigation) and an assessment of the extractable water from the soil (mostly derived from actual water content in the root zone, wilting point and field capacity), whereas, significant bias are found mainly when dealing with large areas and long periods, due to the spatial variability of the water inputs uncertainties as well as the inaccuracy in estimating other flux components such as the deep drainage (Calera *et al.*, 2017). Hence, the major limitation of the SWB method is the high number of needed inputs whose estimations are likely uncertain especially over a heterogeneous land surface due to hydrologic processes complexity. Moreover, spatially distributed SWB models (typically those using the FAO guidelines (Allen *et al.*, 1998) for crop ET estimation) generally parameterize the vegetation characteristics on the basis of land use maps (Bounoua *et al.*, 2015; Xie *et al.*, 2008), and different parameters are used for different land use classes. Nevertheless, SWB modelers generally do not have the possibility to carry out remote sensing-based land use change mapping due to time, budget, or capacity constraints and use often very generic classes potentially leading to modeling errors (Hunink *et al.*, 2017). In addition, the lack of data about the soil properties (controlling field capacity, wilting point and the water retention) as well as the actual root depths for heterogeneous areas crops, lead to limited practical use of the SWB models (Calera *et al.*, 2017). The same apply to the soil evaporation whose estimation generally rely on the FAO guidelines (Allen *et al.*, 1998). Although, it was shown that under high evaporation conditions, immediately after rain or irrigation for instance, the FAO-56 daily evaporation computed on the basis of the readily evaporable water (REW) is overestimated (Mutziger *et al.*, 2005; Torres and Calera, 2010). Hence, to improve the estimation of E at the beginning of each drydown, a reduction factor proposed by Torres and Calera (2010) was applied to deal with this problem in several studies (e.g. Odi-Lara *et al.* (2016) and Saadi *et al.* (2015)). Furthermore, since actual ET is computed based on actual soil moisture status, the limited knowledge of the actual farmers' irrigation scheduling is a further critical limitation for SWB modeling. Therefore, SWB modelers must deal with the lack of information about real irrigation, which induces unreliable estimations. Some approaches assimilate either water stress estimates based on canopy temperature (Colaizzi *et al.*, 2003) or ET estimates based on SEB models into the soil water balance models (Anderson *et al.*, 2007; Crow *et al.*, 2008; Neale *et al.*, 2012; Schuurmans *et al.*, 2003), in order to calibrate the fraction of water depleted derived from the water balance model. In a slightly different approach, some authors propose the integration of actual ET values in order to calibrate the soil water balance model in terms of the root zone storage capacity (Campos *et al.*, 2016; Hain *et al.*, 2009; Wang-Erlandsson *et al.*, 2016).

At regional scale, ET estimation is often achieved using SEB approaches, by combining surface temperature from medium to low-resolution (kilometer scale) remote sensing data with vegetation parameters and meteorological variables (Liou and Kar, 2014). Recently, many efforts have been made to feed remotely-sensed surface temperature into ET modeling platforms in combination with other critical variables, e.g., NDVI and albedo (Kalma *et al.*, 2008; Kustas and Anderson, 2009). A wide range of satellite-based ET models were developed, and these methods are reviewed in (Liou and Kar, 2014). The majority of SEB-based models are "single source" models". However, as mentioned before, separate estimates of evaporation and transpiration makes the "dual-source" models more useful for agro-hydrological applications (water stress detection, irrigation monitoring etc.) (Boulet *et al.*, 2015).

Contrarily to SWB models, most SEB models are run in their most standardized version, using observed remote sensing-based parameters such as albedo in conjunction with a set of input parameters taken from literature or *in situ* data; results are mostly instantaneous images of surface fluxes of which the extrapolation (instantaneous satellite overpass to the daily accumulation) and the interpolation (between acquisition two dates) are sources of uncertainty. On the other hand, the SEB model validation with enough data in space and time is difficult to achieve, due to the lack of enough ET field measurements but also to the limited availability of high-resolution thermal images (Chirouze *et al.*, 2014). Therefore, it is usually possible to evaluate SEB models results only at similar scale (km) to medium or low-resolution images. Indeed, the pixel size of thermal remote sensing images, except for the scarce Landsat7 images (60 m), covers a range of 1000 m (MODIS), to the order of 4000 m (GOES).

1.3 Irrigation

The irrigation schedule indicates how much irrigation water has to be given to the crop, and how often or when this water is given. How much and how often water has to be applied depends on the irrigation water requirement (IR) of the crop. IR is defined as the amount of irrigation water required to be delivered in the field to meet the CWR.

1.3.1 How much water is given?

The amount of irrigation water, usually expressed in $mm.day^{-1}$ or $mm.month^{-1}$, which can be given during one irrigation application is influenced by the soil type (influences the maximum amount of water which can be stored in the soil per meter depth), the root depth (frequent - but small - irrigation applications shallow root system and less frequently and more water for deep rooting crops) and the irrigation method (surface, sprinkler or drip irrigation).

Surface irrigation consists of a broad class of irrigation methods in which water is distributed over the soil surface by gravity flow. The irrigation water is introduced into level or graded furrows or basins, using siphons, gated pipe, or turnout structures, and is allowed to advance across the field. Surface irrigation is best suited to flat terrain, and medium to fine textured soil types which promote the lateral spread of water down the furrow row or across the basin.

Sprinkler irrigation is a method of irrigation in which water is sprayed, or sprinkled through the air in rain like drops. The spray and sprinkling devices can be permanently set in place (solid set), temporarily set and then moved after a given amount of water has been applied (portable set or intermittent mechanical move), or they can be mounted on booms and pipelines that continuously travel across the land surface (wheel roll, linear move, central pivot).

Drip Irrigation is sometimes called trickle irrigation and involves dripping water onto the soil at very low rates (2-20 litres/hour) from a system of small diameter plastic pipes fitted with outlets called emitters or drippers. Water is applied close to plants so that only part of the soil in which the roots grow is wetted, unlike surface and sprinkler irrigation, which involves wetting the whole soil surface. With drip irrigation water, applications are more frequent (usually every 1-3 days) than with other methods and this provides a very favorable high moisture level in the soil in which plants can flourish.

In the Kairouan plain, the main used irrigation techniques are drip and sprinkler irrigation. Cereals are mainly irrigated by sprinkling. The olive tree, with a density of less than or equal to 200 trees per hectare, is most often irrigated by gravity. The development of drip irrigation since 1999, facilitated by state subsidies (NOURY *et al.*, 2007), has concerned vegetables crops and fruit trees (apple, pear, peach and apricot trees), as well as new olive plantations. At the time, these crops were irrigated mainly by surface irrigation (Koukou-Tchamba, 2000). The work of (Feuillette, 2001; Kadi, 2002) showed that the conversion to drip irrigation allowed not only a reduction in labor but also an increase in the yields and the financial benefit of vegetable crops.

In most cases, CWR is supplied by rainfall and the remaining part by irrigation. In such cases IR is computed as a residual term of the water balance equation *i.e.* as the difference between the CWR and the rainfall part which is effectively used by the plants *i.e.* the effective rainfall defined as the fraction of the total amount of rainwater retained in the root zone and useful for meeting the water need of the crops.

$$IR = \mathrm{CWR} - P_{eff} + [\pm \Delta S]_0^r \tag{1.38}$$

IR is mainly estimated using RS-based SWB models, since irrigation is a component of the water balance equation on which SWB models are based. The crop coefficient method (FAO56 method) is currently the main method used for scheduling irrigations around the world (Glenn *et al.*, 2007). IR was rarely directly estimated using SEB models. Indeed, SEB outputs are generally actual ET *i.e.* its energy equivalent LE, and if irrigation is estimated, it should be computed as a residual term of the water balance equation. Exception exists, for example, Courault *et al.* (1998) used surface temperature derived from NOAA data and a SVAT model called MAGRET to find parameters linked to the irrigation over the agricultural region "la Crau" in South-Eastern France ; the predicted parameters were the beginning and the end of irrigation, frequency and water quantity diverted. IR for a typical crop and an assumed rainfall pattern may be illustrated as in figure 1.9; it is rather a dynamic variable.

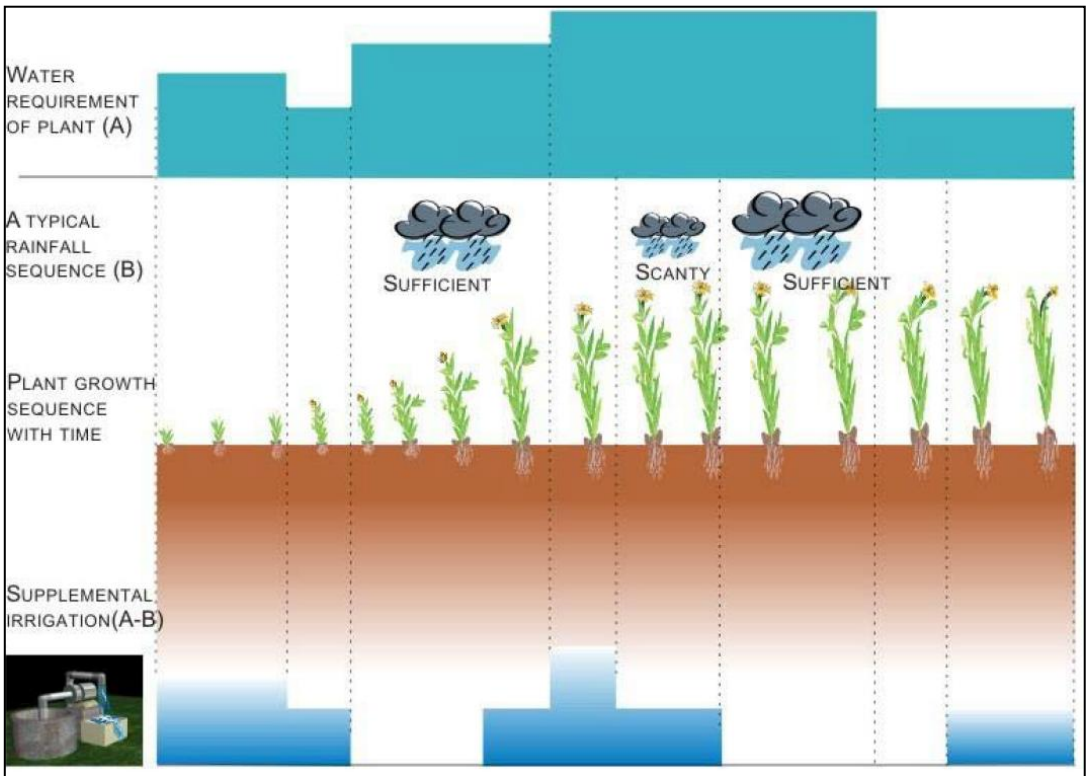

Figure 1. 9: Typical crop water requirement and corresponding water provided naturally by rain or artificially by irrigation

1.3.2 When water is given?

The total water required for crop growth is not uniformly distributed over its entire life span. The total growing season of an annual crop can be divided into four growth stages; the initial stage, the crop development stage, the mid-season stage (including flowering and grain setting or yield formation) and the late season stage (including ripening and harvest).

Since it is the period of the highest crop water needs, the mid-season stage is most sensitive to water scarcity in which water shortages occurrence lead to negative effects on the crop yield. The least sensitive to water shortages is the late season stage. Water shortages in this stage - especially if the crop is harvested dry - have only a slight effect on the yield. Care should, however, be taken even during this stage with crops which are harvested fresh (lettuce as example) which are also sensitive to water shortages during the late season stage. The initial and crop development stages are between the mid-season and late season stages with respect to sensitivity to water shortages. Some crops react favorably to water shortage during the crop development stage: they react by developing a deeper root system, which is helpful during the later stages (Brouwer *et al.*, 1989).

1.3.3 How often water is given?

Soon after irrigation, when the soil is saturated, up to the field capacity, the extraction of water from the soil by the plants is at the peak. This rate of water withdrawal decreases as the soil moisture depletes. A critical threshold is reached in the moisture content of the soil, below which the plant is stressed. Unless the soil moisture is increased by application of water, the plant production would decrease. The difference of moisture content between the maximum content of available water *i.e.* field capacity and the lowest allowable moisture content *i.e.* wilting point is called the optimum soil water, from which the interval period of irrigation water may be estimated

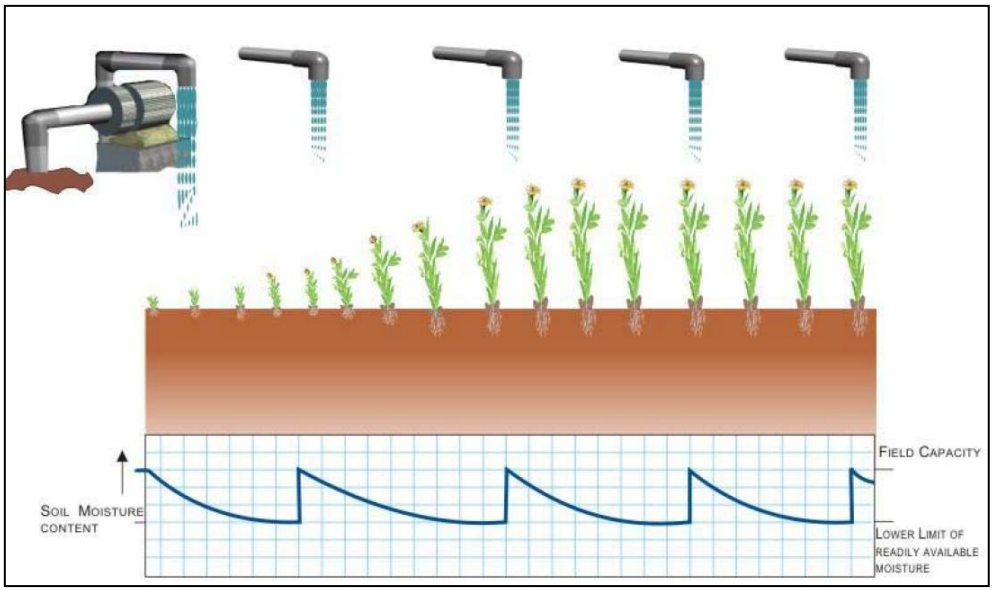

Figure 1. 10: Rise and fall of soil moisture content due to irrigation and evapotranspiration (Source: Dhrubajyoti (2009))

When sprinkler and drip irrigation methods are used, it may be possible and practical to vary both the irrigation depth and interval during the growing season. Whereas, when surface irrigation methods are used, it is not very practical to vary the irrigation depth and frequency, and it is very confusing for the farmers to change the schedule all the time. Therefore, farmers usually fix the most suitable irrigation depth and interval and keep them constant over the growing season.

Irrigation schedule can be determined either by plant observation method or by estimation method:

- **Plant observation method** is based on observing changes in the plant characteristics (plants color, curling of the leaves and ultimately plant wilting). The changes can often only be detected by looking at the crop as a whole rather than at the individual plants. The disadvantage of this method is that by the time the symptoms are evident, the irrigation water has already been withheld too long for most crops and yield losses are already unavoidable.
- **Estimation method** is based on the estimated depth (in mm) of the irrigation application, and the calculated irrigation water need of the crop during the growing

season. Thus, the influence of the climate, *i.e.* radiation, air temperature and humidity, wind speed and rainfall, is more accurately taken into account.

1.3.4 Plant response to water stress

In order to increase water savings and enhance agricultural sustainability, early detection of water stress in crops, before it causes irreversible damage and yield loss, is crucial. In water deficit settings, ET will be less than in fully irrigated conditions because deficit-irrigated plants cannot transpire water at the same rate as fully watered, healthy, and actively growing plants (NebGuide, 2009). Under the same microclimatic conditions, irrigated crops will have higher ET rates than rainfed crops. Under rainfed or deficit irrigation, the plant leaf stomata will close when the soil cannot supply water at a sufficient rate, or the root system is not extensive and efficient enough to withdraw water from the soil system to meet the atmospheric demand. Rainfed crops usually will have deeper and more extensive root systems than irrigated crops and can withdraw water from deeper soil layers. However, in the absence of rain, when the available soil water is depleted, rainfed plants will experience wilting and ET will be reduced. Beyond a certain water stress threshold, crop yield will decrease. Water stress indicators are therefore useful to diagnose the causes of crop yield variability and develop management strategies in water-limited environments.

Conventional methods for monitoring crop water stress rely on *in situ* soil moisture measurements, however, recent studies have focused on the use of remotely-sensed data as an alternative to traditional field measurements of plant stress parameters, as this provides information about the spatial and temporal variability of crops, these methods are reviewed in Ihuoma and Madramootoo (2017). The most classical indicator of crop water stress that uses RS data without using direct measurements is the crop water stress index (CWSI) based on the difference between air and canopy temperature (Idso *et al.*, 1981).

1.3.5 Irrigation efficiencies

The water that is required to irrigate a field or plot of land growing a particular crop not only has to satisfy the evapotranspiration needs for growing the crop (*i.e.* CWR), but would also include i) losses in the form of deep percolation and surface runoff while conveying water from the inlet of the field up to its tail end and ii) water requirement for special operations like land preparation, transplanting, leaching of salts, etc.

The net irrigation requirement (NIR) is defined as the amount of irrigation water required to be delivered in the field to meet the irrigation water requirement of crop (IR) as well as other needs such as leaching, pre-sowing, etc. The Gross Irrigation Requirement (GIR) is defined as the amount of water required to meet NIR plus the amount of water lost as surface runoff and through deep percolation. Hence, to reflect water losses at field scale, the field application efficiency (e_a) defined as the ratio of NIR and GIR, is used; it depends on the irrigation method and the level of farmer discipline.

$$NIR = e_a \times GIR \quad (1.\ 39)$$

1.4 Synthesis

This chapter is a state of art of the different estimation methods of the two main soil water balance components, ET and irrigation, with a special care to VIS-NIR and TIR remote sensing contribution in ET modeling. Finally, a comparative analysis between the two main approaches using remote sensing data to estimate spatially distributed ET: the SWB-based approach and the SEB-based approach, was performed, since, in this dissertation, the two applied models to our study area; SAMIR and SPARSE; and aiming to estimate ET either at field or regional scale are SWB model and SEB model, respectively.

The study area as well as the used dataset is presented in the next chapter.

Chapter 2: Study area and data processing

In this chapter, the general framework of the study area (location, climate, natural resources, land use etc.) is presented. Then, the different experimental sets and satellite data that have been collected and used during this thesis are detailed. Climate and soil data as well as land use maps are useful for agrometeorological models implementation. Other data are used for models calibration (soil moisture, evapotranspiration flux) and validation (irrigation volumes on the main irrigated areas of the region, scintillometer measurements). The processing steps of these data are also described. Finally, satellite images series and associated pre-processing are detailed. The high spatial resolution SPOT5 images series are used to feed the SAMIR model with VIS-NIR data for four agricultural seasons (2008-2009, 2011-2012, 2012-2013 and 2013-2014). The atmospheric and radiometric correction of the SPOT5 images series were based (among other pre-processing methods) on the SPOT4-Take5 high repetitivity images series acquired by CNES in the beginning of the year 2013. The low spatial resolution images series Terra-MODIS and Aqua-MODIS are used to feed the SPARSE model with VIS-NIR and TIR data.

2.1 Study area description

2.1.1 Geographic location

The Merguellil watershed (Figure 2.1) is a large watershed in Tunisia (1540 km²), it has a relatively mountainous upstream part (1200 km²) with contrasting topography and land use, and a downstream part, a vast plain mostly devoted to agriculture; the outlet of the upstream subcatchment is the el Haouareb dam, built in 1989 which receives the waters of the Merguellil wadi (Leduc *et al.*, 2005). The downstream plain is the Kairouan plain, our study area (Figure 2.1), located 9°30' E - 10°15' E and 35°N - 35°45' N, southwest of Kairouan city and surrounding the village of "Sidi Ali Ben Salem".

The Kairouan plain is a low-lying plain (less than 100 m) whose water flows reach closed depressions *i.e.* sebkhas; Sebkha of el-Kalbia and Sebkha of sidi-el-Heni; acting as a base level for the two main wadis in the region; Merguellil wadi and Zeroud wadi, respectively. It is surrounded by the Sahel hills to the east and by mountains to the west (Jebel Ouesslat, Jebel Cherichira, and Jebel Touila) (Figure 2.1).

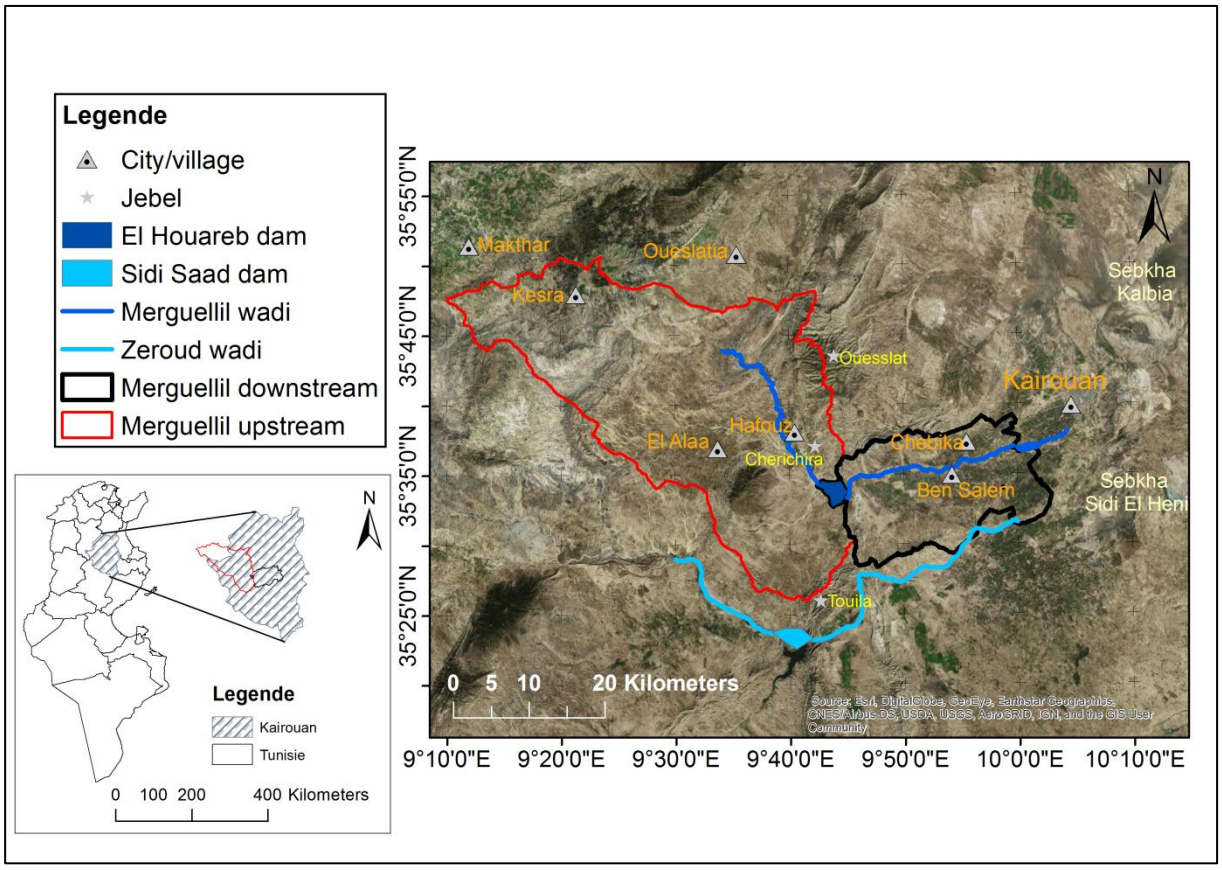

Figure 2. 1: The upstream and downstream parts of the Merguellil watershed in central Tunisia

The climate of this region is a semi-arid climate with very high precipitation variability (average annual rainfall ranging from 250 to 500 mm/year); dry summers, wet winters and large thermal amplitudes.

Various water and soil conservation works were carried out in the Merguellil basin such as hill lakes and dams, which significantly reduce surface runoff and therefore protect the El Haouareb dam from rapid siltation; contour ridges that locally reduce

erosion processes and retain rainwater; and artificial groundwater recharge areas. However, these structures have been poorly maintained and managed, resulting in successive drying of the El Houareb dam (Cudennec *et al.*, 2003). The dam has altered the balance of water intakes in the plain which leads, outside of flood periods, to dry out the portions of wadis situated downstream of the dam (Leduc *et al.*, 2007).

2.1.2 Climat data

The Kairouan plain is part of the arid bioclimatic zone with a temperate winter (Barbery and Mohdi, 1987). Indeed, the Merguellil basin is sometimes influenced by a temperate climate, specific to the cold and rainy Tellian mountainous of northern Tunisia and at other times by the arid desert climate typical of southern Tunisia. However, du to its topography, this basin is more influenced by Southern climate than by the North one (Bouzaiane and Laforgue, 1986).

2.1.2.1 Rainfall

In central Tunisia, the rainy season extends from September to April, and in summer the rains are almost absent. Precipitation is mainly rainfall, with dew and mist are insignificant due to quasi-permanent atmosphere dryness. In the Kairouan region, annual mean rainfall ranges from 265 mm in the plain to 515 mm in the highest part of the catchment (Alazard *et al.*, 2015).

The Merguellil watershed is characterized by high interannual and spatial precipitation variability with intense floods and droughts. The annual rainfall measured between 1986 and 2016 at the Kairouan SM meteorological station (9°32' 40" E - 35°22' 60" N) is illustrated in figure 2.2. In this figure, totals are computed for hydrological years, from September to August. The average annual precipitation is about 320 mm. 2000-2001 was the driest hydrological year, with a total annual rainfall of 160 mm. The wettest hydrological year was 1989-1990, with 575 mm of annual rainfall.

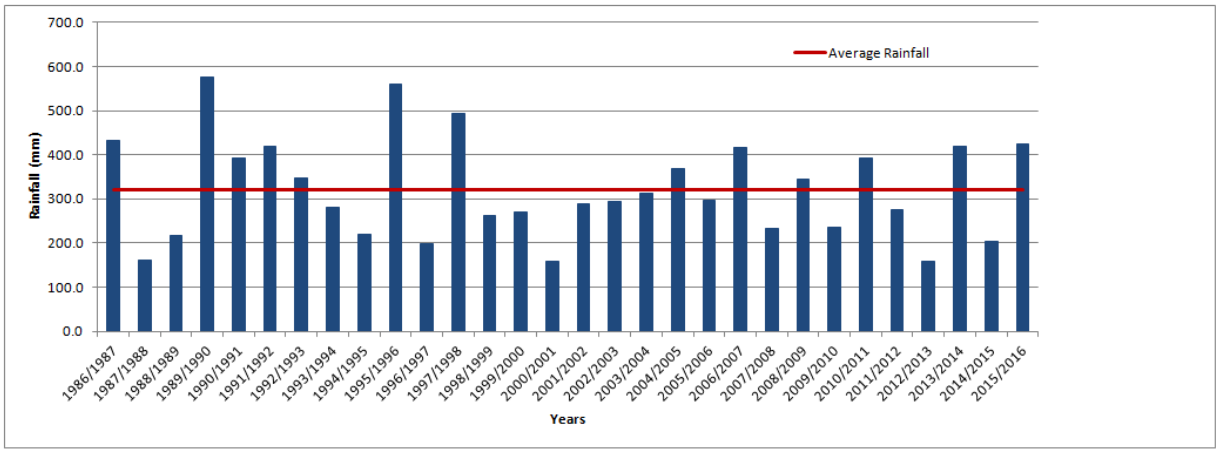

Figure 2. 2: Kairouan SM station annual precipitation during the time series period 1986-2016

Moreover, average monthly precipitation measured in the same meteorological station is shown in figure 2.3, showing significant irregularities in inter-monthly rainfall throughout the year. The most intense downpours are recorded in September and October. Generally, winter rains are often of low intensity compared to autumn rains,

whereas in summer rains are rare or absent, which is a characteristic of semi-arid regions. As annual rainfall averages fall below 400 mm, summer and spring drought affects plant development and yields (Gorrab, 2016).

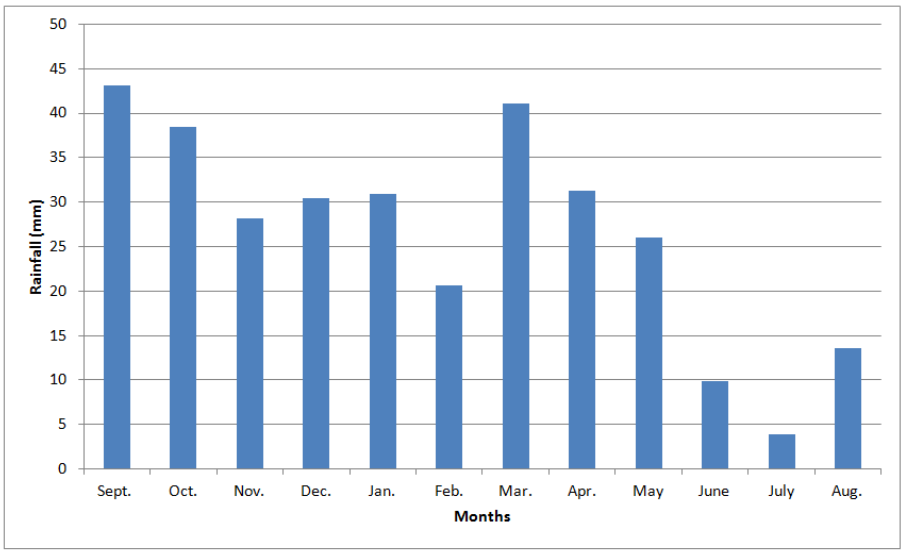

Figure 2. 3: Average monthly rainfall variation of the Kairouan SM station (1986-2016).

2.1.2.2 Temperature

Analyzing the temperature data for the Kairouan station during the last 30 years (1986-2016) (Figure 2.4), it can be seen that the average monthly temperature oscillates between 10°C and 28°C. Generally the coldest months are December, January and February with average monthly temperatures below 15°C. The warmest months are July and August with an average temperature of about 28°C. This temperature variation in proves the region climate aridity. Warming at Kairouan during the last 50 years (1951–2002) is statistically significant (0.29°C/10 years), also minimum temperatures have increased significantly (Mougou *et al.*, 2011).

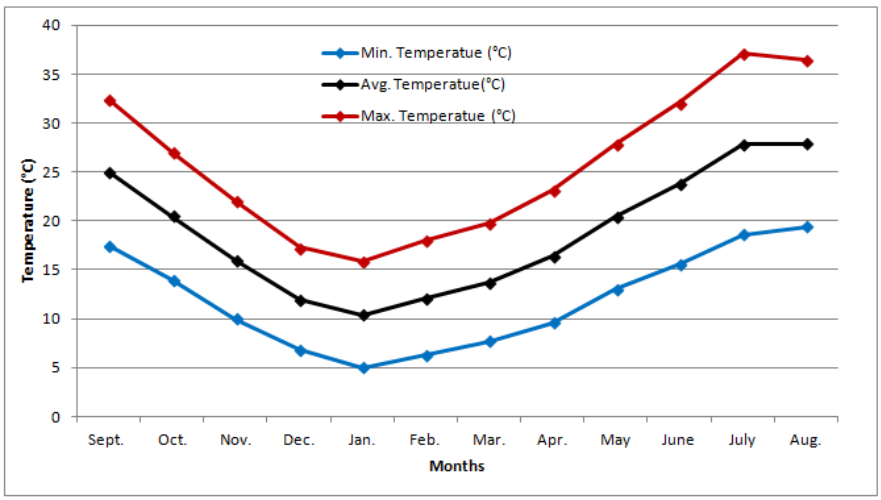

Figure 2. 4: Monthly average air temperature variation in the Kairouan Station (1986-2016)

2.1.2.3 Relative humidity

The average monthly relative humidity in the region varies between 55% and 70% during the cold season and between 40% and 55% during the warm season. The climate is therefore moderately dry from September to April and very dry from May to August, which explains the atmospheric clarity (Bouzaiane and Laforgue, 1986).

2.1.2.4 Wind conditions

The prevailing wind is from the north and north-west direction in winter and from the south and south-west in summer. Winds are generally light winds (speed less than 50 $km.h^{-1}$). Two characteristic winds of the region are worth noting:

i- The sirocco is a warm, dry wind of Saharan origin, often accompanied by sand. It blows between April and September (between 20 and 55 days per year) and causes significant temperature increases of up to 50°C and can last for 12 successive days. Annual mean sirocco days recorded during 1975 to 1995 were 41 (minimum 13; maximum 60) (Mougou and Henia, 1998).

ii- Jebbali is a cold winter wind. It begins on the Algerian massifs (Bouzaiane and Lafforgue, 1986).

2.1.3 Water Resources

The water resources of the Merguellil watershed are characterized by a very high complexity, linked in particular to a spatial disparity in rainfall, to the interconnection of surface and underground flows, to water withdrawals for various uses (agricultural, domestic and industrial), to water and soil conservation works, and to large dams (El Haouareb and Sidi Saad) located in the downstream part of the watershed (Kingumbi *et al.*, 2007).

2.1.3.1 Surface water resources

The Merguellil watershed (Figure 2.5) is mainly drained by the Merguellil wadi. It drains a vast basin of about 8600 km and collects surface water from most of central Tunisia from the Tunisian-Algerian border. When large floods occur, usually during the months of September, October or April, the waters of the Wadi Zeroud flooded a large part of the Kairouan plain, especially its southern shore.

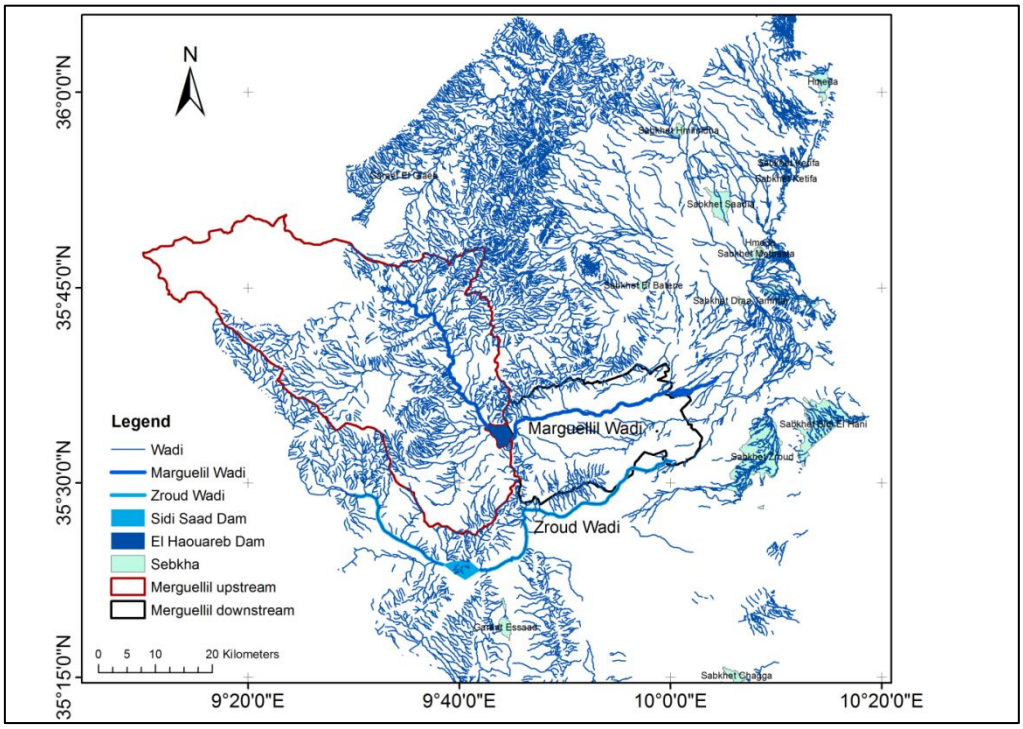

Figure 2. 5: Hydrographic Network of the Merguelil and Zeroud wadi (Source: SIG Merguellil, AMETHYST project)

During the autumn of 1969, the region of Kairouan experienced intense floods. In September 1969, the rainfall was 145 mm (with 127 mm over six days), four times the monthly average. This flood was followed by a second more intense flood in October 1969 (three times larger than in September, 428 mm). These exceptional floods are part of the remarkable rainfall events in the Merguellil watershed (Bouzaiane and Laforgue, 1986).

2.1.3.2 Groundwater resources

The aquifer system of the plain of Kairouan is considered as the most important reservoir of Central Tunisia (about 3000 km), with several aquifers stacked on top of each other and communicating most often between them. The natural recharge of the Kairouan aquifers was estimated at 57 Mm^3/year (Besbes, 1975; Chaieb, 1988). The outlets of this hydrogeological system are the hydraulic boundaries of the Cherbai, Sidi El Hani and Kalbia border sebkhas. The discharge of the water table takes place towards the sebkhas where the waters are subjected to a strong evapotranspiration (natural discharge).

The Kairouan aquifer, of regional importance, is overexploited for irrigation as well as for drinking water supply. This is due to the continued increase in the population occupying the plain (564900 inhabitants in 2011) and the fact that water withdrawals increasingly exceed natural inputs. The intensification of agriculture since the 1970–1980s has relied on groundwater supply. The tendency is to intensify agriculture, not necessarily with additional wells, but by the deepening of existing wells to increase their capacity. The main irrigated crops are horticultural crops, cereals and orchards. The Tunisian State has invested in public and collective wells in some areas, whereas others are private and individually managed. However, illicit drilling and pumping were rapidly developed, while water authorities tried to maintain situational awareness by conducting regional inventory

of the pumping wells and maintaining a regional network to monitor water-table levels (Massuel *et al.*, 2017). The evolution of the number of private wells in the Kairouan plain from an inventory done in 2010 (approximately 2,066 private pumping wells; dug wells and boreholes, for a total irrigated area of 12,000 ha within the 700 km² of the northern part of the plain) was studied by Massuel *et al.* (2017); they found that this evolution follows a steep growth often qualified as exponential (Figure 2.6).

The increase in water withdrawals from the Kairouan aquifer is the cause of its overexploitation. The overexploitation of aquifers is perceptible through a general decline in the piezometric level from 0.25 to 1 m per year for the last two decades and an average annual drawdown of around 0.30 m for the period 1995-2007 (Leduc *et al.*, 2007). The Kairouan plain aquifer has presented a general drop of the piezometric head of about 30 m over the last 40 years (Jerbi *et al.*, 2014). Figure 2.7 shows an example of a piezometer in the Kairouan Plain in which a considerable decline in the piezometric level is noted.

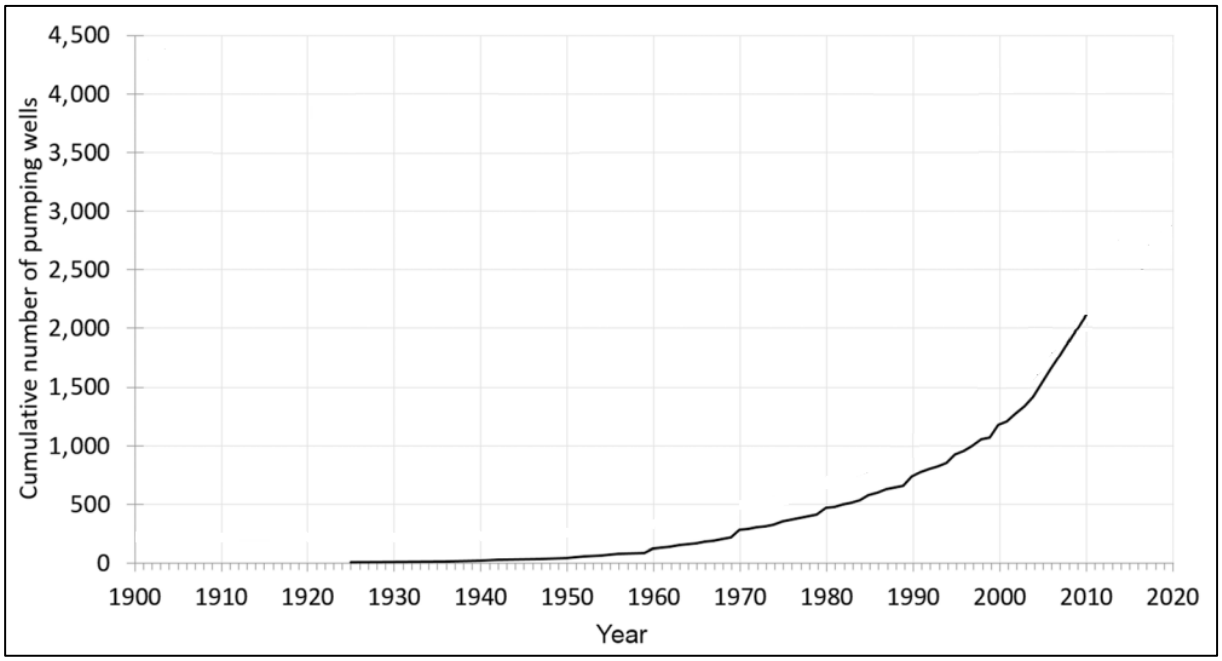

Figure 2. 6: Exponential evolution of the cumulative number of private pumping wells from the 2010 inventory (Source: Massuel *et al.* (2017))

In an attempt to stop overexploitation, the authorities initially intervened on supply through the management of dams and then on demand, by setting up a "back-up area" (areas where drilling is prohibited) supposed to compel the drilling of new wells, since 1991. However, the Kairouan aquifer remains a collective resource in free access: the restrictive regulations are not respected and the wells continue to proliferate especially after the revolution (January 2011).

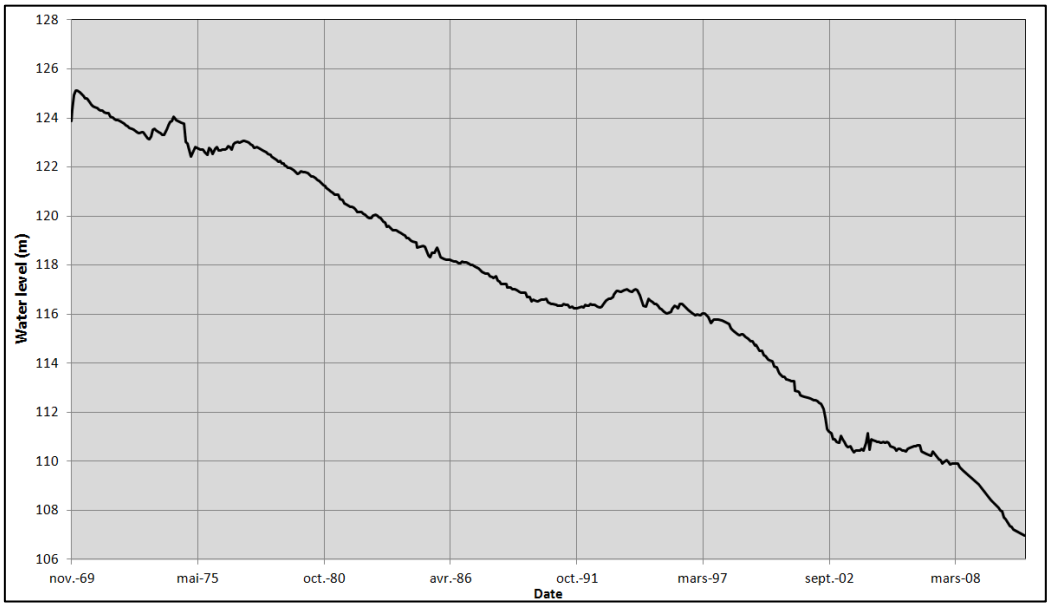

Figure 2. 7: Variation of the Kairouan aquifer piezometeric level during 1969-2008: Example of the El Grin piezometer (9°50' 52" E; 35° 36' 13" N) (Source, DGRE)

2.2 Land use maps

Land use in the Kairouan plain is intimately linked to climatic factors as well as soil and available water resources. Land use maps were available for 2008–2009 (Shabou, 2010), 2011–2012 (Chahbi *et al.*, 2014), 2012-2013 (Chahbi, 2015) and 2013–2014 (Chahbi, 2016); they include eight, six, six and seven land use classes, respectively (only agricultural area is taken into account). These classifications were obtained by applying a multi temporal decision tree, which allows the identification of crop types based on NDVI thresholds derived from ground truth datasets.

In order to validate these remotely-sensed classifications, confusion matrix were produced for each map by comparing the classification results to actual land use for more than 100 validation fields (independent from the training data). Test fields data collection (land use, crop characteristics, estimated crop coverage rate, etc.) was a periodic work to which I took part since 2014. This analysis showed an overall accuracy of approximately 97%, 80%, 85% and 88%, for the 2008–2009, 2011-2012, 2012-2013 and 2013-2014 seasons, respectively.

The most recent land use map (2013-2014) of the study area, given in figure 2.8, shows that the main occupation of agricultural land in the Kairouan plain is non-irrigated olive trees that occupy 41% of the plain. The olive tree is particularly adapted to the specific characteristics of the arid zones. Irrigated tree crops (4%) and annual crops (12%, mainly durum wheat and barley) are the other major land uses. Market gardening crops occupy also a significant percentage of areas such as autumn vegetables (4.5%) and summer vegetables (4%). During the summer, they consist mostly of tomatoes and peppers, and in smaller proportions watermelons and melon, while in autumn many plots are used for growing peppers and beans. The percentage of bare soils (rangeland and fallow) is important (18.4%) due to the hydric constraint that becomes more and more limiting in the plain. The lack of rain often incites farmers to decide not to sow or to abandon the plots originally planted in cereals. Moreover, the unfavorable soil characteristics and the extension of the zones affected by the salinization are other factors explaining the

increase of the uncultivated soils. These soils are vulnerable areas exposed to various degradation forms (water and wind erosion).

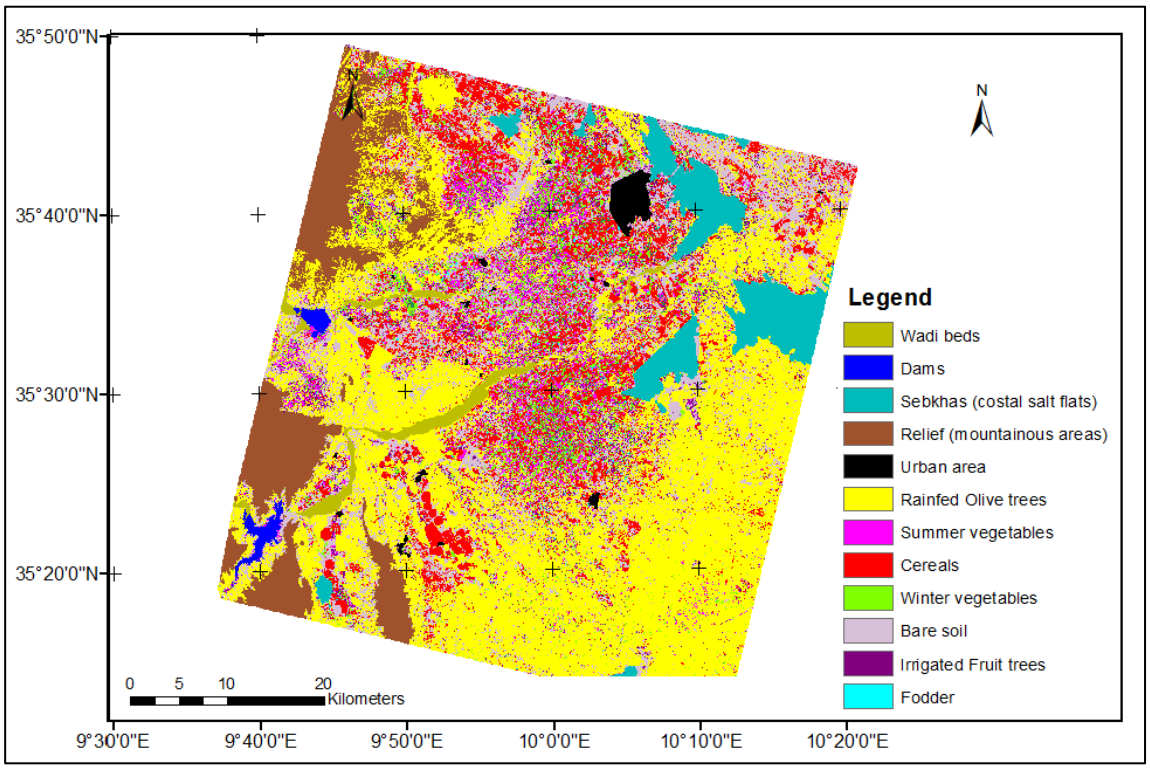

Figure 2. 8: Land use map of the Kairouan plain obtained by the classification of SPOT 5 multi-date images for the 2013/2014 agricultural season.

2.3 Observed irrigation data

Information on actual irrigation volumes at scales ranging from plot to perimeter is essential for the validation of the SAMIR model irrigation estimates.

a. Perimeter scale

The dominant structure for irrigation in the Kairouan plain is the Agricultural Development Group (Groupement de Développement Agricole, GDA —in French) (Figure 2.9). Monthly irrigation volumes were obtained at the scale of each GDA irrigated sector. It was assumed that these data were trustworthy since these entities manage a collective well equipped with a meter, providing the water to the plots inside the perimeter. However, some plots outside the official perimeter also benefit from this water and in the frame of the acquisition of our validation data, they were delineated with the help of the irrigation manager. Conversely, no private well is exploited inside the GDAs, so that the monthly volumes collected can be reliably linked to the declared cultivated area.

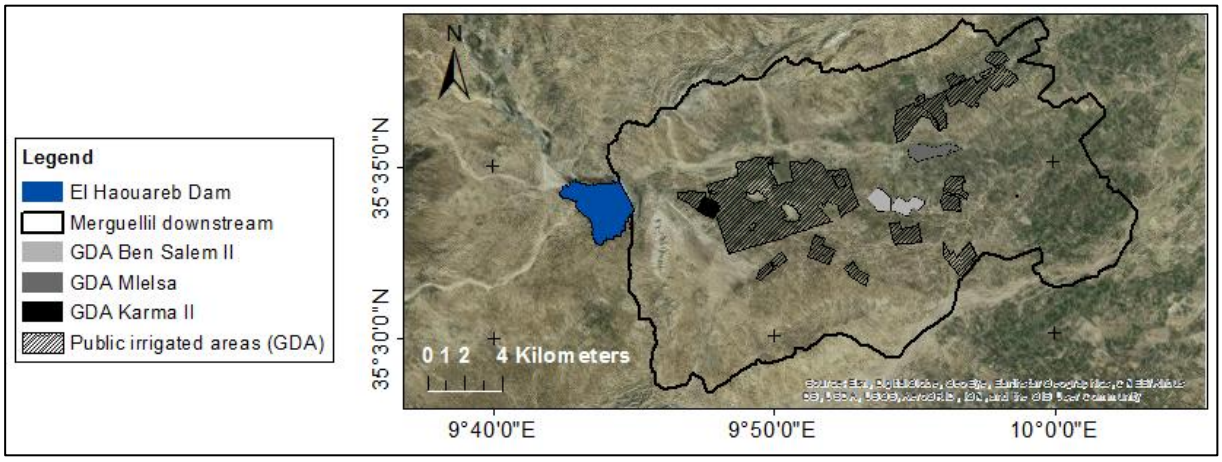

Figure 2. 9: Geographic location of the GDAs in the study area

The irrigation data (2008-2015) of three GDAs, Ben Salem II, Mlelsa and Karma II extending on 267 ha, 225 ha and 106 ha, respectively, were collected within the framework of this thesis (figure 2.10). The pumped volumes are obviously dependent on each GDA area, however, the general shape is the same and the peaks are always reached in summer with the decrease in rainfall and the summer vegetables requiring a lot of water.

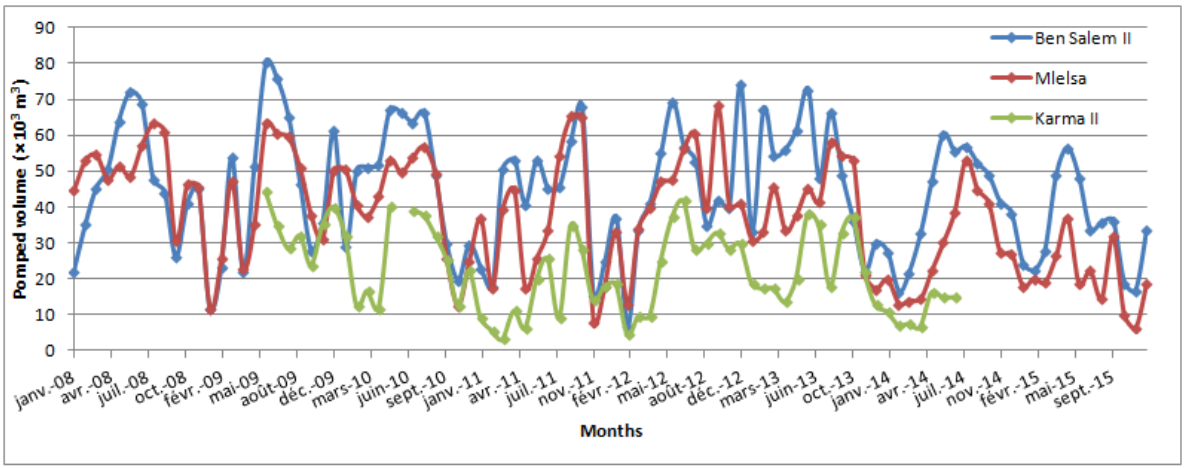

Figure 2. 10: Monthly pumped water volume in the Ben Salem II, Mlelsa and Karma II GDAs.

b. Plot scale

Field surveys conducted in 2013 in Ben Salem II, Mlelsa and Karma I and Karma II GDAs were carried out to collect plot-scale irrigation data. The irrigation volumes invoiced to the owners (or farmers) obtained from the managers of the collective perimeters (GDA) were combined with the identification of each owner's plot (or plots) carried out in the field thanks to the aid of the managers in charge of the water distribution. Thus, one irrigation volume was obtained per "name". The term "name" refers to one or more plots belonging to the same owner, or cultivated by the same farmer, corresponding to a single invoiced volume. Finally, 106, 76 and 34 "names" were identified for the GDAs Mlelsa, Karma I and Karma II respectively. For the GDA of Ben Salem II the invoicing was done at the level of only eight blocks.

2.4 Remote sensing data

2.4.1 High-resolution satellite imagery

Acquisition of SPOT5 image time series were planned over the plain: Nine, six, thirteen and nine SPOT5 images were acquired for the 2008–2009, 2011–2012 , 2012–2013 and 2013-2014 seasons, respectively (Figure 2.11). These images were used to feed the SAMIR model with NDVI data allowing the vegetation dynamic monitoring.

For the 2012-2013 season, we benefited also from images acquired in the frame of the SPOT4-Take5 experiment (SPOT4-Take5, 2013) which occurred during the first half of 2013 and whose main purpose was to simulate the revisit frequency and resolution of Sentinel-2 images to help users set up and test their applications and methods before the mission is launched. In this frame, SPOT4-Take5 images at 20 meters resolution were acquired every 5 days from 3 February to 18 June 2013 over the Kairouan plain, but only 14 dates were cloud free among the 28 images acquired (Figure 2.11).

The longest gap in the SPOT4-take5 time series was at the beginning of the period, as the first correct image was acquired on 10 March 2015, which means 40 days without image data. This is quite long regarding vegetation monitoring and emphasizes the limitation of a five-day revisit frequency even in semi-arid areas (frequent cirrus clouds can be observed over the study site). However, in our case, this gap was filled using the SPOT5 satellite, which successfully acquired two images, thanks to the programming capabilities of this sensor and its oblique viewing agility allowing observing areas on cloud free days. This is interesting since it shows that combining Sentinel-2 data with other sensors (Landsat 8, SPOT6, etc.) may still be necessary in many places to get consistent high-resolution time series. Another way to bridge the gaps in the time series would be to use fusion methods using medium-resolution images to estimate high-resolution signatures (Gao *et al.*, 2006).

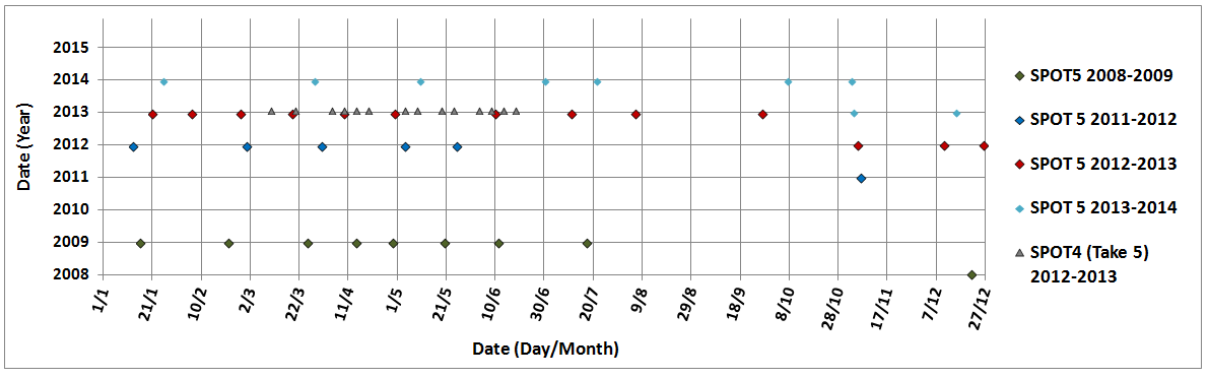

Figure 2. 11: Acquisition dates of the SPOT images.

SPOT images processing

Those images require processing in order to get rid of geometric and radiometric measurement errors.

a. Geometric corrections

A raw satellite image is affected by geometrical deformations due to the relative movement of the sensor during acquisition, its angle of view, the rotation of the Earth and the geometry of the Earth surface (curvature and relief). These images cannot be

stacked with maps of the same area. Hence, satellite image geometric correction is paramount since it allows remote sensing derived information to be related to other thematic information in Geographical Information System. In our case, the coordinate system chosen is UTM, 32nd Zone, North.

The image acquired on 5 November 2012 was first corrected using orthorectification and georeferenced using GPS points. This image was used as a reference image for the geometric correction of the subsequent SPOT5 campaigns. The subsequent images were first orthorectified and then georeferenced regarding the reference image using a first-degree polynom adjusted on a set of 20-30 points control points selected manually all over the image. The resulting Root Mean Square (RMS) was usually less than 0.5 pixel, the equivalent of 5 m for SPOT images, which is valid for this type of data. Geometric correction was performed using ENVI software.

b. Radiometric corrections of SPOT5 image time series

There are three types of radiometric corrections: calibration of sensor values to get physical data, correction for the geometric variation in the image acquisition (satellite view angle and topography) and atmospheric correction (absorption and scattering of solar radiation).

SPOT5 images (2008-2009 and 2011-2013) were radiometrically corrected to obtain top of canopy (TOC) reflectance on the basis of physical modeling corrections using the Simplified Method for Atmospheric Corrections (SMAC) algorithm based on the 6S radiative transfer model (Rahman and Dedieu, 1994). The SMAC 6S model was applied for each image using values of atmospheric optical depth and water content taken from a photometer located in the area and part of the AERONET network (Aeronet). The corrections for the 2008-2009 and 2011-2012 image time series were done by Zaghouani (2013) and for the 2012-2013 and 2013-2014 seasons, pre-processing was done in the frame of this thesis.

The SPOT4-take5 series were provided already corrected using the Multi-sensor Atmospheric Correction and Cloud Screening (MACCS) algorithm taking into account both temporal and spectral approaches for retrieving the aerosol optical thickness (AOT)(Hagolle *et al.*, 2015).

c. Internal radiometric normalization of 2012-2013 season's SPOT5 and SPOT4-take5 images time series

Due to the uncertainties in the atmospheric parameters, and in order to eliminate time profile artifacts due to radiometric correction discrepancies within the time series, an additional inter-calibration between images acquired in 2012-2013 was achieved (both SPOT5 and SPOT4-take5 time series) and was applied only to the two SPOT bands used for the NDVI computation, *i.e.* XS2 (red band) and XS3 (NIR band). Among the several methods of radiometric normalization (Furby and Campbell, 2001), the pseudo-invariant features (PIFs) method is widely used (Eckhardt *et al.*, 1990; Paolini *et al.*, 2006; Schott *et al.*, 1988; Schroeder *et al.*, 2006). Indeed, the radiative transfer model shows that for a flat topography and an assumed spatially homogeneous atmosphere, the reflectance can be linearly related to the image digital numbers DNs (Schott *et al.*, 1988). This relative approach allows calibrating all images with similar atmospheric conditions with one image used as a reference. In our case, the seasonal average image was used. Hence, pseudo-invariant features were identified for which a constant reflectance value could be assumed

over time. Thus, an additional normalization of the image time series was achieved by linear correction of the identified inconsistent dates as it was done by Houlès *et al.* (2006) and Simonneaux *et al.* (2008).

The PIFs method was applied to the SPOT5 and SPOT4-take5 image time series. 28 invariant objects were identified manually in the scene by visually comparing pairs of distant dates in the SPOT5 2012-2013 image time series (*i.e.*, 5 November 2012 and 10 June 2013). Then, for these 28 objects, the reflectance of one band at each date is plotted against the reflectance of the average image of this band (Figures 2.12 and 2.13). The quality of the invariant objects is confirmed by the determination of the linear fit. However, whereas in some cases the regression fits the 1:1 line (Figures 2.12a and 2.13a), in other cases the regression line is significantly different from the 1:1 line, showing a problem in the quality of the atmospheric correction Figures 2.12b and 2.13b). These discrepancies are more frequent for the SPOT5 time series, which is not surprising as each date was corrected independently, whereas the SPOT4-take5 series was corrected using the MACCS algorithm taking into account the temporal dimension of the series. When the deviation from the 1:1 line was important, the linear correction was applied to the image to match it with the average image.

For the SPOT5 time series, eight images were corrected while for the SPOT4-take5 time series, seven dates were linearly corrected, and one date was discarded (20th of March) because of the strong scattering of the reflectance due to haze (Figure 2.13c). Figures showing the comparison, between each SPOT5 and SPOT4-take5 images and the average image of the time series for the 28 invariant sites are given in annex 4.1.

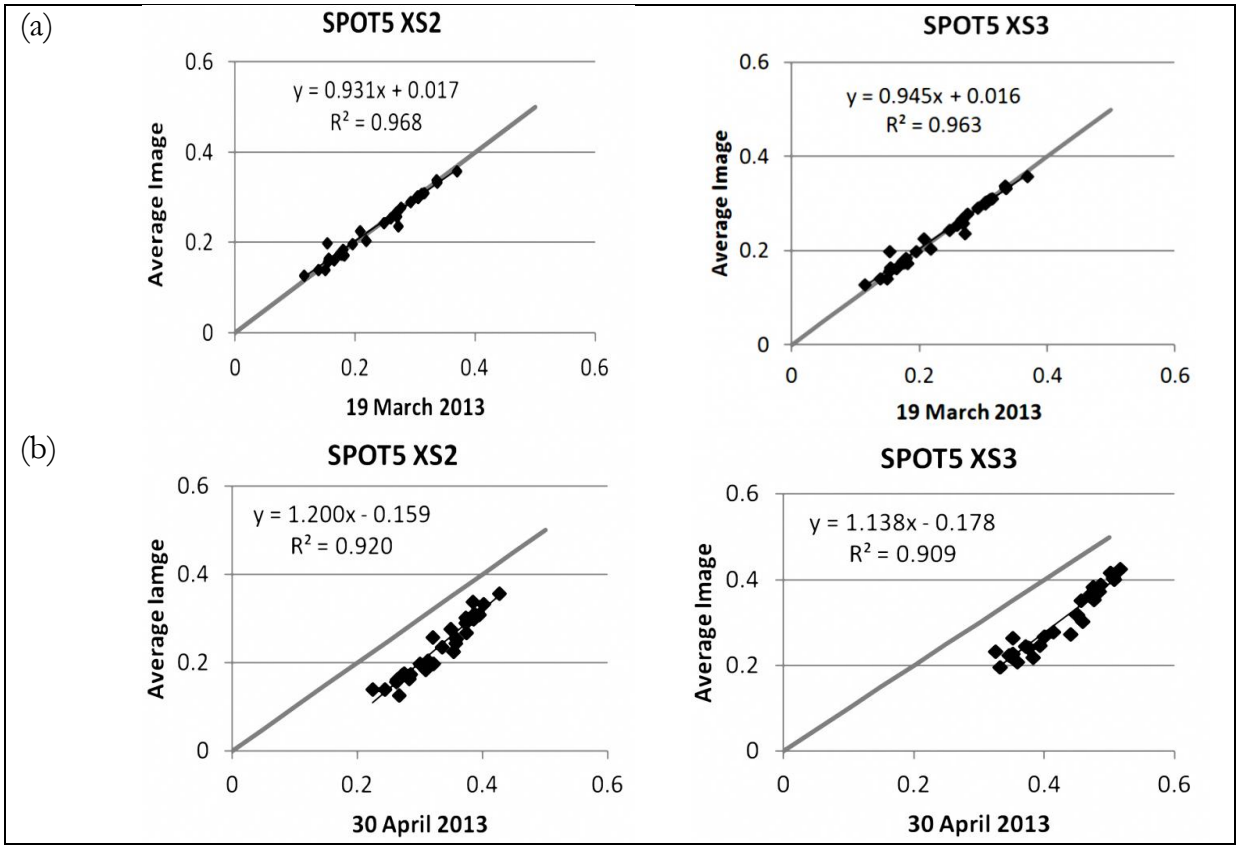

Figure 2. 12: Comparison between the 2012-2013 SPOT5 images after atmospheric correction using SMAC6S and the average reflectance image of this series for the 28 invariant sites, for spectral bands XS2 and XS3. Example of (a) an image for which no additional correction is required and (b) an image needing an additional correction.

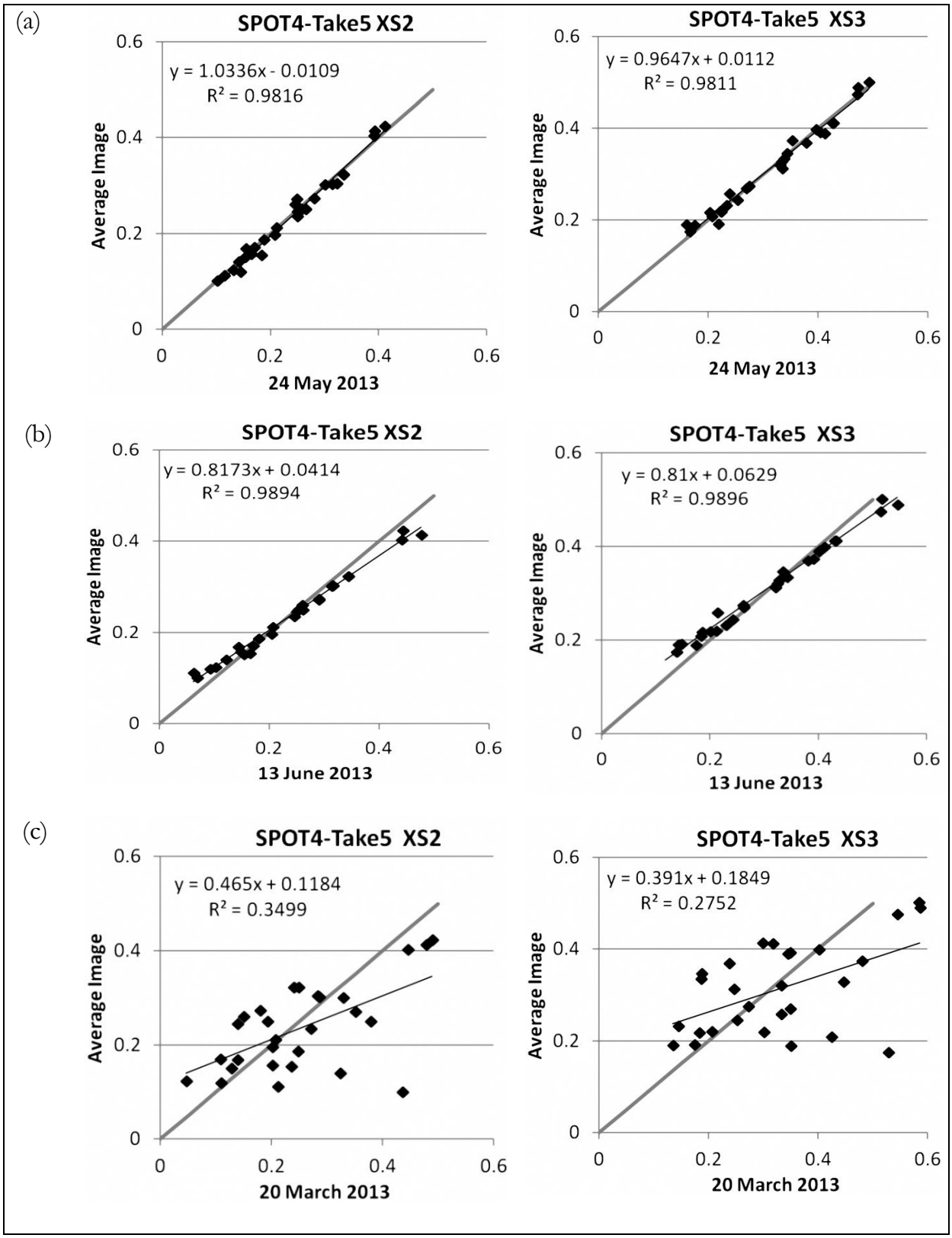

Figure 2. 13: Comparison between the SPOT4-take5 atmospherically corrected images and the average SPOT4-take5 reflectance for the 28 invariant sites, for spectral bands XS2 and XS3.

Example of (a) an image for which no additional correction is required, (b) an image needing an additional correction and (c) a hazy image (discarded from the final time series).

d. Additional 2012-2013 season's SPOT5 images radiometric normalization (SPOT4-take5 images as reference)

Once the consistency of reflectance levels within the two time series had been checked, a similar analysis is performed between the SPOT5 (2012-2013 season) and SPOT4-take5 images time series by plotting the average reflectance of the invariant objects (Figure 2.14). A significant bias was observed which can be explained by:

i) Differences in the atmospheric correction algorithm used;
ii) Difference in band definition between SPOT4-take5 and SPOT5;
iii) The variations in viewing angle between both sets of images. Indeed the SPOT4-take5 images were acquired at a fixed angle different from nadir, whereas SPOT5 images were acquired at any angle.

The observed bias had a strong impact on maximum NDVI values observed in the images, which was 0.9 for the SPOT4-take5 series, and only 0.7 for the SPOT5 series. Considering that fully covering vegetations were certainly present in the area (*i.e.*, cereals or forage fields), a realistic maximum NDVI value of 0.9 was expected for all seasons. Therefore, the SPOT5 series was linearly normalized to match the SPOT4-take5 radiometry on the basis of the linear regression established between the reflectance of the SPOT5 and SPOT4-take5 average images (Figure 2.14). Figures showing the comparison between the reflectance of the 2012-2013 SPOT5 images (after internal normalization using the PIFs method) and the average SPOT4-take5 reflectance (after internal normalization using the PIFs method) for the 28 invariant sites for all images are given in annex 4.2.

Finally, a NDVI profile was generated for each pixel, for all 2012-2013 SPOT5 and SPOT4-take5 images.

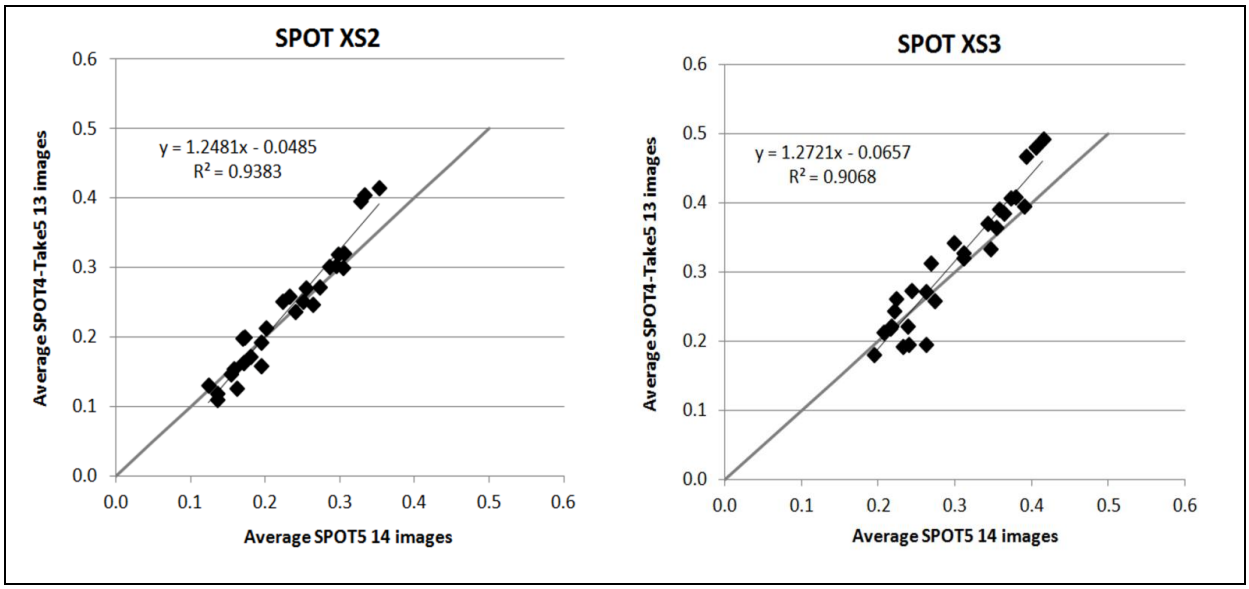

Figure 2. 14: Comparison between the average reflectances of the 28 invariants for the 2012-2013 SPOT5 and SPOT4-take5 time series before correction.

e. NDVI standardization of 2008-2009, 2011-2012 and 2012-2013 SPOT5 images (SPOT4-take5 images as reference)

For the 2008-2009 and 2011-2012 seasons, the NDVI time series were already computed by Zaghouani (2013) using the XS2 and XS3 bands. Maximum NDVI as well as bare soil NDVI were identified for the 2008-2009, 2011-2012 and 2012-2013 SPOT5 time series images, and an average maximum NDVI and an average bare soil NDVI were computed for each season. Then, these values were compared to those obtained with the SPOT4-take5 series. As mentioned above, considerable NDVI bias was observed not only for the 2008-2009 and 2011-2012 seasons but even for the 2012-2013 season. However, intra-annual maximum vegetation and bare soil NDVI are supposed to be the same in a context of an irrigated area. Therefore, the NDVI values for the three SPOT5 series were linearly normalized (based on maximum vegetation and bare soil) to match the SPOT4-take5 series (Table 2.1). Although ideally we should have go back to the Red and NIR bands for correction, this direct NDVI correction, although approximative, was achieved for the sake of simplicity, considering errors remain low.

Table 2. 1: linear regressions for NDVI standardization

SPOT campaigns	Bare soil NDVI	Maximum vegetation NDVI	Linear regressions
SPOT5 2008-2009	0.14	0.84	$Y = 1.15\,X - 0.06$
SPOT5 2011-2012	0.16	0.85	$Y = 1.17\,X - 0.09$
SPOT5 2012-2013	0.09	0.72	$Y = 1.27\,X - 0.02$
SPOT4-take5 2012-2013	0.10	0.90	

f. Radiometric corrections of 2013-2014 SPOT5 image time series

Since the SPOT4-take5 image series was taken as reference to radiometrically correct the SPOT5 images, we also used it to directly correct the 2013-2014 seasons' SPOT5 images series using the PIF approach, without applying the SMAC 6S model. Hence, 31 invariant objects were identified manually in the scene by visually comparing pairs of distant dates, *i.e.* 26 February 2013 and 15 February 2014. For these 31 objects, the DNs of each date were plotted against the reflectance of the average SPOT4-take5 image (Figures 2.15). Each date was then linearly corrected to match the SPOT4-Take5 radiometry based on the established linear regressions. The figure 3.15 shows example of two images, all the other figures are given in annex 4.3.

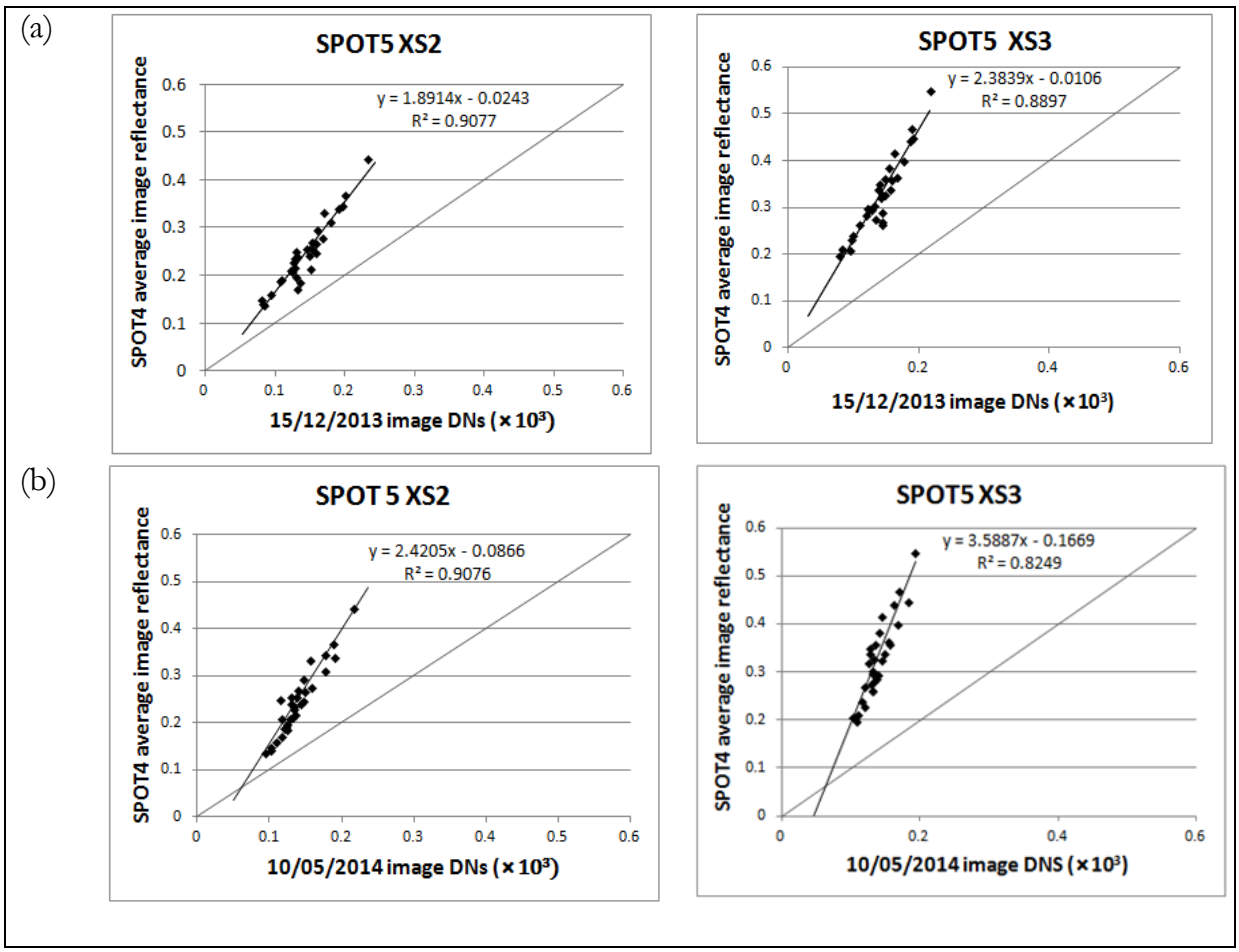

Figure 2. 15: Comparison between the 2013-2014 SPOT5 images DNs and the average SPOT4-take5 reflectance for the 31 invariant sites, for spectral bands XS2 and XS3. Example of (a) an image in early season and (b) an image in mid-season.

g. Cloud masking

The SPOT4-take5 series was delivered with cloud masks that were applied to avoid anomalies in the NDVI, while for the SPOT5 images, only two images included small cumulus clouds (5 November 2012 and 21 January 2013) which were manually masked. The clouds were identified using a simple threshold since they have a strong reflectance in the green band. The cloud shadows were also easy to identify because they had the lowest reflectance in the near infrared band. As small clouds were rarely at the same place, they have limited impact on the resulting NDVI profiles.

2.4.2 Low-resolution satellite imagery

To feed the SPARSE energy balance model, we used products of the MODIS sensor embarked on board of the satellites Terra (overpass time around 10:30 local solar time) and Aqua (overpass time around 13:30 local solar time) (Table 2.2). MODIS products were acquired for the study period, from 1 September 2012 to 30 June 2015, at the resolution of 1 km. The data used were: land surface temperature (T_{surf}), surface emissivity (ε_{surf}) and viewing angle (ϕ) (MOD11A1 and MYD11A1 products for Terra and Aqua, respectively; NDVI (MOD13A2 and MYD13A2 products for Terra and Aqua,

respectively) and albedo (α) (the combined products MCD43B1, MCD43B2 and MCD43B3).

All MODIS products are stored in a hierarchical format of enhanced data, HDF (Hierarchical Data Format) files, consisting of multidimensional data tables and descriptive metadata. The structure of the MODIS data directory is based on the short names of the MODIS products. TERRA MODIS products are abbreviated "MOD", AQUA MODIS products are abbreviated "MYD" and the combined products TERRA and AQUA MODIS are abbreviated "MCD". Abbreviated names also include the version number. The classification of MODIS data (Earth, atmosphere and cryptosphere data) is done in a hierarchy of five levels according to the applied processing to these data:

- Level 0: This is the first level in which the raw data are stored in PDS (Production Data Set) format. Raw data are reconstructed, unprocessed instrument and payload data at full resolution, with all communications artefacts removed.
- Level 1A: Reconstructed, unprocessed instrument data at full resolution, time-referenced, and annotated with ancillary information, including radiometric and geometric calibration coefficients and georeferencing parameters computed and appended but not applied to Level 0 data.
- Level 1B: Level 1A data that have been processed to sensor units (not all instruments have Level 1B source data).
- Level 2: This is the level where the geophysical parameters are derived at the same resolution and location. These are data of level 1B to which the atmospheric corrections have been applied. They are directly exploitable to process the surface parameters.
- Level 3: This is the level at which the data are averaged over a time scale. Variables are mapped on uniform space-time grid scales, usually with some completeness and consistency.
- Level 4: Model output or results from analyses of lower-level data (e.g., variables derived from multiple measurements).

The Characteristics of the used MODIS data are detailed in annex 5.

MODIS images pre-processing

Most standard MODIS Land products use the Sinusoidal grid tiling system (Figure 2.16). Tiles are 10 degrees by 10 degrees at the equator. The tile coordinate system starts at (0, 0) (horizontal tile number, vertical tile number) in the upper left corner and proceeds right (horizontal) and downward (vertical).

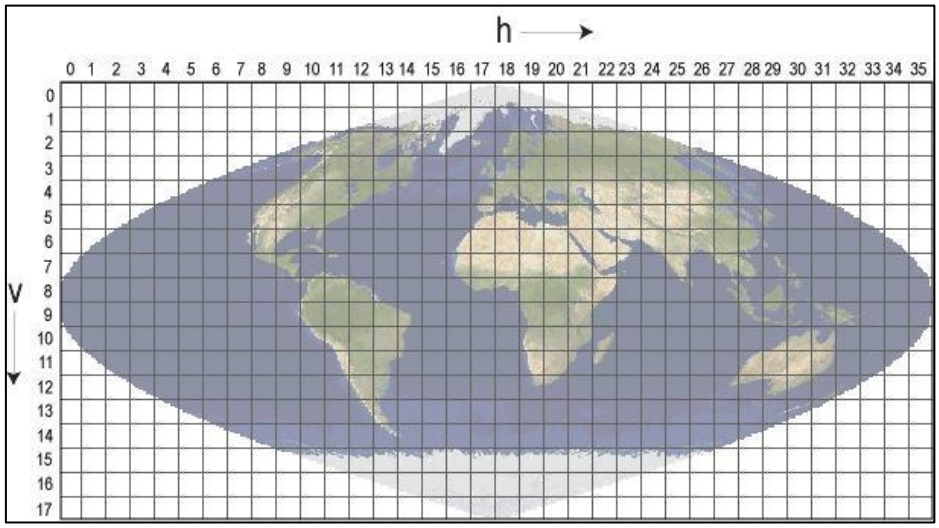

Figure 2. 16: MODIS sinusoidal tiling system (Source: https://lpdaac.usgs.gov/)

a. Data reprojection , extraction and temporal interpolation

The sinusoidal projection is used for the storage of MODIS images at the Land Processes Distributed Active Archive Center (LP-DAAC). This projection is not suitable for displaying images. The composite data was therefore reprojected using MODIS Reprojection Tool (MRT). The MRT free software is developed by the Land Processes Distributed Active Archive Centre (LP-DAAC); it enables users to i) read data files in HDF format (MODIS Level-2G, Level-3, and Level-4 land data products), ii) specify a geographic subset or specific science data sets as input to processing, iii) perform geographic transformation to a different coordinate system/cartographic projection, and iv) write the output to file formats other than HDF (Dwyer and Schmidt, 2006)

A MATLAB (matrix laboratory programming language https://fr.mathworks.com/) code was used to apply MRT and retrieve the images for each MODIS product in order to extract the variables that will be used as input data into the SPARSE model. A 10 km × 8 km sub-image centered on the scintillometer transect (see section 2.5.3) was extracted (Figure 2.17).

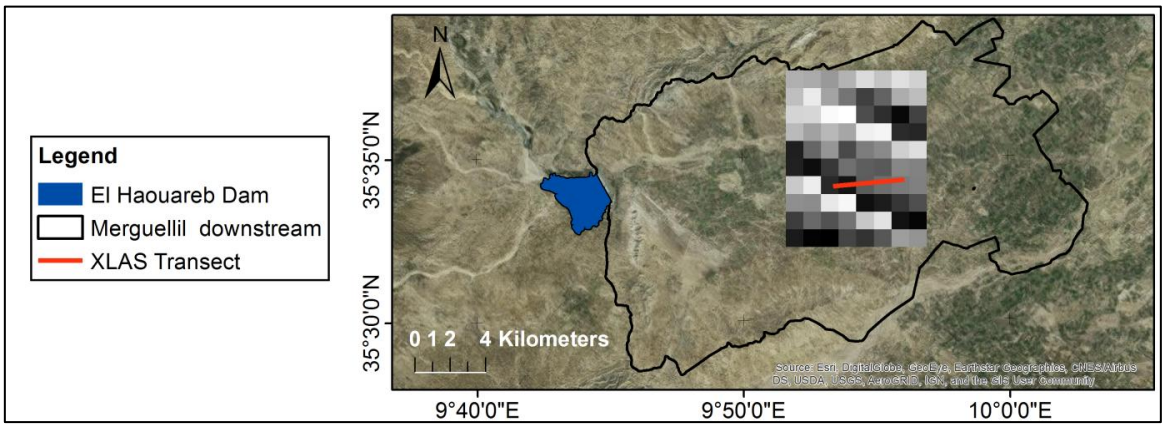

Figure 2. 17: Geographic location of the extracted 10 km× 8 km MODIS sub-image (MODIS grid)

The daily MODIS T_{surf} and viewing angle, 8-day MODIS albedo, and 16-day MODIS NDVI contain some missing or unreliable data; hence, days with missing data in MODIS pixels regarding the scintillometer footprint were excluded. Linear temporal interpolation of albedo and NDVI data were done to get daily images. For each pixel, only the good RS data was taken into account (based on the quality index supplied with the product); hence, the temporal interpolation was specific for each pixel.

b. Remote sensed leaf area index

LAI is a key variable functionally related to plant biomass production. Accurate estimation of leaf area index (LAI) is important for monitoring vegetation dynamics. Indeed, early research showed that there is a strong correlation between a red to near-infrared transmittance ratio and LAI (Jordan, 1969) and spectral measurements are strongly related to the LAI (Tucker, 1979). The NDVI is one of the most extensively applied vegetation indices related to LAI, hence, a single equation (Clevers, 1989) was used to compute remotely-sensed LAI of all crops in the study area from the MODIS NDVI product:

$$LAI = -\frac{1}{k} ln\left(\frac{NDVI_{\infty} - NDVI}{NDVI_{\infty} - NDVI_{soil}}\right) \quad (2.\ 1)$$

Soil and vegetation NDVI threshold, $NDVI_{\infty}$ and $NDVI_{soil}$, are often difficult to obtain, particularly in sparsely or highly vegetated areas (Song *et al.*, 2017). The traditional methods for their estimation are: i) maximum and minimum NDVI in a study area (Gutman and Ignatov, 1998), ii) the accumulative maximum and minimum over a long-term series dataset (Zeng *et al.*, 2000) or iii) $NDVI_{\infty}$ and $NDVI_{soil}$ based on field measurements or high-resolution remotely-sensed data (Jiapaer *et al.*, 2011; Zhang *et al.*, 2013). It has been reported that the underestimation of $NDVI_{soil}$ in sparse vegetation areas may cause the overestimation of LAI as high as 0.2 (Montandon and Small, 2008).

The calibration of this relationship was done over the Yaqui irrigated perimeter (Mexico) during the 2007-2008 growing season using hemispherical LAI measured in all the studied fields and NDVI, derived from Formosat-2 images (Chirouze *et al.*, 2014) . Calibration results gave the asymptotical values of NDVI, $NDVI_{\infty}$ = 0.97 and $NDVI_{soil}$ = 0.05, as well as the extinction factor k = 1.13. The $NDVI_{soil}$ obtained by Chirouze *et al.* (2014) over the Yaqui perimeter was different from the bare soil NDVI computed using the SPOT images (see sect. 2.4.1 table 2.1). In fact, bare soil NDVI depends on the used remotely-sensed data and on the study area which are different in our case (SPOT vs. Formosat-2 and Yaqui perimeter vs. Kairouan plain) but it is always assumed that NDVI of 0.1 and below correspond to bare soil (Weier and Herring, 2000). However, as this relationship was calibrated over a heterogeneous land surface but on herbaceous vegetation only, its relevance for trees was checked. For that purpose, clump-LAI measurements on an olive tree, as well as allometric measurements, *i.e.* mean distance between trees and mean crown size were obtained using Pleiades satellite data (Mougenot *et al.*, 2014; Touhami, 2013). We checked that the pixels with tree dominant cover showed LAI values close to the results of allometric measurements (of the order of 0.3 given the interrow distance of 12 m on average).

2.5 *In situ* data

2.5.1 Meteorological data

Half hourly standard meteorological measurements including global incoming radiation i.e incident short wavelengths radiation [$W.m^{-2}$], wind speed [$m.s^{-1}$], air temperature [°C], air humidity [%] and rainfall [mm] have been recorded using an automated weather station installed in the study area (delegation of Chebika, Sidi Ali Ben Salem sector) since December 2011(Figure 2.18) in the frame of the SudMed programm[1]. Hereafter, this weather station is referred as the Ben Salem meteorological station (35° 33' 1" N; 9° 55' 18" E). It is an automatic Campbell Scientific (Logan, USA) station. The global radiation is measured using a Sr11 pyranometer (Wittich, Netherland). Wind speed and direction [°] are measured using a Windvane-Anenometer R.M.010305 (Young, USA); wind speed is measured at 2.32m above the ground. The air temperature and air humidity are measured using a HMP45C thermo-hygrometer (Vaisala, Finland). Rainfall is measured with a Tipping Bucket Raingauge SBS500 (Campbell Scientific, USA).

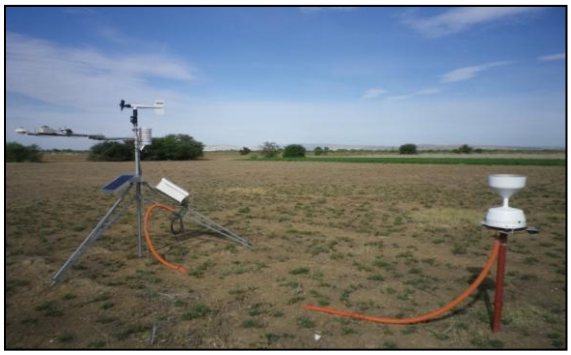

Figure 2. 18: Ben Salem meteorological station set-up

Required meteo data over periods prior to the Ben Salem meteorological station installation date (from 2008 to 2011) were taken from the nearest weather station referred as the INGC (National Institute of Field Crops, Institut National des Grandes cultures—in French) meteorological station (35° 37' 14" N; 9° 56' 16"E). This wheather station is managed by the National Meteorological Institute (INM, Institut National météorologique—in French).

Processing of meteorological data

The processing of INGC meteorological data aquired from January 2008 to December 2011 was done in the frame of Zaghouani (2013) master thesis, while the Ben Salem meteorological data sets acquired from December 2011 to June 2015 and used in this

[1] The SUDMED program has been launched by the CESBIO (Center for Space Studies of the BIOsphere, Centre d'Etudes Spatiales de la BIOsphère—in French) to address the issue of improving understanding of the hydrological functioning of semi-arid watersheds. Study sites are the Tensift in central Morocco since 2002, the Merguellil catchment since 2008 and the Mount Lebanon for snow hydrology since 2011.

PhD thesis work required primary processing to make them relevant and usable; thus the reliability and accuracy of each climate variable was checked by identifying periods with missing data as well as outliers and measurement artefacts. Depending on the nature of the errors found, they have been corrected as follows by linear interpolation if only a half an hour data is missing or erroneous; otherwise, missing or erroneous data over several hours or several days were substituted by data from the Ben Salem flux station or the INGC weather station (subject to availability). Thus, for each meteorological variable, a complete data set was generated at a half-hour time step, which enabled us to compute half hourly reference ET (ETo) using the FAO "reduced form" equation for application to both 24-h and hourly or shorter time steps (Allen *et al.*, 2005a; Allen *et al.*, 2006):

$$ET_o = \frac{0.408\,\Delta(R_n - G) + \gamma\,\frac{C_n}{T_{0.5h} + 273}\,U_2(e^o(T_{0.5h}) - e_a)}{\Delta + \gamma\,(1 + C_d U_2)} \qquad (2.\ 2)$$

where where ETo is in mm $(0.5h)^{-1}$ for half hourly time steps, Rn-G [MJ m^{-2} $(0.5h)^{-1}$] is half hourly available energy, γ [kPa.C-1] is the psychrometric constant, $T_{0.5h}$ [K] is half hourly air temperature, Δ [kPa C^{-1}] is saturation slope vapour pressure curve at $T_{0.5h}$, U_2 [$m.s^{-1}$] is average half-hourly wind speed, e°($T_{0.5h}$) [kPa] is saturation vapour pressure at air temperature $T_{0.5h}$, e_a [kPa] is the average half-hourly actual vapour pressure and C_n and C_d are respectively the numerator and denominator constants that change with reference type and calculation time step (C_n= 0.5×37 and C_d=0.34 (Allen *et al.*, 2006)).

The relationships allowing calculation of the equation 2.2 parameters are detailed in annex 6. Once calculated at the half-hour time step, the daily ETo was computed. The following graph (Figure 2.19) represents the two series of daily ETo and rainfall of the Ben Salem meteorological station from December 2011 to June 2015, higher values of about 10 mm/day are reached in summer.

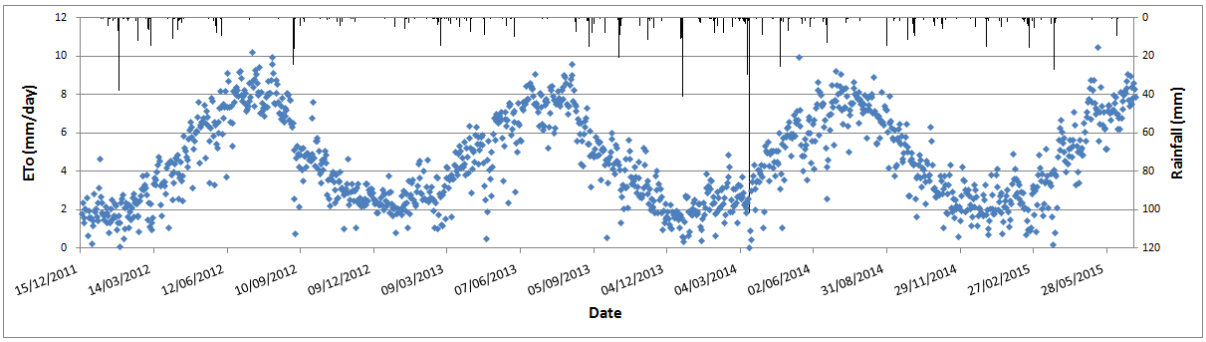

Figure 2. 19: Daily variation of reference evapotranspiration and rainfall over the period December 2011-June 2015 (Ben Salem meteorological station)

2.5.2 Flux and soil moisture data

The flux data sets used in this PhD thesis works were measured by three automatic Campbell Scientific (Logan, USA) flux stations (Figure 2.20) based on the eddy correlation (EC) method. Moreover, soil properties (moisture, temperature and heat flux) measurement is carried out in soil pits near the flux towers.

The first station was installed few tens of meters away from the Ben Salem meteorological station, in an irrigated field (delegation of Chebika, Sidi Ali Ben Salem

sector) from December 2011 until November 2014. Hereafter, this station is referred as the Ben Salem 1 station (35° 33' 1" N; 9° 55' 18" E). It was operated to measure the four components of the surface energy budget as well as soil properties of i) an irrigated barley from December 2011 to June 2012 and ii) an irrigated wheat from November 2012 to June 2013 and iii) an irrigated pepper from June to November 2014. The second station was installed in a rainfed wheat field (delegation of Chebika, Sidi Ali Ben Salem sector) from January to June 2012. Hereafter, this station is referred as the Ben Salem 2 station (35° 33' 32" N; 9° 56' 25" E). The third station was installed in a rainfed olive orchard (delagtion of Nasrallah) from March 2012 to September 2016. It consists of two stations: one on the olive tree and the other on the bare soil. Hereafter, this station is referred as Nasrallah station (35° 18' 17" N; 9° 54' 56" E). The measured parameters as well as the measuring sensor are detailed in table 2.3 for the three stations.

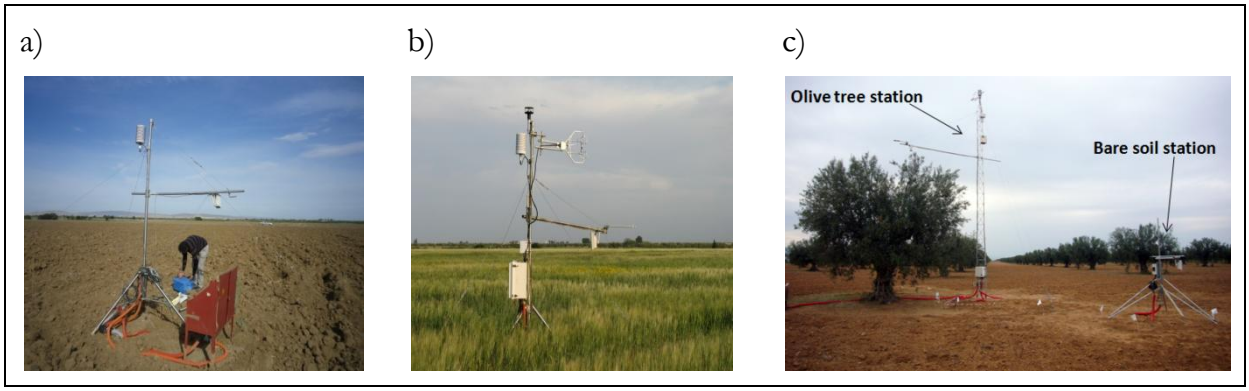

Figure 2. 20: set-up of a) Ben Salem 1 b) Ben Salem 2 and c) Nasrallah stations

These three stations measure the convective fluxes exchanged between the surface and the atmosphere (H and LE) by the turbulent covariance method, combined with measurements of the net radiation Rn and the soil heat flux G (15mn recording time step).

The components of the radiative surface balance which are short wavelength radiations (incoming and outgoing) and long wavelength radiations (incoming and outgoing) are measured by net radiometer). From these measurements, the net radiation is deduced since it represents the balance between short and long wavelengths radiation according to the equation 1.19 (see section 1.2.2.1). G is measured by three soil heat flux plates uniformly distributed at a soil pit (2-3 cm depth) close to the flux towers of the Ben Salem 1 and Ben Salem 2 stations. Five soil heat flux plates were used in the Nasrallah station. A correction was performed to bring the soil heat flux measured in depth to a surface heat flux by taking into account the heat stored between the surface and the measurement depth. H and LE are measured using i) a CSAT3 anemometer recording high-frequency fluctuations (20 Hz) of the three components of wind speed; the component u horizontal and parallel to the wind direction, the component v horizontal and perpendicular to the wind direction and the vertical component w; as well as the air temperature fluctuations (20 Hz) from the sound velocity; and ii) an optical hygrometer KH20 recording high-frequency (20 Hz) fluctuations of water vapor in the atmosphere *i.e* water vapor. Since the KH20 sensor cannot measure the absolute vapor pressure, it is coupled with a thermo-hygrometer installed at the same height which measures the air humidity and temperature

(Table 2.2). Moreover, soil moisture and temperature are measured using respectively five thetaprobes and five thermistors (Table 2.2)

Table 2. 2: Measured parameters and measuring instruments in the Ben Salem 1, Ben Salem 2 and Nasrallah stations

Flux stations		Measured parameters	Sensor	Model and Manufacturer
Ben Salem 1	Flux tower	Wind speed (u, v, w) [m.s^{-1}]	3D Sonic Anemometer	CSAT3 (Campbell Scientific, USA)
		Specific air humidity [kg.kg^{-1}]	Hygrometer	KH20 (Campbell Scientific, USA)
		Temperature air [°C]	Thermo-hygrometer	HMP155 (Vaisala, Finland)
		Relative humidity [%]	Thermo-hygrometer	HMP155 (Vaisala, Finland)
	Radiations	Net radiation [W.m^{-2}]	Net Radiometer	NR01 (Hukesflux, Netherlands)
		Infrared temperature [°K]	Infrared thermometer	IR120 (Campbell Scientific, USA)
		NDVI [-]	NDVI sensor	SKR1800 (Skye, UK)
	Soil	Soil hat flux [W.m^{-2}]	Simple soil heat flux plates (×4)	HFP01 (Hukseflux, Netherlands)
			Self calibrated soil heat flux plate	HFP01SC (Hukseflux, Netherlands)
		Soil Temperature [°C]	Thermistors (×5)	TH108 (Campbell Scientific, USA)
		Soil moisture [m^3.m^{-3}]	Thetaprobes	ML2x (×5) and PR2/6 (×1) (DeltaT, UK)
Ben Salem 2	Flux tower	Wind speed (u, v, w) [m.s^{-1}]	3D Sonic Anemometer	CSAT3 (Campbell Scientific, USA)
		Specific air humidity [kg.kg^{-1}]	Hygrometer	KH20 (Campbell Scientific, USA)
		Air temperature [°C]	Thermo-hygrometer	HMP155 (Vaisala, Finland)
		Air relative humidity [%]	Thermo-hygrometer	HMP155 (Vaisala, Finland)
	Radiations	Net radiation [W.m^{-2}]	Net Radiometer	NRLITE 2 (Kipp&Zonen, Netherlands)
	Soil	Soil hat flux [W.m^{-2}]	Soil heat flux plates (×5)	HFP01 (Hukseflux, Netherlands)
		Soil Temperature [°C]	Thermistors (×5)	TH108 (Campbell Scientific, USA)
		Soil moisture [m^3.m^{-3}]	Thetaprobes (×5)	ML2x (DeltaT, UK)
Nasrallah (olive tree)	Flux tower	Wind speed (u, v, w) [m.s^{-1}]	3D Sonic Anemometer	CSAT3 (Campbell Scientific, USA)
		Specific air humidity [kg.kg^{-1}]	Hygrometer	KH20 (Campbell Scientific, USA)
		Air temperature [°C]	Thermo-hygrometer	HMP155 (Vaisala, Finland)
		Air relative humidity [%]	Thermo-hygrometer	HMP155 (Vaisala, Finland)

Flux stations		Measured parameters	Sensor	Model and Manufacturer
Nasrallah (olive tree)	Radiations	Net radiation [W.m^{-2}]	Net Radiometer (×2)	CNR4 (Kipp&Zonen, Netherlands) and NR01 (Hukesflux, Netherlands)
		Infrared temperature [°K]	Infrared thermometer	IR120 (Campbell Scientific, USA)
	Soil	Soil hat flux [W.m^{-2}]	Soil heat flux plates (×5)	HFP01 (Hukseflux, Netherlands)
		Soil Temperature [°C]	Thermistors (×5)	TH108 (Campbell Scientific, USA)
		Soil moisture [m^3.m^{-3}]	Thetaprobes (×5)	ML2x (DeltaT, UK)
Nasrallah (bare soil)	Flux tower	Air temperature [°C]	Humidity and Temperature Probe	HMP155 (Vaisala, Finland)
		Relative humidity [%]	Humidity and Temperature Probe	HMP155 (Vaisala, Finland)
		Wind speed [m.s^{-1}]	Windvane-Anenometer	R.M. 010305 (Young, USA)
		Wind direction [°]	Windvane-Anenometer	R.M. 010305 (Young, USA)
		Rainfall [mm]	Raingauge	SBS500 (Campbell Scientific, USA)
	Radiations	Infrared temperature [°K]	Infrared thermometer	IR120 (Campbell Scientific, USA)
	Soil	Soil hat flux [W.m^{-2}]	Soil heat flux plates (×5)	HFP01 (Hukseflux, Netherlands)
		Soil Temperature [°C]	Thermistors (×5)	TH108 (Campbell Scientific, USA)
		Soil moisture [m^3.m^{-3}]	Thetaprobes (×5)	ML2x (DeltaT, UK)

Processing of flux data

The processing of the Ben Salem 1 irrigated wheat (2012/2013) flux data was done in the frame of this PhD thesis work. The processing of the Ben salem 1 irrigated barley (2011/2012) and the Ben Salem 2 rainfed wheat (2011/2012) flux data was done in the frame of Zaghouani (2013) master thesis while Nasrallah flux data processing was done by Chebbi *et al.* (2017, in progress) . It is all the same for the irrigated fields soil moisture data.

The EC processing sequence to calculate turbulent fluxes from raw, high-frequency data is complex, depending on the chosen instruments, their deployment, the site characteristics and the atmospheric turbulence peculiarities (Fratini and Mauder, 2014). Several software programs allowing the calculation of convective flows using the turbulent covariance method have been developed and made available to the scientific community in recent years (Foken *et al.*, 2012). They allow the application of required instrument corrections, applying calibration coefficients if needed, rotating coordinates; correcting for time delays; and conducting quality control. The most used are: TK2, developed at the University of Bayreuth, Germany (Mauder and Foken, 2011); EDIRE,

developed at the University of Edinburgh, UK (Clement and Moncreif, 2007), ECPACK developed in the University of Wageningen, Netherlands (Van Dijk *et al.*, 2004), and EDDYPRO developed by LI-COR, USA (LI-COR, 2016). In our case, post-processing of 20 Hz EC data was done using the EddyPro software in order to get half hourly convective fluxes (LE and H).

In a subsequent step, the energy balance closure was calculated by statistical regression of half hourly turbulent energy fluxes against available energy for the irrigated barley (2011/2012), the irrigated wheat (2012/2013) and the rainfed wheat (2011/2012) fields. The result indicates a lack of closure with an imbalance of 14% (Figure 2.21), 40% (Figure 2.22) and 20% (Figure 2.23) for the irrigated barley, irrigated wheat and rainfed wheat fields, respectively. The low closure value (60%) for the irrigated wheat field can be explained by the quality of EC measurements which is influenced not only by possible deviations from the theoretical assumptions but also by problems of sensor configurations and meteorological conditions (Foken and Wichura, 1996). However, it is difficult to isolate the causes of measurement errors. Instrumental errors, uncorrected sensor configurations, problems of heterogeneities in the area and atmospheric conditions are the main problems that affect data quality (Foken, 2008). Figure 2.24 shows statistical regression of half hourly turbulent energy fluxes against available energy of the Nasrallah station

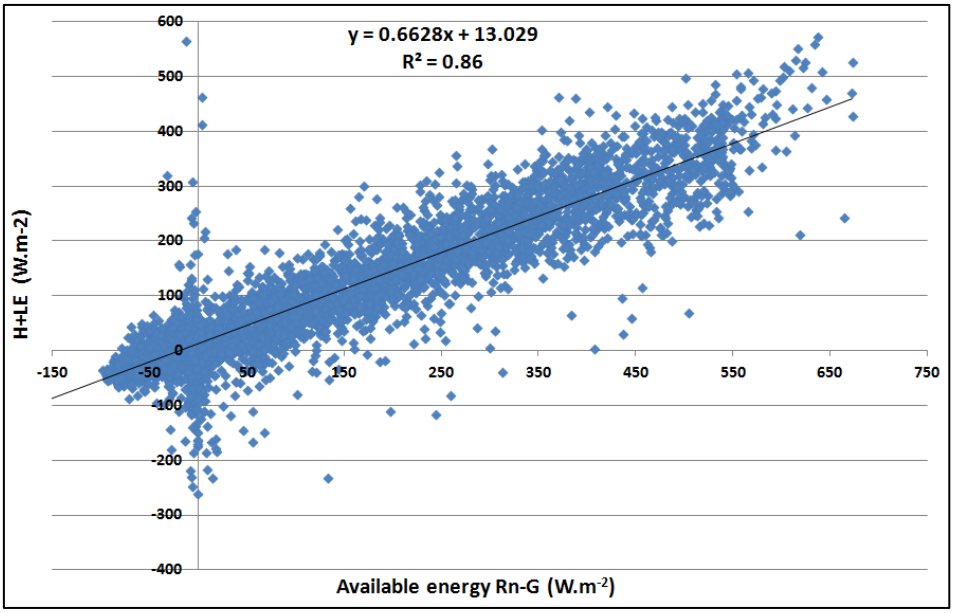

Figure 2. 21: Statistical regression of half hourly turbulent energy fluxes against available energy of the Ben salem 1 station (irrigated barley 2011/2012)

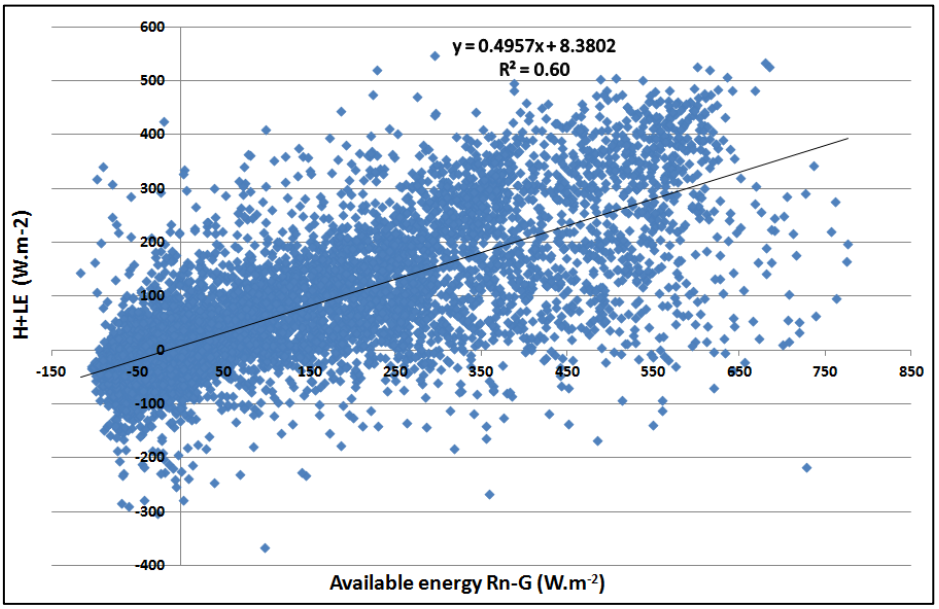

Figure 2. 22: Statistical regression of half hourly turbulent energy fluxes against available energy of the Ben salem 1 station (irrigated wheat 2012/2013)

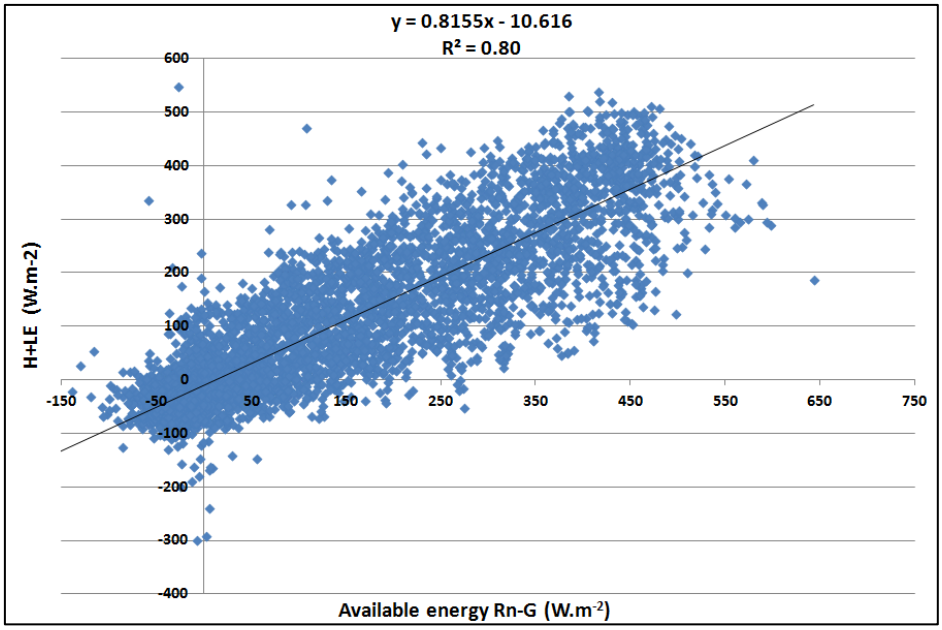

Figure 2. 23: Statistical regression of half hourly turbulent energy fluxes against available energy of the Ben salem 2 station (rainfed wheat 2011/2012)

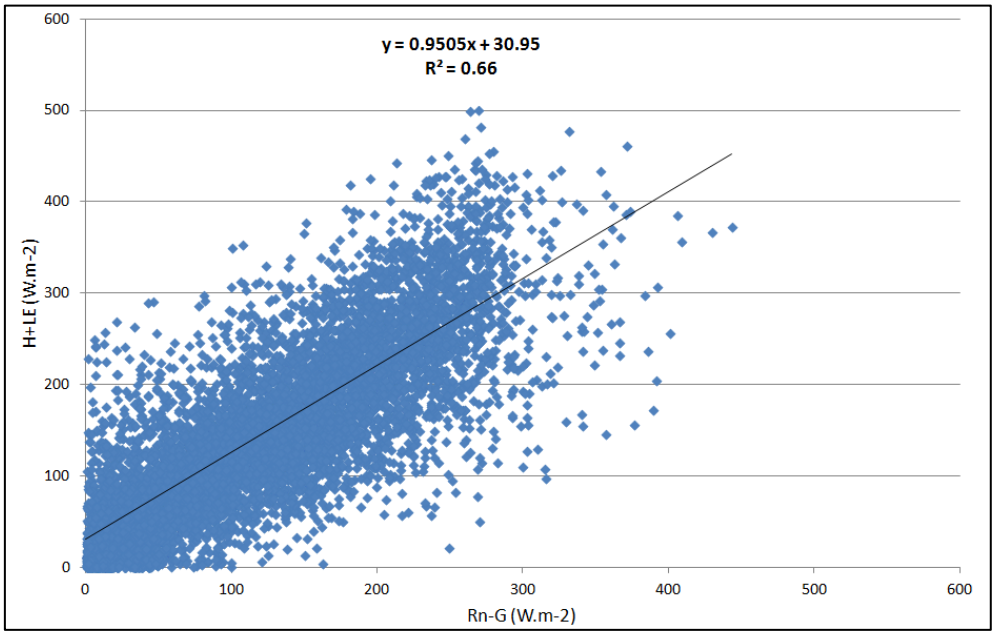

Figure 2. 24: Statistical regression of half hourly turbulent energy fluxes against available energy of the Nasrallah station (olive orchard 2012-2015) (Source: Chebbi *et al.* (2017, in progress))

Since the energy balance closure found is low, the measured LE was not taken into account and a LE_{res} was computed as the residual term of the energy balance equation using the EC measurement of H, Rn and G as follows:

$$LE_{res} = R_n - G - H \quad (2.\ 3)$$

On the other hand, the Bowen ratio (β) method was applied to compute a LE_{Bowen} as follows:

$$\beta = \frac{H}{LE} \rightarrow LE_{Bowen} = \frac{R_n - G}{1+\beta} \text{ and } H_{Bowen} = (Rn - G).\left(\frac{\beta}{(1+\beta)}\right) \quad (2.\ 4)$$

where LE and H , Rn and G are the half hourly EC measured fluxes.

Finally, daily LE_{res} and LE_{Bowen} were computed from the half hourly LE and an average daily observed LE (Figures 2.25, 2.26 and 2.27) was computed and converted from [$W.m^{-1}$] to [mm/day], since these observed LE *i.e.* ET will be used to calibrate the parameters of SAMIR model (see sections 3.2 and 4.1) which computes a daily soil water balance. Figures 2.28 shows observed daily latent heat flux LE and reference evapotranspiration (ETo) of the Nasrallah station (November 2012 to December 2015).

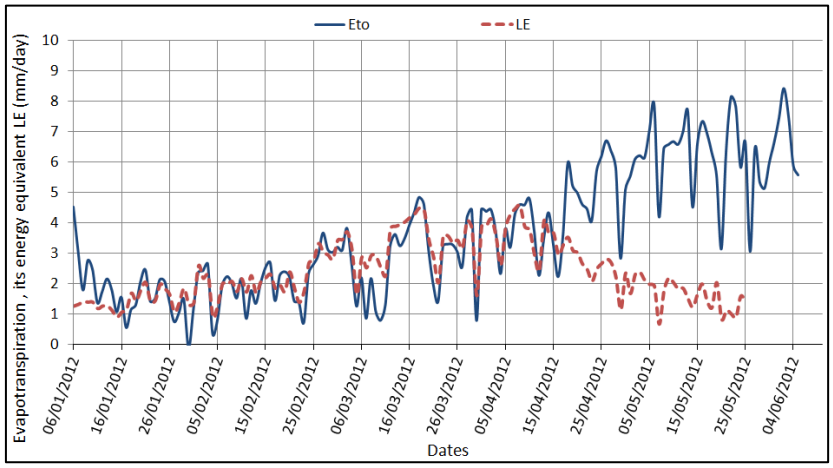

Figure 2. 25: Observed daily latent heat flux LE of the Ben salem 1 flux station (irrigated barley 2011/2012 agricultural season) and reference evapotranspiration (ETo) computed at the Ben Salem meteorological station for the same period.

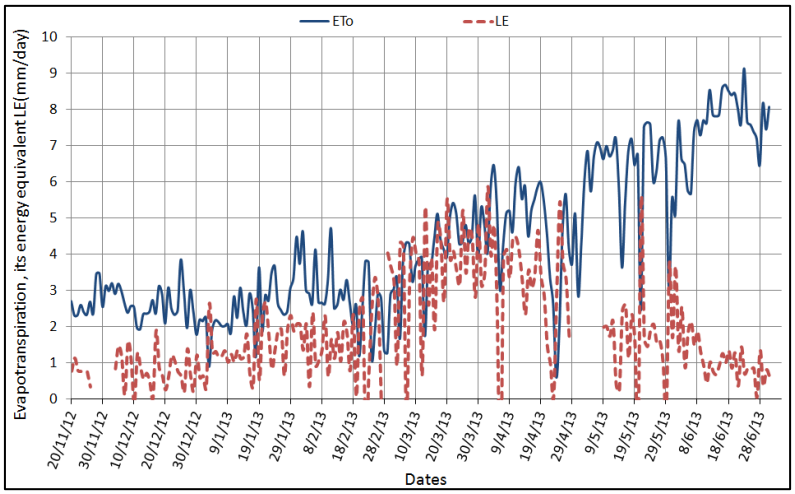

Figure 2. 26: Observed daily latent heat flux LE of the Ben salem 1 flux station (irrigated wheat 2012/2013 agricultural season) and reference evapotranspiration (ETo) computed at the Ben Salem meteorological station for the same period.

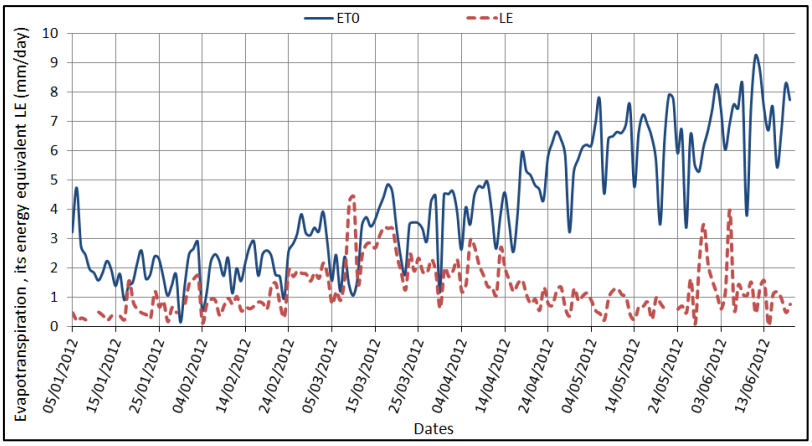

Figure 2. 27: Observed daily latent heat flux LE of the Ben salem 2 flux station (rainfed wheat 2011/2012 agricultural season) and reference evapotranspiration (ETo) computed at the Ben Salem meteorological station for the same period.

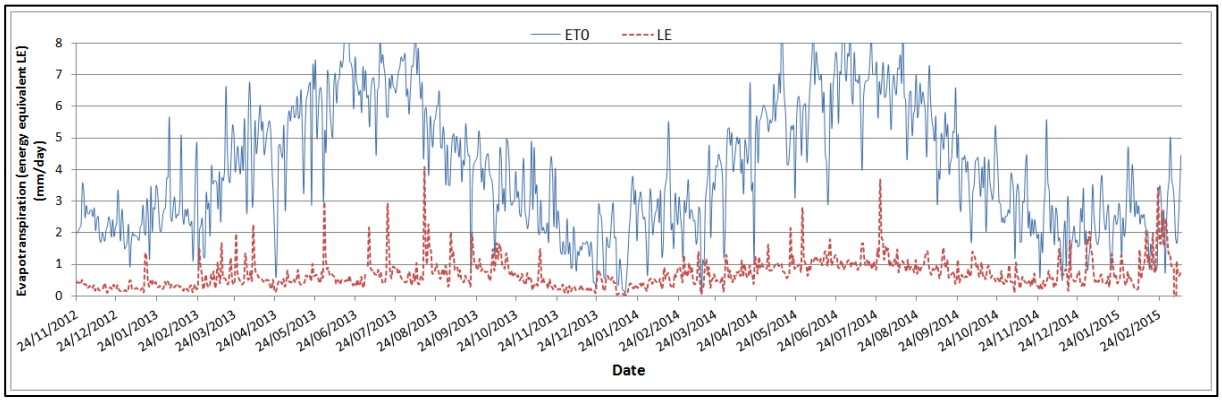

Figure 2. 28: Observed daily latent heat flux LE and reference evapotranspiration (ETo) of the Nasrallah station (olive orchard 2012-2015)

Processing of soil moisture data and irrigation doses calculation

Information on irrigation practices at our experimental plots has several shortcomings, as the farmer does not always have precise irrigation dates. Thus, half-hourly measurements of soil moisture at the flux stations were used to estimate irrigation doses and application days.

At the Ben Salem 1 flux station, there are two sensors for measuring soil moisture (Table 2.3); five theta probes ML2x (at 0.05 m, 0.10 m, 0.20 m, 0.40 m and 1.00 m soil depth) and one theta probe PR2 (at 0.10 m, 0.20 m, 0.30 m, 0.40 m, 0.60 m and 1.00 m soil depth). The half hourly measured soil moisture by the two sensors were processed together in order to compare them and thus keep the most reliable data. Soil moisture measurements calibration consists in the conversion of these electric measurements millivolts (mV) to volumetric water content $\boldsymbol{\theta}_{vol}$ [% or $m^3.m^{-3}$], based on gravimetric measurements (Baize, 2000) and soil bulk density estimation (Duchaufour, 1995) done by Gorrab (2016). Calibration parameters coming from gravimetric method as well as soil bulk density for each soil depth are detailed in table 2.4.

Table 2. 3: Calibration coefficients of the measured soil moisture in the Ben Salem 1 flux station (irrigated wheat field 2012/2013)

Measurement depth (m)			0.05	0.10	0.20	0.30	0.40	0.60	1.00
Soil moisture sensor calibration parameters	**Ml2x**	a	0.050	0.036	0.046	-	0.044	-	0.008
		b	-3.65	-6.228	-8.188	-	-8.928	-	6.801
	PR2	a	-	0.032	0.032	0.049	0.064	0.051	-0.016
		b	-	-6.298	-7.704	-26.082	-43.247	-34.796	28.98
Soil bulk density [-]			1.1	1.19	1.28	1.28	1.28	1.34	1.4

Source: SudMed Project

Hence, for each sensor, and for each measurement depth, the following relationship was applied to compute volumetric soil moisture $\boldsymbol{\theta}_{vol}$:

$$\theta_{vol} = \theta_p \times \gamma_{bulk} = (a \times \theta_{el} + b) \times \gamma_{bulk} \quad (2.\ 5)$$

where $\boldsymbol{\theta}$p [% or g.g^{-1}] is the moisture content, $\boldsymbol{\theta}_{el}$ [mV] is the theta probe measured soil moisture, $\boldsymbol{\gamma}_{bulk}$ [-] is the soil bulk density and a and b are the calibration coefficients.

Half hourly soil moisture measurements using the ML2x sensor and the PR2 sensor are illustrated in figures 2.27a and 2.27b showing measurements errors in PR2 measurements in particular for the measurement depth 60 cm, in addition, peaks of soil moistures are sharper with ML2x rather than with PR2. Hence, the Ml2x data, which are a priori more reliable, have been chosen for further elaborations.

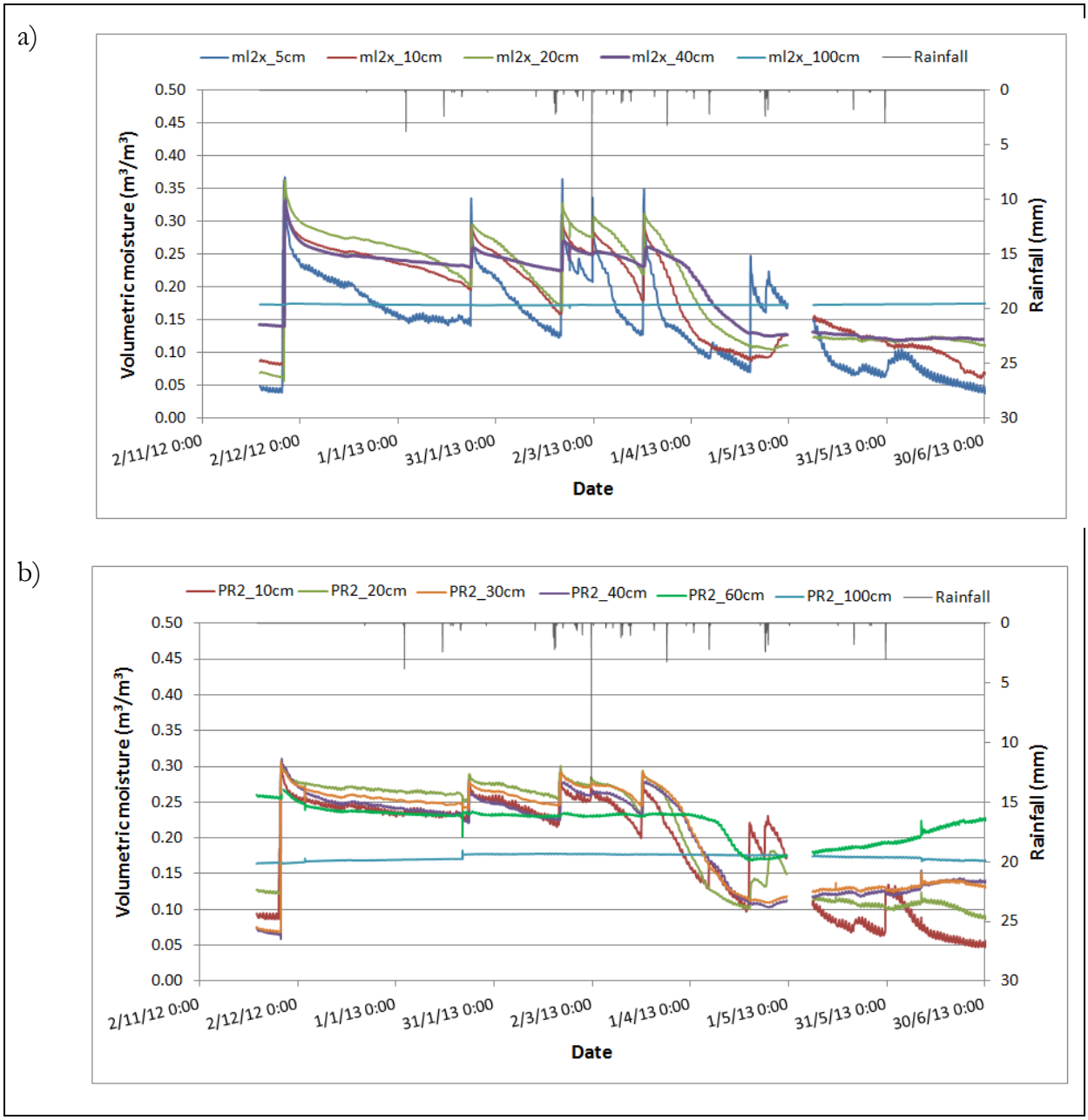

Figure 2. 29: Half hourly a) ML2x and b) PR2 soil moisture measurement in the Ben Salem 1 station from November 2012 to June 2013 and rainfall from the Ben Salem meteorological station for the same period.

In a subsequent step, daily soil moisture was computed from the half hourly ML2x measurements. Since measured soil moisture is a punctual measurement of a specific soil depth in which the sensor is put, each measurement was supposed to be representative of a soil horizon (referred as i) having a certain depth determined on the basis of the depth were the sensor is put, for example, soil moisture measurement at 5 cm ($\boldsymbol{\theta}_{vol,1}$) corresponds to the moisture of a 0.075 m deep soil horizon , from the soil surface $z_{1,1}$=0 cm to $z_{2,1}$=0.075 cm soil depth. Likewise, the other measurement depths: soil moisture measurement at 0.1 m, 0.2 m, 0.4 m and 1 m corresponds to the moisture of $z_{1,2}$=0.075 m to $z_{2,2}$=0.15 m, $z_{1,3}$=0.15 m to $z_{2,3}$=0.30 m, $z_{1,4}$=0.30 m to $z_{2,4}$=0.70 m and $z_{1,5}$=0.70 m to $z_{2,5}$=1.00 m soil horizons, respectively. Thus, water content of each horizon w_d [mm] was computed as follow:

$$w_{d,i} = \theta_{vol,i} \times 1000 * (z_{2,i} - z_{1,i}) \quad (2.\ 6)$$

Then, cumulative soil moisture for the total depth (1.00 m) was computed. In order to get the daily irrigation doses, the moisture inversion method was used to eliminate the moisture peaks corresponding to rainfall. The remaining peaks are assumed to be irrigations (Figure 2.30). A subtraction between moisture at the date of the alleged irrigation (day j) and humidity at the previous date (day j-1) gives us approximately the irrigation dose.

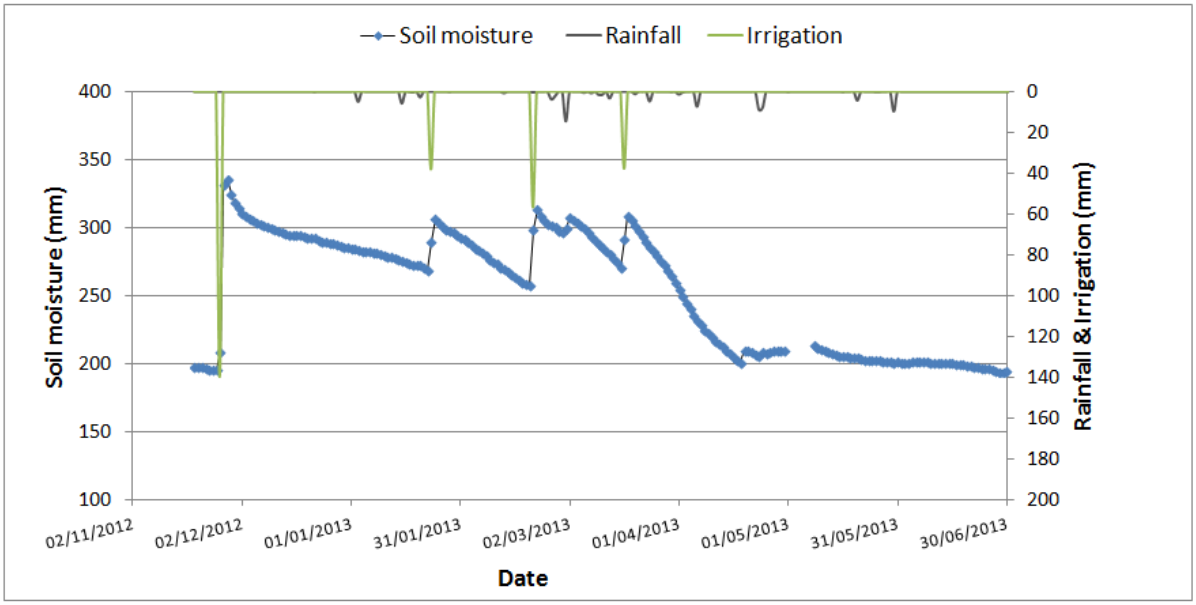

Figure 2. 30: Computed irrigations doses from the cumulative soil moisture in 1.00 m soil deep (the Ben Salem 1 soil moisture measurement from November 2012 to June 2013) and rainfall from the Ben Salem meteorological station for the same period.

2.5.3 Extra large aperture scintillomter (XLAS)

An optical Kipp and Zonen Extra Large Aperture Scintillometer (XLAS) was operated continuously for more than two years (1 March 2013 to 3 June 2015) over a relatively flat terrain (difference in levels of about 18 m). The scintillometer consists in a transmitter and a receiver both with an aperture diameter of 0.3 m. The wavelength of the light beam emitted by the transmitter is 940 nm. The transmitter was located on an eastern water

tower (coordinates: 35° 34' 0.7" N; 9° 53' 25.19" E; 127 m above sea level) and the receiver on a western water tower (coordinates: 35° 34' 17.22" N; 9° 56' 7.30"E; 145 m above sea level) separated by a path length of 4 km (Figure 2.31). Both instruments were installed at 20 m height. The scintillometer transect was above mixed vegetation canopy: trees (mainly olive orchards) with some annual crops (cereals and market gardening).

Furthermore, two automatic Campbell Scientific (Logan, USA) eddy correlation stations were also positioned at the same level on the two water tower top platforms. Half hourly turbulent fluxes in the eastern and the western EC stations were measured used a sonic anemometer CSAT3 (Campbell Scientific, USA) at a rate of 20 Hz and a sonic anemometer RM 81000 (Young, USA) at a rate of 10 Hz, respectively. These EC set-ups were used to initialise friction velocity u* values in the scintillometer derived flux computation.

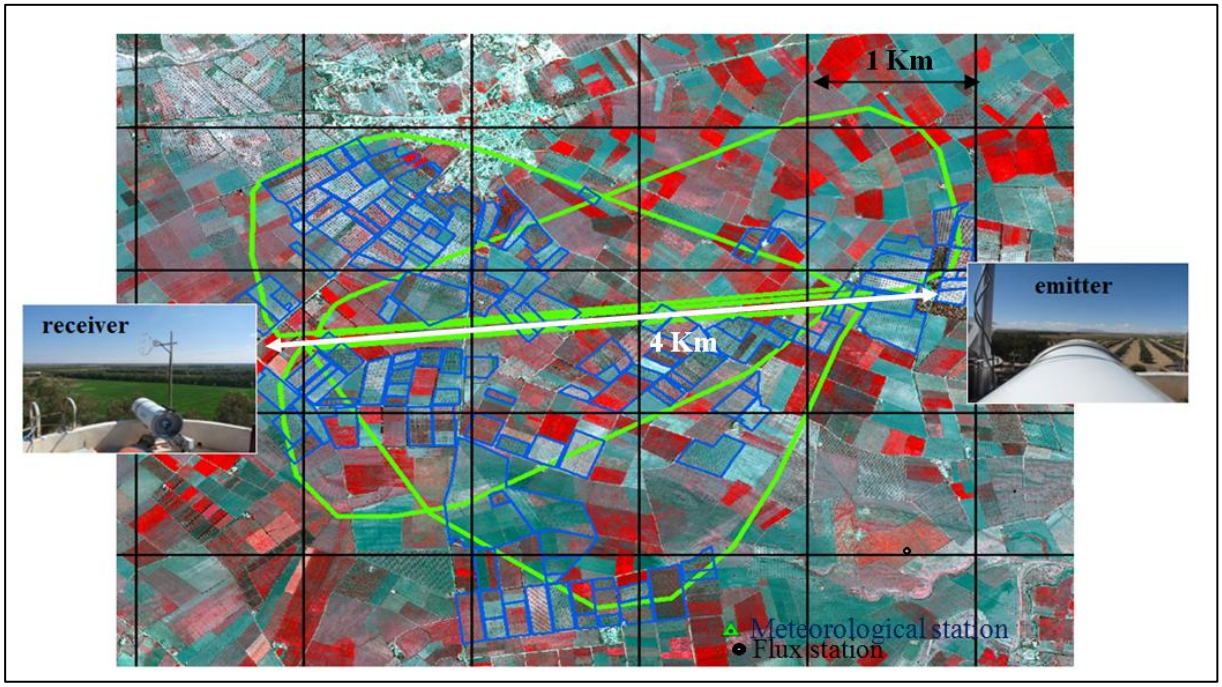

Figure 2. 31 : XLAS Set-up : XLAS transect (white), emitter and receiver are located at the extremity of each white arrow and half-hourly XLAS footprint for selected typical wind conditions (green), MODIS grid (black), trees plots (blue) and the location of the Ben Salem meteorological and the Ben Salem 1 flux station. This figure illustrates three colour (red, green, blue) composite of SPOT5 bands 3, 2 and 1 aquired acquired on 9th April 2013 and showing in red the cereal plots.

2.5.3.1 Scintillometer derived fluxes

In order to compute the XLAS sensible heat flux, the refractive index of air integrated along the optical path C_{n^2} [$m^{-2/3}$] was converted to the structure parameter of temperature C_T^2 [$K^2\ m^{-2/3}$] by introducing the Bowen ratio (ratio between sensible and latent heat fluxes), hereafter referred to as β, which is a temperature /humidity correlation factor. Moreover, the height of scintillometer beam above the surface varies along the path. Consequently, C_n^2 and therefore C_T^2 are not only averaged horizontally but vertically as well.

At visible wavelengths, the refractive index is more sensitive to temperature than humidity fluctuations Then, we can relate the C_{n^2} to C_{T^2} :

$$C_{n^2} \approx \left(\frac{-0.78 \times 10^{-6} \times P}{T^2}\right)^2 C_{T^2} \left(1 + \frac{0.03}{\beta}\right)^2 \quad (2.\ 7)$$

with T is the air temperature [°K] and P is the atmospheric pressure [Pa].

Green and Hayashi (1998) proposed another method to compute the sensible heat flux (H) assuming full energy budget closure and using an iterative process without the need of the Bowen ratio as an input parameter (Solignac *et al.*, 2009; Twine *et al.*, 2000). Then, the similarity relationship proposed by Andreas (1988) is used to relate the C_{T^2} to the temperature scale T_* in unstable atmospheric conditions:

$$\frac{C_{T^2}\,(z_{LAS} - d)^{\frac{2}{3}}}{T_*^2} = 4.9 \times \left(1 - 6.1 \times \left(\frac{z_{LAS} - d}{L_O}\right)^{-\frac{2}{3}}\right) \quad (2.\ 8)$$

and for stable atmospheric conditions:

$$\frac{C_{T^2}\,(z_{LAS} - d)^{\frac{2}{3}}}{T_*^2} = 4.9 \times \left(1 + 2.2 \times \left(\frac{z_{LAS} - d}{L_O}\right)^{\frac{2}{3}}\right) \quad (2.\ 9)$$

where L_O [m] is the Obukhov length , Z_{LAS} [m] is the scintillometer effective height, and d (m) is the displacement height, which corresponds to 2/3 of the averaged vegetation height z_v (see section 5.2).

From T_* and the friction velocity, u_* , the sensible heat flux can be derived as follows:

$$H = -\rho c_p T_* u_* \quad (2.\ 10)$$

where ρ [kg.m^{-3}] is the density of air and c_p [J.Kg^{-1}.K^{-1}] is the specific heat of air at constant pressure.

XLAS sensible heat flux (H_XLAS) was computed at a half hourly time step. Negative night-time data were set to zero and daytime flux missing data (one to three 30mn-data) were gap filled using simple interpolation. Flux anomalies in early morning (around sunrise) and late afternoon (around sunset) were corrected on the basis of the ratio between sensible heat flux and half hourly incoming short wavelengths radiation (Rg) measurements using the Ben Salem meteorological station. Furthermore, aberrant values of XLAS sensible heat flux were ruled out.

2.5.3.2 XLAS footprint computation

The footprint of a flux measurement defines the spatial context of the measurement and the source area that influences the sensors. In case of inhomogeneous surfaces like patches of various land covers and moisture variability due to irrigation, the measured signal is dependent on the fraction of the surface having the strongest influence on the sensor and thus on the footprint size and location. Footprint models (Horst and Weil, 1992; Leclerc and Thurtell, 1990) have been developed to determine what area is contributing the heat fluxes to the sensors as well as the relative weight of each particular

cell inside the footprint limits. Contributions of upwind locations to the measured flux depend on the height of the vegetation, height of the instrumentation, wind speed, wind direction, and atmospheric stability conditions (Chávez *et al.*, 2005).

According to the model of Horst and Weil (1992), for one-point measurement system, the footprint function *f* relates the spatial distribution of surface fluxes, $F_0(x,y)$ *to* the measured flux at height z_m, $F(x,y,z_m)$, as follows:

$$F(x,y,z_m) = \int_{-\infty}^{\infty}\int_{-\infty}^{x} F_0(x',y')f(x-x',y-y',z_m)dx'dy' \quad (2.\ 11)$$

The footprint function *f* is computed as:

$$f^y(x,z_m) \cong \frac{d\bar{z}}{dx}\frac{z_m}{\bar{z}^2}\frac{\bar{u}(z_m)}{\bar{u}(c\bar{z})}Ae^{-(z_m/b\bar{z})^r} \quad (2.\ 12)$$

where $\bar{u}(z)$ is the mean wind speed profile and $\bar{z}$ is the mean plume height for diffusion from a surface source. The variables *A, b* and *c* are scale factors and r a scale factor of the Gamma function. In the case of a scintillometer measurement, the footprint function has to be combined with the spatial weighting function *W(x)* of the scintillometer to account for the sensor integration along its path. Thus, the sensible heat flux footprint mainly depends on the scintillometer effective height z_{LAS} (Hartogensis *et al.*, 2003), which includes the topography below the path and the transmitter and receiver heights, the wind direction and the Obukhov length L_O, which characterizes the atmospheric stability (Solignac *et al.*, 2009). In a subsequent step, having the half hourly footprints (Fp_{30}), daily footprints (Fp_{day}) were computed as a weighted sum by the sensible heat flux (H_{30}), as follows:

$$Fp_{day} = \frac{\sum_{i=10:00}^{16:00} Fp_{30}(i) \times H_{30}(i)}{\sum_{i=10:00}^{16:00} H_{30}(i)} \quad (2.\ 13\ )$$

Only daytime observations from 10:00 to 16:00 UTC are considered, since the most important latent heat fluxes occur during this period. An example of a daily footprint is shown in figure 2.32. In the chosen day two wind directions are noted, south wind in the morning and then a north wind in the afternoon.

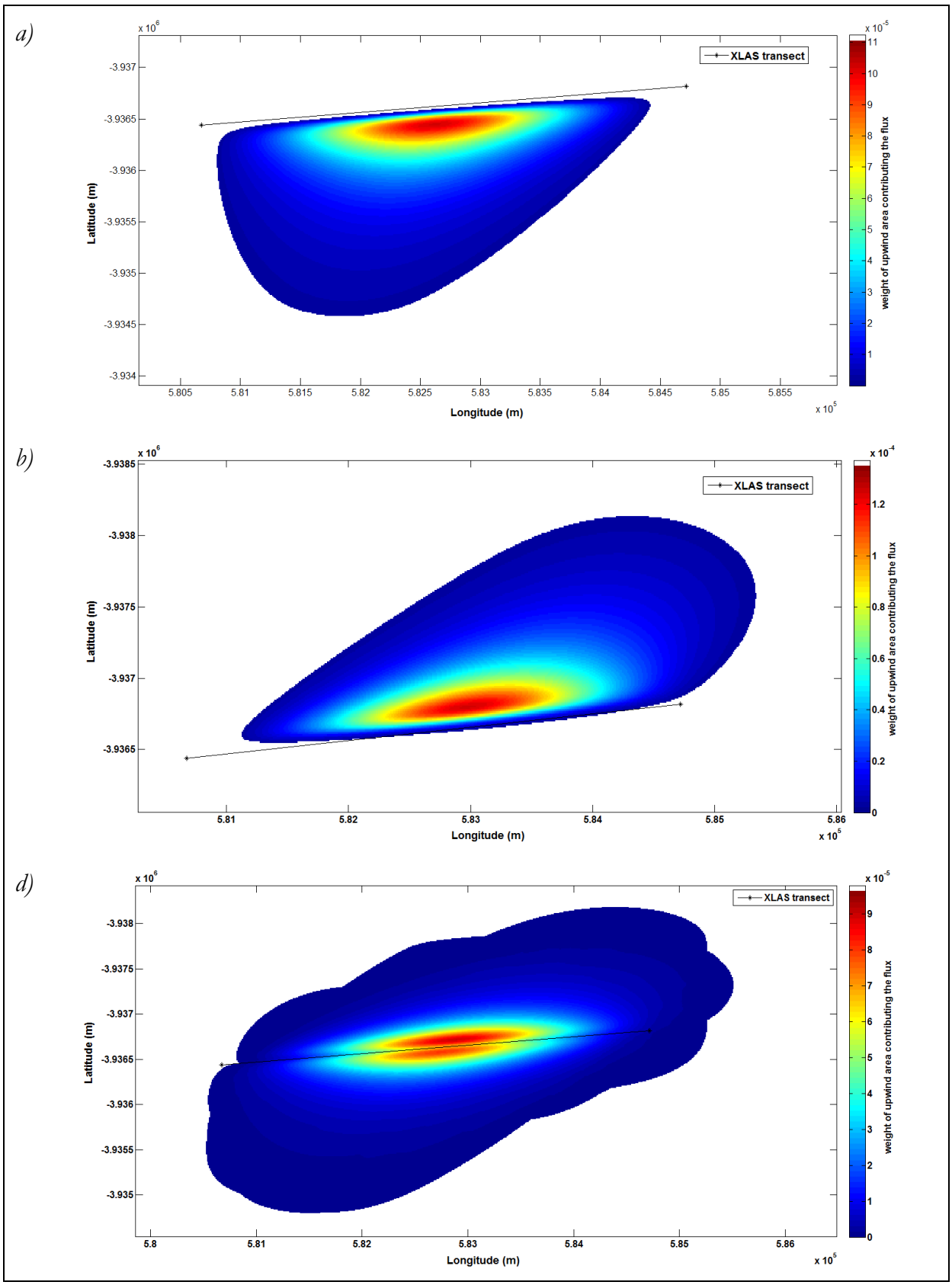

Figure 2. 32: Variation in source area contributions for 12 April 2013 at (a) 10:30 South Wind and (b) 16:00 North Wind and (c) resultant daily computed footprint

2.5.3.3 XLAS derived latent heat flux

Since the scintillometer only provides spatially averaged sensible heat flux (H_XLAS), the latent heat flux (LE_XLAS), energy equivalent of ET, can then be computed as the energy balance rest-term, hence, the estimation of a representative value for net surface radiation Rn combined with soil heat flux G, as available energy (AE=Rn-G) is always crucial for the accuracy of the retrieved values of LE_XLAS.

Instantaneous ($LE\_residual\_XLAS_{t\text{-}FP}$) and daily ($LE\_residual\_XLAS_{day\text{-}FP}$) XLAS derived latent heat flux (*i.e* residual latent heat flux) of the XLAS upwind area were computed assuming 100% energy budget closure of the XLAS measured sensible heat flux (H_XLAS) with additional estimations of AE as follows:

$$LE\_residual\_XLAS_{t-FP} = AE_{t-FP} - H\_XLAS_{t} \quad (2.\ 14)$$

$$LE\_residual\_XLAS_{day-FP} = AE_{day-FP} - H\_XLAS_{day} \quad (2.\ 15)$$

H_XLAS_t is the scintillometer sensible heat flux at the time of the satellite overpass interpolated from the half hourly fluxes measurements. Daily H (H_XLAS_{day}) was computed as the average of the half hourly XLAS-measured H. Daily available energy ($AE_{day\text{-}FP}$) was computed from instantaneous available energy (AEt-FP) as detailed the following paragraphs. The subscripts "day" and "t" refer to daily and instantaneous (at the time of Terra and Aqua overpasses) variables, respectively; while the subscript "FP" means that the footprint is taken into account *i.e.* instantaneous or the daily (depending on time scale) footprint was multiplied by the variable.

This assumption of 100% Energy Balance closure is valid only under the similarity hypothesis of Monin-Obukhov implying homogenous surface and stationary flows which is the case of our study area. In fact, above the XLAS transect, topography is flat, and landscape is heterogeneous only from an agronomic point of view since we find different land uses (cereals, vegetables and fruit trees mainly olive trees with considerable spacing of bare soil); however, this heterogeneity in landscape features at field scale is randomly distributed and there is no drastic change in height and density of the vegetation at the scale of the XLAS transect (*i.e.* little heterogeneity at the km scale, most MODIS pixels have similar NDVI values for instance). In order to provide a first guess on these relative heterogeneities, land use classes within each MODIS pixel of the 10 × 8 km sub-image were studied based on the land use map of the 2013-2014 season (see section 5.2).

a. Instantaneous available energy

Net surface radiation is the balance of energy between incoming and outgoing shortwave and longwave radiation fluxes at the land-atmosphere interface. Remote sensed surface radiative budget components provide unparalleled spatial and temporal information, thus several studies have attempted to estimate net radiation by combining remote sensing observations with surface and atmospheric data. Net radiation was computed using the equation 1.17 (see section 1.2.2.1)

The soil heat flux G depends on the soil type and water content as well as the vegetation type (Allen *et al.*, 2005b). The direct estimation of G by remote sensing data is not possible (Allen *et al.*, 2011a), however, empirical relations could estimate the fraction G/Rn as a function of soil and vegetation characteristics using satellite image data, such

as the LAI, NDVI, α and T_{surf}. In order to estimate the G/Rn ratio, several methods have been tested for various types of surfaces at different locations (Bastiaanssen, 1995; Burba *et al.*, 1999; Choudhury *et al.*, 1987; Jackson *et al.*, 1987; Kustas and Daughtry, 1990; Kustas *et al.*, 1993; Ma *et al.*, 2002; Payero *et al.*, 2001) .

Danelichen *et al.* (2014) evaluated the parameterization of these different models in three sites in Mato Grosso state in Brazil and found that the model proposed by Bastiaanssen (1995) showed the best performance for all sites, followed by the model from Choudhury *et al.* (1987) and Jackson *et al.* (1987). Hence, to estimate G, we tested three methods:

Bastiaanssen (1995):

$$G = Rn \times (T_{surf} - 273.16) \times (0.0038 + 0.0074\,\alpha) \times (1 - 0.98NDVI^4) \quad (2.\ 16)$$

Choudhury *et al.* (1987):

$$G = 0.4 \times Rn(\exp(-0.5LAI)) \quad (2.\ 17)$$

Jackson *et al.* (1987)

$$G = 0.583 \times Rn(\exp(-2.13NDVI)) \quad (2.\ 18)$$

Remote sensing variables α, T_{surf}, ε_s, LAI and NDVI were calculated at the resolution of the sensor (MODIS, 1 km resolution). The Ben Salem meteorological station was used to provide Rg and R_{atm}. MODIS Available Energy AE_t was computed for a 10 km × 8 km sub-image centered on the XLAS transect at Terra-MODIS and Aqua-MODIS overpass time, using the three methods estimating G. Since, the measured heat fluxes H_XLAS_t represents only the weighted contribution of the fluxes from the upwind area to the tower (footprint) then instantaneous footprint at the time of Terra and Aqua overpass were selected among the two half hour preceding and following the satellite's time of overpass (lowest time interval) and then was multiplied by AE_t to get the available energy of the upwind area $AE_{t\text{-}FP}$.

b. Daily available energy

Most methods using TIR domain data rely on once-a-day acquisitions, late morning (such as Terra-MODIS overpass time) or early afternoon (such as Aqua-MODIS overpass time). Thus, they provide a single instantaneous estimate of energy budget components, since the diurnal cycle of the energy budget is not recorded. In order to obtain daily AE from these instantaneous measurements and to reconstruct hourly variations of AE, we considered that its evolution was proportional to another variable whose diurnal evolution can be easily known.

The extrapolation from an instantaneous flux estimate to a daytime flux assumes that the surface energy budget is "self-preserving" *i.e.* the relative partitioning among components of the budget remains constant throughout the day. However, many studies (Brutsaert and Sugita, 1992; Gurney and Hsu, 1990; Sugita and Brutsaert, 1990) showed that the self-preservation method gives day- time latent heat estimates that are smaller than observed values by 5-10%. Moreover, Anderson *et al.* (1997) found that the evaporative fraction computed from instantaneous measured fluxes tends to

underestimate the daytime average by about 10%, hence, corrected parameterization was used and a coefficient=1.1 was applied. Similarly, Delogu *et al.* (2012) found an overestimation of about 10% between estimated and measured daily component of the available energy thus, a coefficient =0.9 was applied. The Delogu *et al.* (2012) corrected parameterization were tested, but this coefficient did not give consistent results, therefore, the extrapolation relationship was calibrated in order to get accurate daily results of AE .

Thereby, the applied extrapolation method was tested using *in situ* Ben Salem 1 (2012-2013) flux station measurements, but only for clear sky days for which MODIS images can be acquired and remote sensing data used to compute AE are available. Clear sky days were selected based on the ratio of daily measured Rg to the theoretical clear sky radiation Rso as proposed by the FAO-56 method (Allen *et al.*, 1998). A day was defined as clear if the measured Rg is higher than 85 % of the theoretical clear sky radiation at the satellite overpass time (Delogu *et al.*, 2012). Daily measured available energy $AE_{BS\text{-}day}$ computed as the average of half-hourly measured $AE_{BS\text{-}30}$, was compared to daily available energy ($AE_{BS\text{-}day\text{-}Terra}$ and $AE_{BS\text{-}day\text{-}Aqua}$) computed using the extrapolation method from instantaneous measured $AE_{BS\text{-}t\text{-}Terra}$ and $AE_{BS\text{-}t\text{-}Aqua}$ at Terra and Aqua overpass time, respectively (Equations 2.19 and 2.20).

$$AE_{BS-day-Terra} = a_{Terra} Rg_{day} \frac{AE_{BS-t-Terra}}{Rg_{t-Terra}} + b_{Terra} \quad (2.\ 19)$$

$$AE_{BS-day-Aqua} = a_{Aqua} Rg_{day} \frac{AE_{BS-t-Aqua}}{Rg_{t-Aqua}} + b_{Aqua} \quad (2.\ 20)$$

where Rg_{day} is the daily measured incoming short wavelengths radiation in the Ben Salem meteorological station; $Rg_{t\text{-}Terra}$ and $Rg_{t\text{-}Aqua}$ are the instantaneous incoming short wavelengths radiations measured at Terra and Aqua overpass time, respectively and $AE_{BS\text{-}t\text{-}Terra}$ and $AE_{BS\text{-}t\text{-}Aqua}$ are the instantaneous measured available energy in the Ben Salem flux station, at Terra and Aqua overpass time.

Results gave an overestimation of about 15 % (Figure 2.33). The corrected parameterizations of AE (Table 2.5), needed to remove the bias between measured ($AE_{BS\text{-}day}$) and computed AE ($AE_{BS\text{-}day\text{-}Terra}$ and $AE_{BS\text{-}day\text{-}Aqua}$), were applied to compute daily remotely sensed AE (AE_{day}) from instantaneous AE (AE_t) following the extrapolation method shown in equations 2.19 and 2.20.

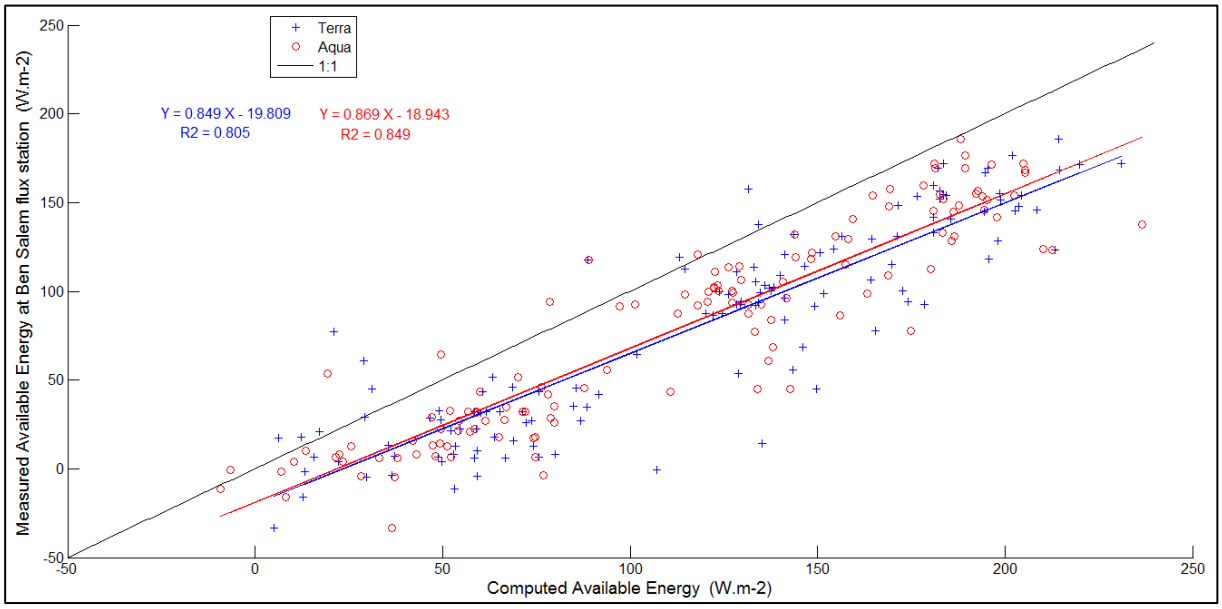

Figure 2. 33: Comparison of daily AE observed at Ben Salem 1 flux station (2012-2013) and daily AE estimated using the scaling method based on Rg.

Table 2. 4: Corrected parameterizations of available energy extrapolation method

Terra	a_{Terra}	0.85
	b_{Terra}	-19.81
Aqua	a_{Aqua}	0.87
	b_{Aqua}	-18.94

Daily available energy was computed for the 10 km × 8 km sub-image, and then was weighted by the corresponding daily footprint to get the daily available energy of the upwind area $AE_{day\text{-}FP}$. Finally, estimates of observed daily LE ($LE\_residual\_XLAS_{day\text{-}FP}$) were obtained based on the three methods used to compute the soil heat flux G.

2.6 Synthesis

In this chapter, the geographic and climatic framework as well as ground and surface water resources of our study area was presented. In addition, the experimental set-ups and *in situ* data were described. Experimental measurements are used either for model forcing (meteorological data), calibration (Eddy Covariance measurement for SAMIR model) or validation (XLAS measurement).

The different remote sensing data used in this PhD work were also presented; high-resolution SPOT image time series for four agricultural seasons are used to feed SAMIR model with NDVI data while low-resolution MODIS data are used to feed SPARSE model with NDVI and TIR data. This chapter detailed also the processing of all *in situ* and remote sensing data in order to get reliable and accurate data

Chapter 3: Evapotranspiration and irrigation volumes estimation at high spatial resolution: application of the soil water balance model SAMIR

The results of this chapter are taken from the article:

Saadi, S., Simonneaux, V., Boulet, G., Raimbault, B., Mougenot, B., Fanise, P., Ayari, H., Lili-Chabaane, Z., 2015. Monitoring Irrigation Consumption Using High-resolution NDVI Image Time Series: Calibration and Validation in the Kairouan Plain (Tunisia). Remote Sensing 7, 13005.

- Posted in « Remote Sensing » journal.

In this chapter, the operationality and accuracy of the SAMIR tool in computing distributed water balance components was assessed at both plot scale (calibration based on evapotranspiration ground measurements) and perimeter scale (irrigation volumes) when several land use types, irrigation and agricultural practices are intertwined in a given landscape.

3.1 SAMIR model description

The SAMIR tool (SAtellite Monitoring of IRrigation) (Simonneaux *et al.*, 2009) is based on the coupling of the FAO-56 dual crop coefficient model with time series of high-resolution NDVI imagery which provide estimates of the actual basal crop coefficient (Kcb) and the vegetation fraction cover (fc).

The basis of SAMIR is the FAO dual crop method under non standard conditions, *i.e.* considering the actual soil water status, as described in the FAO paper 56 (Allen *et al.*, 1998) and summarized in a subsequent paper (Allen *et al.*, 2005b). The main originality of SAMIR lies in the use of remote sensing NDVI time series for the monitoring of vegetation development, from which crop coefficients and vegetation fraction covers are derived, instead of using standard values. The NDVI, derived from near infra red (NIR) and red (R) reflectances, is available from most Earth observation sensors. SAMIR has been written in IDL/ENVI language as a plug-in to the ENVI software package, and is accessible through a Graphic User Interface. The FAO-56 basis of SAMIR has been described in chapter 1. All additional specific features of this tool are described in the paper included hereafter (section 3.2, Saadi *et al.*, 2015).

The input data in SAMIR are (i) meteorological data (*i.e.* reference evapotranspiration and rainfall), (ii) landuse map, (iii) NDVI time series, (iv) soil data and (v) irrigation rules.

Meteorological data (global radiation, air humidity, wind speed, and air temperature) are required to compute the Penman-Monteith reference evapotranspiration ETo (see section 2.5.1). SAMIR allows the user to use either uniform (one single station) or spatialized (e.g. several stations interpolated) input values of ETo. Rainfall data may also be considered homogeneous if a single station is available or spatially interpolated based on several stations.

The knowledge of land use is required for relating NDVI to the vegetation fraction cover (fc) and the basal crop coefficient (Kcb) and to define rooting parameters and irrigation rules. Since a land use map can usually be obtained only once some images have been acquired, which means several days after the beginning of the vegetation cycle, real time application would require the use of a land use assumption at the beginning of the season, based for example on the maps of the previous year along with crop rotation rules. This constraint emphasizes the need for developing new methods for monitoring the land use in quasi real time.

Moreover, the model requires calibrated NDVI time series based on soil reflectances. The user defines the NDVI-fc and the NDVI-Kcb or fc-Kcb relationships for each land use class. The values are then interpolated at daily step between the dates of imagery. For some annual crops, while NDVI drops during senescence due to drying, vegetation fraction cover remains high and affects turbulent and radiative transfers (shadowing). To account for this phenomenon, the fc profile can be kept steady during a given numbers of days after reaching its peak value, or until NDVI drops below a threshold indicating that harvest has occurred. For trees, considering the potential impact of the shades on

evaporation, we used a formalism defining the effective fraction cover; hypothesis of spherical canopies (Allen *et al.*, 1998).

The water content at field capacity and wilting point (θ_{fc}, θ_{wp}) are specified by the user. They can be considered uniform over the study area or spatialized based on a soil map. Following the FAO-56 recommendations, evaporation is controlled by the surface layer, whereas transpiration is controlled by the root zone. An additional layer was considered below the root compartment to account for deep water storage (Zhang and Wegehenkel, 2006). In order to allow water stored in this deep layer to be used by the plant, a diffusion process was introduced to simulate capillary water movement between deep and root layer. For coherence, diffusion was also introduced between the root and evaporation layer, allowing evaporation to last longer after a wetting event, and also to the deeper layers to keep drying after harvest. These additions to the FAO-56 aim to enable the simulation of rainfed cultivation or non-optimal irrigation. Lateral circulation of water (overland and subsurface runoff) is assumed negligible. During rainfall or irrigation events, the water fills the compartments successively from top to bottom by gravity. When all compartments are full, the excess water flows out of the system as deep drainage. For each land use class, the user specifies the minimum and maximum rooting depths (Zr_{min}, Zr_{max}) and the depletion fraction beyond which stress begins (p). The root depth Zr varies according to the plant development and is assumed to be linearly linked to the vegetation fraction cover (fc) (see section 3.2).

If irrigation volumes are known at the daily scale for any plot, they can be forced in SAMIR, but this is rarely the case, except for some experimental plots. For this reason, a set of rules triggering irrigation automatically has been built for SAMIR. These rules have to be specified by the user based on the known or assumed farmer's behaviour. Rules can be specific to each land use class and/or any irrigation unit. The main parameters to define are (i) the maximum allowable depletion for irrigation triggering, (ii) the irrigation depth to apply and (iii) the soil fraction wetted by irrigation (few). Irrigation may be triggered based on the level of readily available water (RAW), the level of total available water (TAW), for a given depletion of the root zone (Dr) or at any fixed time step. The water input depth may be either a fraction of the depletion or a fixed amount. Additionally, for annual crops which are not irrigated during senescence, inputs can be stopped once the Kcb decreases below a given fraction of the peak value reached. Finally, management constrains can give further control on the delivery of water at the seasonal scale. These are the maximum cumulated input depth for a plot during the whole season, the maximum number of water inputs, the minimum and maximum depth for each water input and a minimum time lapse between two inputs.

The rationale for daily water budget update is summarized as follows:

- Updating the soil configuration resulting from crop development

  - Updating the root depth (Zr)

  - Updating the soil moisture depletions (root zone depletion Dr and deep layer depletion Dd)

  - Updating the water capacities (TAW, RAW and the total available water in the deep compartment TDW)

- Applying water inputs (rainfall and irrigation)

  - Computing the automatic irrigation (based on irrigation rules) or forcing them if known

  - Updating the depletions with rainfall and irrigation

- Applying evapotranspiration and diffusion

  - Computing the evapotranspiration

  - Computing the diffusive fluxes

  - Updating the depletions with evaporation, transpiration and diffusion.

Actually, all these processes occur either during the whole day (e.g. evapotranspiration and diffusion) or at any random hour of the day (rainfall, irrigation). Thus, the order in which they are computed is somewhat arbitrary.

The output data of SAMIR are distributed daily values of ET [mm], irrigation [mm], stress coefficient (Ks), soil moisture [m^3/m^3] for the three soil layers, and percolation below the deeper soil layer (DP).

3.2 Irrigation volumes results validation at perimeter scale: Published results (article)

The soil water balance model SAMIR was run in our study area for four agricultural seasons 2008-2009, 2011-2012, 2012-2013 and 2013-2014 using NDVI time series of SPOT images. The following article shows results for only the first three seasons, because for the last one the satellite data was not yet available. The simulation was achieved on an area of about 18 km × 5 km encompassing three irrigated perimeters (GDAs) of the kairouan plain. The irrigation volumes observed in these GDAs were used to validate the irrigation volumes estimated using SAMIR.

Remote Sens. **2015**, *7*, 13005-13028; doi:10.3390/rs71013005

remote sensing

ISSN 2072-4292

www.mdpi.com/journal/remotesensing

Article

Monitoring Irrigation Consumption Using High-resolution **NDVI Image Time Series: Calibration and Validation in the Kairouan Plain (Tunisia)**

Sameh Saadi [1,2,*], Vincent Simonneaux [2], Gilles Boulet [1,2], Bruno Raimbault [1,2], Bernard Mougenot [1,2], Pascal Fanise [2], Hassan Ayari [1,2] and Zohra Lili-Chabaane [1]

[1] Institut National Agronomique de Tunisie/Université de Carthage, 43 Avenue Charles Nicolle,
1082 Tunis Mahrajène, Tunisie; E-Mail: zohra.lili.chabaane@gmail.com

[2] Centre d'Etudes Spatiales de la Biosphère, 18 Av. Edouard Belin, BP 2801,
31401 Toulouse Cedex 9, France; E-Mails: Vincent.simonneaux@ird.fr (V.S.); gilles.boulet@ird.fr (G.B.); raimbault.bruno@gmail.com (B.R.); bernard.mougenot@ird.fr (B.M.); Pascal.fanise@ird.fr (P.F.); hassan.ayari@ird.fr (H.A.)

***** Author to whom correspondence should be addressed; E-Mail: saadi_sameh@hotmail.fr; Tel.: +216-71-286-825; Fax: +216-71-750-254.

Academic Editors: Benjamin Koetz, Magaly Koch and Prasad S. Thenkabail

Received: 1 June 2015 / Accepted: 9 September 2015 / Published: 1 October 2015

Abstract: Water scarcity is one of the main factors limiting agricultural development in semi-arid areas. Remote sensing has long been used as an input for crop water balance monitoring. The increasing availability of high-resolution high repetitivity remote sensing (forthcoming Sentinel-2 mission) offers an unprecedented opportunity to improve this monitoring. In this study, regional crop water consumption was estimated with the SAMIR software (SAtellite Monitoring of IRrigation) using the FAO-56 dual crop coefficient water balance model fed with high-resolution NDVI image time series providing estimates of both the actual basal crop coefficient and the vegetation fraction cover. Three time series of SPOT5 images have been acquired over an irrigated area in central

Tunisia along with a SPOT4 time series acquired in the frame of the SPOT4-Take5 experiment, which occurred during the first half of 2013. Using invariant objects located in the scene, normalization of the SPOT5 time series was realized based on the SPOT4-Take5 time series. Hence, a NDVI time profile was generated for each pixel. The operationality and accuracy of the SAMIR tool was assessed at both plot scale (calibration based on evapotranspiration ground measurements) and perimeter scale (irrigation volumes) when several land use types, irrigation and agricultural practices are intertwined in a given landscape. Results at plot scale gave after calibration an average Nash efficiency of 0.57 between observed and modeled evapotranspiration for two plots (barley and wheat). When aggregated for the whole season, modeled irrigation volumes at perimeter scale for all campaigns were close to observed ones (resp. 135 and 121 mm, overestimation of 11.5%). However, spatialized evapotranspiration and irrigation volumes need to be improved at finer timescales.

Keywords: Remote sensing; water balance; FAO paper 56; evapotranspiration; irrigation; semi-arid Mediterranean; SPOT.

1. Introduction

In arid and semi-arid regions, water availability is a major limitation for crop production. In the Kairouan plain (Central Tunisia), the combined effect of drought spells and the increase of irrigated surfaces during the last decades have had a negative impact on the available water resources. Efficient agricultural water management is therefore a major issue, especially in irrigated areas. The design of tools that provide regional estimates of the water balance may help the sustainable management of water resources in these regions.

Evapotranspiration (ET) is one of the most important fluxes of the water balance in semi-arid areas; it is a key factor for optimizing irrigation water management [1]. Direct measurements of ET are only possible at local scale (single plot) using for example eddy-covariance devices. Scintillometers measure sensible heat flux along a given path and then latent heat flux (ET) is returned as a residual term of the surface energy budget. Furthermore, remote sensing (RS) capabilities for monitoring vegetation and its physical properties on large areas have been identified for years now (UNEP). It provides spatialized and periodic information about some major drivers of ET such as albedo, surface temperature and vegetation properties. Several methods for estimating ET using remotely-sensed data have been developed [3-7]. Most of them solve the surface energy budget for latent heat using thermal imagery. Instantaneous estimates at the time of satellite overpass have been successfully used to estimate ET at daily scale [8]. However, the main limitations of these methods are the difficulties in obtaining valid estimates of the aerodynamic surface

temperature and the atmospheric resistance to heat transfer in single-pixel methods or the difficulty in identifying the wet and dry edges when using triangle-based methods (UNEP). A further limitation arises when trying to extrapolate ET beyond one day due to the limited availability of high-resolution thermal imagery.

Another possible approach is to use Soil Vegetation Atmosphere Transfer models (SVAT) to simulate ET. These models can benefit from remote sensing since the latter provides periodic information about the vegetation development which is a primary factor driving evapotranspiration. The use of high-resolution image time series for monitoring irrigated crops was more recently discussed [10-12]. The low availability of such data, for financial as well as technical reasons, combined with the intermittent presence of cloud, has been a restraint to their use [13-15]. However, the forthcoming Sentinel-2 mission offers a unique opportunity to improve this monitoring thanks to high-resolution (10 m) and high repetitivity (5 days) visible and near infrared (VIS-NIR) remote sensing.

For the operational monitoring of soil-plant water balance, the most common and practical approach used for estimating crop water requirement is the FAO-56 method [16]. The FAO 56 dual crop coefficient approach uses two coefficients to separate the respective contribution of plant transpiration (Kcb) and soil evaporation (Ke). However, standard basal crop coefficients (Kcb) profiles provided by FAO tables are average values not suited for specific growth conditions that can largely differ between plots. Remote sensing is a valuable asset to derive those temporal profiles of crop coefficients. It has been shown that the crop coefficients were linked to the spectral response of the cover, especially vegetation indices [12,17-20]. Ke is linked to the bare soil fraction, complementary of the fractional vegetation cover (fc) which can also be related to visible RS data [21]. Although the relations proposed between Kcb, fc and vegetation indices are not theoretically fully linear, they can usually be approximated by linear relations [22-23]. Moreover, establishing a unique relationship between crop coefficient and spectral vegetation indices is an ongoing research topic [24] and many empirical linear relationships available in the literature have been derived experimentally.

The FAO-56 method has long been used to monitor water budget at plot scale with tools like CROPWAT [25]. The interest for coupling the FAO-56 method with remotely-sensed crop coefficients is rising alongside the increasing availability of high-resolution Normalized Difference Vegetation Index (NDVI) time series [26-30]. The SAMIR tool (SAtellite Monitoring of IRrigation) [31] used in this paper computes spatially distributed estimates of ET and crop water budget at regional scale. It is based on the coupling of the FAO-56 dual crop coefficient model with time series of high-resolution NDVI imagery (Normalized Difference Vegetation Index) providing estimates of the actual basal crop coefficient (Kcb) and the vegetation fraction cover (fc).

In this study, regional evapotranspiration and crop water consumption were estimated over an irrigated area located in the Kairouan plain using the SAMIR model fed by SPOT high-resolution time series. The model was calibrated on the basis of local ET measurements from flux towers and was validated at perimeter scale using known irrigation volumes. The objective

of the work was to assess the operationality and accuracy of SAMIR outputs at plot and perimeter scales, in a context of high land cover complexity (*i.e.*, trees, winter cereals, summer vegetables) and limited data available for parameterization.

2. Material and methods

2.1. Study Area

The experimental site is located in the Kairouan plain, a semi-arid region in central Tunisia (9°30′E to 10°15′E, 35°N to 35°45′N) (Figure 1), covering an area of more than 3000 km^2, which is part of the Merguellil watershed. The rainfall patterns are highly variable in time and space with an average annual rainfall of approximately 320 mm (extreme values recorded in Kairouan city are 108 mm in 1950/51 and 703 mm in 1969/70). The mean daily temperature in the city of Kairouan is 19.2 °C (minimum of 10°C in January and maximum of 28 °C in August). The relative humidity ranges between 70% and 55% in winter and 40% and 55% in summer. The mean annual reference evapotranspiration estimated by the Penman-Monteith method is close to 1600 mm. Dominant crops in this region are cereals, olive and fruit trees and market gardening [32].

Water management in the Merguellil basin is characteristic of semi-arid regions with an upstream sub-basin that collects surface and subsurface flows to a dam (the El Haouareb dam), and a downstream plain supporting irrigated agriculture (Figure 1). Irrigation water comes exclusively from the groundwater, except for a very small part of the plain on the edge of the dam: the major part of dam water infiltrates to the downstream aquifer. The main user of the Kairouan aquifer is agriculture, which consumes more than 80% of the total amount extracted each year [1]. Most farmers in the Kairouan plain extract water for irrigation directly from private wells, while a few rely on public irrigation schemes based on collective networks of water distribution pipelines stemming from a main gauged borehole. Each borehole corresponds to one organizational unit named GDA ("*Groupement de Développement Agricole*"). Annual consumption exceeds the annual recharge of the water table resulting in a piezometric decrease of between 0.5 m and 1 m per year [33].

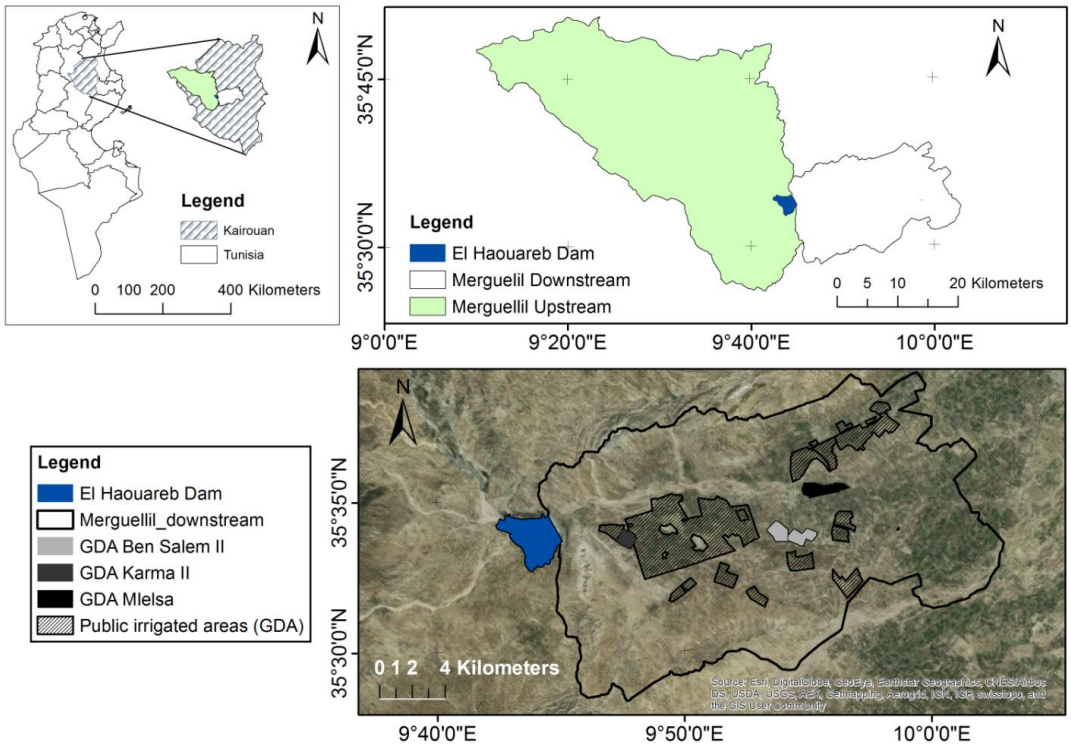

Figure 1. The study area

2.2. Experimental Setup and Data Pre-Processing

Half hourly meteorological measurements were recorded using an automated weather station installed in the study area. It includes measurements of solar radiation, air temperature and humidity, wind speed and rainfall. Cumulative precipitation and reference evapotranspiration (ETo) values between November and June were respectively 238 mm and 1008 mm, for the 2008/2009 season, 142 mm and 666 mm for the 2011/2012 season and 97 mm and 992 mm for the 2012/2013 season.

A flux station was installed in a plot located in the study area. It measures the various energy balance components using the eddy correlation method. Energy fluxes measurements were acquired over irrigated barley and irrigated wheat during the 2011–2012 and 2012–2013 seasons, respectively. These experiments allowed continuous monitoring of actual ET as well as soil moisture measurements. Energy balance closure of the EC measurements was checked and corrected using the residual method. The low uncorrected value obtained at both sites (around 60% of closure) led to discard fast response psychrometer measurements. Few isolated inconsistent peaks were also removed. Overall, the quality of eddy covariance measurements is mainly affected by instrumental errors, uncorrected sensor configurations or problems of heterogeneities in the area and atmospheric conditions [34].

Time series of SPOT5 image acquisitions were planned over the plain: Nine, six and ten SPOT5 images were acquired for the 2008–2009, 2011–2012 and 2012–2013 seasons, respectively (Figure 2).The SPOT5 images for the three campaigns were georeferenced using orthorectification and then radiometrically corrected to obtain top of canopy (TOC)

reflectance on the basis of physical modeling corrections using the Simplified Method for Atmospheric Corrections (SMAC) algorithm based on the 6S radiative transfer model [35]. The SMAC 6S model was applied for each image using values of atmospheric optical depth and water content taken from a photometer located in the area and part of the AERONET network [36]. Due to the uncertainties in the atmospheric parameters, and in order to eliminate time profile artifacts due to radiometric correction discrepancies within the time series, an additional inter-calibration between dates was achieved based on the identification of pseudo-invariant features for which a constant reflectance value is assumed over time. Indeed, the radiative transfer model shows that for a flat topography and an assumed spatially homogeneous atmosphere, the reflectance can be linearly related to the image DNs [37]. Thus, an additional normalization of the image time series was achieved by linear correction of the identified inconsistent dates [30,38]. For the last season, we also benefited from images acquired in the frame of the SPOT4-Take5 experiment which occurred during the first half of 2013 [39] and whose main purpose was to simulate the revisit frequency and resolution of Sentinel-2 images to help users set up and test their applications and methods before the mission is launched. In this frame, SPOT4 images at 20 meters resolution were acquired every 5th day from 3rd February to 18th June 2013 over the Kairouan plain, but only 14 dates were cloud free among the 28 images acquired (Figure 2). The SPOT4 series was corrected using the Multi-sensor Atmospheric Correction and Cloud Screening (MACCS) algorithm taking into account both temporal and spectral approaches for retrieving the aerosol optical thickness (AOT) [40].

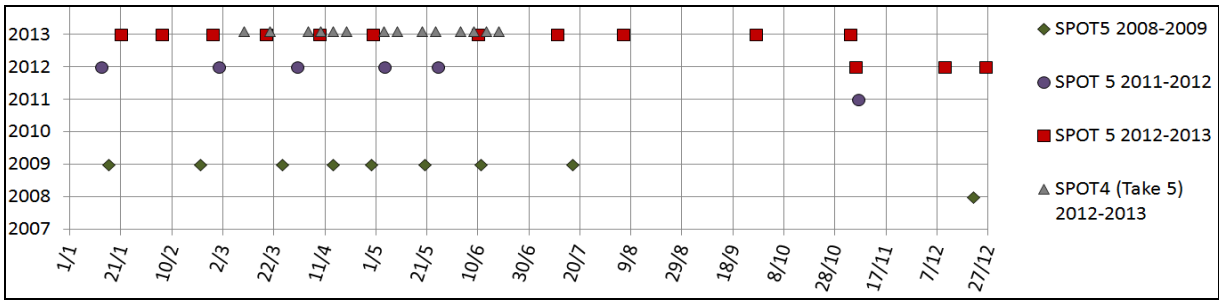

Figure 2. Acquisition dates of the SPOT images.

Monthly irrigation volumes used for validation were obtained at the scale of each GDA irrigated sector. It was assumed that these data were trustworthy since these entities manage a collective well equipped with a meter, providing the water to the plots inside the perimeter. However, some plots outside the official perimeter also benefit from this water and in the frame of the acquisition of our validation data, they were delineated with the help of the irrigation manager. Conversely, no private well is exploited inside the GDAs, so that the monthly volumes collected can be reliably linked to the declared cultivated area.

2.3. Method for Evapotranspiration and Irrigation Estimates

2.3.1. Model Description

The algorithmic basis of SAMIR is the FAO dual crop coefficient method under stress conditions, *i.e.*, considering actual soil water status [16]. This approach has been largely used for irrigation scheduling and to compute crop evapotranspiration for operational purpose. It is based on the concept of reference evapotranspiration for a standard well-watered grass, modulated by crop coefficients to account for the specific development of any vegetation cover as well as its actual water status. We present here only the major equations of the model and the modifications implemented within SAMIR. The reader should refer to the FAO paper N°56 for other equations; we kept for clarity the same notations as FAO paper 56 [16]. The actual (adjusted) evapotranspiration ETa of a crop is defined as:

$$ET_a = (K_s \cdot K_{cb} + K_e)ET_o \quad (1)$$

where Kcb is the basal crop coefficient representing unstressed crop transpiration, Ke is the evaporation coefficient representing soil evaporation and Ks is a stress coefficient accounting for the reduction of transpiration due to water shortage in the root zone.

ET_0 was computed following the FAO paper 56 and is thus not presented here. Regarding Ke, in order to account for frequent overestimations of bare soil evaporation as observed by [41], we used the same formalism as the latter reference to modify the Kr coefficient, *i.e.*, the evaporation reduction coefficient accounting for water availability in the evaporation layer which is used to compute Ke.

$$Kr = m \cdot \frac{TEW - De}{TEW - REW} \leq 1 \quad (2)$$

with TEW the total evaporable water, REW the easily evaporable water and De the depletion (water deficit) in the shallow surface layer used to compute soil evaporation. The m coefficient lies within [0,1] and allows to further reduce the maximum evaporation level when REW = 0 and is functionally equivalent to a minimum surface resistance to evaporation of the soil.

As an extension to the standard FAO-56 formalism, an additional layer of depth Zd was considered beyond the root depth Zr to account for capillary flow from below the root zone [42]. The total depth of soil involved in crop functioning Zsoil is defined as Zsoil = Zr + Zd. To allow the water stored in this deep layer to be used by the plant, a diffusion process was introduced in the SAMIR model to simulate capillary flow between deep and root layers (Dif_{rd}). For coherence, diffusion was also introduced between the root zone and the shallow evaporation layer (Dif_{er}), allowing especially evaporation to last long after a wetting event, and also to the deeper layers to sustain low evaporation fluxes observed after harvest. The depth of the root and deep layers evolves dynamically with root growth: when root depth increases, a portion of the deep layer is included in the root zone. The total available water in

the deep compartment (TDW) is computed similarly to total available water in the root layer (TAW) using the following formula:

$$TDW = (\theta fc - \theta wp) \cdot Zd \quad (3)$$

with θfc the water content at field capacity and θwp the water content at wilting point. Water diffusion is driven by the water gradient between layers as follows:

$$Dif_{er} = cdE.\left(\frac{\frac{(TAW - Dr)}{Zr} - \frac{(TEW - De)}{Ze}}{\theta fc}\right) \quad (4)$$

$$Dif_{rd} = cdR.\left(\frac{\frac{(TDW - Dd)}{Zd} - \frac{(TAW - Dr)}{Zr}}{\theta fc}\right) \quad (5)$$

where De, Dr and Dd are the depletions in the evaporation , root and deep layers, respectively, while cdE and cdR are the diffusion coefficients for the transfers between the root zone and the surface layer, and the root zone and the deep layer, respectively (mm·day^{-1}).

Regarding the vegetation development, instead of using standard values provided by the FAO paper 56, the major specificity of SAMIR is to use remote sensing data to estimate the actual basal crop coefficient Kcb using a linear relationship:

$$Kcb = a_{Kcb} \cdot NDVI + b_{Kcb} \quad (6)$$

where NDVI is the Normalized Difference Vegetation Index, depending on near infra red (NIR) and red (R) reflectances:

$$NDVI = \frac{NIR - R}{NIR + R} \quad (7)$$

The NDVI time series is linearly interpolated for each day between the successive dates of image acquisition.

In the same manner, the vegetation fraction cover fc was derived from NDVI using the following linear relation:

$$fc = a_{fc} \cdot NDVI + b_{fc} \quad (8)$$

Then the root depth is linked to the vegetation fraction cover using the following formula:

$$\mathrm{Zr} = Zrmin + \frac{fc}{fcmax} \cdot (Zrmax - Zrmin) \quad (9)$$

where fc_{max} is the maximum fraction cover for which the maximum rooting depth Zrmax is reached and Zrmin is the minimum rooting depth when the vegetation is detected by the satellite (fc > 0).

Finally, the model updates the water content of the three soil layers at a daily time step in order to compute the water budget using equations similar to those in the FAO paper 56 [16].

The main difference lies in the added Dif_{er} and Dif_{rd} terms for water diffusion, and the addition of the deep layer. The surface runoff is neglected.

The water content in the evaporation layer is updated as follows:

$$\begin{cases} De_j = De_{j-1} - P_j - \dfrac{I_j}{f_w} + \dfrac{E_j}{f_{ew}} + Tew_j - Dif_{er} \\ 0 \le De_j \le TEW \end{cases} \quad (10)$$

where De_j is the cumulative depth of evaporation (depletion) at the end of day j (mm), De_{j-1} is the same variable at the end of day j − 1 (mm), P_j is the precipitation, I_j is irrigation depth, E_j is the soil evaporation, Tew_j is the depth of transpiration from the exposed and wetted fraction of the soil surface layer, all on day j (mm), f_w is the fraction of soil surface wetted by irrigation and f_{ew} is the wetted soil fraction exposed to evaporation.

The water content in the root layer is updated as follows:

$$\begin{cases} Dr_j = Dr_{j-1} - P_j - I_j + ETc_j - Dif_{rd} \\ With\ 0 \le Dr_j \le TAW \end{cases} \quad (11)$$

where Dr_j is the depletion in the root layer at the end of day j (mm), Dr_{j-1} is the same variable on day j − 1, ETc_j is the soil evaporation on day j (mm). If the water content goes beyond field capacity after a heavy rain or irrigation (*i.e.*, $Dr_j < 0$), it is assumed that the amount of water above field capacity is lost the same day by percolation to the deep layer ($DPr_j = -Dr_j$) and then Dr is set to zero.

The depletion in the deep layer is computed as follows:

$$\begin{cases} D_{d,j} = D_{d,j-1} - DP_r + Dif_{er} \\ 0 \le D_{d,j} \le TDW \end{cases} \quad (12)$$

where Dd_j is the depletion in the deep layer at the end of day j (mm), Dd_{j-1} is the same variable on day j − 1. In the same manner as for the root zone, if $Dd_j < 0$ then an amount DPd_j of deep percolation is assumed to be lost for the crop ($DPd_j = -Dd_j$) and Ddj is set to zero.

The water stress of vegetation in the FAO method is expressed by a coefficient Ks related to the actual root zone water content. A fraction p of TAW named Readily Available Water (RAW) is supposed to be available for the plant without stress (Ks = 1). The stress is presumed to start when Dr > RAW and is calculated using Equation (13) (Ks < 1). Conversely, when Dr ≤ RAW then Ks = 1.

$$K_s = \frac{TAW - Dr}{TAW - RAW} = \frac{TAW - Dr}{(1 - p)\,TAW} \quad (13)$$

whereas rainfall inputs can be estimated using meteorological data, the irrigation inputs are very variable in space and time and cannot be known practically on large areas. Thus, the SAMIR tool simulates irrigations based on the daily soil water balance of the root zone. Irrigation is modeled specifically for each land cover class, so as to reproduce the various irrigation

practices applied by the farmers on the ground. These practices are described by several parameters that the user has to set. A major parameter is the threshold water content in the root layer to trigger a water input, defining the management allowable depletion MAD [16], *i.e.*, the amount of water which can be depleted between two irrigations. When the root zone depletion reaches this value, irrigation is automatically triggered to fill up the soil. Other parameters to set are the fraction of soil surface wetted by irrigation (fw) depending on the irrigation system, the minimum depth of each input (Min_ir) and the minimum number of days between two water inputs (Min_days). Finally, the Kcb threshold to stop irrigation during the senescence stage (Kcb stop) is defined as a percentage of the peak Kcb value (maximum development) below which irrigation is stopped. In simulating irrigations, SAMIR does not aim at detecting an actual vegetation stress at the time it occurs. Instead, the hypothesis is that if a significant stress occurs, it will have an effect on the NDVI in the following days which will be accounted for by SAMIR.

2.3.2. Model Calibration and Validation at Plot Scale

The model was calibrated at plot scale using latent heat flux measurements for two seasons. Calibration consists in maximizing the Nash efficiency computed between observed and modeled ET. The Nash-Sutcliffe efficiency coefficient is a non-dimensional statistical performance index that determines the relative magnitude of the residual variance compared to the observed variance [43].

$$NASH = 1 - \frac{\sum_{i=1}^{n}(ET_i^{obs} - ET_i^{sim})^2}{\sum_{i=1}^{n}(ET_i^{obs} - \overline{ET^{obs}})^2} \quad (14)$$

where ET_i^{obs} is the observation of evapotranspiration on day i, ET_i^{sim} is the modeled value of evapotranspiration on day i and $\overline{ET^{obs}}$ is the observed mean over the entire growing season. The Nash efficiency ranges from $-\infty$ to 1; an efficiency of 1 corresponds to a perfect match between model outputs and observations.

Some of the model parameters were taken from the FAO paper 56 [16] or measured *in situ* (e.g., soil water content), while others were calibrated either because they were not available from the bibliography or because the model was particularly sensitive to these parameters. The procedure to prescribe each parameter value is detailed in the results section. For irrigation, a two-step approach was implemented. First, actual irrigations values resulting from soil moisture measurement analysis were used as inputs in the calibration of the model, then, known irrigations were removed from the model inputs and the automatic irrigation mode was switched on in order to calibrate the irrigation parameters.

2.3.3. Spatialization of ET and Irrigation.

SAMIR was run over the whole irrigated plain using the image time series for the three seasons to compute spatially distributed estimates of irrigation depths. Water balance components, including irrigation, are computed for each pixel. Land use information is required for each pixel

since many parameters of the model are crop specific. This is the case for the root zone parameters, the irrigation rules and the fc(NDVI) and Kcb(NDVI) relations. Land cover maps were available for 2008–2009 [44], 2011–2012 [45] and 2012–2013 [46]; they include eight, six and six land use classes, respectively. These classifications were obtained by applying a multi temporal decision tree, which allows the identification of crop types on the basis of NDVI thresholds derived from ground truth datasets. The SAMIR parameters required for each land use class were taken either from the previous calibration step (*i.e.*, for cereals) or from bibliographic data since there was no calibration data for market gardening and fruit trees classes. The climatic forcing was considered homogeneous over the plain and meteorological data was taken from the sole station present in the area. Finally, the irrigation parameterization for crops other than cereals was defined from our knowledge of the farmers' practices, while considering the main differences in irrigation practices between classes (e.g., aspersion for cereals, drip irrigation for orchards). In order to validate the SAMIR estimates, irrigation depths were cumulated to monthly values at the scale of irrigation sectors (GDA) and compared to available official irrigation volumes gathered through our ground survey.

3. Results and Discussion

3.1. Remote Sensing Data Preprocessing

For the SPOT4-take5 time series acquired in 2012–2013, the longest gap was at the beginning of the period, as the first correct image was acquired on 10/03/2015, which means 40 days without image data. This is quite long regarding vegetation monitoring and emphasizes the limitation of a five-day revisit frequency even in semi-arid areas (frequent cirrus clouds can be observed over the study site). However, in our case, this gap was filled using the SPOT5 satellite, which successfully acquired two images, thanks to the programming capabilities of this sensor and its oblique viewing agility allowing to observe areas on cloud free days. This is an interesting result showing that combining Sentinel-2 data with other sensors (Landsat 8, SPOT6, *etc*.) may still be necessary in many places to get consistent high-resolution time series. Another way to bridge the gaps in the time series would be to use fusion methods using medium resolution images to estimate high-resolution signatures [47].

We present hereafter the outcome of the images pre-processing for the 2012–2013 season; the same approach was applied to the 2008–2009 and 2011–2012 images. After application of an atmospheric correction, we identified manually 28 invariant objects in the scene by visually comparing pairs of distant dates (*i.e.*, 5 November 2012 and 10 June 2013). Then, for these 28 objects, the reflectance of one band at each date is plotted against the reflectance of the average image of this band (Figures 3 and 4). The quality of the invariant objects is confirmed by the determination of the linear fit. However, whereas in some cases the regression fits the 1:1 line (Figures 3a and 4a), in other cases the regression line is significantly different from the 1:1 line, showing a problem in the quality of the atmospheric correction. These discrepancies are more frequent for the SPOT5 time series, which is not

surprising as each date was corrected independently, whereas the SPOT4 series was corrected using the MACCS algorithm taking into account the temporal dimension of the series. When the deviation from the 1:1 line was important (Figures 3b and 4b), the linear correction was applied to the image to match it with the average image. For the SPOT4 series, seven dates were linearly corrected, and one date was discarded (20 March) because of the strong scattering of the reflectance due to haze (Figure 4c). For the SPOT5 time series, eight images were corrected.

Once the consistency of reflectance levels within the two time series had been checked, a similar analysis is performed between the two time series by plotting the average reflectance of the invariant objects (Figure 5). A significant bias was observed which can be explained by (i) differences in the atmospheric correction algorithm used, (ii) difference in band definition between SPOT4 and 5 and (iii) the variations in viewing angle between both sets of images. Indeed the SPOT4 images were acquired at a fixed angle different from nadir, whereas SPOT5 images were acquired at any angle. The observed bias had a strong impact on maximum NDVI values observed in the images, which was 0.9 for the SPOT4 series, and only 0.7 for the SPOT5 series. Considering that fully covering vegetations were certainly present in the area (*i.e.*, cereals or forage fields), a realistic maximum NDVI value of 0.9 was expected for all seasons. Therefore, the SPOT5 series was linearly normalized to match the SPOT4-Take5 radiometry on the basis of the linear regression established between the reflectance of the SPOT5 and SPOT4-Take5 average images (Figure 5).

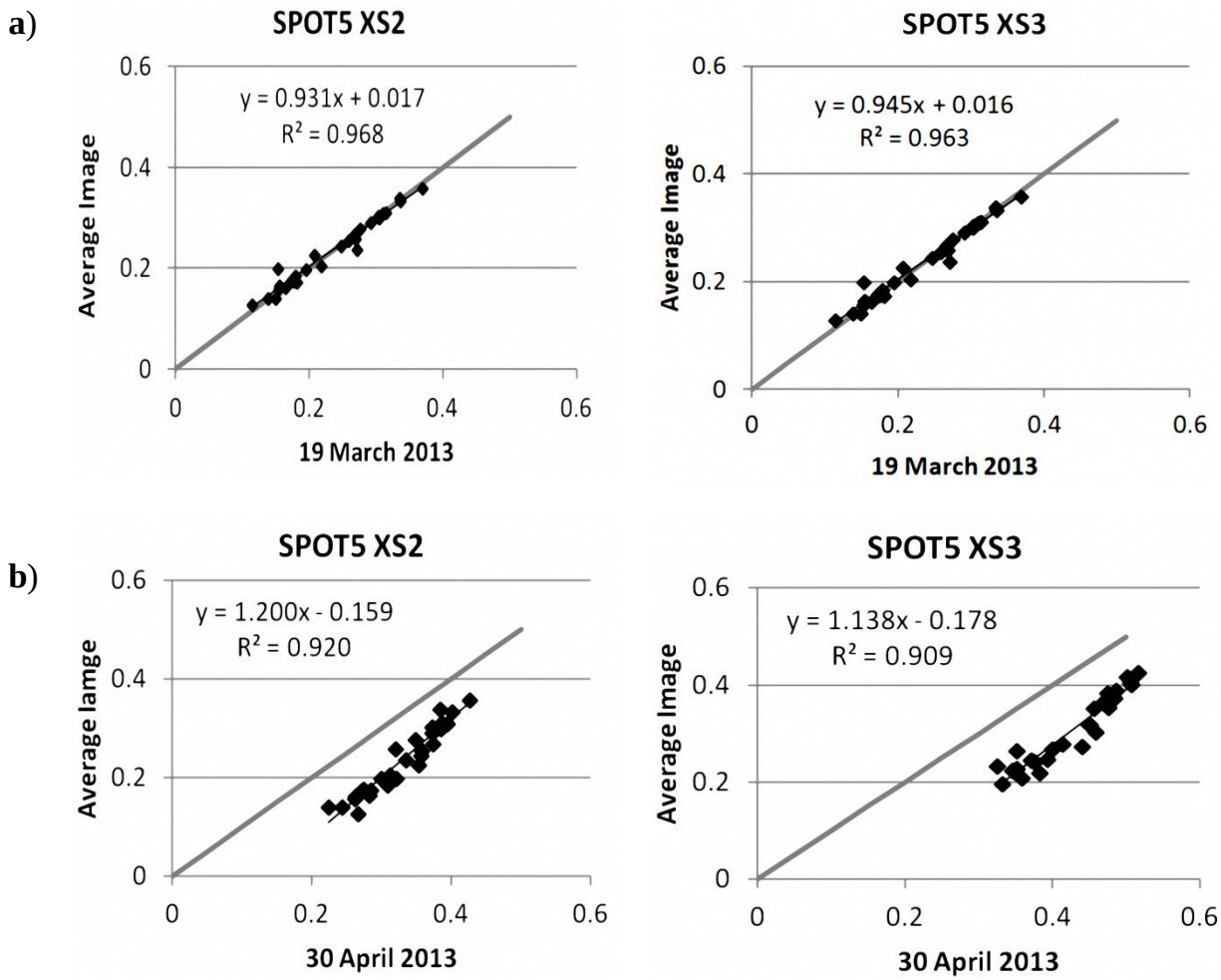

Figure 3. Comparison between the SPOT5 images after atmospheric correction using SMAC6S and the average SPOT5 reflectance for the 28 invariant sites, for spectral bands XS2 and XS3. Example of (**a**) an image for which no additional correction is required and (**b**) an image needing an additional correction.

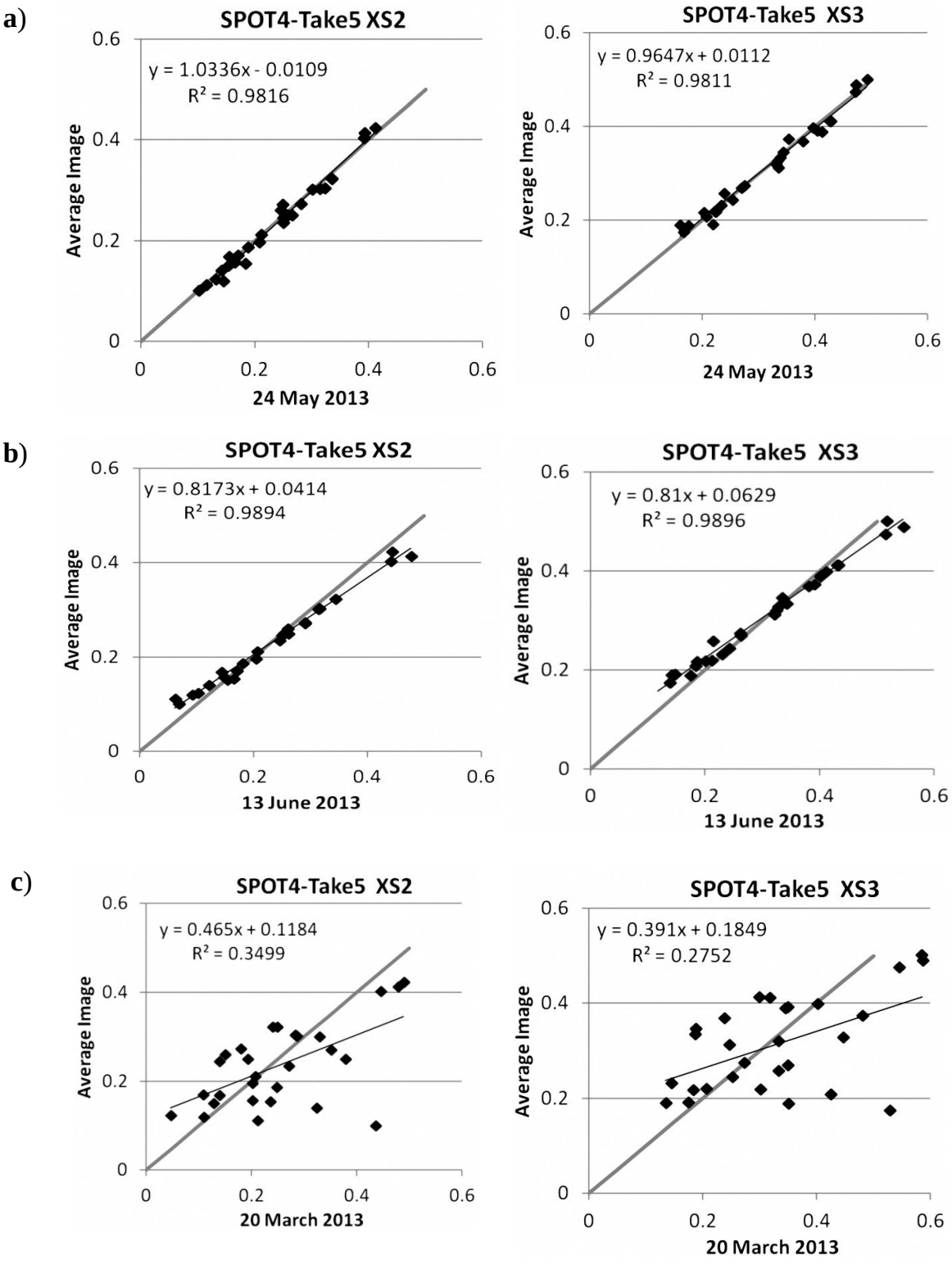

Figure 4. Comparison between the SPOT4-Take5 atmospherically corrected images and the average SPOT4 reflectance for the 28 invariant sites, for spectral bands XS2 and XS3. Example of (**a**) an image for which no additional correction is required, (**b**) an image needing an additional correction and (**c**) a hazy image (discarded from the final time series).

The SPOT4 series was delivered with cloud masks that were applied to avoid anomalies in the NDVI. For the SPOT5 series, two images included small cumulus clouds (5 November 2012 and 21 January 2013) which were masked. The clouds were identified using a simple threshold since they have a strong reflectance in the blue band. The cloud shadows were also easy to identify because they had the lowest reflectance in the near infra-red band. As small clouds were rarely at the same place, they have limited impact on the resulting NDVI profiles.

Finally, from the combination of these two time series, a NDVI profile was generated for each pixel.

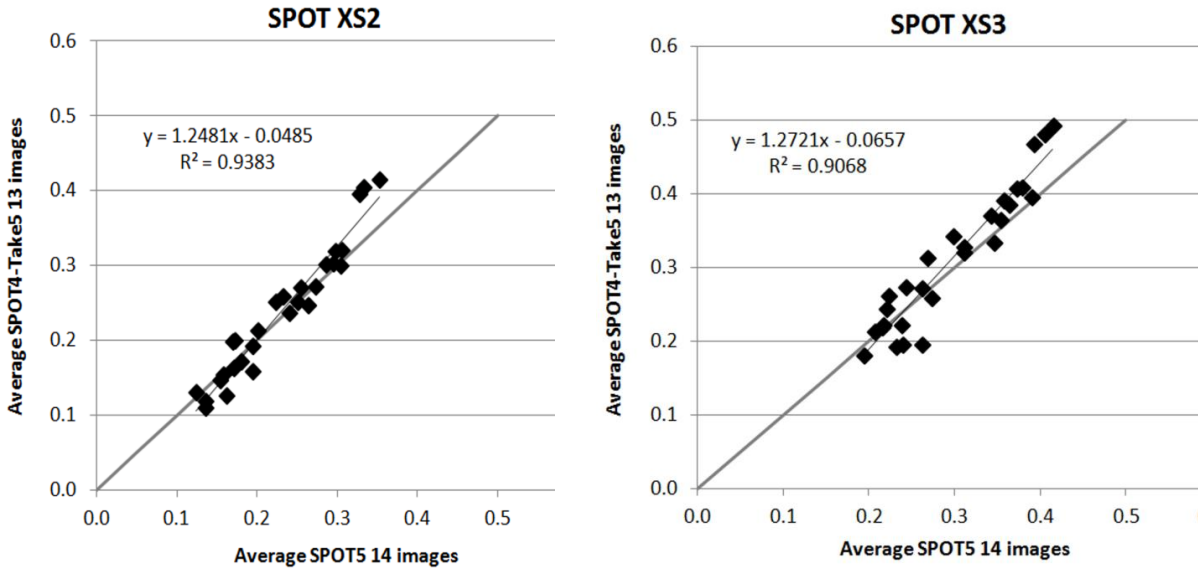

Figure 5. Comparison between the average reflectances of the 28 invariants for the SPOT5 and SPOT4-Take5 time series before correction.

3.2. Plot Scale Calibration of Evapotranspiration Parameters

In a subsequent step, the NDVI time profile for each flux site was extracted from the SPOT time series and was used in the SAMIR model for calibration. The NDVI-fc relationship was determined empirically considering that for a bare soil (NDVI = 0.1) the fraction cover was null (fc = 0) and that at full coverage (fc = 1) the NDVI was the maximum value observed in the image (0.9). The characteristic volumetric soil water contents were determined from soil texture analysis (clay loam, θ_{fc} = 0.29, θ_{wp} = 0.15). An initial water content of 10% was considered for the two plots since soils were mostly dry after the summer and before the first autumnal rainfalls. The soil fraction wetted by rain or irrigation (fw) was set to one because the irrigation technique for cereals was sprinkler irrigation. The depth of the evaporation layer (Ze) and the proportion of easily available water (p) were fixed following FAO paper 56 recommendations [16]. All other parameters were fixed by calibration (REW, m, Zr_{max}, Z_{soil}, Dif_{er}, Dif_{rd}, Kcb) and are summarized in Tables 1 and 2. In a second phase, irrigation parameters were calibrated by assuming an optimal management to avoid stress (*i.e.*, water

input when RAW is empty) and the depth of water inputs was selected in order to fill the depletion
(Dr = 0). The calibration was applied simultaneously to both seasons to get a unique set of parameters for cereals. The results (Table 3) show that cereals are irrigated only a short time after the vegetation peak is reached (Kcb_stop = 99%) which is consistent with the conventional agricultural practice for cereals (no more water is needed after grain filling during the maturation stage.

The results showed that although evapotranspiration simulations are on the whole correct (Figure 6), they are better for the barley plot than for the wheat plot (Nash efficiency of 0.6 and 0.53 respectively and a root mean square deviation RMSD of 0.63 and 0.94 mm respectively). However, we also see that this difference might be due to problems in the observed data, as it is very clear that the daily variations of observed ET for wheat are much stronger than for barley and should be considered with care. However, they might be mainly noisy and we see no clue of any significant bias since they reproduce well the seasonal cycle and they are also coherent with the independent ET0 measurements. The discrepancies were more frequent at the end and at the beginning of the growing season (Figure 6), when vegetation cover is low and soil evaporation process dominates. The calibrated parameters are shown in Table 1.

Table 1. Parameters obtained after calibration on observed ET for wheat and barley plots. Grey cells show calibrated parameters.

	Definition	**Value**	**Data Sources**
	Vegetation Parameters		
a_{fc}	NDVI-fc relation's slope	1.25	Satellite imagery
b_{fc}	NDVI-fc relation's intercept	−0.13	Satellite imagery
a_{Kcb}	NDVI-Kcb relation's slope	1.35	Calibrated
b_{Kcb}	NDVI-Kcb relation's intercept	−0.18	Calibrated
	Soil Parameters		
θ_{fc} (m^3/m^3)	Volumetric water content at field capacity	0.29	Ground observation
θ_{wp} (m^3/m^3)	Volumetric water content at wilting point	0.15	Ground observation
Init_RU (%)	Soil initial water content	10	Ground observation
Ze (mm)	Height of the surface layer	125	FAO-56
REW (mm)	Readily evaporable water at surface layer	0	Calibrated
m	Coefficient de reduction	0.264	Calibrated
Zr_{min} (mm)	Minimum root depth	125	FAO-56
Zr_{max} (mm)	Maximum root depth	1650	Calibrated
p	Maximum Root Water Depletion Fraction before stress	0.55	FAO-56
Z_{soil} (mm)	Total soil thickness	2000	Calibrated
Dif_{er} (%)	Diffusion between surface and root layers	10	Calibrated
Dif_{rd} (%)	Diffusion between deep and root layers	20	Calibrated

Table 2. Relations used for fc and Kcb estimates from NDVI

NDVI-fc	**NDVI min**	**NDVI max**	**fc min**	**fc max**	**Relations**	**Sources**
Cereals	0.1	0.9	0	1	$fc = 1.25 \times NDVI - 0.13$	Satellite imagery
Market gardening	0.1	0.9	0	1		
Fruit trees	0.1	0.8	0	0.9	$fc = 1.34 \times NDVI - 0.17$	
NDVI-kcb	NDVI min	NDVI max	Kcb min	Kcb max	Relations	Sources
Cereals	-	-	-	-	$K_{cb} = 1.36 \times NDVI - 0.18$	Calibration (barley and wheat experiment field).
Market gardening	0.1	0.9	0	0.98	$K_{cb} = 1.23 \times NDVI - 0.12$	FAO paper 56 [16] and Satellite imagery.
Fruit trees	-	-	-	-	$K_{cb} = 0.76 \times fc$	Calibration (olive trees experimental field in Morocco)

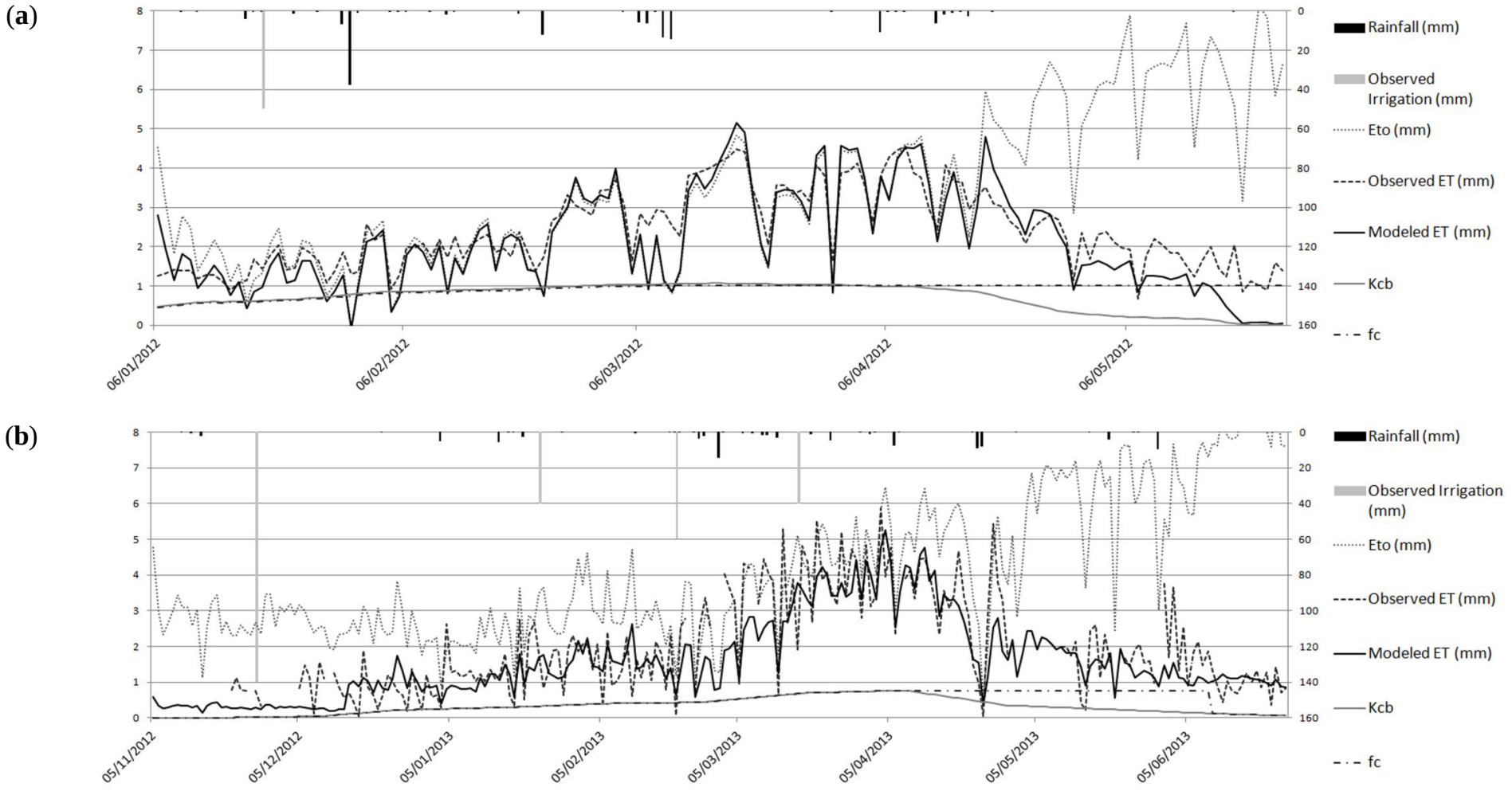

Figure 6. Simulations of ET for the (**a**) barley and (**b**) winter wheat experiment fields for the calibrated model using observed irrigations (Nash = 0.6 and 0.53, respectively).

Table 3. Soil and Irrigation parameters used for spatialization.

		Cereals	Market Gardening	Fruit Trees
Soil parameters				
Zrmax (mm)		1650	1000	1600
p		0.55	0.55	0.65
Initial RU (%)	2008/2009	10	10	
	2011/2012	32	32	50
	2012/2013	10	10	
Irrigation rules				
Fw, fraction wetted (%)		100	25	100
MAD, management allowable depletion for irrigation triggering		MAD = RAW	MAD = 0.2 * TAW	MAD = RAW
Kcb_stop, Kcb threshold to stop irrigation (% of Kcbmax)		99	75	0
Irrigation constraints				
Min_ir, minimum water depth per turn (mm)		20	0	20
Min_days, minimum number of days between two water turns		7	7	7

3.3. Validation of Irrigation Volumes at Perimeter Scale

3.3.1. Model Parameters Setting for Evapotranspiration and Irrigation Spatialization

Evapotranspiration and irrigation estimates were spatially distributed at perimeter scale for the seasons 2008–2009 (December to June), 2011–2012 (November to May) and 2012–2013 (November to June). Considering the difficulty to get individual parameter values for specific crop types, the land cover typology was grouped into three major classes: market gardening (about 35% of the GDAs' areas), cereals (about 17%) and orchards (about 34%, mainly olive trees). The linear relationship linking fc and Kcb with NDVI for the market gardening were estimated using the FAO paper 56 [16] and satellite data (Table 2). For bare soil conditions, we assumed like [23] that fc and Kcb values were zero, with NDVI values for bare soils extracted from the images. For full vegetation cover, fc was assumed to be 1 and Kcb was taken as Kcb-mid in the FAO paper 56, while NDVI was also extracted from the images. For olive trees, the same method was applied to estimate the NDVI-fc relation. For Kcb, a relationship between fc and Kcb was obtained from a previous calibration achieved on experimental data for irrigated olive trees in the Haouz plain in Morocco (not shown here) which was considered more representative of the Merguellil area than using bibliographic data. In absence of a detailed soil map, soil properties (θ_{fc}, θ_{wp}, REW, Ze, Z_{soil}, $Dif_{er,}$ Dif_{rd}) were considered homogeneous in the study area and the parameters were taken from calibration at plot scale (Section 3.2). Crop specific parameters (Zrmax and p) were set to calibrated values for cereals and taken from FAO paper 56 [16] for the other land use classes (Table 3). The initial soil water content (Init_RU) for annual crops was estimated considering the previous precipitations. For the 2008–2009 and 2012–2013, it was also set to 10% of the soil available water (between θ_{fc} and θ_{wp}) because no significant precipitations were observed since summer, while for the 2011–2012 season initial water content was set at a relatively larger value of 32% of the soil available water due to 85 mm of precipitations recorded ten days before the starting date of the simulation. Higher initial soil filling rate was used for trees (50%) since they

are almost continuously irrigated. Regarding irrigation rules (Table 3), market gardening was irrigated using drip irrigation which means that less soil surface is wetted (fw = 25%) and irrigation lasts longer because vegetable require water until harvest (Kcb_stop = 75%). In addition, to reproduce the drip irrigation, MAD was set to a low value (MAD = 0.2 * TAW), which triggers frequent irrigation inputs. Trees are mainly irrigated by gravity all year round (fw = 100%, Kcb_stop = 0).

3.3.2. Comparison between Modeled and Observed Irrigation Volumes

After running the SAMIR model using the image time series over the plain for the three seasons (Figure 7), the monthly values of modeled irrigation were computed for three irrigated perimeters (GDAs) for which validation data were available (Ben Salem II, Mlelsa and Karma II, Figure 8). The cumulated ET values are also plotted on the figure in order to scale irrigation totals to the total water loss occurring during the month. The seasonal water budget was computed for all campaigns (Figure 9) and shows that on the whole the inputs (P and I) are close to evaporative consumption (ET) with little water remaining in the soil.

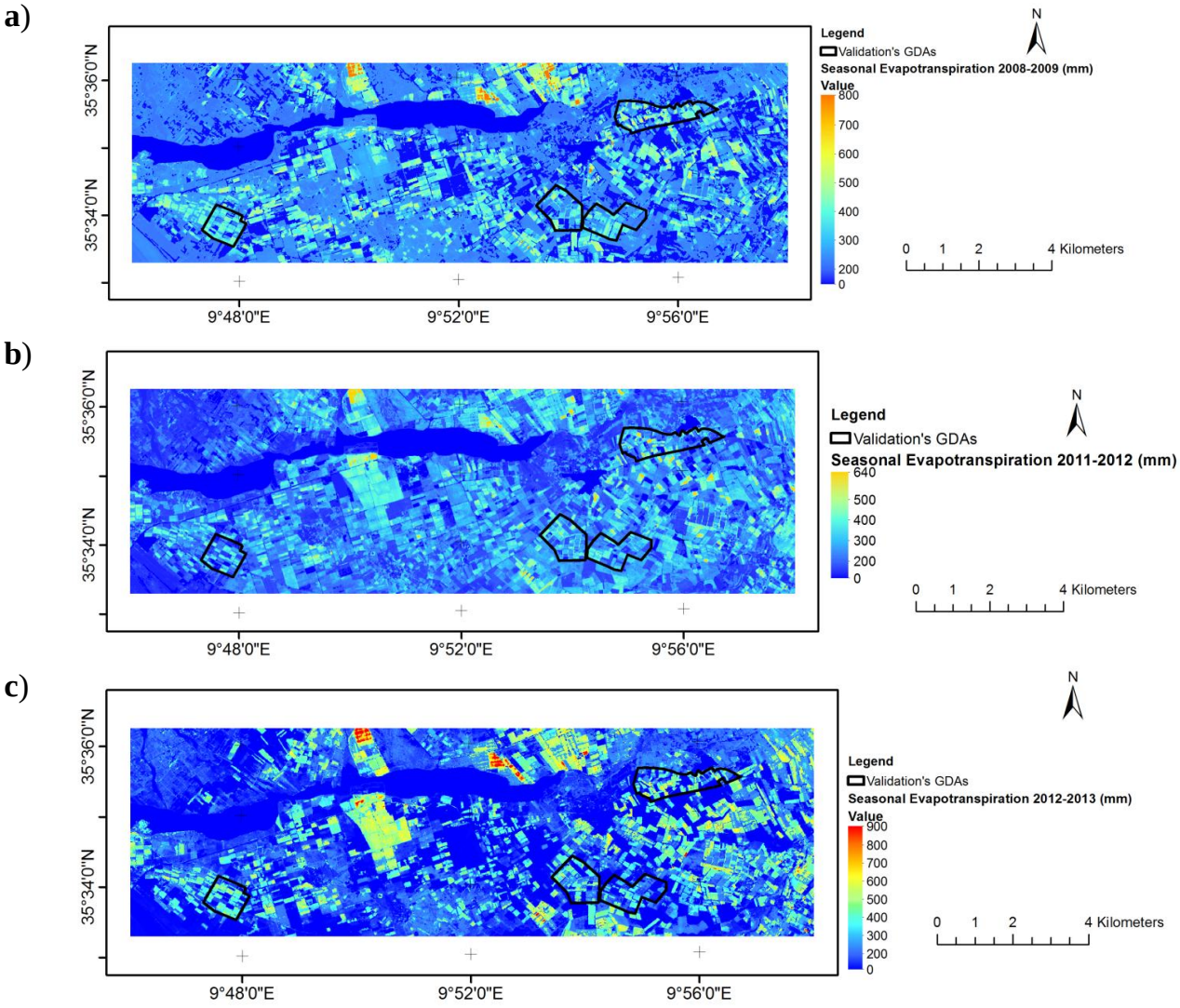

Figure 7. Modeled ET over the study area for the (**a**) 2008–2009, (**b**) 2011–2012 and (**c**) 2012–2013 seasons.

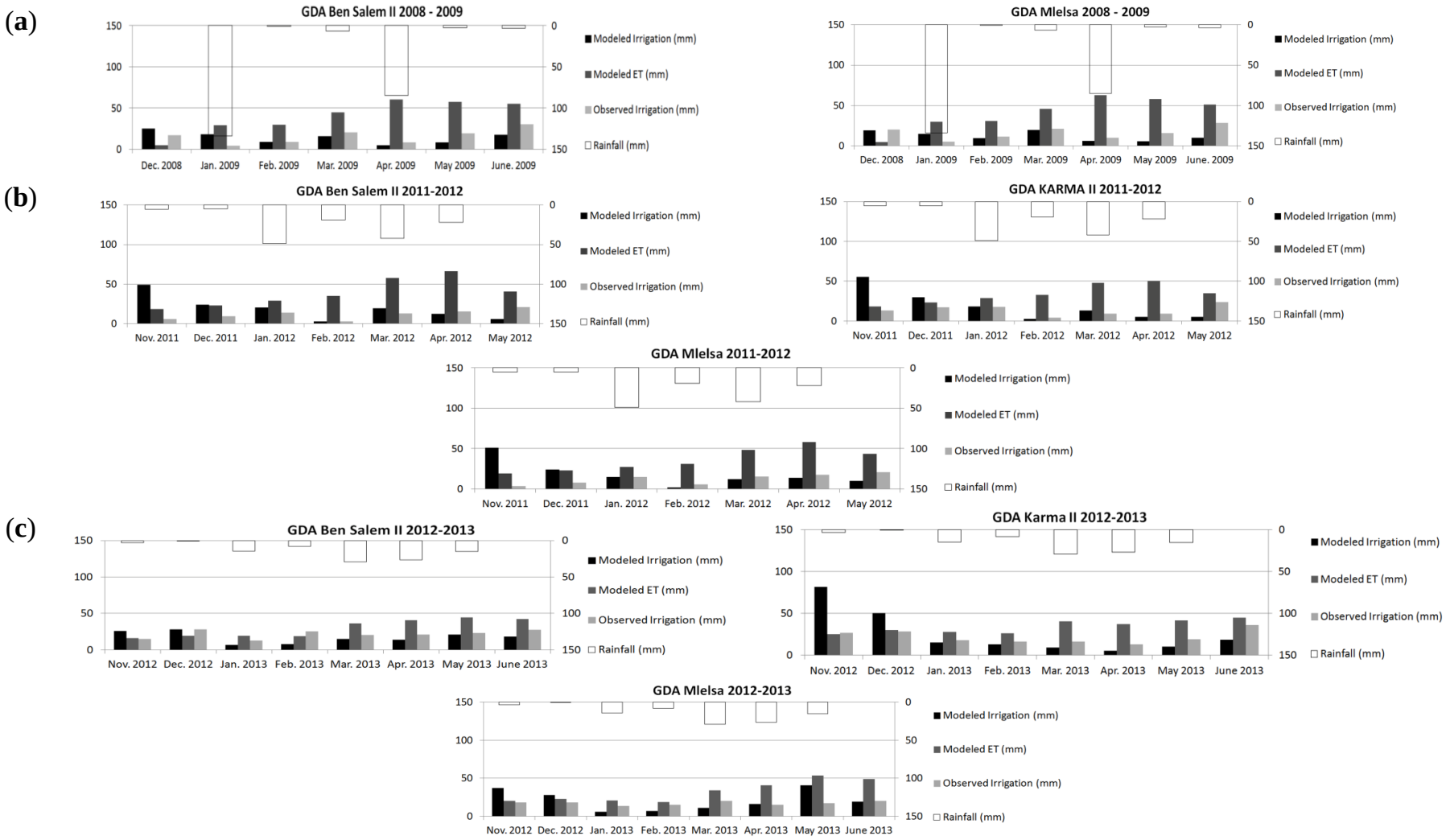

Figure 8. Comparison between surveyed and SAMIR (SAtellite Monitoring of IRrigation) estimated irrigation depth at seasonal scale for the (**a**) 2008–2009, (**b**) 2011–2012 and (**c**) 2012–2013 seasons.

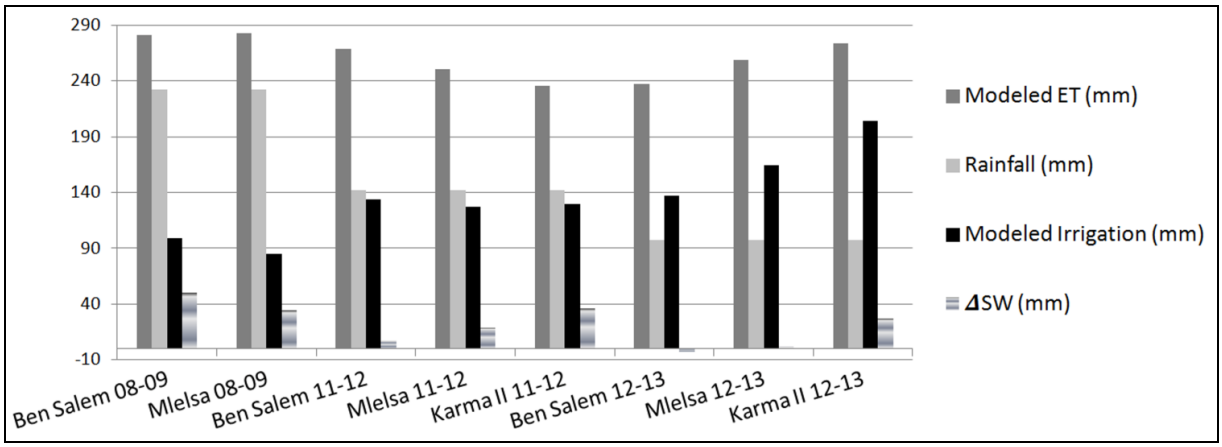

Figure 9. Seasonal water budget for the eight campaigns (**Δ**SW is the variation of soil water content).

For the 2008–2009 season (Figure 8a), the modeled irrigations are quite close to the observed values, although irrigations are small compared to ET, especially in summer. The larger discrepancy visible in June can be due to market gardening which dominates at this time as cereals are harvested (beginning of June). Indeed the parameters used for these crops are rather uncertain. For the 2011–2012 season (Figure 8b), the estimated irrigations are also on the whole satisfying with two noticeable exceptions for the first and last months of the simulation. Indeed, November exhibits a strong overestimation of irrigation which can be due to an error in soil water content initialization but is also at least partially due to the fact that late vegetables (e.g., pepper or tomatoes) are not all removed although still green and not irrigated. The model is not able to manage such partial vegetation cycles and irrigates as if it was the crop that will follow in the crop rotation (*i.e.*, the crop mentioned in the land use map). In May, the discrepancy is not clearly explained but can be also due to the growing importance of vegetables planted mainly in April. For the 2012–2013 season (Figure 8c), irrigations are also on the whole correct but with several exceptions. Overestimations in November and December for Karma II and November for Mlelssa are linked to previous crops as explained for 2011–2012. The problem of May for Mlessa and June for Karma II can be also related to market gardening which is poorly parameterized. When aggregated at seasonal scale, the irrigation estimates for the eight campaigns give a mean absolute percentage error (MAPE) of 25% (Figure 10) and the overall difference for all campaigns is very low (121 mm irrigation observed for 135 mm modeled). This is an encouraging result considering the fact that (i) the calibration dataset is minimal, and (ii) the calibration protocol affects a limited number of parameters for a limited number of LU classes. Progress in parameterization would require ideally crop specific information, e.g., flux measurements on vegetables of trees, or at least irrigation volumes collected at plot scale so as to be crop specific. However, even with the current irrigation volumes at

perimeter scale, it might be possible to achieve a global calibration of some parameters. Although there would be too many degrees of freedom to correctly calibrate all parameters with such aggregated data, we could focus on irrigation practices which are much uncertain though quite sensitive.

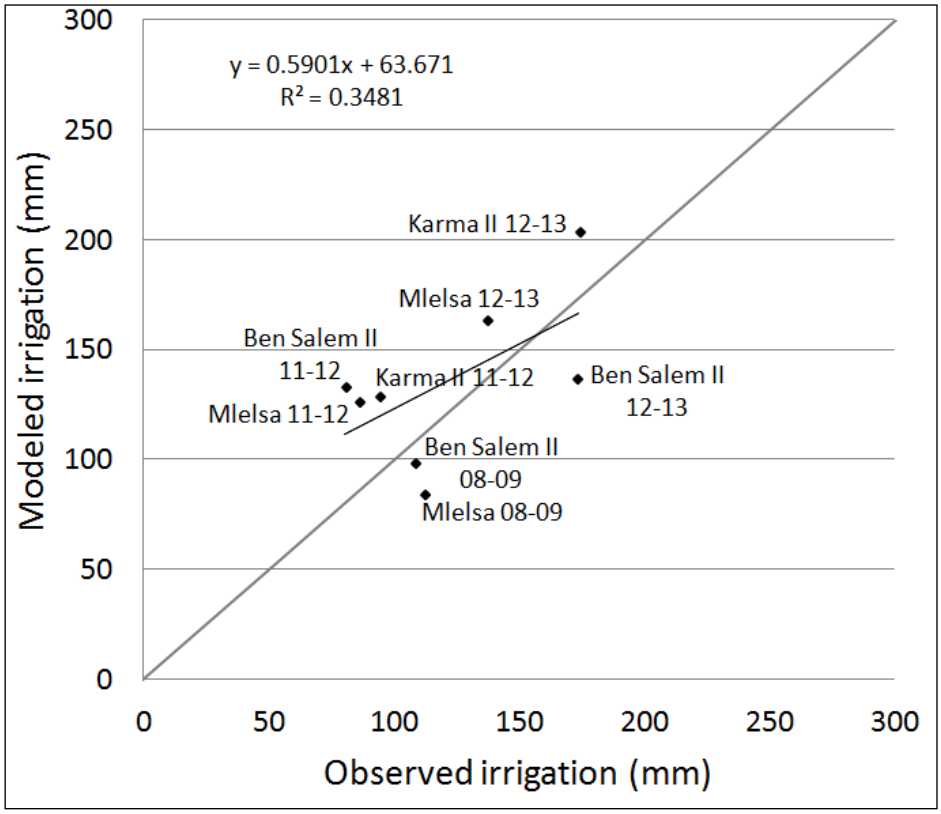

Figure 10. Comparison between observed and SAMIR modeled seasonal irrigation depths.

4. Conclusions

We show in this study that the five days acquisition frequency of Sentinel-2, as simulated in the SPOT4-Take5 experiment, will not completely solve the problem of cloudiness even in semi-arid areas like Tunisia. The combination with other VIS-NIR high-resolution sensors like Landsat 8 or SPOT should still be useful. We also showed that although the radiometric correction of images was performed with special care using the state-of-the-art MACCS algorithm, the invariant analysis proposed here can help improving the time series quality, especially in semi-arid areas where such objects can be easily found. Moreover, although a cloud masking is performed during the MACCS implementation, the subsequent invariant analysis helps identifying and discarding some remaining hazy images. Using these high-resolution time series including clear images approximately every 20 days, we have shown that with limited local data and literature review it was possible to estimate irrigation volumes at perimeters scale. The seasonal volumes estimated by this method

appear acceptable, even though results at finer timescales (monthly and below) need to be improved, in particular by translating our knowledge of the agricultural practices into algorithmic constraints in the model. Despite these shortcomings, we have demonstrated that combining HR data and simple water balance modeling offers an interesting method to monitor irrigation volumes.

Acknowledgments

We are grateful to the CNES for supplying image time series in the frame of the SPOT4-Take5 experiment, and also for helping us acquiring SPOT5 images thanks to several ISIS actions. This work was also permitted with the collaboration of the CRDA (Centre Regional de Développement Agricole) of Kairouan, the GDAs of Mlelssa, Karma and Ben Salem and Mr Abderazak Selmi from CTV-Chebika who provided irrigation data. We also thank the Tunisian Ministry of Research for granting students involved in this study. Financial support from the MISTRALS/SICMED program for the ReSAMEd project, from the CNES/TOSCA program for the EVA2IRT project and from the ANR/TRANSMED program for the AMETHYST project (ANR-12-TMED-0006-01) are gratefully acknowledge, as well as the mobility support from PHC Maghreb program (N° 32592VE). Finally, this work has benefited from the financial support of the ARTS program ("Allocations de recherche pour une thèse au Sud") of IRD (Institut de Recherche pour le Développement).

Authors' Contributions

Sameh Saadi: data processing and analysis.
Vincent Simonneaux: data analysis and results interpretation.
Gilles Boulet: flux experiment management.
Bruno Raimbault: ground data management (flux, meteorology).
Bernard Mougenot: soil data and site management.
Pascal Fanise: site instrumentation.
Hassan Ayari: irrigation ground survey.
Zohra Lili-Chabaane: image processing.

Conflicts of Interest

The authors declare no conflict of interest.

References

1. Poussin, J.; Imache, A.; Béji, R.; Le Grusse, P.; Ben Mihoub, A. Exploring regional irrigation water demand using typologies of farms production units: An example from tunisia. *Agricultural Water Management Agricultural Water Management* **2008**, *95*, 973-983.

2. Tucker, C.J. Red and photographic infrared linear combinations for monitoring vegetation. *Remote Sensing of Environment* **1979**, *8*, 127-150.

3. Calcagno, G.; Mendicino, G.; Monacelli, G.; Senatore, A.; Versace, P. Distributed estimation of actual evapotranspiration through remote sensing techniques. In *Methods and tools for drought analysis and management*, Rossi, G.; Vega, T.; Bonaccorso, B., Eds. Springer Netherlands: 2007; Vol. 62, pp 125-147.

4. Courault, D.; Seguin, B.; Olioso, A. Review about estimation of evapotranspiration from remote sensing data: From empirical to numerical modeling approach. *Irrigation and Drainage system* **2005**, *19*, 223-249.

5. Gowda, P.; Chavez, J.; Colaizzi, P.; Evett, S.; Howell, T.; Tolk, J. Et mapping for agricultural water management: Present status and challenges. *Irrig Sci* **2008**, *26*, 223-237.

6. Kustas, W.P.; Norman, J.M. Use of remote sensing for evapotranspiration monitoring over land surfaces. *Hydrol. Sci.* **1996**, *41*, 495–516.

7. Zhao-Liang, L.; Ronglin, T.; Zhengming, W.; Yuyun, B.; Chenghu, Z.; Bohui, T.; Guangjian, Y.; Xiaoyu, Z. A review of current methodologies for regional evapotranspiration estimation from remotely sensed data *Sensors* **2009**, *9*, 3801-3853.

8. Delogu, E.; Boulet, G.; Olioso, A.; Coudert, B.; Chirouze, J.; Ceschia, E.; Le Dantec, V.; Marloie, O.; Chehbouni, G.; Lagouarde, J.P. Reconstruction of temporal variations of evapotranspiration using instantaneous estimates at the time of satellite overpass. *Hydrol. Earth Syst. Sci.* **2012**, *16*, 2995-3010.

9. Chirouze, J.; Boulet, G.; Jarlan, L.; Fieuzal, R.; Rodriguez, J.C.; Ezzahar, J.; Er-Raki, S.; Bigeard, G.; Merlin, O.; Garatuza-Payan, J., *et al.* Intercomparison of four remote-sensing-based energy balance methods to retrieve surface evapotranspiration and water stress of irrigated fields in semi-arid climate. *Hydrol. Earth Syst. Sci.* **2014**, *18*, 1165-1188.

10. Allen, T.R. Topographic normalization of landsat thematic mapper data in three mountain environments. *Geocarto International* **2000**, *15*, 15-22.

11. Bastiaanssen, W.G.M.; Molden, D.J.; Makin, I.W. Remote sensing for irrigated agriculture: Examples from research and possible applications. *Agricultural Water Management* **2000**, *46*, 137-155.

12. Hunsaker, D.; Pinter, P., Jr.; Barnes, E.; Kimball, B. Estimating cotton evapotranspiration crop coefficients with a multispectral vegetation index. *Irrig Sci* **2003**, *22*, 95-104.

13. J. Trout, T.; F. Johnson, L.; Gartung, J. Remote sensing of canopy cover in horticultural crops. *HortScience* **2008**, *43*, 333-337

14. Pinter, P.J.; Hatfield, J.L.; Schepers, J.S.; Barnes, E.M.; Moran, M.S.; Daughtry, C.S.; Upchurch, D.R. Remote sensing for crop management. *Photogrammetric Eng. Remote Sensing* **2003**, *69*, 647– 664.

15. Takeuchi, W.; Tamura, M.; Yasuoka, Y. Estimation of methane emission from west siberian wetland by scaling technique between noaa avhrr and spot hrv. *Remote Sensing of Environment* **2003**, *85*, 21–29.

16. Allen, R.G.; Pereira, L.S.; Raes, D.; Smith, M. Crop evapotranspiration-guidelines for computing crop water requirements-fao irrigation and drainage paper 56. *FAO, Rome* **1998**, *300*.

17. Bausch, W.C.; Neale, C.M.U. Crop coefficients derived from reflected canopy radiation: A concept. *Trans. ASAE* **1987**, *32*, 703-709.

18. Er-Raki, S.; Chehbouni, A.; Guemouria, N.; Duchemin, B.; Ezzahar, J.; Hadria, R. Combining fao-56 model and ground-based remote sensing to estimate water consumptions of wheat crops in a semi-arid region. *Agricultural Water Management* **2007**, *87*, 41-54.

19. Glenn, E.P.; Neale, C.M.U.; Hunsaker, D.J.; Nagler, P.L. Vegetation index-based crop coefficients to estimate evapotranspiration by remote sensing in agricultural and natural ecosystems. *Hydrological Processes* **2011**, *25*, 4050–4062.

20. Neale, C.M.U.; Bausch, W.; Heermann, D. Development of reflectance-based crop coefficients for corn. *Trans. ASAE* **1989**, *32*, 1891–1899.

21. Huete, A.; Jackson, R.; Post, D. Spectral response of a plant canopy with different soil backgrounds. *Remote Sensing of Environment* **1985**, *17*, 37-53.

22. Choudhury, B.J.; Ahmed, N.U.; Idso, S.B.; Reginato, R.J.; Daughtry, C.S.T. Relations between evaporation coefficients and vegetation indices studied by model simulations. *Remote Sens. Environ* **1994**, *50*, 1-17.

23. Gonzalez-Dugo, M.; Mateos, L. Spectral vegetation indices for benchmarking water productivity of irrigated cotton and sugarbeet crops. *Agricultural Water Management* **2008**, *95*, 48-58.

24. Er-Raki, S.; Chehbouni, A.; Duchemin, B. Combining satellite remote sensing data with the fao-56 dual approach for water use mapping in irrigated wheat fields of a semi-arid region. *Remote Sensing* **2010**, *2*, 375-387.

25. Clarke, D.; Smith, M.; El-Askari, K. In *Cropwat for windows: User guide*, 2001; IHE.

26. González-Dugo, M.; Escuin, S.; Cano, F.; Cifuentes, V.; Padilla, F.; Tirado, J.; Oyonarte, N.; Fernández, P.; Mateos, L. Monitoring evapotranspiration of irrigated crops using crop coefficients derived from time series of satellite images. Ii. Application on basin scale. *Agricultural Water Management* **2013**, *125*, 92-104.

27. Gonzalez-Dugo, M.; Neale, C.; Mateos, L.; Kustas, W.; Prueger, J.; Anderson, M.; Li, F. A comparison of operational remote sensing-based models for estimating crop evapotranspiration. *Agricultural and Forest Meteorology* **2009**, *149*, 1843-1853.

28. Mateos, L.; González-Dugo, M.P.; Testi, L.; Villalobos, F.J. Monitoring evapotranspiration of irrigated crops using crop coefficients derived from time series of satellite images. I. Method validation. *Agricultural Water Management* **2013**, *125*, 81-91.

29. Neale, C., Gonzales-Dugo, M. P., Mateos, L., Kustas, W.P., Kaheil, Y., . In *A hybrid approach for estimating spatial evapotranspiration from satellite imagery*, Remote sensing for agriculture, ecosystems, and hydrology IX, Florence, Italy, 2007; SPIE Eds., Bellingham, Wash., Etats-Unis: Florence, Italy, pp 674209.674201-674209.674208

30. Simonneaux, V.; Duchemin, B.; Helson, D.; Er-Raki, S.; Olioso, A.; Chehbouni, A.G. The use of high-resolution image time series for crop classification and evapotranspiration estimate over an irrigated area in central morocco. *International Journal of Remote Sensing* **2008**, *29*, 95-116.

31. Simonneaux, V.; Lepage, M.; Helson, D.; Métral, J.; Thomas, S.; Duchemin, B.; Cherkaoui, M.; Kharrou, H.; Berjami, B.; Chebhouni, A. Estimation spatialisée de l'évapotranspiration des cultures irriguées par télédétection : Application à la gestion de l'irrigation dans la plaine du haouz (marrakech, maroc). *Sécheresse* **2009**, *20*, 123-130.

32. Zribi, M.; Chahbi, A.; Shabou, M.; Lili-Chabaane, Z.; Duchemin, B.; Baghdadi, N.; Amri, R.; Chehbouni, A. Soil surface moisture estimation over a semi-arid region using envisat asar radar data for soil evaporation evaluation. *Hydrology and Earth System Sciences Discussions* **2011**, *15*, 345-358.

33. Leduc, C.; Calvez, R.; Beji, R.; Nazoumou, Y.; Lacombe, G.; Aouadi, C. Evolution de la ressource en eau dans la vallée du merguellil (tunisie centrale). In *Séminaire Euro-Méditerranéen sur la Modernisation de l'Agriculture Irriguée*, La modernisation de l'agriculture irriguée. IAV Hassan II: Rabat, 2005; p 10.

34. Masseroni, D.; Corbari, C.; Mancini, M. Limitations and improvements of the energy balance closure with reference to experimental data measured over a maize field. *Atmósfera* **2014**, *27*, 335-352.

35. Rahman, H.; Dedieu, G. Smac: A simplified method for the atmospheric correction of satellite measurements in the solar spectrum. *Remote Sensing* **1994**, *15*, 123-143.

36. Aeronet. http://aeronet.gsfc.nasa.gov/ (10 June 2014),

37. Schott, J.R.; Salvaggio, C.; Volchock, W.J. Radiometric scene normalization using pseudo invariant features. *Remote Sens.* **1988**, *26*, 1-16.

38. Houlès, V.; El Hajj, M.; Bégué, A. Radiometric normalization of a spot-4 and spot-5 time series of images (isle-reunion) for agriculture applications. *Revue Française de Photogrammetrie et de Teledetection* **2006**, *181*, 31-37.

39. Spot4 (take5). http://www.cesbio.ups-tlse.fr/multitemp/?page_id=406 (16 February 2015),

40. Hagolle, O.; Huc, M.; Villa Pascual, D.; Dedieu, G. A multi-temporal and multi-spectral method to estimate aerosol optical thickness over land, for the atmospheric correction of formosat-2, landsat, venμs and sentinel-2 images. *Remote Sensing* **2015**, *7*, 2668.

41. Torres, E.A.; Calera, A. Bare soil evaporation under high evaporation demand: A proposed modification to the fao-56 model. *Hydrological Sciences Journal–Journal des Sciences Hydrologiques* **2010**, *55*, 303-315.

42. Zhang, Y.; Wegehenkel, M. Integration of modis data into a simple model for the spatial distributed simulation of soil water content and evapotranspiration. *Remote Sensing of Environment* **2006**, *104*, 393-408.

43. Nash, J.E.; Sutcliffe, J.V. River flow forecasting through conceptual models part i — a discussion of principles. *Journal of Hydrology* **1970**, *10*, 282-290.

44. S'habou, M. Suivi de la dynamique du couvert végétal par télédetection spatiale sur le site semi-aride de merguellil (tunisie centrale). Institut National Agronomique de Tunisie, Université de Carthage, Tunis, 2010.

45. Chahbi, A.; Zribi, M.; Lili-Chabaane, Z.; Duchemin, B.; Shabou, M.; Mougenot, B.; Boulet, G. Estimation of the dynamics and yields of cereals in a semi-arid area using remote sensing and the safy growth model. *International Journal of Remote Sensing* **2014**, *35*, 1004-1028.

46. Chahbi, A. Prévision du rendement des céréales à partir des mesures de télédétection, application sur le bassin de merguellil. nstitut National Agronomique de Tunisie, Université de Carthage, Tunis, 2015.

47. Gao, F.; Masek, J.; Schwaller, M.; Hall, F. On the blending of the landsat and modis surface reflectance: Predicting daily landsat surface reflectance. *IEEE Transactions on geosciences and remote sensing* **2006**, *44*, 2207 - 2218.

3.3 Unpublished results and additional analyzes

This part presents a set of analyzes and results that are not included in the previous publication.

- SAMIR was also run on the same area for the 2013-2014 season. It was a wet season in comparison to the three other ones, which was interesting to assess SAMIR in different climatic conditions.
- The validation of modeled irrigation volumes of the 2012-2013 season was also carried out at field-scale using an irrigation dataset collected from field surveys conducted in the Ben Salem II, Mlelsa, Karma I and Karma II GDAs. Moreover, a comparison was also made between measured groundwater withdrawals obtained for some private farms with irrigation volumes estimated by SAMIR.
- For the 2012-2013 and 2013-2014 seasons, SAMIR was also applied on a 10 km × 8 km sub-image centered on the XLAS using the same parameters as in the article. In this case, the modeled ET was validated using the XLAS derived ET.

3.3.1 Irrigation volumes results validation at perimeter scale for the 2013-2014 season

Evapotranspiration and irrigation estimates were spatially distributed at perimeter scale for the seasons 2013-2014 (November to October) following the same approach detailed in the paper and applying the same model parameters. Figure 3.1 shows modeled ET over the study area for the 2013–2014's season. This season was the wettest one with a cumulated rainfall of about 341 mm.

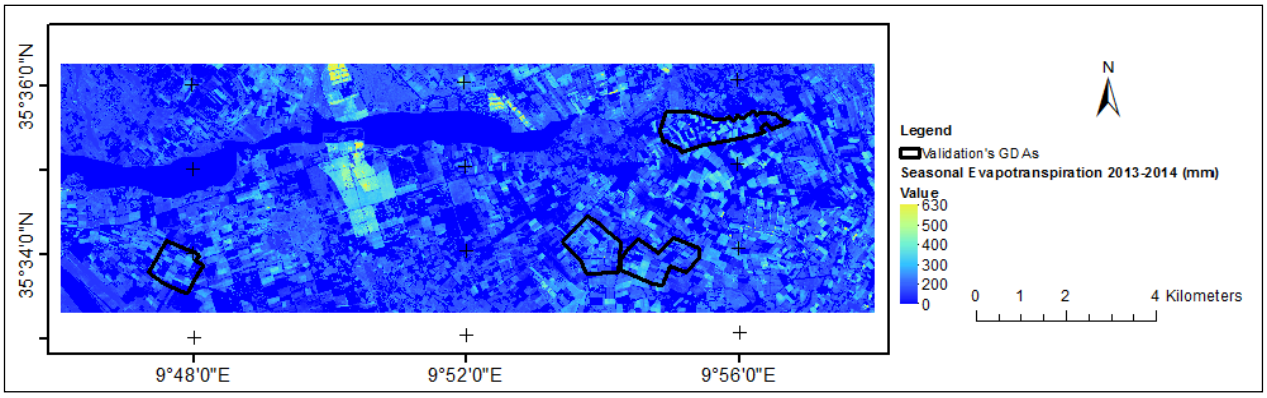

Figure 3. 1: Modeled ET over the study area for the 2013–2014 season.

Then, the monthly values of modeled irrigation were computed for the three GDAs and compared to the observed irrigation volume (Figure 3.2).

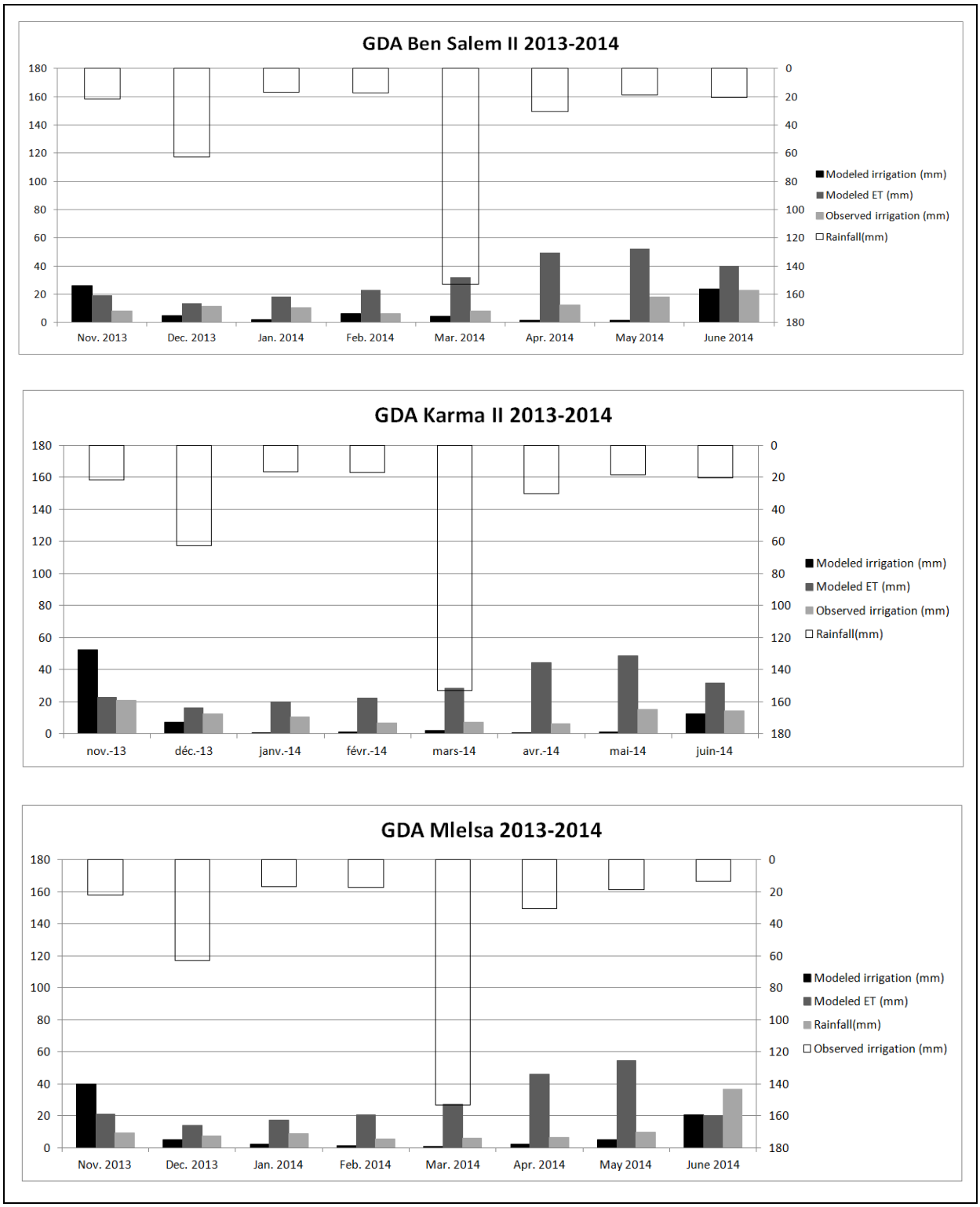

Figure 3. 2: Comparison between surveyed and SAMIR estimated irrigation depth at seasonal scale for the 2013–2014's season.

The cumulated ET values are also plotted on the figure in order to give a scale to irrigation totals. SAMIR overestimates irrigation in November for the three GDAs. This

error may be due to an error in soil water content initialization which was estimated based only on rainfall during the previous month, without taking into account the impact of the previous crops. One other possible explanation is that late vegetables (e.g., pepper or tomatoes) are not all removed at the beginning of the simulation in November and are still green although no more irrigated. As it was already mentioned, SAMIR is not able to manage such partial vegetation cycles and irrigates these remaining crops as if it was the crop that will follow in the crop rotation, since only one land use map is used for the whole season.

The figure 10 of the article was redone considering the 2013/2014 results of irrigation volume aggregated at seasonal scale and inversing the two axis since traditionally observations are plotted on the Y-axis (figure 3.3). All seasonal values were calculated using the months available for the four seasons, *i.e* from November to June. The seasonal water budget computed for all campaigns (Figure 3.4) and the observed irrigation volume are detailed in the following table:

Table 3. 1 : Estimated and observed seasonal water budget components for all campaigns

Campaigns	Modeled irrigation (mm)	Modeled ET (mm)	Rainfall (mm)	ΔSW (mm)	Observed irrigation (mm)
Ben Salem 08-09	98.8	281.2	232.5	50.1	108.3
Mlelsa 08-09	84.7	283.0	232.5	34.2	112.2
Ben Salem 11-12	133.6	268.8	142.0	6.8	80.5
Mlelsa 11-12	126.8	250.3	142.0	18.5	86.0
Karma II 11-12	129.2	235.2	142.0	36.0	94.0
Ben Salem 12-13	137.4	237.2	96.9	-2.9	172.9
Mlelsa 12-13	164.0	259.0	96.9	1.9	136.9
Karma II 12-13	204.2	274.0	96.9	27.1	173.9
Ben Salem 13-14	70.4	248.1	340.9	163.1	97.3
Mlelsa 13-14	77.6	221.3	340.9	197.1	67.6
Karma II 13-14	76.2	234.1	340.9	183.0	93.2
Seasonal results (November to June)	118.4	253.8	200.4	65.0	111.2

The irrigation estimates for the eleven campaigns give a mean absolute percentage error (MAPE) of 25% and a root mean square error (RMSE) of 30 mm. The overall difference for all campaigns decreases as compared to the results based only on the eight campaigns: 111 mm of total observed irrigation compared to the 118 mm simulated by SAMIR. The regression is also better with R^2=0.42.

Although the overall results are encouraging, SAMIR always overestimates the monthly irrigation volumes at the beginning of the season and the largest discrepancy is recorded in November for all campaigns. Hence, we highlight a real problem in the initialization parameters, especially parameters linked to the soil water content. Another limiting factor is the land use map. One single annual land use map is usually far from the reality of the major part of our study area characterized by crop rotation (up to three crop per year) and by intercropping of cereals (winter) and vegetables (summer) between the rows of irrigated trees fields which can lead to error in model simulation since it remains unable to take into account these aspects.

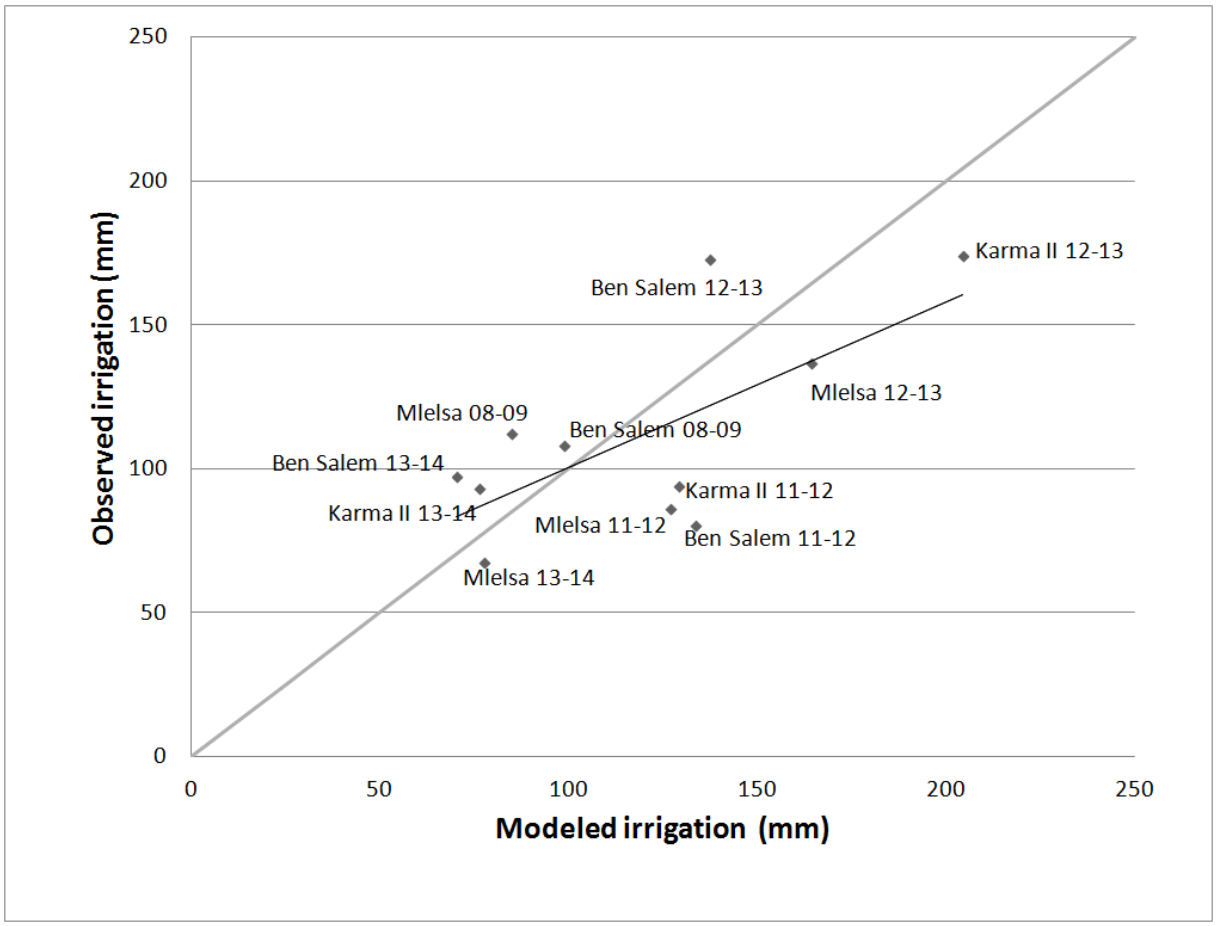

Figure 3. 3 : Comparison between observed and SAMIR modeled seasonal irrigation depths (improvement of fig. 10 of (Saadi *et al.*, 2015) paper including the 13-14 season).

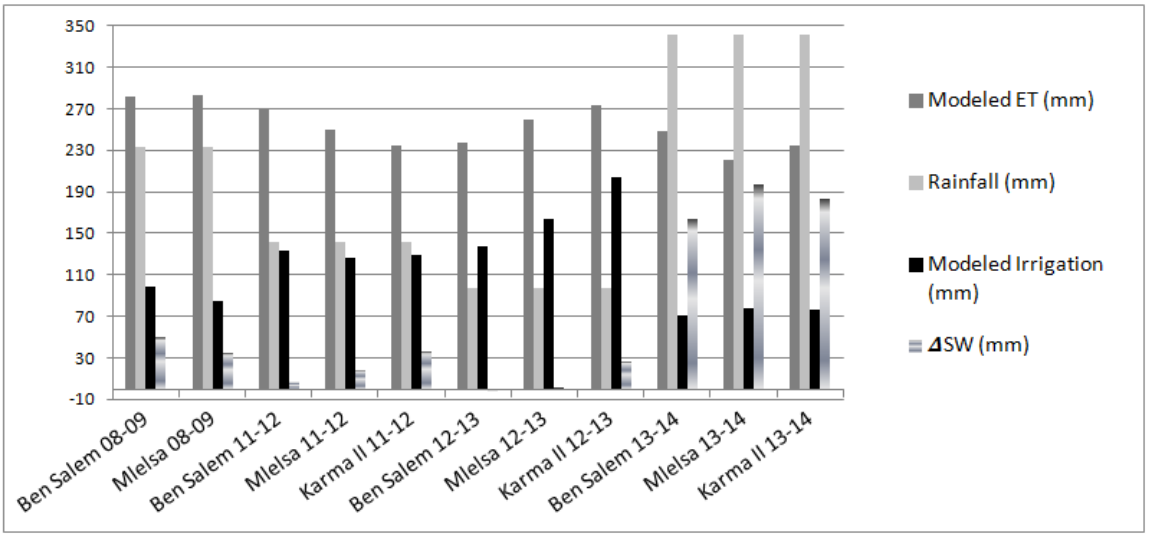

Figure 3. 4 : Seasonal water budget for the eight campaigns (**Δ**SW is the variation of soil water content).

3.3.2 Irrigation volumes results validation at field and farm scales

Field scale

Modeled irrigation volumes were also compared to plot-scale irrigation dataset collected during field surveys conducted in 2013 in Ben Salem II, Mlelsa and Karma I and Karma II GDAs.

Although the overall difference between simulated and averaged irrigation volumes at perimeter scale is coherent (Table 3.2), property-level results (Figures 3.5, 3.6, 3.7 and 3.8) are disappointing. The detailed results are presented in Annex 7. However, the discrepancies observed are not so surprising considering the complexity of the invoice system, the frequent redistribution of water between farmers, and the difficulty to identify people in large families. As a clue, we have to say that the names' list collected during the ground survey to map the plots was very different from the list of names corresponding to invoices. After discussion with the managers, it was possible to match the two list considering family relations and also owner-farmer links, but it seems that it was not so successful. We are not surprised to see also that for the Mlelsa GDA the relation between estimated and observed irrigation is better, as this GDA was clearly better organized and managed ("here we all belong to the same great family" said the manager).

Table 3. 2: Comparison between simulated SAMIR irrigation and irrigation observed at the "name" / block scale for the 2012/2013 season

GDA	"name" / block number	Modeled irrigation (mm)	Observed irrigation (mm)
Karma I	76 names	196.0	146.4
Karma II	34 names	278.0	272.1
Mlelsa	106 names	186.6	148.6
Ben salem II	8 blocks	145.30	173.75

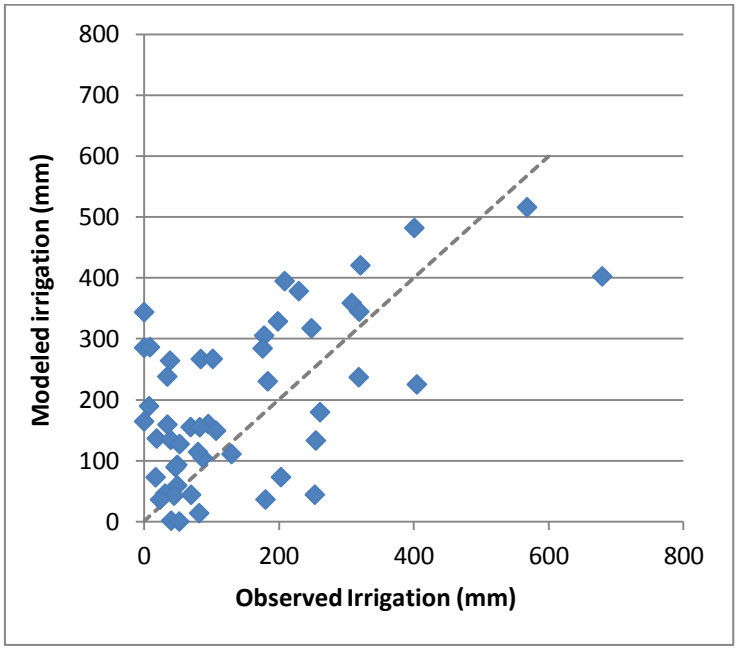

Figure 3. 5: Modeld vs. obsereved irrigation volumes in the GDA Karma I

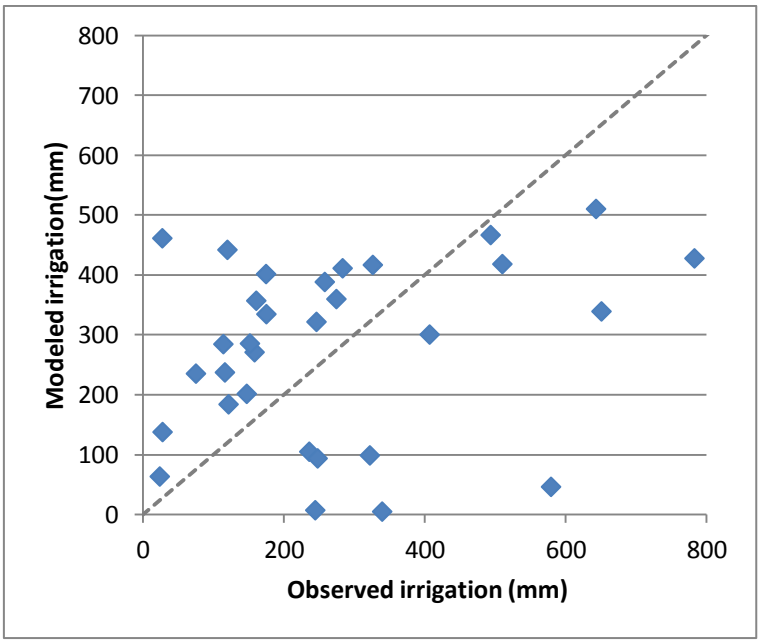

Figure 3. 6 : Modeld vs. obsereved irrigation volumes in the GDA Karma II

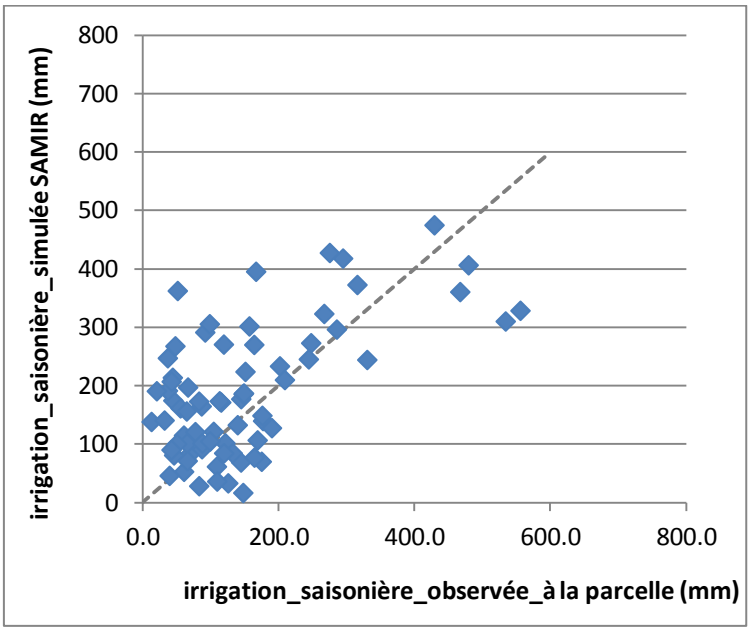

Figure 3. 7 : Modeld vs. obsereved irrigation volumes in the GDA Mlelsa

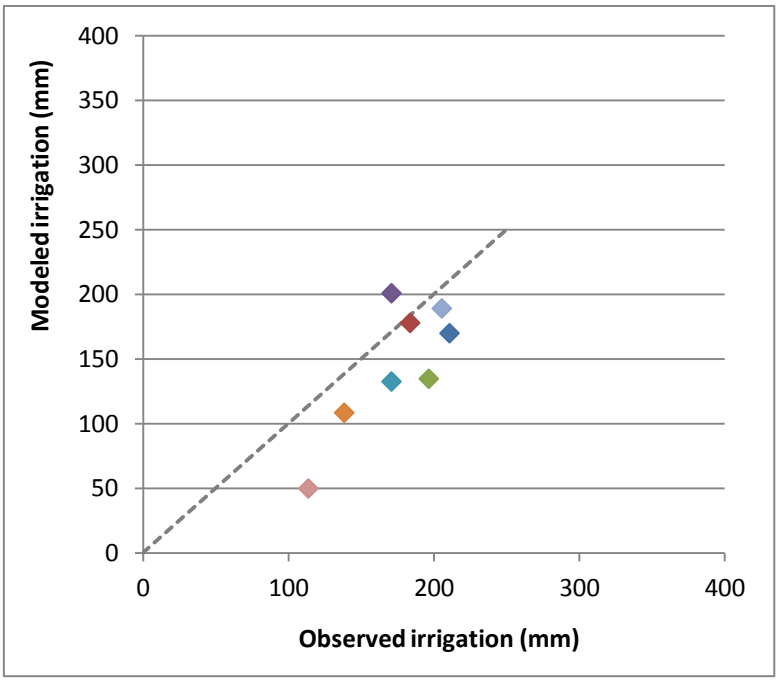

Figure 3. 8 : Modeled vs. observed irrigation volumes in the irrigation blocks of the Ben Salem II GDA.

Farm scale

SAMIR estimates of irrigation volumes were also assessed at farm scale in the frame of Fradi (2017) master thesis. The main objective was to report and evaluate the farmers' irrigation practices. A comparison was made between measured groundwater withdrawals obtained for three farms in the Kairouan plain, with irrigation volumes estimated by

SAMIR. These farms were chosen because they used only a private well for irrigation, and it was possible to install a meter on these wells. The results showed first that the tabulated standard Kcb values proposed in the FAO-56 paper were far from the remotely sensed Kcb values used by SAMIR, showing the advantage of remote sensing for actual vegetation monitoring. However, the most interesting results came from the comparison between the pumped volumes and the estimated irrigation requirements, showing strong discrepancies. Three water consumption scenarios were applied in SAMIR to account for uncertainties in parameters, *i.e.* (1) the economic scenario with minimum Kcb and economic irrigation allowing limited stress, (2) a standard scenario with medium parameters and optimal irrigation management (irrigation triggered when RAW is empty) and (3) a scenario with maximum Kcb and frequent irrigations, without generating drainage however. The results showed that actual irrigations were always greater or equal even to the maximum water consumption scenario simulations. The over irrigation was also observed after rainfall events: while the amount of simulated irrigation depth decreases, this drop is not observed on actual farmer's inputs. This shows that farmers do not account much for rainfall events and prefer to secure their production. Over irrigation is also recorded in plots using drip irrigation, showing that the use of this technique does not always imply an economic irrigation management.

The differences between modeled and observed irrigation volume may be partially explained by the modeling uncertainties. Also, the efficiency of the irrigation scheme may be questioned although the short distance between the pump and the plots and the use of plastic pipes may limit these losses. However, the fact that even the most water consuming parameters' set doesn't allow to reach the observed water consumption advocates for a clear over irrigation by farmers. This strategy has been confirmed by ground enquiries showing that they usually pump water as much as possible, to secure their production, and that the cost of pumping is not a limitation. The logic of the famers is not only driven by hydrological considerations and constraints.

3.3.3 Evapotranspiration results validation using the XLAS data

The daily distributed ET simulated by SAMIR were also validated using the daily XLAS derived ET (*i.e.* LE_residual_XLAS$_{day\text{-}FP}$). Daily observed ET was computed using the residual method; hence, six estimates of the daily observed ET were obtained by combining the two satellite overpasses and three methods to compute G and thus AE (see Section 2.5.3.3). From the daily observed ET estimates, minimum and maximum ET were selected for each day and minimum and maximum daily ET time series were interpolated between successive days based on the preservation of the ratio of the available energy (AE) to the global incoming radiation Rg as scale factor (Figure 3.10). On the other hand, SAMIR was run for the 10 km × 8 km sub-image centered on the XLAS transect (see figure 2.17 section 2.4.2). Computed daily ET was then weighted by the corresponding daily XLAS footprint in order to get an ET comparable to XLAS derived ET. Figure 3.9 shows two examples of daily footprint overlying the daily modeled ET.

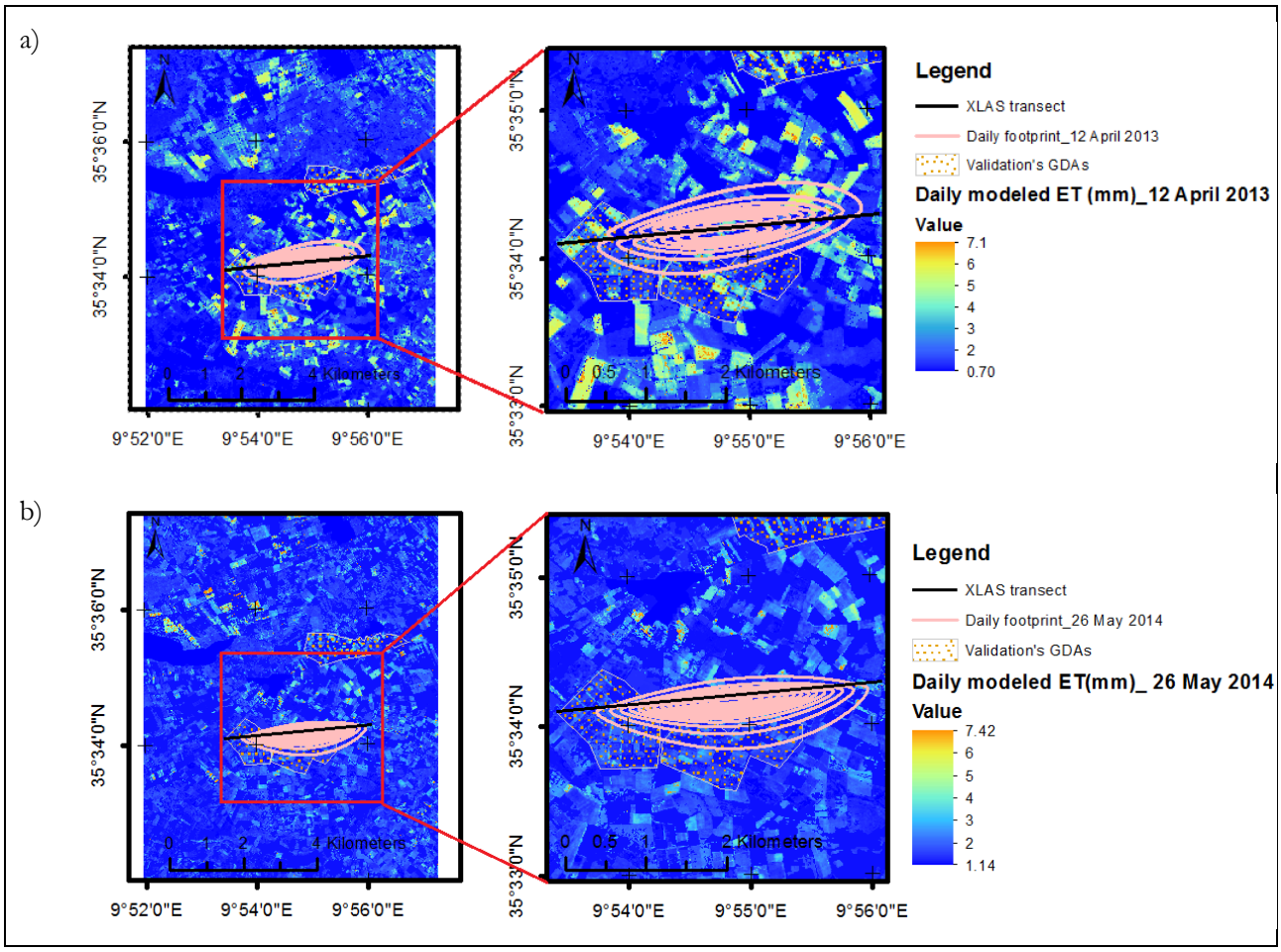

Figure 3. 9 : Daily SAMIR modeled evapotranspiration over the 10 km × 8 km sub-image and daily XLAS footprint for (a) 12th April 2013 and (b) 26th May 2014

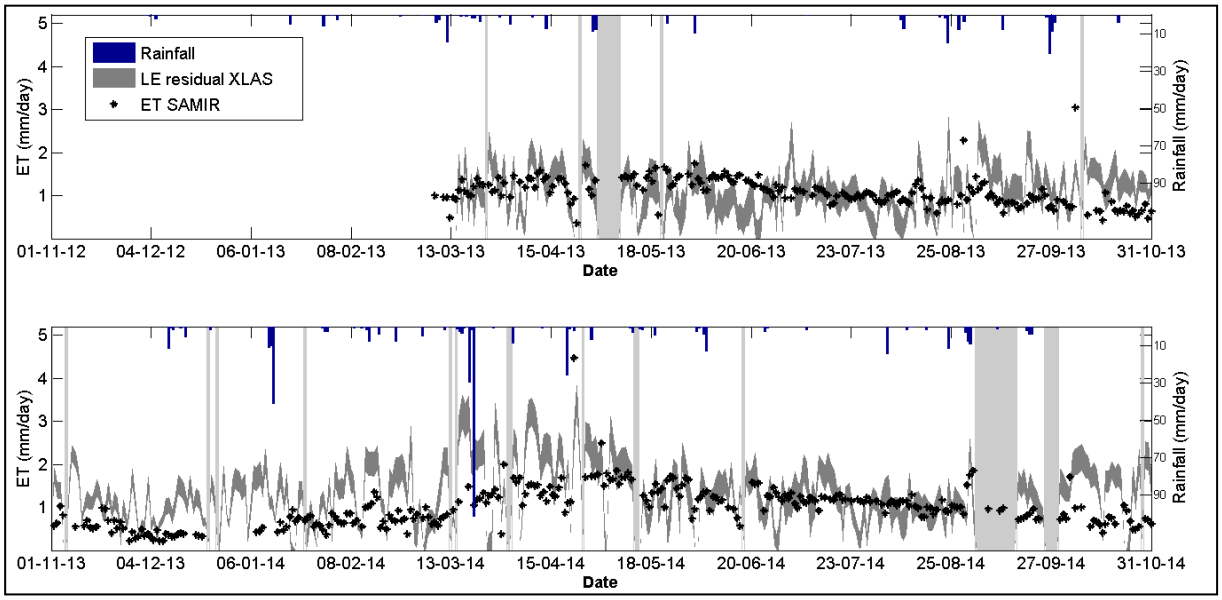

Figure 3. 10 : Daily SAMIR modeled evapotranspiration vs. observed daily latent heat fluxes. Light grey bars show gaps in XLAS data.

Observed ET ranged from zero and 2.8 mm and from zero and 3.8 mm for 2012-2013 and 2013-2014, respectively; this is consistent with the fact that 2013-2014 is a wet season in comparison with 2012-2013. The comparison between XLAS derived and SAMIR ET values shows better results for 2012-2013 than 2013-2014. Results show a good agreement between observed and modeled ET for the first mid-season of cereals crops from March to May 2013, and for the subsequent season of market gardening (e.g. tomato, water melon, pepper etc.) from May to August 2013. In addition, a good agreement is observed for the second market gardening season (May to August 2014). However, discrepancies are observed for the remaining periods which may correspond to periods when bare soil fraction (fallow and trees fields) outweighs the vegetation covered fraction or when evaporation process. Also the discrepancy observed for the second wheat period and not for the first may be due to a bad simulation of evaporation processes occurring more during the second wet year. This highlights the known problems of the FAO method to simulate evaporation from bare soil, mainly the readily evaporable water at surface layer REW, as observed during the SAMIR calibration (Saadi *et al.* 2015) and as mentioned by other authors (Torres et Calera, 2010, Odi-Lara, 2016).

With the current parameterization, SAMIR is not able to well reproduce the ET interseasonality and modeled ET range from 0.3 mm and 2 mm for both seasons. The average annual levels are not bad but the slight difference between seasons is insufficient, given that the two seasons are different in terms of climatic conditions. The transpiration component is assumed more stable between years because it is linked to external water inputs by irrigation, and thus mainly link to the cropped surfaces. Conversely, the evaporation component is more linked to soil surface moisture and thus correlated with rainfall events and partially with irrigation. Then, the fact that the contrast between years is not well reproduced advocates for a problem with evaporation, in this case an underestimation. The fact that the evaporation peaks present in the XLAS derived ET after each rainfall event are not observed in the SAMIR ET corroborates this evaporation problem. The area below XLAS transect is mainly cropped by trees with considerable fractions of bare soil, especially during the dry season (rain-fed cereals did not develop), which explains the importance of the contrast observed for ET between years but not with SAMIR.

This problem with evaporation may be because of the REW parameter controlling the evaporation rate (REW=0 and m=0.246) has been obtained by the calibration of cereals. Having not much information or other crops, and considering this parameter was linked mainly to soil properties, we have decided to use this parameter for all crops in the area, which may be the reason for the observed problem. Therefore, in order to improve SAMIR results, we have decided to revisit the calibration of cereals using more standard REW values, and to apply in any case standard REW values (*i.e.* between 0 and 8) to other crops, assuming this parameter cannot be extrapolate simply from one crop to another. This will be presented in chapter 4.

3.4 Synthesis and partial conclusion

The major originality of SAMIR relies on the use of remote sensing NDVI time series for vegetation monitoring, from which crop coefficients and vegetation fraction covers are derived, instead of using standard values. The irrigations are simulated based on the soil water budget. Irrigation volume estimates have been evaluated at perimeter, farm and field scales. The seasonal volumes estimated at perimeter scale were acceptable, although comparison at finer spatial scales (farm and field scales) were not significant. Indeed, at plot scale we faced the difficulty to collect accurate information. At farm scale, the result gave significant information about the farmer's behavior but the data set did not allow assessing accurately SAMIR estimates themselves. At perimeter scale, it was shown that the modeled monthly irrigations are on the whole satisfying with some noticeable exceptions pointing out the limitations of SAMIR regarding (1) the initialization of the soil moisture, and (2) the impossibility to take into account changes of land use during the same season. This last point emphasizes the necessity to develop methods for monthly land use mapping instead of the traditional annual or seasonal mapping frequency used for now. Finally, SAMIR ET estimates were compared with ET derived from XLAS measurements over four kilometers transect during two years. Although the values were on the whole coherent, discrepancies revealed some possible problems in the evaporation simulations with SAMIR. Therefore, further elaborations are carried out to enhance SAMIR parameterization which will be presented in the next chapter.

Chapter 4: Revisiting SAMIR parameters setting for evapotranspiration and irrigation spatialization

The SAMIR overall results of modeled ET and irrigation volumes are encouraging. However, with the current parameterization, in the sparsely vegetated area observed by the XLAS, SAMIR is not able to well reproduce the seasonal variations of ET and the modeled ET is located within the same range for the 2012-2013 and 2013-2014 seasons although XLAS measurements are more contrasted, because of significant differences in precipitations for these two years. Moreover, the issue of parameterization, regarding mainly the soil water content initialization and the soil evaporation (REW), has been already highlighted. Therefore, in order to improve SAMIR results, the input parameters are revisited. New cereals parameters calibration is carried out based simultaneously on evaporation and soil moisture measurements for the three observed plots. A further attempt to get calibrated parameters for trees was performed based on ET and soil moisture measurements of the rainfed olive orchard (Nasrallah flux station).

4.1 SAMIR model calibration

4.1.1 Second calibration on cereals fields

The SAMIR model was recalibrated at plot scale using simultaneously latent heat flux and soil moisture measurements (section 2.5.2) of the irrigated barley (20111-2012), irrigated wheat (2012-2013) and rainfed wheat (2011-2012) plots. The goal of this calibration is to get a unique set of parameters for cereals taking into account irrigated and rainfed cereals in order to get a robust parameterization in a context of various cropping practices. Another difference with the first calibration described in (Saadi *et al.*, 2015) is that the Nash efficiency between observed and modeled values was maximized for both ET and soil moisture for the three soil layers (*i.e.* evaporation layer, root zone and deep layer).

The NDVI time profile for each flux site was extracted from the SPOT time series. The NDVI-fc relationship was determined empirically considering that for a bare soil (NDVI = 0.1) the fraction cover was null (fc = 0) and that at full coverage (fc = 1) the NDVI was the maximum value observed in the image (0.9). The NDVI-kcb relations were calibrated. Differently from the first calibration, wilting point (θ_{wp}) and field capacity (θ_{fc}) were determined for each plot on the basis of the soil moisture measurements as the upper and lower limits of the soil moisture measurement range. The field capacity was determined after discarding the water content peaks observed after strong wetting events before soil drainage. An initial water content of 45%, 70% and 10% of the water holding capacity was considered for the rainfed winter wheat (2011-2012), irrigated barley (2011-2012) and irrigated winter wheat (2012-2013) plots, respectively, based on previous rainfall as soil water measurements when usually not yet available. For 2012–2013, it was set to 10% because no significant precipitations were observed since summer, while for the 2011–2012 season, the initial water content was set at a relatively larger value of 45% and 70% due to 85 mm of precipitations recorded ten days before the starting date of the simulation. Higher percentage was considered for the irrigated barley because this plot is irrigated and barley was preceded by a market gardening crop (during summer 2011). The soil fraction wetted by rain or irrigation (fw) was set to one because the irrigation technique for cereals is sprinkler irrigation. The depth of the evaporation layer (Ze) and the proportion of easily available water (p) were fixed following FAO paper 56 recommendations (Allen *et al.*, 1998). The calibrated parameters (REW, m, Zr_{max}, Z_{soil}, Dif_{er}, Dif_{rd}, and Kcb) are summarized in table 4.1.

Table 4. 1: Parameters obtained after calibration on observed ET and soil moisture for the three cereals plots.

	Definition	Value	Data Sources
	Vegetation Parameters		
a_{fc}	NDVI-fc relation's slope	1.25	Satellite imagery
b_{fc}	NDVI-fc relation's intercept	−0.13	Satellite imagery
a_{Kcb}	NDVI-Kcb relation's slope	1.31	Calibrated
b_{Kcb}	NDVI-Kcb relation's intercept	−0.13	Calibrated
	Soil Parameters		
θ_{fc} [m^3/m^3]	Volumetric water content at field capacity	0.22	Rainfed wheat ground observation
		0.27	Irrigated barley ground observation
		0.25	Irrigated wheat ground observation
θ_{wp} [m^3/m^3]	Volumetric water content at wilting point	0.07	Rainfed wheat ground observation
		0.14	Irrigated barley ground observation
		0.11	Irrigated wheat ground observation
Init_RU [%]	Soil initial water content	45	Rainfed wheat ground observation
		70	Irrigated barley ground observation
		10	Irrigated wheat ground observation
Ze [mm]	Depth of the surface layer	125	FAO-56
REW [mm]	Readily evaporable water at surface layer	0	Calibrated
m [-]	Coefficient de reduction	0.264	Calibrated
Zr_{min} [mm]	Minimum root depth	125	FAO-56
Zr_{max} [mm]	Maximum root depth	800	Calibrated
p	Fraction of readily available water holding capacity	0.55	FAO-56
Z_{soil} [mm]	Total soil thickness	1550	Calibrated
Dif_{er} [%]	Diffusion coeff. between surface and root layers	5	Calibrated
Dif_{rd} [%]	Diffusion coeff. between deep and root layers	10	Calibrated

The results showed that the dynamics of ET are on the whole correctly simulated (Figures 4.1). One important result is that it was not possible to obtain correct results without decreasing the m factor down to 0.264. When trying to keep it to one, even with REW at a value of zero, the average Nash decreases significantly around 0.4. This confirms that the evaporation process is difficult to described using the standard FAO method, and confirms the usefulness of the m factor. However, some important discrepancies explain that the final Nash and RMSD values are not so good. For rainfed wheat, we see that SAMIR does not reproduces ET peaks due to rainfall events, showing, if observations are correct, that the low m factor is not appropriate during this period of bare soil and high ET0. SAMIR increases evaporation after harvest (around May, 27th), but the raise is not as pronounced as for observations. For the irrigated barley, we see also a significant underestimation of ET by SAMIR starting mid-April, which can be explained also by soil evaporation problems. Finally, the problem of the irrigated wheat is quite different and seems to be linked to measurement errors. Indeed, especially when compared with irrigated barley, the strong variability of ET is probably due to errors in observed ET, quite obvious considering the dozen of ET values which are not associated

with null values of ETo and are anyway not realistic. Calibrating rainfed and irrigated crops together appears to be successful here, showing that except the difference in water inputs, they have roughly similar behavior. Nevertheless, observed ET for the rainfed wheat seems to be lower than modeled one, which could be interpreted by a lower Kcb, but this lower value may also be the result of compensation, through the calibration, of the higher observed values during the last month.

The soil moisture simulation for the surface and root layer is correct with Nash values better than for ET simulations (Table 4.2). The results for the deep layer soil moisture were not considered because calibration was unsuccessful. This can be explained either by the complex hydrological behavior of this layer or by soil moisture measurement errors (e.g. the raise of moisture in the deep layer for rainfed wheat is quite surprising). In fact, the evaporation and root layers have fairly simple behaviors; they are well constrained by water inputs (rainfall and/or irrigation) and ET outputs, so basically they look like a tank. On the other hand, the deep layer receives by gravity only the excess water drained from the above horizons and it is affected by capillarity fluxes with the layers below. These processes are more complex to simulate.

Table 4. 2: NASH efficiencies of SAMIR calibration on observed ET and soil moisture for wheat and barley plots.

NASH			**Irrigated barley 2011-2012**	**Rainfed wheat 2011-2012**	**Irrigated wheat 2012-2013**	**Average**
Evapotranspiration		Nash	0.55	0.45	0.53	0.51
		RMSD	0.66	0.75	0.68	0.70
Soil moisture	**Evaporation layer**	Nash	0.66	0.77	0.67	0.70
	Root layer	Nash	0.89	0.81	0.77	0.82
	Deep layer	Nash	-120.76	-26.40	-4.56	-
Average			0.66	0.62	0.62	**0.63**

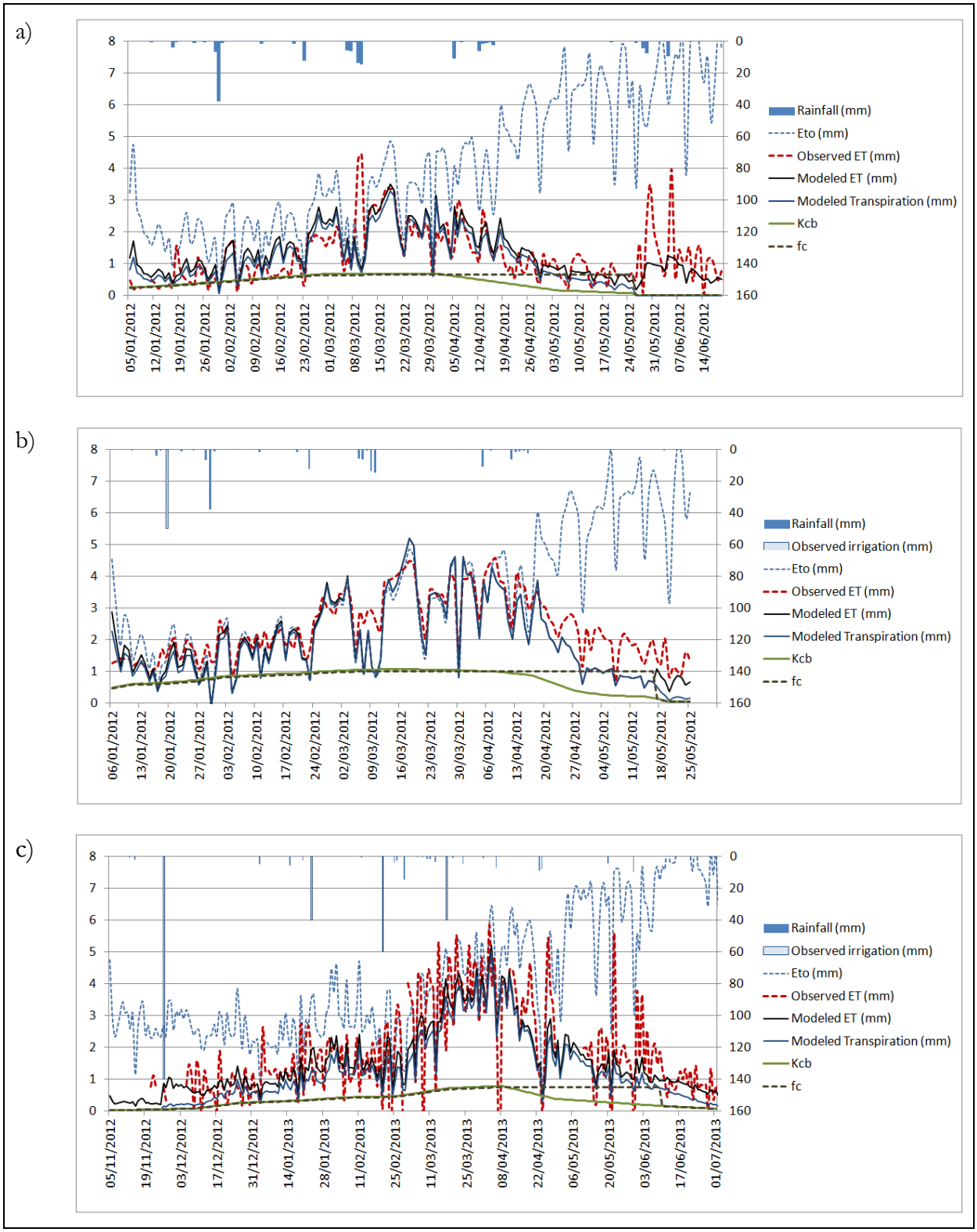

Figure 4. 1: Simulations of ET for the (**a**) rainfed winter wheat (**b**) irrigated barley and (**c**) irrigated winter wheat experiment fields for the calibrated model (NASH = 0.45, 0.55 and 0.53, respectively).

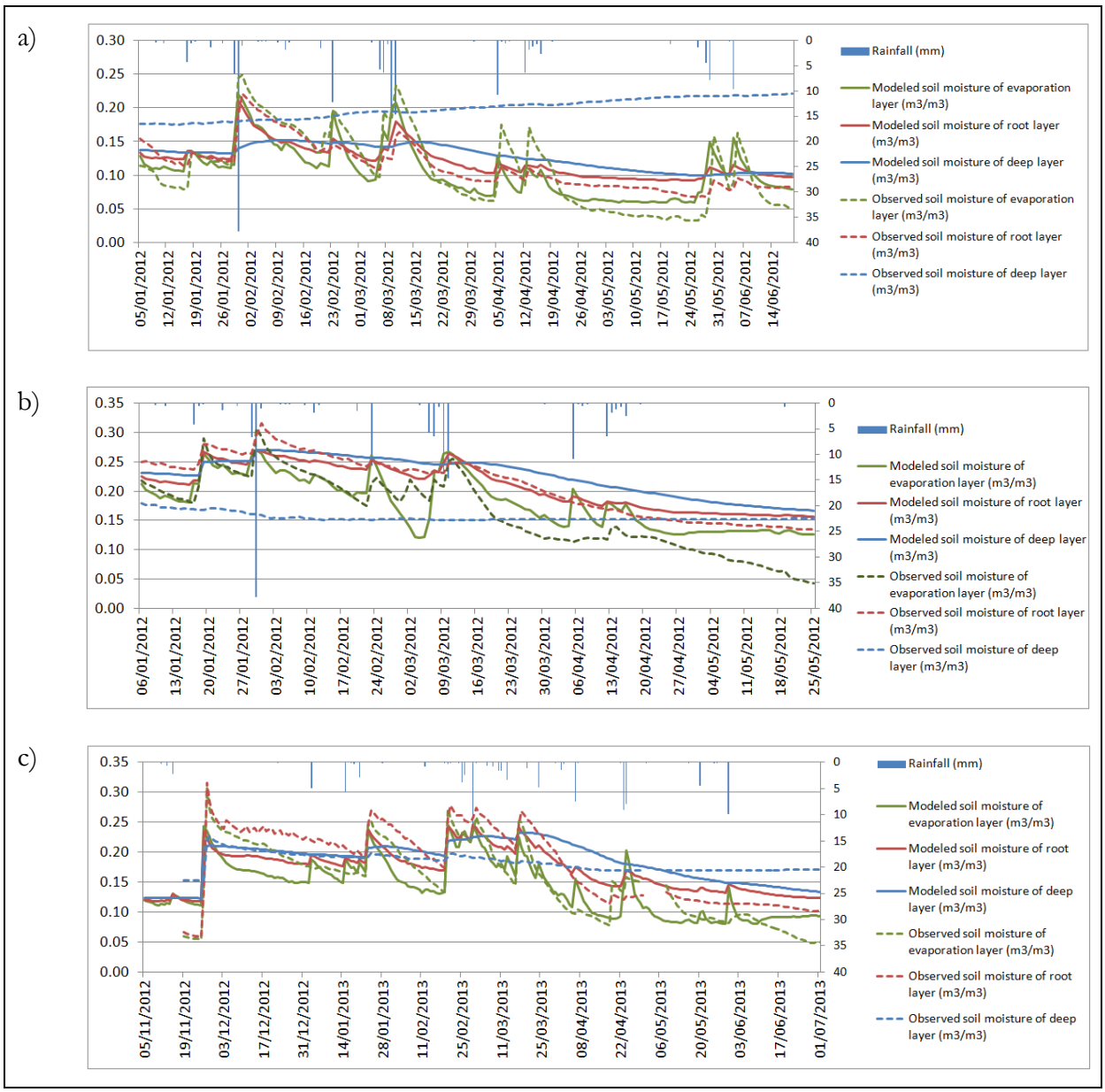

Figure 4. 2: Simulations of soil moisture for the (**a**) rainfed winter wheat, (**b**) irrigated barley and (**c**) irrigated winter wheat fields for the calibrated model. Average NASH for evaporation and root layers: 0.79, 0.77 and 0.72 for the three plots, respectively.

4.1.2 Calibration for the olive orchard

In order to better understand tree crops functioning regarding the FAO-56 model, the SAMIR model was also calibrated at plot scale using latent heat flux measurements and soil moisture of the rain-fed olive orchard (section 2.5.2). One important stake was to get insight in the evaporation process that has shown to be tricky in previous results. However, calibration on a rain-fed orchard with very low vegetation cover would hardly be applicable below the XLAS transect were all trees are denser and irrigated.

The simultaneous calibration with flux and soil moisture measurements has failed since negative NASH efficiencies are always obtained. These problems may be due either to measurements problems, or to the fact that water flux for such a rainfed system, with deep rooting system, may not be correctly represented by the simple FAO soil model. However, calibration using only ET measurement gave a Nash efficiency of 0.40 (Figure

4.3); the parameters are shown in Table 4.3. It is interesting to see, although disturbing, that it was not possible to get correct calibration without a strong reduction of the evaporation intensity, with a null value for REW and a very low m factor (0.108). This confirm the evaporation problem with FAO-56, but will not provide any solution to our hypothesis that evaporation should be higher under the XLAS transect. So we decided to withdraw these results, considering that this rainfed orchard is not representative of our XLAS irrigated area.

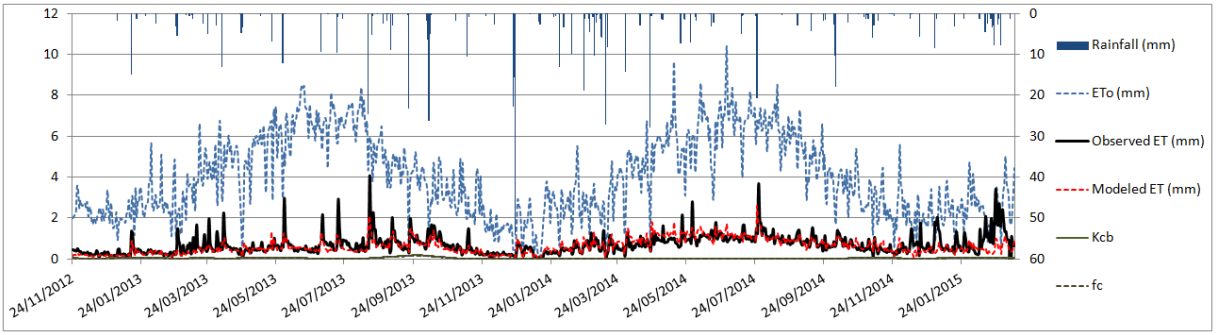

Figure 4. 3: Simulation of ET for the rainfed olive orchard field for the calibrated model (NASH Spatialization of ET and Irrigation)

Table 4. 3: Parameters obtained after calibration on observed ET for the rain-fed olive field.

	Definition	**Value**	**Data Sources**
Soil Parameters			
θ_{fc} [m^3/m^3]	Volumetric water content at field capacity	0.22	ground observation
θ_{wp} [m^3/m^3]	Volumetric water content at wilting point	0.04	ground observation
Init_RU [%]	Soil initial water content	10	Estimation
Ze [mm]	Height of the surface layer	125	FAO-56
REW [mm]	Readily evaporable water at surface layer	0	Calibrated
m [-]	Coefficient de reduction	0.108	Calibrated
Zr_{min} [mm]	Minimum root depth	1550	FAO-56
Zr_{max} [mm]	Maximum root depth	1550	Calibrated
p [-]	Fraction of readily available water holding capacity	0.65	FAO-56
Z_{soil} [mm]	Total soil thickness	5000	Calibrated
Dif_{er} [%]	Diffusion between surface and root layers	15	Calibrated
Dif_{rd} [%]	Diffusion between deep and root layers	25	Calibrated

4.2 Model parameters setting

The fc-NDVI relations for all land use classes and the Kcb-NDVI relation for market gardening were kept unchanged (Table 4.4). The revised calibrated Kcb-NDVI relation was used for cereals crops (Table 4.4). For tree crops, the previously relation for fc and Kcb achieved on experimental data for irrigated olive trees in the Haouz plain in Morocco was questioned. Indeed, this olive orchard with high vegetation cover is well maintained and well irrigated leading to high transpiration against limited evaporation. These conditions are not verified in our study area context, and although the trees are irrigated, they are occasionally subject to water stress (mainly olive trees) especially in dry season when they are in competition with more profitable crops such market gardening. A literature review on Kcb values was carried out and it was assumed that a NDVI-Kcb relation derived from Kcb values provided by (Allen *et al.*, 1998) and (Testi *et al.*, 2004) for olive trees was more suitable.

Soil properties (θ_{fc}, θ_{wp}, Ze, Z_{soil}, Dif_{er}, Dif_{rd}) were considered homogeneous in the study area and these parameters were taken from cereal plots calibration. As no other accurate information was available, the averaged value of the observed θ_{fc} and θ_{wp} in the three cereals plots were used (Table 4.5). Calibrated value of REW and m was used only for cereals crops, while for trees and market gardening crops, because no other reliable information was available, we used bibliographic values: m was set to 1 and REW was taken from the table 19 of the FAO-56 paper (Allen *et al.*, 1998) based on the estimated soil water content (Table 4.5).

Crop specific parameters (Zr_{max} and p) were set to calibrated values for cereals and taken from FAO paper 56 (Allen *et al.*, 1998) for the other land use classes (Table 4.5). For tree crops, maximum root zone depth was set to match the calibrated maximum soil depth (Table 4.5). In order to overcome parameters initialization problem, the initial soil water content (Init_RU) was also revisited and for all season it was set to 50% of the soil available water (between θ_{fc} and θ_{wp}) for all land use classes except for bare soils where it was set to 10% (Table 4.5). These assumptions were done based on field observation of our study area, because cereals crops sown at the beginning of the simulation (November) are often preceded by an irrigated summer crop which lead to a significant residual soil water content. For bare soils, the 10% Init_RU accounts for the fact that these soil receive only rainfall and are mostly dry at the end of October.

The irrigation parameters were also revisited (Table 4.5). Drip irrigation was assumed for trees since gravity irrigation become increasingly rare in our study area (fw = 25%, MAD = 0.5 * TAW), trees are irrigated throughout the year (no threshold to stop irrigation during senescence: Kcb_stop = 0). Market gardening was also irrigated using drip irrigation (fw = 25%) and irrigation lasts longer because vegetables require water until harvest (Kcb_stop = 50%). This parameter was set to 50% instead of 75% previously because farmers tend to irrigate market gardening as long as possible to get high fruit caliber for more profit, even against low quality. Cereals irrigation parameters were kept unchanged.

Table 4. 4: Relations used for fc and Kcb estimates from NDVI

NDVI-fc	NDVI min	NDVI max	fc min	fc max	Relations	Sources
Cereals	0.1	0.9	0	1	$fc = 1.25 \times NDVI - 0.13$	Satellite imagery
Market gardening	0.1	0.9	0	1		
Fruit trees	0.1	0.8	0	0.9	$fc = 1.34 \times NDVI - 0.17$	
NDVI-kcb	**NDVI min**	**NDVI max**	**Kcb min**	**Kcb max**	**Relations**	**Sources**
Cereals	-	-	-	-	$K_{cb} = 1.31 \times NDVI - 0.13$	Calibration (our field experiments).
Market gardening	0.1	0.9	0	0.98	$K_{cb} = 1.23 \times NDVI - 0.12$	(Allen *et al.*, 1998) and Satellite imagery.
Fruit trees	-	-	-	-	$K_{cb} = 1.16 \times fc$	(Allen *et al.*, 1998) and ((Testi *et al.*, 2004)

Table 4. 5: Soil and crop parameters and irrigation rules used for spatialization. Grey cells show calibrated parameters.

		Cereals	Market Gardening	Fruit Trees
Soil parameters				
	θ_{fc} (m^3/m^3)		0.26	
	θ_{wp} (m^3/m^3)		0.11	
	Z_{soil}(mm)		1550	
	Dif_{er} (%)		5	
	Dif_{rd} (%)		10	
Initial RU (%)	Bare soil		10	
	Cropped soil		50	
	REW (mm)	0	6	6
	m	0.264	1	1
Crop parameters				
	Zr_{min} (mm)	125	125	1550
	Zr_{max} (mm)	800	1000	1550
	p	0.55	0.55	0.65
Irrigation rules				
	Fw, fraction wetted (%)	100	25	25
	MAD, management allowable depletion for irrigation triggering	MAD = RAW	MAD = 0.2 * TAW	MAD = 0.5 * TAW
	Kcb_{stop}, Kcb irrigation threshold to stop (% of Kcb_{max})	99	50	-
Irrigation constraints				
	Min_{ir}, minimum water depth per turn (mm)	20	-	-
	Min_{days}, minimum number of days between two water turns	7	-	-

4.3 Validation of new modeled irrigation volumes at perimeter scale

With the new parameter set, evapotranspiration and irrigation estimates were spatially computed for the seasons 2008–2009 (December to June), 2011–2012 (November to May), 2012–2013 (November to June) and 2013-2014 (November to June). Evapotranspiration was validated on the scintillometer transect for the 2012-2013 and 2013-2014 seasons, and irrigation volumes were validated for the four GDAs.

The results of the comparison between the modeled and observed monthly irrigation volumes show a significant improvement of monthly results for all seasons (Figures 4.4 to 4.7 and Table 4.6). Moreover, the large discordances observed previously for the beginning of the simulation period, *i.e.* in November and December, were reduced thanks probably to the modification of soil moisture initialization.

However, bad results are still found for the 2011-2012 season for the three GDAs (Figure 4.5). Observed irrigation data may hardly be questioned since the overestimation is observed for the three independent GDAs. As the revisited parameters provide good results for the other seasons, we are more inclined to question the quality of the land use map for this season, especially the problem already mentioned in chapter 3 regarding crop changes occurring at this period of the year which are not captured by unique annual land use maps. The larger discrepancies are generally visible in June (e.g. Mlelsa 2008-2009, Karma II 2011-2012, Karma II 2012-2013), which can be due to land cover changes which are not managed by SAMIR, *i.e.* to market gardening appearing at this time after winter cereals harvest (beginning of June). Moreover, even for market gardening present in the land cover map, the parameters for these crops are rather uncertain.

The seasonal results for all campaigns are summarized in table 4.6 and plotted in Figure 4.8. Despite the improvements observed for the monthly distribution (Table 4.6), the overall results remain almost the same: the average seasonal modeled irrigation depth is now of 120 mm (118 mm previously), as compared to the observed value of 111 mm. However, the regression is less good than for the previous calibration with R^2=0.31.

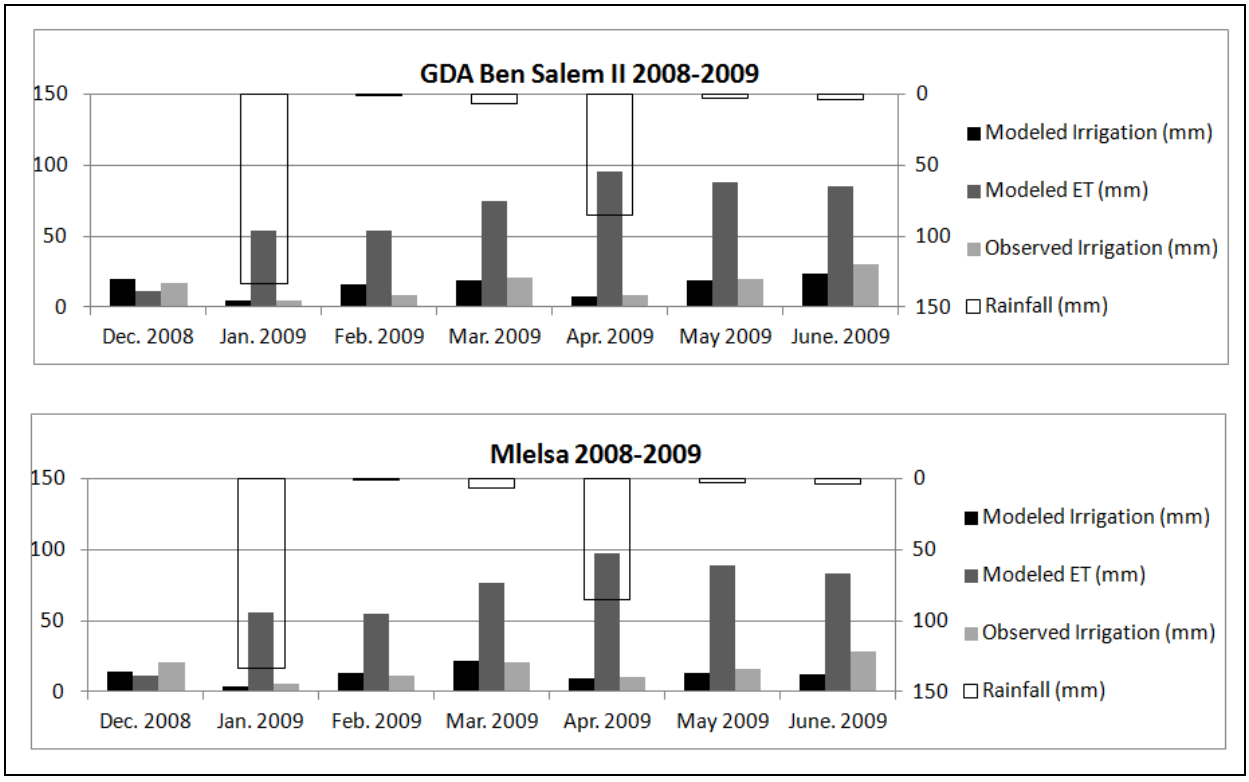

Figure 4. 4: Comparison between surveyed and SAMIR estimated irrigation depth at seasonal scale for the 2008–2009 season

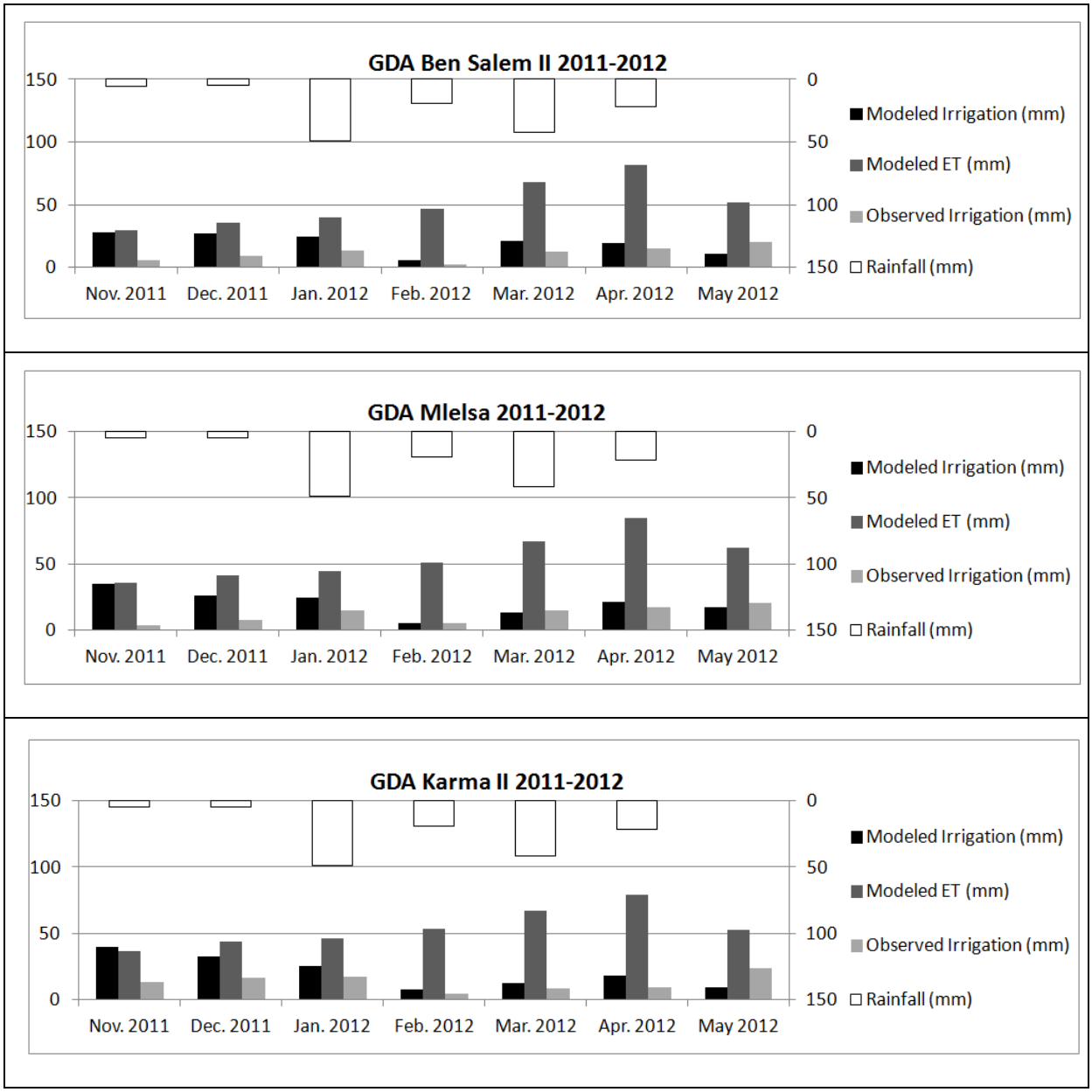

Figure 4. 5: Comparison between surveyed and SAMIR estimated irrigation depth at seasonal scale for the 2011–2012 season

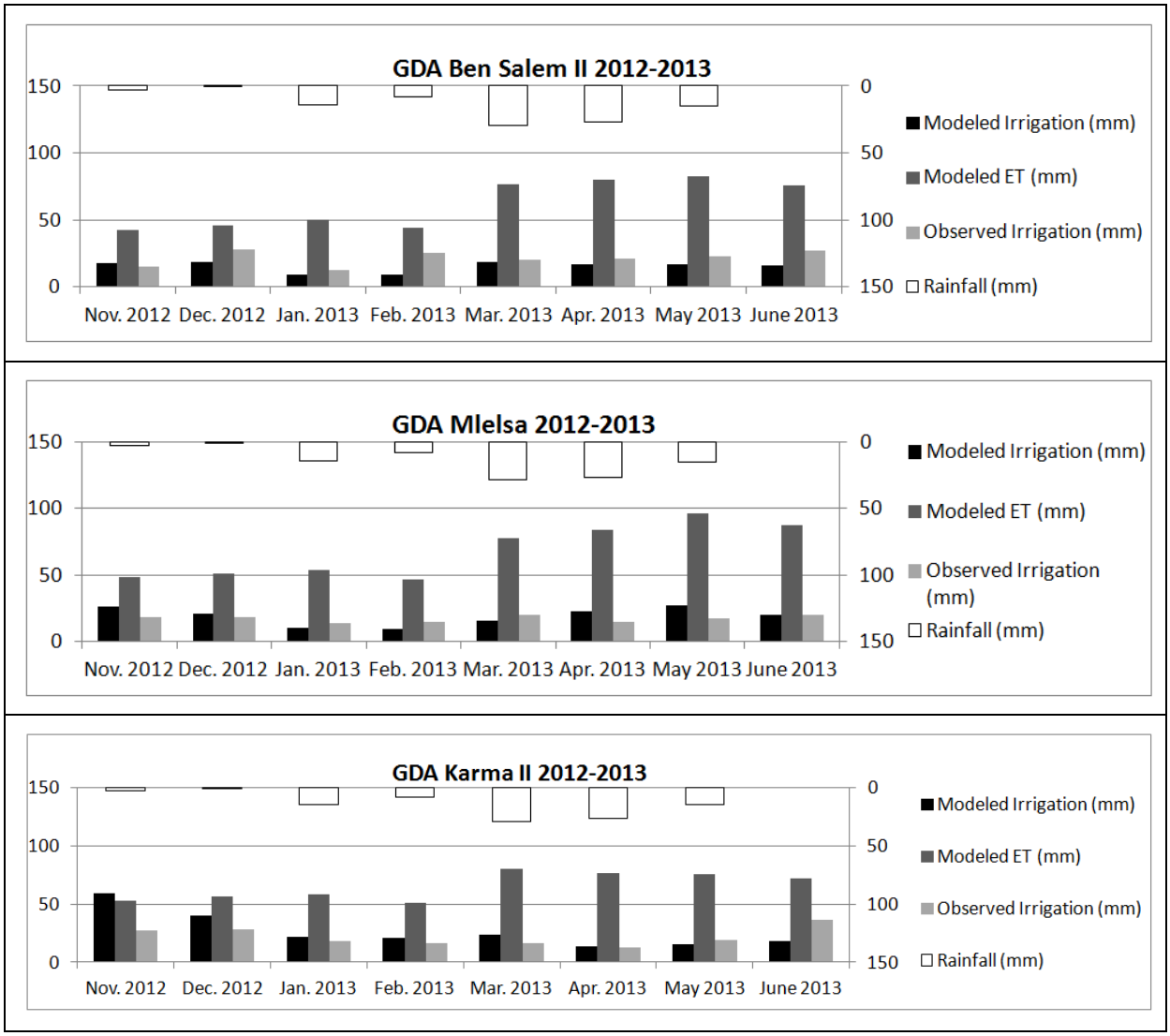

Figure 4. 6: Comparison between surveyed and SAMIR estimated irrigation depth at seasonal scale for the 2012–2013 season

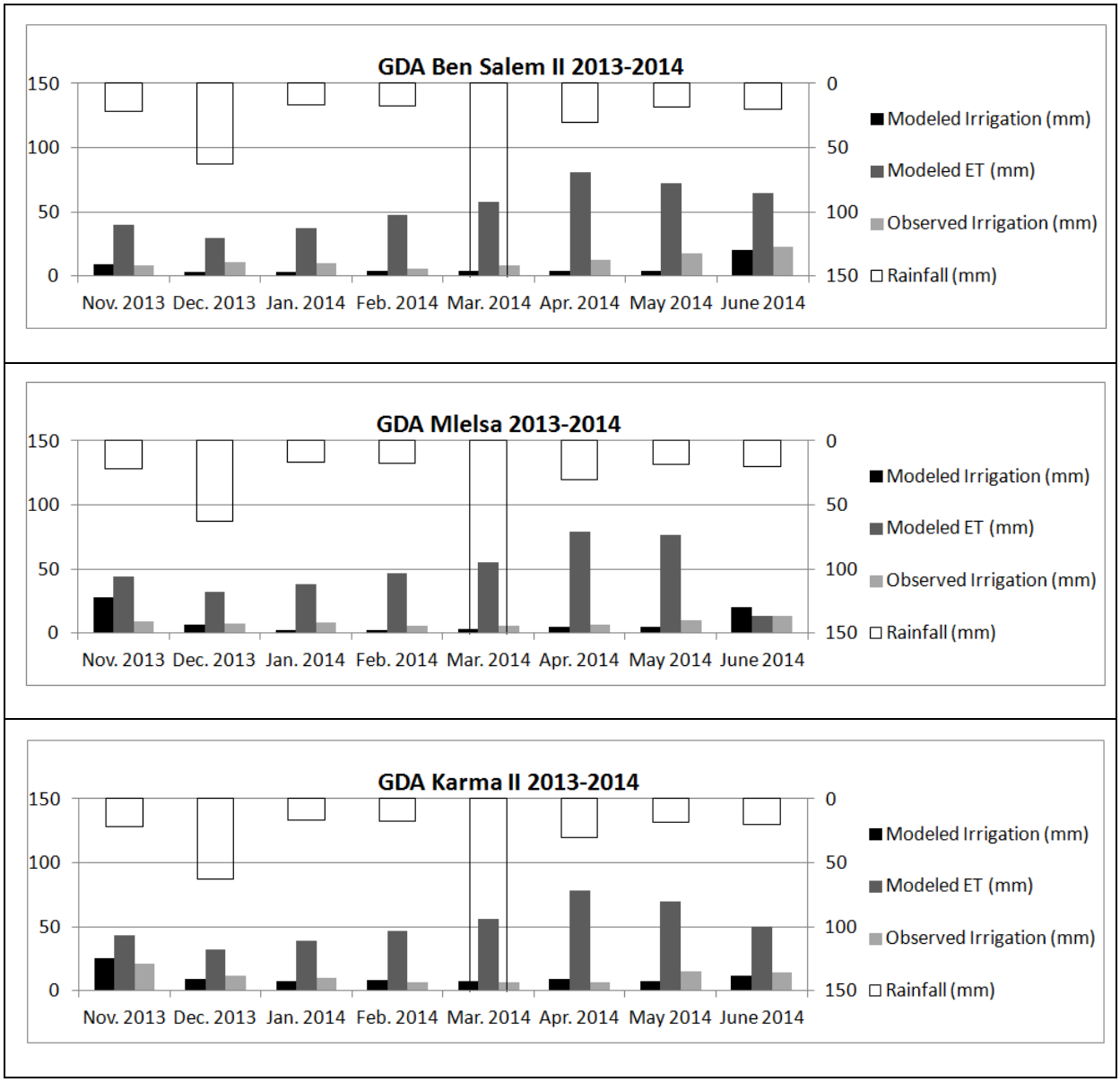

Figure 4. 7: Comparison between surveyed and SAMIR estimated irrigation depth at seasonal scale for the 2013-2014 season

Table 4. 6: Estimated and observed seasonal water budget components for all campaigns. Irr. is irrigation; Obs. Irr. and Mod. Irr. are the monthly observed and modeled irrigation volumes, respectivelely; Mod. ET is the modeled evapotranspiraion

Campaigns	Mod. Irr. (mm)	Mod. ET (mm)	Rainfall (mm)	ΔSW (mm)	Obs. Irr. (mm)	Monthly Irr. RMSE Old parameters	Monthly Irr. RMSE Revisted parameters
Ben Salem 08-09	109.0	463.6	232.5	-122.1	108.3	9.0	3.7
Mlelsa 08-09	87.1	467.9	232.5	-148.3	112.2	9.0	6.6
Ben Salem 11-12	136.3	353.0	142.0	-74.6	80.5	21.0	12.6
Mlelsa 11-12	143.1	387.9	142.0	-102.8	86.0	20.8	14.2
Karma II 11-12	145.3	378.5	142.0	-91.2	94.0	19.2	13.8
Ben Salem 12-13	123.7	497.7	96.9	-277.1	172.9	8.7	8.3
Mlelsa 12-13	151.4	543.4	96.9	-295.1	136.9	12.5	6.4
Karma II 12-13	212.6	521.9	96.9	-212.4	173.9	22.3	14.3
Ben Salem 13-14	53.3	430.3	340.9	-36.1	97.3	10.2	6.9
Mlelsa 13-14	73.4	386.3	340.9	28.0	67.6	11.8	7.8
Karma II 13-14	86.0	416.2	340.9	10.7	93.2	13.3	4.0
Seasonal results (November to June)	120.1	440.6	200.4	-120.1	111.2	14.3	9.0

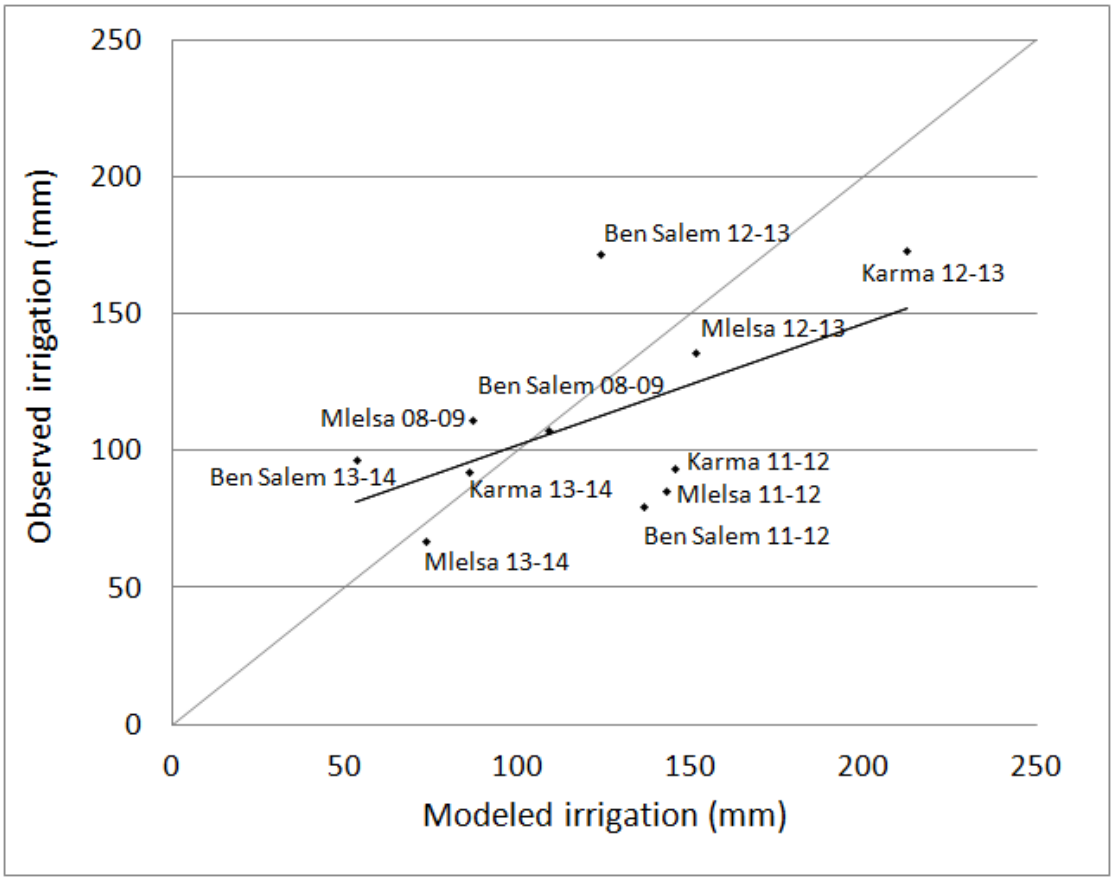

Figure 4. 8: Comparison between observed and SAMIR modeled seasonal irrigation depths

4.4 New evapotranspiration results validation using the XLAS data

The daily-distributed ET simulated by SAMIR using the old and the new parameters was compared to the daily XLAS derived ET (figure 4.9). Results were enhanced for the 2013-2014 season and the new-modeled ET matches well the observed one. On the other hand, a strong degradation is obtained for 2012-2013. Although more ET peaks corresponding to rainfall events were recorded for this season in comparison with the old parameters, there is a clear overestimation of ET. It is important to keep in mind that despite this bad result for ET, the 2012-2013 irrigation volumes were correctly estimated. There are several possible explanations for this discrepancy. First, the area concerned is not the same as for GDAs and errors in land cover are possible in the XLAS area. Indeed, the land cover maps for the two seasons where not obtained by the same methods, which, added to the usual errors in such maps, could increase the bias between the two years. Indeed, the class statistics computed on the XLAS area for the two seasons show a clear incoherence, with two times more trees 2012-2013 than in 2013-2014 (Table 4.8), which is not realistic for these permanent crops. This problem emphasize the difficult task of land use mapping in semi arid areas where crops cycles are not synchronous, vegetation cover are sometimes very low especially for trees and intercropping is widely encountered (Simonneaux *et al.*, 2008). The second possible explanation for the ET errors at 2012-2013 is that SAMIR does not account for actual irrigation but simulates them with the same rules, and the possible variation of stress level between years. Thus, the contrast of performance between the two seasons can be linked to the also contrasted hydrological functioning of these years, due to climate and possible variations of irrigation practices. We know that in this area irrigation is not only driven by actual crop requirements but also but by water availability and farmers behavior. Thus, it is possible that the already mentioned failures of evaporation modeling depend on the hydrological regime. One clue corroborating both hypotheses is that despite a dryer year, the averaged ET is higher for 2012-2013. If we assume that the vegetation amount evolution is correctly controlled by NDVI time series, this anomaly can be linked to errors in the soil evaporation process or to land use errors having impact on crop water budget simulation. Finally, although the ET problem is not solved yet, the comparison between the two parameterizations, affecting mainly the evaporation parameters, shows the high impact of this factor in such sparsely vegetated semi-arid areas. Further work is necessary to improve this aspect.

Table 4. 7: Land use statistics of the XLAS area (%)

	2012-2013	**2013-2014**
Cereals	5	14
Market gardening	20	28
Tree crops	37	17
Bare soil	31	41

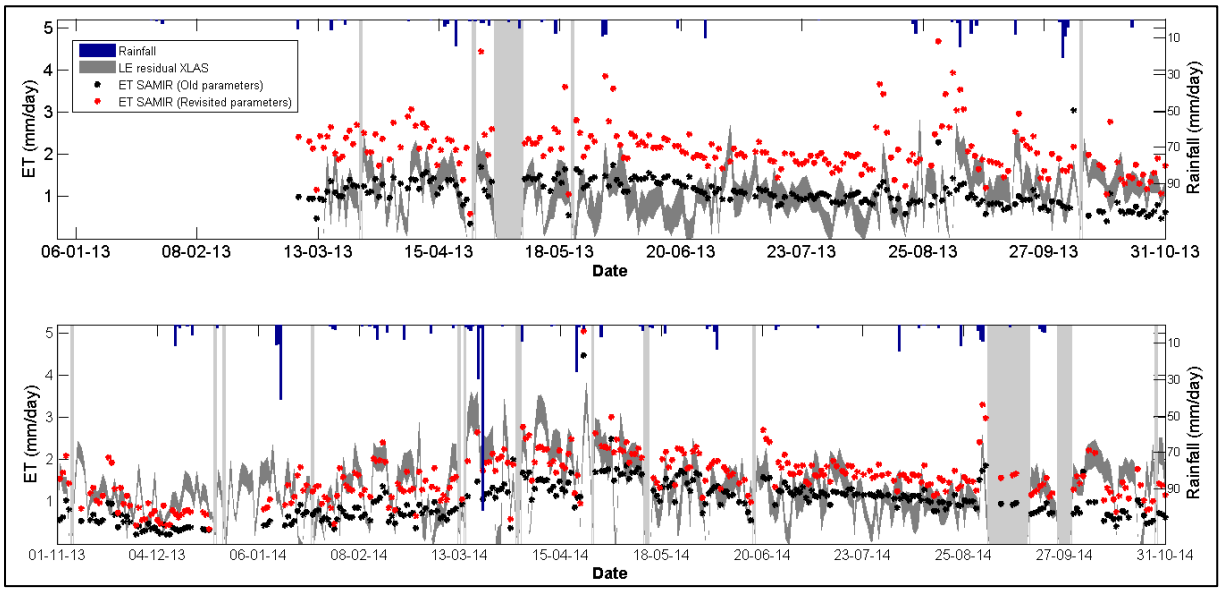

Figure 4.9: Observed daily latent heat fluxes vs. daily SAMIR modeled evapotranspiration obtained with the old and the revisited parameters

4.5 Synthesis and partial conclusion

The overall results of the water balance spatialization by the SAMIR model are encouraging. Although the modeled irrigation volumes remain almost the same in comparison to previous parameters setting, monthly results improved significantly. Strong overestimation of irrigation in the first two months of the simulation was corrected. Regarding the ET estimates, although we still did not get yet a good agreement simultaneously for both seasons, we have identified the levers to fix this issue, namely the evaporation parameters and the land cover characterization. However, it is still difficult to determine reliable evaporation parameters without calibration or validation data, which may be a problem in areas with high bare soil fractions.

Our results are difficult to compare to previous works in the Mediterranean context. Indeed, at plot scale, several studies validated ETa estimates using eddy correlation measurements, but it is difficult to compare the RMS values obtained. The average RMS that we obtained for the three plots (0.7 mm day^{-1}) was of the same order of magnitude of the values obtained by Cammalleri *et al.* (2013) on olive orchards (RMS between 0.3 and 0.5 mm day^{-1}), or by Padilla *et al.* (2011) 0.8 and 0.67 mm day^{-1} respectively) or by Mateos *et al.* (2013) on irrigated fields located in southern Spain (RMS of 0.75 mm day^{-1}). Generally, the FAO-56 approach coupled with remote sensing simulates well ETa at plot scale, as it was the case for our cereal plots, especially when a calibration is applied. The discrepancies are often specific of the crops studied and of the quality of the data used (meteorological data, ground measured ETa and remote sensing data quality), so that it is difficult to compare the RMS figures between study cases.

Actually, the problems arise when trying to extend from plot to regional scale irrigation estimates. Besides, several studies compare between variants of ETa estimation methods based on the coupling of FAO-56 and remote sensing, but they don't actually compare the results to ground measured ETa or irrigation volumes

(Guermazi *et al.*, 2016), so that it is difficult to compare with our work. However, Akdim *et al.* (2014) used the penman monteith equation forced by remote sensing data (NDVI derived from SPOT4 and Landsat8 images) to estimate irrigation water requirements in the semi-arid region of Doukkala (Morocco). The comparison between these monthly irrigation requirements and sensed monthly water delivery provided by the irrigation office showed discrepencies much larger than ours.

The main originality of our study is to achieve validation of ETa and irrigation volumes on large areas using ground data.. However, the main limitation of crop water balance models fed by HR RS data in estimating the water balance components rely in the high number of inputs parameters required by those models, whose estimation is largely uncertain remains the main drawback of these models. For this reason, ET estimation in a context of heterogeneous landscape is often achieved using SEB approaches based models, such as the SPARSE model.

Chapter 5: Energy fluxes estimation at low spatial resolution: Application of the energy balance model SPARSE

The results of this chapter are taken from the article:

Saadi, S., Boulet, G., Bahir, M., Brut, A., Mougenot, B., Fanise, P., Simonneaux, V., and Lili Chabaane, Z.: Assessment of actual evapotranspiration over a semi-arid heterogeneous land surface by means of coupled low-resolution remote sensing data with energy balance model: comparison to extra Large Aperture Scintillometer measurements, Hydrol. Earth Syst. Sci. Discuss., https://doi.org/10.5194/hess-2017-454, in review, 2017

- In review in « Hydrology and Earth Systems Sciences » journal.

In this chapter, the operational use of the SPARSE model and the accuracy of the modeled sensible heat flux (H) and daily ET over a heterogeneous semi-arid landscape with a complex land cover (i.e. trees, winter cereals, summer vegetables) was assessed.

5.1 SPARSE model description

The SPARSE model (Boulet *et al.*, 2015) constraints the surface energy budgets of both the soil and the vegetation (considered as the main heat and vapor sources) with a remotely-sensed radiative surface temperature in order to retrieve instantaneous evaporation and transpiration rates. It also computes those two components in any prescribed water stress conditions, from fully stressed to potential rates. Those values are used as bounding terms in order to secure realistic outputs of the model.

5.1.1 Input data

SPARSE input data are RS and meteorological data. RS data are radiative surface temperature as well as green or total Leaf Area Index (LAI) and vegetation height; both can be deduced from NDVI estimates and, if possible, land use type. Meteorological data are half hourly to hourly estimates of incoming solar radiation, wind speed, air temperature and humidity at reference level.

5.1.2 Algorithm

SPARSE is a two-sources model made of two independent versions; "layer" and "patch" (Figure 5.1) and two modes; "retrieval" and "prescribed", which can be also used independently. The "patch" approach assumes that the soil and the vegetation interact almost independently with the atmosphere corresponding to a parallel resistance scheme while the "layer" approach assumes that soil vegetation and atmosphere are tightly coupled corresponding to a series resistance scheme. In this PhD dissertation, the "Layer approach" was used, based on the results obtained by Boulet *et al.* (2015). The algorithm is very close to the soil–plant–atmosphere interface of the SiSPAT model (Braud *et al.*, 1995). The full set of equations can be solved either in prescribed conditions (for example, in fully stressed or potential conditions) to compute transpiration and evaporation rates for given stress levels or in retrieval (or inverse) mode, identically to TSEB (Norman *et al.*, 1995).

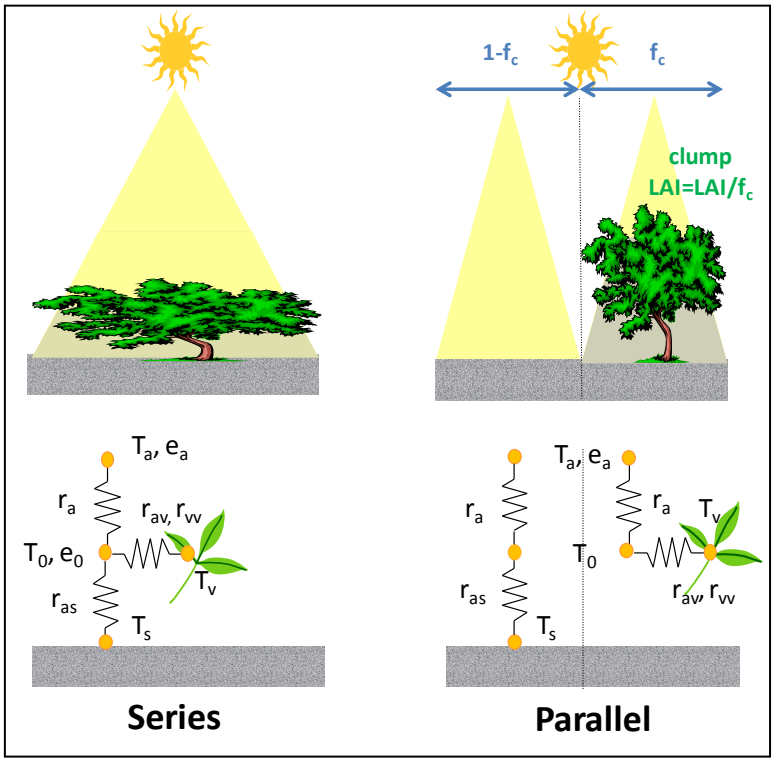

Figure 5. 1: Resistance scheme showing the series and parallel model approaches (Source: Boulet *et al.* (2015))

The SPARSE model computes the equilibrium surface temperatures of the soil (Ts) and the vegetation (Tv) at the meteorological time step as a signature of the energy budget equations of each source. Five main equations are solved simultaneously. The first two express the continuity of the sensible and latent heat fluxes from the soil and the canopy to the aerodynamic level and above, the third and the fourth represent the energy budget of the soil and the vegetation, and the fifth describes the link between the radiative temperature as observed by the satellite and its two component temperature sources (soil Ts and vegetation Tv).

$$\begin{cases} H = H_s + H_v \\ LE = LE_s + LE_v \\ R_{ns} = G + H_s + LE_s \\ R_{nv} = H_v + LE_v \\ \sigma T_{rad}^4 = R_{atm} - R_{an} \end{cases} \quad (5.\ 1)$$

H [W.m^{-2}] is the total sensible heat flux; H_s [W.m^{-2}] and H_v [W.m^{-2}] are the sensible heat flux from the soil and the canopy, respectively; LE [W.m^{-2}] is the total latent heat flux; LE_s [W.m^{-2}] and LE_v [W.m^{-2}] are the latent heat flux from the soil and the canopy, respectively; G [W.m^{-2}] is soil het flux; R_{ns} [W.m^{-2}] and R_{nv} [W.m^{-2}] are net radiation over the soil and the canopy, respectively; T_{rad} is the radiative temperature, σ [W.m^{-2}.K^4] is Stefan-Boltzmann constant, R_{atm} [W.m^{-2}] is the incoming atmospheric radiation and R_{an} [W.m^{-2}] is the net longwave radiation which depends on Ts and Tv.

Radiative temperature is linked to the land surface temperature T_{surf} and the surface emissivity ε_{surf} as follows:

$$\sigma T_{rad}^4 = \varepsilon_{surf}\sigma T_{surf}^4 + (1 - \varepsilon_{surf})R_{atm} \quad (5.\ 2)$$

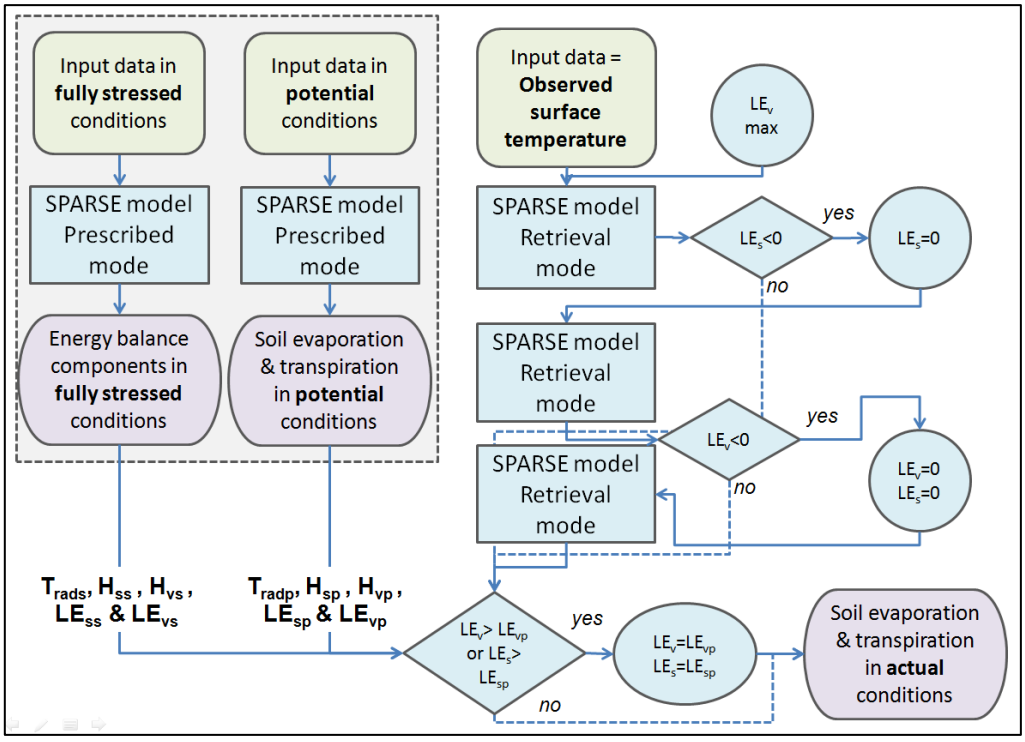

Figure 5. 2: Flowchart of the SPARSE algorithm; Trads, Hss , Hvs LEss and LEvs are radiative surface temperature, soil sensible heat flux , vegetation sensible heat flux, soil latent heat flux and vegetation latent heat flux at stressed conditions, respectively; Tradp, Hsp, Hvp, LEsp and LEvp are radiative surface temperature, soil sensible heat flux , vegetation sensible heat flux, soil latent heat flux and vegetation latent heat flux at potential conditions, respectively (Source: Boulet *et al.* (2015), modified)

The latent heat flux components for the soil (LEs) and the vegetation (LEv) are representative averages for the surface as a whole. The continuity of the latent heat and sensible heat fluxes below and above the aerodynamic level implies that the first two continuity equations (Eq. 5.1) can be written as follows:

$$\begin{cases} H_s = \rho c_p \dfrac{T_s - T_0}{r_{as}}, H_v = \rho c_p \dfrac{T_v - T_0}{r_{av}} \rightarrow H = H_s + H_v = \rho c_p \dfrac{T_0 - T_a}{r_a} \\ LE_s = \dfrac{\rho c_p}{\gamma}\beta_s \dfrac{e_{sat}(T_s) - e_0}{r_{as}}, LE_v = \dfrac{\rho c_p}{\gamma}\beta_v \dfrac{e_{sat}(T_v) - e_0}{r_{vv}} \rightarrow LE = LE_s + LE_v = \dfrac{\rho c_p}{\gamma}\dfrac{e_0 - e_a}{r_a} \end{cases} \quad (5.\ 3)$$

where ϱ.cp [m^{-3}.J. K^{-1}] is the product of air density and specific heat, $\boldsymbol{\gamma}$ [K.Pa.C^{-1}] is the psychrometric constant, T_0 [K] is the aerodynamic temperature, T_a [K] is the air temperature, e_{sat} (Ts) and e_{sat} (Tv) are the saturated vapour pressure at soil temperature Tv [K] and vegetation temperature Tv [K], respectively, e_0 is the partial pressure of vapour at the aerodynamic level, r_{as} [$m.s^{-1}$] is the aerodynamic resistance between the soil and the

aerodynamic level, r_{av} [m.s^{-1}] is the aerodynamic resistance between the canopy and the aerodynamic level, r_a is the aerodynamic resistance between the aerodynamic level and the reference level, r_{as} is the soil to aerodynamic level resistance and r_{vv} is the minimum total resistance for latent heat exchange between the vegetation and the aerodynamic level. Efficiencies βx (x referring to "s" for soil, "v" for vegetation, and left blank for the total evapotranspiration flux) are functionally equivalent to surface resistances. Their range of validity is [0,1]: if βv= 1, then the vegetation transpires at the potential rate, and if βs= 1, the soil evaporation rate is that of a saturated surface, while βv= 0 or βs= 0 corresponds to a non-transpiring or non-evaporating surface, respectively.

In order to reduce the computational cost of solving the system for all unknown variables including Ts and Tv, non-linear expressions in LEs and LEv equations are linearized though Taylor expansion around air temperature (Eqs. 5.3 and 5.4) so that the model can be solved through a simple matrix inversion. This is especially useful when SPARSE is run for a large number of pixels.

$$LE_s \approx \frac{\rho c_p}{\gamma}\beta_s \frac{e_{sat}(T_a) + \Delta(T_s - T_a) - e_0}{r_{as}} \quad (5.\ 4)$$

$$LE_v \approx \frac{\rho c_p}{\gamma}\beta_v \frac{e_{sat}(T_a) + \Delta(T_v - T_a) - e_0}{r_{vv}} \quad (5.\ 5)$$

where $\boldsymbol{\Delta}$ [kPa C^{-1}] is the slope of the saturation vapour curve at air temperature T_a.

The expression of the various resistances according to Shuttleworth and Gurney (1990) are as follows:

$$r_a = \frac{Ln\left(\frac{z-d}{z_{om}}\right)^2}{k^2 u_a (1+Ri)^m} \quad (5.\ 6)$$

$$r_{as} = \frac{z_v e^{n_{SW}} Ln\left(\frac{z-d}{z_{om}}\right)\left(e^{\frac{-n_{SW} z_{om,s}}{z_v}} - e^{\frac{-n_{SW}(d+z_{om})}{z_v}}\right)}{n_{SW} k^2 u_a (z_v - d)} \quad (5.\ 7)$$

$$r_{av} = \left(\frac{w}{u_a}\frac{Ln\left(\frac{z-d}{z_{om}}\right)}{Ln\left(\frac{z_v-d}{z_{om}}\right)}\right)^{0.5} \frac{n_{SW}}{4\alpha_0 LAI(1-e^{-0.5 n_{SW}})} \quad (5.\ 8)$$

$$r_{vv} = r_{av} + \frac{r_{stmin}\prod f}{LAI_g} \quad (5.\ 9)$$

where u_a [m.s^{-1}] is the wind speed measured at height z, z_v [m] is the vegetation height, d [m] is the displacement height, z_{om} the roughness length for momentum exchange, n_{SW}=2.5, w (Fassnacht *et al.*) is the width of the leaves, α_o=0.005, r_{stmin} [m.s^{-1}] is the minimum stomatal resistance and $z_{om,s}$=0.005 m is the roughness length for momentum exchange over bare soil. $\mathrm{Ri} = \frac{5g(z-d)(T_0-T_a)}{T_a u_a^2}$ is the stability correction (Richardson number); m=0.75 in unstable conditions and m=2 in stable conditions. Πf represent the

product of weighting stress functions related to environmental factors affecting the stomatal resistance (temperature, solar radiation, vapour pressure deficit) and are taken from Braud *et al.* (1995). The rule of thumb applies: $z_{om}=0.13*z_v$ and $d=0.66*z_v$.

Net radiation is computed according to the radiative transfer scheme of Merlin and Chehbouni (2004) which takes into account the multiple reflections between the soil and the vegetation layer in the shortwave and longwave domains, hence:

$$R_{ns} = A_{ss} - \rho c_p \frac{T_s - T_a}{r_{radss}} - \rho c_p \frac{T_v - T_a}{r_{radsv}} \, , R_{nv} = A_{vv} - \rho c_p \frac{T_s - T_a}{r_{radvs}} - \rho c_p \frac{T_v - T_a}{r_{radvv}} \quad (5.\ 10)$$

$$\rightarrow R_n = R_{ns} + R_{nv}$$

where A_{ss} [W.m^{-2}] is the forcing term of the soil net radiation for the series model, A_{vv} [W.m^{-2}] is the forcing term of the vegetation net radiation for the series model, r_{radss} [m.s^{-1}] is the soil radiative resistance for the soil net radiation in the series model, r_{radsv} [m.s^{-1}] is the canopy radiative resistance for the soil net radiation in the series model, r_{radvs} [m.s^{-1}] is the soil radiative resistance for the vegetation net radiation in the series model and r_{radvv} [m.s^{-1}] is the canopy radiative resistance for the vegetation net radiation in the series model.

The soil heat flux G is a fraction ξ of the net radiation available for the whole of the soil surface ($G = \xi R_{ns}$). If the model is run at the same time of the day, for instance with surface temperatures acquired with a sun-synchronous satellite, ξ depends mostly on the bare soil fraction cover.

The resulting energy balance for the soil and the canopy for the series model (the third and the fourth equation of the system 5.1) can be written as follows:

$$\begin{cases} (1-\xi)A_{ss} = (1-\xi)\rho c_p \frac{T_s - T_a}{r_{radss}} + (1-\xi)\rho c_p \frac{T_v - T_a}{r_{radsv}} + \rho c_p \frac{T_s - T_0}{r_{as}} + \frac{\rho c_p}{\gamma}\beta_s \frac{e_{sat}(T_a) + \Delta(T_s - T_a) - e_0}{r_{as}} \\ A_{vv} = (1-\xi)\rho c_p \frac{T_s - T_a}{r_{radvs}} + (1-\xi)\rho c_p \frac{T_v - T_a}{r_{radvv}} + \rho c_p \frac{T_v - T_0}{r_{av}} + \frac{\rho c_p}{\gamma}\beta_v \frac{e_{sat}(T_a) + \Delta(T_v - T_a) - e_0}{r_{vv}} \end{cases} \quad (5.\ 2)$$

Finally, the final equation of system 4.1 is linking radiative surface temperature Trad to the net longwave radiation components R_{atm} and R_{an} which depends on Ts and Tv and can be expressed as follows:

$$R_{an} = A_{atm} - \rho c_p \left(\frac{1}{r_{radss}} + \frac{1}{r_{radvs}}\right)(T_s - T_a) - \rho c_p \left(\frac{1}{r_{radvv}} + \frac{1}{r_{radsv}}\right)(T_v - T_a) \quad (5.\ 3)$$

Forcing terms A_{ss}, A_{vv} and A_{atm} as well as radiative resistances of the net radiation model for the series version of SPARSE are detailed in annex 8. Consequently, the fifth equation of system 4.1 is written as:

$$\sigma T_{rad}^4 + A_{atm} - R_{atm} = \rho c_p \left(\frac{1}{r_{radss}} + \frac{1}{r_{radvs}}\right)(T_s - T_a) - \rho c_p \left(\frac{1}{r_{radvv}} + \frac{1}{r_{radsv}}\right)(T_v - T_a) \quad (5.\ 4)$$

Prescribed mode

If the soil and the vegetation efficiencies *i.e* stress levels (named β_s and β_v [0,1]) are known, then the model is run in a forward mode from prescribed water stress conditions (from fully stressed to potential). In that case the system is solved for the following unknowns: Trad, Ts, Tv, e_0 and T_0 (Figure 5.2). T_{rad} in this prescribed mode is then an output of the system computed from Eq. (5.12) after solving the other four equations (Eqs. 5.2 and 5.9) for Ts, Tv, e_0 and T_0. This mode has two direct applications. It can be used independently of the retrieval mode to generate an equilibrium surface temperature at the time of the satellite overpass in order to assimilate surface temperature measurements from known βs and βv values computed at the daily or sub-daily time steps from a hydrological model. It is also implemented as a final step in the retrieval mode to provide theoretical limits corresponding to maximum reachable levels of sensible heat (fully stressed conditions) or latent heat (potential conditions) for each component (the soil and the vegetation). Output fluxes from the retrieval run are bounded by those limiting cases. In full potential conditions, βs= βv= 1, while in fully stressed conditions, βs= βv= 0.

Retrieval mode

In retrieval conditions, Trad is known and is derived from satellite observations or *in situ* measurements in the thermal infra-red domain. In order to compute the various fluxes of the energy balance, the full set of five equations for the series model (Eq. 5.1) must be solved simultaneously by inverting the same matrix corresponding to Eqs. (5.3), (5.11) and (5.13). In that case, contrarily to the prescribed mode, the problem is initially ill-posed since the system includes six unknowns: evaporation LEs and transpiration LEv, surface temperature components Ts and Tv, and aerodynamic level conditions e_0 and T_0.

LEs and LEv values are directly converted into stress levels βs and βv using Eqs. (5.4) and (5.5). In order to downsize the number of unknowns, SPARSE carries out the same rationale as the TSEB model: as a first guess, the vegetation is supposed to transpire at potential rate; therefore, βv is set to 1, and the system is solved for unknown LEs (thus βs), Ts, Tv, e_0 and T_0. If negative LEs is obtained, then the assumption of an unstressed canopy proves to be inconsistent with the observed surface temperature level. In that case, one assumes that the vegetation is suffering from water stress. This means that root zone soil moisture is depleted under critical levels, and that, most probably, the soil surface is already long dry. Therefore, βs is set to 0 and the system is solved for LEv (thus βv) instead of LEs. Finally, if LEv is negative, fully stressed conditions are imposed for both the soil and the vegetation independently of T_{rad}. Finally, in order to ensure that LEs and LEv outputs are within realistic bounds, their values obtained by running SPARSE in "retrieval" conditions are limited by the evapotranspiration components in potential conditions (βs=1, βv=1) computed by SPARSE in prescribed potential conditions (Figure 5.2). Moreover, LEs is set to minimum positive threshold for vegetation stress detection of 30 W.m-2 instead of LEs=0. This threshold accounts for the small but non neglectable vapor flow reaching the surface (Boulet *et al.*, 1997).

5.2 Validation of instantaneous and daily SPARSE model estimates using the XLAS data: Published results (article)

The "layer" version of the energy balance model SPARSE was run to compute distributed energy balance componentsn for three agricultural seasons 2012-2013 , 2013-2014 and 2014-2015. Simulation concerned an area of 10 km ×8 km centered on the XLAS transect. SPARSE instantaneous estimates of H, LE and stress factor at the time of Terra-MODIS and Aqua-MODIS overpasses, after being weighted by the instantaneous XLAS footrpint, were validated using XLAS measured H , XLAS derived LE and observed stress index, respectively. Furthermore, three methods were tested to carry out the extrapolation from instantaneous to daily LE based on the stress index, the evaporative fraction and the residual approach. And then, daily modeled LE, weighted by the daily XLAS footprint, was compared to daily XLAS derived LE. Finally, in order to highlight seasonal variation of ET, monthly modeled ET with the SPARSE model was computed and compared to monthly observed ET (XLAS derived LE) and also to monthly ET modeled by SAMIR model.

Hydrol. Earth Syst. Sci. Discuss., https://doi.org/10.5194/hess-2017-454
Manuscript under review for journal Hydrol. Earth Syst. Sci.
Discussion started: 28 August 2017

Hydrology and Earth System Sciences Discussions

Assessment of actual evapotranspiration over a semi-arid heterogeneous land surface by means of coupled low-resolution remote sensing data with energy balance model: comparison to extra Large Aperture Scintillometer measurements

Sameh Saadi[1,2], Gilles Boulet[1], Malik Bahir[1], Aurore Brut[1], Bernard Mougenot[1], Pascal Fanise[1], Vincent Simonneaux[1], and Zohra Lili Chabaane[2]

[1]Centre d'Etudes Spatiales de la Biosphère, Université de Toulouse, CNRS, CNES, IRD, UPS, Toulouse, France
[2] Université de Carthage / Institut National Agronomique de Tunisie/ LR17AGR01-GREEN-TEAM, Tunis, Tunisie;

Correspondence to: Sameh Saadi (saadi_sameh@hotmail.fr)

Abstract.

In semi-arid areas, agricultural production is restricted by water availability; hence efficient agricultural water management is a major issue. The design of tools providing regional estimates of evapotranspiration (ET), one of the most relevant water balance fluxes, may help the sustainable management of water resources.

Remote sensing provides periodic data about actual vegetation temporal dynamics (through the Normalized Difference Vegetation Index NDVI) and water availability under water stress (through the surface temperature T_{surf}) which are crucial factors controlling ET.

In this study, spatially distributed estimates of ET (or its energy equivalent, the latent heat flux LE) in the Kairouan plain (Central Tunisia) were computed by applying the Soil Plant Atmosphere and Remote Sensing Evapotranspiration (SPARSE) model fed by low resolution remote sensing data (Terra and Aqua MODIS). The work goal was to assess the operational use of the SPARSE model and the accuracy of the modeled i) sensible heat flux (H) and ii) daily ET over a heterogeneous semi-arid landscape with a complex land cover (*i.e.* trees, winter cereals, summer vegetables).

SPARSE was run to compute instantaneous estimates of H and LE fluxes at the satellite overpass time. The good correspondence (R^2= 0.60 and 0.63 and RMSE=57.89 Wm^{-2} and 53.85 Wm^{-2}; for Terra and Aqua, respectively) between instantaneous H estimates and large aperture scintillometer (XLAS) H measurements along a path length of 4 km over the study area showed that the SPARSE model presents satisfactory accuracy. Results showed that, despite the fairly large scatter, the instantaneous LE can be suitably estimated at large scale (RMSE=47.20 Wm^{-2} and 43.20 Wm^{-2}; for Terra and Aqua, respectively and R^2= 0.55 for both satellites). Additionally, water stress was investigated by comparing modeled (SPARSE) and observed (XLAS) water stress values; we found that most points were located within a 0.2 confidence interval, thus the general tendencies are well reproduced. Even though extrapolation of instantaneous latent heat flux values to daily totals was less obvious, daily ET estimates are deemed acceptable.

KEYWORDS: Evapotranspiration, Remote sensing, SPARSE model, scintillometer, water stress.

Hydrol. Earth Syst. Sci. Discuss., https://doi.org/10.5194/hess-2017-454
Manuscript under review for journal Hydrol. Earth Syst. Sci.
Discussion started: 28 August 2017

Hydrology and Earth System Sciences Discussions

1 Introduction

In water scarce regions, especially arid and semi-arid areas, the sustainable use of water by resource conservation as well as the use of appropriate technologies to do so is a priority for agriculture (Amri et al., 2014; Pereira et al., 2002).

Water use rationalization is needed especially for countries actually suffering from water scarcity, or for countries that probably would suffer from water restrictions according to climate change scenarios. Indeed, the Mediterranean region is one of the most prominent "hot spots" in future climate change projections (Giorgi and Lionello, 2008) due to an expected larger warming than the global average and to a pronounced increase in precipitation inter-annual variability. The major part of the southern Mediterranean countries, among others Tunisia, already suffer from water scarcity and show a growing water deficit, due to the combined effect of the water needs growth (soaring demography and irrigated areas extension), and the reduction of resources (temporary drought and/or climate change). This implies that closely monitoring the water budget components is a major issue (Oki and Kanae, 2006).

The estimation of evapotranspiration (ET) is of paramount importance since it represents the preponderant component of the terrestrial water balance; it is the second largest component after precipitation (Glenn et al., 2007); hence ET quantification is a key factor for scarce water resources management. Direct measurement of ET is only possible at local scale (single field) using the eddy covariance method for example; whereas, it is much more difficult at larger scales (irrigated perimeter or watershed) due to the complexity not only of the hydrological processes (Minacapilli et al., 2007) but also of the hydro-meteorological processes. Indeed, at landscape scale, surface heterogeneity influences regional and local climate, inducing for example cloudiness, precipitation and temperature patterns differences between areas of higher elevation (hills and mountains surrounding the Kairouan plain) and the plain downstream. Moreover, at these scales, land cover is usually heterogeneous and this affects the land-atmosphere exchanges of heat, water and other constituents (Giorgi and Avissar, 1997). ET estimates for various temporal and spatial scales, from hourly to monthly to seasonal time steps, and from field to global scales, are required for hydrologic applications in water resource management (Anderson et al., 2011). Techniques using remote sensing (RS) information are therefore essential when dealing with processes that cannot be represented by point measurements only (Su, 2002).

In fact, the contribution of RS in vegetation's physical characteristics monitoring on large areas have been identified for years (Tucker, 1978); RS provides periodic data about some major ET drivers, amongst others, surface temperature and vegetation properties (e.g. Normalized Difference Vegetation Index NDVI and Leaf Area Index LAI) from field to regional scales (Li et al., 2009; Mauser and Schädlich, 1998). Many methods using remotely-sensed data to estimate ET are reviewed in Courault et al. (2005). ICARE (Gentine et al., 2007) and SiSPAT (Braud et al., 1995) are examples of complex physically based Land Surface Models (LSM) using RS data. They include a detailed description of the vegetation water uptake in the root zone, the interactions between groundwater, root zone and surface water. However, the lateral surface and subsurface flows are neglected. This can lead to inaccurate results when applied in areas where such interactions are important (Overgaard et al., 2006).

Hydrol. Earth Syst. Sci. Discuss., https://doi.org/10.5194/hess-2017-454
Manuscript under review for journal Hydrol. Earth Syst. Sci.
Discussion started: 28 August 2017

Moreover, RS can provide estimates of large area fluxes in remote locations, but those estimates are based on the spatial and temporal scales of the measuring systems and thus vary one from another. Hence, one solution is to upscale local micrometeorological measurements to larger spatial scales in order to acquire an optimum representation of land-atmosphere interactions (Samain et al., 2012). However, such up-scaling process is not always possible and results might not be reliable in comparison to the RS distributed products.

Water and energy exchange in the soil-plant-atmosphere continuum have been simulated through several land surface models (Bastiaanssen et al., 2007; Feddes et al., 1978). Among them, two different approaches use remote sensing data to estimate spatially distributed ET (Minacapilli et al., 2009): one is based on the soil water balance (SWB) and one that solves the surface energy budget (SEB). The SWB approach exploits only visible-near-infrared (VIS-NIR) observations to perceive the spatial variability of crop parameters. The SEB modeling approach uses visible (VIS), near infrared (NIR) and thermal (TIR) data to solve the SEB equation by forcing remotely sensed estimates of the SEB components (mainly the surface temperature T_{surf}). In fact, there is a strong link between water availability in the soil and surface temperature under water stress, hence, in order to estimate soil moisture status as well as actual ET at relevant space and timescales, information in the TIR domain (8–14 µm) is frequently used (Boulet et al., 2007). The SWB approach has the advantage of high resolution and frequency VIS-NIR remote sensing data availability against limited availability of high resolution thermal imagery for the SEB approach. Indeed, satellite data such as Landsat or Advanced Spaceborne Thermal Emission and Reflection Radiometer (ASTER) provide field scale (30–100 m) estimates of ET (Allen et al., 2011), but they have a low temporal resolution (16 day-monthly) (Anderson et al., 2011).

The RS-based SWB models provide estimates of ET, soil water content, and irrigation requirements in a continuous way. For instance, at field scale, estimates of seasonal ET and irrigation can be obtained by SWB modeling using high resolution remote sensing forcing as done in the study with the SAtellite Monitoring of IRrigation (SAMIR) model by Saadi et al. (2015) over the Kairouan plain. However, for an appropriate estimation of ET, the SWB model requires knowledge of the water inputs (precipitation and irrigation) and an assessment of the extractable water from the soil (mostly derived from the soil moisture characteristics: actual available water content in the root zone, wilting point and field capacity), whereas, significant biases are found mainly when dealing with large areas and long periods, due to the spatial variability of the water inputs uncertainties as well as the inaccuracy in estimating other flux components such as the deep drainage (Calera et al., 2017). Hence, the major limitation of the SWB method is the high number of needed inputs whose estimation is highly uncertain especially over a heterogeneous land surface due to hydrologic processes complexity. Moreover, spatially distributed SWB models, typically those using the Food and Agriculture Organization-FAO guidelines (Allen et al., 1998) for crop ET estimation, generally parameterize the vegetation characteristics on the basis of land use maps (Bounoua et al., 2015; Xie et al., 2008), and different parameters are used for different land use classes. Nevertheless, SWB modelers generally do not have the possibility to carry out remote sensing-based land use change mapping due to time, budget, or capacity constraints and use often very generic classes potentially leading to modeling errors (Hunink et al., 2017). In addition, the lack of data about the soil properties (controlling field capacity, wilting point and

Hydrol. Earth Syst. Sci. Discuss., https://doi.org/10.5194/hess-2017-454
Manuscript under review for journal Hydrol. Earth Syst. Sci.
Discussion started: 28 August 2017

the water retention) as well as the actual root depths, lead to limited practical use of the SWB models (Calera et al., 2017). The same apply to the soil evaporation whose estimation generally rely on the FAO guidelines approach (Allen et al., 1998). Although, it was shown that under high evaporation conditions, the FAO-56 (Allen et al., 1998) daily evaporation computed on the basis of the readily evaporable water (REW) is overestimated at the beginning of the dry down phase (*i.e.* the period after rain or irrigation where the soil moisture is decreasing due to evapotranspiration and drainage, Mutziger et al., 2005; Torres and Calera, 2010). Hence, to improve its estimation a reduction factor proposed by Torres and Calera (2010) was applied to deal with this problem in several studies (e.g. Odi-Lara et al., 2016; Saadi et al., 2015). Furthermore, SWB models such as SWAP (Kroes, 2017), Cropsyst (Stöckle et al., 2003), AquaCrop (Steduto et al., 2009) and SAMIR (Simonneaux et al., 2009) are able to take irrigation into account, either as an estimated amount provided by the farmer (as an input if available) or a predicted amount through a module triggering irrigation according to, say, critical soil moisture levels (as an output). However, the limited knowledge of the actual irrigation scheduling is a critical limitation for the validation protocol of irrigation requirements estimates by SWB modeling. Therefore, SWB modelers must deal with the lack of information about real irrigation which induces unreliable estimations.

Consequently, ET estimation at regional scale is often achieved using SEB approaches, by combining surface temperature from medium to low resolution (kilometer scale) remote sensing data with vegetation parameters and meteorological variables (Liou and Kar, 2014). Recently, many efforts have been made to feed remotely sensed surface temperature into ET modeling platforms in combination with other critical variables, e.g., NDVI and albedo (Kalma et al., 2008; Kustas and Anderson, 2009). A wide range of satellite-based ET models were developed, and these methods are reviewed in (Liou and Kar, 2014). The majority of SEB-based models are single-source models; their algorithms compute a total latent heat flux as the sum of the evaporation and the transpiration components using a remotely sensed surface temperature. However, separate estimates of evaporation and transpiration makes the dual-source models more useful for agrohydrological applications (water stress detection, irrigation monitoring etc.) (Boulet et al., 2015).

Contrarily to SWB models, most SEB models are run in their most standardized version, using observed remote sensing-based parameters such as albedo in conjunction with a set of input parameters taken from literature or *in situ* data. On the other hand, the SEB model validation with enough data in space and time is difficult to achieve, due to the limited availability of high resolution thermal images (Chirouze et al., 2014). Therefore, it is usually possible to evaluate SEB models results only at similar scale (km) to medium or low resolution images. Indeed, the pixel size of thermal remote sensing images, except for the scarce Landsat7 images (60 m), covers a range of 1000 m (Moderate Sensors Resolution Imaging Spectroradiometer MODIS), to the order of 4000 m (Geostationary Operational Environmental Satellite GEOS). However, direct methods measuring sensible heat fluxes (eddy covariance for example) only provide point measurements with a footprint considerably smaller than a satellite pixel. Therefore, scintillometry techniques have emerged as one of the best tools aiming to quantify averaged fluxes over heterogeneous land surfaces (Brunsell et al., 2011). They provide area-averaged sensible heat flux over areas comparable to those observed by satellites (Hemakumara et al., 2003; Lagouarde et al., 2002). Scintillometry can provide sensible heat using different wavelengths (optical and microwave wavelength ranges),

Hydrol. Earth Syst. Sci. Discuss., https://doi.org/10.5194/hess-2017-454
Manuscript under review for journal Hydrol. Earth Syst. Sci.
Discussion started: 28 August 2017

aperture sizes (15-30 cm) and configurations (long-path and short-path scintillometry) (Meijninger et al., 2002). The upwind area contributing to the flux (*i.e.* the flux footprint) varies as wind direction and atmospheric stability, and must be estimated for the surface measurements in order to compare them to SEB estimates of the flux which are representative of the pixel (Brunsell et al., 2011). Assessing the upwind area contributing to the flux can be done using several footprint models (Schmid, 2002). Although footprint analysis ensures ad hoc spatial intersecting area between ground measurements and satellite-based surface fluxes, the spatial heterogeneity at subpixel scale should be further considered in validating low resolution satellite data (Bai et al., 2015). The LAS technique has been validated over heterogeneous landscapes against eddy covariance measurements (Bai et al., 2009; Chehbouni et al., 2000; Ezzahar et al., 2009) and also against modeled fluxes (Marx et al., 2008; Samain et al., 2012; Watts et al., 2000). Few studies dealt with eXtra Large Aperture Scintillometer (XLAS) data (Kohsiek et al., 2006; Kohsiek et al., 2002; Moene et al., 2006). Historical survey, theoretical background as well as recent works in applied research concerning scintillometry are reviewed in De Bruin and Wang (2017). Since the scintillometer provides large-scale area-average sensible heat flux (H_XLAS), the corresponding latent heat flux (LE_XLAS) can then be computed as the energy balance residual term (LE_XLAS =Rn-G-H_XLAS), hence, the estimation of a representative value for the available energy (AE =Rn-G) is always crucial for the accuracy of the retrieved values of LE_XLAS. This assumption is valid only under the similarity hypothesis of Monin-Obukhov (MOST) (Monin and Obukhov, 1954), *i.e.* surface homogeneity and stationary flows. These hypothesis are verified in our study area where topography is flat, and landscape is heterogeneous only from an agronomic point of view since we find different land uses (cereals, market gardening and fruit trees mainly olive trees with considerable spacing of bare soil); however, this heterogeneity in landscape features at field scale is randomly distributed and there is no drastic change in height and density of the vegetation at the scale of the XLAS transect (*i.e.* little heterogeneity at the km scale, most MODIS pixels have similar NDVI values for instance).

In this study, spatially distributed estimates of surface energy fluxes (sensible heat H and latent heat fluxes LE) over an irrigated area located in the Kairouan plain (Central Tunisia) were obtained by the SEB method, using the Soil Plant Atmosphere and Remote Sensing Evapotraspiration (SPARSE) model (Boulet et al., 2015) fed by 1-km thermal data and 1-km NDVI data from MODIS sensors on Terra and Aqua satellites. The main objective of this paper is to compare the modeled H and LE simulated by the SPARSE model with, respectively, the H measured by the XLAS and the LE reconstructed from the XLAS measurements acquired during two years over a large, heterogeneous area. We explore the consistency between the instantaneous H and LE estimates at the satellite overpass time, the water stress estimates and also ET derived at daily time step from both approaches.

2 Experimental site and datasets

2.1 Study area

The study site is a semi-arid region located in central Tunisia, the Kairouan plain (9°23′−10°17′E, 35°1′−35°55′N, (Figure 1). The landscape is mainly flat, and the vegetation is dominated by agricultural production (cereals, olive groves, fruit trees, market gardening,

Hydrol. Earth Syst. Sci. Discuss., https://doi.org/10.5194/hess-2017-454
Manuscript under review for journal Hydrol. Earth Syst. Sci.
Discussion started: 28 August 2017

Zribi et al., 2011). Water management in the study area is typical of semi-arid regions with an upstream sub-catchment that transfers surface and subsurface flows collected by a dam (the El Haouareb dam), and a downstream plain (Kairouan plain) supporting irrigated agriculture (Figure 1). Agriculture consumes more than 80% of the total amount of water extracted each year from the Kairouan aquifer (Poussin et al., 2008). Most farmers in the plain uses their own wells to extract water for irrigation (Pradeleix et al., 2015), while a few depends on public irrigation schemes based on collective networks of water distribution pipelines all linked to a main borehole. The crop intensification in the last decades, associated to increasing irrigation, has led to growing water demand, and an overexploitation of the groundwater (Leduc et al., 2004).

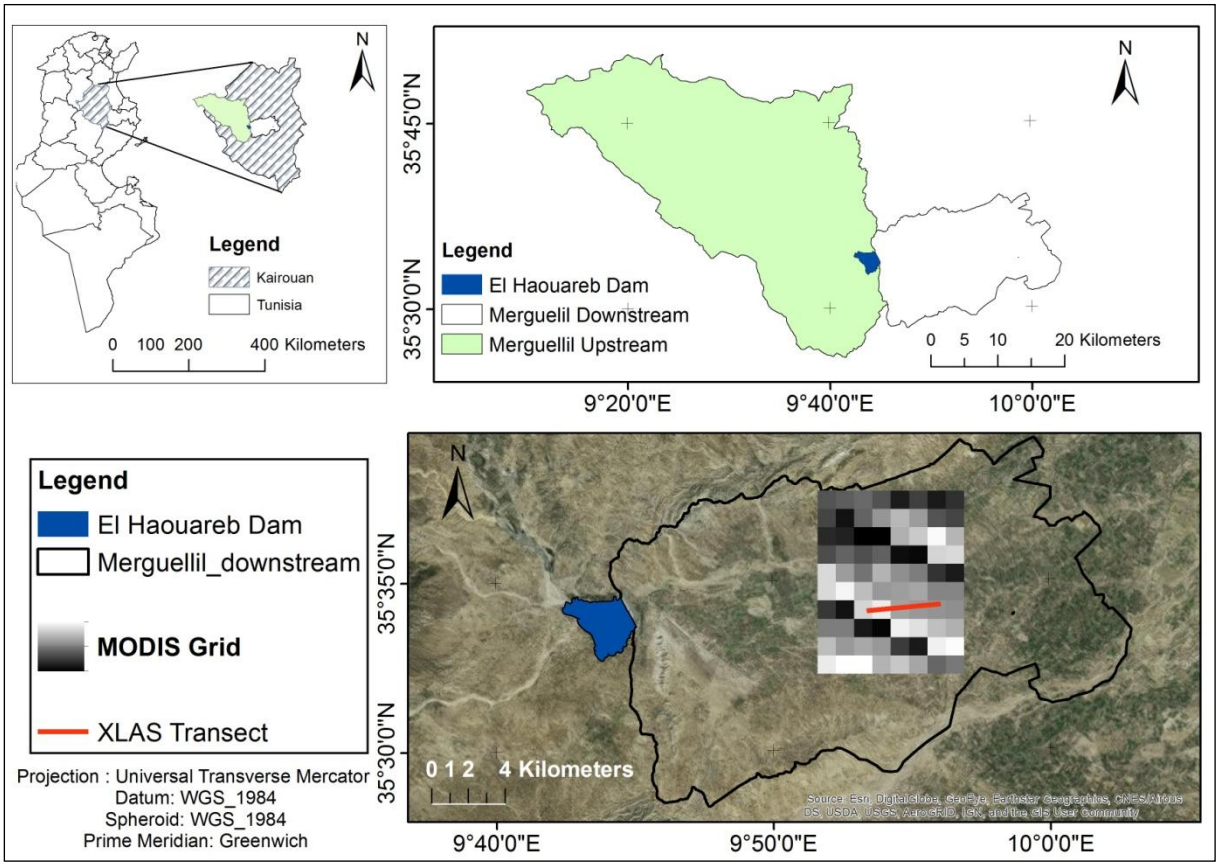

Figure 1: The study area: the downstream Merguellil sub-basin is the so called Kairouan plain; MODIS grid is the extracted 10 km × 8 km MODIS sub-image and in red the scintillomter XLAS transect

2.2 Experimental set-up and remote sensing data

An optical Kipp and Zonen Extra Large Aperture Scintillometer (XLAS) was operated continuously for more than two years (1 March 2013 to 3 June 2015) over a relatively flat terrain (maximum difference in elevation of about 18 m). The scintillometer consists in a transmitter and a receiver both with an aperture diameter of 0.3 m, which allows longer path length. The wavelength of the light beam emitted by the transmitter is 940 nm. The transmitter was located on an eastern water tower (coordinates: 35° 34' 0.7" N; 9° 53' 25.19"

Hydrol. Earth Syst. Sci. Discuss., https://doi.org/10.5194/hess-2017-454
Manuscript under review for journal Hydrol. Earth Syst. Sci.
Discussion started: 28 August 2017

E; 127 m above sea level) and the receiver on a western water tower (coordinates: 35° 34' 17.22" N; 9° 56' 7.30"E; 145 m above sea level) separated by a path length of 4 km (Figure 2).

The scintillometer transect was above mixed vegetation canopy: trees (mainly olive orchards) with some annual crops (cereals and market gardening) and the mean vegetation height is estimated about 1.17m along the transect. Both instruments were installed at 20 m height as recommended in the Kipp & Zonen instruction manual for LAS & XLAS (KIPP&ZONEN, 2007). At this height and for a 4-km path length, the devices are high enough to minimize measurement saturation and assumed to be above or close to the blending height where MOST applied.

Furthermore, two automatic Campbell Scientific (Logan, USA) eddy covariance (EC) flux stations were also positioned at the same level on the two water tower top platforms. Half hourly turbulent fluxes in the western and the eastern EC stations were measured used a sonic anemometer CSAT3 (Campbell Scientific, USA) at a rate of 20 Hz and a sonic anemometer RM 81000 (Young, USA) at a rate of 10 Hz, respectively. The western station data were more reliable with less measurement errors and gaps, hence, the western EC set-up was used to initialise friction velocity u* values and the Obukhov length Lo in the scintillometer flux computation (sect.3.1).

Half hourly standard meteorological measurements including incoming long wave radiation *i.e.* global incoming radiation (Rg_{30}), the incoming longwave radiation *i.e* atmospheric radiation ($R_{atm\text{-}30}$), wind speed (u_{30}), wind direction ($u_{d\text{-}30mn}$), air temperature ($T_{a\text{-}30}$) and relative humidity ($RH_{a\text{-}30}$) and barometric pressure (P_{30}) were recorded using an automated weather station installed in the study area (Figure 2), referred as the Ben Salem meteorological station (35° 33' 1.44" N; 9° 55' 18.11"E). Meteorological data were used either to force the SPARSE model or as input data in XLAS derived sensible and latent heat flux. The global incoming radiation was also used in the extrapolation method to scale instantaneous observed (sect. 3.3.2) and modeled (sect. 4.2) available energy as well as modeled sensible heat flux (sect. 4.2) to daily values.

In addition, an EC flux station, referred as the Ben Salem flux station (few tens of meters away from the meteorological station) was installed from November 2012 to June 2013 in an irrigated wheat field (Figure 2) measuring half hourly convective fluxes exchanged between the surface and the atmosphere ($H_{BS\text{-}30}$ and $LE_{BS\text{-}30}$) combined with measurements of the net radiation $Rn_{BS\text{-}30}$ and the soil heat flux $G_{BS\text{-}30}$. Net radiation and soil heat flux measurements were transferred to the meteorological station from June 2013 till June 2015. Since, there are no Rn and G measurements in the two water towers EC stations, Rn_{BS} and G_{BS} measurements were among the inputs data to derive sensible and latent heat fluxes from the XLAS measurements. In addition, measured available energy ($AE_{BS}=Rn_{BS}—G_{BS}$) and H_{BS} were used to calibrate the extrapolation relationship of the available energy and the sensible heat flux, respectively (sect. 3.3.2 and 4.2).

Remotely sensed data were acquired for the study period (1st September 2012 to 30th June 2015) at the resolution of the MODIS sensor at 1 km, embarked on board of the satellites Terra (overpass time around 10:30 local solar time) and Aqua (overpass time around 13:30 local solar time). Downloaded MODIS products were (*i*) MOD11A1 and MYD11A1 for Terra and Aqua, respectively (surface temperature T_{surf}, surface emissivity ε_{surf} and viewing angle

Hydrol. Earth Syst. Sci. Discuss., https://doi.org/10.5194/hess-2017-454
Manuscript under review for journal Hydrol. Earth Syst. Sci.
Discussion started: 28 August 2017

ϕ), (*ii*) MOD13A2 and MYD13A2 for Terra and Aqua, respectively (NDVI) and (*iii*) MCD43B1, MCD43B2 and MCD43B3 (albedo α). These MODIS data provided in sinusoidal projection were reprojected in UTM using the MODIS Reprojection Tool. Then, sub-images of 10 km × 8 km centered on the XLAS transect (Figure 1) were extracted. The daily MODIS T_{surf} and viewing angle, 8-day MODIS albedo, and 16-day MODIS NDVI contain some missing or unreliable data; hence, days with missing data (35% of all dates) in MODIS pixels regarding the scintillometer footprint (see later footprint computation in sect.3.2) were excluded. Albedo products (MCD43) are available every 8 days; the day of interest is the central date. Both Terra and Aqua data are used in the generation of this product, providing the highest probability for quality input data and designating it as a combined product. Moreover, the 1km/16days NDVI products (MOD13A2/MYD13A2) are available every 16 days and separately for Terra and Aqua. Algorithms generating this product operate on a per-pixel basis and require multiple daily observations to generate a composite NDVI value that will represent the full period (16 days). For both products, data are linearly interpolated over the available dates in order to get daily estimates. For each pixel, the quality index supplied with each product is used to select the best data.

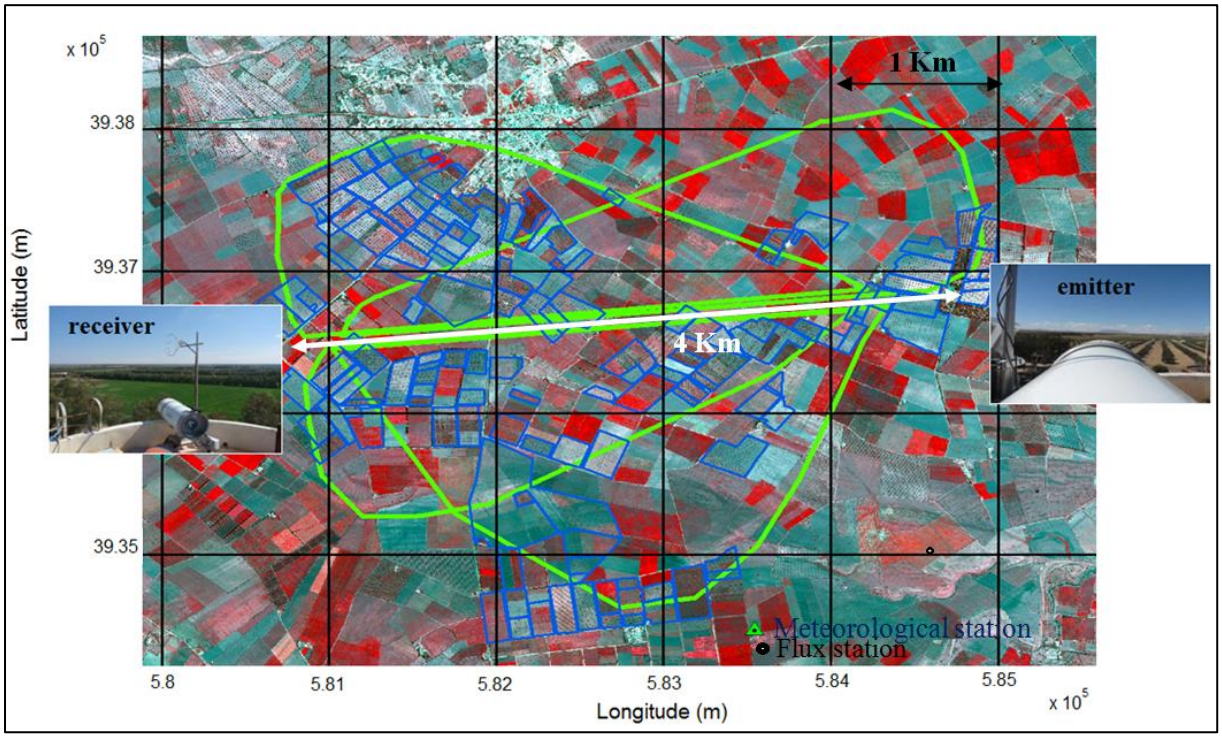

Figure 2: XLAS set-up: XLAS transect (white), for which the emitter and the receiver are located at the extremity of each white arrow, half-hourly XLAS footprint for selected typical wind conditions (green), MODIS grid (black), orchards (blue) and the location of the Ben Salem meteorological and flux stations. Background is a three color (red, green, blue) composite of SPOT5 bands 3 (NIR), 2 (VIS-red) and 1(VIS-green) acquired on 9th April 2013 and showing in red the cereal plots.

Hydrol. Earth Syst. Sci. Discuss., https://doi.org/10.5194/hess-2017-454
Manuscript under review for journal Hydrol. Earth Syst. Sci.
Discussion started: 28 August 2017

Hydrology and Earth System Sciences Discussions

3 Extra Large aperture scintillometer (XLAS): data processing

3.1 Scintillometer derived fluxes

Scintillometer measurements are based on the scintillation theory; fluxes of sensible heat and momentum cause atmospheric turbulence close to the ground, and create, with surface evaporation, refractive index fluctuations due mainly to air temperature and humidity fluctuations (Hill et al., 1980). The fluctuations intensity of refractive index is directly linked to sensible and latent heat fluxes. The light beam emitted by the XLAS transmitter towards the receiver is dispersed by the atmospheric turbulence. The scintillations representing the intensity fluctuations are analyzed at the XLAS receiver and are expressed as the structure parameter of the refractive index of air integrated along the optical path C_{n^2} ($m^{-2/3}$) (Tatarskii, 1961). The sensitivity of the scintillometer to C_{n^2} along the beam is not uniform and follows a bell-shape curve due to the symmetry of the devices. This means that the measured flux is more sensitive to sources located towards the transect centre and is less affected by those close to the transect extremities.

In order to compute the XLAS sensible heat flux, C_n^2 was converted to the structure parameter of temperature turbulence C_T^2 ($K^2m^{-2/3}$) by introducing the Bowen ratio (ratio between sensible and latent heat fluxes), hereafter referred to as β, which is a temperature /humidity correlation factor. Moreover, the height of the scintillometer beam above the surface varies along the path. In our study site, the terrain is very flat leading to little beam height variation across the landscape, except for what is induced by the different roughness of the individual fields. Since the interspaces between trees are large, the effective roughness of the orchards is not significantly different from that of annual crops fields. Consequently, C_n^2 and therefore C_T^2 are not only averaged horizontally but vertically as well.

At visible wavelengths, the refractive index is sensitive to temperature fluctuations. Then, we can relate the C_{n^2} to C_{T^2} as follows:

$$C_{n^2} = \left(\frac{-0.78 \times 10^{-6} \times P}{T^2}\right)^2 C_{T^2} \left(1 + \frac{0.03}{\beta}\right)^2 \quad (1)$$

with T the air temperature (°K) and P the atmospheric pressure (Pa).

Green and Hayashi (1998) proposed another method to compute XLAS sensible heat flux (H_XLAS) assuming full energy budget closure and using an iterative process without the need of β as an input parameter. This method is called the "β-closure method" (BCM, Twine et al., 2000). In the calculation algorithm, β is estimated iteratively with the BCM method, as described in Solignac et al. (2009) with initial guess using Rn_{BS} and G_{BS} from the Ben Salem flux station and initial u_* coming from the western water tower EC station.

Then, the similarity relationship proposed by Andreas (1988) is used to relate the C_{T^2} to the temperature scale T_* in unstable atmospheric conditions as follows:

$$\frac{C_{T^2}\,(z_{LAS} - d)^{\frac{2}{3}}}{T_*^2} = 4.9\left(1 - 6.1\left(\frac{z_{LAS} - d}{L_O}\right)^{-\frac{2}{3}}\right) \quad (2)$$

Hydrol. Earth Syst. Sci. Discuss., https://doi.org/10.5194/hess-2017-454
Manuscript under review for journal Hydrol. Earth Syst. Sci.
Discussion started: 28 August 2017

Hydrology and Earth System Sciences Discussions

And for stable atmospheric conditions:

$$\frac{C_{T^2}\,(z_{LAS}-d)^{\frac{2}{3}}}{T_*^2} = 4.9\left(1+2.2\left(\frac{z_{LAS}-d}{L_O}\right)^{\frac{2}{3}}\right) \quad (3)$$

where L_O (m) the Obukhov length , Z_{LAS} (m) the scintillometer height, and d (m) the displacement height, which corresponds to 2/3 of the averaged vegetation height z_v.

From T_* and the friction velocity u_* (computed based on an iteration approach in the BCM method), the sensible heat flux can be derived as follows:

$$H = -\rho c_p T_* u_* \quad (4)$$

where ρ (kgm^{-3}) the density of air and c_p (Jkg^{-1}K^{-1}) the specific heat of air at constant pressure.

H_XLAS was computed at a half hourly time step. Before flux computation, a strict filtering was applied to the XLAS data to remove outliers depending on weak demod signal. Negative night-time data were set to zero and daytime flux missing data (one to three 30 mn-data) were gap filled using simple interpolation. Furthermore, half hourly H_XLAS aberrant values due to measurement errors and values higher than 400 Wm^{-2}, arising from measurement saturation, were ruled out (3% of the total measurement throughout the experiment duration). Finally, daily H_XLAS was computed as the average of the half hourly H_XLAS.

3.2 XLAS footprint computation

The footprint of a flux measurement defines the spatial context of the measurement and the source area that influences the sensors. In case of inhomogeneous surfaces like patches of various land covers and moisture variability due to irrigation, the measured signal is dependent on the fraction of the surface having the strongest influence on the sensor and thus on the footprint size and location. Footprint models (Horst and Weil, 1992; Leclerc and Thurtell, 1990) have been developed to determine what area is contributing to the heat fluxes as well as the relative weight of each particular cell inside the footprint limits. Contributions of upwind locations to the measured flux depend on the height of the vegetation, height of the instrumentation, wind speed, wind direction, and atmospheric stability conditions (Chávez et al., 2005).

According to the model of (Horst and Weil, 1992), for one-point measurement system, the footprint function *f* relates the spatial distribution of surface fluxes, $F_0(x,y)$ *to* the measured flux at height z_m, $F(x,y,z_m)$, as follows:

$$F(x,y,z_m) = \int_{-\infty}^{\infty}\int_{-\infty}^{x} F_0(x',y')f(x-x',y-y',z_m)dx'dy' \quad (5)$$

Hydrol. Earth Syst. Sci. Discuss., https://doi.org/10.5194/hess-2017-454
Manuscript under review for journal Hydrol. Earth Syst. Sci.
Discussion started: 28 August 2017

Hydrology and Earth System Sciences Discussions

The footprint function *f* is computed as:

$$\bar{f}^{y}(x, z_m) = \frac{d\bar{z}}{dx}\frac{z_m}{\bar{z}^2}\frac{\bar{u}(z_m)}{\bar{u}(c\bar{z})}Ae^{-(z_m/b\bar{z})^r} \quad (6)$$

where $\bar{u}(z)$ the mean wind speed profile and $\bar{z}$ the mean plume height for diffusion from a surface source. The variables *A*, *b* and *c* are scale factors and r a scale factor of the Gamma function. In the case of a scintillometer measurement, the footprint function has to be combined with the spatial weighting function *W(x)* of the scintillometer to account for the sensor integration along its path. Thus, the sensible heat flux footprint mainly depends on the scintillometer effective height z_{LAS} (Hartogensis et al., 2003), which includes the topography below the path and the transmitter and receiver heights, the wind direction and the Obukhov length L_O, which characterizes the atmospheric stability (Solignac et al., 2009). In a subsequent step, daily footprints were computed as a weighted sum of the half hourly footprints by the XLAS sensible heat flux.

In fact, there is an issue with the MODIS pixel heterogeneity and notably the distribution of the land use classes at the intersection between the square pixel and the XLAS footprint (Bai et al., 2015). Hence, in order to provide a first guess on these relative heterogeneities, land use classes within each MODIS pixel of the 10 km × 8 km sub-image were studied based on the land use map of the 2013-2014 season (Chahbi, 2016). The average footprint of all half hourly footprints for the whole study period was computed and overlaid on the MODIS grid in order to identify the MODIS pixels partially or totally covered by footprint (Figure 3).

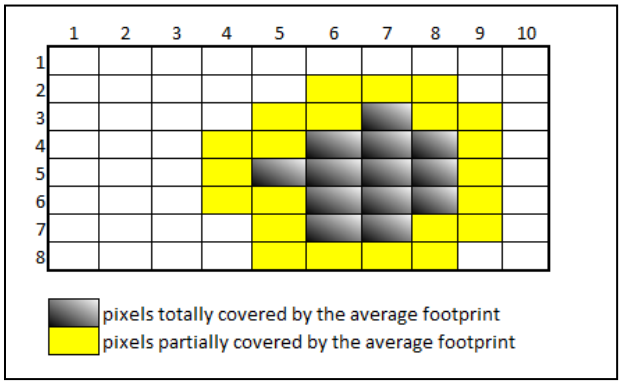

Figure 3: MODIS pixels partially or totally covered by XLAS source area

The percentage of land use classes was computed for i) the part of each pixel that lies within the footprint, and ii) the complementary part of the pixel located outside of the footprint (Figure 4). Results show that difference in percentages of each land use classes for the pixel fractions located within or outside the footprint is low with 1.8%, 1.7%, 1.0% and 3.5% for cereals, market gardening, trees and bare soil, respectively. Moreover, the major part of the area above transect is covered by fallow and orchards. The land use classes' partition inside the 13 MODIS pixels totally covered by the average footprint is comparable.

Hydrol. Earth Syst. Sci. Discuss., https://doi.org/10.5194/hess-2017-454
Manuscript under review for journal Hydrol. Earth Syst. Sci.
Discussion started: 28 August 2017

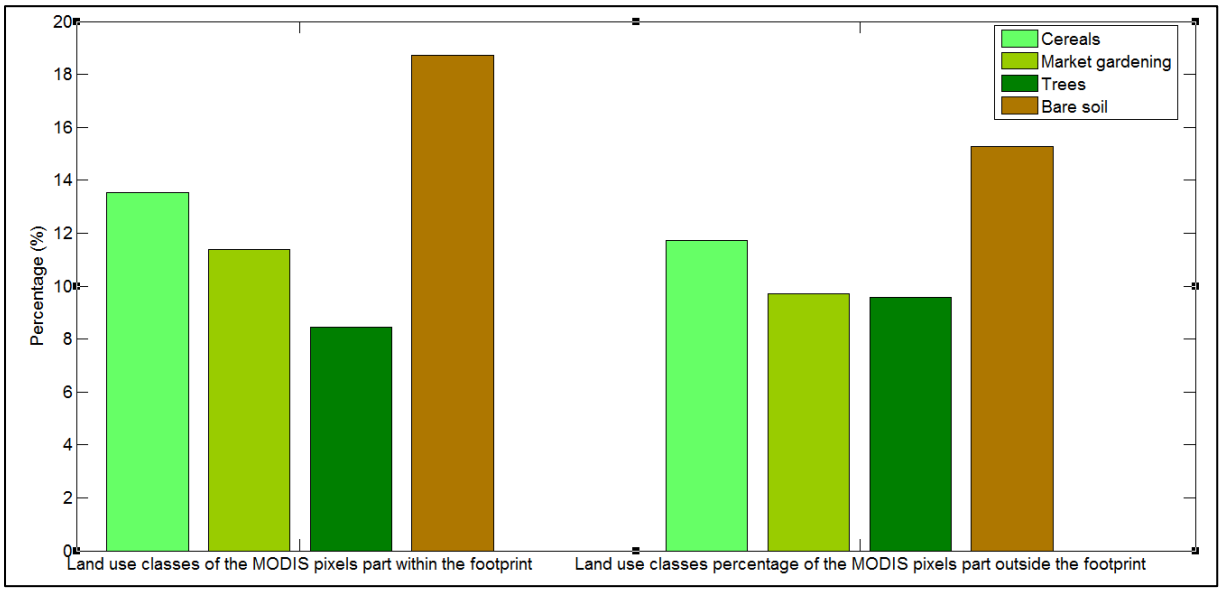

Figure 4: Land use classes' percentage of the MODIS pixels within or outside the footprint

3.3 XLAS derived latent heat flux

Instantaneous (LE_residual_XLAS$_{t\text{-}FP}$) and daily (LE_residual_XLAS$_{day\text{-}FP}$) XLAS derived latent heat flux (*i.e.* residual latent heat flux) of the XLAS upwind area were computed using the energy budget closure of the XLAS measured sensible heat flux (H_XLAS) with additional estimations of remotely sensed net surface radiation Rn and soil heat flux G, as available energy (AE=Rn-G), as follows:

$$\mathrm{LE\_residual\_XLAS_{t-FP}} = \mathrm{AE_{t-FP}} - H\_XLAS_t \quad (7)$$

$$\mathrm{LE\_residual\_XLAS_{day-FP}} = \mathrm{AE_{day-FP}} - \mathrm{H\_XLAS_{day}} \quad (8)$$

H_XLAS$_t$ and H_XLAS$_{day}$ are respectively the instantaneous and daily measured H at the time of the satellite overpass interpolated from the half hourly fluxes measurements. Daily available energy within the footprint (AE$_{day\text{-}FP}$) was computed from instantaneous available energy (AE$_{t\text{-}FP}$) as detailed in Sect. 3.3.1 and Sect. 3.3.2. The subscripts "30", "day" and "t" refer to half hourly, daily and instantaneous (at the time of Terra and Aqua overpasses) variables, respectively; while the subscript "FP" means that the footprint is taken into account *i.e.* instantaneous or the daily (depending on time scale) footprint was multiplied by the variable.

3.3.1 Instantaneous available energy

Net surface radiation is the balance of energy between incoming and outgoing shortwave and longwave radiation fluxes at the land-atmosphere interface. Remotely sensed surface radiative budget components provide unparalleled spatial and temporal information, thus several studies have attempted to estimate net radiation by combining remote sensing observations with surface and atmospheric data. Net radiation equation can be written as follows:

Hydrol. Earth Syst. Sci. Discuss., https://doi.org/10.5194/hess-2017-454
Manuscript under review for journal Hydrol. Earth Syst. Sci.
Discussion started: 28 August 2017

Hydrology and Earth System Sciences Discussions

$$\mathrm{Rn} = (1-\alpha)Rg + \varepsilon_{surf}R_{atm} - \varepsilon_{surf}\sigma T_{surf}^4 \quad (9)$$

where Rg the incoming shortwave radiation (W.m^{-2}), R_{atm} the incoming longwave radiation (W.m^{-2}), α the albedo, ε_{surf} the surface emissivity, T_{surf} the surface temperature (°K) and σ Stefan-Boltzmann constant (W.m^{-2}.K^4) .The soil heat flux G depends on the soil type and water content as well as the vegetation type (Allen et al., 2005).The direct estimation of G by remote sensing data is not possible (Allen et al., 2011), however, empirical relations can estimate the fraction ξ=G/Rn as a function of soil and vegetation characteristics using satellite image data, such as the LAI, NDVI, α and T_{surf}. Generally, G represents 5-20% of Rn during daylight hours (Kalma et al., 2008). In order to estimate the G/Rn ratio, several methods have been tested for various types of surfaces at different locations. The most common methods parameterize ξ as a constant for the entire day or at satellite overpass time (Ventura et al., 1999), according to NDVI (Jackson et al., 1987; Kustas and Daughtry, 1990), LAI (Choudhury et al., 1987; Kustas et al., 1993; Tasumi et al., 2005), vegetation fraction (fc) (Su, 2002), T_{surf} and α (Bastiaanssen, 1995), or only T_{surf} (Santanello Jr and Friedl, 2003). These empirical methods are suitable for specific conditions; therefore, estimating G, especially in this type of environment where NDVI values are low and thus G/Rn values are large, is a critical issue. The approach adopted here was drawn on Danelichen et al. (2014) who evaluated the parameterization of these different models in three sites in Mato Grosso state in Brazil and found that the model proposed by (Bastiaanssen, 1995) showed the best performance for all sites, followed by the model from Choudhury et al. (1987) and Jackson et al. (1987):

Bastiaanssen (1995):

$$\mathrm{G} = \mathrm{Rn}(T_{\mathrm{surf}} - 273.16)(0.0038 + 0.0074\alpha)(1 - 0.98\mathrm{NDVI}^4) \quad (10)$$

Choudhury et al. (1987):

$$G = 0.4Rn(\exp(-0.5LAI)) \quad (11)$$

Jackson et al. (1987)

$$G = 0.583Rn(\exp(-2.13NDVI)) \quad (2)$$

Hence, these three methods were tested for the Ben Salem flux station measurements, by comparing the measured $G_{BS\text{-}t}$ and the computed G using measured $Rn_{BS\text{-}t}$, $T_{surf\text{-}BS\text{-}t}$, α_{BS}, $NDVI_{BS}$ and LAI_{BS} at Terra and Aqua overpass time (results not shown). The best results are issued from Bastiaanssen (1995) method with a Root Mean Square Error (RMSE) of 0.09 (average value of the two satellites overpass time) followed by Jackson et al. (1987) and Choudhury et al. (1987) with RMSE values of 0.15 and 0.2, respectively. Moreover, daily measured $G_{BS\text{-}day}$ was computed and a G accumulation is generally found as it has been already mentioned by (Clothier et al., 1986) who showed that G is neither constant nor negligible on diurnal timescales, and can constitute as much as 50% of Rn over sparsely vegetated area. Since G estimation was the most uncertain variable, the three above methods were tested to compute the distributed remotely sensed AE. The Ben Salem meteorological

Hydrol. Earth Syst. Sci. Discuss., https://doi.org/10.5194/hess-2017-454
Manuscript under review for journal Hydrol. Earth Syst. Sci.
Discussion started: 28 August 2017

Hydrology and Earth System Sciences Discussions

station was used to provide Rg_t and $R_{atm\text{-}t}$. Remote sensing variables α, T_{surf}, ε_{surf} and NDVI came from MODIS products. Remotely sensed LAI was computed from the MODIS NDVI using a single equation (Clevers, 1989) for all crops in the study area:

$$LAI = -\frac{1}{k} ln\left(\frac{NDVI_\infty - NDVI}{NDVI_\infty - NDVI_{soil}}\right) \quad (13)$$

The calibration of this relationship was done over the Yaqui irrigated perimeter (Mexico) during the 2007-2008 growing season using hemispherical LAI measured in all the studied fields (Chirouze et al., 2014). Calibration results gave the asymptotical values of NDVI, $NDVI_\infty$ = 0.97 and $NDVI_{soil}$ = 0.05, as well as the extinction factor k=1.13. As this relationship was calibrated over a heterogeneous land surface but on herbaceous vegetation only, its relevance for trees was checked. For that purpose, clump-LAI measurements on an olive tree, as well as allometric measurements *i.e.* mean distance between trees and mean crown size done using Pleiades satellite data (Mougenot et al., 2014;Touhami, 2013) were obtained. Clump LAI is the value of the LAI of an isolated element of vegetation (tree, shrub...); if this element occupies a fraction cover f and is surrounded by bare soil, then the clump LAI value is equal to the area average LAI divided by f. Hence, we checked that the pixels with tree dominant cover show LAI values close to what was expected (of the order of 0.3 to 0.4 given the interrow distance of 12 m on average).

Remote sensed available energy was computed for the 10 km × 8 km MODIS sub-images at Terra-MODIS and Aqua-MODIS overpass time, using the three methods estimating G. Since the measured heat fluxes H_XLAS_t represent only the weighted contribution of the fluxes from the upwind area to the tower (footprint), then instantaneous footprint at the time of Terra and Aqua overpass were selected among the two half hour preceding and following the satellite's time of overpass (lowest time interval) and then was multiplied by the instantaneous remote sensed available energy AE_t to get the available energy of the upwind area $AE_{t\text{-}FP}$.

3.3.2 Daily available energy

Most methods using TIR domain data rely on once-a-day acquisitions, late morning (such as Terra-MODIS overpass time) or early afternoon (such as Aqua-MODIS overpass time). Thus, they provide a single instantaneous estimate of energy budget components. In order to obtain daily AE from these instantaneous measurements and to reconstruct hourly variations of AE, we considered that its evolution was proportional to another variable whose diurnal evolution can be easily known.

The extrapolation from an instantaneous flux estimate to a daytime flux assumes that the surface energy budget is "self-preserving" *i.e.* the relative partitioning among components of the budget remains constant throughout the day. However, many studies (Brutsaert and Sugita, 1992; Gurney and Hsu, 1990; Sugita and Brutsaert, 1990) showed that the self-preservation method gives day-time latent heat estimates that are smaller than observed values by 5-10%. Moreover, (Anderson et al., 1997) found that the evaporative fraction computed from instantaneous measured fluxes tends to underestimate the daytime average by about 10%, hence, a corrected parameterization was used and a coefficient=1.1 was applied. Similarly, Delogu et al. (2012) found an overestimation of about 10% between estimated and

Hydrol. Earth Syst. Sci. Discuss., https://doi.org/10.5194/hess-2017-454
Manuscript under review for journal Hydrol. Earth Syst. Sci.
Discussion started: 28 August 2017

Hydrology and Earth System Sciences Discussions

measured daily component of the available energy thus, a coefficient =0.9 was applied. The corrected parameterization proposed by Delogu et al. (2012) was tested, but this coefficient did not give consistent results, therefore, the extrapolation relationship was calibrated in order to get accurate daily results of AE .

Thereby, the applied extrapolation method was tested using *in situ* Ben Salem flux station measurements. The incoming short wavelengths radiation was used to scale available energy from instantaneous to daily values; but only for clear sky days for which MODIS images can be acquired and remote sensing data used to compute AE are available. Clear sky days were selected based on the ratio of daily measured incoming short wavelengths radiation Rg_{day} to the theoretical clear sky radiation Rso as proposed by the FAO-56 method (Allen et al., 1998). A day was defined as clear if the measured Rg_{day} is higher than 85 % of the theoretical clear sky radiation at the satellite overpass time (Delogu et al., 2012).

Daily measured available energy $AE_{BS\text{-}day}$ computed as the average of half-hourly measured $AE_{BS\text{-}30}$, was compared to daily available energy ($AE_{BS\text{-}day\text{-}Terra}$ and $AE_{BS\text{-}day\text{-}Aqua}$) computed using the extrapolation method from instantaneous measured $AE_{BS\text{-}t\text{-}Terra}$ and $AE_{BS\text{-}t\text{-}Aqua}$ at Terra and Aqua overpass time, respectively (Equation 14).

$$AE_{BS-day-Terra} = a_{Terra} Rg_{day} \frac{AE_{BS-t-Terra}}{Rg_{t-Terra}} + b_{Terra}$$
$$AE_{BS-day-Aqua} = a_{Aqua} Rg_{day} \frac{AE_{BS-t-Aqua}}{Rg_{t-Aqua}} + b_{Aqua} \quad (1\,4)$$

where Rg_{day} is the daily measured incoming short wavelengths radiation in the Ben Salem meteorological station; $Rg_{t\text{-}Terra}$ and $Rg_{t\text{-}Aqua}$ are the instantaneous incoming short wavelengths radiations measured at Terra and Aqua overpass time, respectively and $AE_{BS\text{-}t\text{-}Terra}$ and $AE_{BS\text{-}t\text{-}Aqua}$ are the instantaneous measured available energy in the Ben Salem flux station, at Terra and Aqua overpass time.

Results gave an overestimation of about 15 %. The corrected parameterizations of AE (Table 1), needed to remove the bias between measured ($AE_{BS\text{-}day}$) and computed AE ($AE_{BS\text{-}day\text{-}Terra}$ and $AE_{BS\text{-}day\text{-}Aqua}$), were applied to compute daily remotely sensed AE (AE_{day}) from instantaneous AE (AE_t) following the extrapolation method shown in equation 14.

Table 1: Corrected parameterizations of available energy for the diurnal reconstitution

Terra	a_{Terra}	0.85
	b_{Terra}	-19.81
Aqua	a_{Aqua}	0.87
	b_{Aqua}	-18.94

Then AE_{day} was multiplied by the weighting coefficients ranging from zero and one of the corresponding daily footprint to get the daily available energy of the upwind area $AE_{day\text{-}FP}$. Finally, estimates of Terra and Aqua observed daily LE ($LE\_residual\_XLAS_{day\text{-}FP}$) were obtained based on the three methods used to compute G.

Hydrol. Earth Syst. Sci. Discuss., https://doi.org/10.5194/hess-2017-454
Manuscript under review for journal Hydrol. Earth Syst. Sci.
Discussion started: 28 August 2017

Hydrology and Earth System Sciences Discussions

4 SPARSE model

4.1 Energy fluxes derived from SPARSE model

The SPARSE dual-source model solves the energy budgets of the soil and the vegetation. Here we use the "layer approach", for which the resistance network relating the soil and vegetation heat sources to a main reference level through a common aerodynamic level use a series electrical branching. Main unknowns are the component temperatures, *i.e.* soil (T_s) and vegetation (T_v) temperatures. Totals at the reference height (the measurement height of the meteorological forcing), as well as the longwave radiation budget, are also solved so that altogether a system of five equations can be built:

$$\begin{cases} H = H_s + H_v \\ LE = LE_s + LE_v \\ R_{ns} = G + H_s + LE_s \\ R_{nv} = H_v + LE_v \\ \varepsilon_{surf}\sigma T_{surf}^4 = \varepsilon_{surf} R_{atm} - R_{an} \end{cases} \quad (15)$$

where R_{atm} the atmospheric radiation (Wm^{-2}), R_{an} net longwave radiation which depends on Ts and Tv (Wm^{-2}), T_{surf} and ε_{surf} are respectively the surface temperature (°K) and emissivity as observed by the satellite; indexes "s" and "v" designate the soil and the vegetation, respectively.

The first two (Eq. (15)) express the continuity of the latent and sensible heat fluxes from the sources to the aerodynamic level through to the reference level, the third and the fourth (Eq. (15)) are the soil and vegetation energy budgets, and the fifth (Eq. (15)) relates the surface temperature T_{surf} to T_s and T_v.

The SPARSE model system of equations is fully described in Boulet et al. (2015). SPARSE is similar to the TSEB model (Kustas and Norman, 1999) but includes the expressions of the aerodynamic resistances of Choudhury and Monteith (1988) and Shuttleworth and Gurney (1990). This system can be solved in a forward mode for which the surface temperature is an output (prescribed conditions), and an inverse mode when the surface temperature is an input derived from satellite observations or *in situ* measurements in the thermal infra-red domain (retrieval conditions). Figure 5 illustrates a diagram showing the flowchart of the model algorithm. System (15) is solved step-by-step by following similar guidelines as in the TSEB model: the first step assumes that the vegetation transpiration (LE_v) is maximum, and evaporation (LE_s) is computed. If this soil latent heat flux (LE_s) is below a minimum positive threshold for vegetation stress detection of 30 Wm^{-2}, the hypothesis that the vegetation is unstressed is no longer valid. In that case, the vegetation is assumed to suffer from water stress and the soil surface is assumed to be already long dry. Then, LE_s is set to 30 Wm^{-2}. This value accounts for the small but non negligible vapor flow reaching the surface (Boulet et al., 1997). The system is then solved for vegetation latent heat flux (LE_v). If LE_v is also negative, both LE_s and LE_v values are set to zero, whatever the value of T_{surf}. The system of equation can also be solved for T_s and T_v only if the efficiencies representing stress levels (dependent on surface soil moisture for the evaporation, and root zone soil moisture for the transpiration) are known. In that case the sole first four equations are solved. This prescribed mode allows computing all the fluxes in known limiting soil moisture levels (very dry, e.g.

Hydrol. Earth Syst. Sci. Discuss., https://doi.org/10.5194/hess-2017-454
Manuscript under review for journal Hydrol. Earth Syst. Sci.
Discussion started: 28 August 2017

fully stressed, and wet enough, e.g. potential). It limits unrealistically high values of component fluxes, latent heat flux values above the potential rates or sensible heat flux values above that of a non-evaporating surface. The potential evaporation and transpiration rates used later on are computed using this prescribed mode with minimum surface resistance to evaporation and transpiration, respectively.

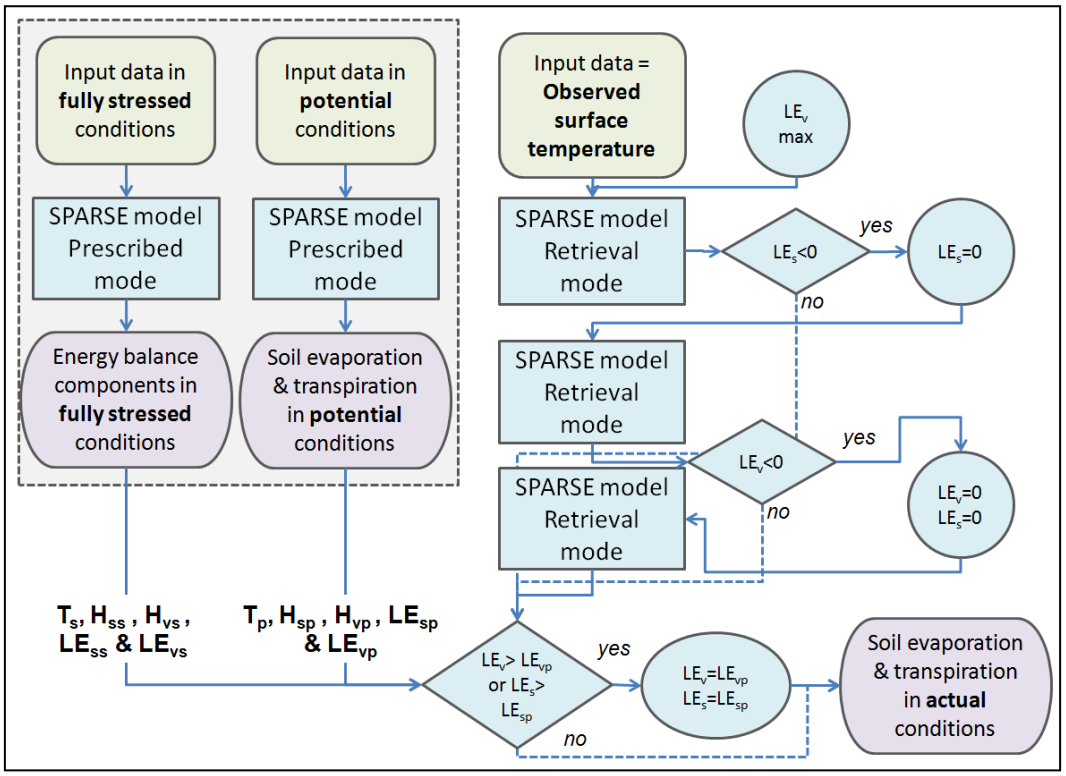

Figure 5: Flowchart of the SPARSE algorithm; T_s, H_{ss} , H_{vs} LE_{ss} and LE_{vs} are surface temperature, soil sensible heat flux, vegetation sensible heat flux, soil latent heat flux and vegetation latent heat flux in fully stressed conditions, respectively; T_p, H_{sp}, H_{vp}, LE_{sp} and LE_{vp} are surface temperature, soil sensible heat flux , vegetation sensible heat flux, soil latent heat flux and vegetation latent heat flux in potential conditions, respectively.

Some of the model parameters were remotely sensed data while others were taken from the bibliography or measured *in situ*. Remotely sensed data fed into SPARSE are T_{surf}, ε_{surf}, ϕ, NDVI, LAI and α. A grid of the vegetation height (z_v) was also necessary as input in the SPARSE model; for herbaceous crops, vegetation height was interpolated with the help of NDVI time series between fixed minimum (0.05 m) and maximum (0.8 m) values, while for trees, the roughness length (z_{om}) was linked to the allometric measurements (mentioned before) and computed as a function of canopy area index, drag coefficient and canopy height using the drag partition approach proposed by Raupach (1994) for tall sparse vegetative environments. Then, since SPARSE deals with vegetation height and not roughness length, the same simple rule of the thumb as the one used in SPARSE was used to reconstruct z_v for the tree cover types ($z_v=z_{om}/0.13$). In a final step, to get spatial vegetation height, z_v was averaged over the MODIS pixels. *In situ* parameters used in SPARSE were mainly meteorological data: Rg, R_{atm}, Ta, Ha and u. No calibration was performed on the model parameters shown in Table 2.

Hydrol. Earth Syst. Sci. Discuss., https://doi.org/10.5194/hess-2017-454
Manuscript under review for journal Hydrol. Earth Syst. Sci.
Discussion started: 28 August 2017

Table 2. SPARSE parameters

	Definition	Value	Data Sources
Remote sensing parameters			
NDVI	Normalized Difference Vegetation Index		Satellite imagery
T_{surf} (K)	Surface temperature (K)		Satellite imagery
α	Albedo		Satellite imagery
ε_{surf}	Surface emissivity		Satellite imagery
Φ (rad)	View zenith angle		Satellite imagery
Meteorological parameters			
R_g (Wm^{-2})	Incoming solar radiation		*In situ* data
R_{atm} (Wm^{-2})	Incoming atmospheric radiation		*In situ* data
T_a (K)	Air temperature at reference level		*In situ* data
RH_a (%)	Air relative humidity		*In situ* data
u_a (ms^{-1})	Horizontal wind speed at reference level		*In situ* data
Fixed parameters			
z_a (m)	Atmospheric forcing height	2.32	*In situ* data
z_v (m)	Vegetation height		Derived from land cover
β_{pot}	Evapotranspiration efficiency in full potential conditions	1.000	
β_{stress}	Evapotranspiration efficiency in fully stressed conditions	0.001	
r_{stmin} (sm^{-1})	Minimum stomatal resistance	100	(Boulet et al., 2015)
w (m)	Leaf width	0.05	(Braud et al., 1995)
ε_v	Vegetation emissivity	0.98	(Braud et al., 1995)
α_v	Vegetation albedo	0.25	Estimation
Constants			
ρ_{cp} ($J.kg^{-1}.K^{-1}$)	Product of air density and specific heat	1170	(Braud et al., 1995)
σ ($W.m^{-2}.k^4$)	Stefan–Boltzmann constant	$5.66.10^{-8}$	(Braud et al., 1995)
γ ($Pa.K^{-1}$)	Psychrometric constant	0.66	(Braud et al., 1995)
$z_{om,s}$(m)	Equivalent roughness length of the underlying bare soil in the absence of vegetation	5.10^{-3}	(Braud et al., 1995)
n_{SW}	Coefficient in r_{av} (Aerodynamic resistance between the vegetation and the aerodynamic level)	2.5	(Boulet et al., 2015)
ξ	Ratio between soil heat flux G and available net radiation on the bare soil Rn_s	0.4	(Braud et al., 1995)

Hydrol. Earth Syst. Sci. Discuss., https://doi.org/10.5194/hess-2017-454
Manuscript under review for journal Hydrol. Earth Syst. Sci.
Discussion started: 28 August 2017

Hydrology and Earth System Sciences Discussions

The retrieval and prescribed modes of the SPARSE model were run for the 10 km × 8 km sub-images at the time of Terra and Aqua overpasses, to get instantaneous modeled fluxes H_SPARSE_t, LE_SPARSE_t and AE_SPARSE_t as well as sensible heat flux ($H_{s\text{-}t} = H_{ss\text{-}t} + H_{vs\text{-}t}$) in fully stressed conditions and latent heat ($LE_{p\text{-}t} = LE_{sp\text{-}t} + LE_{vp\text{-}t}$) and sensible heat ($H_{p\text{-}t} = H_{sp\text{-}t} + H_{vp\text{-}t}$) fluxes in potential conditions. Modeled values were then multiplied by the nearest half hourly footprint to the satellite overpass time, in order to get fluxes corresponding to the upwind area: $H\_SPARSE_{t\text{-}FP}$, $LE\_SPARSE_{t\text{-}FP}$, $AE\_SPARSE_{t\text{-}FP}$, $H_{s\text{-}t\text{-}FP}$, $H_{p\text{-}t\text{-}FP}$ and $LE_{p\text{-}t\text{-}FP}$.

In a subsequent step, the prescribed mode of SPARSE model at potential conditions was run at a half hourly time step using the half hourly meteorological measurements to get half hourly latent heat flux at potential conditions $LE_{p\text{-}30}$. This potential LE weighted by the corresponding half hourly footprint ($LE_{p\text{-}30\text{-}FP}$) is used later when computing daily LE based on the stress factor method (section 4.2).

4.2 Reconstruction of daily modeled ET from instantaneous latent heat flux

Daily ET is usually required for applications in hydrology or agronomy for instance, whereas most SEB methods provide a single instantaneous latent heat flux because the energy budget is only computed at the satellite overpass time (Delogu et al., 2012). In order to scale daily ET from one instantaneous estimate, there are various methods relying on the preservation, during the day, of the ratio of the latent heat flux to a scale factor having known diurnal evolution. Either the stress factor SF (Eq. (16)) or the evaporative fraction EF (Eq. (17)) are assumed invariant during the same day, the diurnal modeled fluxes are accounted for by recovering the diurnal course of either potential ET or available energy.

$$SF = 1 - \frac{LE\_SPARSE_{t-FP}}{LE_{p-t-FP}} \tag{16}$$

$$EF = \frac{LE\_SPARSE_{t-FP}}{AE\_SPARSE_{Ft-P}} \tag{17}$$

- ***Stress Factor (SF) method***

Assuming that the stress factor is constant during the day, the daily modeled ET ($LE\_SPARSE_{day\text{-}FP}$) can be expressed as the product of the instantaneous estimate of SF at the satellite overpass time and the daily potential evapotranspiration :

$$LE\_SPARSE_{day-FP} = (1 - SF) LE_{p-day-FP} \tag{18}$$

$LE_{p\text{-}day\text{-}FP}$ was calculated as the sum of the half hourly modeled latent heat fluxes at potential conditions $LE_{p\text{-}30\text{-}FP}$.

- ***Evaporative Fraction method***

The daily modeled ET ($LE\_SPARSE_{day\text{-}FP}$) can be expressed as the product of the instantaneous estimate of EF at the satellite overpass time and the daily modeled available energy:

Hydrol. Earth Syst. Sci. Discuss., https://doi.org/10.5194/hess-2017-454
Manuscript under review for journal Hydrol. Earth Syst. Sci.
Discussion started: 28 August 2017

Hydrology and Earth System Sciences Discussions

$$LE\_\mathrm{SPARSE}_{day-FP} = EF \times \mathrm{AE\_SPARSE}_{day-FP} \quad (19)$$

$\mathrm{AE\_SPARSE}_{day}$ was computed from instantaneous modeled available energy ($\mathrm{AE\_SPARSE}_t$) using the same approach detailed in Sect. 3.3.2 and applying equation (14). $\mathrm{AE\_SPARSE}_{day}$ was weighted by the corresponding daily footprint to get the daily modeled AE of the upwind area $\mathrm{AE\_SPARSE}_{day\text{-}FP}$.

- ***Residual method***

Besides, daily modeled ET ($\mathrm{LE\_SPARSE}_{day\text{-}FP}$) was also estimated as a residual term of the surface energy budget using daily modeled sensible heat flux ($\mathrm{H\_SPARSE}_{day\text{-}FP}$) and available energy ($\mathrm{AE\_SPARSE}_{day\text{-}FP}$) as follows:

$$\mathrm{LE\_SPARSE}_{\mathrm{day-FP}} = \mathrm{AE\_SPARSE}_{\mathrm{day-FP}} - \mathrm{H\_SPARSE}_{\mathrm{day-FP}} \quad (20)$$

$\mathrm{H\_SPARSE}_{day}$ was computed from modeled sensible heat flux ($\mathrm{H\_SPARSE}_t$) following the same extrapolation method used for the available energy (see Sect. 3.3.2). The corrected parameterizations of H were got from the comparison of daily measured sensible heat flux $H_{BS\text{-}day}$ computed as the average of half-hourly measured $H_{BS\text{-}30}$ and daily sensible heat flux ($H_{BS\text{-}day\text{-}Terra}$ and $H_{BS\text{-}day\text{-}Aqua}$) computed using the extrapolation method from instantaneous measured $H_{BS\text{-}t\text{-}Terra}$ and $H_{BS\text{-}t\text{-}Aqua}$ at Terra and Aqua overpass time, respectively (Equation 21).

$$\begin{aligned} H_{BS-day-Terra} &= \mathrm{a'_{Terra}}\mathrm{Rg_{day}}\frac{\mathrm{H_{BS-t-Terra}}}{\mathrm{Rg_{t-Terra}}} + \mathrm{b'_{Terra}} \\ H_{BS-day-Aqua} &= \mathrm{a'_{Aqua}}\mathrm{Rg_{day}}\frac{\mathrm{H_{BS-t-Aqua}}}{\mathrm{Rg_{t-Aqua}}} + \mathrm{b'_{Aqua}} \end{aligned} \quad (21)$$

where $H_{BS\text{-}t\text{-}Terra}$ and $H_{BS\text{-}t\text{-}Aqua}$ are the instantaneous measured sensible heat flux in the Ben Salem flux station.

Therefore, the corrected parameterizations of H (Table 3), needed to remove the bias between measured ($H_{BS\text{-}day}$) and computed H ($H_{BS\text{-}day\text{-}Terra}$ and $AE_{BS\text{-}day\text{-}Aqua}$), were applied to compute daily modeled H ($\mathrm{H\_SPARSE}_{day}$) from instantaneous modeled H ($\mathrm{H\_SPARSE}_t$) following the extrapolation method shown in equation 21. Finally, $\mathrm{H\_SPARSE}_{day}$ was weighted by the corresponding daily footprint to get the daily modeled H of the upwind area $\mathrm{H\_SPARSE}_{day\text{-}FP}$.

Table 3: Corrected parameterizations of sensible heat flux for the diurnal reconstitution

Terra	a'_{Terra}	1.02
	b'_{Terra}	-17.31
Aqua	a'_{Aqua}	1.00
	b'_{Aqua}	-14.83

Hydrol. Earth Syst. Sci. Discuss., https://doi.org/10.5194/hess-2017-454
Manuscript under review for journal Hydrol. Earth Syst. Sci.
Discussion started: 28 August 2017

5 Water stress estimates

Water stress estimation is crucial to deduce the root zone soil moisture level using remote sensing data, (Hain et al., 2009). Water stress results in a drop of actual evapotranspiration below the potential rate. Its intensity is usually represented by a stress factor as defined in Sect. 4.2, ranging between 0 (unstressed surface) and 1 (fully stressed surface).

Modeled values of SF at the time of Terra and Aqua overpass (SF_{mod}) have been computed from modeled potential LE (LEp_{-t-FP}) as follows:

$$SF_{mod} = 1 - \frac{LE\_SPARSE_{t-FP}}{LE_{p-t-FP}} \quad (22)$$

where LE_SPARSE_{t-FP} and LE_{p-tFP} are the modeled latent heat fluxes in actual and potential conditions, respectively.

Furthermore, surface water stress factor derived from XLAS measurement, named SF_{obs}, at the time of Terra and Aqua overpass was computed as follows (Su, 2002):

$$SF_{obs} = \frac{H\_XLAS_t - H_{p-t-FP}}{H_{s-t-FP} - H_{p-t-FP}} \quad (23)$$

where H_{s-t-FP} and H_{p-t-FP} are the modeled sensible heat flux in actual and potential conditions, respectively; and H_XLAS_t is the XLAS sensible heat flux at the satellite overpass time.

6 Results and discussion

6.1 XLAS and model derived instantaneous sensible heat fluxes

Our primary focus is the comparison between scintillometer measurements and the modeled sensible heat fluxes computed using the Terra and Aqua remotely sensed data. The scintillometer H at the time of the two satellites overpass (H_XLAS_t) are interpolated from the half hourly H measurements. Heat flux determination was possible for typically about 87% of the daytime measurements during the summer, availability of XLAS heat flux values was lower during the cold season due to poor visibility and/or stable stratification.

H_SPARSE was weighted by the XLAS footprint in order to be able to compare the modeled values (H_SPARSE_{t-FP}) with the XLAS measurements (H_XLAS_t). Therefore, due to XLAS and remote sensing data availability, we got 175 and 118 values for Terra and Aqua respectively. In order to highlight H inter-seasonality between the drier 2012-2013 and the wetter 2013-2014 seasons, we present an example of two days each in one season, DOY 2013-083 shows H value ranging between 25 Wm^{-2} and 757 Wm^{-2} while DOY 2014-185 shows H value ranged between 128 Wm^{-2} and 470 Wm^{-2} (Figure 6). The colored area shows the modeled flux and the contours shows the surface source area contributing to the scintillometer measurements. The Day 2013-86 (24th March 2013) is chosen in the cold season while day 185-2014 (4th July 2014) is in the warm season to focus on land cover impact on T_{surf} and thus on modeled H, (trees and cereals in winter vs. only irrigated trees and market gardening in summer). Moreover, the first day experiences a strong southern wind

Hydrol. Earth Syst. Sci. Discuss., https://doi.org/10.5194/hess-2017-454
Manuscript under review for journal Hydrol. Earth Syst. Sci.
Discussion started: 28 August 2017

Hydrology and Earth System Sciences Discussions

while there is a light northern wind during the second day. Generally, a little number of MODIS pixels brings a high contribution to the signal; among them two are hot pixels (pixel with high T_{surf} and low NDVI) in which the land use is mainly arboriculture.

Prediction performance is assessed using RMSE and the coefficient of determination (R^2). Results for the sensible heat flux are illustrated in figure 7 and show good agreement between modeled and measured H at the time of satellites overpass. This is illustrated by linear regressions of $H\_SPARSE_{t\text{-}FP}$ = 1.065 H_XLAS_t -14.788 (R^2 = 0.6; RMSE = 57.89 Wm^{-2}) and $H\_SPARSE_{t\text{-}FP}$ = 1.12 H_XLAS_t -10.57 (R^2 = 0.63; RMSE = 53.85 Wm^{-2}) for Terra and Aqua, respectively. This result is of great interest considering that the SPARSE model was run with no prior calibration. However, we noted that bias is a function of the flux level and most outliers are recorded for H greater than 200 Wm^{-2}. This can be explained by (i) the XLAS measurement saturation (according to the "Kipp & Zonen LAS and XLAS instruction manual" (KIPP&ZONEN, 2007), for a path length of 4 km and a scintillometer height of 20 m, saturation measurement problem starts from H values higher than 300 Wm^{-2}), (ii) uncertainties on the correction of stability using the universal stability function and (iii) potential inconsistencies between the area average MODIS surface temperature and the air temperature measured locally at the meteorological station.

Whereas there are several studies dealing with large aperture scintillometer (LAS) data whose measurements are compared to modeled fluxes, in the few studies dealing with extra large aperture scintillometer (XLAS) data, the comparison is generally done with Eddy Covariance station measurements (Kohsiek et al., 2002; Moene et al., 2006). Indeed, our results are in agreement with those found by Marx et al. (2008) who compared LAS-derived and satellite-derived H (SEBAL was applied with NOAA-AVHRR images providing maps of surface energy fluxes at a 1 km × 1 km spatial resolution), and found that modeled H is underestimated with a RMSE of 39 Wm^{-2} for the site Tamale and 104 Wm^{-2} for the site Ejura. Moreover, Watts et al.(2000) compared the satellite (AVHRR radiometer) estimates of H to those from LAS over semi-arid grassland in northwest Mexico during the summer of 1997. They found RMSE values of 31 Wm^{-2} and 43 Wm^{-2} for LAS path lengths of 300 m and 600 m respectively and showed that LAS measurements are less good than those derived from a 3D sonic anemometer. They also suggested longer LAS path length (greater than 1.1 km) since the LAS is rather insensitive to the surface near the receiver and the emitter.

Hydrol. Earth Syst. Sci. Discuss., https://doi.org/10.5194/hess-2017-454
Manuscript under review for journal Hydrol. Earth Syst. Sci.
Discussion started: 28 August 2017

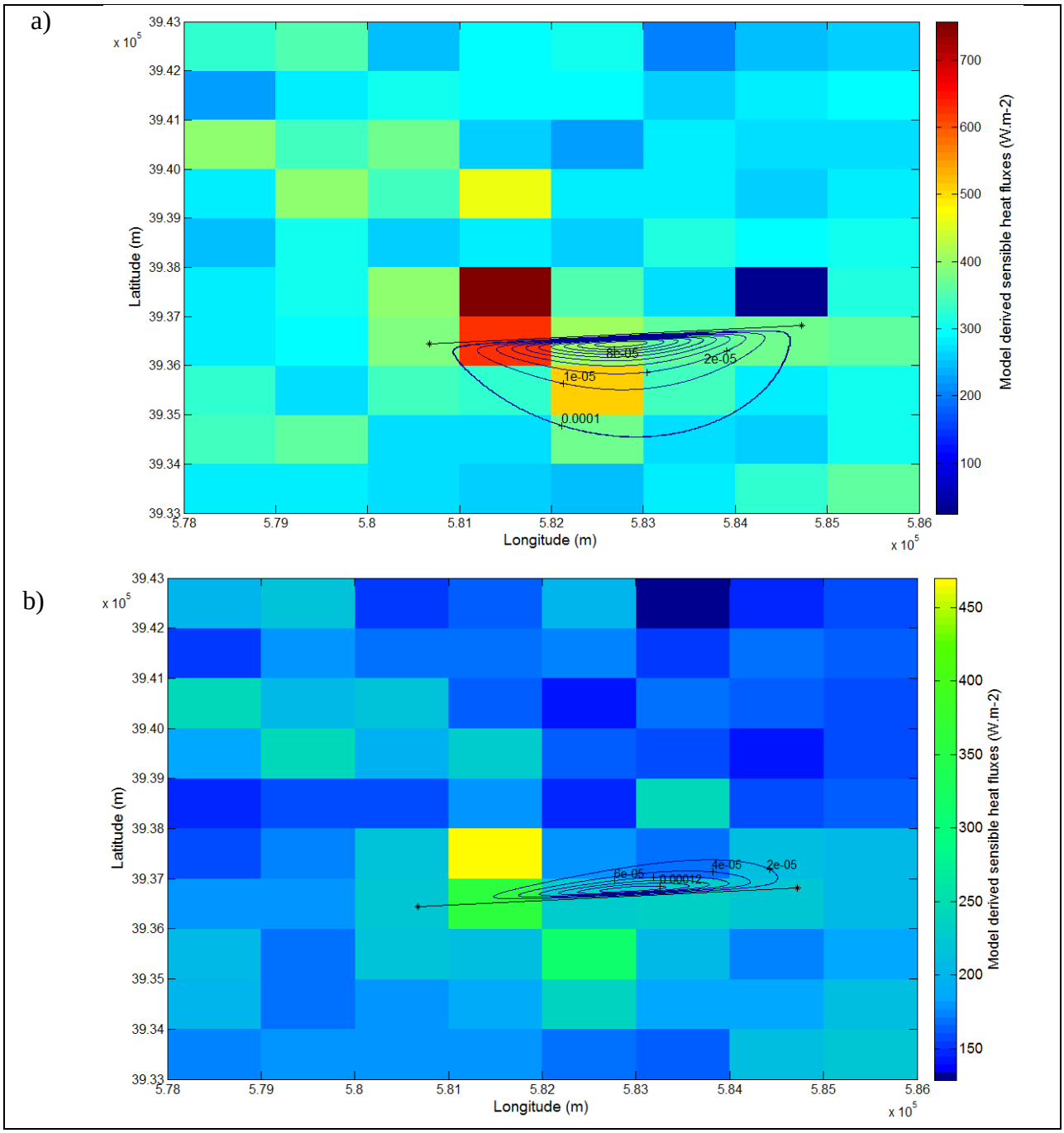

Figure 6: : Model derived sensible heat fluxes and footprints for (a) DOY 2013-082 at Aqua time overpass and (b) DOY 2014-185 at Terra time overpass. The colored area shows the modeled flux and the contours shows the surface source area contributing to the scintillometer measurements.

Hydrol. Earth Syst. Sci. Discuss., https://doi.org/10.5194/hess-2017-454
Manuscript under review for journal Hydrol. Earth Syst. Sci.
Discussion started: 28 August 2017

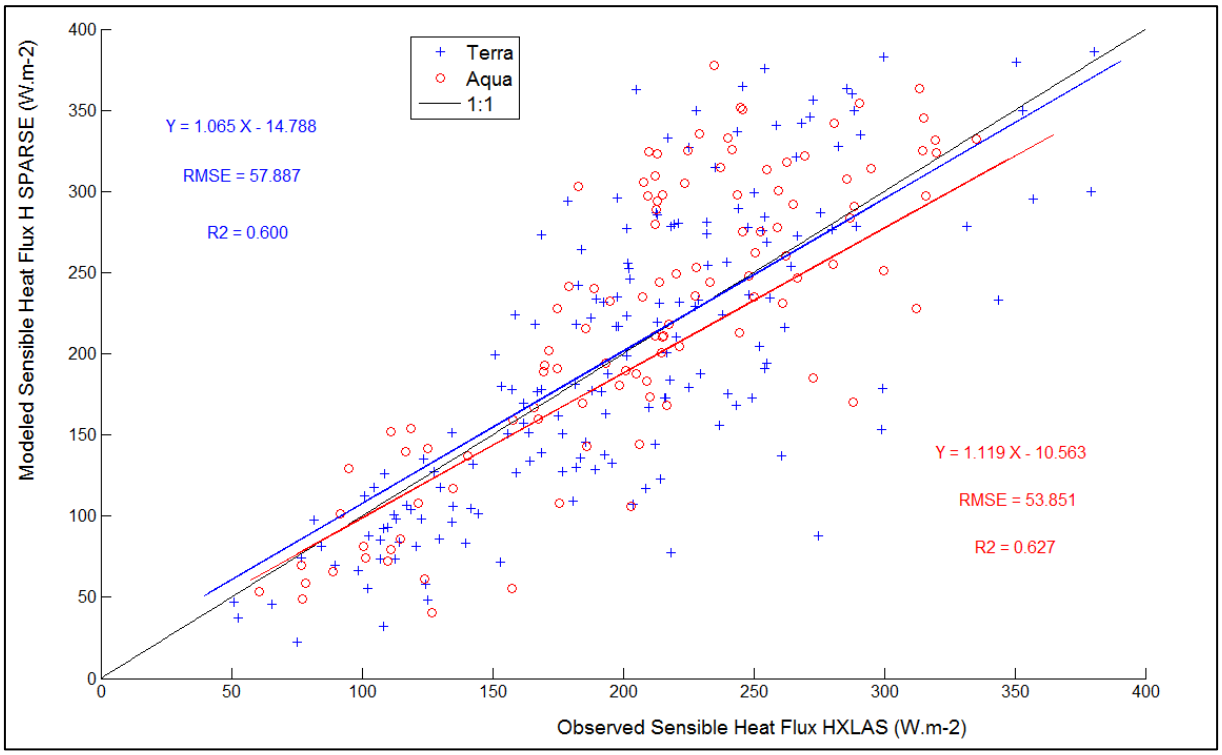

Figure 7: Modeled vs. observed sensible heat fluxes at Terra and Aqua time overpass

6.2 XLAS and model derived instantaneous latent heat fluxes

In a subsequent step, SPARSE derived LE ($LE\_SPARSE_{t\text{-}FP}$) was compared to observed LE ($LE\_residual\_XLAS_{t\text{-}FP}$). Results are illustrated in figure 8 showing a good agreement between modeled and observed LE. However, these results are less good than for the H results, as shown by the linear regressions: $LE\_SPARSE_{t\text{-}FP}$ =0.94 $LE\_residual\_XLAS_{t\text{-}FP}$ + 12.47 (RMSE = 47.20 Wm^{-2}) and $LE\_SPARSE_{t\text{-}FP}$ = 0.85 $LE\_residual\_XLAS_{t\text{-}FP}$ +11.51 (RMSE = 43.20 Wm^{-2}) for Terra and Aqua respectively, with an overall R^2 of 0.55 for both satellites. We note a greater scatter for latent heat flux than for the sensible heat flux (Figure 7), which can be explained by the fact that LE is here a residual term affected by estimation errors in both AE and H. Despite this moderate discrepancy, the good agreement between both approaches indicates that the methodology adopted in SPARSE for estimating H and AE using MODIS imagery is appropriate for modeling latent heat fluxes.

Hydrol. Earth Syst. Sci. Discuss., https://doi.org/10.5194/hess-2017-454
Manuscript under review for journal Hydrol. Earth Syst. Sci.
Discussion started: 28 August 2017

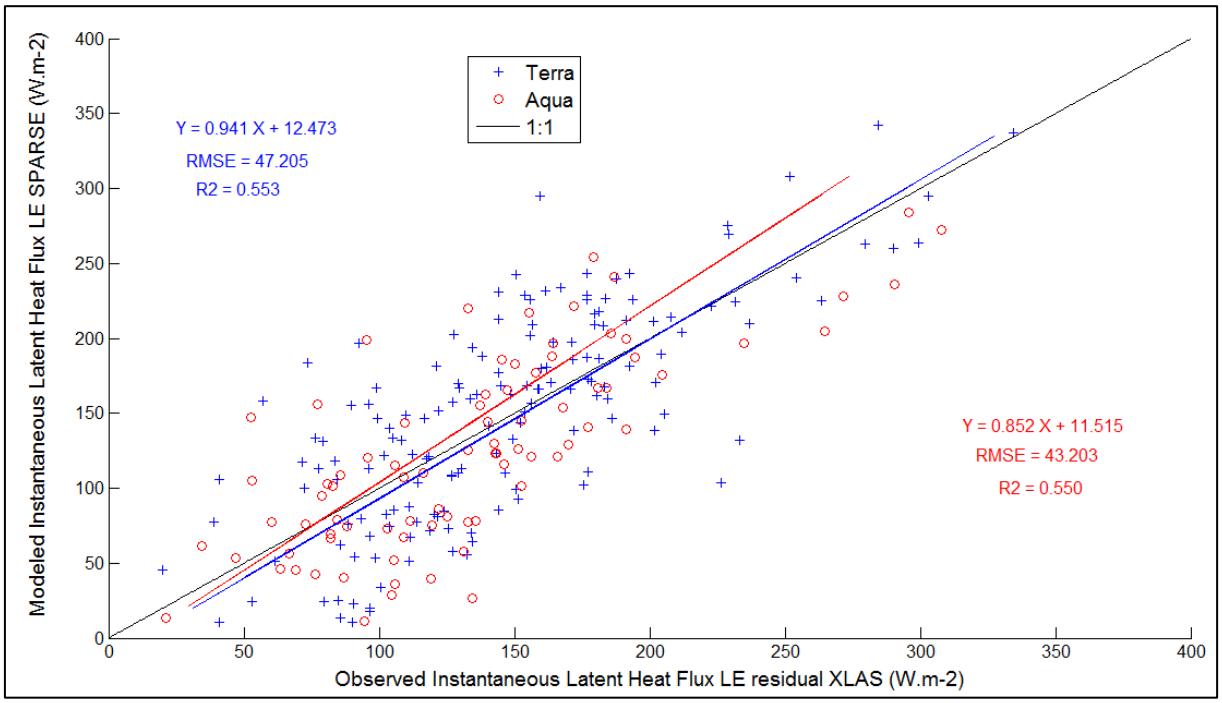

Figure 8: : Modeled vs. observed latent heat fluxes at Terra and Aqua time overpass

6.3 Water stress

The scattered values of the Stress Factor as shown in figure 9 are consistent with previous studies such as Boulet et al. (2015). SEB retrieval of stress is limited by the scale mismatch between the instantaneous estimate of the surface temperature during the satellite overpass (which can be influenced by high frequency turbulence) and the aggregated values of other forcing data which are derived from half hourly averages (Lagouarde et al., 2013; Lagouarde et al., 2015). However, general tendencies are well reproduced, with most points located within a 0.2 confidence interval (illustrated by dotted lines along the 1:1 line) as found by Boulet et al. (2015) at field scale, which is encouraging in a perspective of assimilating ET or SF in a water balance model for example. Moreover, it is noted that results include small LE and LE_p values having the same order of magnitude as the measurement uncertainty itself. Most outliers having greater water stress (~1) correspond to high evaporation from bare soil since the dominant land use in the study area is arboriculture, but also, this could be due to saturation of scintillation which led to an underestimation of H XLAS measurements as pointed by Frehlich and Ochs (1990) and Kohsiek et al. (2002).

Hydrol. Earth Syst. Sci. Discuss., https://doi.org/10.5194/hess-2017-454
Manuscript under review for journal Hydrol. Earth Syst. Sci.
Discussion started: 28 August 2017

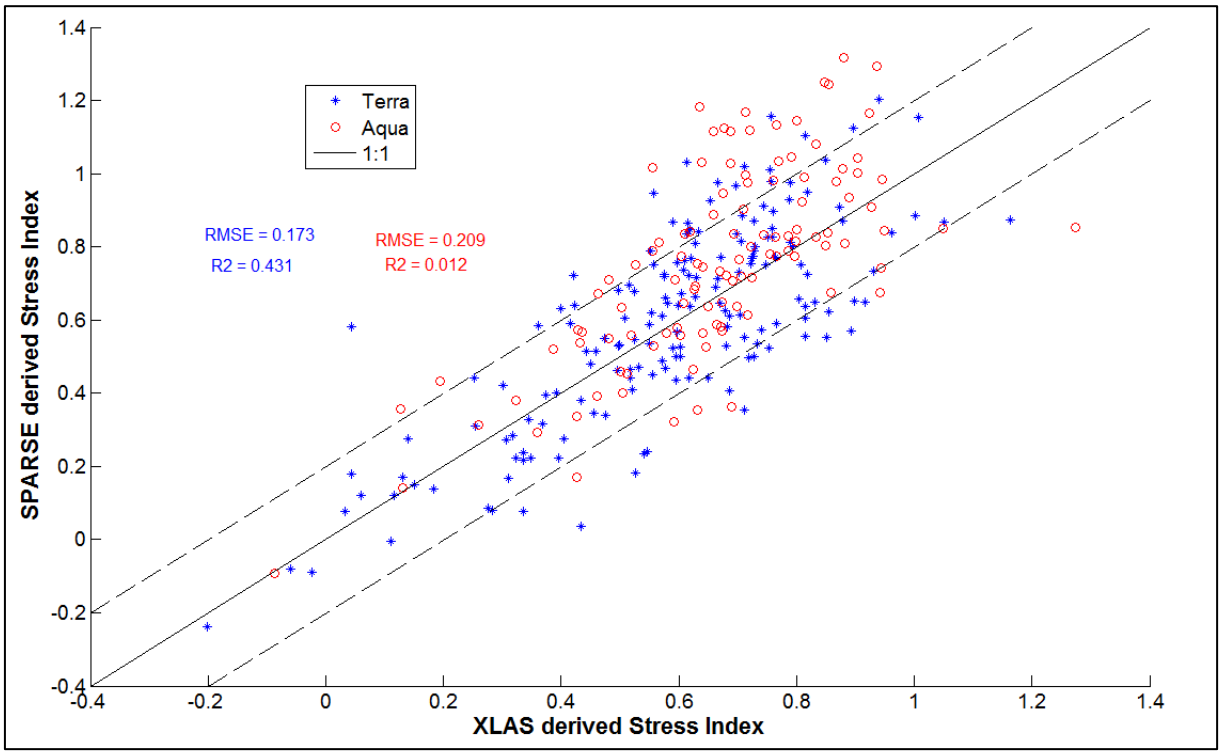

Figure 9: : Modeled vs. XLAS derived stress index SF at Terra and Aqua time overpass

Modeled and observed stress index at Terra and Aqua time overpass show a consistent evolution with daily rainfall (Figure 10), although the modeled stress show a greater dispersion than the observed one. During a rainy episode (or an eventual irrigation period), the surface temperature decreases towards the unstressed surface temperature, thus marking an unstressed state, and SF tends to 0. Conversely, after a long dry down, the water stress appears and the surface temperature increases towards the equilibrium surface temperature computed by SPARSE under stressed conditions, and SF tends towards 1. Besides, it is noted that modeled stress indexes computed on the basis of Aqua MODIS's T_{surf} are often greater than those computed used Terra MODIS's T_{surf} due to higher T_{surf} (higher global solar radiation) at the time of Terra overpass (around midday).

Hydrol. Earth Syst. Sci. Discuss., https://doi.org/10.5194/hess-2017-454
Manuscript under review for journal Hydrol. Earth Syst. Sci.
Discussion started: 28 August 2017

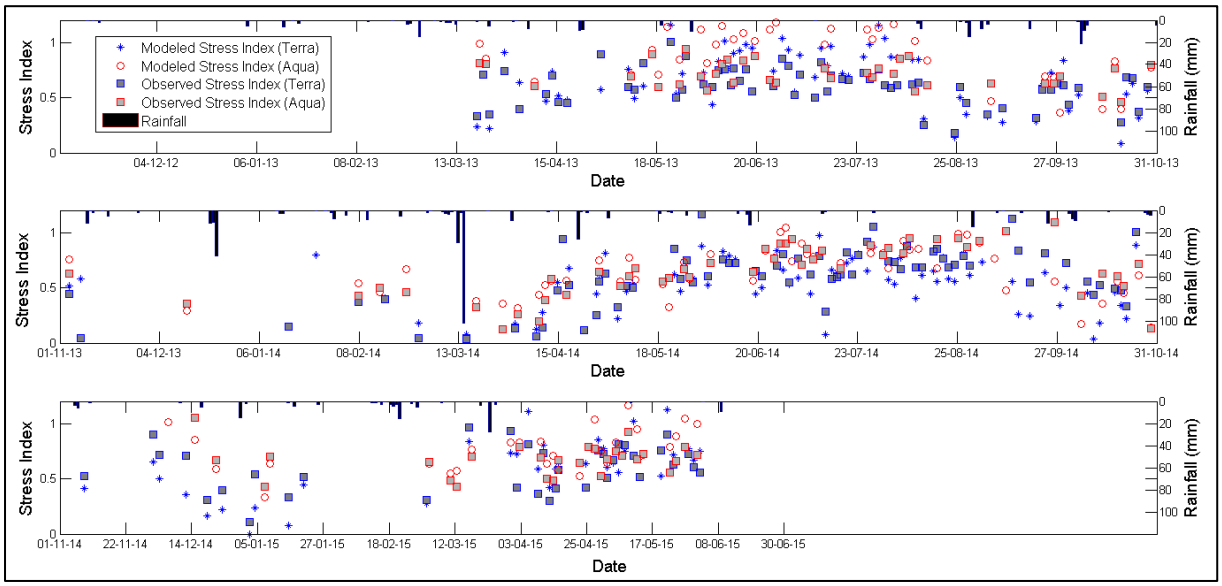

Figure 10: Modeled and observed stress index evolution at Terra and Aqua time overpass compared to daily rainfall

6.4 XLAS and model derived daily latent heat fluxes

Daily observed ET, *i.e.* LE_residual_XLAS$_{day\text{-}FP}$, was computed using the residual method; hence, six estimates of the daily observed ET were obtained by combining the two satellite datasets and three methods to compute G and thus AE (see Sect. 3.3). Only the residual method was used to estimate daily observed ET for two reasons; on the first hand, to reduce the computations approach since, already, three methods to compute AE have been tested and on the other hand, the application of the EF method was not possible because we do not have a measured spatially distributed potential evapotranspiration (only point potential evapotranspiration data at the Ben Salem meteorological station are available). From daily observed ET estimates, minimum and maximum ET were selected for each day and minimum and maximum daily ET time series were interpolated between successive days based on the self preservation of the ratio of AE to Rg as scale factor (Figure 11).

In addition, three methods were used to compute SPARSE daily ET for the Terra and Aqua overpasses (see Sect. 4.2), providing six estimates of the daily modeled ET. For each day average ET was plotted (260 days) with error bars figuring minimum and maximum values, along with precipitation to understand the rainfall impact on the ET evolution (Figure 11).

Despite the uncertainty in reconstructing the daily ET from instantaneous ET, overall results show a good agreement between XLAS derived and SPARSE derived ET values with similar seasonal dynamics. Daily observed and modeled ET over the whole study period were both in the range of 0-4 mmday^{-1} with an RMSE of 0.7 mmday^{-1} which is consistent with the land use present in the XLAS path: mainly trees spaced by a considerable fraction of bare soil, and less herbaceous soil-covering crops (see Sect.3.2). As expected, ET rates decrease significantly during dry periods (summers) since arid conditions limit the latent heat flux in favor of sensible heat flux and increase immediately after rainfall events due to the high amount of water evaporated from soil. The rainfall peaks that occurred on 3rd September 2013

Hydrol. Earth Syst. Sci. Discuss., https://doi.org/10.5194/hess-2017-454
Manuscript under review for journal Hydrol. Earth Syst. Sci.
Discussion started: 28 August 2017


Hydrology and Earth System Sciences Discussions

(about 10 mm), 6th October 2013 (about 20 mm), 15th March 2014 (about 100 mm) and 22nd April 2014 (about 25 mm) are followed by well-reproduced drydowns.

At seasonal scale, we note a good agreement between modeled and observed daily ET for the 2013-2014 and 2014-2015 seasons, especially when vegetation cover was more developed: from March to July 2014 and from March to Mai 2015; these periods correspond to cereals vegetation peak in some plots (March-April) and to market gardening crops (e.g. tomato, water melon, pepper, etc.) cultivated generally from spring to the beginning of autumn in the interrow area of trees plots, which is a common farming practice in the Kairouan plain. However, the 2012-2013 season was dry compared with the two other ones, and less accurate results were obtained. Some points with little to null ET were recorded from May to July 2013 which can be explained by the very dry conditions and scattered vegetation cover with a considerable amount of bare soil. This behavior was not observed in the same period of 2014, because 2014 was a rainy year in comparison to 2013, therefore, even supposing that the farmers have the same attitude and cultivate the same crop types between the two years (which is not true in the context of our study area and farmers always change crop types), precipitations favor the growth of spontaneous vegetation over fallows which contribute to ET rise. On the other hand, since this year experiences more rain, farmers cultivate a larger part of the land and diversify the crop types; the vegetation cover is denser and contributes to an overall increase in ET. Overall, lower ET values are recorder in autumn (October and November) which correspond to evapotranspiration from trees only, since the latest summer crops (market gardening crops) have been already harvested and the winter crops (mainly cereals) are not yet sown.

Moreover, it can be seen that occasionally SPARSE overestimated ET. As example, three dates can be selected in August 2013 (15th, 25th and 29th August 2013) for which modeled ET were 3.30 mm, 3.80 mm and 2.80 mm while maximum observed ET were 2.0 mm, 2.40 mm and 1.20 mm, respectively; broader amplitude between modeled (4.00 mm) and observed ET (1.40 mm) was also recorded on the 18th of May 2013. SPARSE also overestimates ET throughout ten days in August 2014 with an average difference of 1.1 mm and a maximum difference of 1.60 mm recorded in 23rd August 2014. These discrepancies are always recorded under wet conditions (minimum stress factor) which show the difficulty in representing accurately the conditions close to the potential ET. This might be related to the theoretical limit of the model for low vegetation stress especially when coupled with low evaporation efficiencies (*i.e.* dry soil surface) as already reported by Boulet et al. (2015) for senescent vegetation. Average difference between SPARSE and XLAS derived LE estimates when both are available indicate that SPARSE can predict evapotranspiration with accuracies approaching 5% of that of the XLAS.

Hydrol. Earth Syst. Sci. Discuss., https://doi.org/10.5194/hess-2017-454
Manuscript under review for journal Hydrol. Earth Syst. Sci.
Discussion started: 28 August 2017

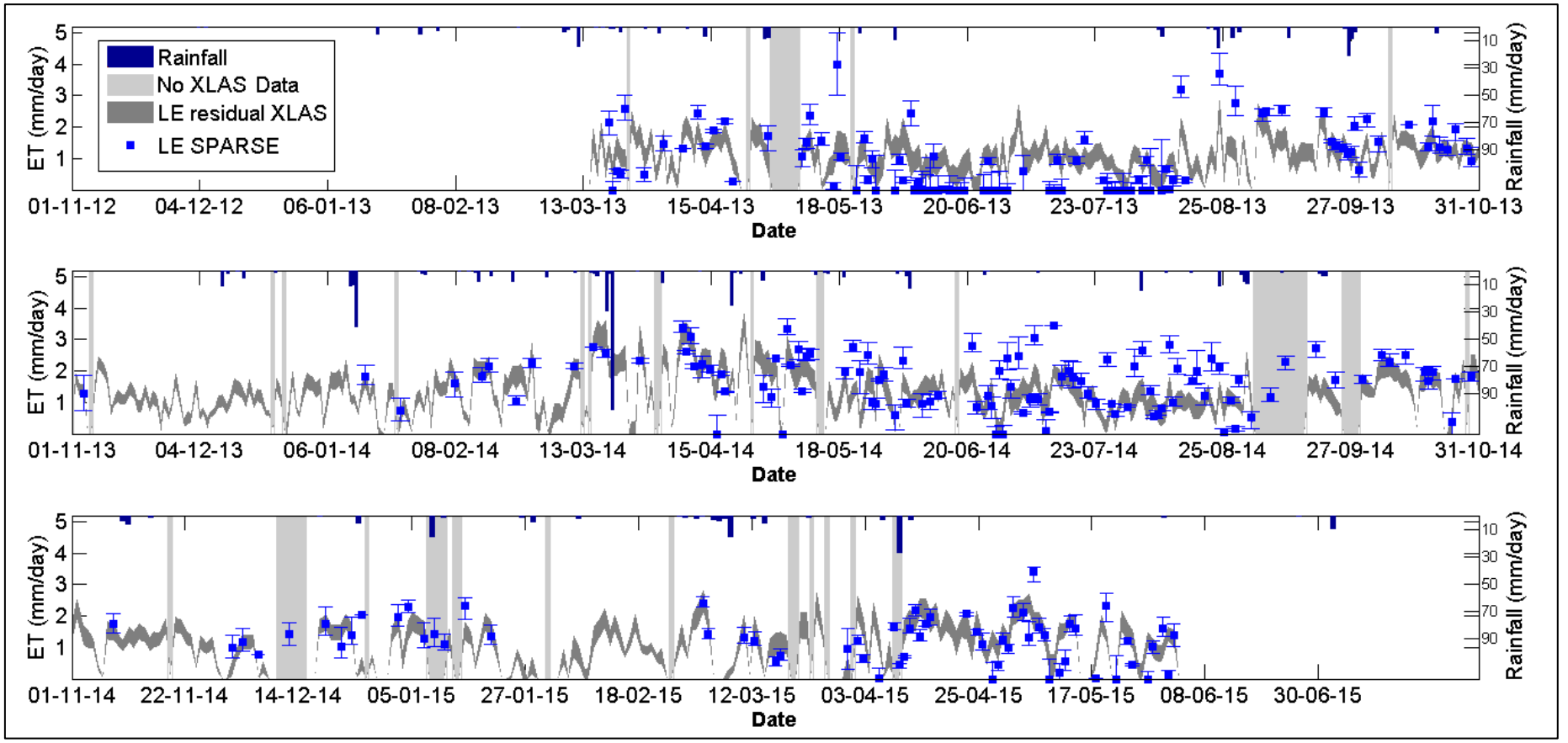

Figure 11: Modeled vs. observed daily latent heat fluxes. Dark grey color shows minimum and maximum daily observed LE. Light grey vertical bars show gaps in XLAS data. Error bars for the modeled ET show the minimum and the maximum daily ET resulting from the three methods used to compute daily ET from instantaneous modeled ET.

Hydrol. Earth Syst. Sci. Discuss., https://doi.org/10.5194/hess-2017-454
Manuscript under review for journal Hydrol. Earth Syst. Sci.
Discussion started: 28 August 2017

7 Conclusions

This study evaluated the performances of the SPARSE model forced by MODIS remote sensing products in an operational context (no model calibration) to estimate instantaneous and daily evapotranspiration. The validation protocol was based on an unprecedented dataset with an extra large aperture scintillometer. Indeed, up to our knowledge, this is the first work based on XLAS measurements acquired during more than 2 years, as compared to three months in previous works (Kohsiek et al., 2002; Moene et al., 2006). The estimates of the sensible heat flux derived from the SPARSE model are in close agreement with those obtained from the XLAS. These results indicate that the XLAS can be fruitfully used to validate large-scale sensible heat flux derived from remote sensing data (and residual latent heat flux), in particular for the results obtained at the satellite overpass time, providing a feasible alternative to local micrometeorological techniques for measuring the sensible heat flux and validating satellite-derived estimates (*i.e.* eddy correlation). Furthermore, the extrapolation from instantaneous to daily evapotranspiration is less obvious and three methods were tested based on the stress index, the evaporative fraction and the residual approach. The daily latent heat fluxes derived from the XLAS agreed rather well with those modeled using SPARSE model, which shows the potential of the SPARSE model in water consumption monitoring over heterogeneous landscape in semi-arid conditions, and especially to locate areas most affected by water stress. However, the precision in ET prediction with the SPARSE model is restricted by several assumptions and uncertainties. For instance, the instantaneous remote sensing data and mainly T_{surf} which is paramount in stress coefficient computation are assumed to be reliable. Moreover, there is an issue with the MODIS pixel heterogeneity and notably the distribution of components at the intersection between the square pixel and the XLAS footprint. Uncertainties are also due to half hourly forcing (meteorological and flux data) and XLAS data as well as to the extrapolation method from instantaneous to daily results. Furthermore, the empirical estimation methods of soil heat flux G (three methods were tested) as well as the possible daily heat accumulation lead to possible errors in available energy estimation and in turn in residual LE estimation.

Even if overall results are encouraging, further work is needed to improve results by i) being most efficient in the SPARSE model application using calibrated input data specific to our study area, especially input parameters to which the model is particularly sensitive such as the mean leaf width and the minimum stomatal resistance, ii) taking into account the heterogeneity of the 1km MODIS pixel by applying MODIS footprint, which is determined by the sensor's observation geometry and (iii) using a Land Surface Model applied at the field scale (Etchanchu et al., 2017) to analyze the scaling properties from the field to the footprint of the XLAS and the MODIS pixels similarly.

Finally, in a future work, we plan to take advantage of the complementarities between the Soil Water Balance and Surface Energy Balance approaches (*i.e.* continuous but uncertain estimates using SWB due to poor soil water content control on one hand and sensitivity of SEB to the actual water stress on the other hand) to implement an assimilation scheme of the remotely sensed surface temperature into land surface models. In fact, in order to provide further information about distributed soil water status over the studied areas, the TIR-derived

evapotranspiration products could be assimilated directly either in land surface or hydrological models.

Author contribution:

Sameh Saadi: data processing, data analysis and results interpretation.

Gilles Boulet: data analysis and results interpretation.

Malik Bahir: SPARSE inputs and XLAS data processing and analysis.

Aurore Brut: XLAS data processing and analysis.

Bernard Mougenot and Zohra Lili Chabaane: site management.

Pascal Fanise: site instrumentation.

Vincent Simonneaux and Zohra Lili-Chabaane contributed with ideas and discussions.

Competing interests:

The authors declare that they have no conflict of interest.

Acknowledgements

The authors are thankful to the GDAs of Ben Salem I and Ben Salem II which enabled the scintillometer set-up and access above the two water towers. Funding from the CNES/TOSCA program for the EVA2IRT project, from the MISTRALS/SICMED program for the ReSAMEd project, from the ORFEO/CNES Program for Pléiades images (© CNES 2012, Distribution Airbus DS, all rights reserved), and from the ANR/TRANSMED program for the AMETHYST project (ANR-12-TMED-0006-01) as well as the mobility support from PHC Maghreb program (N° 32592VE) are gratefully acknowledged,. This work has benefited also from the financial support of the ARTS program ("Allocations de recherche pour une thèse au Sud") of IRD (Institut de Recherche pour le Développement).

References

Allen, R. G., Pereira, L. S., Raes, D., and Smith, M.: Crop evapotranspiration-Guidelines for computing crop water requirements-FAO Irrigation and drainage paper 56, FAO, Rome, 300, D05109, 1998.

Allen, R., Irmak, A., Trezza, R., Hendrickx, J. M., Bastiaanssen, W., and Kjaersgaard, J.: Satellite-based ET estimation in agriculture using SEBAL and METRIC, Hydrological Processes, 25, 4011-4027, 2011.

Amri, R., Zribi, M., Lili-Chabaane, Z., Szczypta, C., Calvet, J. C., and Boulet, G.: FAO-56 dual model combined with multi-sensor remote sensing for regional evapotranspiration estimations, Remote Sensing, 6, 5387-5406, 2014.

Anderson, M. C., Kustas, W. P., Norman, J. M., Hain, C. R., Mecikalski, J. R., Schultz, L., González-Dugo, M. P., Cammalleri, C., d'Urso, G., Pimstein, A., and Gao, F.: Mapping daily evapotranspiration at field to continental scales using geostationary and polar orbiting satellite imagery, Hydrol. Earth Syst. Sci., 15, 223-239, 10.5194/hess-15-223-2011, 2011.

Anderson, M., Norman, J., Diak, G., Kustas, W., and Mecikalski, J.: A two-source time-integrated model for estimating surface fluxes using thermal infrared remote sensing, Remote sensing of environment, 60, 195-216, 1997.

Andreas, E. L.: Atmospheric stability from scintillation measurements, Applied optics, 27, 2241-2246, 1988.

Bai, J., Jia, L., Liu, S., Xu, Z., Hu, G., Zhu, M., and Song, L.: Characterizing the footprint of eddy covariance system and large aperture scintillometer measurements to validate satellite-based surface fluxes, IEEE Geoscience and Remote Sensing Letters, 12, 943-947, 2015.

Bastiaanssen, W. G. M., Allen, R. G., Droogers, P., D'Urso, G., and Steduto, P.: Twenty-five years modeling irrigated and drained soils: State of the art, Agricultural Water Management, 92, 111-125, http://dx.doi.org/10.1016/j.agwat.2007.05.013, 2007.

Bastiaanssen, W. G. M.: Regionalization of surface flux densities and moisture indicators in composite terrain; a remote sensing approach under clear skies in mediterranean climates, SC-DLO, Wageningen, 1995.

Boulet, G., Braud, I., and Vauclin, M.: Study of the mechanisms of evaporation under arid conditions using a detailed model of the soil–atmosphere continuum. Application to the EFEDA I experiment, Journal of Hydrology, 193, 114-141, https://doi.org/10.1016/S0022-1694(96)03148-4, 1997.

Boulet, G., Chehbouni, A., Gentine, P., Duchemin, B., Ezzahar, J., and Hadria, R.: Monitoring water stress using time series of observed to unstressed surface temperature difference, Agricultural and Forest Meteorology, 146, 159-172, https://doi.org/10.1016/j.agrformet.2007.05.012, 2007.

Boulet, G., Mougenot, B., Lhomme, J. P., Fanise, P., Lili-Chabaane, Z., Olioso, A., Bahir, M., Rivalland, V., Jarlan, L., Merlin, O., Coudert, B., Er-Raki, S., and Lagouarde, J. P.: The SPARSE model for the prediction of water stress and evapotranspiration components from thermal infra-red data and its evaluation over irrigated and rainfed wheat, Hydrol. Earth Syst. Sci., 19, 4653-4672, 10.5194/hess-19-4653-2015, 2015.

Bounoua, L., Zhang, P., Thome, K., Masek, J., Safia, A., Imhoff, M. L., and Wolfe, R. E.: Mapping Biophysical Parameters for Land Surface Modeling over the Continental US Using MODIS and Landsat, Dataset Papers in Science, 2015, 11, 10.1155/2015/564279, 2015.

Braud, I., Dantas-Antonino, A. C., Vauclin, M., Thony, J. L., and Ruelle, P.: A simple soil-plant-atmosphere transfer model (SiSPAT) development and field verification, Journal of Hydrology, 166, 213-250, http://dx.doi.org/10.1016/0022-1694(94)05085-C, 1995.

Brunsell, N. A., Ham, J. M., and Arnold, K. A.: Validating remotely sensed land surface fluxes in heterogeneous terrain with large aperture scintillometry, International Journal of Remote Sensing, 32, 6295-6314, 10.1080/01431161.2010.508058, 2011.

Brutsaert, W., and Sugita, M.: Application of self-preservation in the diurnal evolution of the surface energy budget to determine daily evaporation, Journal of Geophysical Research: Atmospheres, 97, 18377-18382, 1992.

Calera, A., Campos, I., Osann, A., D'Urso, G., and Menenti, M.: Remote Sensing for Crop Water Management: From ET modeling to Services for the End Users, Sensors, 17, 1104, 2017.

Chahbi, A., Zribi, M., Saadi, S., Simonneaux, V., Lili Chabaane, Z. : Classification et caractérisation de la couverture végétale dans un milieu semi aride en utilisant des images SPOT 5, Deuxième Workshop AMETHYST, 11 Février 2016, Marrakech, Maroc, 2016,

Chávez, J., Neale, C. M. U., Hipps, L. E., Prueger, J. H., and Kustas, W. P.: Comparing Aircraft-Based Remotely Sensed Energy Balance Fluxes with Eddy Covariance Tower Data Using Heat Flux Source Area Functions, Journal of Hydrometeorology, 6, 923-940, 10.1175/jhm467.1, 2005.

Chirouze, J., Boulet, G., Jarlan, L., Fieuzal, R., Rodriguez, J. C., Ezzahar, J., Er-Raki, S., Bigeard, G., Merlin, O., Garatuza-Payan, J., Watts, C., and Chehbouni, G.: Intercomparison of four remote-sensing-based energy balance methods to retrieve surface evapotranspiration and water stress of irrigated fields in semi-arid climate, Hydrol. Earth Syst. Sci., 18, 1165-1188, 10.5194/hess-18-1165-2014, 2014.

Choudhury, B. J., Idso, S. B., and Reginato, R. J.: Analysis of an empirical model for soil heat flux under a growing wheat crop for estimating evaporation by an infrared-temperature based energy balance equation, Agricultural and Forest Meteorology, 39, 283-297, http://dx.doi.org/10.1016/0168-1923(87)90021-9, 1987.

Choudhury, B., and Monteith, J.: A four-layer model for the heat budget of homogeneous land surfaces, Quarterly Journal of the Royal Meteorological Society, 114, 373-398, 1988.

Clevers, J. G. P. W.: Application of a weighted infrared-red vegetation index for estimating leaf Area Index by Correcting for Soil Moisture, Remote Sensing of Environment, 29, 25-37, http://dx.doi.org/10.1016/0034-4257(89)90076-X, 1989.

Clothier, B., Clawson, K., Pinter, P., Moran, M., Reginato, R. J., and Jackson, R.: Estimation of soil heat flux from net radiation during the growth of alfalfa, agricultural and forest meteorology, 37, 319-329, 1986.

Danelichen, V. H. d. M., Biudes, M. S., Souza, M. C., Machado, N. G., Silva, B. B. d., and Nogueira, J. d. S.: Estimation of soil heat flux in a neotropical Wetland region using remote sensing techniques, Revista Brasileira de Meteorologia, 29, 469-482, 2014.

De Bruin, H.A.R., Kohsiek, W., Van Den Hurk, B.J.J.M., 1993. A verification of some methods to determine the fluxes of momentum, sensible heat, and water vapour using standard deviation and structure parameter of scalar meteorological quantities. Boundary-Layer Meteorology 63, 231-257.

Delogu, E., Boulet, G., Olioso, A., Coudert, B., Chirouze, J., Ceschia, E., Le Dantec, V., Marloie, O., Chehbouni, G., and Lagouarde, J. P.: Reconstruction of temporal variations of evapotranspiration using instantaneous estimates at the time of satellite overpass, Hydrol. Earth Syst. Sci., 16, 2995-3010, 10.5194/hess-16-2995-2012, 2012.

Etchanchu, J., Rivalland, V., Gascoin, S., Cros, J., Brut, A., and Boulet, G.: Effects of multi-temporal high-resolution remote sensing products on simulated hydrometeorological variables in a cultivated area (southwestern France), Hydrol. Earth Syst. Sci. Discuss., 2017, 1-23, 10.5194/hess-2016-661, 2017.

Feddes, R. A., Kowalik, P. J., and Zaradny, H.: Simulation of Field Water Use and Crop Yield, Wiley, 1978.

Frehlich, R. G., and Ochs, G. R.: Effects of saturation on the optical scintillometer, Applied optics, 29, 548-553, 1990.

Gentine, P., Entekhabi, D., Chehbouni, A., Boulet, G., Duchemin, B., 2007. Analysis of evaporative fraction diurnal behaviour. Agricultural and Forest Meteorology 143, 13-29.

Giorgi, F., and Avissar, R.: Representation of heterogeneity effects in Earth system modeling: Experience from land surface modeling, Reviews of Geophysics, 35, 413-437, 1997.

Giorgi, F., and Lionello, P.: Climate change projections for the Mediterranean region, Global and planetary change, 63, 90-104, 2008.

Glenn, E. P., Huete, A. R., Nagler, P. L., Hirschboeck, K. K., and Brown, P.: Integrating remote sensing and ground methods to estimate evapotranspiration, Critical Reviews in Plant Sciences, 26, 139-168, 2007.

Green, A. E., and Hayashi, Y.: Use of the scintillometer technique over a rice paddy, Journal of Agricultural Meteorology, 54, 225-234, 1998.

Gurney, R., and Hsu, A.: Relating evaporative fraction to remotely sensed data at the FIFE site, 1990.

Hain, C. R., Mecikalski, J. R., and Anderson, M. C.: Retrieval of an Available Water-Based Soil Moisture Proxy from Thermal Infrared Remote Sensing. Part I: Methodology and Validation, Journal of Hydrometeorology, 10, 665-683, 10.1175/2008jhm1024.1, 2009.

Hartogensis, O. K., Watts, C. J., Rodriguez, J.-C., and Bruin, H. A. R. D.: Derivation of an Effective Height for Scintillometers: La Poza Experiment in Northwest Mexico, Journal of Hydrometeorology, 4, 915-928, 10.1175/1525-7541(2003)004<0915:doaehf>2.0.co;2, 2003.

Hemakumara, H. M., Chandrapala, L., and Moene, A. F.: Evapotranspiration fluxes over mixed vegetation areas measured from large aperture scintillometer, Agricultural Water Management, 58, 109-122, http://doi.org/10.1016/S0378-3774(02)00131-2, 2003.

Horst, T., and Weil, J.: Footprint estimation for scalar flux measurements in the atmospheric surface layer, Boundary-Layer Meteorology, 59, 279-296, 1992.

Hunink, J., Eekhout, J., Vente, J., Contreras, S., Droogers, P., and Baille, A.: Hydrological modeling using Satellite-Based Crop Coefficients: A Comparison of Methods at the Basin Scale, Remote Sensing, 9, 174, 2017.

Jackson, R. D., Moran, M. S., Gay, L. W., and Raymond, L. H.: Evaluating evaporation from field crops using airborne radiometry and ground-based meteorological data, Irrigation Science, 8, 81-90, 10.1007/bf00259473, 1987.

Kalma, J. D., McVicar, T. R., and McCabe, M. F.: Estimating land surface evaporation: A review of methods using remotely sensed surface temperature data, Surveys in Geophysics, 29, 421-469, 2008.

Kohsiek, W., Meijninger, W. M. L., Moene, A. F., Heusinkveld, B. G., Hartogensis, O. K., Hillen, W. C. A. M., and De Bruin, H. A. R.: An Extra Large Aperture Scintillometer For Long Range Applications, Boundary-Layer Meteorology, 105, 119-127, 10.1023/a:1019600908144, 2002.

Kroes, J. G., J.C. van Dam, R.P. Bartholomeus, P. Groenendijk, M. Heinen, R.F.A. Hendriks, H.M. Mulder, I. Supit, P.E.V. van Walsum: SWAP version 4; Theory description and user manual. Report 2780. Wageningen, Wageningen Environmental Research.Available at: http://library.wur.nl/WebQuery/wurpubs/fulltext/416321, 2017.

Kustas, W. P., and Daughtry, C. S. T.: Estimation of the soil heat flux/net radiation ratio from spectral data, Agricultural and Forest Meteorology, 49, 205-223, http://dx.doi.org/10.1016/0168-1923(90)90033-3, 1990.

Kustas, W. P., and Norman, J. M.: Evaluation of soil and vegetation heat flux predictions using a simple two-source model with radiometric temperatures for partial canopy cover, Agricultural and Forest Meteorology, 94, 13-29, https://doi.org/10.1016/S0168-1923(99)00005-2, 1999.

Kustas, W. P., Daughtry, C. S. T., and Van Oevelen, P. J.: Analytical treatment of the relationships between soil heat flux/net radiation ratio and vegetation indices, Remote Sensing of Environment, 46, 319-330, http://dx.doi.org/10.1016/0034-4257(93)90052-Y, 1993.

Kustas, W., and Anderson, M.: Advances in thermal infrared remote sensing for land surface modeling, Agricultural and Forest Meteorology, 149, 2071-2081, 2009.

Lagouarde, J.-P., Bach, M., Sobrino, J. A., Boulet, G., Briottet, X., Cherchali, S., Coudert, B., Dadou, I., Dedieu, G., and Gamet, P.: The MISTIGRI thermal infrared project: scientific objectives and mission specifications, International journal of remote sensing, 34, 3437-3466, 2013.

Lagouarde, J.-P., Irvine, M., and Dupont, S.: Atmospheric turbulence induced errors on measurements of surface temperature from space, Remote Sensing of Environment, 168, 40-53, https://doi.org/10.1016/j.rse.2015.06.018, 2015.

Lagouarde, J.-P., Jacob, F., Gu, X. F., Olioso, A., Bonnefond, J.-M., Kerr, Y., Mcaneney, K. J., and Irvine, M.: Spatialization of sensible heat flux over a heterogeneous landscape, Agronomie-Sciences des Productions Vegetales et de l'Environnement, 22, 627-634, 2002.

LAS and X-LAS instruction manual: http://www.kippzonen.fr/Download/244/LAS-and-X-LAS-Scintillometers-Manual?ShowInfo=true, access: 7th December, 2007.

Leclerc, M. Y., and Thurtell, G. W.: Footprint prediction of scalar fluxes using a Markovian analysis, Boundary-Layer Meteorology, 52, 247-258, 10.1007/bf00122089, 1990.

Leduc, C., Calvez, R., Beji, R., Nazoumou, Y., Lacombe, G., and Aouadi, C.: Evolution de la ressource en eau dans la vallée du Merguellil (Tunisie centrale), Séminaire sur la modernisation de l'agriculture irriguée, 2004, 10 p.,

Li, Z.-L., Tang, R., Wan, Z., Bi, Y., Zhou, C., Tang, B., Yan, G., and Zhang, X.: A review of current methodologies for regional evapotranspiration estimation from remotely sensed data, Sensors, 9, 3801-3853, 2009.

Liou, Y.-A., and Kar, S.: Evapotranspiration Estimation with Remote Sensing and Various Surface Energy Balance Algorithms—A Review, Energies, 7, 2821, 2014.

Marx, A., Kunstmann, H., Schüttemeyer, D., and Moene, A. F.: Uncertainty analysis for satellite derived sensible heat fluxes and scintillometer measurements over Savannah environment and comparison to mesoscale meteorological simulation results, Agricultural and Forest Meteorology, 148, 656-667, https://doi.org/10.1016/j.agrformet.2007.11.009, 2008.

Mauser, W., and Schädlich, S.: modeling the spatial distribution of evapotranspiration on different scales using remote sensing data, Journal of Hydrology, 212, 250-267, 1998.

Meijninger, W. M. L., Hartogensis, O. K., Kohsiek, W., Hoedjes, J. C. B., Zuurbier, R. M., and De Bruin, H. A. R.: Determination of Area-Averaged Sensible Heat Fluxes with a Large Aperture Scintillometer over a Heterogeneous Surface – Flevoland Field Experiment, Boundary-Layer Meteorology, 105, 37-62, 10.1023/a:1019647732027, 2002.

Minacapilli, M., Agnese, C., Blanda, F., Cammalleri, C., Ciraolo, G., D'Urso, G., Iovino, M., Pumo, D., Provenzano, G., and Rallo, G.: Estimation of actual evapotranspiration of Mediterranean perennial crops by means of remote-sensing based surface energy balance models, Hydrology and Earth System Sciences, 13, 1061-1074, 2009.

Minacapilli, M., Ciraolo, G., D Urso, G., and Cammalleri, C.: Evaluating actual evapotranspiration by means of multi-platform remote sensing data: a case study in Sicily, IAHS PUBLICATION, 316, 207., 2007.

Moene, A. F., Meijninger, W., Kohsiek, W., Gioli, B., Miglietta, F., and Bosveld, F.: Validation of fluxes of an extra large aperture scintillometer at Cabauw using sky arrow aircraft flux measurements, Proceedings of 17th symposium on boundary layers and turbulence. American Meteorological Society, San Diego, CA, 2006, 22-25,

Monin, A., and Obukhov, A.: Basic laws of turbulent mixing in the surface layer of the atmosphere, Contrib. Geophys. Inst. Acad. Sci. USSR, 151, e187, 1954.

Mougenot, B., Touhami, N., Lili Chabaane, Z., Boulet, G., Simonneaux, V., and Zribi, M.: Trees detection for water resources management in irrigated and rainfed arid and semi-arid agricultural areas, Pléiades Days, Toulouse, April 1-3, 2014, 2014.

Mutziger, A. J., Burt, C. M., Howes, D. J., and Allen, R. G.: Comparison of measured and FAO-56 modeled evaporation from bare soil, Journal of irrigation and drainage engineering, 131, 59-72, 2005.

Odi-Lara, M., Campos, I., Neale, C., Ortega-Farías, S., Poblete-Echeverría, C., Balbontín, C., and Calera, A.: Estimating Evapotranspiration of an Apple Orchard Using a Remote Sensing-Based Soil Water Balance, Remote Sensing, 8, 253, 2016.

Oki, T., and Kanae, S.: Global Hydrological Cycles and World Water Resources, Science, 313, 1068-1072, 10.1126/science.1128845, 2006.

Pereira, L. S., Oweis, T., and Zairi, A.: Irrigation management under water scarcity, Agricultural water management, 57, 175-206, 2002.

Poussin, J. C., Imache, A., Beji, R., Le Grusse, P., and Benmihoub, A.: Exploring regional irrigation water demand using typologies of farms and production units: An example from Tunisia, Agricultural Water Management, 95, 973-983, https://doi.org/10.1016/j.agwat.2008.04.001, 2008.

Pradeleix, L., Roux, P., Bouarfa, S., Jaouani, B., Lili-Chabaane, Z., and Bellon-Maurel, V.: Environmental Impacts of Contrasted Groundwater Pumping Systems Assessed by Life Cycle Assessment Methodology: Contribution to the Water–Energy Nexus Study, Irrigation and Drainage, 64, 124-138, 2015.

Raupach, M. R.: Simplified expressions for vegetation roughness length and zero-plane displacement as functions of canopy height and area index, Boundary-Layer Meteorology, 71, 211-216, 10.1007/bf00709229, 1994.

Saadi, S., Simonneaux, V., Boulet, G., Raimbault, B., Mougenot, B., Fanise, P., Ayari, H., and Lili-Chabaane, Z.: Monitoring Irrigation Consumption Using High-resolution NDVI Image Time Series: Calibration and Validation in the Kairouan Plain (Tunisia), Remote Sensing, 7, 13005, 2015.

Samain, B., Simons, G. W., Voogt, M. P., Defloor, W., Bink, N.-J., and Pauwels, V.: Consistency between hydrological model, large aperture scintillometer and remote sensing based evapotranspiration estimates for a heterogeneous catchment, Hydrology and Earth System Sciences, 16, 2095-2107, 2012.

Santanello Jr, J. A., and Friedl, M. A.: Diurnal covariation in soil heat flux and net radiation, Journal of Applied Meteorology, 42, 851-862, 2003.

Shuttleworth, W. J., and Gurney, R. J.: The theoretical relationship between foliage temperature and canopy resistance in sparse crops, Quarterly Journal of the Royal Meteorological Society, 116, 497-519, 1990.

Simonneaux, V., Lepage, M., Helson, D., Metral, J., Thomas, S., Duchemin, B., Cherkaoui, M., Kharrou, H., Berjami, B., and Chehbouni, A.: Estimation spatialisée de l'évapotranspiration des cultures irriguées par télédétection: application à la gestion de l'irrigation dans la plaine du Haouz (Marrakech, Maroc), Science et changements planétaires/Sécheresse, 20, 123-130, 2009.

Solignac, P. A., Brut, A., Selves, J. L., Béteille, J. P., Gastellu-Etchegorry, J. P., Keravec, P., Béziat, P., and Ceschia, E.: Uncertainty analysis of computational methods for deriving sensible heat flux values from scintillometer measurements, Atmos. Meas. Tech., 2, 741-753, 10.5194/amt-2-741-2009, 2009.

Steduto, P., Hsiao, T. C., Raes, D., and Fereres, E.: AquaCrop—The FAO crop model to simulate yield response to water: I. Concepts and underlying principles, Agronomy Journal, 101, 426-437, 2009.

Stöckle, C. O., Donatelli, M., and Nelson, R.: CropSyst, a cropping systems simulation model, European journal of agronomy, 18, 289-307, 2003.

Su, Z.: The Surface Energy Balance System (SEBS) for estimation of turbulent heat fluxes, Hydrology and Earth System Sciences Discussions, 6, 85-100, 2002.

Sugita, M., and Brutsaert, W.: Regional surface fluxes from remotely sensed skin temperature and lower boundary layer measurements, Water Resources Research, 26, 2937-2944, 1990.

Tasumi, M., Trezza, R., Allen, R. G., and Wright, J. L.: Operational aspects of satellite-based energy balance models for irrigated crops in the semi-arid US, Irrigation and Drainage Systems, 19, 355-376, 2005.

Tatarskii, V. I.: Wave propagation in turbulent medium, Wave Propagation in Turbulent Medium, by Valerian Ilich Tatarskii. Translated by RA Silverman. 285pp. Published by McGraw-Hill, 1961., 1961.

Torres, E. A., and Calera, A.: Bare soil evaporation under high evaporation demand: a proposed modification to the FAO-56 model, Hydrological Sciences Journal–Journal des Sciences Hydrologiques, 55, 303-315, 2010.

Touhami, N.: Détection des arbres par imagerie Très Haute Résolution Spatiale sur la plaine de Kairouan Engineer, Institut National Agronomqiue de Tunisie, Tunis, 78 pp., 2013.

Tucker, C. J.: A comparison of satellite sensor bands for vegetation monitoring, 1978.

Twine, T. E., Kustas, W., Norman, J., Cook, D., Houser, P., Meyers, T., Prueger, J., Starks, P., and Wesely, M.: Correcting eddy-covariance flux underestimates over a grassland, Agricultural and Forest Meteorology, 103, 279-300, 2000.

Ventura, F., Spano, D., Duce, P., and Snyder, R.: An evaluation of common evapotranspiration equations, Irrigation Science, 18, 163-170, 1999.

Xie, Y., Sha, Z., and Yu, M.: Remote sensing imagery in vegetation mapping: a review, Journal of Plant Ecology, 1, 9-23, 2008.

Zribi, M., Chahbi, A., Shabou, M., Lili-Chabaane, Z., Duchemin, B., Baghdadi, N., Amri, R., and Chehbouni, A.: Soil surface moisture estimation over a semi-arid region using ENVISAT ASAR radar data for soil evaporation evaluation, Hydrology and Earth System Sciences Discussions, 15, 345-358, 2011.

5.3 Synthesis and partial conclusion

In order to analyze an independent estimate of ET from the SEB approach, SPARSE model computed ET for three agricultural seasons 2012-2013, 2013-2014 and 2014-2015 over the 10 km × 8 km sub-image centered on the scintillometer XLAS transect. Overall results of the SPARSE energy balance spatialization are encouraging, in particular for the results obtained at the satellite overpass time, hence the interest of low spatial resolutions satellite data for crop monitoring under water stress conditions and water stress indicators assessment over heterogeneous surface. However, the extrapolation from instantaneous to daily evapotranspiration was less obvious and three methods were tested based on the stress index, the evaporative fraction and the residual approach. Daily ET estimates were deemed acceptable and the daily LE derived from the XLAS agreed rather well with those modeled using SPARSE model. Nevertheless, ET prediction with the SPARSE model is restricted by several assumptions and uncertainties (remote sensing data, meteorological and flux data, XLAS data, etc).

Several earlier studies were conducted in the Mediterranean context dealing with the integration of remotely sensed data into energy balance models to better estimate all energy budget fluxes, they show good agreement with SPARSE results mainly instantaneous ones. A physically based method for the energy budget partitioning following the Two Source model has been applied over a heterogeneous agricultural area located in southern Spain by Andreu *et al.* (2011) the comparison between instantaneous H and LE estimates to eddy covariance data of five plots gave a RMSD of 14 and 29 Wm^{-2}, respectively. Daytime ET showed a relative error of 10%. Furthermore, Calcagno *et al.* (2007) tested the performance given of the SEBAL model using MODIS images on areas characterized by different physiographic and vegetative conditions (sparse vegetation, crop canopy and high mountain vegetation) in southern Italy. The distributed results obtained for different days from summer 2004 to summer 2006 pointed out generally good ET predictions in the eddy covariance sites RMSE of 46 and 29 Wm^{-2} for H and LE, respectively.

General conclusion and perspectives

Water scarcity is one of the main factors limiting agricultural development in semi-arid areas. This work deals with the **spatial estimation of actual evapotranspiration and irrigation volumes using water balance and energy balance models forced by optical remote sensing data (VIS / NIR / TIR)**. It aims at estimating the regional crop water consumption based on physical and empirical models adapted to the available distributed information: *in situ* and multi-sensor/multi-resolution remote sensing data.

During this thesis, we enhanced several methodological developments (data forcing and assimilation, soil water balance models, surface energy balance models) around the estimation of evapotranspiration and irrigation with a spatio-temporal resolution adapted to the water resources management in semi-arid regions (field and irrigated perimeter scales). These methods have been applied to our study area: the Kairouan Plain in central Tunisia; where efficient agricultural water management is a major issue since the main user of the overexploited Kairouan aquifer is agriculture.

The major innovative aspect of this thesis is the development of methods to estimate the crop water budget and its related hydrological variables at different scales by valuing both high and low remote sensing data into soil water balance surface and energy balance modelization. Results are in synergy with previous works dealing with water resources management in the emblematic site of the Merguellil watershed. Since this study provides information about irrigation water consumption, and therefore implicitly about water pumping from the Kairouan aquifer, its results complement the previous works dealing either with hydrogeology, agronomy or water policy and management. Moreover, the results presented here can be improved based on results of other previous and current studies as it is detailed in the perspective section (e.g. radar synergy to better constraint soil evaporation).

■ Major findings

The first part of this PhD thesis was dedicated to the spatialization of evapotranspiration (ET) and irrigation volumes over the study area using the SAMIR model for four agricultural seasons. The input data in SAMIR are meteorological data, land use map, NDVI time series, crop and soil parameters, and irrigation rules. SAMIR operates on a daily basis and simulates water balance components according to the formalism developed by the FAO-56 with a simplified description of the soil in three horizons (surface, root and deep horizons). Crop and soil parameters for cereals crops were calibrated based on eddy covariance measurement of ET in irrigated barley and irrigated wheat fields. Crop specific parameters were set to calibrated values for cereals and taken from literature for the other land use classes. In absence of a detailed soil map, soil properties for all land use classes were considered homogeneous and the parameters were taken from calibration. The climatic forcing was considered homogeneous over the plain and meteorological data was taken from the sole station present in the study area. The

major originality of SAMIR relies on the use of remote sensing NDVI time series for vegetation monitoring, from which crop coefficients and vegetation fraction covers are derived, instead of using standard values. In order to establish a high-resolution water balance, SAMIR was fed with time series of SPOT images. Four time series of SPOT5 images (2008-2009, 2011-2012, 2012-2013 and 2013-2014) have been acquired over the study site along with a SPOT4 time series acquired in the frame of the SPOT4-Take5 experiment, which took place during the first half of 2013. A special attention was paid to the SPOT5 time series pre-processing based on the SPOT4-Take5 data. The irrigation volume estimates have been evaluated on three irrigated sectors (total area of about 600 ha) and compared to observed irrigation volumes. It was shown that the modeled monthly irrigations are on the whole satisfying with two noticeable exceptions for the first (November) and last (June) months of the simulation. When aggregated to the whole season, modeled irrigation volumes at perimeter scale for all campaigns were close to observed ones (resp. 118 and 111 mm; RMSE of about 35 mm for average irrigations of about 118 mm). SAMIR simulations were also analysed for 2012-2013 and 2013-2014 seasons over a 10 km × 8 km sub-image centered on the scintillometer XLAS transect along a path length of 4 km. Modeled ET weighted by the XLAS footprint was validated using daily ET estimates derived from the XLAS observations. Better results are obtained for 2012-2013 than 2013-2014, and it is shown that current SAMIR parameterization does not allow the simulation of interseasonal variations in ET. Moreover, results show a good agreement between observed and modeled ET especially in the mid-season of cereals crops (March to May) for both seasons; and during the cropping period of market gardening crops (cultivated generally from spring to the beginning of autumn). However, less accurate results are obtained when bare soil fraction (fallow and trees fields) outweighs the vegetation covered fraction *i.e.* at the beginning of both seasons.

In the second part, based on a more regional evaluation of the model performance with the XLAS dataset, the parameterization of SAMIR was revisited; parameters concerning the soil evaporation and related to the soil hydrodynamic properties were reevaluated. A new SAMIR parameters calibration was obtained from ET and soil moisture measurements of three irrigated and rainfed cereals fields. SAMIR was run over the study area for the four agricultural seasons; calibrated soil and crop parameters were only used for cereals while for the other land use classes parameters were derived from the FAO-56. Furthermore, the previous Kcb-NDVI relation for trees was discussed and replaced by another relation enabling a more realistic evapotranspiration. The irrigation rules were also revised and both market gardening and fruit trees were irrigated using drip irrigation which means that less soil surface is wetted. In addition, to reproduce the drip irrigation practice, manageable allowable depletion (MAD) was set to a low value (MAD = 0.2TAW and MAD=0.5TAW for both market gardening and fruit trees, respectively), which triggers frequent irrigation inputs. Although the overall results of modeled irrigation volumes remain almost the same (120 mm; RMSE of about 37 mm), monthly results improved significantly. Strong overestimation of irrigation in the first two months of the simulation was corrected. However, if the ET estimates agreed with XLAS observed ET for the wettest 2013-2014 season with significant improvement of modeled ET in the beginning of the simulation, we also observe a strong degradation for the 2012-2013 season.

In order to analyze an independent estimate of ET with the SEB approach, in the third part, a distributed energy balance model computed ET for three agricultural seasons 2012-2013, 2013-2014 and 2014-2015 using the "layer" version of the two-sources energy balance model SPARSE over the 10 km × 8 km sub-image centered on the scintillometer XLAS transect. Some of SPARSE parameters were remotely-sensed data while others were taken from the bibliography or taken from routine *in situ data* (meteorological data). Remotely-sensed data were acquired at the resolution of the MODIS sensor at 1 km, embarked on board of the satellites Terra and Aqua. No calibration was performed on the model parameters. SPARSE instantaneous estimates of sensible heat flux (H), latent heat flux (LE) and stress factor (SF) at Terra-MODIS and Aqua-MODIS overpass time, after being weighted by the instantaneous XLAS footrpint, were validated using XLAS measured H as well as XLAS derived LE and stress index, respectively. The good correspondence (R^2= 0.60 and 0.63 and RMSE=57.89 Wm^{-2} and 53.85 Wm^{-2}; for Terra and Aqua, respectively) between instantaneous H estimates and XLAS H measurements showed that the SPARSE model presents satisfactory accuracy. Results showed that, despite the fairly large scatter, the instantaneous LE can be suitably estimated at large scale (RMSE=47.20 Wm^{-2} and 43.20 Wm^{-2}; for Terra and Aqua, respectively and R^2= 0.55 for both satellites). Additionally, the comparison of modeled and observed water stress showed that most points were located within a 0.2 confidence interval, thus the general tendencies are well reproduced. Furthermore, the extrapolation from instantaneous to daily evapotranspiration was less obvious and three methods were tested based on the stress index, the evaporative fraction and the residual approach. Daily ET estimates were deemed acceptable and the daily LE derived from the XLAS agreed rather well with those modeled using SPARSE model (RMSE of 0.7 $mmday^{-1}$), which shows the potential of the model in water consumption monitoring over heterogeneous landscapes in semi-arid conditions, and especially to determine the average water stress.

■ Limitations of the methods and models

In summary, the results of the present work show that remote sensing based on multispectral images may be used, with a correct degree of accuracy and spatial representation, to calculate crop water and irrigation requirement. These results are in agreement with several previous studies with the same focuses in the Mediterranean region or under the Mediterranean climate. However, the methods developed in this thesis are, nevertheless limited by several corresponding assumptions. It is therefore useful to identify their applicability in order to allow them to be applied in appropriate cases and to identify possible improvement of these methods.

SAMIR model limitations

Despite the advantage of the SAMIR model in estimating the water balance components at field or perimeter scale with high spatial resolution, the high numbers of needed inputs whose estimations are likely uncertain at large scales remain the main drawback of this model.

For an appropriate estimation of ET, the SWB model requires knowledge of the water inputs (precipitation and irrigation) and an assessment of the extractable water from the soil, mostly derived from the soil moisture characteristics, whereas, significant biases are found mainly when dealing with large areas and long periods, due to the spatial variability of the water inputs uncertainties as well as the inaccuracy in estimating other flux components such as the deep drainage. Moreover, unknown initial soil moisture is a real issue in SAMIR parameters setting. Spin-up could be used to force the net change in soil moisture from the beginning to the end of agricultural season as it was shown in several researches (e.g.Lim *et al.*, 2012; Rodell *et al.*, 2005; Yang *et al.*, 2011).

In addition, the absence of a detailed soil map and the assumption of homogeneous soil properties for all land use classes is one of the main limitations of the SAMIR model.

The agricultural practices, especially irrigation, are difficult to parameterize. Indeed, the lack of information about real irrigation can induce unreliable estimations since irrigation is modeled by SAMIR as a predicted amount through a module triggering irrigation according to critical soil moisture levels. Moreover, the limited knowledge of the actual irrigation scheduling is a critical limitation for the validation protocol of modeled irrigation volumes.

Furthermore, the land use map is a crucial input data of SAMIR since all parameters setting is based on the land use classes. However, due to unavailability, one annual land use map was considered per season which does not take into account crop rotation which is common practice in the Kairouan plain (up to three crops per agricultural season). Hence, the strong overestimation of irrigation by SAMIR during the two first months of the simulation can be explained by the fact that late vegetables (e.g., pepper or tomatoes) are not completely removed while they are still green and not irrigated. The SAMIR model is not able to manage such partial vegetation cycles and irrigates as if it was the crop that will follow in the crop rotation (*i.e.*, the crop mentioned in the land use map).

Furthermore, the calibration dataset is minimal and the calibration protocol affects a limited number of parameters for a limited number of land uses classes. During this work, we noticed that the readily evaporable water (REW) parameter which constrains the soil evaporation is very sensitive parameter of SAMIR in our study context. In fact, in semi arid regions, the bare soil fraction (fallows and fruit trees interspaces) in a cropped area is considerable, especially during dry seasons. The estimation of this parameter generally relies on the FAO guidelines approach (Allen *et al.*, 1998). Although it was shown that under high evaporation conditions, the FAO-56 daily evaporation computed based on REW, is overestimated at the beginning of the dry down phase. Hence, to improve its estimation a reduction factor (m) proposed by Torres and Calera, (2010) and derived from the cereals crops calibration was applied for all land use class to deal with this problem in our case. However, for the fruit trees and market gardening crops, the calibrated REW was not a successful choice and gave less accurate results of ET estimates in comparison to the XLAS derived ET. Hence, this parameter was revisited and calibrated value was kept only for cereals crops while literature values were used for the other land use classes. Hence, results at monthly timescale were clearly improved but it remains that we have no clear idea of the way to reliably determine this parameter.

Finally, even though SPOT5 images were carefully pre-processed in order to get accurate remote sensing data, there could also be some uncertainties related to RS data. The fc-NDVI and Kcb-NDVI determination for each land use class was not an easy task and several assumptions (e.g. minimum NDVI of bare soil, maximum NDVI for fully covering crop, maximum Kcb, etc.) were necessary.

SPARSE model limitations

The precision in ET prediction with the SPARSE model is restricted by several assumptions and uncertainties. For instance, the instantaneous remote sensing data and mainly Tsurf are assumed reliable. Moreover, there is an issue with the MODIS pixel heterogeneity and notably the distribution of components at the intersection between the pixel and the XLAS footprint. Uncertainties are also due to half hourly forcing (meteorological and flux data) and XLAS data as well as to the extrapolation method from instantaneous to daily results.

In addition, H estimation depends mainly on T_{surf} and near surface air temperature (T_{air}). There is a strong relationship between T_{surf} and T_{air}, although the two temperatures have different physical meaning and responses to atmospheric conditions. In complex terrain, these differences are amplified; yet it is in these environments that remotely sensed T_{surf} may be most valuable in prediction and characterization of spatial-temporal patterns of T_{air}. Furthermore, the empirical estimation methods of soil heat flux G (three methods were tested) as well as the possible daily heat accumulation lead to possible errors in available energy estimation and in turn in residual LE estimation.

In situ data limitations

Although the scintillometer XLAS provides a feasible alternative to local micrometeorological techniques for measuring the sensible heat flux and validating satellite-derived estimates, it provides measurements of only large-scale area-average H but not the latent heat flux. Computation of LE as the energy balance residual term assumes that the Monin-Obukhov (MOST) similarity hypothesis (Monin and Obukhov, 1954), *i.e.* surface homogeneity and stationary flows are verified in our study area where topography is flat. This assumption can lead to possible uncertainties in observed ET computation.

■ Perspectives and future plans

➢ Operational perspectives

Regarding the impact on operational management of water, the main outcomes of this work are a potential contribution to decision support tools for decision makers in the Kairoun region. They could be applied at the GDA or the CRDA ("Commissariat Regional de Developpement Agricole", agricultural development regional office) scales, which are entities managing respectively groups of fields and groups of irrigated perimeters.

Indeed, irrigation requirement estimation in the irrigated perimeters (GDA) can be a valuable source of information for watershed arrangement, since it provides estimates of

the volumes of pumped water from the overexploited Kairouan aquifer. Moreover, water consumption in irrigated fields outside the GDAs limits, when associated with land use surveys and confronted to the known lawful drilling cartography, can help the CRDA water resources administrators to better locate the undeclared drillings. In addition, irrigation water consumption in the irrigated perimeters managed by the CRDA help assessing the efficiencies of these perimeters (Kharrou *et al.*, 2013). Furthermore, the adopted approach and methodologies in this PhD thesis can be applied at the national level or tested in other Tunisian regions. However, it should be mentioned that the outcomes of this work do not specifically target the field scale level, *i.e.* tools to be used at the farm level. Indeed, due to hypothesis regarding irrigation simulation, SAMIR results are not accurate enough at plot scale to provide actual irrigation requirements. In this respect, farmers can benefit from the SAT-IRR tool (Le Page, 2015), a Web tool that addresses the needs of irrigators. The main goal of this online application is to propose a date and dose of irrigation at plot scale. The theoretical bases and operational modus operandi of SAT-IRR are similar to those of SAMIR model with the major difference that the farmer interacts with the system to introduce the actual water inputs applied, a condition to compute the actual water budget of the plot. A water balance very close to the one described in the FAO-56 (Allen *et al.*, 1998) is calculated by combining satellite imagery as well as weather data and forecasts or projection into the future for crop development.

Finally, the following question must be asked: how to technically implement this potential information system (server, interface ...)? Presumably, it should be centralized at national level, with user interfaces at regional level in the CRDAs, etc. Moreover, the issue of decision makers and even farmers awareness about the research outcomes and their practical use should be mentioned. This can be achieved through meetings and training sessions on the information system data (e.g. estimated evapotranspiration, irrigation consumption…) that administers and farmers can use. Indeed, in the frame of AMETHYST project, a training session of SAMIR software was held in the CRDA of Kairouan, and a winter school was organized in which researchers, and administrators working on the Kairouan plain participated.

- Scientific perspectives

The increasing availability of high-resolution high repetitively remote sensing data (e.g. Sentinel-2 mission) offers an unprecedented opportunity to improve crop water balance monitoring. The Copernicus Sentinel-2 program makes it possible to have a full coverage of the major part of the Earth at least every 5 days in 13 different multispectral bands. This temporal resolution can allow real-time monitoring of crop development and its water status through the use of vegetation indices such as NDVI and/or Normalized Difference Water Index (NDWI), hence of the crop water consumption estimation. On the other hand, the possible cloudiness problem even in semi-arid areas like Tunisia can be resolved by combination of VIS-NIR high-resolution data of different sensors like Landsat8 or SPOT in a kind of "virtual constellation" of sensors.

Progress in SAMIR parameterization would require ideally crop specific information. Setup of flux measurements on vegetables and trees would allow parameters calibration

on these land use classes. In addition, careful consideration should be given to irrigation practices which are much uncertain although quite sensitive.

Improving the parameterization of the ET partition into transpiration and evaporation and further analysis of the evaporation coefficient Ke is an important research path especially over areas covered with trees; this is currently done by Chebbi *et al.* (2017, in progress) in a rainfed olive orchard in the Kairouan plain. This partition is generally studied at field scale for annual crops (e.g.Aouade *et al.*, 2016; Wu *et al.*, 2016; Xiao *et al.*, 2016) or orchards (e.g. Er-Raki, 2009; López-Olivari *et al.*, 2016). However, global- and regional-scale partitioning of ET is not accurately known since large-scale observations of ET, notwithstanding its partitioning, are not available. Perhaps, consequently, few researchers have diagnosed ET partitioning issues in land surface schemes, even though a better knowledge on this information would provide a powerful constraint on model physics, and is also of major interest for water management.

Moreover, efforts are undertaken to establish methods allowing the elaboration of seasonal land use maps (summer and winter maps) of the Kairouan plain using the Sentinel-2 images (Mabrouki, 2018 in progress). This would allow overcoming the problem of the only one land use map as input data of SAMIR.

Since SAMIR allows the use of either uniform or distributed soil properties data, the clay content map at 100 m spatial resolution produced by Shabou *et al.* (2015), which covers the Kairouan plain, can be used to enhance realism of the soil properties. The soil moisture and texture map produced by Gorrab *et al.* (2015) at the spatial resolution of the radar TerraSAR-X data (9m), but within a limited area (9 km × 5 km) of the Kairouan plain, can be also used. Efforts are undertaken to improve this work and reproduce soil moisture and texture map of the whole Kairouan plain using the high-resolution high repetitively Sentinel-1 data (Bousbih, 2018 in progress).

On the other hand, SPARSE results can be improved by i) being more efficient in the SPARSE model application using calibrated input data specific to our study area, especially input parameters to which the model is particularly sensitive such as the mean leaf width and the minimum stomatal resistance, ii) taking into account the heterogeneity of the 1km MODIS pixel by applying MODIS footprint, which is determined by the sensor's observation geometry and (iii) using a Land Surface Model applied at the field scale (Etchanchu *et al.*, 2017) to analyze the scaling properties from the field to the footprint of the XLAS and the MODIS pixels.

In addition, since agrometeorological models are sensitive to meteorological data, distributed meteo data can be used instead of single weather station data. Spatial interpolation of meteo data can be achieved based on meteorological measurements of one or more weather stations according to a Digital Elevation Model (Li and Heap, 2008). Otherwise, forcing agrometeorological model with the latest global atmospheric reanalysis ERA-Interim (Dee *et al.*, 2011) weather data is rather a promising research path. First efforts are undertaken by Farhani (2017) to statistically analyze these data in the Kairouan plain context and confront them to several meteorological stations data. The forcing of the SPARSE model by ERA-Interim data showed satisfactory results (instantaneous and daily ET) in comparison to those obtained using meteorological stations data.

Moreover, ET estimation by the SPARSE model depends mainly on TIR remote sensing data availability. Hence, the combination of TIR low-resolution data of different sensors such as MODIS and Sentinel-3 with high-resolution TIR data (when available) from sensors like Landsat8 can enhance the temporal continuity of ET estimates.

In fact, in order to provide further information about distributed soil water status over the studied areas, the TIR-derived ET products could be assimilated directly either in land surface or hydrological models. Moreover, the estimation of water stress coefficient K_s in the FAO-56 crop coefficient approach requires computing daily water balance for soil and root zone, including several parameters whose estimation is not straightforward. Consequently, K_s can be derived from remote sensing data using surface temperature derived from thermal infrared observations, since surface temperature and water status are intimately linked (Moran, 1994). TIR remote sensing data were assimilated into several SVAT models (Boegh *et al.*, 2004; Pellenq and Boulet, 2004), but also into FAO-56 method (Er-Raki *et al.*, 2008) on which is based the SAMIR model. Because of the complexity of most land surface models as well as the difficulty to specify the observation error on T_{surf}, , assimilation of TIR data in the SAMIR model to get actual soil water status remains very challenging.

However, in a future work, we plan to take advantage of the complementarities between the Soil Water Balance and Surface Energy Balance approaches (*i.e.* continuous but uncertain estimates using SWB due to poor soil water content control on one hand and sensitivity of SEB to the actual water stress but infrequent T_{surf} observations, on the other) to implement an assimilation scheme of the remotely-sensed surface temperature into land surface models. Therefore, since SAMIR is a state-space model, simulating continuous water balance components, in case of failure in estimating accurate values of ET, modeled actual ET using the observation model SPARSE, can be directly assimilated into SAMIR. SPARSE estimates corresponding to a high-resolution thermal infrared image acquisition (e.g. Landsat image, the 50-100 m/2-3 days mission project TRISHNA) would be specifically of high importance in order to likely steer the SAMIR model estimates to the right path.

References

A.

Abrams, M., 2000. The Advanced Spaceborne Thermal Emission and Reflection Radiometer (ASTER): data products for the high spatial resolution imager on NASA's Terra platform. international Journal of Remote sensing 21, 847-859.

Aeronet, Available online: http://aeronet.gsfc.nasa.gov/ (accessed on 10 June 2014).

Akdim, N., Alfieri, S., Habib, A., Choukri, A., Cheruiyot, E., Labbassi, K., Menenti, M., 2014. Monitoring of Irrigation Schemes by Remote Sensing: Phenology versus Retrieval of Biophysical Variables. Remote Sensing 6, 5815.

Alazard, M., Leduc, C., Travi, Y., Boulet, G., Ben Salem, A., 2015. Estimating evaporation in semi-arid areas facing data scarcity: Example of the El Haouareb dam (Merguellil catchment, Central Tunisia). Journal of Hydrology: Regional Studies 3, 265-284.

Allen, R., Irmak, A., Trezza, R., Hendrickx, J.M., Bastiaanssen, W., Kjaersgaard, J., 2011a. Satellite-based ET estimation in agriculture using SEBAL and METRIC. Hydrological Processes 25, 4011-4027.

Allen, R., Walter, I., Elliott, R., Howell, T., Itenfisu, D., Jensen, M., Snyder, R., 2005a. The ASCE standardized reference evapotranspiration equation. 2005. Reston, Virginia: American Society of Civil Engineers, 69.

Allen, R.G., Pereira, L.S., Howell, T.A., Jensen, M.E., 2011b. Evapotranspiration information reporting: I. Factors governing measurement accuracy. Agricultural Water Management 98, 899-920.

Allen, R.G., Pereira, L.S., Raes, D., Smith, M., 1998. Crop evapotranspiration-Guidelines for computing crop water requirements-FAO Irrigation and drainage paper 56. FAO, Rome 300, D05109.

Allen, R.G., Pereira, L.S., Smith, M., Raes, D., Wright, J.L., 2005b. FAO-56 dual crop coefficient method for estimating evaporation from soil and application extensions. Journal of irrigation and drainage engineering 131, 2-13.

Allen, R.G., Pruitt, W.O., Wright, J.L., Howell, T.A., Ventura, F., Snyder, R., Itenfisu, D., Steduto, P., Berengena, J., Yrisarry, J.B., Smith, M., Pereira, L.S., Raes, D., Perrier, A., Alves, I., Walter, I., Elliott, R., 2006. A recommendation on standardized surface resistance for hourly calculation of reference ETo by the FAO56 Penman-Monteith method. Agricultural Water Management 81, 1-22.

Allen Richard, G., Tasumi, M., Morse, A., Trezza, R., Wright James, L., Bastiaanssen, W., Kramber, W., Lorite, I., Robison Clarence, W., 2007. Satellite-Based Energy Balance for Mapping Evapotranspiration with Internalized Calibration (METRIC)—Applications. Journal of Irrigation and Drainage Engineering 133, 395-406.

Amri, R., 2013. Estimation régionale de l'évapotranspiration sur la plaine de Kairouan (Tunisie) à partir de données satellites multi-capteurs. Université Paul Sabatier - Toulouse III, p. 176.

Amri, R., Zribi, M., Lili-Chabaane, Z., Szczypta, C., Calvet, J.C., Boulet, G., 2014. FAO-56 dual model combined with multi-sensor remote sensing for regional evapotranspiration estimations. Remote Sensing 6, 5387-5406.

Anderson, M., Norman, J., Diak, G., Kustas, W., Mecikalski, J., 1997. A two-source time-integrated model for estimating surface fluxes using thermal infrared remote sensing. Remote sensing of environment 60, 195-216.

Anderson, M.C., Kustas, W.P., Norman, J.M., Hain, C.R., Mecikalski, J.R., Schultz, L., González-Dugo, M.P., Cammalleri, C., d'Urso, G., Pimstein, A., Gao, F., 2011. Mapping daily evapotranspiration at field to continental scales using geostationary and polar orbiting satellite imagery. Hydrol. Earth Syst. Sci. 15, 223-239.

Anderson, M.C., Norman, J.M., Mecikalski, J.R., Otkin, J.A., Kustas, W.P., 2007. A climatological study of evapotranspiration and moisture stress across the continental United States based on thermal remote sensing: 1. Model formulation. Journal of Geophysical Research: Atmospheres 112.

Andreas, E.L., 1988. Atmospheric stability from scintillation measurements. Applied optics 27, 2241-2246.

Andreu, A., González-Dugo, M., Polo, M., Padilla, F., Gavilán, P., 2011. Energy balance modeling of agricultural areas by remote sensing, Remote Sensing for Agriculture, Ecosystems, and Hydrology XIII. International Society for Optics and Photonics, p. 81740M.

Aouade, G., Ezzahar, J., Amenzou, N., Er-Raki, S., Benkaddour, A., Khabba, S., Jarlan, L., 2016. Combining stable isotopes, Eddy Covariance system and meteorological measurements for partitioning evapotranspiration, of winter wheat, into soil evaporation and plant transpiration in a semi-arid region. Agricultural Water Management 177, 181-192.

Arkin, P.A., Xie, P., 1994. The global precipitation climatology project: first algorithm intercomparison project. Bulletin of the American Meteorological Society 75, 401-419.

Assessment Millennium Ecosystem, 2005. Ecosystems and human well-being: wetlands and water. World resources institute, Washington, DC 5.

B.

Baccour, H., Slimani, M., Cudennec, C., 2012. Structures spatiales de l'évapotranspiration de référence et des variables climatiques corrélées en Tunisie. Hydrological Sciences Journal 57, 818-829.

Bacour, C., Baret, F., Béal, D., Weiss, M., Pavageau, K., 2006. Neural network estimation of LAI, fAPAR, fCover and LAI× C ab, from top of canopy MERIS reflectance data: Principles and validation. Remote sensing of environment 105, 313-325.

Bai, J., Liu, S., Mao, D., 2009. Area-averaged evapotranspiration fluxes measured from large aperture scintillometer in the Hai River basin, River Basin Research And Planning Approach, edited by: Zhang, H., Zhao, R., and Zhoa, H., Orient ACAD Forum, Marrickville, Australia, pp. 331-340.

Baize, D., 2000. Guide des analyses en pédologie. 2nd edition. INRA, France.

Baldocchi, D.D., 2003. Assessing the eddy covariance technique for evaluating carbon dioxide exchange rates of ecosystems: past, present and future. Global Change Biology 9, 479-492.

Barbery, J., Mohdi, M., 1987. Carte des ressources en sols de la Tunisie (1/200 000). Feuille de Kairouan, Ministère de l'Agriculture, Tunis, Tunisie.

Baret, F., Guyot, G., Major, D., 1989. Crop biomass evaluation using radiometric measurements. Photogrammetria 43, 241-256.

Bastiaanssen, W.G., Molden, D.J., Makin, I.W., 2000. Remote sensing for irrigated agriculture: examples from research and possible applications. Agricultural water management 46, 137-155.

Bastiaanssen, W.G.M., 1995. Regionalization of surface flux densities and moisture indicators in composite terrain; a remote sensing approach under clear skies in mediterranean climates. SC-DLO, Wageningen.

Beringer, J., McIlwaine, S., Lynch, A., Chapin, F., Bonan, G., 2002. The use of a reduced form model to assess the sensitivity of a land surface model to biotic surface parameters. Climate Dynamics 19, 455-466.

Berni, J.A.J., Zarco-Tejada, P.J., Suarez, L., Fereres, E., 2009. Thermal and Narrowband Multispectral Remote Sensing for Vegetation Monitoring From an Unmanned Aerial Vehicle. IEEE Transactions on Geoscience and Remote Sensing 47, 722-738.

Beven, K., 2006. A manifesto for the equifinality thesis. Journal of Hydrology 320, 18-36.

Black, T.A., Tanner, C., Gardner, W., 1970. Evapotranspiration from a snap bean crop. Agronomy Journal 62, 66-69.

Boegh, E., Soegaard, H., 2004. Remote sensing based estimation of evapotranspiration rates. International Journal of Remote Sensing 25, 2535-2551.

Boegh, E., Thorsen, M., Butts, M.B., Hansen, S., Christiansen, J.S., Abrahamsen, P., Hasager, C.B., Jensen, N.O., van der Keur, P., Refsgaard, J.C., Schelde, K., Soegaard, H., Thomsen, A., 2004. Incorporating remote sensing data in physically based distributed agro-hydrological modelling. Journal of Hydrology 287, 279-299.

Bonan, G.B., 2008. Forests and climate change: forcings, feedbacks, and the climate benefits of forests. science 320, 1444-1449.

Boudhina, N., Masmoudi, M.M., Mechlia, N.B., Zitouna, R., Mekki, I., Prévot, L., Jacob, F., 2017. Evapotranspiration of Wheat in a Hilly Topography: Results from Measurements Using a Set of Eddy Covariance Stations, Water and Land Security in Drylands. Springer, pp. 67-76.

Boulet, G., 1999. Modélisation des changements d'échelle et prise en compte des hétérogénéités de surface et de leur variabilité spatiale dans les interactions sol-végétation-atmosphère. Université de Joseph Fourier, Grenoble, France, p. 216.

Boulet, G., 2003. Calcul de l'évapotranspiration de référence ET0 selon la méthode FAO (Allen *et al.* 98). Université Cady Ayyad, Marrakech, Maroc.

Boulet, G., Braud, I., Vauclin, M., 1997. Study of the mechanisms of evaporation under arid conditions using a detailed model of the soil–atmosphere continuum. Application to the EFEDA I experiment. Journal of Hydrology 193, 114-141.

Boulet, G., Chehbouni, A., Gentine, P., Duchemin, B., Ezzahar, J., Hadria, R., 2007. Monitoring water stress using time series of observed to unstressed surface temperature difference. Agricultural and Forest Meteorology 146, 159-172.

Boulet, G., Mougenot, B., Lhomme, J.P., Fanise, P., Lili-Chabaane, Z., Olioso, A., Bahir, M., Rivalland, V., Jarlan, L., Merlin, O., Coudert, B., Er-Raki, S., Lagouarde, J.P., 2015. The SPARSE model for the prediction of water stress and evapotranspiration components from thermal infra-red data and its evaluation over irrigated and rainfed wheat. Hydrol. Earth Syst. Sci. 19, 4653-4672.

Boulet, G., Olioso, A., Ceschia, E., Marloie, O., Coudert, B., Rivalland, V., Chirouze, J., Chehbouni, G., 2012. An empirical expression to relate aerodynamic and surface temperatures for use within single-source energy balance models. agricultural and forest meteorology 161, 148-155.

Bounoua, L., Zhang, P., Thome, K., Masek, J., Safia, A., Imhoff, M.L., Wolfe, R.E., 2015. Mapping Biophysical Parameters for Land Surface Modeling over the Continental US Using MODIS and Landsat. Dataset Papers in Science 2015, 11.

Bousbih, S., 2017 (In progress). Synergie optique/radar pour l'estimation des états de surfaces continetales. Carthage University, INAT, Tunis, Tunisie.

Bouttier, F., Courtier, P., 2002. Data assimilation concepts and methods March 1999. Meteorological training course lecture series. ECMWF, 59.

Bouzaiane, S., Laforgue, A., 1986. Monographie hydrologique des oueds Zéroud et Merguellil. . DGRE–ORSTOM Tunis, Tunisie. .

Brouwer, C., Prins, K., Heibloem, M., 1989. Training manual no. 4 : Irrigation Water Management: Irrigation Scheduling. Food and Agriculture Organization of the United Nations, Rome, Italy.

Brunet Y., L.P., Flura D., Baculat B., 1995. La mesure des flux turbulents, Tome 1 : De la plante au couvert végétal, INRA Editions ed, Presented at Ecole-Chercheurs en Bioclimatologie, Le Croisic, FRA (1995-04-03 - 1995-04-07).Paris (France), pp. 441-459.

Brunsell, N.A., Ham, J.M., Arnold, K.A., 2011. Validating remotely sensed land surface fluxes in heterogeneous terrain with large aperture scintillometry. International Journal of Remote Sensing 32, 6295-6314.

Brutsaert, W., 2013. Evaporation into the atmosphere: theory, history and applications. Springer Science & Business Media.

Brutsaert, W., Sugita, M., 1992. Application of self-preservation in the diurnal evolution of the surface energy budget to determine daily evaporation. Journal of Geophysical Research: Atmospheres 97, 18377-18382.

Burba, G.G., Verma, S.B., Kim, J., 1999. Surface energy fluxes of Phragmites australis in a prairie wetland. Agricultural and Forest Meteorology 94, 31-51.

C.

Calcagno, G., Mendicino, G., Monacelli, G., Senatore, A., Versace, P., 2007. Distributed estimation of actual evapotranspiration through remote sensing techniques, Methods and tools for drought analysis and management. Springer, pp. 125-147.

Calera-Belmonte, A., Jochum, A.M., GarcÍa, A.C., Rodríguez, A.M., Fuster, P.L., 2005. Irrigation management from space: Towards user-friendly products. Irrigation and Drainage Systems 19, 337-353.

Calera, A., Campos, I., Osann, A., D'Urso, G., Menenti, M., 2017. Remote Sensing for Crop Water Management: From ET Modelling to Services for the End Users. Sensors 17, 1104.

Cammalleri, C., Anderson, M., Gao, F., Hain, C., Kustas, W., 2014. Mapping daily evapotranspiration at field scales over rainfed and irrigated agricultural areas using remote sensing data fusion. Agricultural and forest meteorology 186, 1-11.

Cammalleri, C., Ciraolo, G., Minacapilli, M., Rallo, G., 2013. Evapotranspiration from an Olive Orchard using Remote Sensing-Based Dual Crop Coefficient Approach. Water Resources Management 27, 4877-4895.

Campos, I., González-Piqueras, J., Carrara, A., Villodre, J., Calera, A., 2016. Estimation of total available water in the soil layer by integrating actual evapotranspiration data in a remote sensing-driven soil water balance. Journal of Hydrology 534, 427-439.

Carlson, T., 2007. An Overview of the "Triangle Method" for Estimating Surface Evapotranspiration and Soil Moisture from Satellite Imagery. Sensors (Basel, Switzerland) 7, 1612-1629.

Čermák, J., Deml, M., Penka, M., 1973. A new method of sap flow rate determination in trees. Biologia plantarum 15, 171-178.

Chahbi, A., 2015. Prévision du Rendement des Céréales à Partir des Mesures de Télédétection, Application sur le Bassin de Merguellil. University of Carthage, National Agronomic Institute of Tunisia (INAT), Tunis, Tunisia.

Chahbi, A., Zribi, M., Lili-Chabaane, Z., Duchemin, B., Shabou, M., Mougenot, B., Boulet, G., 2014. Estimation of the dynamics and yields of cereals in a semi-arid area using remote sensing and the safy growth model. . Int. J. Remote Sens. 35, 1004–1028.

Chahbi, A., Zribi, M., Saadi, S., Simonneaux, V., Lili Chabaane, Z. , 2016. Classification et caractérisation de la couverture végétale dans un milieu semi aride en utilisant des images SPOT 5, Deuxième Workshop AMETHYST, 11 Février 2016, Marrakech, Maroc.

Chávez, J., Neale, C.M.U., Hipps, L.E., Prueger, J.H., Kustas, W.P., 2005. Comparing Aircraft-Based Remotely Sensed Energy Balance Fluxes with Eddy Covariance Tower Data Using Heat Flux Source Area Functions. Journal of Hydrometeorology 6, 923-940.

Chebbi, W., Boulet, G., Le Dantec, V., Lili Chabaane, Z., Fanise, P., Mougenot, B., Ayari, H., 2017 (In progress). Analysis of evapotranspiration components of a rain-fed olive orchard during three contrasting years in a semi-arid climate. agricultural and forest meteorology.

Chehbouni, A., Lo Seen, D., Njoku, E.G., Lhomme, J.P., Monteny, B., Kerr, Y.H., 1997. Estimation of sensible heat flux over sparsely vegetated surfaces. Journal of Hydrology 188-189, 855-868.

Chehbouni, A., Watts, C., Lagouarde, J.P., Kerr, Y.H., Rodriguez, J.C., Bonnefond, J.M., Santiago, F., Dedieu, G., Goodrich, D.C., Unkrich, C., 2000. Estimation of heat and momentum fluxes over complex terrain using a large aperture scintillometer. Agricultural and Forest Meteorology 105, 215-226.

Chirouze, J., 2009. L'estimation spatialisé de l'évapotranspiration et le suivi de l'irrigation en milieu semi-aride à partir des données de l'infrarouge thermique, SDUEE: Hydrologie,Hydrochimie, sol, Environnement. Université Toulouse 3 Paul Sabatier, Toulouse, France, p. 193.

Chirouze, J., Boulet, G., Jarlan, L., Fieuzal, R., Rodriguez, J.C., Ezzahar, J., Er-Raki, S., Bigeard, G., Merlin, O., Garatuza-Payan, J., Watts, C., Chehbouni, G., 2014. Intercomparison of four remote-sensing-based energy balance methods to retrieve

surface evapotranspiration and water stress of irrigated fields in semi-arid climate. Hydrol. Earth Syst. Sci. 18, 1165-1188.

Choudhury, B.J., Ahmed, N.U., Idso, S.B., Reginato, R.J., Daughtry, C.S.T., 1994. Relations between evaporation coefficients and vegetation indices studied by model simulations. Remote Sens. Environ 50, 1-17.

Choudhury, B.J., Idso, S.B., Reginato, R.J., 1987. Analysis of an empirical model for soil heat flux under a growing wheat crop for estimating evaporation by an infrared-temperature based energy balance equation. Agricultural and Forest Meteorology 39, 283-297.

Clark, P., Roberts, N., Lean, H., Ballard, S.P., Charlton-Perez, C., 2016. Convection-permitting models: a step-change in rainfall forecasting. Meteorological Applications 23, 165-181.

Clement, R., Moncreif, J., 2007. EdiRe Software VS 1.4. 3.1170. University of Edinburgh. https://www.geos.ed.ac.uk/homes/jbm/micromet/EdiRe/ accessible on 13th October 2017.

Clevers, J.G.P.W., 1989. Application of a weighted infrared-red vegetation index for estimating leaf Area Index by Correcting for Soil Moisture. Remote Sensing of Environment 29, 25-37.

Colaizzi, P.D., Barnes, E.M., Clarke, T.R., Choi, C.Y., Waller, P.M., 2003. Estimating soil moisture under low frequency surface irrigation using crop water stress index. Journal of irrigation and drainage engineering 129, 27-35.

Courault, D., Clastre, P., Cauchi, P., Delécolle, R., 1998. Analysis of spatial variability of air temperature at regional scale using remote sensing data and a SVAT model, Proceedings of the First International Conference on Geospatial Information in Agriculture and Forestry.

Courault, D., Seguin, B., Olioso, A., 2005. Review on estimation of evapotranspiration from remote sensing data: From empirical to numerical modeling approaches. Irrigation and Drainage Systems 19, 223-249.

Crow, W.T., Kustas, W.P., Prueger, J.H., 2008. Monitoring root-zone soil moisture through the assimilation of a thermal remote sensing-based soil moisture proxy into a water balance model. Remote Sensing of Environment 112, 1268-1281.

Cudennec, C., Beji, R. Le Goulven, P., et Bachta, M. S., 2005. Analyse des interactions entre ressources en eau et usages agricoles dans le bassin versant de l'oued Merguellil, Tunisie Centrale. In :

Gestion intégrée de l'eau au sein d'un bassin versant, Le Goulven P., Bouarfa S., Kuper M. (Ed.), CEMAGREFCIRAD-IRD, Montpellier, 5p. .

Cudennec, C., Calvez, R., Pouget, J.-C., Kingumbi, A., Le Goulven, P., 2003. Constitution et structuration territoriales des ressources, des impacts et des risques hydrologiques au sein du bassin du Merguellil. Perspectives de modélisation hydrologique pour la transposition d'approches de gestion, Atelier du PCSI (Programme Commun Systèmes Irrigués) sur la Gestion Intégrée de l'Eau au Sein d'un Bassin Versant. Cirad - IRD - Cemagref, Montpellier, France, p. 11 p.

D.

Danelichen, V.H.d.M., Biudes, M.S., Souza, M.C., Machado, N.G., Silva, B.B.d., Nogueira, J.d.S., 2014. Estimation of soil heat flux in a neotropical Wetland region using remote sensing techniques. Revista Brasileira de Meteorologia 29, 469-482.

De Bruin, H.A.R., Wang, J., 2017. Scintillometry: a review, 21st April 2017 ed. Researchgate, p. 44.

Deardorff, J., 1978. Efficient prediction of ground surface temperature and moisture, with inclusion of a layer of vegetation. Journal of Geophysical Research: Oceans 83, 1889-1903.

Dee, D.P., Uppala, S.M., Simmons, A.J., Berrisford, P., Poli, P., Kobayashi, S., Andrae, U., Balmaseda, M.A., Balsamo, G., Bauer, P., Bechtold, P., Beljaars, A.C.M., van de Berg, L., Bidlot, J., Bormann, N., Delsol, C., Dragani, R., Fuentes, M., Geer, A.J., Haimberger, L., Healy, S.B., Hersbach, H., Hólm, E.V., Isaksen, L., Kållberg, P., Köhler, M., Matricardi, M., McNally, A.P., Monge-Sanz, B.M., Morcrette, J.J., Park, B.K., Peubey, C., de Rosnay, P., Tavolato, C., Thépaut, J.N., Vitart, F., 2011. The ERA-Interim reanalysis: configuration and performance of the data assimilation system. Quarterly Journal of the Royal Meteorological Society 137, 553-597.

Delogu, E., Boulet, G., Olioso, A., Coudert, B., Chirouze, J., Ceschia, E., Le Dantec, V., Marloie, O., Chehbouni, G., Lagouarde, J.P., 2012. Reconstruction of temporal variations of evapotranspiration using instantaneous estimates at the time of satellite overpass. Hydrol. Earth Syst. Sci. 16, 2995-3010.

Dhrubajyoti, S., 2009. Water Resources Engineering. . IIT Kharagpur, India.

Doorenbos, J., Pruitt, W.O., 1977. Crop water requirements.FAO Irrigation and Drainage Paper No. 24. FAO, Rome, Italy.

Douglas, E.M., Jacobs, J.M., Sumner, D.M., Ray, R.L., 2009. A comparison of models for estimating potential evapotranspiration for Florida land cover types. Journal of Hydrology 373, 366-376.

Duan, S.-B., Li, Z.-L., Cheng, J., Leng, P., 2017. Cross-satellite comparison of operational land surface temperature products derived from MODIS and ASTER data over bare soil surfaces. ISPRS Journal of Photogrammetry and Remote Sensing 126, 1-10.

Duchaufour, P., 1995. Pédologie. Sol, végétation, environnement. 4th Edition. Masson, Paris, France.

Dwyer, J., Schmidt, G., 2006. The MODIS Reprojection Tool, in: Qu, J.J., Gao, W., Kafatos, M., Murphy, R.E., Salomonson, V.V. (Eds.), Earth Science Satellite Remote Sensing: Vol. 2: Data, Computational Processing, and Tools. Springer Berlin Heidelberg, Berlin, Heidelberg, pp. 162-177.

Dyer, A., 1961. Measurements of evaporation and heat transfer in the lower atmosphere by an automatic eddy-correlation technique. Quarterly Journal of the Royal Meteorological Society 87, 401-412.

Dyer, A., Hicks, B., 1970. Flux-gradient relationships in the constant flux layer. Quarterly Journal of the Royal Meteorological Society 96, 715-721.

E.

Eckhardt, D., Verdin, J., Lyford, G., 1990. Automated update of an irrigated lands GIS using SPOT HRV imagery. Photogrammetric Engineering and Remote Sensing 56, 1515-1522.

Er-Raki, S., Chehbouni, A., Duchemin, B., 2010. Combining Satellite Remote Sensing Data with the FAO-56 Dual Approach for Water Use Mapping In Irrigated Wheat Fields of a Semi-Arid Region. Remote Sensing 2, 375-387.

Er-Raki, S., Chehbouni, A., Guemouria, N., Duchemin, B.ı., Ezzahar, J., Hadria, R., 2007. Combining FAO-56 model and ground-based remote sensing to estimate water consumptions of wheat crops in a semi-arid region. Agricultural water management 87, 41-54.

Er-Raki, S., Chehbouni, A., Guemouria, N., Ezzahar, J., Khabba, S., Boulet, G., Hanich, L., 2009. Citrus orchard evapotranspiration: comparison between eddy covariance measurements and the FAO-56 approach estimates. Plant Biosystems 143, 201-208.

Er-Raki, S., Chehbouni, A., Hoedjes, J., Ezzahar, J., Duchemin, B., Jacob, F., 2008. Improvement of FAO-56 method for olive orchards through sequential assimilation of thermal infrared-based estimates of ET. Agricultural Water Management 95, 309-321.

Er-Raki, S., Chehbouni, A., Ezzahar, J., Khabba, S., Boulet, G., Hanich, L. and Williams, D., 2009. Evapotranspiration partitioning from Sap Flow and Eddy Covariance techniques for olive orchards in semi-arid region. . Acta Hort. (ISHS) 846, 201-208.

ESA, 2017. SENTINEL Overview. https://sentinels.copernicus.eu, (accessed on 1st November 2017).

Etchanchu, J., Rivalland, V., Gascoin, S., Cros, J., Tallec, T., Brut, A., Boulet, G., 2017. Effects of high spatial and temporal resolution Earth observations on simulated hydrometeorological variables in a cropland (southwestern France). Hydrol. Earth Syst. Sci. 21, 5693-5708.

Ezzahar, J., Chehbouni, A., Hoedjes, J., Ramier, D., Boulain, N., Boubkraoui, S., Cappelaere, B., Descroix, L., Mougenot, B., Timouk, F., 2009. Combining scintillometer measurements and an aggregation scheme to estimate area-averaged latent heat flux during the AMMA experiment. Journal of Hydrology 375, 217-226.

F.

Falge, E., M. Aubinet, P.S. Bakwin, D. Baldocchi, P. Berbigier, C. Bernhofer, T.A. Black, R. Ceulemans, K.J. Davis, A.J. Dolman, A. Goldstein, M.L. Goulden, A. Granier, D.Y. Hollinger, P.G. Jarvis, N. Jensen, K. Pilegaard, G. Katul, P. Kyaw Tha Paw, B.E. Law, A. Lindroth, D. Loustau, Y. Mahli, R. Monson, P. Moncrieff, E. Moors, J.W. Munger, T. Meyers, W. Oechel, E.-D. Schulze, H. Thorgeirsson, J. Tenhunen, R. Valentini, S.B. Verma, T. Vesala, and S.C. Wofsy. , 2017. FLUXNET Research Network Site Characteristics, Investigators, and Bibliography, 2016. ORNL DAAC, Oak Ridge, Tennessee, USA. https://doi.org/10.3334/ORNLDAAC/1530.

Fang, H., Wei, S., Liang, S., 2012. Validation of MODIS and CYCLOPES LAI products using global field measurement data. Remote Sensing of Environment 119, 43-54.

Farahani, H.J., Howell, T.A., Shuttleworth, W.J., Bausch, W.C., 2007. Evapotranspiration: progress in measurement and modeling in agriculture. Transactions of the ASABE 50, 1627-1638.

Farhani, N., 2017. Spatialisation des variables météorologiques à l'aide des variables auxiliaires sur le bassin de la plaine du Merguellil, Tunisie. University of Carthage, Tunis, Tunisia.

Fassnacht, K.S., Gower, S.T., Norman, J.M., McMurtric, R.E., 1994. A comparison of optical and direct methods for estimating foliage surface area index in forests. agricultural and forest meteorology 71, 183-207.

Fensholt, R., Sandholt, I., Rasmussen, M.S., 2004. Evaluation of MODIS LAI, fAPAR and the relation between fAPAR and NDVI in a semi-arid environment using in situ measurements. Remote Sensing of Environment 91, 490-507.

Feuillette, S., 2001. Vers une gestion de la demande en eau en accès libre : exploration des interactions entre ressource et usages par les systèmes Multi-Agent. Application à la nappe de Kairouan. University of Montpellier II, Montpellier, France, p. 344.

Foken, T., 2008. The energy balance closure problem: an overview. Ecological Applications 18, 1351-1367.

Foken, T., Leuning, R., Oncley, S.R., Mauder, M., Aubinet, M., 2012. Corrections and data quality control, Eddy covariance. Springer, pp. 85-131.

Foken, T., Wichura, B., 1996. Tools for quality assessment of surface-based flux measurements. agricultural and forest meteorology 78, 83-105.

Fradi, F., 2017. Comparison between irrigation groundwater withdrawals and crop water requirements estimated using remote sensing in the Kairouan plain. IRA-Médenine/INAT, Tunisia.

Fratini, G., Mauder, M., 2014. Towards a consistent eddy-covariance processing: an intercomparison of EddyPro and TK3. Atmos. Meas. Tech. 7, 2273-2281.

Frérot, A., 2011. Water: Towards a Culture of Responsibility. UPNE.

Furby, S., Campbell, N., 2001. Calibrating images from different dates to 'like-value'digital counts. Remote Sensing of Environment 77, 186-196.

G.

Gao, B.-C., 1996. NDWI—A normalized difference water index for remote sensing of vegetation liquid water from space. Remote sensing of environment 58, 257-266.

Gao, F., Masek, J., Schwaller, M., Hall, F., 2006. On the blending of the Landsat and MODIS surface reflectance: Predicting daily Landsat surface reflectance. IEEE Transactions on Geoscience and Remote sensing 44, 2207-2218.

Garatuza-Payan, J., Watts, C.J., 2005. The use of remote sensing for estimating ET of irrigated wheat and cotton in Northwest Mexico. Irrigation and Drainage Systems 19, 301.

Gassert, F., Landis, M., Luck, M., Reig, P., Shiao, T., 2013. Aqueduct global maps 2.0. Water Resources Institute (WRI): Washington, DC, 202011-202012.

Ghosh, S.N., 2016. Eco-hydrological background, Environmental hydrology and hydraulics: eco-technological practices for sustainable development. CRC Press.

Gillespie, A., Rokugawa, S., Matsunaga, T., Cothern, J.S., Hook, S., Kahle, A.B., 1998. A temperature and emissivity separation algorithm for Advanced Spaceborne Thermal Emission and Reflection Radiometer (ASTER) images. IEEE transactions on geoscience and remote sensing 36, 1113-1126.

Giorgi, F., Avissar, R., 1997. Representation of heterogeneity effects in earth system modeling: Experience from land surface modeling. Reviews of Geophysics 35, 413-437.

Giorgi, F., Lionello, P., 2008. Climate change projections for the Mediterranean region. Global and planetary change 63, 90-104.

Glenn, E.P., Huete, A.R., Nagler, P.L., Hirschboeck, K.K., Brown, P., 2007. Integrating remote sensing and ground methods to estimate evapotranspiration. Critical Reviews in Plant Sciences 26, 139-168.

Glenn, E.P., Neale, C.M., Hunsaker, D.J., Nagler, P.L., 2011. Vegetation index-based crop coefficients to estimate evapotranspiration by remote sensing in agricultural and natural ecosystems. Hydrological Processes 25, 4050-4062.

Gonzalez-Dugo, M., Mateos, L., 2008. Spectral vegetation indices for benchmarking water productivity of irrigated cotton and sugarbeet crops. Agricultural Water Management 95, 48-58.

González-Dugo, M.P., Escuin, S., Cano, F., Cifuentes, V., Padilla, F.L.M., Tirado, J.L., Oyonarte, N., Fernández, P., Mateos, L., 2013. Monitoring evapotranspiration of irrigated crops using crop coefficients derived from time series of satellite images. II. Application on basin scale. Agricultural Water Management 125, 92-104.

Gorrab, A., 2016. Développement et validation de méthodologies pour le suivi des états de surface des sols agricoles nus par Télédetection radar (bande X). Université Toulouse 3 Paul Sabatier, Toulouse, France, p. 217.

Gorrab, A., Zribi, M., Baghdadi, N., Mougenot, B., Fanise, P., Chabaane, Z., 2015. Retrieval of Both Soil Moisture and Texture Using TerraSAR-X Images. Remote Sensing 7, 10098.

Gorrab. A, 2016. Développement et validation de méthodologies pour le suivi des états de surface des sols agricoles nus par Télédetection radar (bande X). Université Toulouse 3 Paul Sabatier, Toulouse, France, p. 217.

Gowda, P.H., Chávez, J.L., Howell, T.A., Marek, T.H., New, L.L., 2008. Surface energy balance based evapotranspiration mapping in the Texas high plains. Sensors 8, 5186-5201.

Grant, D., 1975. Comparison of evaporation measurements using different methods. Quarterly Journal of the Royal Meteorological Society 101, 543-550.

Green, A.E., Hayashi, Y., 1998. Use of the scintillometer technique over a rice paddy. Journal of Agricultural Meteorology 54, 225-234.

Gu, J., Li, X., Huang, C., Okin, G.S., 2009. A simplified data assimilation method for reconstructing time-series MODIS NDVI data. Advances in Space Research 44, 501-509.

Guermazi, E., Bouaziz, M., Zairi, M., 2016. Water irrigation management using remote sensing techniques: a case study in Central Tunisia. Environmental Earth Sciences 75, 202.

Gurney, R., Hsu, A., 1990. Relating evaporative fraction to remotely sensed data at the FIFE site.

Gutman, G., Ignatov, A., 1998. The derivation of the green vegetation fraction from NOAA/AVHRR data for use in numerical weather prediction models. International Journal of Remote Sensing 19, 1533-1543.

Guyot, G., 1999. Climatologie de l'environnement, Dunod Edition.Paris, France.

H.

Habaieb, H., Masmoudi Charfi, C., 2003. Calcul des besoins en eau des principales cultures exploitées au nord de la Tunisie : estimation de l'évapotranspiration de référence par différentes formules empiriques (cas des régions de Tunis, Béja et Bizerte) . Science et changements planétaires. Sécheresse 14(4), 257-265.

Hagolle, O., Huc, M., Villa Pascual, D., Dedieu, G., 2015. A multi-temporal and multi-spectral method to estimate aerosol optical thickness over land, for the atmospheric correction of formosat-2, Landsat, venμs and Sentinel-2 images. Remote Sensing 7, 2668-2691.

Hain, C.R., Mecikalski, J.R., Anderson, M.C., 2009. Retrieval of an Available Water-Based Soil Moisture Proxy from Thermal Infrared Remote Sensing. Part I: Methodology and Validation. Journal of Hydrometeorology 10, 665-683.

Hartogensis, O.K., Watts, C.J., Rodriguez, J.-C., Bruin, H.A.R.D., 2003. Derivation of an Effective Height for Scintillometers: La Poza Experiment in Northwest Mexico. Journal of Hydrometeorology 4, 915-928.

Heilman, J.L., Heilman, W.E., Moore, D.G., 1982. Evaluating the Crop Coefficient Using Spectral Reflectance1. Agronomy Journal 74, 967-971.

Hemakumara, H.M., Chandrapala, L., Moene, A.F., 2003. Evapotranspiration fluxes over mixed vegetation areas measured from large aperture scintillometer. Agricultural Water Management 58, 109-122.

Hicks, B., 1970. The measurement of atmospheric fluxes near the surface: a generalized approach. Journal of Applied Meteorology 9, 386-388.

Hill, R., Clifford, S.F., Lawrence, R.S., 1980. Refractive-index and absorption fluctuations in the infrared caused by temperature, humidity, and pressure fluctuations. JOSA 70, 1192-1205.

Hoedjes, J., Chehbouni, A., Ezzahar, J., Escadafal, R., De Bruin, H., 2007. Comparison of large aperture scintillometer and eddy covariance measurements: Can thermal infrared data be used to capture footprint-induced differences? Journal of Hydrometeorology 8, 144-159.

Hoedjes, J.C.B., Chehbouni, A., Jacob, F., Ezzahar, J., Boulet, G., 2008. Deriving daily evapotranspiration from remotely sensed instantaneous evaporative fraction over olive orchard in semi-arid Morocco. Journal of Hydrology 354, 53-64.

Holmes, J., 1984. Measuring evapotranspiration by hydrological methods. Agricultural Water Management 8, 29-40.

Horst, T., Weil, J., 1992. Footprint estimation for scalar flux measurements in the atmospheric surface layer. Boundary-Layer Meteorology 59, 279-296.

Houlès, V., El Hajj, M., Bégué, A., 2006. Radiometric normalization of a Spot 4 and Spot 5 time series of images (ISLE-REUNION) for agriculture applications.

Howell, T.A., Schneider, A.D., Jensen, M.E., 1991. History of lysimeter design and use for evapotranspiration measurements, Lysimeters for evapotranspiration and environmental measurements. ASCE, pp. 1-9.

Huete, A., Jackson, R., Post, D., 1985. Spectral response of a plant canopy with different soil backgrounds. Remote sensing of environment 17, 37-53.

Huete, A.R., 1988. A soil-adjusted vegetation index (SAVI). Remote sensing of environment 25, 295-309.

Huffman, G.J., Bolvin, D.T., Nelkin, E.J., Wolff, D.B., Adler, R.F., Gu, G., Hong, Y., Bowman, K.P., Stocker, E.F., 2007. The TRMM multisatellite precipitation analysis (TMPA): Quasi-global, multiyear, combined-sensor precipitation estimates at fine scales. Journal of hydrometeorology 8, 38-55.

Hunink, J., Eekhout, J., Vente, J., Contreras, S., Droogers, P., Baille, A., 2017. Hydrological Modelling using Satellite-Based Crop Coefficients: A Comparison of Methods at the Basin Scale. Remote Sensing 9, 174.

Hunsaker, D., Barnes, E., Clarke, T., Fitzgerald, G., Pinter Jr, P.J., 2005a. Cotton irrigation scheduling using remotely sensed and FAO-56 basal crop coefficients. Transactions of the ASAE 48, 1395-1407.

Hunsaker, D.J., Pinter, P.J., Kimball, B.A., 2005b. Wheat basal crop coefficients determined by normalized difference vegetation index. Irrigation Science 24, 1-14.

Hunt, E.R., Rock, B.N., 1989. Detection of changes in leaf water content using near-and middle-infrared reflectances. Remote sensing of environment 30, 43-54.

I.

Idso, S.B., Jackson, R.D., Pinter, P.J., Reginato, R.J., Hatfield, J.L., 1981. Normalizing the stress-degree-day parameter for environmental variability. Agricultural Meteorology 24, 45-55.

Ihuoma, S.O., Madramootoo, C.A., 2017. Recent advances in crop water stress detection. Computers and Electronics in Agriculture 141, 267-275.

J.

J. Trout, T., F. Johnson, L., Gartung, J., 2008. Remote Sensing of Canopy Cover in Horticultural Crops. HortScience 43, 333-337

Jabloun, M., Sahli, A., 2008. Evaluation of FAO-56 methodology for estimating reference evapotranspiration using limited climatic data: Application to Tunisia. Agricultural Water Management 95, 707-715.

Jackson, R.D., Moran, M.S., Gay, L.W., Raymond, L.H., 1987. Evaluating evaporation from field crops using airborne radiometry and ground-based meteorological data. Irrigation Science 8, 81-90.

Jensen, M.E., Burman, R.D., Allen, R.G., 1990. Evapotranspiration and irrigation water requirements. ASCE.

Jerbi, H., Massuel, S., Tarhouni, J., Lachaal, F., Riaux, J., Burte, J., Leduc, C., 2014. La nappe de la plaine de Kairouan soumise aux changements globaux: quels effets sur la ressource ?, 3ème Colloque International Eau-Climat'2014: Regards Croisés Nord-Sud,October 2014, Tunis, Tunisia, p. 6.

Jiapaer, G., Chen, X., Bao, A., 2011. A comparison of methods for estimating fractional vegetation cover in arid regions. agricultural and forest meteorology 151, 1698-1710.

Johnson, C., 2012. Mathematical Physics of BlackBody Radiation. Icarus iDucation, School of Computer Science and Communication, Royal Institute of Technology, Stockholm.

Jordan, C.F., 1969. Derivation of leaf-area index from quality of light on the forest floor. Ecology 50, 663-666.

Jupp, D.L., Tian, G., McVicar, T.R., Qin, Y., Fuqin, L., 1998. Soil moisture and drought monitoring using remote sensing I: theoretical background and methods. EOC Report1, 16-21.

K.

Kadi, A., 2002. Modèle de simulation régional agricole et aide à la décision pour une gestion stratégique de la demande en eau. Cas de la plaine de Kairouan en Tunisie. CIHEAM-IAMM, Montpellier, France, p. 140.

Kalma, J., Jupp, D., 1990. Estimating evaporation from pasture using infrared thermometry: evaluation of a one-layer resistance model. Agricultural and Forest Meteorology 51, 223-246.

Kalma, J.D., McVicar, T.R., McCabe, M.F., 2008. Estimating land surface evaporation: A review of methods using remotely sensed surface temperature data. Surveys in Geophysics 29, 421-469.

Kanemasu, E.T., 1974. Seasonal canopy reflectance patterns of wheat, sorghum, and soybean. Remote Sensing of Environment 3, 43-47.

Kaufman, Y.J., Tanre, D., 1992. Atmospherically resistant vegetation index (ARVI) for EOS-MODIS. IEEE transactions on Geoscience and Remote Sensing 30, 261-270.

Kharrou, M.H., Le Page, M., Chehbouni, A., Simonneaux, V., Er-Raki, S., Jarlan, L., Ouzine, L., Khabba, S., Chehbouni, G., 2013. Assessment of Equity and Adequacy of Water Delivery in Irrigation Systems Using Remote Sensing-Based Indicators in Semi-Arid Region, Morocco. Water Resources Management 27, 4697-4714.

Kingumbi, A., Bargaoui, Z., Ledoux, E., Besbes, M., Hubert, P., 2007. Modélisation hydrologique stochastique d'un bassin affecté par des changements d'occupation: cas du Merguellil en Tunisie centrale / Hydrological stochastic modelling of a basin affected by land-use changes: case of the Merguellil basin in central Tunisia. Hydrological Sciences Journal 52, 1232-1252.

Kjelgaard, J., Stockle, C., Black, R., Campbell, G., 1997. Measuring sap flow with the heat balance approach using constant and variable heat inputs. Agricultural and Forest Meteorology 85, 239-250.

Kohsiek, W., Meijninger, W.M.L., Debruin, H.A.R., Beyrich, F., 2006. Saturation of the Large Aperture Scintillometer. Boundary-Layer Meteorology 121, 111-126.

Kohsiek, W., Meijninger, W.M.L., Moene, A.F., Heusinkveld, B.G., Hartogensis, O.K., Hillen, W.C.A.M., De Bruin, H.A.R., 2002. An Extra Large Aperture Scintillometer For Long Range Applications. Boundary-Layer Meteorology 105, 119-127.

Koukou-Tchamba, A., 2000. Analyse des choix des techniques d'irrigation : cas de la zone de Melalsa (gouvernorat de Kairouan). INAT/IRD, Tunis, Tunisia, p. 103.

Kustas, W., Anderson, M., 2009. Advances in thermal infrared remote sensing for land surface modeling. Agricultural and Forest Meteorology 149, 2071-2081.

Kustas, W., Norman, J., 1996. Use of remote sensing for evapotranspiration monitoring over land surfaces. Hydrological Sciences Journal 41, 495-516.

Kustas, W.P., Daughtry, C.S.T., 1990. Estimation of the soil heat flux/net radiation ratio from spectral data. Agricultural and Forest Meteorology 49, 205-223.

Kustas, W.P., Daughtry, C.S.T., Van Oevelen, P.J., 1993. Analytical treatment of the relationships between soil heat flux/net radiation ratio and vegetation indices. Remote Sensing of Environment 46, 319-330.

Kustas, W.P., French, A.N., Hatfield, J.L., Jackson, T.J., Moran, M.S., Rango, A., Ritchie, J.C., Schmugge, T.J., 2003. Remote sensing research in hydrometeorology. Photogrammetric Engineering & Remote Sensing 69, 631-646.

Kustas, W.P., Norman, J.M., 1999. Evaluation of soil and vegetation heat flux predictions using a simple two-source model with radiometric temperatures for partial canopy cover. agricultural and forest meteorology 94, 13-29.

L.

Lagouarde, J.-P., Jacob, F., Gu, X.F., Olioso, A., Bonnefond, J.-M., Kerr, Y., Mcaneney, K.J., Irvine, M., 2002. Spatialization of sensible heat flux over a heterogeneous landscape. Agronomie-Sciences des Productions Vegetales et de l'Environnement 22, 627-634.

Lagouarde, J., Boulet, G., 2016. Energy Balance of Continental Surfaces and the Use of Surface Temperature, in: Nicolas, B., Mehrez, Z. (Eds.), Land Surface Remote Sensing in Continental Hydrology in Remote Sensing Observations of Continental Surfaces. ISTE_ELSEVIER, France, p. 502.

Le Goulven, P., Leduc, C., Bachta, M.S., Poussin, J.-C., 2009. Sharing scarce resources in a Mediterranean river basin: Wadi Merguellil in central Tunisia. River Basin Trajectories: Societies, Environments and Development, Wallingford, CABI, 147-170.

Le Page, M., 2015. SAT-IRR: Satellite for Irrigation Scheduling, CESBIO, Toulouse, France. http://www.cesbio.ups-tlse.fr/multitemp/?p=4824. (accessed on 31 January 2018).

Leclerc, M.Y., Thurtell, G.W., 1990. Footprint prediction of scalar fluxes using a Markovian analysis. Boundary-Layer Meteorology 52, 247-258.

Leduc, C., Ammar, S.B., Favreau, G., Beji, R., Virrion, R., Lacombe, G., Tarhouni, J., Aouadi, C., Chelli, B.Z., Jebnoun, N., Oi, M., Michelot, J.L., Zouari, K., 2007. Impacts of hydrological changes in the Mediterranean zone: environmental modifications and rural development in the Merguellil catchment, central Tunisia / Un exemple d'évolution hydrologique en Méditerranée: impacts des modifications environnementales et du développement agricole dans le bassin-versant du Merguellil (Tunisie centrale). Hydrological Sciences Journal 52, 1162-1178.

Leduc, C., Beji, R., Calvez, R., 2005. Les ressources en eau du barrage d'el Haouareb et des nappes adjacentes, vallée du Mergellil, Tunisie centrale, in: Le Goulven Patrick (ed.), B.S.e., Kuper M. (ed.) (Ed.), Gestion intégrée de l'eau au sein d'un bassin versant. Cirad, 7 p. Atelier du PCSI.Programme Commun Systèmes Irrigués : Thème 2 : Dynamiques Ressources-Usages dans le Bassin de Merguellil, Montpellier (FRA), 2003/12/02-03. .

Leduc, C., Calvez, R., Beji, R., Nazoumou, Y., Lacombe, G., Aouadi, C., 2004. Evolution de la ressource en eau dans la vallée du Merguellil (Tunisie centrale), Séminaire sur la modernisation de l'agriculture irriguée. IAV Hassan II, p. 10 p.

Lhomme, J.-P., Monteny, B., Amadou, M., 1994. Estimating sensible heat flux from radiometric temperature over sparse millet. agricultural and forest meteorology 68, 77-91.

Lhomme, J.P., Montes, C., Jacob, F., Prévot, L., 2012. Evaporation from Heterogeneous and Sparse Canopies: On the Formulations Related to Multi-Source Representations. Boundary-Layer Meteorology 144, 243-262.

LI-COR, 2016. EDDYPRO software:Instruction manual https://www.licor.com/documents/1ium2zmwm6hl36yz9bu4 accessible on 13th October 2017., p. 322.

Li, H., Sun, D., Yu, Y., Wang, H., Liu, Y., Liu, Q., Du, Y., Wang, H., Cao, B., 2014. Evaluation of the VIIRS and MODIS LST products in an arid area of Northwest China. Remote Sensing of Environment 142, 111-121.

Li, J., Heap, A.D., 2008. A review of spatial interpolation methods for environmental scientists. Geoscience Australia Canberra, 137-145.

Li, Z.-L., Tang, R., Wan, Z., Bi, Y., Zhou, C., Tang, B., Yan, G., Zhang, X., 2009. A review of current methodologies for regional evapotranspiration estimation from remotely sensed data. Sensors 9, 3801-3853.

Liang, S., Wang, K., Zhang, X., Wild, M., 2010. Review on estimation of land surface radiation and energy budgets from ground measurement, remote sensing and model simulations. IEEE Journal of Selected Topics in Applied Earth Observations and Remote Sensing 3, 225-240.

Lienhard, J.H., 1981. A heat transfer textbook. Prentice Hall PTR, Michigan University,USA.

Lim, Y.-J., Hong, J., Lee, T.-Y., 2012. Spin-up behavior of soil moisture content over East Asia in a land surface model. Meteorology and Atmospheric Physics 118, 151-161.

Liou, Y.-A., Kar, S., 2014. Evapotranspiration Estimation with Remote Sensing and Various Surface Energy Balance Algorithms—A Review. Energies 7, 2821.

Liu, S., Xu, Z., Song, L., Zhao, Q., Ge, Y., Xu, T., Ma, Y., Zhu, Z., Jia, Z., Zhang, F., 2016. Upscaling evapotranspiration measurements from multi-site to the satellite pixel scale over heterogeneous land surfaces. Agricultural and Forest Meteorology 230, 97-113.

López-Olivari, R., Ortega-Farías, S., Poblete-Echeverría, C., 2016. Partitioning of net radiation and evapotranspiration over a superintensive drip-irrigated olive orchard. Irrigation Science 34, 17-31.

M.

M. U. Neale, C., C. Bausch, W., F. Heermann, D., 1990. Development of Reflectance-Based Crop Coefficients for Corn. Transactions of the ASAE 32, 1891.

Ma, Y., Su, Z., Li, Z., Koike, T., Menenti, M., 2002. Determination of regional net radiation and soil heat flux over a heterogeneous landscape of the Tibetan Plateau. Hydrological Processes 16, 2963-2971.

Mabrouki, R., 2017 (In progress). Utilisation des images sattelitaires pour la cartographie des occupations du sol dans la plaine de Kairouan: compraison des methodes de classification arbre de décision, random forest et orienté objet. University of Carthage,INAT, Tunis, Tunisia.

Makkink, G., 1959. Limitations and perspectives of lysimeter research, Colloque de Hannoversch-Muenden 8-14 September 1959= Symposium of Hannoversch-Muenden 8-14 September 1959. AIHS, pp. 13-25.

Malbéteau, Y., 2016. Suivi des ressources en eau par une approche combinant la télédétection multi-capteur et la modélisation phénoménologique, SDU2E : Surfaces et Interfaces continentales, Hydrologie. Université Toulouse 3 Paul Sabatier Toulouse-France, p. 157.

Mandel, L., Wolf, E., 1995. Quantum theory of photoelectric detection of light, Optical Coherence and Quantum Optics. Cambridge University Press.

Marx, A., Kunstmann, H., Schüttemeyer, D., Moene, A.F., 2008. Uncertainty analysis for satellite derived sensible heat fluxes and scintillometer measurements over Savannah environment and comparison to mesoscale meteorological simulation results. Agricultural and Forest Meteorology 148, 656-667.

Massuel, S., Amichi, F., Ameur, F., Calvez, R., Jenhaoui, Z., Bouarfa, S., Kuper, M., Habaieb, H., Hartani, T., Hammani, A., 2017. Considering groundwater use to improve the assessment of groundwater pumping for irrigation in North Africa. Hydrogeology Journal 25, 1565-1577.

Mateos, L., González-Dugo, M., Testi, L., Villalobos, F., 2013. Monitoring evapotranspiration of irrigated crops using crop coefficients derived from time series of satellite images. I. Method validation. Agricultural water management 125, 81-91.

Matsushima, D., 2005. Relations between aerodynamic parameters of heat transfer and thermal-infrared thermometry in the bulk surface formulation. Journal of the Meteorological Society of Japan. Ser. II 83, 373-389.

Mauder, M., Foken, T., 2011. Documentation and instruction manual of the eddy-covariance software package TK3.

Mauser, W., Schädlich, S., 1998. Modelling the spatial distribution of evapotranspiration on different scales using remote sensing data. Journal of Hydrology 212, 250-267.

Melton, F.S., Johnson, L.F., Lund, C.P., Pierce, L.L., Michaelis, A.R., Hiatt, S.H., Guzman, A., Adhikari, D.D., Purdy, A.J., Rosevelt, C., 2012. Satellite irrigation management support with the terrestrial observation and prediction system: A framework for integration of satellite and surface observations to support improvements in agricultural water resource management. IEEE Journal of Selected Topics in Applied Earth Observations and Remote Sensing 5, 1709-1721.

Minacapilli, M., Agnese, C., Blanda, F., Cammalleri, C., Ciraolo, G., D'Urso, G., Iovino, M., Pumo, D., Provenzano, G., Rallo, G., 2009. Estimation of actual evapotranspiration of Mediterranean perennial crops by means of remote-sensing based surface energy balance models. Hydrology and Earth System Sciences 13, 1061-1074.

Minacapilli, M., Ciraolo, G., D Urso, G., Cammalleri, C., 2007. Evaluating actual evapotranspiration by means of multi-platform remote sensing data: a case study in Sicily. IAHS PUBLICATION, 316, 207.

Minacapilli, M., Iovino, M., D'Urso, G., 2008. A distributed agro-hydrological model for irrigation water demand assessment. Agricultural water management 95, 123-132.

Mjejra, M., Dubreuil, V., Hénia, L., 2014. Evaluation de l'évapotranspiration maximale par télédétection à moyenne résolution spatiale : cas du bassin versant de la Mejerda en Tunisie, CLIMAT : SYSTÈME & INTERACTIONS - XXVIIème colloque de l'AIC, Dijon, France, pp. 54-59.

Moene, A.F., Meijninger, W., Kohsiek, W., Gioli, B., Miglietta, F., Bosveld, F., 2006. Validation of fluxes of an extra large aperture scintillometer at Cabauw using sky arrow aircraft flux measurements, Proceedings of 17th symposium on boundary layers and turbulence. American Meteorological Society, San Diego, CA, pp. 22-25.

Montandon, L.M., Small, E.E., 2008. The impact of soil reflectance on the quantification of the green vegetation fraction from NDVI. Remote Sensing of Environment 112, 1835-1845.

Monteith, J., Unsworth, M., 2007. Principles of environmental physics. Academic Press.

Monteith, J.L., 1965. Evaporation and Environment. Symposia of the Society for Experimental Biology 19, 205-234.

Monteith, J.L., Unsworth, M., 1990. Principles of Environmental Physics. Butterworth-Heinemann, London.

Moran, M.S., 1994. Irrigation management in Arizona using satellites and airplanes. Irrigation Science 15, 35-44.

Moran, M.S., Jackson, R.D., Raymond, L.H., Gay, L.W., Slater, P.N., 1989. Mapping surface energy balance components by combining Landsat Thematic Mapper and ground-based meteorological data. Remote Sensing of Environment 30, 77-87.

Mougenot, B., Touhami, N., Lili Chabaane, Z., Boulet, G., Simonneaux, V., Zribi, M., 2014. Trees detection for water resources management in irrigated and rainfed arid and semi-arid agricultural areas, Pléiades Days, Toulouse.

Mougou, R., Henia, L., 1998. Contribution à l'étude des phénomènes à risques en Tunisie. Cas du sirocco. Publications de 1'Association Internationale de Climatologie 9.

Mougou, R., Mansour, M., Iglesias, A., Chebbi, R.Z., Battaglini, A., 2011. Climate change and agricultural vulnerability: a case study of rain-fed wheat in Kairouan, Central Tunisia. Regional Environmental Change 11, 137-142.

Mutziger, A.J., Burt, C.M., Howes, D.J., Allen, R.G., 2005. Comparison of measured and FAO-56 modeled evaporation from bare soil. Journal of irrigation and drainage engineering 131, 59-72.

N.

Neale, C.M., Jayanthi, H., Wright, J.L., 2005. Irrigation water management using high-resolution airborne remote sensing. Irrigation and Drainage Systems 19, 321-336.

Neale, C.M.U., Dugo, M.P.G., Mateos, L., Kustas, W.P., Kaheil, Y., 2007. A hybrid approach for estimating spatial evapotranspiration from satellite imagery, SPIE Remote Sensing. SPIE, p. 8.

Neale, C.M.U., Geli, H.M.E., Kustas, W.P., Alfieri, J.G., Gowda, P.H., Evett, S.R., Prueger, J.H., Hipps, L.E., Dulaney, W.P., Chávez, J.L., French, A.N., Howell, T.A., 2012. Soil water content estimation using a remote sensing based hybrid evapotranspiration modeling approach. Advances in Water Resources 50, 152-161.

NebGuide, 2009. Estimating crop evapotranspiration from reference evapotranspiration and crop coefficients. University of Nebraska, Lincoln, USA.

Norman, J.M., Kustas, W.P., Humes, K.S., 1995. Source approach for estimating soil and vegetation energy fluxes in observations of directional radiometric surface temperature. Agricultural and Forest Meteorology 77, 263-293.

NOURY, H., ALBOUCHI, L., POUSSIN, J.C., 2007. Dynamique des investissements agricoles dans le gouvernorat de Kairouan (Tunisie). . Programme MERGUSIE, IRD/INAT, , p. 16 p.

O.

Odi-Lara, M., Campos, I., Neale, C., Ortega-Farías, S., Poblete-Echeverría, C., Balbontín, C., Calera, A., 2016. Estimating Evapotranspiration of an Apple Orchard Using a Remote Sensing-Based Soil Water Balance. Remote Sensing 8, 253.

Olioso, A., Inoue, Y., Ortega-Farias, S., Demarty, J., Wigneron, J.-P., Braud, I., Jacob, F., Lecharpentier, P., Ottlé, C., Calvet, J.-C., 2005. Future directions for advanced evapotranspiration modeling: Assimilation of remote sensing data into crop simulation models and SVAT models. Irrigation and Drainage Systems 19, 377-412.

Overgaard, J., Rosbjerg, D., Butts, M., 2006. Land-surface modelling in hydrological perspective? a review. Biogeosciences 3, 229-241.

P.

Padilla, F., González-Dugo, M., Gavilán, P., Domínguez, J., 2011. Integration of vegetation indices into a water balance model to estimate evapotranspiration of wheat and corn. Hydrology and Earth System Sciences 15, 1213.

Paolini, L., Grings, F., Sobrino, J.A., Jiménez Muñoz, J.C., Karszenbaum, H., 2006. Radiometric correction effects in Landsat multi-date/multi-sensor change detection studies. International Journal of Remote Sensing 27, 685-704.

Paulson, C.A., 1970. The mathematical representation of wind speed and temperature profiles in the unstable atmospheric surface layer. Journal of Applied Meteorology 9, 857-861.

Payero, J.O., Neale, C.M.U., Wright, J.L., 2001. Estimating Diurnal Variation of Soil Heat Flux for Alfalfa and Grass. Proceedings of the 2001 ASAE Annual Meeting Sacramento, California.

Pellenq, J., Boulet, G., 2004. A methodology to test the pertinence of remote-sensing data assimilation into vegetation models for water and energy exchange at the land surface. Agronomie 24, 197-204.

Penman, H.L., 1948. Natural evaporation from open water, bare soil and grass, Proceedings of the Royal Society of London A: Mathematical, Physical and Engineering Sciences. The Royal Society, pp. 120-145.

Pieri, P., Fuchs, M., 1990. Comparison of Bowen ratio and aerodynamic estimates of evapotranspiration. Agricultural and forest meteorology 49, 243-256.

Pinter, P.J., Hatfield, J.L., Schepers, J.S., Barnes, E.M., Moran, M.S., Daughtry, C.S., Upchurch, D.R., 2003. Remote sensing for crop management. Photogrammetric Eng. Remote Sensing 69, 647– 664.

Pradeleix, L., Roux, P., Bouarfa, S., Jaouani, B., Lili-Chabaane, Z., Bellon-Maurel, V., 2015. Environmental Impacts of Contrasted Groundwater Pumping Systems Assessed by Life Cycle Assessment Methodology: Contribution to the Water–Energy Nexus Study. Irrigation and Drainage 64, 124-138.

Prata, A., Caselles, V., Coll, C., Sobrino, J., Ottle, C., 1995. Thermal remote sensing of land surface temperature from satellites: Current status and future prospects. Remote Sensing Reviews 12, 175-224.

R.

Rahman, H., Dedieu, G., 1994. SMAC: a simplified method for the atmospheric correction of satellite measurements in the solar spectrum. Remote Sensing 15, 123-143.

Rana, G., Katerji, N., 2000. Measurement and estimation of actual evapotranspiration in the field under Mediterranean climate: a review. European Journal of Agronomy 13, 125-153.

Raupach, M., Clark, J., Jarvis, P., Gardiner, B., Shuttleworth, W., Crowther, J., Leuning, R., Di Giovanni, F., Stewart, J., De Bruin, H., 1989. Stand overstorey processes. Philosophical Transactions of the Royal Society of London. Series B, Biological Sciences, 175-190.

Raupach, M., Finnigan, J., 1988. Single layer models of evaporation from plant canopies are incorrect but useful, whereas multilayer models are correct but useless: Discuss. Australian Journal of Plant Physiology 15, 705-716.

Reicosky, D., Peters, D., 1977. A portable chamber for rapid evapotranspiration measurements on field plots. Agronomy journal 69, 729-732.

Reicosky, D.C., Sharratt, B.S., Ljungkull, J.E., Baker, D.G., 1983. Comparison of alfalfa evapotranspiration measured by a weighing lysimeter and a portable chamber. Agricultural Meteorology 28, 205-211.

Richards, L.A., 1931. Capillary conduction of liquids through porous mediums. Physics 1, 318-333.

Richardson, A.J., Everitt, J.H., 1992. Using spectral vegetation indices to estimate rangeland productivity. Geocarto International 7, 63-69.

Richardson, A.J., Wiegand, C., 1977. Distinguishing vegetation from soil background information. Photogrammetric Engineering and Remote Sensing 43, 1541-1552.

Robinson, A.R., Lermusiaux, P.F., 2000. Overview of data assimilation. Harvard reports in physical/interdisciplinary ocean science 62, 1-13.

Rodell, M., Houser, P.R., Berg, A.A., Famiglietti, J.S., 2005. Evaluation of 10 Methods for Initializing a Land Surface Model. Journal of Hydrometeorology 6, 146-155.

Roerink, G.J., Su, Z., Menenti, M., 2000. S-SEBI: A simple remote sensing algorithm to estimate the surface energy balance. Physics and Chemistry of the Earth, Part B: Hydrology, Oceans and Atmosphere 25, 147-157.

Rouse Jr, J.W., Haas, R., Schell, J., Deering, D., 1974. Monitoring vegetation systems in the Great Plains with ERTS.

S.

Saadi, S., Simonneaux, V., Boulet, G., Raimbault, B., Mougenot, B., Fanise, P., Ayari, H., Lili-Chabaane, Z., 2015. Monitoring Irrigation Consumption Using High-resolution NDVI Image Time Series: Calibration and Validation in the Kairouan Plain (Tunisia). Remote Sensing 7, 13005.

Samain, B., Simons, G.W., Voogt, M.P., Defloor, W., Bink, N.-J., Pauwels, V., 2012. Consistency between hydrological model, large aperture scintillometer and remote sensing based evapotranspiration estimates for a heterogeneous catchment. Hydrology and Earth System Sciences 16, 2095-2107.

Sánchez, N., Martínez-Fernández, J., Calera, A., Torres, E., Pérez-Gutiérrez, C., 2010. Combining remote sensing and in situ soil moisture data for the application and

validation of a distributed water balance model (HIDROMORE). Agricultural Water Management 98, 69-78.

Sánchez, N., Martínez-Fernández, J., González-Piqueras, J., González-Dugo, M.P., Baroncini-Turrichia, G., Torres, E., Calera, A., Pérez-Gutiérrez, C., 2012. Water balance at plot scale for soil moisture estimation using vegetation parameters. agricultural and forest meteorology 166-167, 1-9.

Sauer, T., Havlík, P., Schneider, U.A., Schmid, E., Kindermann, G., Obersteiner, M., 2010. Agriculture and resource availability in a changing world: The role of irrigation. Water Resources Research 46.

Saugier, B., Ripley, E., 1978. Evaluation of the aerodynamic method of determining fluxes over natural grassland. Quarterly Journal of the Royal Meteorological Society 104, 257-270.

Schott, J.R., Salvaggio, C., Volchok, W.J., 1988. Radiometric scene normalization using pseudoinvariant features. Remote sensing of Environment 26, 1IN115-1416.

Schroeder, T.A., Cohen, W.B., Song, C., Canty, M.J., Yang, Z., 2006. Radiometric correction of multi-temporal Landsat data for characterization of early successional forest patterns in western Oregon. Remote sensing of environment 103, 16-26.

Schuurmans, J.M., Troch, P.A., Veldhuizen, A.A., Bastiaanssen, W.G.M., Bierkens, M.F.P., 2003. Assimilation of remotely sensed latent heat flux in a distributed hydrological model. Advances in Water Resources 26, 151-159.

Semmens, K.A., Anderson, M.C., Kustas, W.P., Gao, F., Alfieri, J.G., McKee, L., Prueger, J.H., Hain, C.R., Cammalleri, C., Yang, Y., Xia, T., Sanchez, L., Mar Alsina, M., Vélez, M., 2016. Monitoring daily evapotranspiration over two California vineyards using Landsat 8 in a multi-sensor data fusion approach. Remote Sensing of Environment 185, 155-170.

Shabou, M., 2010. Suivi de la dynamique du couvert végétal par télédetection spatiale sur le site semi-aride de merguellil (tunisie centrale). Université de Carthage-Institut National Agronomique de Tunisie, Tunis.

Shabou, M., Mougenot, B., Chabaane, Z., Walter, C., Boulet, G., Aissa, N., Zribi, M., 2015. Soil Clay Content Mapping Using a Time Series of Landsat TM Data in Semi-Arid Lands. Remote Sensing 7, 6059.

Shiklomanov, I.A., 2000. Appraisal and assessment of world water resources. Water international 25, 11-32.

Shuttleworth, W.J., Gurney, R.J., 1990. The theoretical relationship between foliage temperature and canopy resistance in sparse crops. Quarterly Journal of the Royal Meteorological Society 116, 497-519.

Shuttleworth, W.J., Wallace, J., 1985. Evaporation from sparse crops an energy combination theory. Quarterly Journal of the Royal Meteorological Society 111, 839-855.

Siebert, S., Döll, P., Hoogeveen, J., Faures, J.-M., Frenken, K., Feick, S., 2005. Development and validation of the global map of irrigation areas. Hydrology and Earth System Sciences Discussions 2, 1299-1327.

Simonneaux, V., Duchemin, B., Helson, D., Er-Raki, S., Olioso, A., Chehbouni, A., 2008. The use of high-resolution image time series for crop classification and

evapotranspiration estimate over an irrigated area in central Morocco. International Journal of Remote Sensing 29, 95-116.

Simonneaux, V., Lepage, M., Helson, D., Metral, J., Thomas, S., Duchemin, B., Cherkaoui, M., Kharrou, H., Berjami, B., Chehbouni, A., 2009. Estimation spatialisée de l'évapotranspiration des cultures irriguées par télédétection: application à la gestion de l'irrigation dans la plaine du Haouz (Marrakech, Maroc). Science et changements planétaires/Sécheresse 20, 123-130.

Soil-Quality, 2017. Fact Sheets Water Availability.

Solignac, P.A., Brut, A., Selves, J.L., Béteille, J.P., Gastellu-Etchegorry, J.P., Keravec, P., Béziat, P., Ceschia, E., 2009. Uncertainty analysis of computational methods for deriving sensible heat flux values from scintillometer measurements. Atmos. Meas. Tech. 2, 741-753.

Song, W., Mu, X., Ruan, G., Gao, Z., Li, L., Yan, G., 2017. Estimating fractional vegetation cover and the vegetation index of bare soil and highly dense vegetation with a physically based method. International Journal of Applied Earth Observation and Geoinformation 58, 168-176.

SPOT4-Take5, 2013. Available online: http://www.cesbio.ups-tlse.fr/multitemp/?page_id=406 (accessed on 16 February 2015). .

Steinberg, S.L., Van Bavel, C., McFarland, M., 1990. Improved sap flow gauge for woody and herbaceous plants. Agronomy Journal 82, 851-854.

Stewart, J.B., Kustas, W.P., Humes, K.S., Nichols, W.D., Moran, M.S., De Bruin, H., 1994. Sensible heat flux-radiometric surface temperature relationship for eight semiarid areas. Journal of Applied Meteorology 33, 1110-1117.

Stull, R.B., 2012. An introduction to boundary layer meteorology. Springer Science & Business Media.

Su, Z., 2002. The Surface Energy Balance System (SEBS) for estimation of turbulent heat fluxes. Hydrology and Earth System Sciences Discussions 6, 85-100.

Sugita, M., Brutsaert, W., 1990. Regional surface fluxes from remotely sensed skin temperature and lower boundary layer measurements. Water Resources Research 26, 2937-2944.

Szeicz, G., Long, I., 1969. Surface resistance of crop canopies. Water Resources Research 5, 622-633.

Szeicz, G., Van Bavel, C., Takami, S., 1973. Stomatal factor in the water use and dry matter production by sorghum. Agricultural Meteorology 12, 361-389.

T.

Takeuchi, W., Tamura, M., Yasuoka, Y., 2003. Estimation of methane emission from West Siberian wetland by scaling technique between NOAA AVHRR and SPOT HRV. Remote Sensing of Environment 85, 21–29.

Tardy, B., Rivalland, V., Huc, M., Hagolle, O., Marcq, S., Boulet, G., 2016. A Software Tool for Atmospheric Correction and Surface Temperature Estimation of Landsat Infrared Thermal Data. Remote Sensing 8, 696.

Tasumi, M., 2003. Progress in operational estimation of regional evapotranspiration using satellite imagery.

Tatarskii, V.I., 1961. Wave propagation in turbulent medium. Wave Propagation in Turbulent Medium, by Valerian Ilich Tatarskii. Translated by RA Silverman. 285pp. Published by McGraw-Hill, 1961.

Testi, L., Villalobos, F., Orgaz, F., Fereres, E., 2006. Water requirements of olive orchards: I simulation of daily evapotranspiration for scenario analysis. Irrigation Science 24, 69-76.

Testi, L., Villalobos, F.J., Orgaz, F., 2004. Evapotranspiration of a young irrigated olive orchard in southern Spain. agricultural and forest meteorology 121, 1-18.

Torres, A.F., Walker, W.R., McKee, M., 2011. Forecasting daily potential evapotranspiration using machine learning and limited climatic data. Agricultural Water Management 98, 553-562.

Torres, E.A., Calera, A., 2010. Bare soil evaporation under high evaporation demand: a proposed modification to the FAO-56 model. Hydrological Sciences Journal–Journal des Sciences Hydrologiques 55, 303-315.

Touhami, N., 2013. Détection des arbres par imagerie Très Haute Résolution Spatiale sur la plaine de Kairouan Institut National Agronomqiue de Tunisie, Tunis, p. 78.

Troufleau, D., Lhomme, J.-P., Monteny, B., Vidal, A., 1997. Sensible heat flux and radiometric surface temperature over sparse Sahelian vegetation. I. An experimental analysis of the kB− 1 parameter. Journal of Hydrology 188, 815-838.

Tucker, C.J., 1978. A comparison of satellite sensor bands for vegetation monitoring.

Tucker, C.J., 1979. Red and photographic infrared linear combinations for monitoring vegetation. Remote Sensing of Environment 8, 127-150.

Turk, J.T., Mostovoy, G.V., Anantharaj, V., 2010. The NRL-Blend High-resolution Precipitation Product and its Application to Land Surface Hydrology, in: Gebremichael, M., Hossain, F. (Eds.), Satellite Rainfall Applications for Surface Hydrology. Springer Netherlands, Dordrecht, pp. 85-104.

Twine, T.E., Kustas, W., Norman, J., Cook, D., Houser, P., Meyers, T., Prueger, J., Starks, P., Wesely, M., 2000. Correcting eddy-covariance flux underestimates over a grassland. agricultural and forest meteorology 103, 279-300.

U.

UNEP, 2000. Global Environment Outlook (GEO). http://web.unep.org/geo/assessments/global-assessments/geo-2000.

UNEP, 2009. Blue Plan Note N°11. www.planbleu.org.

USGS, 2016. The World's Water. U.S. Department of the Interior. http://water.usgs.gov/edu/earthwherewater.html.

Ushio, T., Sasashige, K., Kubota, T., Shige, S., Okamoto, K.i., Aonashi, K., Inoue, T., Takahashi, N., Iguchi, T., Kachi, M., 2009. A Kalman filter approach to the Global Satellite Mapping of Precipitation (GSMaP) from combined passive microwave and infrared radiometric data. Journal of the Meteorological Society of Japan. Ser. II 87, 137-151.

V.

Van Dijk, A., Moene, A., De Bruin, H., 2004. The principles of surface flux physics: theory, practice and description of the ECPACK library. Internal Rep 1, 99.

Van Dijk, A.I., 2004. Estimates of CO2 uptake and release among European forests based on eddy covariance data. Global Change Biology 10, 1445-1459.

Velluet, C., 2014. Modélisation et analyse pluriannuelles du fonctionnement hydrologique et énergétique de deux écosystèmes dominants au Sahel agropastoral (Sud-Ouest Niger). Université de Montpellier 2, Montpellier, France, p. 286.

Verstraeten, W.W., Veroustraete, F., Feyen, J., 2008. Assessment of Evapotranspiration and Soil Moisture Content Across Different Scales of Observation. Sensors (Basel, Switzerland) 8, 70-117.

W.

Wada, Y., Beek, L.P., Sperna Weiland, F.C., Chao, B.F., Wu, Y.H., Bierkens, M.F., 2012. Past and future contribution of global groundwater depletion to sea-level rise. Geophysical Research Letters 39.

Waggoner, P.E., Furnival, G., Reifsnyder, W., 1969. Simulation of the microclimate in a forest. Forest Science 15, 37-45.

Wan, Z., Zhang, Y., Zhang, Q., Li, Z.-l., 2002. Validation of the land-surface temperature products retrieved from Terra Moderate Resolution Imaging Spectroradiometer data. Remote Sensing of Environment 83, 163-180.

Wang-Erlandsson, L., Bastiaanssen, W.G.M., Gao, H., Jägermeyr, J., Senay, G.B., van Dijk, A.I.J.M., Guerschman, J.P., Keys, P.W., Gordon, L.J., Savenije, H.H.G., 2016. Global root zone storage capacity from satellite-based evaporation. Hydrol. Earth Syst. Sci. 20, 1459-1481.

Wang, L., Qu, J.J., 2009. Satellite remote sensing applications for surface soil moisture monitoring: A review. Frontiers of Earth Science in China 3, 237-247.

Watts, C.J., Chehbouni, A., Rodriguez, J.C., Kerr, Y.H., Hartogensis, O., de Bruin, H.A.R., 2000. Comparison of sensible heat flux estimates using AVHRR with scintillometer measurements over semi-arid grassland in northwest Mexico. Agricultural and Forest Meteorology 105, 81-89.

Webb, E., 1965. Aerial microclimate, Agricultural Meteorology. Springer, pp. 27-58.

Weier, J., Herring, D., 2000. Measuring Vegetation (NDVI and EVI). NASA.

Wierngа, J., 1993. Representative roughness parameters for homogeneous terrain. Boundary-Layer Meteorology 63, 323-363.

Wik, M., Pingali, P., Broca, S., 2008. Global agricultural performance: past trends and future prospects. Background paper for the WDR.

Williams, D.G., Cable, W., Hultine, K., Hoedjes, J.C.B., Yepez, E.A., Simonneaux, V., Er-Raki, S., Boulet, G., de Bruin, H.A.R., Chehbouni, A., Hartogensis, O.K., Timouk, F., 2004. Evapotranspiration components determined by stable isotope, sap flow and eddy covariance techniques. Agricultural and Forest Meteorology 125, 241-258.

Wilson, K., Goldstein, A., Falge, E., Aubinet, M., Baldocchi, D., Berbigier, P., Bernhofer, C., Ceulemans, R., Dolman, H., Field, C., 2002. Energy balance closure at FLUXNET sites. agricultural and forest meteorology 113, 223-243.

Wisser, D., Frolking, S., Douglas, E.M., Fekete, B.M., Vörösmarty, C.J., Schumann, A.H., 2008. Global irrigation water demand: Variability and uncertainties arising from agricultural and climate data sets. Geophysical Research Letters 35.

Wösten, J., Pachepsky, Y.A., Rawls, W., 2001. Pedotransfer functions: bridging the gap between available basic soil data and missing soil hydraulic characteristics. Journal of hydrology 251, 123-150.

Wu, Y., Du, T., Ding, R., Tong, L., Li, S., Wang, L., 2016. Multiple Methods to Partition Evapotranspiration in a Maize Field. Journal of Hydrometeorology 18, 139-149.

X.

Xiao, X., Sauer, T.J., Singer, J.W., Horton, R., Ren, T., Heitman, J.L., 2016. Partitioning evaporation and transpiration in a maize field using heat-pulse sensors for evaporation measurement.

Xie, Y., Sha, Z., Yu, M., 2008. Remote sensing imagery in vegetation mapping: a review. Journal of Plant Ecology 1, 9-23.

Y.

Yang, Y., Uddstrom, M., Duncan, M., 2011. Effects of short spin-up periods on soil moisture simulation and the causes over New Zealand. Journal of Geophysical Research: Atmospheres 116, D24108.

Yu, W., Ma, M., Wang, X., Geng, L., Tan, J., Shi, J., 2014. Evaluation of MODIS LST Products Using Longwave Radiation Ground Measurements in the Northern Arid Region of China. Remote Sensing 6.

Yunusa, I., Walker, R., Lu, P., 2004. Evapotranspiration components from energy balance, sapflow and microlysimetry techniques for an irrigated vineyard in inland Australia. Agricultural and Forest Meteorology 127, 93-107.

Z.

Zaghouani, R., 2013. Estimation des besoins en eau pour l'agriculture dans le bassin de Merguelil par imagerie satellite haute resolution. University of Carthage, National Agronomic Institute of Tunisia (INAT), Tunis, Tunisia, p. 80.

Zarco-Tejada, P.J., González-Dugo, V., Berni, J.A.J., 2012. Fluorescence, temperature and narrow-band indices acquired from a UAV platform for water stress detection using a micro-hyperspectral imager and a thermal camera. Remote Sensing of Environment 117, 322-337.

Zeng, X., Dickinson, R.E., Walker, A., Shaikh, M., DeFries, R.S., Qi, J., 2000. Derivation and evaluation of global 1-km fractional vegetation cover data for land modeling. Journal of Applied Meteorology 39, 826-839.

Zhang, K., Kimball, J.S., Nemani, R.R., Running, S.W., 2010. A continuous satellite-derived global record of land surface evapotranspiration from 1983 to 2006. Water Resources Research 46, W09522.

Zhang, X., Liao, C., Li, J., Sun, Q., 2013. Fractional vegetation cover estimation in arid and semi-arid environments using HJ-1 satellite hyperspectral data. International Journal of Applied Earth Observation and Geoinformation 21, 506-512.

Zhang, Y., Wegehenkel, M., 2006. Integration of MODIS data into a simple model for the spatial distributed simulation of soil water content and evapotranspiration. Remote sensing of Environment 104, 393-408.

Zhao, W., Li, A., 2015. A Review on Land Surface Processes Modelling over Complex Terrain. Advances in Meteorology 2015, 17.

Zribi, M., Chahbi, A., Shabou, M., Lili-Chabaane, Z., Duchemin, B., Baghdadi, N., Amri, R., Chehbouni, A., 2011. Soil surface moisture estimation over a semi-arid region using ENVISAT ASAR radar data for soil evaporation evaluation. Hydrology and Earth System Sciences Discussions 15, 345-358.

Zribi, M., Kotti, F., Lili-Chabaane, Z., Baghdadi, N., Issa, N.B., Amri, R., Amri, B., Chehbouni, A., 2012. Soil Texture Estimation Over a Semiarid Area Using TerraSAR-X Radar Data. IEEE Geoscience and Remote Sensing Letters 9, 353-357.

Annexes

Annex 1: TIR missions

○ Landsat satellites

The Landsat program is an important images base of the Earth's surface; it is the oldest one since 1972. With the launch of Landsat 5 in 1984, the thermal band in the Thematic Mapper (TM) sensor appeared with a spatial resolution of 120 m (Table A.1). The TM sensor was operational for 27 years and was stopped in November 2011. Landsat 6 failed to reach its orbit and was lost. Landsat 7 was launched in 1999 and has also a thermal band thanks to the Enhanced Thematic Mapper Plus (ETM +) sensor, which is an enhanced version of the TM sensor. The thermal band has an improved spatial resolution at 60 m and the satellite covers the entire globe in 16 days. Landsat 7 is still operational but has suffered a failure and the images of the ETM + sensor acquire only 75% of each scene data.NASA successfully launched the Landsat 8 satellite on February 2013 and its operation was transferred to the United States Geological Survey (USGS). The data collected by the new thermal sensor, Thermal Infrared Sensor (TIRS), are freely available. The spatial resolution is now 100 m with an overall coverage of 16 days.However, for the three missions, the T_{surf} product is not yet systematically available for downloading, so it is necessary to apply an atmospheric correction model, for example, the joint use of the MODTRAN model and the re-analysis atmospheric data from ERA-Interim (Tardy *et al.*, 2016).

○ Advanced Spaceborne Thermal Emission Reflection radiometer (ASTER)

The ASTER radiometer is one of five instruments on NASA's TERRA satellite. It provides on request maps with high spatial resolution in the visible (15 m), the near infrared (30 m) and in the thermal infrared (90 m). With its 5 bands in the thermal infrared (wavelength between 8 and 12 μm), ASTER allows the inversion of T_{surf} and spectral emissivity at 90 m resolution (Abrams, 2000). In the best case, the temporal resolution is 16 days (Table A.1). ASTER surface temperature product (AST08) is obtained using the same algorithm as for the surface emissivity product. The T_{surf} is thus estimated by applying Planck's law from the estimated values of the Temperature Emissivity Separation (TES) algorithm developed by (Gillespie *et al.*, 1998). The ASTER T_{surf} data are corrected for radiometric, atmospheric and geometric effects.

○ MODerate resolution Imaging Spectroradiometer (MODIS)

The MODIS instrument is a radiometer using 36 spectral bands ranging from 0.4 to 14.4 μm. MODIS is embarked on two satellites: TERRA launched in December 1999 and AQUA in May 2002. Aqua crosses the equator at 1:30 am and 1:30 pm local time, and Terra crosses the equator at 10:30 am and 10:30 pm, which means that MODIS data are generally available 4 times a day (if there are no clouds) with a resolution of 1 km, this

combination makes it possible to have a daily average T_{surf} closer to the real field. MODIS data are free and can be downloaded via *http://lpdaac.usgs.gov/main.asp*.

The surface temperature (T_{surf}) and emissivity daily data are retrieved at 1km pixels by the generalized split-window algorithm and at 6km grids by the day/night algorithm. In the split-window algorithm, emissivities in bands 31 and 32 are estimated from land cover types, atmospheric column water vapor and lower boundary air surface temperature are separated into tractable sub-ranges for optimal retrieval. In the day/night algorithm, daytime and nighttime T_{surf} and surface emissivities are retrieved from pairs of day and night MODIS observations in seven TIR bands. The product is comprised of T_{surf}, quality assessment, observation time, view angles, and emissivities.

Table A. 1: Satellite-based thermal datasets

Satellite	**Sensor**	**Thermal Band**	**Spectral band**	**Spatial resolution**	**Temporal resolution**
Landsat 8	TIRS	B10 (Medium infrared)	10.30 – 11.30 µm	100 m	16 days
		B11(Medium infrared)	11.50 – 12.30 µm		
Landsat 7	ETM+	Band 6 - TIR	10.4 – 12.5 µm	60 m	16 days
Landsat 5	TM	Band 6 - TIR	10.40 – 12.50 µm	120 m	16 days
Terra	ASTER	Band10- TIR	8.12 – 8.47 µm	90 m	On request
		Band11- TIR	8.47– 8.82 µm		
		Band12- TIR	8.92 – 9.27 µm		
		Band13- TIR	10.25 – 10.95 µm		
		Band14- TIR	10.95 – 11.65 µm		
Terra, Aqua	MODIS	Band 31- TIR	10.78 – 11.28 µm	1 km	1-2/day
		Band 32- TIR	11.77 – 12.27 µm		
NOAA	AVHRR	Band 4- TIR	10.3 – 11.3 µm	1 km	2/day
		Band 5- TIR	11.5 – 12.5 µm		
GEOS	GEOS imager	Band 4- TIR	10.2 – 11.2 µm	4 km	1-3 hour
		Band 5- TIR	11.5 – 12.5 µm		

Annex 2: VIS-NIR missions

There are several multispectral (VIS-NIR) high-resolution missions, here after, we cite some European Space Agency (ESA) missions:

- **SPOT** ("*Satellite Pour l'Observation de la Terre*", Satellite for observation of Earth) is a commercial high-resolution optical imaging Earth observation satellite system operating from space. It is run by Spot Image, based in Toulouse, France. It was initiated by the CNES ("Centre national d'études spatiales", the French space agency) in the 1970s. It has been designed to improve the knowledge and management of the Earth by exploring the Earth's resources, detecting and forecasting phenomena involving climatology and oceanography, and monitoring human activities and natural phenomena. The SPOT system includes a series of satellites: SPOT-1 (1986-1990) with 10 panchromatic and 20 meter multispectral picture resolution capability; SPOT-2 (1990-2009) ; SPOT-3 (1993-1997); SPOT-4 (1998-2013); SPOT-5 (2002-2015) with 2.5 m, 5 m and 10 m capability; SPOT-6 launched on September 2012 and SPOT-7 launched on June 2014. Compared to its predecessors, SPOT-5 offered greatly enhanced capabilities due to SPOT-5's improved 5-metre and 2.5-metre resolution. The satellite provided an ideal balance between high-resolution and wide-area coverage. SPOT-5's other key feature was the unprecedented acquisition capability of the on-board HRS imaging instrument, which had the ability to take stereo pair images quasi-simultaneously. SPOT sensors, spectral and spatial resolution and applications are detailed in Table A.2. At the end of life of SPOT-4 and SPOT-5 satellites, the Take 5 experiment was set up: satellite orbit was lowered by 3 kilometres to put it on a 5 day repeat cycle orbit; hence, the satellite flew over the same places on Earth every 5 days. This experiment used SPOT-4 and SPOT-5 as a simulator of the time series that Sentinel-2 mission provide. 45 and 150 sites have been observed every 5 days, by SPOT-4 and SPOT-5, respectively.

- **Sentinel-2** is a polar-orbiting, multispectral high-resolution imaging mission for land monitoring to provide, for example, imagery of vegetation, soil and water cover, inland waterways and coastal areas every 5 days. Sentinel-2 can also deliver information for emergency services. Sentinel-2A was launched on 23 June 2015 and Sentinel-2B followed on 7 March 2017. Sentinel-2 spectral and spatial resolutions as well as applications are detailed in Table A.2.

- **Pleiades** is a constellation of two very-high-resolution satellites; Pleiades-HR 1A and Pleiades-HR 1B, launched in December 2011, capable of acquiring imagery of any point on the globe in less than 24 hours for civil and military users, at a resolution of just 70 cm every day. Pleiades spectral and spatial resolutions as well as applications are detailed in Table A.2.

Table A. 2: Characteristics of SPOT-4, SPOT-5, Sentinel-2 and Pleiades satellites

Satellites	Sensors	Mode	Band	Spectral band	Spatial resolution	Applications
SPOT-4	HRVIR	Multispectral	B1 (green)	0.50 - 0.59 μm	20 m	Telecommunications; Land use and Planning; Infrastructure planning; Environmental assessment.
			B2 (red)	0.61 - 0.68 μm	20 m	
			B3 (near IR)	0.78 - 0.89 μm	20 m	
			MIR (middle IR)	1.58 - 1.75 μm	20 m	
		Panchromatic	PAN	0.61 - 0.68 μm	10 m	
	Vegetation	Multispectral	B0 (blue)	0.43 - 0.47μm	1165 m	Oceanographic applications; Atmospheric corrections.
			B2 (red)	0.61 - 0.68 μm	1165 m	Vegetation photosynthesis activity.
			B3 (near IR)	0.79 - 0.89 μm	1165 m	
			MIR (middle IR)	1.58 - 1.75 μm	1165 m	Ground and vegetation humidity.
SPOT-5	HRG	Multispectral	B1(green)	0.50 - 0.59 μm	10 m	Telecommunications; Land use and Planning; Infrastructure planning; Environmental assessment; Marine studies; Agriculture; Mapping; Civil Engineering; Mapping Natural Resources; Mining and Exploration Oil and Gas.
			B2 (red)	0.61 - 0.68 μm	10 m	
			B3 (near IR)	0.78 - 0.89 μm	10 m	
			SWIR	1.58 - 1.75 μm	10m x 10m	
		Panchromatic	PAN	0.51 - 0.73 μm	5m x 5m	
	Vegetation 2	Remains unchanged in comparison to the one installed on board SPOT-4 sensor.				

Satellites	Sensors	Mode	Band	Spectral band	Spatial resolution	Applications
Sentinel-2	MSI (Imaging multi-spectral radiometers	Multispectral	Band 1 – Coastal aerosol	0.42 - 0.46 μm	60 m	Monitoring land cover change for environmental monitoring; Agricultural applications. such as crop monitoring and management to help food security; Detailed vegetation and forest monitoring and parameter generation (e.g. leaf area index. chlorophyll concentration. carbon mass estimations).
			Band 2 – Blue	0.42 - 0.55 μm	10 m	
			Band 3 – Green	0.52 - 0.60 μm	10 m	
			Band 4 – Red	0.63 - 0.69 μm	10 m	
			Band 5 – Vegetation Red Edge	0.69 - 0.85 μm	20 m	
			Band 5 – Vegetation Red Edge	0.72 - 0.89 μm	20 m	
			Band 5 – Vegetation Red Edge	0.76 - 0.80 μm	20 m	
			Band 8 – NIR	0.73 - 0.96 μm	10 m	
			Band 8A – Narrow NIR	0.84 - 0.88 μm	20 m	
			Band 9 – Water vapour	0.92 - 0.96 μm	60 m	
			Band 10 – SWIR – Cirrus	1.35 - 1.40 μm	60 m	
			Band 11 – SWIR	1.52 - 1.7 μm	20 m	
			Band 12 – SWIR	2.01 - 2.37 μm	20 m	
Pleiades	HiRI (High-resolution optical imagers)	Multispectral	Band 1 – Blue	0.43 - 0.55 μm	2 m	Defense or civil security missions; Critical geophysical phenomena survey (volcanic eruptions; Detailed Mapping especially in urban area.
			Band 2 – Green	0.49-0.61 μm	2 m	
			Band 3 – Red	0.60-0.72 μm	2 m	
			Band 4 – NIR	0.75-0.95 μm	2 m	
		Panchromatic	PAN	0.47-0.82 μm	0.5 m	

Annex 3: Summary table of vegetation indices determined in recent years

Groups	Vegetation index	Formula	Authors	Commentaries
Simpe indices	Difference Vegetation Index	$\mathbf{DVI = NIR - R}$	(Bacour *et al.*, 2006)	They are very sensitive to atmospheric variations, as well as to the spectral contribution of soils. In addition, when the vegetation is very dense, the reflectance in the red band becomes very low, resulting in a saturation of the RVI index.values.
	Ratio Vegetation Index"	$\mathbf{RVI} = {}^{\mathbf{NIR}}/_{\mathbf{R}}$	(Jordan, 1969)	
	Normalized Difference Vegetation Index	$\mathbf{NDVI} = \frac{\mathbf{NIR - R}}{\mathbf{NIR + R}}$	(Rouse Jr *et al.*, 1974; Tucker, 1979)	Reference vegetation index and the most used one. NDVI values are theoretically in the range of -1 (areas other than plant cover, such as snow, water or cloud) to +1 (vegetation). The highest NDVI values correspond to the densest vegetation cover. NDVI allows the analysis of the vegetation cover dynamic.
	Moisture Stress Index & Normalized Difference Water Index	$\boldsymbol{MSI} = {}^{\boldsymbol{MIR}}/_{\boldsymbol{NIR}}$ $\boldsymbol{NDWI} = \frac{\boldsymbol{NIR - MIR}}{\boldsymbol{NIR + MIR}}$	(Gao, 1996; Hunt and Rock, 1989)	They vary depending on the water content of the leaves. They allow detecting the vegetation water stress and are therefore very useful for crop monitoring in dry zone.
Indices taking into account the soils influence	Perpendicular Vegetation Index	$\boldsymbol{PVI} = \frac{\mathbf{1}}{\sqrt{\boldsymbol{\alpha}^{\mathbf{2}} + \mathbf{1}}}(\boldsymbol{NIR - \alpha R - b})$ a and b are respectively the slope and the ordinate at the origin of the soils line.	(Richardson and Wiegand, 1977)	It is based on the use of the soils line which becomes a reference to determine the density of the vegetation (the more a pixel is far from the line, the more its coverage is dense).
	Soil-Adjusted Vegetation Index	$\boldsymbol{SAVI} = \frac{\boldsymbol{NIR - R}}{\boldsymbol{NIR + R + L}}(\mathbf{1} + \boldsymbol{L})$	(Huete, 1988)	It characterizes the soil and its vegetation coverage rate. The parameter L is a constant taking the value of 0.25 for a high density and 1 for a very low density of vegetation.

	Transformed Soil-Adjusted Vegetation Index	$$TSAVI = \frac{\alpha(NIR - \alpha R - b)}{R + NIR - \alpha b + 0.08(1 + \alpha^2)}$$	(Baret *et al.*, 1989)	It has the same characteristics as the PVI except the addition of a corrective constant of the soil effect (0.08).
Indices taking into account the effects of soils and the atmosphere	Atmospherically Resistant Vegetation Index	$$ARVI = \frac{NIR - RB}{NIR + RB}$$ RB = R – γ (B – R) γ: Atmospheric auto correction factor.	(Kaufman and Tanre, 1992)	It takes into account the atmosphere effects.

Annex 4.1: Internal radiometric normalization of 2012-2013 season's SPOT5 and SPOT4-take5 images time series

- ***2012-2013 season's SPOT5 images***

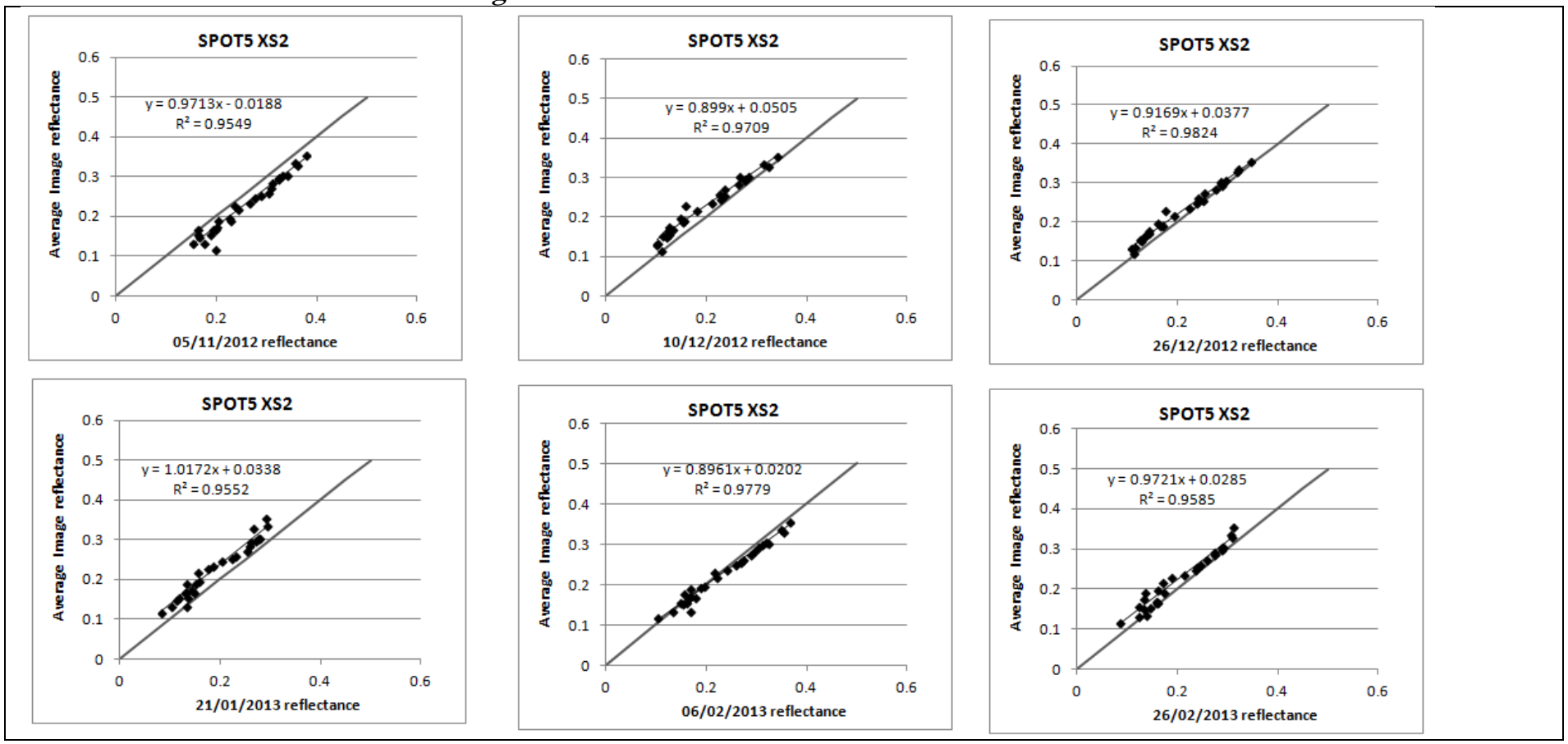

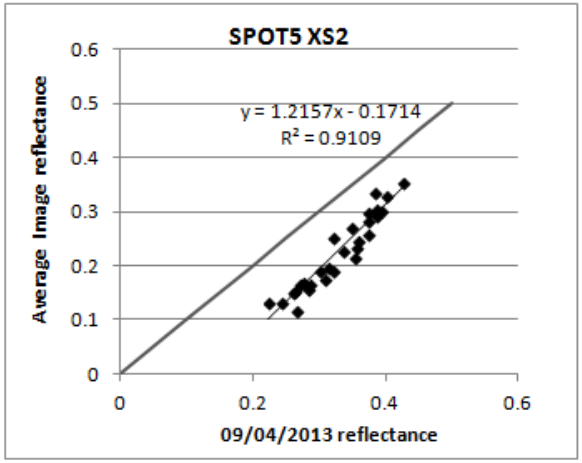
SPOT5 XS2
y = 1.2157x - 0.1714
R² = 0.9109
Average Image reflectance
09/04/2013 reflectance
0
0.1
0.2
0.3
0.4
0.5
0.6
0
0.2
0.4
0.6

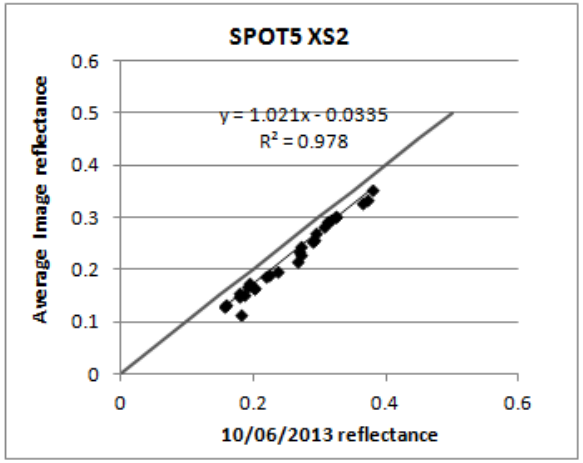
SPOT5 XS2
y = 1.021x - 0.0335
R² = 0.978
Average Image reflectance
10/06/2013 reflectance
0
0.1
0.2
0.3
0.4
0.5
0.6
0
0.2
0.4
0.6

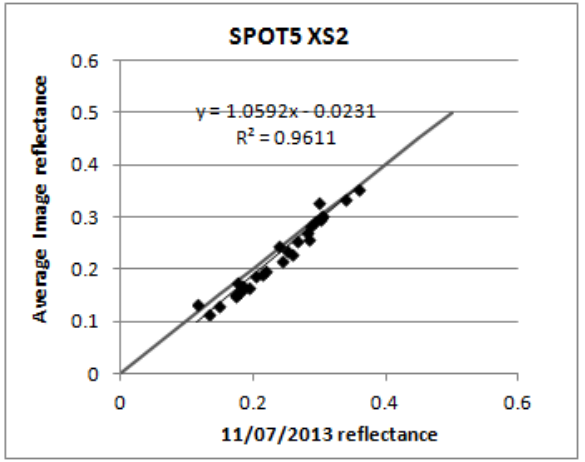
SPOT5 XS2
y = 1.0592x - 0.0231
R² = 0.9611
Average Image reflectance
11/07/2013 reflectance
0
0.1
0.2
0.3
0.4
0.5
0.6
0
0.2
0.4
0.6

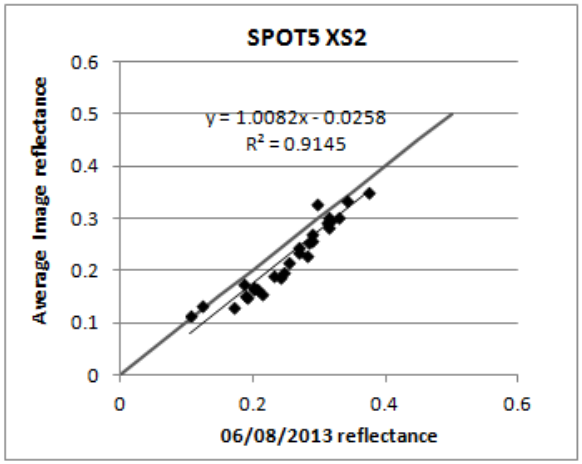
SPOT5 XS2
y = 1.0082x - 0.0258
R² = 0.9145
Average Image reflectance
06/08/2013 reflectance
0
0.1
0.2
0.3
0.4
0.5
0.6
0
0.2
0.4
0.6

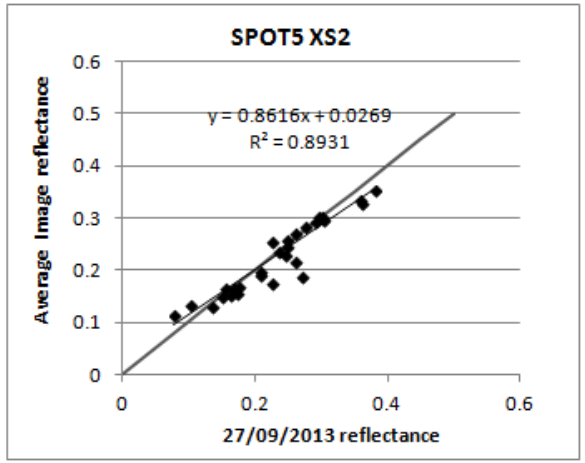
SPOT5 XS2
y = 0.8616x + 0.0269
R² = 0.8931
Average Image reflectance
27/09/2013 reflectance
0
0.1
0.2
0.3
0.4
0.5
0.6
0
0.2
0.4
0.6

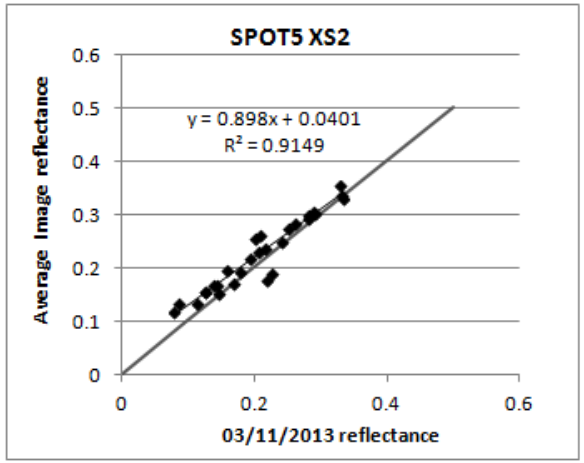
SPOT5 XS2
y = 0.898x + 0.0401
R² = 0.9149
Average Image reflectance
03/11/2013 reflectance
0
0.1
0.2
0.3
0.4
0.5
0.6
0
0.2
0.4
0.6

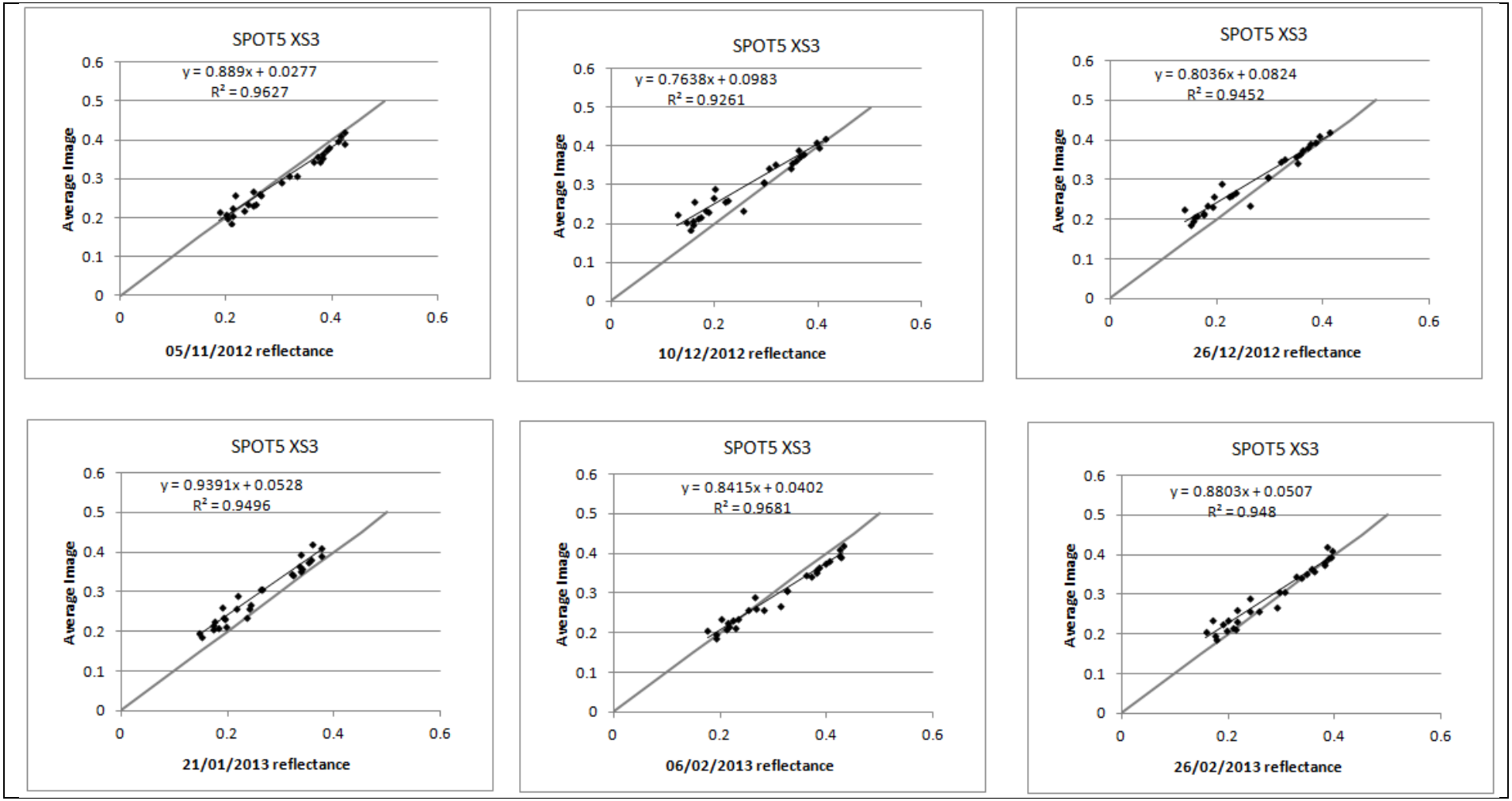
SPOT5 XS3
y = 0.889x + 0.0277
R² = 0.9627
Average Image
05/11/2012 reflectance
SPOT5 XS3
y = 0.7638x + 0.0983
R² = 0.9261
Average Image
10/12/2012 reflectance
SPOT5 XS3
y = 0.8036x + 0.0824
R² = 0.9452
Average Image
26/12/2012 reflectance
SPOT5 XS3
y = 0.9391x + 0.0528
R² = 0.9496
Average Image
21/01/2013 reflectance
SPOT5 XS3
y = 0.8415x + 0.0402
R² = 0.9681
Average Image
06/02/2013 reflectance
SPOT5 XS3
y = 0.8803x + 0.0507
R² = 0.948
Average Image
26/02/2013 reflectance

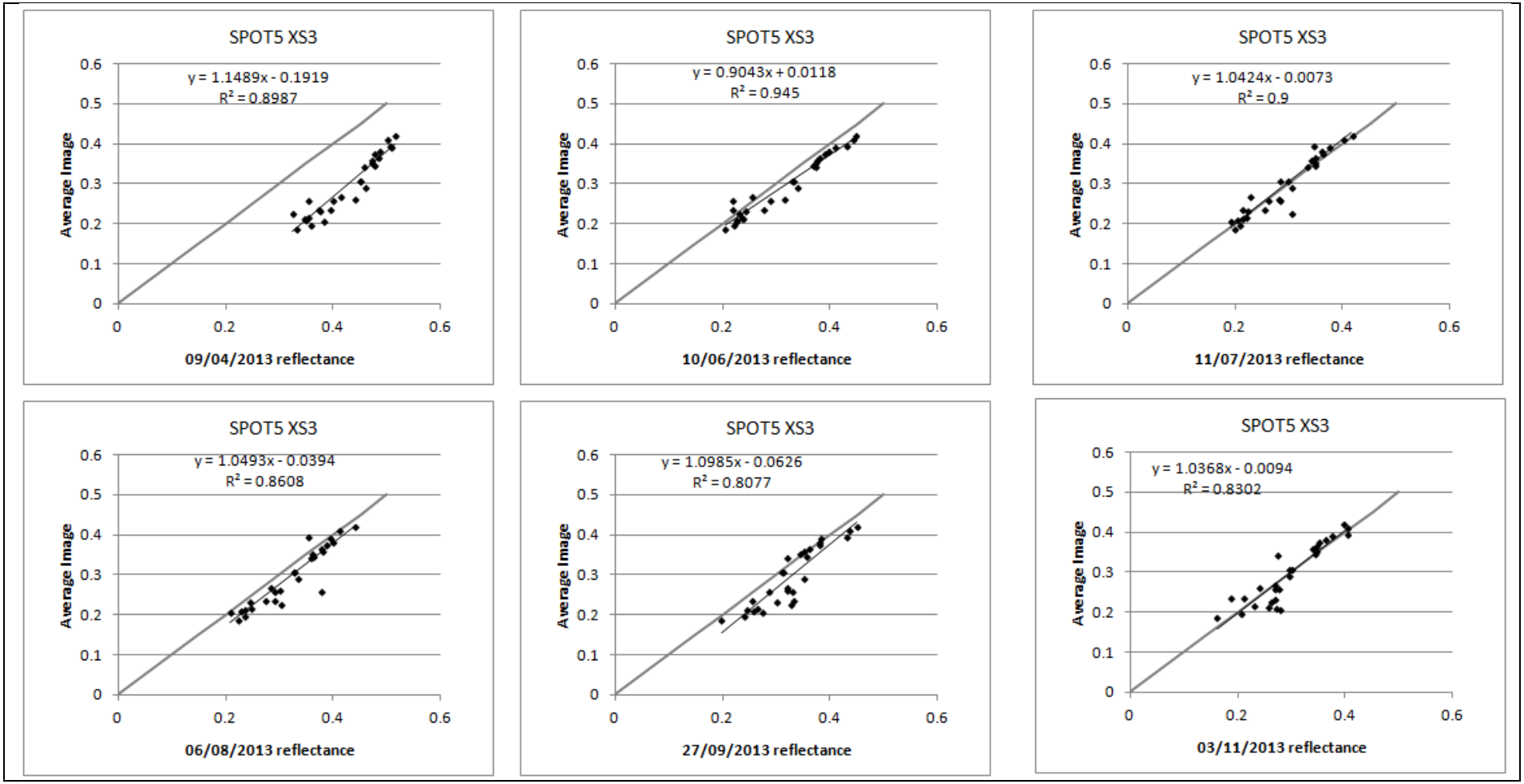
SPOT5 XS3
y = 1.1489x - 0.1919
R² = 0.8987
Average Image
09/04/2013 reflectance
SPOT5 XS3
y = 0.9043x + 0.0118
R² = 0.945
Average Image
10/06/2013 reflectance
SPOT5 XS3
y = 1.0424x - 0.0073
R² = 0.9
Average Image
11/07/2013 reflectance
SPOT5 XS3
y = 1.0493x - 0.0394
R² = 0.8608
Average Image
06/08/2013 reflectance
SPOT5 XS3
y = 1.0985x - 0.0626
R² = 0.8077
Average Image
27/09/2013 reflectance
SPOT5 XS3
y = 1.0368x - 0.0094
R² = 0.8302
Average Image
03/11/2013 reflectance

➢ ***2012-2013 season's SPOT4-Take5 images***

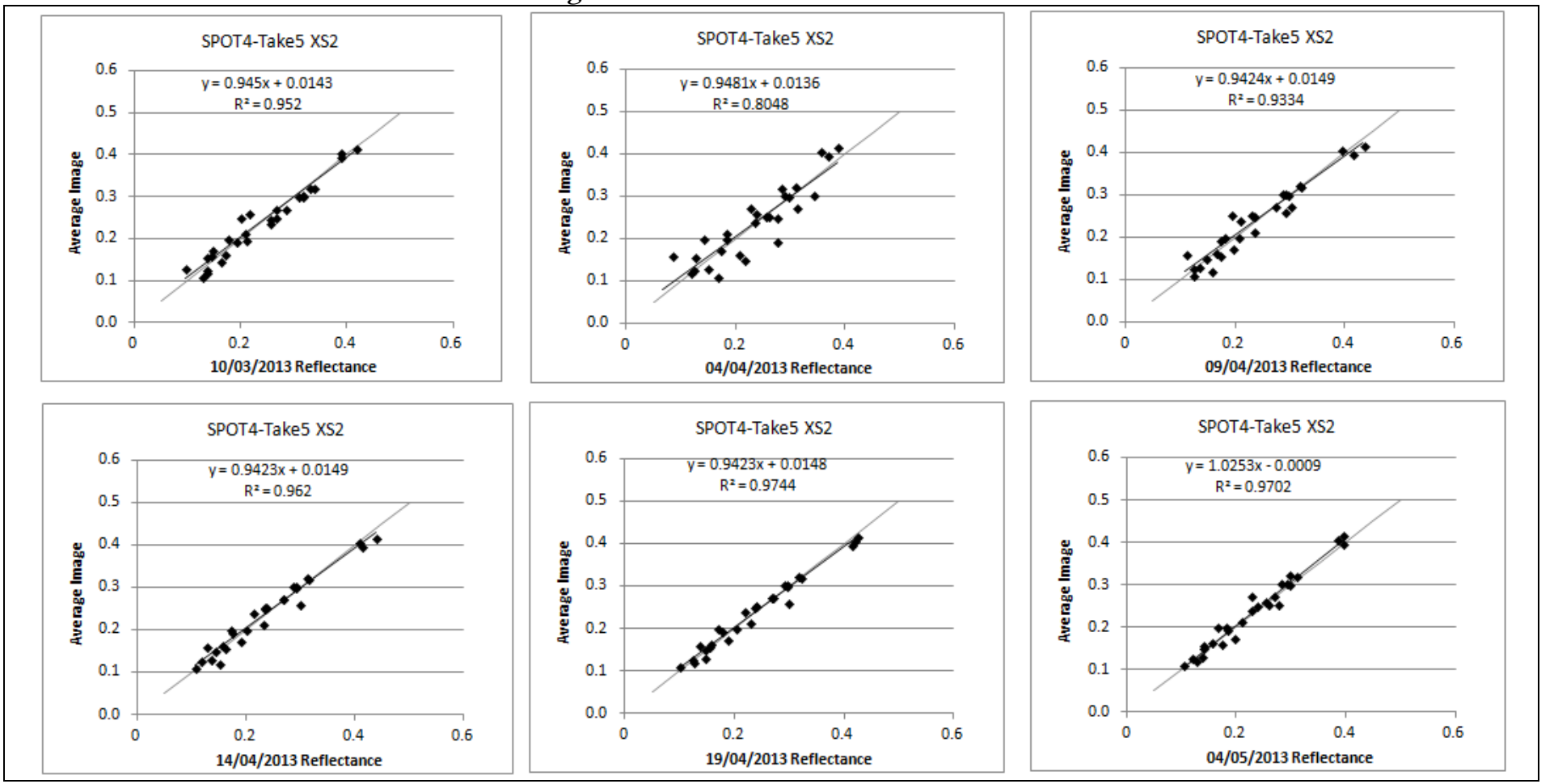

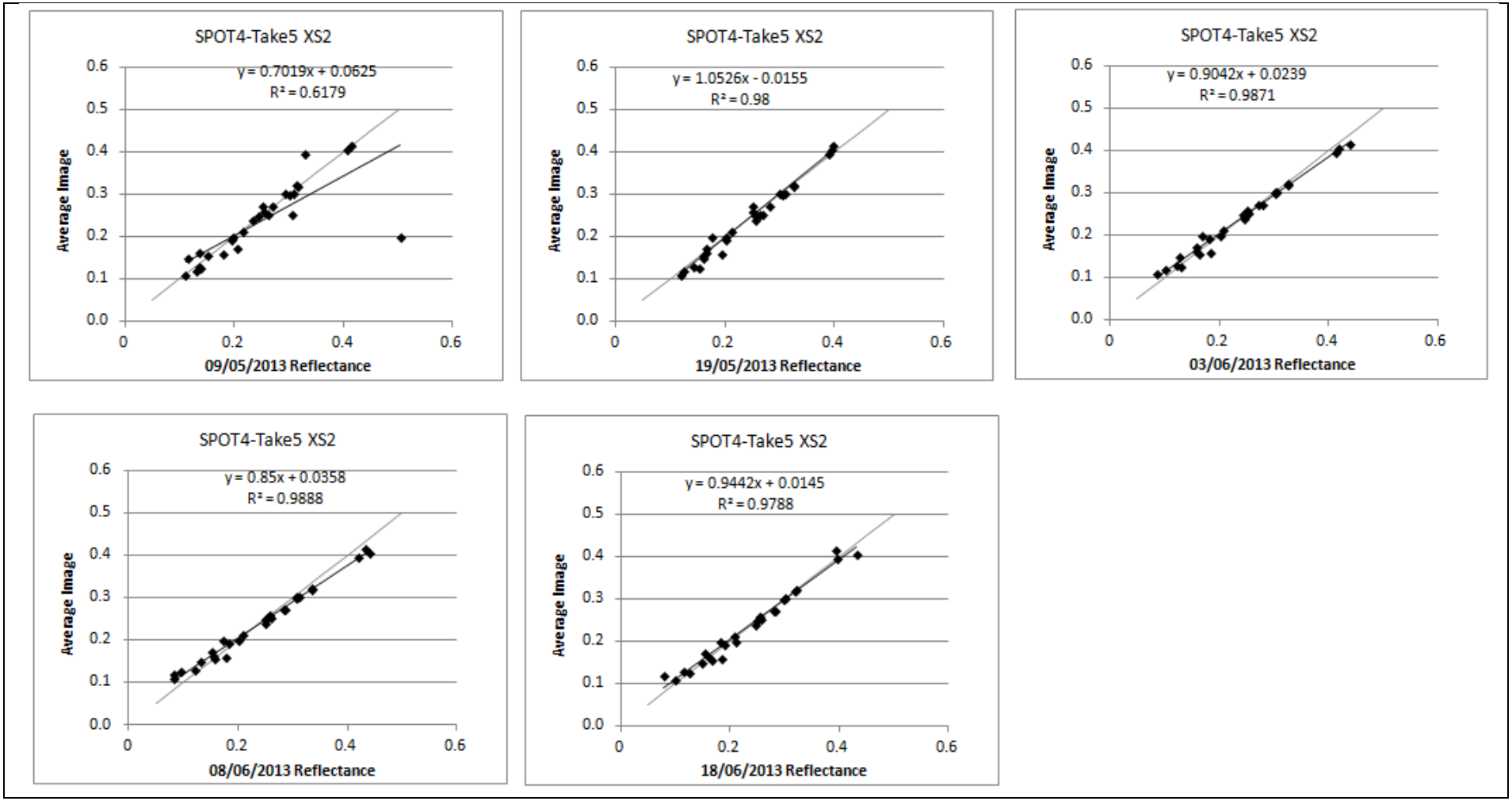
SPOT4-Take5 XS2
y = 0.7019x + 0.0625
R² = 0.6179
Average Image
09/05/2013 Reflectance
SPOT4-Take5 XS2
y = 1.0526x - 0.0155
R² = 0.98
Average Image
19/05/2013 Reflectance
SPOT4-Take5 XS2
y = 0.9042x + 0.0239
R² = 0.9871
Average Image
03/06/2013 Reflectance
SPOT4-Take5 XS2
y = 0.85x + 0.0358
R² = 0.9888
Average Image
08/06/2013 Reflectance
SPOT4-Take5 XS2
y = 0.9442x + 0.0145
R² = 0.9788
Average Image
18/06/2013 Reflectance

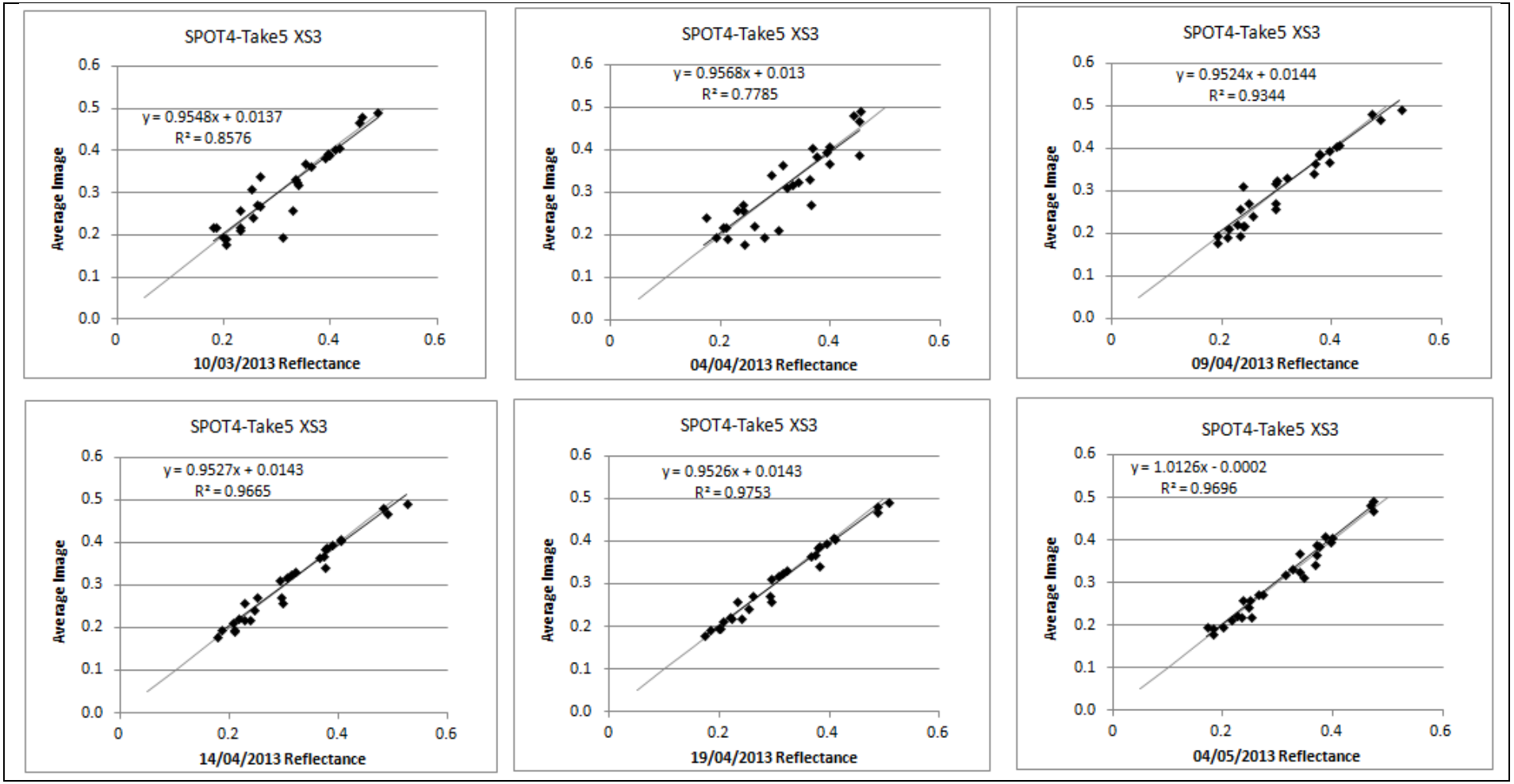
SPOT4-Take5 XS3
y = 0.9548x + 0.0137
R² = 0.8576
Average Image
10/03/2013 Reflectance
SPOT4-Take5 XS3
y = 0.9568x + 0.013
R² = 0.7785
Average Image
04/04/2013 Reflectance
SPOT4-Take5 XS3
y = 0.9524x + 0.0144
R² = 0.9344
Average Image
09/04/2013 Reflectance
SPOT4-Take5 XS3
y = 0.9527x + 0.0143
R² = 0.9665
Average Image
14/04/2013 Reflectance
SPOT4-Take5 XS3
y = 0.9526x + 0.0143
R² = 0.9753
Average Image
19/04/2013 Reflectance
SPOT4-Take5 XS3
y = 1.0126x - 0.0002
R² = 0.9696
Average Image
04/05/2013 Reflectance

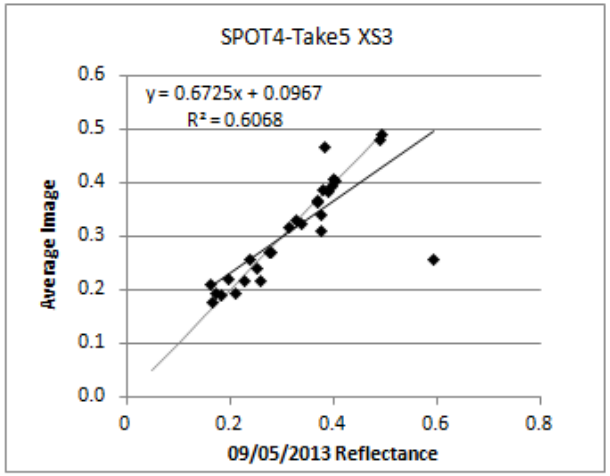
SPOT4-Take5 XS3
y = 0.6725x + 0.0967
R² = 0.6068
Average Image
09/05/2013 Reflectance

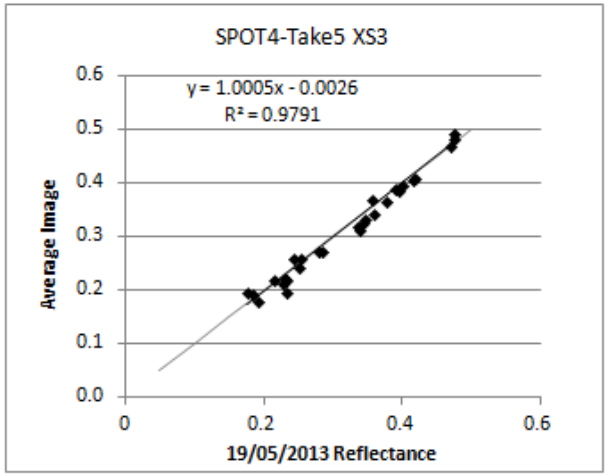
SPOT4-Take5 XS3
y = 1.0005x - 0.0026
R² = 0.9791
Average Image
19/05/2013 Reflectance

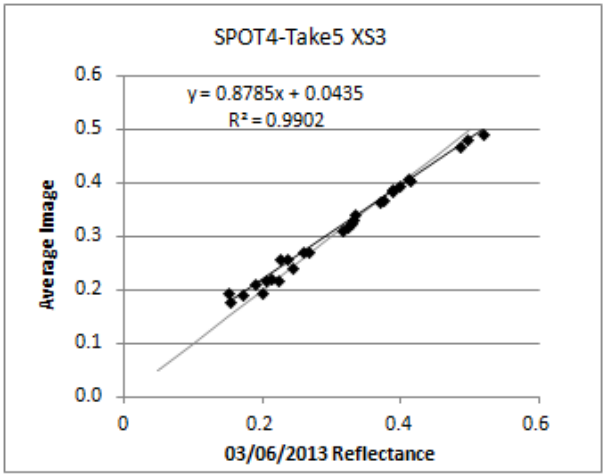
SPOT4-Take5 XS3
y = 0.8785x + 0.0435
R² = 0.9902
Average Image
03/06/2013 Reflectance

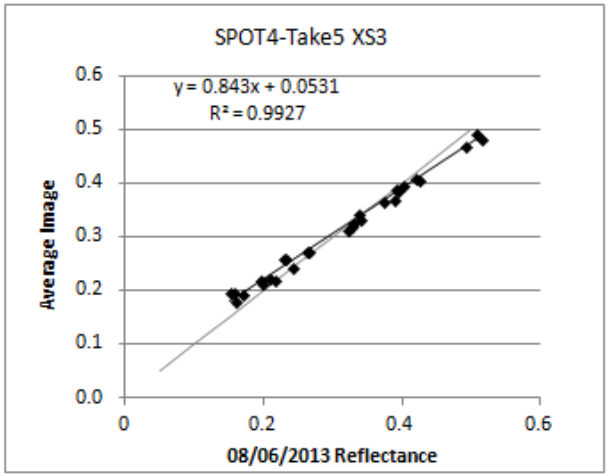
SPOT4-Take5 XS3
y = 0.843x + 0.0531
R² = 0.9927
Average Image
08/06/2013 Reflectance

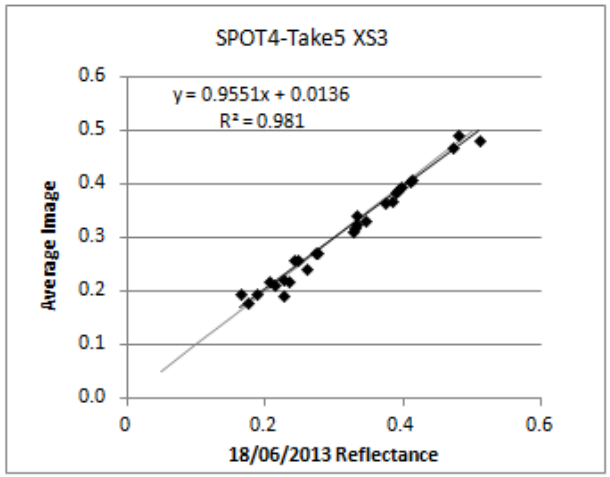
SPOT4-Take5 XS3
y = 0.9551x + 0.0136
R² = 0.981
Average Image
18/06/2013 Reflectance

Annex 4.2: Additional 2012-2013 season's SPOT5 images radiometric normalization (SPOT4-take5 average image as reference)

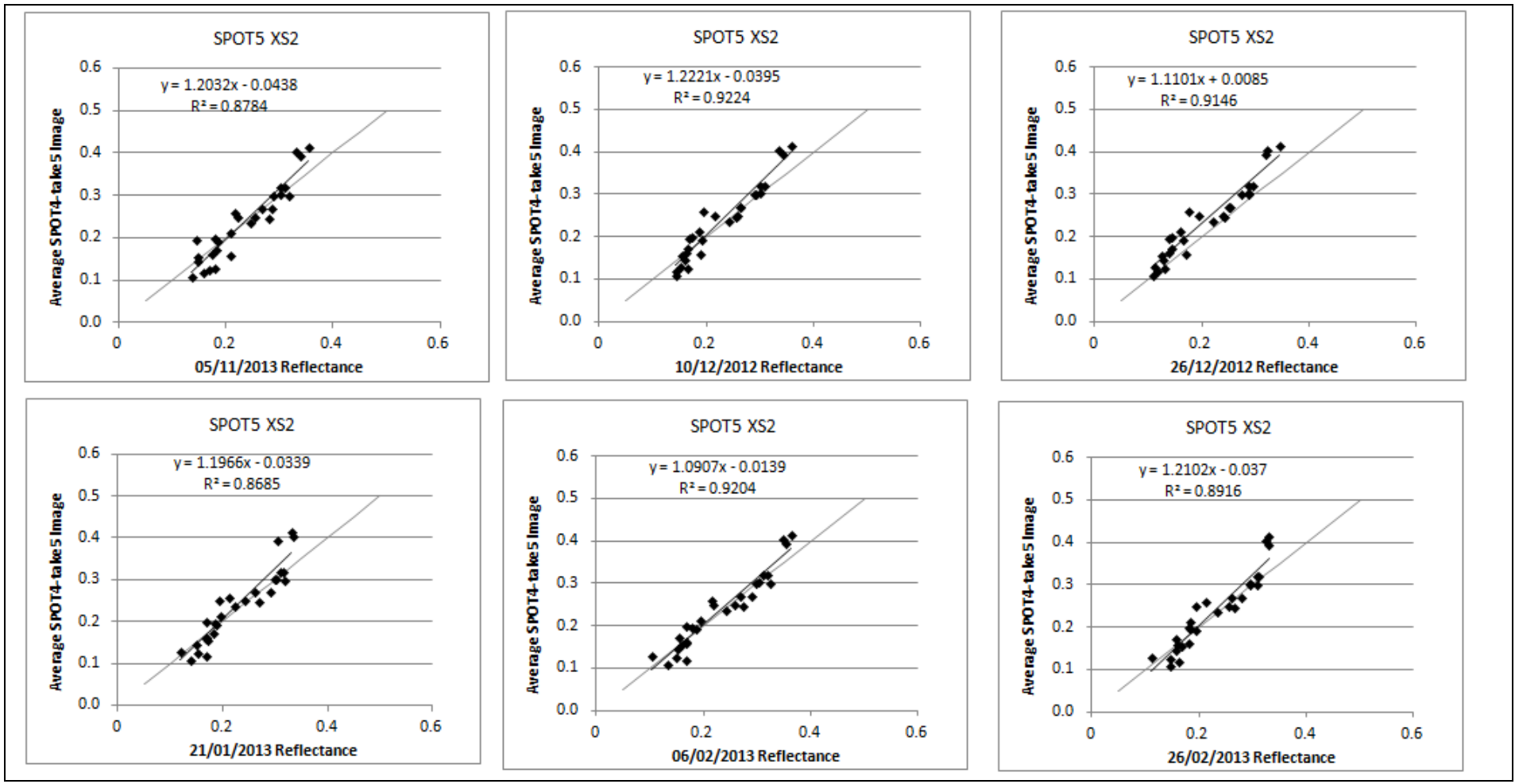

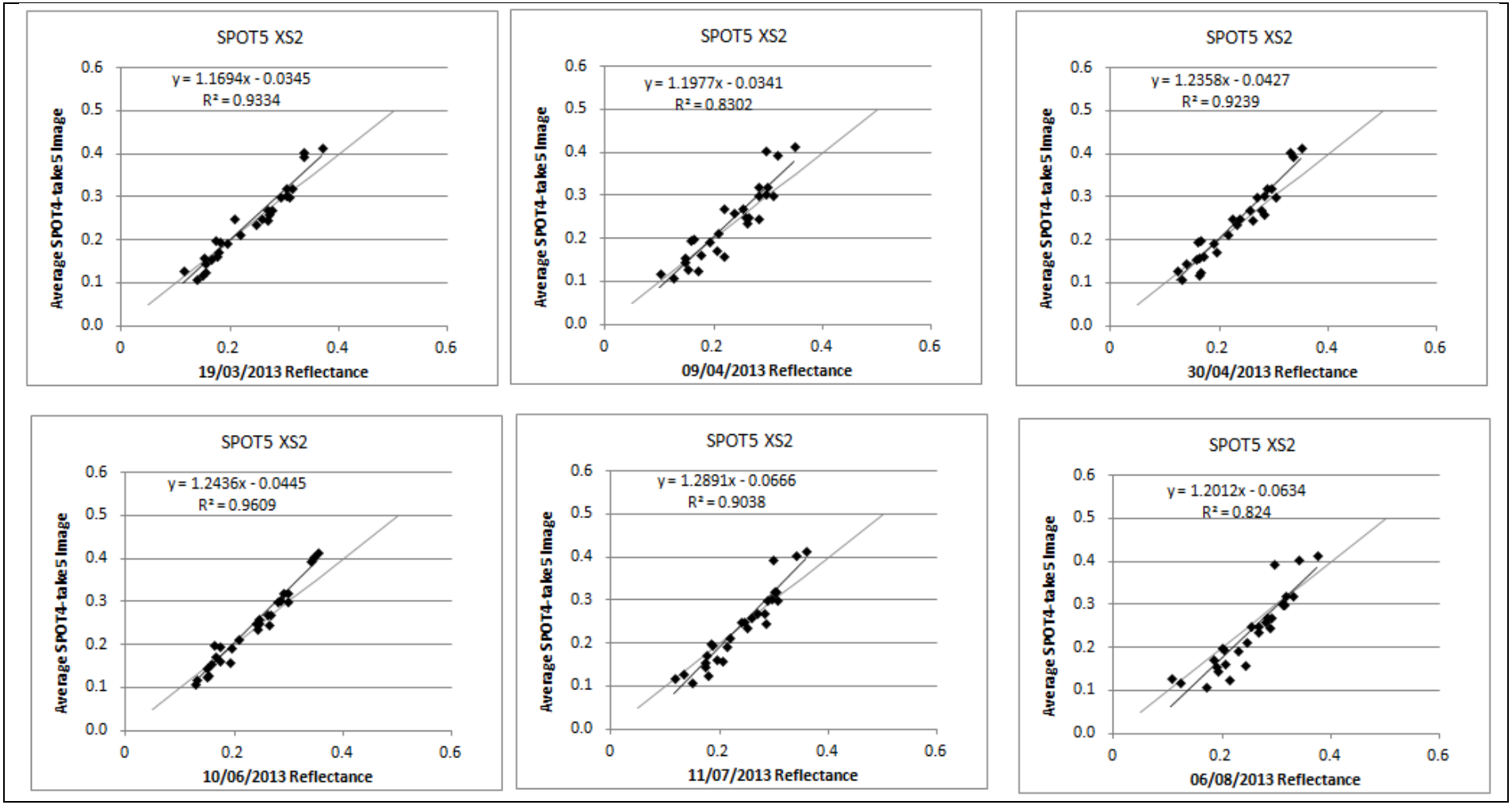
SPOT5 XS2
y = 1.1694x - 0.0345
R² = 0.9334
Average SPOT4-take5 Image
19/03/2013 Reflectance
SPOT5 XS2
y = 1.1977x - 0.0341
R² = 0.8302
Average SPOT4-take5 Image
09/04/2013 Reflectance
SPOT5 XS2
y = 1.2358x - 0.0427
R² = 0.9239
Average SPOT4-take5 Image
30/04/2013 Reflectance
SPOT5 XS2
y = 1.2436x - 0.0445
R² = 0.9609
Average SPOT4-take5 Image
10/06/2013 Reflectance
SPOT5 XS2
y = 1.2891x - 0.0666
R² = 0.9038
Average SPOT4-take5 Image
11/07/2013 Reflectance
SPOT5 XS2
y = 1.2012x - 0.0634
R² = 0.824
Average SPOT4-take5 Image
06/08/2013 Reflectance

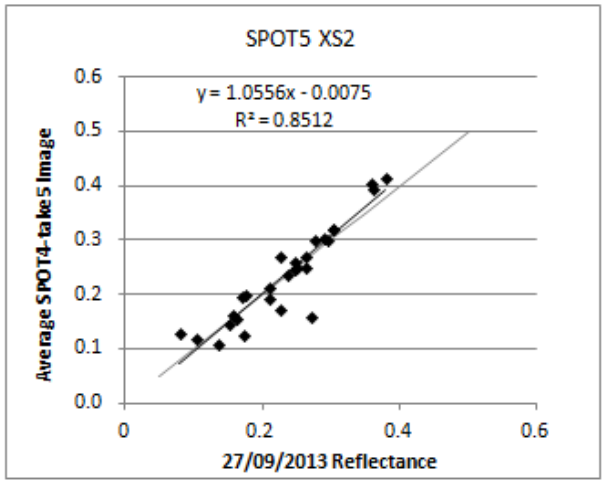
SPOT5 XS2
y = 1.0556x - 0.0075
R² = 0.8512
Average SPOT4-take5 Image
27/09/2013 Reflectance
0.0
0.1
0.2
0.3
0.4
0.5
0.6
0
0.2
0.4
0.6

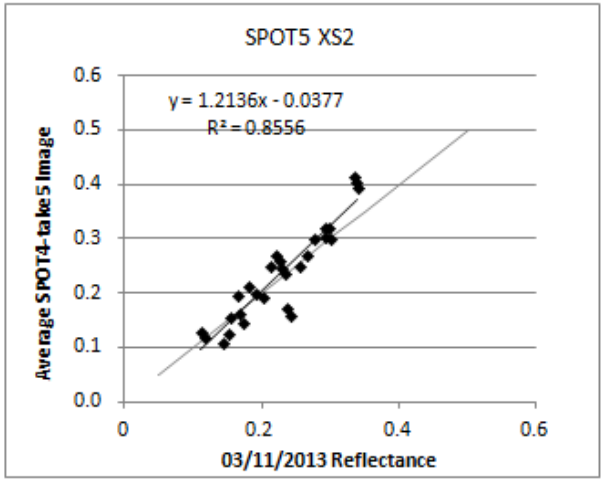
SPOT5 XS2
y = 1.2136x - 0.0377
R² = 0.8556
Average SPOT4-take5 Image
03/11/2013 Reflectance
0.0
0.1
0.2
0.3
0.4
0.5
0.6
0
0.2
0.4
0.6

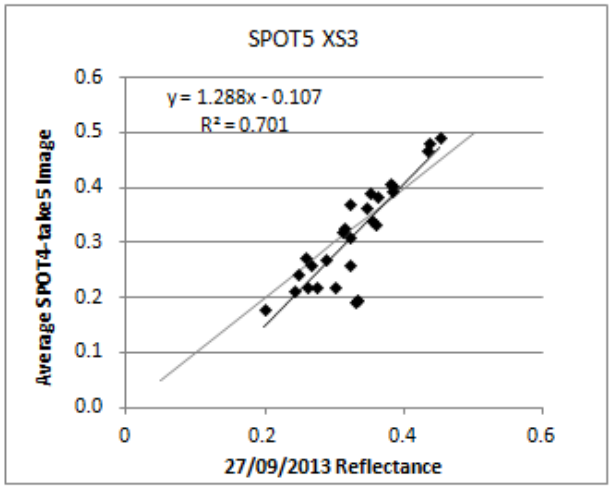
SPOT5 XS3
y = 1.288x - 0.107
R² = 0.701
Average SPOT4-take5 Image
27/09/2013 Reflectance
0.0
0.1
0.2
0.3
0.4
0.5
0.6
0
0.2
0.4
0.6

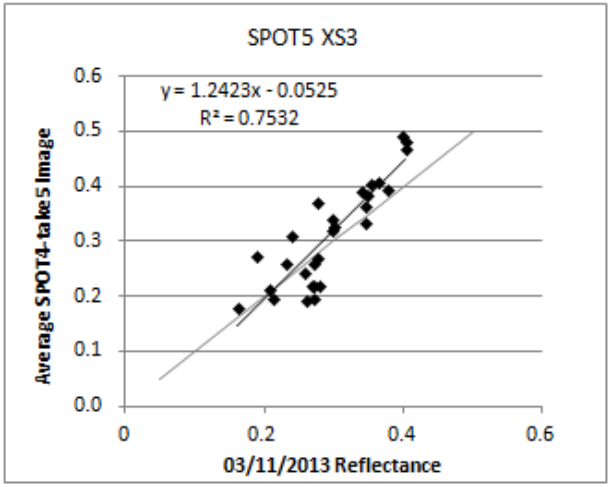
SPOT5 XS3
y = 1.2423x - 0.0525
R² = 0.7532
Average SPOT4-take5 Image
03/11/2013 Reflectance
0.0
0.1
0.2
0.3
0.4
0.5
0.6
0
0.2
0.4
0.6

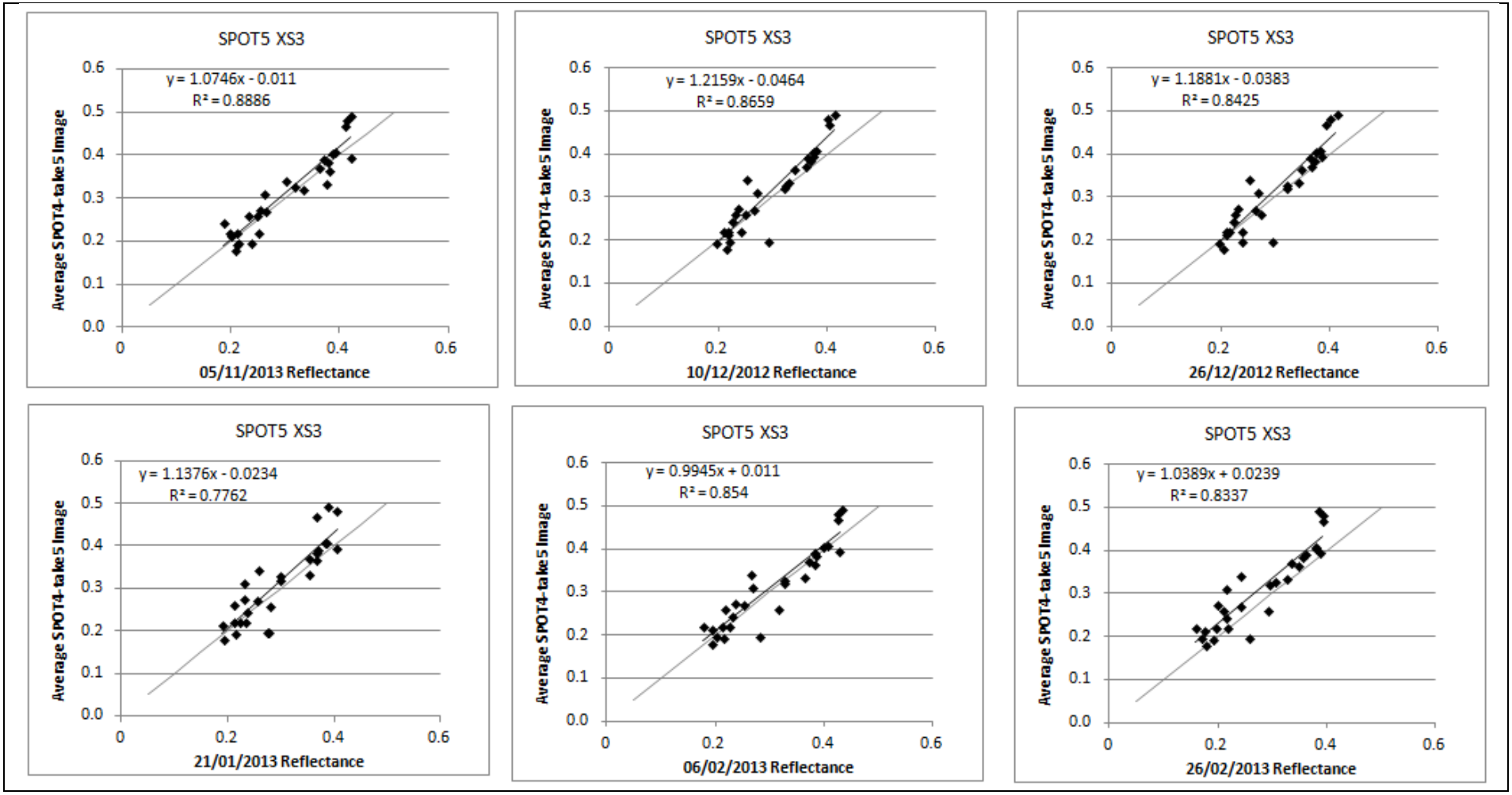
SPOT5 XS3
y = 1.0746x - 0.011
R² = 0.8886
Average SPOT4-take5 Image
05/11/2013 Reflectance
SPOT5 XS3
y = 1.2159x - 0.0464
R² = 0.8659
Average SPOT4-take5 Image
10/12/2012 Reflectance
SPOT5 XS3
y = 1.1881x - 0.0383
R² = 0.8425
Average SPOT4-take5 Image
26/12/2012 Reflectance
SPOT5 XS3
y = 1.1376x - 0.0234
R² = 0.7762
Average SPOT4-take5 Image
21/01/2013 Reflectance
SPOT5 XS3
y = 0.9945x + 0.011
R² = 0.854
Average SPOT4-take5 Image
06/02/2013 Reflectance
SPOT5 XS3
y = 1.0389x + 0.0239
R² = 0.8337
Average SPOT4-take5 Image
26/02/2013 Reflectance

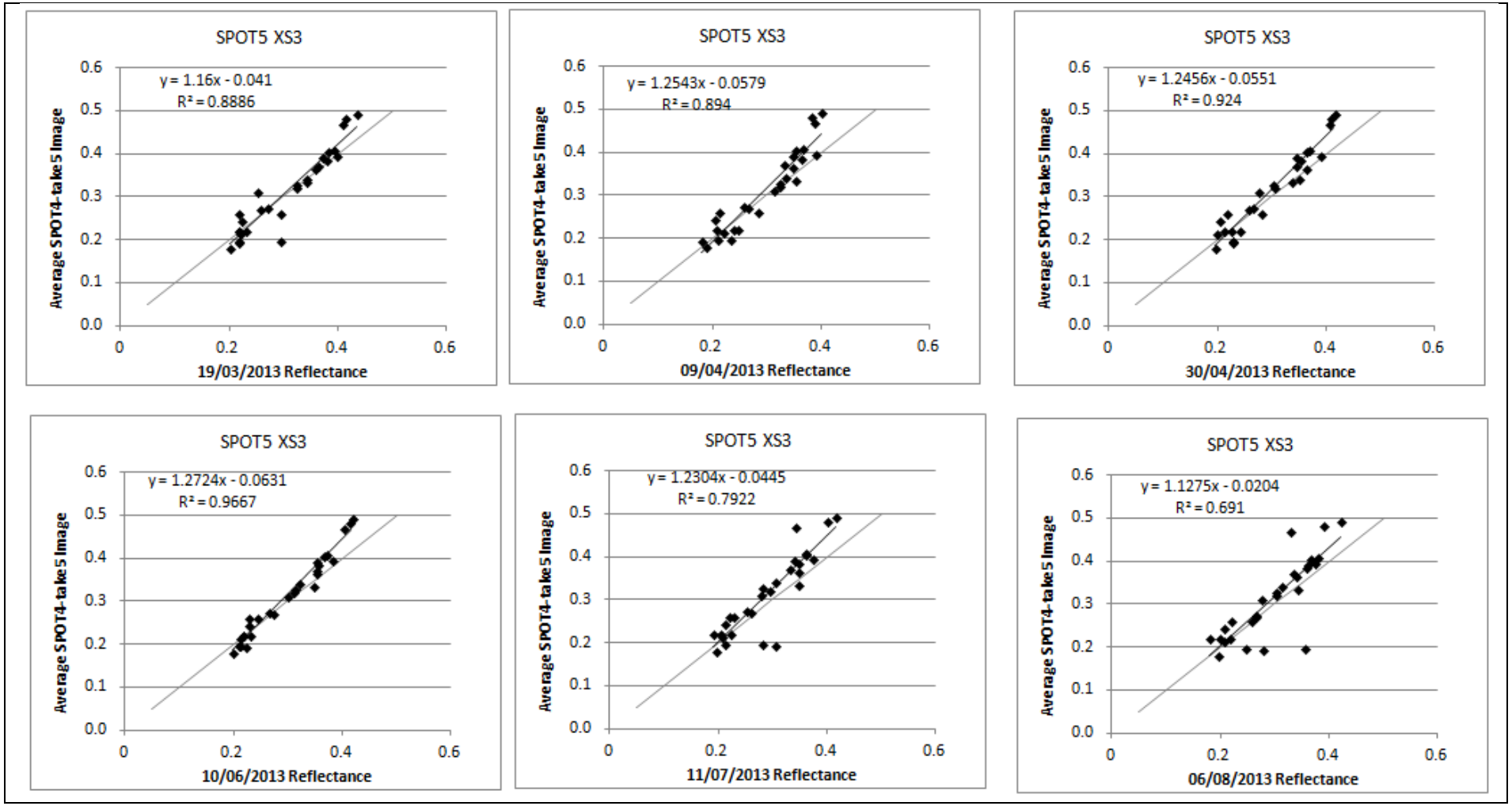
SPOT5 XS3
y = 1.16x - 0.041
R² = 0.8886
Average SPOT4-take5 Image
19/03/2013 Reflectance
SPOT5 XS3
y = 1.2543x - 0.0579
R² = 0.894
Average SPOT4-take5 Image
09/04/2013 Reflectance
SPOT5 XS3
y = 1.2456x - 0.0551
R² = 0.924
Average SPOT4-take5 Image
30/04/2013 Reflectance
SPOT5 XS3
y = 1.2724x - 0.0631
R² = 0.9667
Average SPOT4-take5 Image
10/06/2013 Reflectance
SPOT5 XS3
y = 1.2304x - 0.0445
R² = 0.7922
Average SPOT4-take5 Image
11/07/2013 Reflectance
SPOT5 XS3
y = 1.1275x - 0.0204
R² = 0.691
Average SPOT4-take5 Image
06/08/2013 Reflectance

Annex 4.3: Radiometric corrections of 2013-2014 SPOT5 images time series

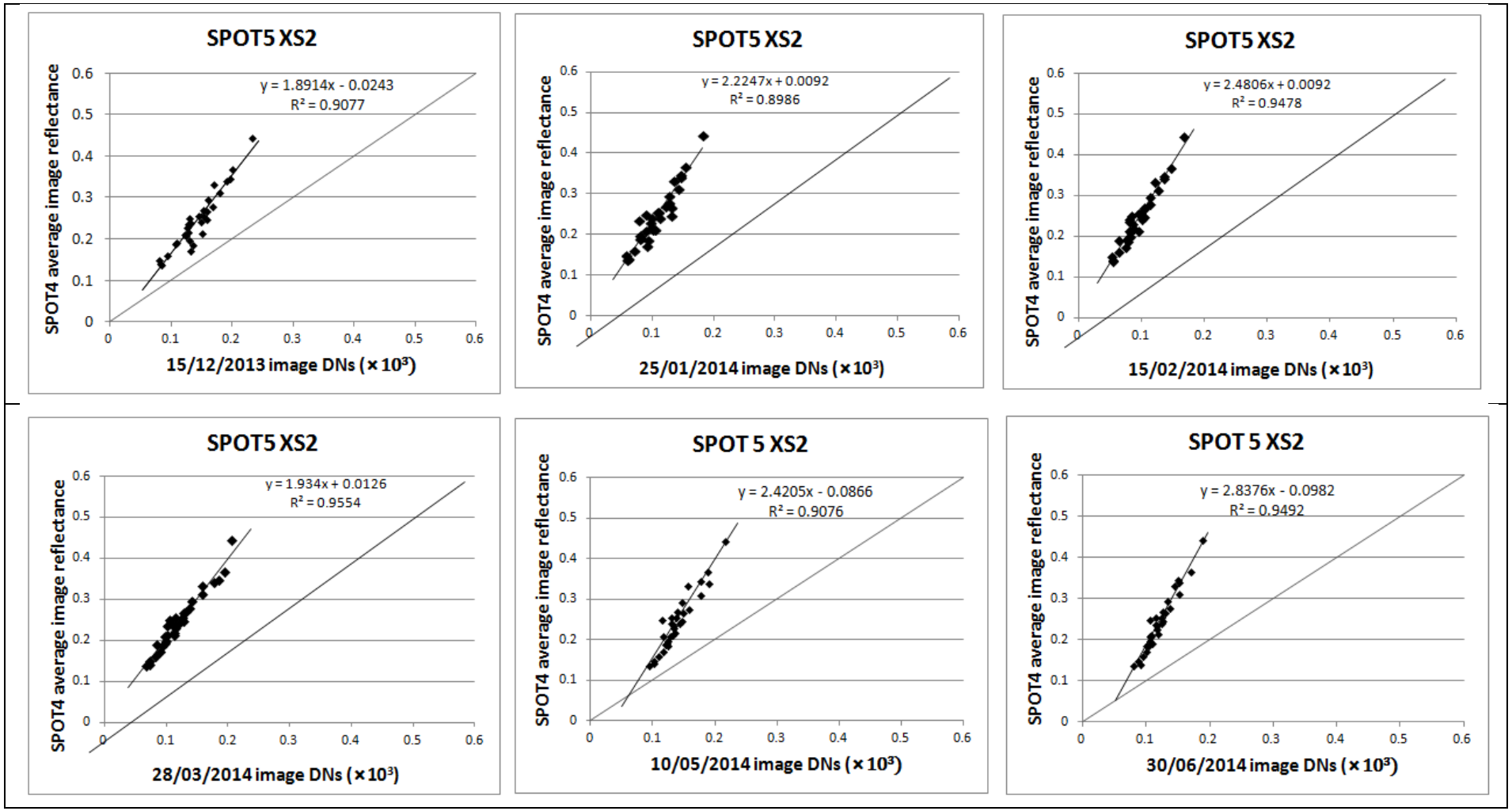

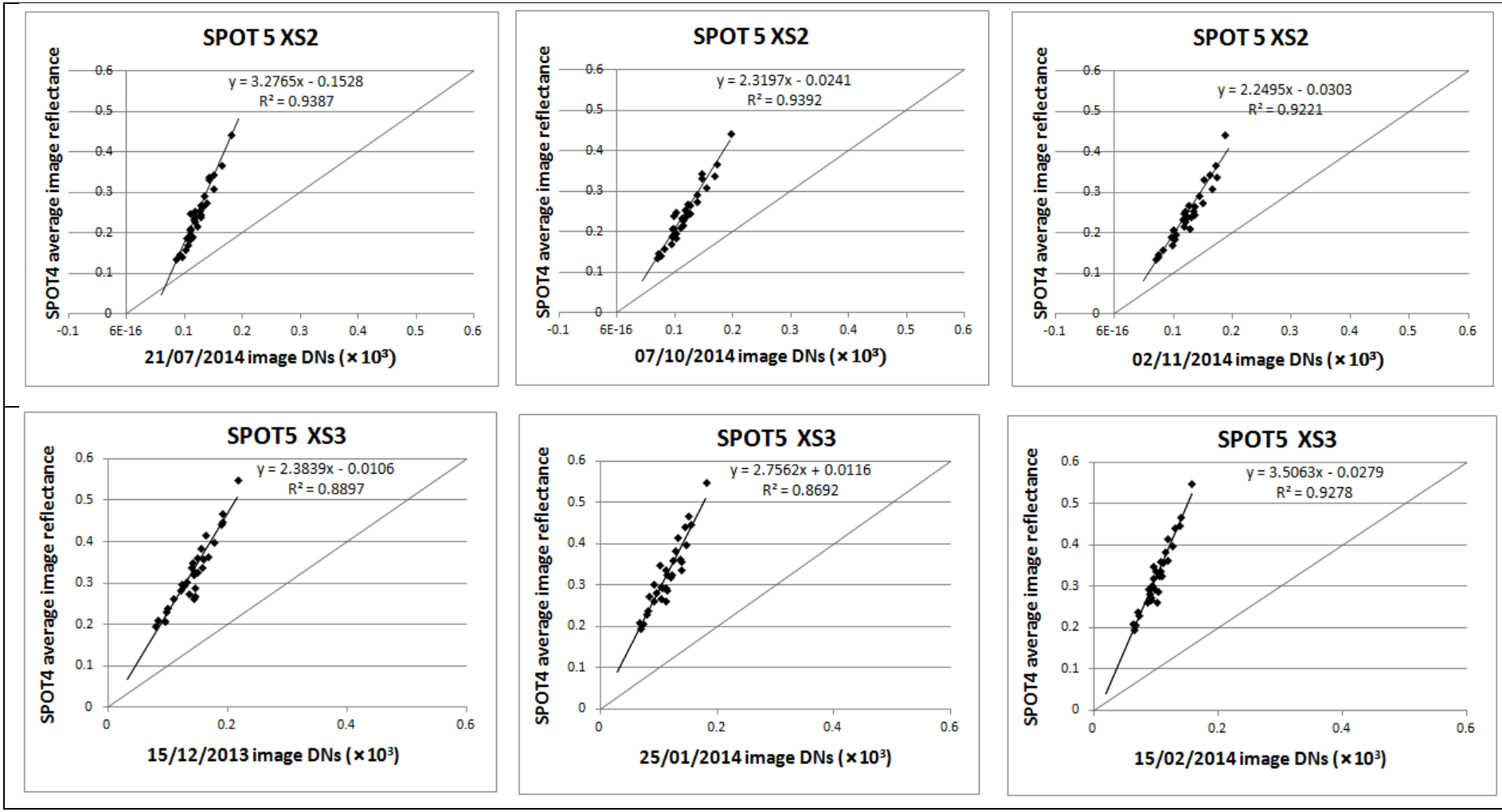
SPOT 5 XS2
y = 3.2765x - 0.1528
R² = 0.9387
SPOT4 average image reflectance
21/07/2014 image DNs (×10³)
SPOT 5 XS2
y = 2.3197x - 0.0241
R² = 0.9392
SPOT4 average image reflectance
07/10/2014 image DNs (×10³)
SPOT 5 XS2
y = 2.2495x - 0.0303
R² = 0.9221
SPOT4 average image reflectance
02/11/2014 image DNs (×10³)
SPOT5 XS3
y = 2.3839x - 0.0106
R² = 0.8897
SPOT4 average image reflectance
15/12/2013 image DNs (×10³)
SPOT5 XS3
y = 2.7562x + 0.0116
R² = 0.8692
SPOT4 average image reflectance
25/01/2014 image DNs (×10³)
SPOT5 XS3
y = 3.5063x - 0.0279
R² = 0.9278
SPOT4 average image reflectance
15/02/2014 image DNs (×10³)

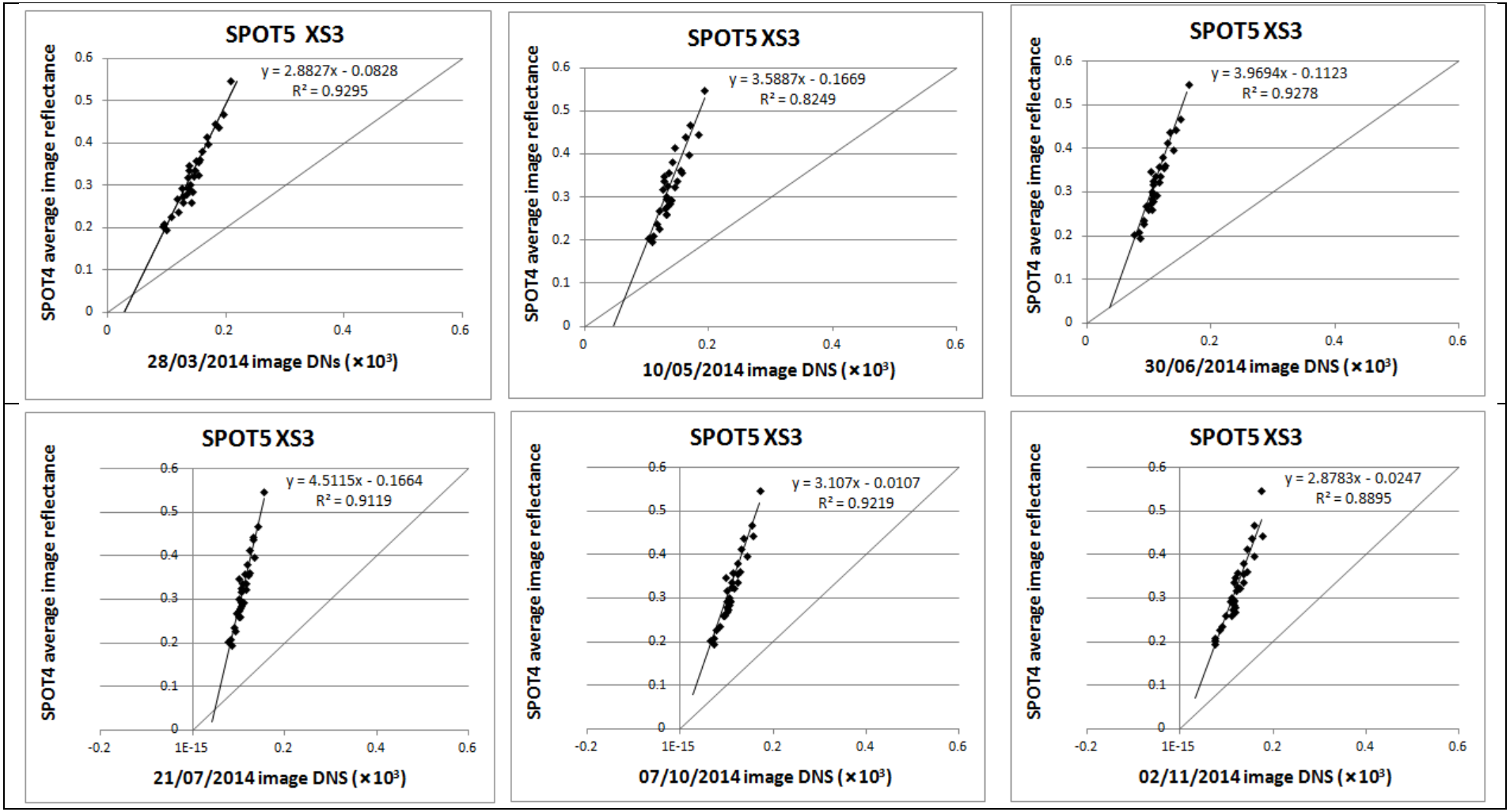
SPOT5 XS3
y = 2.8827x - 0.0828
R² = 0.9295
SPOT4 average image reflectance
28/03/2014 image DNs (×10³)
SPOT5 XS3
y = 3.5887x - 0.1669
R² = 0.8249
SPOT4 average image reflectance
10/05/2014 image DNS (×10³)
SPOT5 XS3
y = 3.9694x - 0.1123
R² = 0.9278
SPOT4 average image reflectance
30/06/2014 image DNS (×10³)
SPOT5 XS3
y = 4.5115x - 0.1664
R² = 0.9119
SPOT4 average image reflectance
21/07/2014 image DNS (×10³)
SPOT5 XS3
y = 3.107x - 0.0107
R² = 0.9219
SPOT4 average image reflectance
07/10/2014 image DNS (×10³)
SPOT5 XS3
y = 2.8783x - 0.0247
R² = 0.8895
SPOT4 average image reflectance
02/11/2014 image DNS (×10³)

Annex 5: Characteristics of the used MODIS data

Products	Spatial resolution/ Temporal resolution	Processing level	Bands	Projection system	Processing Type
MOD11A1 MYD11A1	1 km/Daily	Level 3	31 (1078-1128 nm) 32 (1170-1227 nm)	Sinusoidal	The product is comprised of T_{surf}, quality assessment, observation time, view angles, and emissivities. The Land Surface Temperature (T_{surf}) and emissivity daily data are retrieved at 1km pixels by the generalized split-window algorithm in which emissivities in bands 31 and 32 are estimated from land cover types; atmospheric column water vapor and lower boundary air surface temperature are separated into tractable sub-ranges for optimal retrieval. The surface temperature is computed from the measurements of luminance recovered in the thermal infrared.
MOD13A2 MYD13A2	1 km/16 days	Level 3	1 red (620-670 nm) 2 NIR (841-876 nm) 3 blue (459–479 nm) 7 SWIR (2105-2155 nm)	Sinusoidal	It is the MODIS vegetation index (VI) product. Two VI are derived from atmospherically-corrected reflectance in the red, near-infrared, and blue wavebands; NDVI and EVI (Enhanced Vegetation Index). The two products more effectively characterize the global range of vegetation states and processes. The VI are retrieved from daily, atmosphere-corrected, bidirectional surface reflectance; from the two highest NDVI values it selects the pixel that is closest-to-nadir. Because the MODIS sensors aboard Terra and Aqua satellites are identical, the VI algorithm generates each 16-day composite eight days apart (phased products) to permit a higher temporal resolution product by combining both data records.

MCD43B1 MCD43B2 MCD43B3	1 km/16 days	Level 3	Seven spectral bands spaced throughout the solar shortwave spectrum : 0.4-3.0 μm Three broad band: 0.4-0.7 μm 0.7-3.0 μm 0.4- 3.0 μm	Sinusoidal	These products are part of the MODIS BRDF/ALBEDO product that combines registered, multi date, multiband, atmospherically corrected surface reflectance data from the MODIS and MISR (multi-angle imaging spectroradiometer) instruments to fit a Bidirectional Reactance Distribution Function (BRDF) in seven spectral bands at a 1km spatial resolution on a 16-day cycle. The albedo measures are a directional hemispherical reflectance (black sky albedo) obtained by integrating the BRDF over the existence hemisphere for a single irradiance direction, and a bihemispherical reflectance (white sky albedo) obtained by integrating the BRDF over all viewing and irradiance directions. Both Terra and Aqua data are used in the generation of this product, providing the highest probability for quality input data. The BRDF/Albedo parameters provide: (i) coefficients for mathematical functions that describe the BRDF of each pixel in the seven MODIS 'Land' bands (1- 7); (ii) albedo measurements derived simultaneously from the BRDF for bands 1-7 as well as three broad bands (0.4-0.7, 0.7-3.0, and 0.4- 3.0 micrometers).

Annex 6: Calculation of reference evapotranspiration using FAO Penman-Monteith equation (Allen *et al.*, 1998)

$$ET_o = \frac{0.408\,\Delta(R_n - G) + 0.5\,\gamma\,\frac{37}{T_{0.5h}+273}\,U_2(e^o(T_{0.5h}) - e_a)}{\Delta + \gamma\,(1 + 0.34\,U_2)}$$

Psychometric constant (γ) is calculated by equation:

$\gamma = 0.665 \cdot 10^{-3} \cdot P$ [kPa °C^{-1}]

where: P – atmospheric pressure [kPa]

$$P = 101.3 \cdot \left(\frac{293 - 0.0065 \cdot z}{293}\right)^{5.26}$$

where : Z – altitude above sea level [m]

Slope vapour pressure (Δ) curve is a function of half hourly temperature ($T_{0.5h}$):

$$\Delta = \frac{4098\left[0.6108\,\exp\frac{(17.27 \times T_{0.5h})}{T_{0.5h}+237.3}\right]}{(T+237.3)^2}$$ [kPa °C^{-1}]

Saturation vapour pressure (e_s) half hourly temperature ($T_{0.5h}$) was calculated by equation:

$$e_s = e^0(T_{0.5h}) = 0.6108 \times \exp\left(\frac{17.27 \times T_{0.5h}}{T_{0.5h}+237.3}\right)$$ [kPa]

Actual vapour pressure (e_a) was calculated from half hourly relative humidity $RH_{0.5h}$:

$$e_a = e^0(T_{0.5h})\,\frac{RH_{0.5h}}{100}$$ [kPa]

Net radiation at the crop surface (Rn) is equal to the difference between shortwave and longwaveradiation:

Rn = Rns – Rnl [MJ m^{-2} 0.5h^{-1}]

Net shortwave radiation is calculated from equation:

Rns = (1 – α)Rs [MJ m^{-2} 0.5h^{-1}]

where α represent albedo (0.23)

Net longwave radiation was calculated by equation:

$$R_{nl} = (\boldsymbol{\sigma} T_{0.5h}, K^4) \times (0.34 - 0.14\sqrt{e_a}) \times (1.35\,\frac{R_s}{R_{so}} - 0.35)$$ [MJ m^{-2} 0.5h^{-1}]

where :

$\boldsymbol{\sigma}$ is Stefan-Boltzman constant: $\boldsymbol{\sigma}$= (4.903/24)*0.5 * 10^{-9} [MJ m^{-2} 0.5h^{-1}]

Rso – clear sky solar radiation [MJ m^{-2} 0.5h^{-1}],

Rs – solar radiation [MJ m^{-2} 0.5h^{-1}].

$$Rso = \left(0.75 + 2 \cdot 10^{-5} \cdot z\right) \cdot Ra$$

where: Ra – extraterrestrial radiation [MJ m^{-2} $0.5h^{-1}$].

$$R_a = \frac{12(60)}{\pi} G_{sc} d_r [(\omega_2 - \omega_1)\sin(\varphi)\sin(\delta) + \cos(\varphi)\cos(\delta)(\sin(\omega_1) - \sin(\omega_2))]$$

where : G_{sc} – solar constant, 0.0820 [MJ m^{-2} min^{-1}], φ – latitude [rad], dr – relative distance Earth—Sun [rad], δ – solar declination, ω_1 – solar time angle at beginning of period [rad] and ω_2 – solar time angle at end of period [rad].

$$dr = 1 + 0.033 \cdot \cos\left(\frac{2\pi}{365} \cdot J\right)$$

where: J – the number of the day in the year

$$\delta = 0.409 \cdot \sin\left(\frac{2\pi}{365} \cdot J - 1.39\right)$$

$$\omega_1 = \omega - \frac{\pi t_1}{24} \qquad \text{and } \omega_2 = \omega + \frac{\pi t_1}{24}$$

where ω solar time angle at midpoint of half hourly period [rad], t_1 length of the calculation period [half hour]: *i.e.*, 0.5 for a 30-minute period.

The solar time angle at midpoint of the period is:

$$\omega = \frac{\pi}{12}\left[\left((t - 0.25) + \frac{(L_m - L_z)}{15} + S_c\right) - 12\right]$$

Where t standard clock time at the midpoint of the period [half hour], Lz longitude of the centre of the local time zone [degrees], Lm longitude of the measurement site [degrees] and Sc seasonal correction for solar time [hour].

The seasonal correction for solar time is:

$$S_c = 0.1645\sin(2b) - 0.1255\cos(b) - 0.025\sin(b)$$

$$b = \frac{2\pi(J - 81)}{364}$$

Soil heat flux (G)

Half hourly G can be approximated during daylight periods as:

$$G = 0.1 \times Rn$$

and during nighttime periods as:

$$G = 0.5 \times Rn$$

Wind speed correction

$$u_2 = u_z \cdot \frac{4.87}{\ln(67.8 \cdot z - 5.42)}$$

where: U_z – wind speed measured at Z m above ground.

Annex 7: Comparison between modeled irrigation volumes by SAMIR and observed irrigation at the ownership / block scales for the 2012/2013 season

GDA	ownership / block	Seasonal modeled irrigation SAMIR (mm)	Seasonal observed irrigation (mm)
Karma 1	1	305.3	178.0
	2	110.8	129.6
	3	284.3	175.8
	4	378.3	229.3
	5	155.1	69.0
	6	317.3	248.2
	7	343.8	0.0
	8	36.2	179.9
	10	164.3	0.0
	11	402.4	679.2
	13	44.0	253.1
	14	285.3	0.0
	15	236.9	318.3
	16	358.7	307.9
	17	104.5	86.9
	18	1.3	40.1
	20	179.6	260.9
	21	266.8	84.0
	22	328.6	198.4
	23	267.0	101.7
	24	230.2	183.3
	25	482.0	400.7
	27	23.3	1940.4
	28	394.7	208.4
	33	136.3	18.6
	34	344.6	319.0
	35	238.0	34.4
	36	516.0	567.8
	38	264.1	38.5
	39	286.3	8.7
	40	45.7	31.1
	42	160.0	95.1
	43	43.9	69.7
	48	134.1	39.3
	49	114.1	79.9
	51	127.1	52.6

	53	92.9	49.1
	54	59.2	49.1
	55	420.6	320.8
	56	149.1	106.7
	57	225.1	404.4
	60	72.8	202.9
	61	13.7	81.6
	64	189.4	7.3
	65	0.0	52.1
	66	159.2	34.5
	67	72.6	17.1
	68	154.8	82.5
	69	89.2	46.4
	74	42.4	44.4
	75	133.0	254.6
	76	35.9	23.6
Karma 2	1	510.4	643.0
	2	184.2	121.3
	3	321.9	246.1
	4	105.1	235.9
	5	93.9	247.7
	6	201.7	147.1
	7	271.2	158.3
	8	442.2	119.7
	9	235.5	75.0
	10	5.1	339.4
	11	46.4	579.1
	12	401.8	174.5
	13	339.4	650.7
	15	285.7	151.7
	16	334.8	175.0
	17	300.7	406.8
	18	360.0	274.4
	19	357.2	160.6
	20	427.9	782.7
	21	466.9	493.4
	22	461.5	27.3
	23	237.5	116.1
	24	418.4	510.0
	25	7.4	244.4
	26	388.5	257.9
	27	411.4	283.2

	29	98.9	321.9
	30	284.7	113.9
	31	137.9	27.6
	32	417.0	326.1
	34	63.7	23.6
Mlelsa	1	233.0	201.5
	2	372.4	315.5
	3	296.0	285.3
	5	395.0	166.4
	6	474.6	429.0
	7	272.6	247.5
	9	139.4	176.6
	10	176.9	144.5
	11	246.9	36.4
	12	114.5	60.1
	13	32.7	125.4
	14	328.2	555.6
	15	417.6	294.5
	16	106.3	168.6
	17	82.9	69.2
	19	185.4	147.9
	20	196.8	66.2
	21	148.4	175.7
	22	267.3	47.6
	23	269.7	163.7
	24	223.6	150.7
	25	291.1	91.5
	28	360.2	466.9
	30	127.3	189.7
	32	301.4	156.6
	33	91.2	86.8
	34	80.6	45.6
	35	27.8	82.6
	36	174.3	44.4
	37	137.8	12.5
	38	191.1	36.6
	39	120.4	77.1
	40	244.0	330.0
	43	209.6	208.8
	44	322.8	266.8
	45	305.2	98.2
	46	140.3	31.6

	47	101.3	121.2
	48	270.3	118.9
	49	406.1	479.3
	50	101.0	64.9
	52	190.4	20.2
	53	52.5	60.3
	54	171.1	115.0
	56	427.2	274.9
	57	16.2	147.5
	58	100.9	87.3
	59	245.0	244.0
	60	61.1	108.6
	61	161.1	55.1
	62	173.3	112.8
	63	164.5	86.3
	65	132.3	139.3
	67	70.9	65.6
	69	35.8	109.1
	70	309.9	533.9
	77	45.6	39.1
	79	155.8	64.3
	80	362.1	51.0
	81	68.4	144.3
	83	69.7	174.7
	85	213.5	43.7
	86	120.9	104.0
	87	206.7	42.1
	89	100.0	50.0
	91	172.6	82.5
	92	84.1	131.9
	93	76.8	164.0
	97	104.4	98.9
	98	89.8	41.8
	106	84.1	119.3
Ben Salem 2	Bloc 1	169.80	210.76
	Bloc 2	177.81	183.64
	Bloc 3	134.58	196.50
	Bloc 4	200.72	170.86
	Bloc 5	132.43	170.82
	Bloc 6	108.32	138.32
	Bloc 7	189.01	205.43
	Bloc 8	49.73	113.66

Annex 8: SPARSE forcing terms

$$A_{ss} = (a_{rads} + b_{rads})\,\sigma T_a^4 + c_{rads},$$

$$r_{radss} = -\frac{\rho c_p}{4\sigma T_a^3 a_{rads}},$$

$$r_{radsv} = -\frac{\rho c_p}{b_{rads} 4\sigma T_a^3},$$

$$A_{vv} = (a_{radv} + b_{radv})\,\sigma T_a^4 + c_{radv},$$

$$r_{radvs} = -\frac{\rho c_p}{a_{radv} 4\sigma T_a^3},$$

$$r_{radvv} = -\frac{\rho c_p}{b_{radv} 4\sigma T_a^3} \text{ and}$$

$$A_{atm} = (a_{rads} + b_{rads} + a_{radv} + b_{radv})\,\sigma T_a^4 + c_{ratms} + c_{ratmv},$$

where

$$a_{rads} = -\frac{\varepsilon_s\left[(1 - f_c) + \varepsilon_v f_c\right]}{1 - f_c\,(1 - \varepsilon_s)\,(1 - \varepsilon_v)},$$

$$b_{rads} = a_{radv} = \frac{\varepsilon_v \varepsilon_s f_c}{1 - f_c\,(1 - \varepsilon_s)\,(1 - \varepsilon_v)},$$

$$c_{ratms} = \frac{(1 - f_c)\,\varepsilon_s R_{atm}}{1 - f_c\,(1 - \varepsilon_s)\,(1 - \varepsilon_v)},$$

$$c_{rads} = \frac{R_g\,(1 - \alpha_s)\,(1 - f_c)}{1 - f_c \alpha_s \alpha_v} + c_{ratms},$$

$$b_{radv} = -f_c \varepsilon_v \left[1 + \frac{\varepsilon_s + (1 - f_c)\,(1 - \varepsilon_s)}{1 - f_c\,(1 - \varepsilon_s)\,(1 - \varepsilon_v)}\right],$$

$$c_{ratmv} = f_c \varepsilon_v R_{atm} \left[1 + \frac{(1 - f_c)\,(1 - \varepsilon_s)}{1 - f_c\,(1 - \varepsilon_s)\,(1 - \varepsilon_v)}\right] \text{ and}$$

$$c_{radv} = R_g\,(1 - \alpha_v)\,f_c \left[1 + \frac{\alpha_s\,(1 - f_c)}{1 - f_c \alpha_s \alpha_v}\right] + c_{ratmv}.$$

(α_s and ε_s are the albedo and the emissivity of the soil, α_v and ε_v are the albedo and the emissivity of the canopy, and R_g is the global incoming radiation, $f_c = 1 - e^{-0.5\,\mathrm{LAI}} / \cos\varphi$, where the view zenith angle $\phi = 0°$ for both data sets; $R_{atm} = 1.24\left(e_a / T_a\right)^{1/7} \sigma T_a^4$.)

AUTEUR : Sameh SAADI

TITRE : Estimation spatialisée de l'évapotranspiration réelle et des volumes d'irrigation à l'aide de modèles de bilans hydrique et énergétique forcés par des données de la télédétection optique (VIS/PIR/IRT)

RÉSUMÉ : La gestion efficace de l'eau dans les régions arides et semi-arides est un problème majeur, principalement dans les zones irriguées. La conception d'outils fournissant des estimations régionales des composantes du bilan hydrique peut aider à la gestion durable de la ressource en eau dans ces régions. La télédétection multi-capteurs a démontré un très fort potentiel pour le suivi des ressources hydriques agricoles à différentes échelles.

Cette thèse vise à développer des techniques et des méthodes efficaces pour estimer les variables hydrologiques (évapotranspiration et les volumes d'irrigation) afin d'évaluer, dans l'espace (résolutions "métrique" et "kilométrique"), les besoins en eau des cultures du couvert végétal de la plaine de Kairouan (Tunisie centrale) ainsi que les volumes d'irrigation extraits de son aquifère surexploité. L'approche adoptée combine l'expérimentation, la modélisation et l'utilisation de données de télédétection multi-capteurs / multi-résolutions. Les deux types d'outils utilisés sont le modèle de bilan hydrique SAMIR et le modèle de bilan d'énergie SPARSE. Les variables estimées par SAMIR et SPARSE sont évaluées à l'aide des mesures terrain (mesures d'un scintillomètre XLAS) et des enquêtes de terrain (volumes d'irrigation observés).

Les volumes d'irrigation saisonniers estimés par SAMIR sont acceptables, même si les résultats à des échelles de temps plus fines (mensuelles) doivent être améliorés. Ainsi, les paramètres de SAMIR, en particulier les paramètres non calibrés, sont revisités afin d'améliorer les performances de simulation de l'ET et des volumes d'irrigation. Les estimations des flux de chaleur sensible et latente par SPARSE sont en étroit accord avec celles obtenues à partir du XLAS. Cependant, l'extrapolation de l'évapotranspiration instantanée au pas de temps journalier est moins évidente.

MOTS CLÉS : Evapotranspiration, gestion de l'irrigation, télédétection, modélisation hydrologique, modèle de bilan hydrique, modèle de bilan d'énergie.

TITLE: Spatial estimation of actual evapotranspiration and irrigation volumes using water and energy balance models forced by optical remote sensing data (VIS / NIR / TIR)

ABSTRACT: In arid and semi-arid regions, efficient agricultural water management is a major issue, mainly in irrigated areas. The design of tools that provide an estimate of water balance components at the regional scale may help sustainable management of limited water resources in the water scarce regions. Remotely sensed Earth observation has become a major research field for agricultural water resources management.

The main objective of this thesis is to develop and test efficient techniques and methods to estimate hydrological variables (Evapotranspiration (ET) and irrigation volumes) in order to assess, at "metric" and "kilometric" resolution , the crop water requirements and the extracted irrigation volumes in the Kairouan plain (central Tunisia). The adopted approach combines field experimentation, modeling and the use of multi-sensor / multi-resolution remote sensing data. Two modeling tools are used: the soil water balance model SAMIR and the energy balance model, SPARSE. SAMIR and SPARSE estimates are assessed using field measurements (Scintillometer XLAS measurements) and field surveys (observed irrigation volumes).

The seasonal irrigation volumes estimated by the SAMIR model are acceptable, even though results at finer timescales (monthly and below) needed to be improved. Hence, the SAMIR model parameters, especially the uncalibrated ones are revisited in order to improve the results. SPARSE estimates of sensible and latent heat fluxes are in close agreement with those obtained from the XLAS. However, the extrapolation from instantaneous to daily ET is less obvious.

KEY WORDS: Evapotranspiration, irrigation management, remote sensing, hydrological modeling, water balance model, energy balance model.

DIRECTEUR DE THÈSE : Gilles BOULET

LIEU ET DATE DE SOUTENANCE : CESBIO, 16 février 2018

DISCIPLINE ADMINISTRATIVE : ED SDU2E : Surfaces et interfaces continentales, hydrologie

INTITULÉ ET ADRESSE DE L'U.F.R. OU DU LABORATOIRE : Centre d'Études Spatiales de la BIOsphère- CESBIO (UMR 5126), 18 avenue Édouard Belin, bpi 2801, 31401 Toulouse cedex 9